SOFT ROBOTICS BASED ON ELECTROACTIVE POLYMERS

EDITED BY: Guoying Gu, Herbert Shea, Stefan Seelecke, Gursel Alici and Gianluca Rizzello

PUBLISHED IN: Frontiers In Robotics And Ai

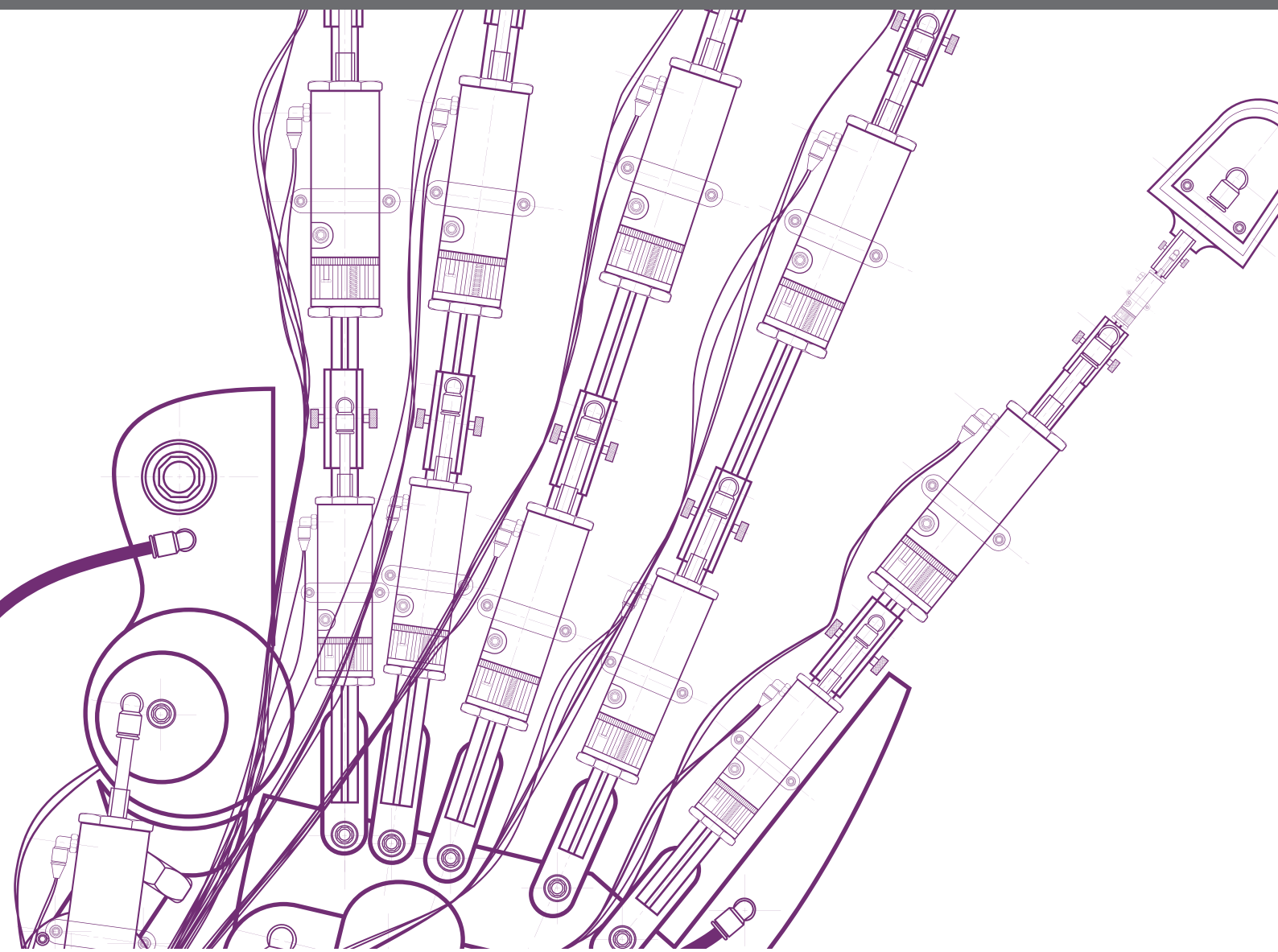

frontiers Research Topics

frontiers

ISSN 1664-8714
ISBN 978-2-88966-935-6
DOI 10.3389/978-2-88966-935-6

About Frontiers

Frontiers is more than just an open-access publisher of scholarly articles: it is a pioneering approach to the world of academia, radically improving the way scholarly research is managed. The grand vision of Frontiers is a world where all people have an equal opportunity to seek, share and generate knowledge. Frontiers provides immediate and permanent online open access to all its publications, but this alone is not enough to realize our grand goals.

Frontiers Journal Series

The Frontiers Journal Series is a multi-tier and interdisciplinary set of open-access, online journals, promising a paradigm shift from the current review, selection and dissemination processes in academic publishing. All Frontiers journals are driven by researchers for researchers; therefore, they constitute a service to the scholarly community. At the same time, the Frontiers Journal Series operates on a revolutionary invention, the tiered publishing system, initially addressing specific communities of scholars, and gradually climbing up to broader public understanding, thus serving the interests of the lay society, too.

Dedication to Quality

Each Frontiers article is a landmark of the highest quality, thanks to genuinely collaborative interactions between authors and review editors, who include some of the world's best academicians. Research must be certified by peers before entering a stream of knowledge that may eventually reach the public - and shape society; therefore, Frontiers only applies the most rigorous and unbiased reviews.
Frontiers revolutionizes research publishing by freely delivering the most outstanding research, evaluated with no bias from both the academic and social point of view. By applying the most advanced information technologies, Frontiers is catapulting scholarly publishing into a new generation.

What are Frontiers Research Topics?

Frontiers Research Topics are very popular trademarks of the Frontiers Journals Series: they are collections of at least ten articles, all centered on a particular subject. With their unique mix of varied contributions from Original Research to Review Articles, Frontiers Research Topics unify the most influential researchers, the latest key findings and historical advances in a hot research area! Find out more on how to host your own Frontiers Research Topic or contribute to one as an author by contacting the Frontiers Editorial Office: frontiersin.org/about/contact

SOFT ROBOTICS BASED ON ELECTROACTIVE POLYMERS

Topic Editors:
Guoying Gu, Shanghai Jiao Tong University, China
Herbert Shea, École Polytechnique Fédérale de Lausanne, Switzerland
Stefan Seelecke, Saarland University, Germany
Gursel Alici, University of Wollongong, Australia
Gianluca Rizzello, Saarland University, Germany

Citation: Gu, G., Shea, H., Seelecke, S., Alici, G., Rizzello, G., eds. (2021). Soft Robotics based on Electroactive Polymers. Lausanne: Frontiers Media SA. doi: 10.3389/978-2-88966-935-6

Table of Contents

frontiers in Robotics and AI

EDITORIAL
published: 30 April 2021
doi: 10.3389/frobt.2021.676406

Editorial: Soft Robotics Based on Electroactive Polymers

Guoying Gu[1,2]*, *Herbert Shea*[3], *Stefan Seelecke*[4], *Gursel Alici*[5,6] *and Gianluca Rizzello*[4]

[1]Robotics Institute, School of Mechanical Engineering, Shanghai Jiao Tong University, Shanghai, China, [2]State Key Laboratory of Mechanical System and Vibration, Shanghai Jiao Tong University, Shanghai, China, [3]Soft Transducers Laboratory (LMTS), School of Engineering, École Polytechnique Fédérale de Lausanne (EPFL), Neuchâtel, Switzerland, [4]Department of Systems Engineering, Department of Materials Science and Engineering, Saarland University, Saarbrucken, Germany, [5]School of Mechanical, Materials, Mechatronic and Biomedical Engineering, University of Wollongong, Wollongong, NSW, Australia, [6]Applied Mechatronics and Biomedical Engineering Research (AMBER) Group, University of Wollongong, Wollongong, NSW, Australia

Keywords: electroactive polymers, soft robots, soft actuators, soft sensors, dielectric elastomer actuator

Editorial on the Research Topic

Soft Robotics Based on Electroactive Polymers

Conventional robots using rigid structural elements and high-output actuators have enabled great progress in automated assembly and manufacturing (Nof, 1999; Yang et al., 2018). An increasing number of robots need to interact safely with humans, manipulate soft and delicate objects or need to move in difficult environments. Soft robotics is a rapidly growing field as compliant robots are capable of sustaining large deformation while maintaining structural compliance, allowing safe operation with people and adaptation to many situations (Rus and Tolley, 2015).

Most soft robots rely on pneumatic actuation which requires a compressor or pump (Shintake et al., 2018). Electroactive polymers (EAPs) are smart soft materials capable of changing sizes and/or shapes in direct response to electrical stimuli (Bar-Cohen, 2002; Gu et al., 2017). They allow combining actuator, sensor and structure in one single topology. For these reasons, soft robotic systems with EAPs (ionic EAPs and Dielectric Elastomer Actuators) have gained great attention.

The goal of this research topic is to provide an overview of the state of the art in design, fabrication, modeling, control and applications of soft robotic systems based on both EAPs. After the peer review process, this topic accepted 13 articles, including 11 research articles and 2 review articles.

There are four articles focusing on the actuator, sensor and structure design. Cacucciolo and co-authors (Cacucciolo et al) describe a new class of electrically driven soft fluidic muscles combining thin McKibben actuators with stretchable pumps based on ElectroHydroDynamics, to directly pump liquid molecules by means of an electric field. This architecture does not require an external pump or compressor, easing integration in textile and wearables. Hashimoto et al. present a novel 3D self-folding structure by combining a rigid frame with a stretchable dielectric elastomer actuator. The novel design has a simple structure, allowing for high-speed and high-precision operations. The proposed design is employed to develop a three-joint gripper which can grasp an object with length of 36.7 mm and weight of 3.28 g. Must et al. explore the use of soft and compliant actuator material based on ionic and capacitive laminate (ICL) for potential use in miniaturized manipulators. Three techniques are demonstrated, rendering a bulk of ICL into a practical manipulator, which is highly compatible with electron optics. After presenting experimental characterization results, the ability of the ICL manipulator in handling a single cell is experimentally demonstrated. Shintake et al. report soft stretchable capacitive strain sensors whose gauge factor is doubled from 0.8 to over 1.6 by using auxetic structures. The sensors consist of liquid metal electrodes separated by an elastomer film, on which silicone auxetic structures exhibiting negative Poisson ratio have been bonded. The authors measure the change in capacitance as the sensor are stretched, measuring capacitance vs. strain. The sensors are robust, with no change in sensitivity after 11,000 cycles under 50% strain.

There are four articles focusing on the robot design and application. Franke et al. present a dielectric elastomer actuator (DEA) driven soft robot consisting of two DEA artificial muscles on the top and

OPEN ACCESS

Edited by:
Cecilia Laschi,
National University of Singapore, Singapore

Reviewed by:
Federico Carpi,
University of Florence, Italy

***Correspondence:**
Guoying Gu
guguoying@sjtu.edu.cn

Specialty section:
This article was submitted to Soft Robotics, a section of the journal Frontiers in Robotics and AI

Received: *05 March 2021*
Accepted: *16 April 2021*
Published: *30 April 2021*

Citation:
Gu G, Shea H, Seelecke S, Alici G and Rizzello G (2021) Editorial: Soft Robotics Based on Electroactive Polymers. Front. Robot. AI 8:676406. doi: 10.3389/frobt.2021.676406

bottom of a soft silicone body. This design prevents the undesired bending when a pre-stretched DEA membrane is applied on the soft robotic structures using a bioinspired stiff skeleton. The robotic structure shows a large and defined bimorph bending curvature under both static and dynamic actuations. An analytical model is developed to study the effects of applied voltage, material stiffness and pre-stretch ratio. A prototype fabricated after the optimal design shows that fast and large dynamic displacements of about 47 mm can be accomplished, while blocking force can be optimized from 1 to 4 mN. Pfeil et al. present a bioinspired worm-like crawling soft robot based on dielectric elastomer actuators, which are cylindrical actuator segments used to set the structure in motion. Textile materials consisting of parallel oriented carbon fibers are used to enhance the stiffness in the supporting areas of the robot. Christianson et al. demonstrate the swimming performance of an untethered jellyfish-inspired robot, propelled by dielectric elastomer actuators. An axisymmetric array of unimorph actuators based on non-prestretched DEAs are used to provide upwards propulsion. After experimentally characterizing and modeling the actuators, they have designed a waterproof power supply to drive the soft actuators based on DEAs. The robot swims at an average speed of 3.2 mm/s. Olsen and Kim present a design method for a small aquatic robot's swimming mechanism based on the jet propulsion mechanism found in jellyfish. Two modeling approaches are proposed: 1) a geometric model to gain qualitative information about the feasibility for the robot design, and 2) a refined mechanics model based on a linear beam theory and an equivalent circuit model. Both models can be used to improve the performance of the P1 swimming mode as compared to that of a typical jellyfish.

There are three articles focusing on the modeling and control. Nalbach et al. report on modeling and design optimization of multi-degrees of freedom (MDOF) dielectric elastomer actuator (DEA) for soft robotic applications. The actuator consists of a pair of cone DEA membranes whose electrodes are partitioned in four sections to be activated separately in order to generate the desired MDOF actuation feature. After experimental characterization, a mathematical model is developed to design optimize a prototype capable of performing bending angles of about 9.6 degrees. Chi et al. develop an iterative learning control method to track the motion trajectory of a circular soft crawling robot, which uses DEA as the robot body and four electro-adhesion actuators as feet. They use a knowledge-based modeling framework to establish the physical model of the DEA, and employ ILC for motion trajectory tracking control. Simulations and experimental results are presented to demonstrate the effectiveness of the developed soft robot and the control scheme. Hoffstadt and Mass report on closed-loop control of DE stack-actuators using a new self-sensing scheme that does not require a superimposed excitation signal. The self-sensing system is experimentally validated, showing performance at up to 400 Hz equivalent to what can be obtained using external sensors. The control of voltage, DEA force or DEA displacement can be achieved by using different feed-forward control structures.

There are two review articles. Hao et al. reviews the current trends, challenges and potential solutions of IPMC as soft actuators and sensors. This review investigates the key factors influencing the actuating performance of IPMC, and potential of IPMCs as soft sensors. Hu et al. provide a review of state-of-the-art PEDOT-based conducting polymer actuators. This review also provides a comprehensive understanding of the actuation mechanism, performance evaluation criteria, fabrication technologies, and possible applications of PEDOT-based actuators. It discusses two actuation mechanisms and three actuation configurations. Evaluation criteria for actuator performances and material properties are surveyed, and the effect of electrode and electrolyte materials are summarized. After presenting their applications in the bionics and biomedicine area, textiles and wearable devices and micro applications, four future research opportunities to improve and widen the applications of PEDOT-based actuators are discussed.

We hope that the articles presented in this research topic can provide in-depth insights and understandings in the field of soft robotics involving with the electroactive polymers and inspire new design of bio-inspired and robust soft robots for comprehensive applications.

AUTHOR CONTRIBUTIONS

All authors listed have made a substantial, direct, and intellectual contribution to the work and approved it for publication.

REFERENCES

Bar-Cohen, Y. (2002). Electroactive Polymers as Artificial Muscles: A Review. *J. Spacecraft Rockets.* 39 (6), 822–827. doi:10.2514/2.3902

Gu, G., Zhu, J., Zhu, L., and Zhu, X. (2017). A Survey on Dielectric Elastomer Actuators for Soft Robots. *Bioinspiration & Biomimetics.* 12 (1), 011003. doi:10.1088/1748-3190/12/1/011003

Nof, S. Y. (1999). *Handbook of Industrial Robotics.* John Wiley & Sons.

Rus, D., and Tolley, M. T. (2015). Design, Fabrication and Control of Soft Robots. *Nature* 521 (7553), 467–475. doi:10.1038/nature14543

Shintake, J., Cacucciolo, V., Floreano, D., and Shea, H. (2018). Soft Robotic Grippers. *Adv. Mater.* 30 (29), 1707035. doi:10.1002/adma.201707035

Yang, G.-Z., Bellingham, J., Dupont, P. E., Fischer, P., Floridi, L., Full, R., et al. (2018). The Grand Challenges of Science Robotics. *Sci. Robot.* 3 (14), eaar7650. doi:10.1126/scirobotics.aar7650

Conflict of Interest: The authors declare that the research was conducted in the absence of any commercial or financial relationships that could be construed as a potential conflict of interest.

frontiers in Robotics and AI

ORIGINAL RESEARCH
published: 01 November 2019
doi: 10.3389/frobt.2019.00112

Design and Modeling of a New Biomimetic Soft Robotic Jellyfish Using IPMC-Based Electroactive Polymers

*Zakai J. Olsen and Kwang J. Kim**

Active Materials and Smart Living (AMSL) Lab, Department of Mechanical Engineering, University of Nevada Las Vegas, Las Vegas, NV, United States

Smart materials and soft robotics have been seen to be particularly well-suited for developing biomimetic devices and are active fields of research. In this study, the design and modeling of a new biomimetic soft robot is described. Initial work was made in the modeling of a biomimetic robot based on the locomotion and kinematics of jellyfish. Modifications were made to the governing equations for jellyfish locomotion that accounted for geometric differences between biology and the robotic design. In particular, the capability of the model to account for the mass and geometry of the robot design has been added for better flexibility in the model setup. A simple geometrically defined model is developed and used to show the feasibility of a proposed biomimetic robot under a prescribed geometric deformation to the robot structure. A more robust mechanics model is then developed which uses linear beam theory is coupled to an equivalent circuit model to simulate actuation of the robot with ionic polymer-metal composite (IPMC) actuators. The mechanics model of the soft robot is compared to that of the geometric model as well as biological jellyfish swimming to highlight its improved efficiency. The design models are characterized against a biological jellyfish model in terms of propulsive efficiency. Using the mechanics model, the locomotive energetics as modeled in literature on biological jellyfish are explored. Locomotive efficiency and cost as a function of swimming cycles are examined for various swimming modes developed, followed by an analysis of the initial transient and steady-state swimming velocities. Applications for fluid pumping or thrust vectoring utilizing the same basic robot design are also proposed. The new design shows a clear advantage over its purely biological counterpart for a soft-robot, with the newly proposed biomimetic swimming mode offering enhanced swimming efficiency and steady-state velocities for a given size and volume exchange.

Keywords: modeling, soft-robotics, biomimetics, ionic polymer-metal composites, electroactive polymers

OPEN ACCESS

Edited by:
Guoying Gu,
Shanghai Jiao Tong University, China

Reviewed by:
Yanjie Wang,
Hohai University, China
Zicai Zhu,
Xi'an Jiaotong University, China

****Correspondence:***
Kwang J. Kim
kwang.kim@unlv.edu

Specialty section:
This article was submitted to Soft Robotics, a section of the journal Frontiers in Robotics and AI

Received: *19 July 2019*
Accepted: *15 October 2019*
Published: *01 November 2019*

Citation:
Olsen ZJ and Kim KJ (2019) Design and Modeling of a New Biomimetic Soft Robotic Jellyfish Using IPMC-Based Electroactive Polymers. Front. Robot. AI 6:112. doi: 10.3389/frobt.2019.00112

INTRODUCTION

Electroactive polymers (EAPs) have emerged and grown into a vast and diverse field of research, with numerous potential applications in soft robotics and smart materials. EAPs are a class of polymeric materials that respond to an external electrical stimulus, this includes size and shape changes which may be used in actuation (O'Halloran et al., 2008). The wide range of EAP materials

may be divided into two categories, electronic EAPs, including ferroelectric polymers, dielectric elastomers, electro-strictive graft elastomers, and liquid crystal elastomers, and ionic EAPs, which include ionic polymer gels, ionic polymer-metal composites, conducting polymers, and others (Bar-Cohen, 2002; O'Halloran et al., 2008). In the model developed within this paper we will focus on the ionic polymer-metal composite (IPMC), though other actuator types may be just as easily used.

An IPMC consists of an ionic polymer, typically Nafion® or Aquivion® (Shahinpoor and Kim, 2001; Trabia et al., 2017), that is composited between two electrodes, most commonly platinum or gold. The IPMC material the capability of both electromechanical transduction, where they can act as actuators (Bonomo et al., 2007; Kim, 2007; Trabia et al., 2017), as well as mechanoelectrical transduction, where they work as sensors (Bonomo et al., 2006; Chen et al., 2007; Porfiri, 2009; Akle and Habchi, 2013). This duality lies in the fundamentals of the electrochemical nature that governs both transduction modes, and is explored throughout literature (Schicker and Wallmersperger, 2013; Cha and Porfiri, 2014; Shen et al., 2015a; Shahinpoor, 2015). As actuators, IPMCs have are capable of exhibiting large mechanical deformations in response to a relatively low voltage (Shahinpoor and Kim, 2001; Bar-Cohen, 2002; Wallmersperger et al., 2007; Jo et al., 2013; Shahinpoor, 2015), making them attractive for compact, low power soft robotics. Furthermore, their ability to actuate in water (Kim et al., 2007; Yim et al., 2007; Brunetto et al., 2008; Abdelnour et al., 2009) has focused the soft robotics development heavily on aquatic animals. The biomimetic applications of IPMCs range from small scale biological structures such as cilia (Sareh et al., 2012) all the way up to full size robots (Shen et al., 2015b).

The jellyfish has been the focus of many researchers in the biology and engineering field, with varying interests in its swimming mechanism. Here, a model for the swimming behavior of jellyfish is used to develop a new biomimetic soft robot design that builds on the basic mechanisms used in biology for locomotion and address any observed limitations. Biological jellyfish swim using one of two methods, rowing or jetting (Michael et al., 2013; Gemmell et al., 2015). The jet propulsion mechanism for locomotion consists of two distinct phases, the contraction and relaxation phase. During contraction, the jellyfish expels water out of an enclosed volume to generate thrust. To refill the fluid volume, the contraction phase is followed by a slower relaxation phase in which the internal volume takes in water through the velar aperture. During this process, a negative acceleration is experienced that slows the animal down. This will be the primary area of focus for developing a modified swimming mechanism for potential soft robotics.

Two approaches are presented and compared. First, a model that is rooted in a geometric description of a material body is used to gain qualitative information about the feasibility of a proposed robot design. After that, a refined mechanics model is proposed and developed. As will be shown throughout the paper, both the design of the biomimetic jellyfish robot as well as the approach taken for the modeling framework differ from what is found in literature. The design of the robot diverges from the traditional biomimetic robots in that the goal is not to take inspiration from the biological world and attempt to recreate a robot that might move or look in a similar fashion. Instead, inspiration from nature is used as a reference point, from which a new concept for locomotion is developed that only loosely mimics the principles found in biology.

METHODS

Biological Inspiration

Kinematics of Swimming Jellyfish

The jet propulsion mechanism used by jellyfish follows a simple equation of motion (EoM) that can be used to simulate the swimming behavior of these animals (Daniel, 1983). This equation also provides a starting point for modeling jellyfish-like robotics and their bioinspired swimming mechanisms. The swimming mechanism is broken down into four components: thrust, drag, inertia, and acceleration reaction. After a brief derivation found in Daniel (1983), the following EoM is obtained.

$$(1+\alpha_{AM})\,\rho_w V_f \frac{du}{dt} = \frac{\rho_w}{A_V}\left(\frac{dV_f}{dt}\right)^2 - \frac{1}{2}C_d\rho_w S_A u^2 \tag{1}$$

wherein α_{AM}, ρ_w, V_f, u, t, A_V, C_d, and S_A are the added mass coefficient, fluid density, volume of fluid within the jellyfish body, linear velocity, time, velar aperture, drag coefficient, and cross-sectional area with respect to the direction of travel. The details of these parameters are given in Daniel (1983), and an illustration of the structure of a jellyfish is provided (**Figure 1**). Note that the direction of flow for the thrusting force is not reflected in this equation obtained from literature, but during implementation the thrust must be made positive during the contraction phase and negative during the relaxation phase due to the nature by which jellyfish perform their jet propulsion mechanism.

We take a brief moment to analyze this equation further. In the presented form, this equation is a result of applying Newton's second law, where we have taken the sum of the forces acting on the jellyfish, i.e., thrust, drag, and acceleration reaction, and related it to the acceleration, i.e., inertia, of the jellyfish. Here, only linear motion in one dimension is considered and the added mass is taken to be a scalar, greatly simplifying the problem. Nevertheless, we are still left with a non-linear equation due to the drag force being quadratic in the swimming velocity, in addition to the drag coefficient typically being a function of the flow conditions, and hence the swimming velocity. Furthermore, the volume and its rate of change, as well as the velar aperture and cross-sectional area, are dependent on the deformation of the jellyfish body and hence nearly all of the terms in Equation (1) are time dependent. Potential areas for simplification are cases in which the added mass is negligible or where its time variations may be ignored, as well as cases where the drag coefficient can be taken as constant or possibly as a small parameter suitable for perturbation techniques. In this paper, a few simplifying assumptions will be made regarding these parameters and will be discussed in detail as they arise.

As modeled in Daniel (1985), the volume rate of change is taken to be constant over both the contraction and relaxation

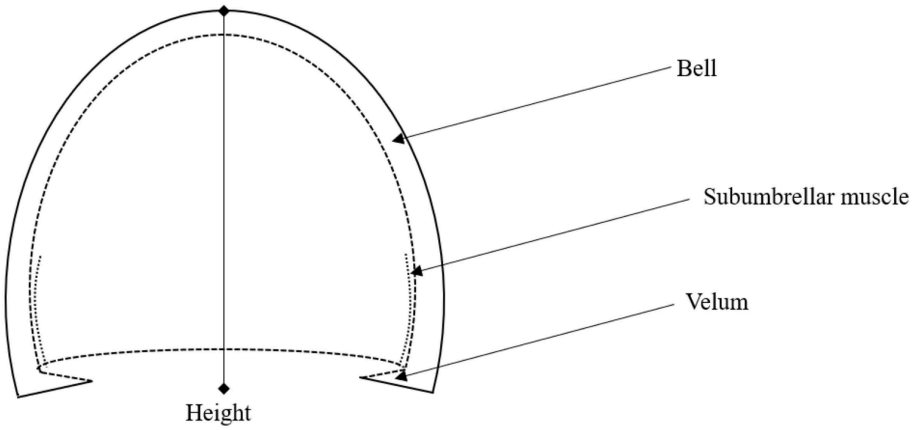

FIGURE 1 | Illustration of jellyfish body structure, highlighting the bell, Subumbrellar muscle, velum, and height. The hemiellipsoid structure of the jellyfish body can be defined through the bell height and the velar aperture radius.

phases. This can be achieved by defining a volume percentage change that should occur over these intervals, denoted ΔV, and calculating the rate of change over each phase as

$$\frac{dV_f}{dt} = \begin{cases} -\frac{\Delta V}{t_c} & \textit{contraction} \\ \frac{\Delta V}{t_r} & \textit{relaxation} \end{cases} \tag{2}$$

in which t_c and t_r are the durations of the contraction and relaxation phases, respectively. During contraction, the internal volume of fluid is ejected at rate given above and by performing this contraction over the duration t_c, the volume changes by exactly $-\Delta V$. Now by relaxing the bell, the internal volume of fluid may be filled at the relaxation rate, and by relaxing over a time t_r the bell volume increases by exactly ΔV, hence at the end of each swimming cycle the internal fluid volume returns to its initial value. This can be conveniently expressed using a variable amplitude square wave Fourier series of the form

$$\begin{aligned} F(t) \;=\; & \frac{At_c + Bt_r}{t_c + t_r} \\ & + \sum_{n=1}^{\infty} \frac{A-B}{n\pi} \left[\sin\left(\frac{2n\pi}{t_c+t_r} t_c\right) \cos\left(\frac{2n\pi}{t_c+t_r} t\right) \right. \\ & \left. + \left(1 - \cos\left(\frac{2n\pi}{t_c+t_r} t_c\right)\right) \sin\left(\frac{2n\pi}{t_c+t_r} t\right) \right] \end{aligned} \tag{3}$$

wherein A and B are the contraction and relaxation phase amplitudes, respectively. This type of input form will be used later when constructing two new models of soft-robotic systems, where it is of interest to see how the swimming behavior changes when this same input waveform is used for the volume rate of change, geometric parameters defining the bell, and electrical inputs to an IPMC model. **Figure 2** illustrates how the waveform is structured, where during the contraction phase a larger volume rate of change occurs over a shorter period when compared to the relaxation phase. Using the Fourier series to describe the phenomena in Equation (2), the volume rate of change is expressed as

$$\begin{aligned} \frac{dV_f}{dt} \;=\; & \sum_{n=1}^{\infty} (-\Delta V) \frac{t_c + t_r}{n\pi t_c t_r} \left[\sin\left(\frac{2n\pi}{t_c+t_r} t_c\right) \cos\left(\frac{2n\pi}{t_c+t_r} t\right) \right. \\ & \left. + \left(1 - \cos\left(\frac{2n\pi}{t_c+t_r} t_c\right)\right) \sin\left(\frac{2n\pi}{t_c+t_r} t\right) \right] \end{aligned} \tag{4}$$

This gives the volume of fluid contained within the jellyfish as

$$\begin{aligned} V_f = \; & V_0 - \sum_{n=1}^{\infty} \Delta V \frac{(t_c+t_r)^2}{2t_c t_r (n\pi)^2} \left[\cos\left(\frac{2n\pi}{t_c+t_r}(t-t_c)\right) \right. \\ & \left. + \; 1 - \left(\cos\left(\frac{2n\pi}{t_c+t_r} t_c\right) + \cos\left(\frac{2n\pi}{t_c+t_r} t\right) \right) \right] \end{aligned} \tag{5}$$

for an initial volume of V_0. Notice the term in Equation (3) outside of the summation does not appear in Equation (4), as this would give rise to a term that is linear in time in Equation (5). Elimination of this term from Equation (3) could be viewed as a kind of constraint on the parameters (t_c, t_r, A, B) to ensure that the integrated result oscillates about some initial value. With proper expressions for the cross-sectional area, drag coefficient, and added mass coefficient as provided in Daniel (1983), Equation (1) constitutes a first order non-homogeneous non-linear ODE in the swimming velocity variable u. The solution of this equation is easily obtained numerically via a state-space representation and 4th order Runge-Kutta integration to calculate position and velocity and integrate forward in time.

Design Principle of a New Biomimetic Jellyfish

As evident from the velocity profile found in Daniel (1983), the jellyfish swimming mechanism has a disadvantage due to the intake of water through the velar aperture during the relaxation phase. This causes a negative momentum exchange that pulls back on the animal, thus slowing it down. Here is where the proposed biomimetic robot seeks to modify the jet propulsion swimming mechanism. If the water that is drawn into the

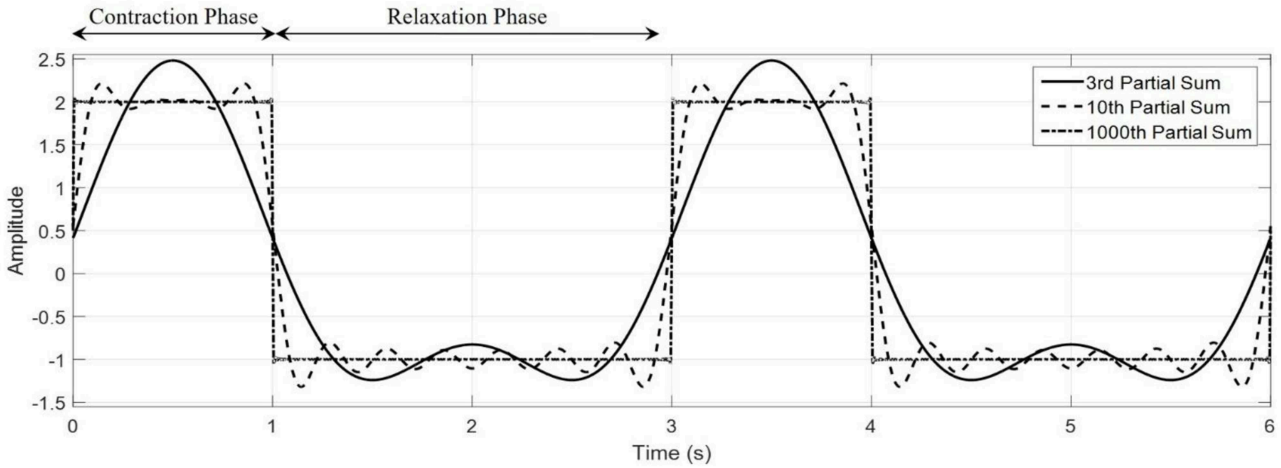

FIGURE 2 | Representative waveforms generated with the Fourier series square wave. The characteristic contraction and relaxation phases of the jellyfish can be captured by the Fourier series shown here. Here, we have taken $t_c = 1$, $t_r = 2$, $A = 2$, $B = -1.5$, to create a purely illustrative waveform that demonstrate the role of these parameters.

enclosed volume is redirected as to assist the propulsion of the device, then continual forward motion is achieved by an always increasing velocity until a steady state is reached. This, theoretically, should allow for a more efficient and effective swimming mechanism for a potential soft robot.

To achieve this necessary modification, the addition of a distinct inlet and outlet to the enclosed volume is proposed. During contraction, only the outlet valve allows fluid flow, thus constraining the direction of the mass flux and hence the momentum exchanged. Then, during relaxation, the inlet would allow for the mass flux to occur along the same direction, therefore contributing a positive acceleration. A simple illustrative cross-section of such a design is given in **Figure 3**.

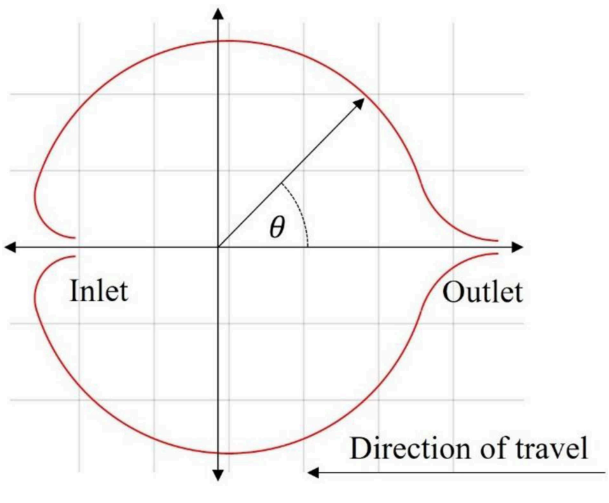

FIGURE 3 | Illustration of the inlet and outlet valves. The direction cosine of an inlet or outlet for the proposed design is based off the polar angle starting on the positive x-axis and increasing in the counterclockwise direction.

Governing Equation and Model Inputs

In deriving Equation (1) there is an implicit assumption that the body of the jellyfish is approximately the same density as water. For arbitrary soft robot designs, this assumption is not valid and so the equation must be recast to account for variations in the density of the materials used to construct the robot as well as any potential onboard control devices. A simple modification is to split the robot's mass into a persistent mass that encompasses the materials that make up the structure and an internal volume of fluid contained within the body of the robot. Further, as added mass effects are by nature an interaction with the surrounding fluids, a distinction must be made between the interior and exterior volume of the robot. To account for the inlet and outlet directions as proposed in the design of this robot, a direction cosine is added to the thrust component. Hence, the equation of motion reads

$$(m_b + \rho_w V_i + \alpha_{AM}\rho_w V_o)\frac{du}{dt} = \cos(\theta(t))\frac{\rho_w}{A_V}\left(\frac{dV_i}{dt}\right)^2 - \frac{1}{2}C_d\rho_w S_A u^2 \quad (6)$$

with the mass of the robot body, m_b, assumed to be fixed with a density not necessarily equal to water, the internal fluid volume, V_i, the external volume of the body, V_o, and the direction cosine, $\cos(\theta(t))$, illustrated in **Figure 3**, which is a function in time as the direction potentially changes for the contraction and relaxation phases. The direction cosine indicates the orientation of the flow through the inlet and outlet valves relative to the direction of forward travel. As mentioned briefly, in biological jellyfish the contraction phase expels fluid rearward through the velar aperture while the relaxation phase intakes fluid in the opposite direction, which in effect changes the direction of the thrust. Incorporating the direction cosine into the model allows

TABLE 1 | Direction cosine angles for inlet and outlet during different swimming modes.

	Propulsion mode 1 (P1)	Propulsion mode 2 (P2)
Inlet	$\theta = 0$	$\theta = \pi$
Outlet	$\theta = 0$	$\theta = 0$

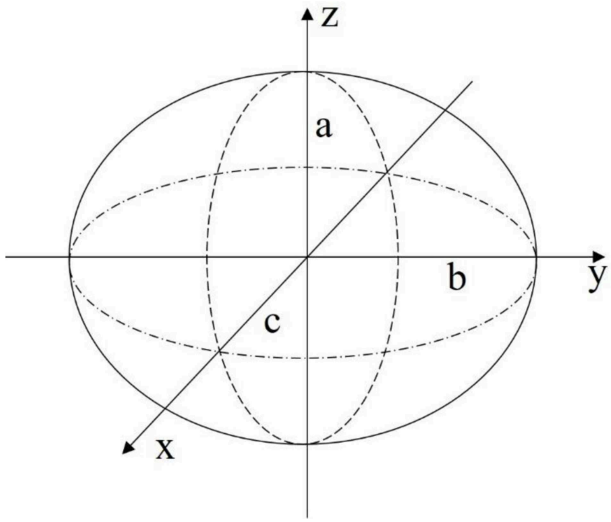

FIGURE 4 | The body of the robot can be approximated as an ellipsoid for initial feasibility study of the proposed design.

for this alternating force to be directly reflected into the model. These modifications are necessary to capture a more accurate swimming behavior of the proposed robot. The time ratio of relaxation time to contraction time is defined in Equation (7).

$$\delta_t = \frac{t_r}{t_c} \tag{7}$$

In the proposed model, the biomimetic robot has a forward-facing inlet that, under ideal circumstances, allows for unidirectional mass flow through the body of the robot, which will be referenced as the P1 swimming mode. This effect manifests itself in the direction cosine term in Equation (6). This kind of control in the model means it can also be used to simulate a jellyfish, P2, mode, in which the inlet is directed rearward, simulating the familiar swimming characteristics seen in Daniel (1983). The direction cosine angle for each mode is given in **Table 1**.

Description of Robot Using a Geometric Model

The first modeling approach describes the body of the robot as a geometric surface. Specifically, the shell of the robot is defined as an ellipsoid with half-axis dimensions *a*, *b*, and *c* as illustrated in **Figure 4**. A constraint is placed on the model that all deformed states of the body can be described though the definition of an ellipsoid.

To use Equation (6) for the EoM, the volume, deformation of the volume, cross-sectional area, drag, and added mass effects must be determined. The internal volume of the given ellipsoid is calculated with Equation (8), and, with an added wall thickness of *d*, the external volume with Equation (9) below.

$$V_i = \frac{4}{3}\pi abc \tag{8}$$

$$V_o = \frac{4}{3}\pi \left(a+d\right)\left(b+d\right)\left(c+d\right) \tag{9}$$

The time rate of change for the internal and external volume are easily obtained by the chain rule for differentiation assuming that all three half-axis dimensions *a*, *b*, and *c* are all able to vary with time. For an input deformation of *a*, the corresponding deformations in *b* and *c* are obtained by enforcing conservation of mass and incompressibility with respect to the material contained between the internal and external volume. Assuming axisymmetric deformation about the z-axis, the rate of change in dimensions *b* and *c* in response to an input deformation to dimension *a* are found to be:

$$\frac{db}{dt} = \frac{dc}{dt} = -\frac{2b+d}{2(a+b+d)}\frac{da}{dt} \tag{10}$$

The cross-sectional area with respect to the swimming direction can be calculated based on the external volume as

$$S_A = \frac{3V_o}{4(c+d)} \tag{11}$$

The drag coefficient is calculated using the formulation found in Morrison (2013). This allows for a wide range of Reynold's numbers, 10^{-1} to 10^6, and assumes a spherical body, for which this approach is valid under small deformations to an originally spherical geometry.

$$C_d = \frac{24}{Re} + \frac{2.6\frac{Re}{5.0}}{1+\left(\frac{Re}{5.0}\right)^{1.52}} + \frac{0.411\left(\frac{Re}{263000}\right)^{-7.94}}{1+\left(\frac{Re}{263000}\right)^{-8.00}} + \frac{0.25\frac{Re}{10^6}}{1+\frac{Re}{10^6}} \tag{12}$$

Finally, the added mass coefficient for an ellipsoid body is found using (Korotkin, 2009).

$$\mathcal{A}_0 = abc\int_0^\infty \frac{du}{(c^2+u)\sqrt{(c^2+u)(b^2+u)(c^2+u)}}$$
$$\alpha_{AM} = \frac{\mathcal{A}_0}{2-\mathcal{A}_0} \tag{13}$$

With these parameters fully defined, the EoM given in Equation (6) can be used to simulate the biomimetic robot swimming.

Description of Robot Using a Mechanics Model

Equivalent Circuit Modeling of an IPMC

In developing a mechanics-based modeling approach a selection of actuator must be made. Here, the actuation model is that of an IPMC actuator, modeled through an equivalent circuit (EC). Similar to Shahinpoor and Kim (2001) and Cha et al. (2012), a circuit model that incorporates resistive, capacitive, and Warburg (RCW) impedances is used. These impedances model the surface and polymer resistance, inherent polymer capacitance

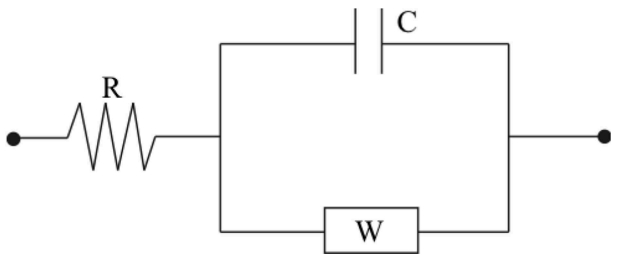

FIGURE 5 | The circuit diagram can be used to construct an accurate model for the electromechanical transduction of IPMC actuators.

and double layer capacitance due to cation migration, and charge transfer and diffusion within the polymer (Bard and Faulkner, 2000; Cha et al., 2012), respectively. A diagram of this circuit is provided in **Figure 5**.

The electrical impedance of each of these lumped circuit elements is written below, where R, C, and W are the lumped electrical resistance, lumped capacitance, and Warburg impedance, respectively

$$Z_R = R,\ Z_{Cap} = \frac{1}{j\omega C},\ Z_{Warburg} = \frac{W}{\sqrt{j\omega}} \tag{14}$$

A transfer function may then be written between an input voltage and the respective current generated through the circuit (Cha et al., 2012).

$$H(s) = \frac{I(s)}{V(s)} = \frac{Cs + W\sqrt{s}}{RCs + RW\sqrt{s} + 1} \tag{15}$$

An electromechanical coupling equation can be written in the following form (Aureli et al., 2010)

$$P = \alpha Q \tag{16}$$

where P, α, and Q are the mechanical loading of the IPMC, electromechanical coupling coefficient, and total charge within the polymer, respectively. Equation (16) links the electrochemical behavior of the IPMC from the EC model to the mechanical deformation of the IPMC which will be detailed later. The actuation response of an IPMC under the EC model can then be obtained from the charge via

$$\begin{aligned} Q(t) &= \int_0^t i(\tau)\, d\tau = \mathcal{L}^{-1}\left\{\frac{1}{s} I(s)\right\} \\ &= \mathcal{L}^{-1}\left\{\frac{1}{s} H(s)\, \mathcal{L}\{\mathcal{V}(t)\}\right\} \end{aligned} \tag{17}$$

where $i(t)$ is the electrical current through the circuit, $\mathcal{V}(t)$ is an external voltage applied to the IPMC electrodes, and $\mathcal{L}$ is the Laplace transform operator and an assumption of zero initial charge was made.

Deformation Modeling With Linear Beam Theory

Relating back to **Figure 4**, the second modeling approach breaks away from the constraint of the robot body being defined by an ellipsoid geometry. Instead, as illustrated in **Figure 6**, the body is broken into active and passive regions, where the active region is physically deformed under the IPMC loading, and the passive region is dictated by the boundary conditions imposed on the geometry. Again, the deformation is assumed to be symmetric about the z-axis and across the xy-plane. This would be achieved by embedded IPMC actuators placed within the active region of the body and placed symmetrically around the z-axis. Other EAP actuators may be used in such a design, but here the model is restricted to just that of an IPMC. A cross-sectional view is provided in **Figure 7** which highlights the placement of the active region of the shell as well as the plane and axis of symmetry.

To describe the deformation of the shell wall, a cross-section slice along the y-z plane is taken and the upper portion of the

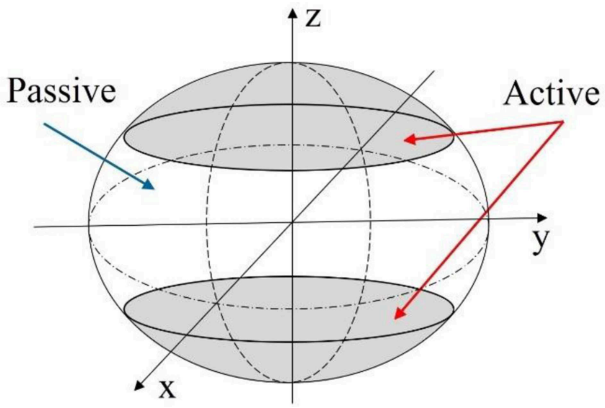

FIGURE 6 | Diagram of the mechanics model description of the robot body. Active portions of the robot body can be deformed using a wide variety of EAP actuators.

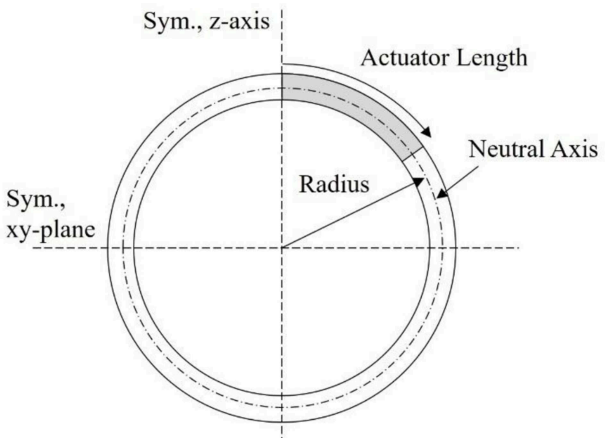

FIGURE 7 | Illustrative cross-section of proposed mechanics model. The symmetry z-axis and xy-plane are highlighted, as well as the actuator length within the active portion of the shell wall, and the radius describing the neutral axis of the beam.

shell is modeled as a curved beam. Using virtual displacement, a functional of the form below is obtained

$$\int_0^L M\delta\kappa + N\delta\epsilon - P_w\delta w - P_v\delta v ds = 0 \tag{18}$$

where M, N, P, w v, and s are the internal bending moment, internal axial load, external loading broken into transverse (P_w) and axial (P_v) directions, transverse and axial displacements, and the local axial coordinate along the length of the beam, respectively. The infinitesimal strain of the beam is defined in terms of the curvature and axial strain, κ and ϵ, given by

$$\kappa = w'' + \left(\frac{v}{\rho}\right)' \tag{19}$$

$$\epsilon = v' - \frac{w}{\rho} \tag{20}$$

wherein ρ is the undeformed radius of curvature of the beam, assumed to be constant for simplicity. The first terms in both strain expressions are the familiar axial and curvature strain found in the Euler-Bernoulli beam theory for straight beams (Byskov, 2013). The second terms are couplings of the transverse and axial deformation to the axial and curvature strains which is found only in curved beams. It can be easily verified that as the radius of curvature tends toward infinity, these terms tend to zero and thus the straight beam theory is recovered.

Now, the assumptions of an inextensible beam, transverse external load, and linear elasticity are taken which yields the new functional

$$\int_0^L EI\left(w'' + \tfrac{w}{\rho^2}\right)\delta\left(w'' + \tfrac{w}{\rho^2}\right) - P_w\delta w ds = 0 \tag{21}$$

with Young's modulus E and cross-sectional moment of inertia I and the product EI is known as the flexural rigidity, or bending stiffness, of the beam. The Galerkin method is used to approximate the deflection in terms of monomials of the local axial coordinate, and is constructed as

$$\widetilde{w} = \sum_{n=0}^{N_w} s^n \widehat{w}_n = \boldsymbol{N_s}\widehat{\boldsymbol{w}} \tag{22}$$

where $\widetilde{w}$ is the trial function, N_w is the number of monomial shape functions used, $\boldsymbol{N_s}$ is a vector of the shape functions and $\widehat{\boldsymbol{w}}$ is a vector of the Galerkin coefficients $\widehat{w}_n$. We may expand out the integrand of the functional and treat the variation on the displacement as a test function. Substitution of the Galerkin trial function into the functional in Equation (21) results in

$$\int_0^L \left[EI\left(\boldsymbol{N_s}''^T\boldsymbol{N_s}'' + \frac{1}{\rho^2}\left(\boldsymbol{N_s}''^T\boldsymbol{N_s} + \boldsymbol{N_s}^T\boldsymbol{N_s}''\right) + \frac{1}{\rho^4}\boldsymbol{N_s}^T\boldsymbol{N_s}\right)\widehat{\boldsymbol{w}} - \boldsymbol{N_s}^T P_w\right] ds = 0 \tag{23}$$

which is a symmetric system of linear equations to solve for the unknown Galerkin coefficients $\widehat{w}_n$. The integration of the stiffness matrix is easily achieved using Gauss-Legendre quadrature. With the transverse deformation calculated from the Galerkin approximation, the condition of inextensibility can be used to determine the local axial deformation induced in the beam.

$$\epsilon = v' - \frac{w}{\rho} = 0 \tag{24}$$

$$\widetilde{v} = \frac{1}{\rho}\int_0^s \widetilde{w}d\zeta = \frac{1}{\rho}\int_0^s \sum_{n=0}^{N_w}\zeta^n\widehat{w}_n d\zeta = \frac{1}{\rho}\sum_{n=0}^{N_w}\frac{s^{n+1}}{n+1}\widehat{w}_n \tag{25}$$

The last step in this process illustrates how the use of monomial shape functions facilitates easier integration in the process of deriving these necessary equations. From here, the volume must be calculated based on the Galerkin approximation using

$$V = \iiint r^2 sin\theta dr d\theta d\varphi \tag{26}$$

Equation (26) is integrated first with respect to the azimuthal angle, ϕ, and the radial distance, r, to obtain

$$V = \tfrac{4\pi}{3}\int_\alpha^\beta R^3 sin\,(\theta_s)\,d\theta_s \tag{27}$$

where the symmetry of the deformation has been leveraged and $\theta_s = \frac{s}{\rho}$ is the polar angle defining the position along the beam. The integration bounds are left as variable because the integrand, which is dependent on the Galerkin trial function, changes as the polar angle transitions from the active portion to the passive portion of the body. Substituting the trial function into the expression for radial position and factoring out the dependence on the loading and bending stiffness from the Galerkin coefficients yields

$$R = (\rho + \widetilde{w}) = \left(\rho + \tfrac{P_w}{EI}\sum_{n=0}^{N_w}\theta_s^n\widetilde{\widehat{w}}_n\right) \tag{28}$$

wherein a change of variable has been made from the local axial coordinate into the polar angle, and the Galerkin coefficients $\widehat{w}_n$ have absorbed the dependence on ρ from this change of variable and become $\widetilde{\widehat{w}}_n$. The radial position is seen to have two components, the nominal radius of curvature with an addition of the transverse deflection along the length of the beam. Substitution of this into the volume integral results in

$$V = \frac{4\pi}{3}\int_0^{\frac{\pi}{2}}\left[\rho^3 + 3\rho^2\frac{P_w}{EI}\sum_{n=0}^{N_w}\theta_s^n\widetilde{\widehat{w}}_n + 3\rho\left(\frac{P_w}{EI}\sum_{n=0}^{N_w}\theta_s^n\widetilde{\widehat{w}}_n\right)^2 + \left(\frac{P_w}{EI}\sum_{n=0}^{N_w}\theta_s^n\widetilde{\widehat{w}}_n\right)^3\right]\sin\,(\theta_s)\,d\theta_s \tag{29}$$

The integration of the volume can be written in a compact form when noticing that the integrand, when expanded, is a series of monomials and sine products as coefficients of the loading and stiffness. The expansion and collection of these terms can be easily written in compact form, the results of which are given in the **Supplementary Material**. Finally, the internal volume is resolved into the cubic polynomial shown in Equation (30). The time dependence of the volume has now been highlighted and

stems solely from the time variations in the loading, which in turn depends on the input voltage to the EC model of the IPMC as will be discussed shortly. The beam theory used has assumed static deflection, and thus the entire model is quasi-static, neglecting inertial effects in the mechanical deformation.

$$V(t) = A_0 + A_1\left(\frac{P_w(t)}{EI}\right) + A_2\left(\frac{P_w(t)}{EI}\right)^2 + A_3\left(\frac{P_w(t)}{EI}\right)^3 \quad (30)$$

The cross-sectional area with respect to the flow direction can be derived with a similar approach as that taken for the volume. Specifically, the area integral necessary is:

$$S_A = \iint r\, dr d\theta_s \quad (31)$$

With the radial distance defined in Equation (28), the integral becomes:

$$S_A = 2\int_0^{\frac{\pi}{2}} \rho^2 + 2\rho\frac{P_w}{EI}\sum_{n=0}^{N_w}\theta_s^n\widetilde{\widetilde{w}}_n + \left(\frac{P_w}{EI}\sum_{n=0}^{N_w}\theta_s^n\widetilde{\widetilde{w}}_n\right)^2 d\theta_s \quad (32)$$

The integral is in terms of only monomials of the polar angle thus its integration is relatively straight forward and can be evaluated to the expression below, with the coefficients B_0, B_1, and B_2 provided in the **Supplementary Material**.

$$S_A(t) = B_0 + B_1\left(\frac{P_w(t)}{EI}\right) + B_2\left(\frac{P_w(t)}{EI}\right)^2 \quad (33)$$

In the derivation of both volume and cross-sectional area the loading, P_w, has been assumed constant along the length of the active portion of the beam. The added mass and drag coefficient, additional assumptions were made that allow the same relations of the geometric model to be used. The added mass was initially calculated based on an ellipsoid of largest volume that fit the material points along the x, y, and z-axis of the robot body. It was found that the added mass coefficient maintained very small oscillations around a value of 0.5, the value for a sphere, and due to the first approximation nature of this model the coefficient has been fixed to this value. Since the deformation to the body is relatively small, the assumption of a roughly spherical geometry is a reasonable approximation and hence drag is calculated again with Equation (12).

To couple the electromechanical transduction of an IPMC to the beam theory model, the mechanical loading of the beam, P_w, is related to the electrochemical behavior of the IPMC through Equation (16). The Fourier series in Equation (3) is used as the model input here, where it defines the input voltage to the IPMC. An approximate inverse Laplace transform of Equation (17) is obtained using the FFT based NILT algorithm without acceleration, discussed in Brančik (2002) and Brancik and Smith (2015).

RESULTS

Evaluation and Comparison of Models

A comparison of the geometric and mechanics models of the robot, in the P2 swimming mode, and an implementation of a biological jellyfish model from Daniel (1983) is provided in **Figure 8**. The biological jellyfish is modeled as being of comparable size and volume exchange to the biomimetic robots. For the jellyfish model a body length dimension of 23.1 mm was chosen with the remaining geometric factors scaling such that the enclosed volume matched that of the next two robot models. For the geometric model the three half-axis dimensions (a, b, c) defining the median surface of the ellipsoid body have an initial dimension of 31.75 mm, and a rate of change in the z-axis dimension of 40 mm/s during the contraction phase was chosen, with the relaxation phase being complementary such that the volume at the end of each swimming cycle returned to its initial state as discussed in section Kinematics of swimming jellyfish. The IPMC EC model used physical dimensions of 28 × 9.94 × 0.57 mm with a maximum input amplitude for the Fourier series of 3 V, with a body radius of 31.75 mm. The shell thickness was made to be 4 mm for both the geometric and mechanics model. All three models utilized a 10 mm velar aperture radius, volume exchange of 10.5%, contraction time of 0.5 s, and a time ratio of 2. Both the geometric and mechanics model assume a persistent mass of 50 g for the robot body, based on the amount of material that would be contained between the internal and external volumes and an approximate density, 1,065 kg/m^3, of common castable silicon materials. The material properties of the IPMC were chosen from literature and use a Young's modulus value of 249 MPa (Trabia et al., 2017), while the shell was assumed to be made of castable silicon with an approximate modulus of 125 kPa. The composite structure for this thin bilayer cross-section was then transformed into an equivalent homogenous material cross-section using standard mechanics of materials approaches in order to calculate the bending stiffness used in the Galerkin approximation of the curved beam deformation.

The jellyfish model utilized Equation (1) for the governing EoM, with a volume rate of change given by Equation (2), or equivalently Equation (3). The remaining parameters are modeled just as in Daniel (1983). The geometric model uses the modified EoM of Equation (6), with the necessary volume, cross-section, drag, and added mass components obtained from Equations (8–13). For the mechanics model, the EoM of Equation (6) is again used, with a voltage input to the EC model, Equation (15), is obtained by a Fourier series of the form given in Equation (3). The charge response obtained from the EC model is used to calculate the mechanical loading through Equation (16), which in turn in controls the volume and cross-section from Equations (30) and (33), respectively.

An important note must be made here. The simulation of the biological jellyfish used was matched to a comparable volume exchange of the two proposed models. From Daniel (1983), the typical volume change for a jellyfish is on the order of 50%, where here a change of only 10.5% is used. While **Figure 8** demonstrates that the two proposed biomimetic robot models do perform comparable to than the biological counter-part,

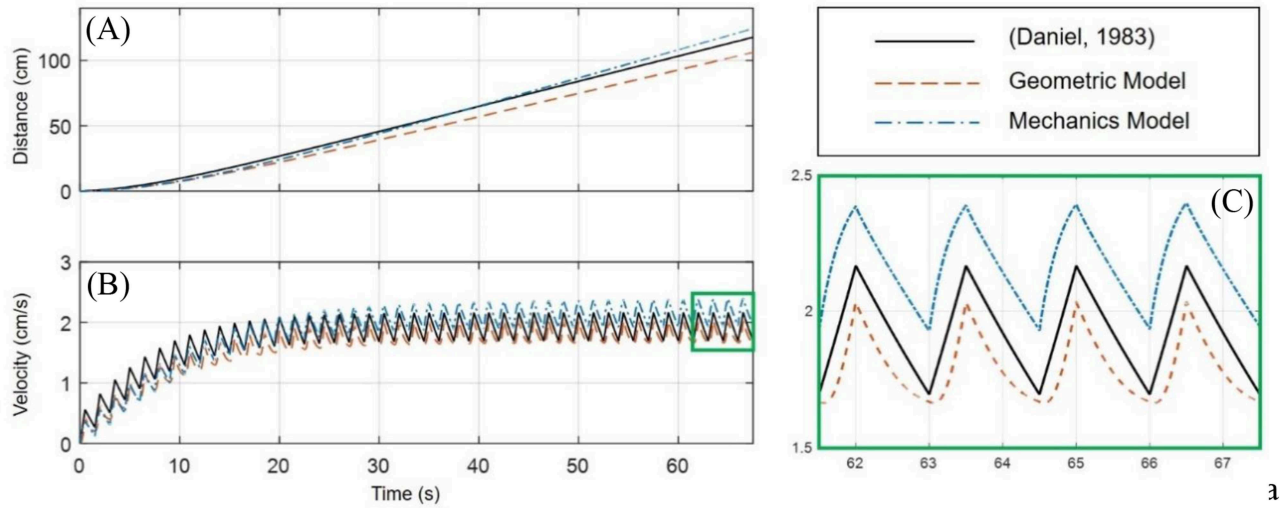

FIGURE 8 | Comparison of the geometric and mechanics descriptions of the designed robot with a biological jellyfish model found in literature. The simulation uses a contraction time of 0.5 s, with a time ratio of 2. All models operate with ∼10.5% volume exchange for thrust generation. **(A)** The position as calculated by the models for the jellyfish and robot show a slight curvature upward during the initial transient swimming phase and approach a nearly linear trend upon reaching steady-state swimming. **(B)** The initial curvature seen in **(A)** is seen to match the build up to steady-state swimming velocity in this plot. Initial transient swimming occurs approximately between 0 and 20 s, after which steady-state is reached and the velocity fluctuates around a steady value. **(C)** An enhanced portion of **(B)** is provided to more easily analyze the waveform of the velocity profiles. It is clearly seen that all three velocity profiles have similar sawtooth like characteristics, with differences in the curvature of the contraction and relaxation phases which is attributed to how the input signal induces deformation of the internal fluid volume.

the biological jellyfish model is not operating at full capacity. This limitation is due to the smaller overall deflection of the body in the mechanics models inherent in the small strain and small deformation assumption used. A more complex non-linear deformation model would allow for a wider range of volume changes to be simulated, but nevertheless the comparisons made here illustrate the swimming kinematics obtained under this new model.

From **Figures 8A,B** and it is clearly seen that all three of the models are operating with roughly the same performance, which is expected given they are exchanging the same amount of fluid and the inlet/outlet orientations are the same. One aspect to note is **Figure 8C**, which is an enhanced view of the boxed region of **Figure 8B**, in which the differences in the velocity profile during contraction and relaxation phases is seen. While the kinematics of the swimming for each model are nearly the same, being based on the two forms of the EoM, Equations (1) and (6), the differences in velocity profile are attributed to how the deformation to the internal fluid volume is obtained. In the standard jellyfish model based on the work in Daniel (1983), the internal volume of a truncated ellipsoid is changed at a constant rate during both the contraction and relaxation phases, as described by the Fourier series in Equation (4). For the geometric model, the z-axis dimension a is being used as an input, where the rate of change of a is driven by Equation (3), with the appropriately chosen values for the constants A and B. Lastly, the mechanics model uses the Fourier series of Equation (3), as the input voltage to the EC model of an IPMC, which then deforms the internal fluid volume according to the curved beam deformation calculated from the Galerkin approximation and Equations (30) and (33).

These three models use the same variable amplitude, variable duty cycle square wave to induce changes to the internal fluid volume through different means. It may be interesting to arrange each model to induce changes to the internal volume by the same means, such as constant rate of volume change, to directly compare the geometric differences between each of the approaches, but here we simply provide a brief discussion on the differences in the velocity profiles under the induced volume deformation described before.

In **Figure 9,** the mechanics model is simulated under both the P1 and P2 swimming modes for the same 10.5% volume exchange. An implementation of the (Daniel, 1983) model is used to interpret the results, wherein a 20% volume exchange was necessary to obtain swimming performance similar to the biomimetic robot under the P1 swimming mode.

The Froude propulsion efficiency may be used to compare the jellyfish and biomimetic robot design ability to generate thrust during the contraction phase (Sfakiotakis et al., 1999; Ford and Costello, 2000; Moslemi and Krueger, 2010; Najem and Leo, 2012; Najem et al., 2012), and is calculated as

$$\eta_P = \frac{1}{t_c} \int \frac{2\, u(\tau)}{u(\tau)+v_e(\tau)} d\tau \tag{34}$$

wherein v_e and u are the ejected fluid velocity, calculated by Equation (35) and robot velocity, respectively. The integral is taken over the duration of the final contraction phase after steady-state swimming is achieved. The efficiency results calculated for the simulations shown in **Figures 8**, **9** are given in **Table 2**.

$$v_e = \frac{\dot{m}}{\rho_w A_v} \tag{35}$$

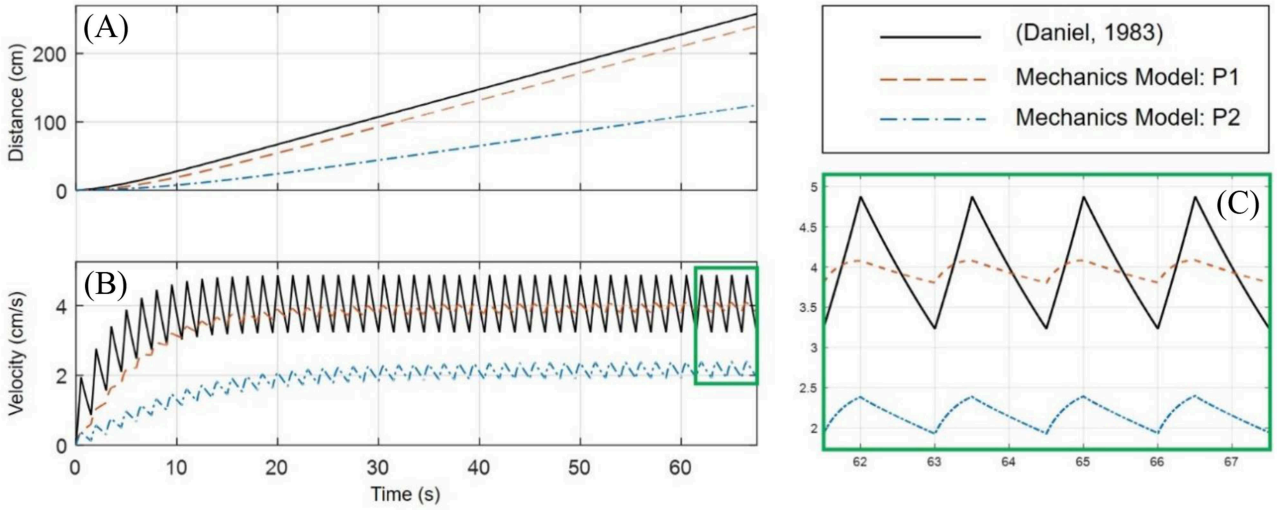

FIGURE 9 | Comparison of the P1 and P2 swimming modes for the mechanics biomimetic robot model. The biological jellyfish as modeled according to Daniel (1983) must operate with nearly twice the volume exchange (20 vs. 10.5%) as the P1 biomimetic robot in order to obtain similar swimming performance. **(A)** As in **Figure 8A**, the position for the three simulations is plotted. The mechanics model in the P1 swimming mode far outpaces the P2 swimming mode, being on par with the biological model operating at a higher volume change. **(B)** The velocity profiles also show that the P1 mode has similar amplitude variations during steady-swimming as the P2 mode, but the biological model has larger variations for a roughly equivalent average steady-state velocity. **(C)** Again, an enhanced view of the velocity profiles at steady-state swimming is given which highlights the differences in the waveform generated by each model.

TABLE 2 | Froude propulsion efficiency of each model is calculated for the 10.5% volume exchange simulations shown before.

Volume exchanged	Jellyfish	Geometric		Mechanics	
		P1	P2	P1	P2
10.5%	39.6%	69.9%	47.6%	62.5%	40.6%
50.0%	59.9%	N/A	N/A	N/A	N/A

The biological jellyfish model reaches the ∼60% propulsion efficiency range of the P1 swimming mode at a volume exchange of ∼50%.

We find that at the simulated volume exchange of 10.5%, both the geometric and mechanics model of the biomimetic robot have propulsion efficiencies on the order of that of the simulated biological jellyfish. These values are reasonable when compared with jet propulsion studies found in literature (Bartol et al., 2009). Leveraging the forward-facing inlet in the P1 swimming mode, the biomimetic robot design can achieve a higher average velocity during steady-state swimming. This effectively makes each thrusting jet during contraction have a higher propulsive efficiency, as evident in the tabulated results. The higher propulsive efficiency achieved is on the same order as that obtained according to the biological jellyfish model of Daniel (1983) when operating with the much greater 50% volume change.

Energetics and Locomotive Cost for Biomimetic Robot

In Daniel (1983) the energetics of the jet propulsion for a model jellyfish are explored in order to characterize biological jellyfish and their locomotion. The locomotive cost is defined as

$$C = \frac{P_i}{Wu} \tag{36}$$

wherein P_i is the rate of energy consumption, W the weight, and u the swimming velocity of the jellyfish. The locomotive efficiency is defined simply in terms of the output power over the input power.

$$\eta_L = \frac{P_o}{P_i} \tag{37}$$

Since the jellyfish and the biomimetic robot design swim in unsteady patterns, the power input and output are averaged over appropriate swimming cycles. The power input is divided into the power required for generating a thrusting jet,

$$P_{i,t} = \frac{1}{t_c} \int T v_e t \tag{38}$$

which is averaged over the duration of a contraction phase, and the power required to expand and refill the internal volume

$$P_{i,f} = \frac{1}{t_r(1-\Delta)} \int T v_e t \tag{39}$$

which is averaged over the duration of a relaxation phase. The term $(1 - \Delta)$ represents the viscous loss through the deformation of the viscoelastic bell material in a jellyfish. Here, the dissipation factor Δ will be taken as zero, neglecting any losses through the deformation of the body material. The summation of these two terms gives the total average power input.

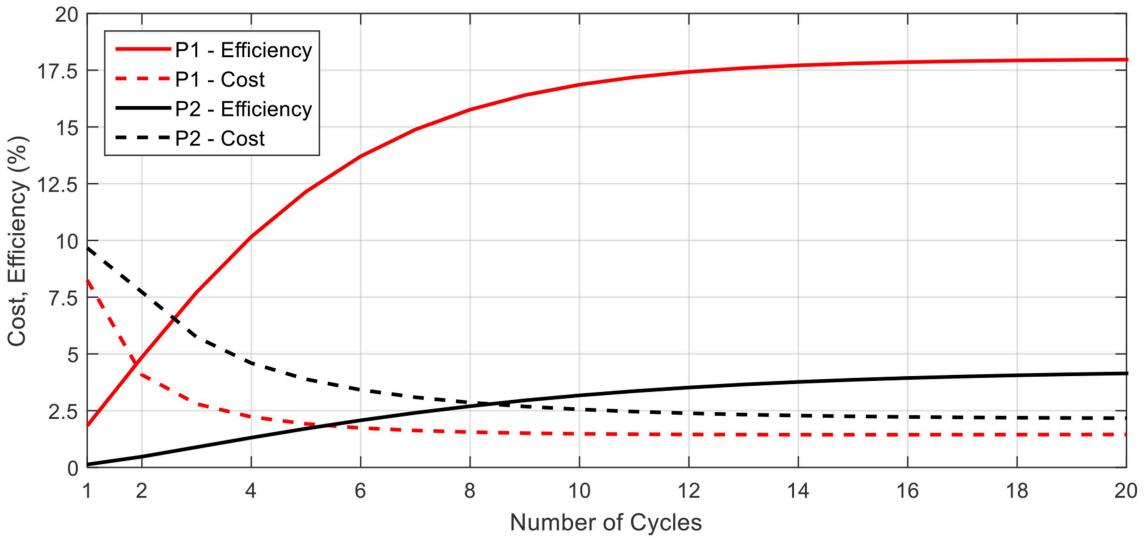

FIGURE 10 | The locomotive cost and efficiency for the P1 and P2 swimming modes are presented here. In both cases, the efficiency increases while cost decreases as more swimming cycles are completed, and each parameter asymptotically approaches a steady state value. P1 curves for efficiency and cost are above and below, respectively, their corresponding P2 curves.

The power output is taken as the power required to overcome the effects of drag and inertia with added mass. These effects are averaged over the entire swimming cycle and are given below.

$$P_{o,d} = \frac{1}{t_c + t_r} \int \frac{1}{2} \rho_w S_A C_d u^3 dt \tag{40}$$

$$P_{o,a} = \frac{1}{t_c + t_r} \int \left(m_b + \rho_w V_i + \alpha_{AM} \rho_w V_o\right) \frac{du}{dt} u \; dt \tag{41}$$

Using these equations, we may characterize the biomimetic robot design in terms of its locomotive efficiency and cost. **Figure 10** provides the cost and efficiency plots for the proposed biomimetic robot as a function of the number of swimming cycles completed. The robot is swimming with a 0.5 s contraction time and a time ratio of 2. From the figure, a similar trend in cost and efficiency as found in the literature for biological jellyfish is seen. As the robot swims, the initial swimming cycles come at a higher cost and with a lower efficiency due to starting from rest and having to overcome the effects of inertia and added mass. As the robot approaches a steady state swimming, the cost and efficiency level off and the robot primarily fights against the drag forces as the average acceleration, and hence inertial effects, tend toward zero.

The data presented in **Figure 10** also highlights the differences between the performance of the P1 and P2 swimming modes. For both the cost and the efficiency, the P1 swimming mode is seen to have better performance, starting and ending with lower cost and higher efficiency as compared to the P2 swimming mode. This, as well as the higher propulsive efficiency, may be attributed to the P1 modes capability to continually generate forward thrusting forces throughout the swimming cycle and hence capable of attaining higher mean velocities at steady state for the same amount of body deformation.

In **Figure 11**, the average acceleration and average velocity over the final swimming cycle of twenty, as simulated in **Figure 10**, are plotted as a function of the time ratio for various contraction times. The results for the P2 swimming mode are similar in form to those found in Daniel (1983). A peak in average velocity is seen near the time ratio of 2, where the peak in acceleration shifts to lower time ratios as the contraction time is increased.

For the P2 swimming mode, the peak average acceleration is seen to decrease as the contraction time is increased, as opposed to the peak average velocity. To explain this, first consider that from the swimming dynamics we know during steady-state swimming, where the peak average velocity would be expected, the average acceleration per cycle should asymptotically approach zero. The lower peak acceleration seen in **Figure 11A** is then not necessarily indicating that the robot is generating lower peak accelerations during the contraction phase, but in fact is swimming in a state that is closer to its steady-state conditions, with a zero average acceleration. This implies that the robot has accelerated to this steady state faster within the 20 cycles that have been simulated, and hence is near its final average swimming velocity. This behavior is readily apparent if one were to examine the average acceleration as a function of the time ratio over a range of completed swimming cycles, wherein as the number of cycles increases the acceleration curves approach zero. The average velocity curves seem to be spread apart from each other based on the contraction time, but this may again be attributed to the fact that at the longer contraction times, the robot is accelerating to steady state in fewer swimming cycles, and hence is achieving a higher average velocity.

To glean more information, we turn to the steady state swimming results as presented in **Figure 12**. Here the locomotive efficiency and average velocity are presented as functions of

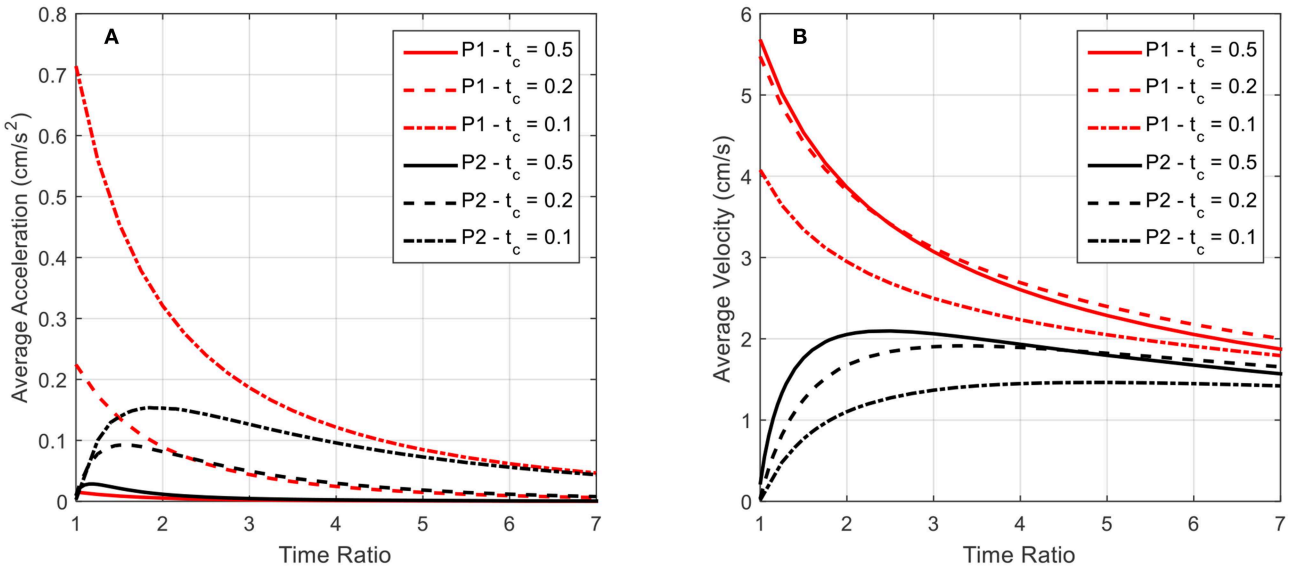

FIGURE 11 | The average acceleration and average velocity after 20 swimming cycles is plotted as a function of the time ratio. Data for both P1 and P2 swimming modes is presented for contraction times of 0.5, 0.2, and 0.1 s. **(A)** As indicated by the above curves, increasing contraction time leads to a decrease in average acceleration after the 20 cycles for all time ratios, indicating that the robot has reached steady-state swimming, which is characterized by a zero average-acceleration. **(B)** In contrast to the average acceleration, the average velocity after the completed swimming cycles does not approach zero with increasing time ratio. As stated before, the near-zero average acceleration is indicative of approaching steady-state swimming, where a finite, non-zero velocity is expected.

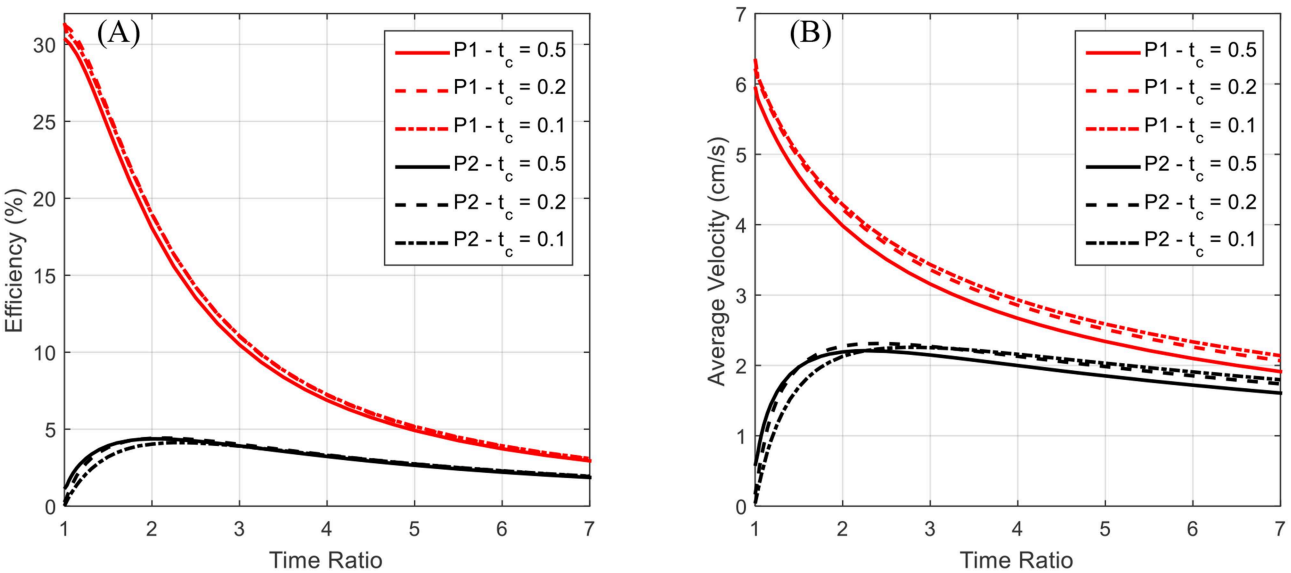

FIGURE 12 | The locomotive efficiency and average velocity after reaching steady state is plotted as a function of the time ratio. Data for both P1 and P2 swimming modes is presented for contraction times of 0.5, 0.2, and 0.1 s. The P1 curves are above the corresponding P2 curves. **(A)** The locomotive efficiency during steady-state swimming is seen to decrease as a function of the time ratio, with the P1 swimming mode having a distinct advantage over P2. **(B)** A decrease in average steady-state swimming velocity with increasing time ratio is seen across all tested contraction times. Both P1 and P2 swimming modes appear to approach a general asymptote and decrease monotonically after a time ratio of ∼3.

the time ratio for various contraction times. Instead of using a consistent number of swimming cycles for each data point, these plots were generated by simulating the robot swimming until steady state was reached for each data point. Hence, average acceleration over a complete swimming cycle has approached zero and these curves are not presented.

Again, for the P2 swimming mode, which corresponds to normal jet propulsion found in the biological jellyfish considered, a peak in efficiency and average velocity is seen near a time ratio of 2 for all contraction times considered. This indicates that under normal jet locomotion, such a time ratio may be ideal in a wide range of circumstances. In both **Figures 11B**, **12B**,

we see that the average velocity for the P1 swimming mode is greater than that in the P2 mode. This is an expected result as the continual forward thrust for the same volume exchange should lead to a higher steady state velocity. Of greater interest is the behavior of these plots for smaller time ratios.

The plots seem to have a singular nature, increasing without bound as the time ratio approaches unity. Simulations were not carried out for time ratios of less than unity for two reasons. The first being that for a biological jellyfish, with time ratios less than unity the relaxation phase is performed over a shorter duration, and hence generates more negative thrust than positive thrust generated on the longer contraction phase. This in effect would result in backwards swimming, which is not of interest in this study. The second reason is that the current IPMC model does not allow for the frequency dependence on actuation amplitude to be accurately reflected. It is commonly found that as an IPMC, as well as other EAPs, are stimulated with higher frequencies, their actuation amplitude decreases. This would in effect generate a smaller volume exchange for the robot and deteriorate performance in the more rapid action regime of small contraction times and sub-unity time ratios. The lack of capability to capture these effects in the rapid actuation regime is due to the quasi-static nature of the beam deflection model. An introduction of inertial effects would allow for a more detailed analysis of the deformation dynamics but is not pursued further here. As indicated in Trabia et al. (2017), actuation decay for a typical IPMC actuating at 5 Hz, which would correspond to an actuation stroke of 0.2 s, is of the same order as one actuating at 1 Hz. Thus, the results for the short contraction time and small time ratio results given in **Figures 11**, **12** are reasonable as first estimations, but a more detailed dynamic analysis for the body deformation is needed in the future.

One final note of interest is that as seen in **Figure 12** both the efficiency and the average velocity obtained at steady state nearly coincide for the various contraction times. This occurs in both the P1 and P2 swimming modes and may indicate that swimming performance is more so a function of overall geometric size, which governs the drag forces experienced in steady swimming, than the duration of the contraction phase.

Device Design for Fluid Pumping and Thrust Vectoring

Aside from the use as a biomimetic jellyfish robot, the current design has other potential applications in the field of soft robotics. Visualizing the mass flux through the robot, during the contraction phase there is a negative flux as water leaves the internal volume. If a control volume is drawn at the outlet of the robot, and if the robot were constrained and fixed in place, the fluid motion through the control volume may be plotted. Assuming a forward-facing inlet as in the proposed design, the velocity through this control volume during the relaxation phase is zero. In this configuration the system now behaves as a unidirectional fluid pump.

For the kinematics described for swimming, where the time ratio between contraction and relaxation phases is larger than unity, the flow through this control volume pulsates. As the time ratio is lowered, the velocity through the control volume becomes more continuous. This is illustrated in **Figure 13**, where velocity profiles for the device in two regimes of contraction time/time ratio are shown. This application transforms the robot into a fluid pump, allowing for a near constant mass flow or a pulsating flow, making it suitable for multiple applications in low volume fluid pumping, akin to the proposed design in Lee et al. (2006). An interesting feature is the unidirectional aspect of this pump, where using one-way valves inherent in the structure of the shell, back flow is restricted. The IPMC driven actuation also makes the system a low voltage component. An alternative input voltage waveform may also allow for a more uniform flow velocity during the contraction phase but was not investigated in this study. The proposed design could further be used in thrusting applications where the device is not intended for self-locomotion as in the case of a biomimetic jellyfish, but for vectoring of a larger vehicle by providing a small thrusting force during a short contraction phase followed by a long relaxation phase that minimizes any additional forces.

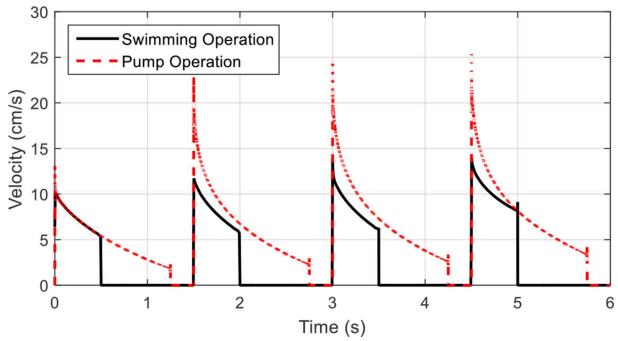

FIGURE 13 | Velocity profiles for fluid pump operations. The outlet fluid velocity during a swimming operation shows the distinct pulse during contraction phases. By extending the contraction phase and shortening the relaxation phase, the outlet velocity becomes more continuous and the device may be used as a fluid pump.

DISCUSSION

Key Findings

Designs and models for biomimetic jellyfish robots typically seek to mimic the structure of natural jellyfish, recreating the hemiellipsoid bell shape and deforming it with artificial muscles in place of the subumbrellar muscles. This approach has seen great success throughout literature (Yeom and Oh, 2009; Villanueva et al., 2010; Xiao et al., 2013), but the design presented here offers an alternative perspective on biomimetic soft robots. Without seeking to exactly mimic the functionality of the biological structure of the jellyfish, inspiration is taken from the physical mechanism of the locomotive jet propulsion used in some jellyfish. The freedom to design the inlet and outlet positions of a soft-robot allowed for the development of the alternative P1 swimming mode, which was shown to result in higher propulsive and locomotive efficiency as well as steady-state swimming velocity as compared to the biological model.

In comparing this design model with some other biomimetic jellyfish robots in literature, we find that the predicted results are in good agreement with the experimental performances. The design found in Xiao et al. (2013) utilizes more traditional robotic actuators to locomote with the P2 swimming of biological jellyfish, and their experiments gave a range of 3–8 cm/s for the forward swimming speed and 1 cm/s during a diving and surfacing operation which are very compatible to the results obtained here. The authors of Nawroth et al. (2012) showed their biomimetic medusoid swimming with a velocity of approximately 0.5 body lengths per stroke (BL/S), while a biological jellyfish had an average near 0.78 BL/s. When the results provided in **Figure 8** are converted into this framework we find the geometric and mechanics models operating at a velocity of 0.14 and 0.18 BL/S, respectively, while the results of **Figure 9** for the jellyfish model and the P1 mechanics model give 0.86 and 0.31 BL/S, respectively, which fit nicely with the results of Nawroth et al. (2012). The authors in Villanueva et al. (2010) and Villanueva et al. (2011) created a biomimetic jellyfish using shape memory alloy materials and demonstrated swimming velocities, with similar characteristics and shown here, in the range of 1–3 cm/s during initial startup swimming, in line with the results of the mechanics model in the P1 swimming mode. Using IPMC actuators, Najem et al. (2012) created a biomimetic jellyfish robot that utilizes a locomotive method more akin to the paddling mode of biological jellyfish, which is expected to generate less deformation of the enclosed fluid and hence less thrust, and achieved experimental speeds in the range 0.36–1.5 mm/s, which are lower than predicted here. This may be attributed to the fact that in the models presented here a small velar aperture is used, which generates a higher thrusting force according to Equation (6), and hence achieves larger average velocities. Overall, the model presented here predicts results that are in line with existing literature and demonstrate the utility of the new design and its capability to utilize a more effective and efficiency swimming method (P1).

As already discussed, the current mechanics model relies on a quasi-static linear beam deformation, which is inadequate for capturing the dynamic nature of the body deformation. Because of this, further investigation on the high frequency actuation for both the P1 and P2 swimming modes is needed. Furthermore, the simple square wave input used for each model may not be ideal for optimizing locomotive efficiency, steady-state velocity, or even initial transient acceleration. The effects of input waveform for each model on the deformation of the internal fluid volume is another avenue of research. Despite this, the newly proposed design shows promise for a novel biomimetic jellyfish robot which utilizes a unique propulsive mechanism for locomotion. The new design also shows promise as a low power, low volume fluid pumping mechanism that utilizes soft EAP actuators.

While this new approach to locomotion is theorized to provide a higher degree of swimming efficiency, it is clearly not the method jellyfish have adapted into their structure. One such reason may be due to the more complex muscular structure required to maintain two apertures that must operate in a synchronous fashion to provide any thrust at all. Any additional efficiency might simply not outweigh the cost of the added complexity. Furthermore, as discussed in Daniel (1983), jellyfish might not have evolved to simply maximize locomotive efficiency or steady-state velocity. Other factors such as their capability to avoid prey or better source food from the environment might have a larger role that makes the design proposed here ill-suited for the biological world. The field of soft robotics however is free of such biological imperatives, and as such the proposed design and P1 swimming mode offer a new perspective on the biomimetic approach for robot development.

CONCLUSION

Biology has been shown to provide invaluable inspiration for the modeling, design, and development of soft robotic systems. Here, insight of the jet propulsion mechanism found in jellyfish lead to a new theory about an improved swimming mechanism for small aquatic robots. This work demonstrated the effects of redirecting the fluid intake direction in a jellyfish type swimming mechanism through two different modeling approaches. The geometric description the proposed robot design is an idealized simplification that gives insight into some of the swimming behaviors of such design and serves as a reasonable approach for conducting initial feasibility studies on new conceptual robot designs. To bring the model closer to reality, the physic-based model used linear beam theory and equivalent circuit models of EAP actuators to construct a new approach to soft-robotic modeling that can be easily expanded to increase accuracy. Both models demonstrated the potential improvements of the P1 swimming mode as compared to that of a typical jellyfish. This new design shows promising applications for biomimetic soft robotics as both an aquatic swimming robot as well as a device for fluid pumping or thrust vectoring.

DATA AVAILABILITY STATEMENT

The datasets generated for this study are available on request to the corresponding author.

AUTHOR CONTRIBUTIONS

ZO performed the study under supervision of KK. ZO wrote the manuscript. KK reviewed the manuscript.

FUNDING

Authors acknowledge partial financial support from the US National Science Foundation (NSF), Partnerships for International Research and Education (PIRE) Program, Grant No. 1545857. Any opinions, findings, and conclusions or recommendations expressed in this material are those of the author(s) and do not necessarily reflect the views of the NSF.

SUPPLEMENTARY MATERIAL

The Supplementary Material for this article can be found online at: https://www.frontiersin.org/articles/10.3389/frobt.2019.00112/full#supplementary-material

REFERENCES

Abdelnour, K., Mancia, E., Peterson, S. D., and Porfiri, M. (2009). Hydrodynamics of underwater propulsors based on ionic polymer-metal composites: a numerical study. *Smart Mater. Struct.* 18:085006. doi: 10.1088/0964-1726/18/8/085006

Akle, B., and Habchi, W. (2013). "Finite element modeling of the sensing and energy harvesting performance in ionic polymer metal composites," in *Proceedings of Electroactive Polymer Actuators and Devices (EAPAD) 2013*, Vol. 8687.

Aureli, M., Kopman, V., and Porfiri, M. (2010). Free-locomotion of underwater vehicles actuated by ionic polymer metal composites. *IEEE/ASME Trans. Mechatr.* 15, 603–614. doi: 10.1109/TMECH.2009.2030887

Bar-Cohen, Y. (2002). Electroactive polymers as artificial muscles: a review. *J. Spacecr. Rockets* 39, 822–827. doi: 10.2514/2.3902

Bard, A. J., and Faulkner, L. R. (2000). *Electrochemical Methods: Fundamentals and Applications. 2nd Edn*. Wiley Publishing.

Bartol, I. K., Krueger, P. S., Stewart, W. J., and Thompson, J. T. (2009). Hydrodynamics of pulsed jetting in juvenile and adult brief squid *Lolliguncula brevis*: evidence of multiple jet 'modes' and their implications for propulsive efficiency. *J. Exp. Biol.* 212, 1889–1903. doi: 10.1242/jeb.027771

Bonomo, C., Fortuna, L., Giannone, P., Graziani, S., and Strazzeri, S. (2006). A model for ionic polymer metal composites as sensors. *Smart Mater. Struct.* 15, 749–758. doi: 10.1088/0964-1726/15/3/010

Bonomo, C., Fortuna, L., Giannone, P., Graziani, S., and Strazzeri, S. (2007). A nonlinear model for ionic polymer metal composites as actuators. *Smart Mater. Struct.* 16, 1–12. doi: 10.1088/0964-1726/16/1/001

Brančik, L. (2002). "Matlab oriented matrix Laplace transforms inversion for distributed systems simulation," in *Proceedings of the 12th Radioelektronika 2002*, 114–117.

Brancik, L., and Smith, N. (2015). "Two approaches to derive approximate formulae of NILT method with generalization," in *2015 38th Int. Conv. Inf. Commun. Technol. Electron. Microelectron* (Opatija), 155–160.

Brunetto, P., Fortuna, L., Graziani, S., and Strazzeri, S. (2008). A model of ionic polymer-metal composite actuators in underwater operations. *Smart Mater. Struct.* 17:025029. doi: 10.1088/0964-1726/17/2/025029

Byskov, E. (2013). "Elementary continuum mechanics for everyone," in *Solid Mechanics and Its Applications*, Vol. 194, ed G. M. L. Gladwell (Springer Netherlands).

Cha, Y., Aureli, M., and Porfiri, M. (2012). A physics-based model of the electrical impedance of ionic polymer metal composites. *J. Appl. Phys.* 111:124901. doi: 10.1063/1.4729051

Cha, Y., and Porfiri, M. (2014). Mechanics and electrochemistry of ionic polymer metal composites. *J. Mech. Phys. Solids* 71, 156–178. doi: 10.1016/j.jmps.2014.07.006

Chen, Z., Tan, X., Will, A., and Ziel, C. (2007). A dynamic model for ionic polymer-metal composite sensors. *Smart Mater. Struct.* 16, 1477–1488. doi: 10.1088/0964-1726/16/4/063

Daniel, T. L. (1983). Mechanics and energetics of medusan jet propulsion. *Can. J. Zool.* 61, 1406–1420. doi: 10.1139/z83-190

Daniel, T. L. (1985). Cost of locomotion: unsteady medusan swimming. *J. Exp. Biol.* 119, 149–164.

Ford, M. D., and Costello, J. H. (2000). Kinematic comparison of bell contraction by four species of hydromedusae. *Sci. Mar.* 64, 47–53. doi: 10.3989/scimar.2000.64s147

Gemmell, B. J., Colin, S. P., Costello, J. H., and Dabiri, J. O. (2015). Suction-based propulsion as a basis for efficient animal swimming. *Nat. Commun.* 6, 1–8. doi: 10.1038/ncomms9790

Jo, C., Pugal, D., Oh, I. K., Kim, K. J., and Asaka, K. (2013). Recent advances in ionic polymer-metal composite actuators and their modeling and applications. *Prog. Polym. Sci.* 38, 1037–1066. doi: 10.1016/j.progpolymsci.2013.04.003

Kim, K. J. (2007). "Ionic polymer-metal composites as a new actuator and transducer material," in *Electroactive Polymers for Robotics Applications*, eds K. J. Kim and S. Tadokoro (London: Springer-Verlag), 165–198.

Kim, K. J., Yim, W., Paquette, J. W., and Kim, D. (2007). Ionic polymer-metal composites for underwater operation. *J. Intell. Mater. Syst. Struct.* 18, 123–131. doi: 10.1177/1045389X06063468

Korotkin, A. I. (2009). Added masses of ship structures. *Fluid Mech. Its Appl.* 88, 1–391. doi: 10.1007/978-1-4020-9432-3

Lee, S., Kim, K. J., and Park, H. C. (2006). Modeling of an IPMC actuator-driven zero-net-mass-flux pump for flow control. *J. Intell. Mater. Syst. Struct.* 17, 533–541. doi: 10.1177/1045389X06058879

Michael, T., Villanueva, A., Joshi, K., and Priya, S. (2013). "Physical modeling of Mastigias papua feeding structures and simulation of their effect on bell stress and kinematics," in *SPIE Bioinspiration, Biomimetics, Bioreplication* (San Diego, CA) 868608.

Morrison, F. A. (2013). *An Introduction to Fluid Mechanics*. New York, NY: Cambridge Univ. Press.

Moslemi, A. A., and Krueger, P. S. (2010). Propulsive efficiency of a biomorphic pulsed-jet underwater vehicle. *Bioinspir. Biomim.* 5:036003. doi: 10.1088/1748-3182/5/3/036003

Najem, J., and Leo, D. J. (2012). "A bio-inspired bell kinematics design of a jellyfish robot using ionic polymer metal composites actuators," *in Proceedings of SPIE - The International Society for Optical Engineering* (San Diego, CA), 41.

Najem, J., Sarles, S. A., Akle, B., and Leo, D. J. (2012). Biomimetic jellyfish-inspired underwater vehicle actuated by ionic polymer metal composite actuators. *Smart Mater. Struct.* 21:11. doi: 10.1088/0964-1726/21/9/094026

Nawroth, J. C., Lee, H., Feinberg, A. W., Ripplinger, C. M., McCain, M. L., Grosberg, A., et al. (2012). A tissue-engineered jellyfish with biomimetic propulsion. *Nat. Biotechnol.* 30, 792–797. doi: 10.1038/nbt.2269

O'Halloran, A., O'Malley, F., and McHugh, P. (2008). A review on dielectric elastomer actuators, technology, applications, and challenges. *J. Appl. Phys.* 104:071101. doi: 10.1063/1.2981642

Porfiri, M. (2009). An electromechanical model for sensing and actuation of ionic polymer metal composites. *Smart Mater. Struct.* 18:015016. doi: 10.1088/0964-1726/18/1/015016

Sareh, S., Rossiter, J., Conn, A., Drescher, K., and Goldstein, R. (2012). Swimming like algae: biomimetic soft artificial cilia. *J. R. Soc. Interface* 10:20120666. doi: 10.1098/rsif.2012.0666

Schicker, D., and Wallmersperger, T. (2013). Modeling and simulation of the chemo-electro-mechanical behavior of ionic polymer-metal composites. *J. Appl. Phys.* 114:163709. doi: 10.1063/1.4826070

Sfakiotakis, M., Lane, D. M. D. M., and Davies, J. B. C. B. C. (1999). Review of fish swimming modes for aquatic locomotion. *IEEE J. Ocean. Eng.* 24, 237–252. doi: 10.1109/48.757275

Shahinpoor, M. (2015). "Fundamentals of ionic polymer metal composites (IPMCs)," in *IONIC Polymer Metal Composites (IPMCs)*, ed M. Shahinpoor (RCR Publishing). doi: 10.1039/9781782622581-00001

Shahinpoor, M., and Kim, K. J. (2001). Ionic polymer-metal composites: I. Fundamentals. *Smart Mater. Struct.* 10, 819–833. doi: 10.1088/0964-1726/10/4/327

Shen, Q., Palmre, V., Stalbaum, T., and Kim, K. J. (2015a). A comprehensive physics-based model encompassing variable surface resistance and underlying physics of ionic polymer-metal composite actuators. *J. Appl. Phys.* 118:124904. doi: 10.1063/1.4931912

Shen, Q., Wang, T., and Kim, K. J. (2015b). A biomimetic underwater vehicle actuated by waves with ionic polymer-metal composite soft sensors. *Bioinspir. Biomim.* 10:055007. doi: 10.1088/1748-3190/10/5/055007

Trabia, S., Olsen, Z. J., and Kim, K. J. (2017). Searching for a new ionomer for 3D printable ionic polymer-metal composites: aquivion as a candidate. *Smart Mater. Struct.* 26:115029. doi: 10.1088/1361-665X/aa919f

Villanueva, A., Priya, S., Anna, C., and Smith, C. (2010). "Robojelly bell kinematics and resistance feedback control," in *2010 IEEE International Conference on Robotics and Biomimetics, ROBIO* (IEEE), 1124–1129. doi: 10.1109/ROBIO.2010.5723486

Villanueva, A., Smith, C., and Priya, S. (2011). A biomimetic robotic jellyfish (Robojelly) actuated by shape memory alloy composite actuators. *Bioinspir. Biomim.* 6:036004. doi: 10.1088/1748-3182/6/3/036004

Wallmersperger, T., Leo, D. J., and Kothera, C. S. (2007). Transport modeling in ionomeric polymer transducers and its relationship to electromechanical coupling. *J. Appl. Phys.* 101:024912. doi: 10.1063/1.2409362

Xiao, J., Duan, J., and Yu, J. (2013). "Design and implementation of a novel biomimetic robotic jellyfish," in *2013 IEEE Int. Conf. Robot. Biomimetics, ROBIO 2013* (Shenzhen), 988–993. doi: 10.1109/ROBIO.2013.6739592

Yeom, S.-W., and Oh, I.-K. (2009). A biomimetic jellyfish robot based on ionic polymer metal composite actuators. *Smart Mater. Struct.* 18:085002. doi: 10.1088/0964-1726/18/8/085002

Yim, W., Lee, J., and Kim, K. J. (2007). An artificial muscle actuator for biomimetic underwater propulsors. *Bioinspir. Biomim.* 2, S31–S41. doi: 10.1088/1748-3182/2/2/S04

Conflict of Interest: The authors declare that the research was conducted in the absence of any commercial or financial relationships that could be construed as a potential conflict of interest.

frontiers in Robotics and AI

ORIGINAL RESEARCH
published: 12 November 2019
doi: 10.3389/frobt.2019.00113

Iterative Learning Control for Motion Trajectory Tracking of a Circular Soft Crawling Robot

*Haozhen Chi[1], Xuefang Li[2], Wenyu Liang[3], Jiawei Cao[4] and Qinyuan Ren[1]**

[1] College of Control Science and Engineering, Zhejiang University, Hangzhou, China, [2] Department of Electrical and Electronic Engineering, Imperial College London, London, United Kingdom, [3] Department of Electrical and Computing Engineering, National University of Singapore, Singapore, Singapore, [4] Temasek Laboratories, National University of Singapore, Singapore, Singapore

Soft robots have recently received much attention with their infinite degrees of freedoms and continuously deformable structures, which allow them to adapt well to the unstructured environment. A new type of soft actuator, namely, dielectric elastomer actuator (DEA) which has several excellent properties such as large deformation and high energy density is investigated in this study. Furthermore, a DEA-based soft robot is designed and developed. Due to the difficulty of accurate modeling caused by nonlinear electromechanical coupling and viscoelasticity, the iterative learning control (ILC) method is employed for the motion trajectory tracking with an uncertain model of the DEA. A D^2 type ILC algorithm is proposed for the task. Furthermore, a knowledge-based model framework with kinematic analysis is explored to prove the convergence of the proposed ILC. Finally, both simulations and experiments are conducted to demonstrate the effectiveness of the ILC, which results show that excellent tracking performance can be achieved by the soft crawling robot.

Keywords: ILC, soft crawling robot, dielectric elastomer actuator, electro-adhesion actuator, knowledge-guided data-driven modeling

OPEN ACCESS

Edited by:
Guoying Gu,
Shanghai Jiao Tong University, China

Reviewed by:
Huichan Zhao,
Tsinghua University, China
Bo Li,
Xi'an Jiaotong University, China

****Correspondence:***
Qinyuan Ren
renqinyuan@zju.edu.cn

Specialty section:
This article was submitted to Soft Robotics, a section of the journal Frontiers in Robotics and AI

Received: *20 July 2019*
Accepted: *16 October 2019*
Published: *12 November 2019*

Citation:
Chi H, Li X, Liang W, Cao J and Ren Q (2019) Iterative Learning Control for Motion Trajectory Tracking of a Circular Soft Crawling Robot. Front. Robot. AI 6:113. doi: 10.3389/frobt.2019.00113

1. INTRODUCTION

Currently, there is a great interest in using the soft robots for practical applications. In contrast to conventional rigid (hard) robots, soft robots are constructed with compliant materials that can be stretched, bent and twisted in new ways. Thus, soft robots possess the potential demonstrating unprecedented adaptation, sensitivity and agility.

Soft actuators play the key role in the soft robots. In previous studies, many soft actuators have been investigated, such as pneumatic muscle actuator (PMA) (Andrikopoulos et al., 2011; Rolf and Steil, 2012; Onal and Rus, 2013), shape memory alloy (SMA) (Koh and Cho, 2009; Yuk et al., 2011) and electroactive polymer (EAP) (Yeom and Oh, 2009; Lau et al., 2014; Godaba et al., 2017). Among these actuators, dielectric elastomer actuators (DEAs) which is one of the EAPs stand out in robotic applications due to their special properties including large deformation, fast response, high energy density, low noise and biological muscle similarities. The muscle-like properties and relatively simple actuation method of DEAs have contributed to developing several bio-inspired soft robots, such as worm-like crawling robots (Shian et al., 2015; Mihai Duduta and Wood, 2017; Cao et al., 2018a), underwater robots (Guo et al., 2012; Li et al., 2017) and human-like robots (Carpi and Rossi, 2005; Liu et al., 2008; Wang and Zhu, 2016). There are two notable work Qin et al. (2018) and Gu et al. (2018) should be pointed out. The work presented in

Qin et al. (2018) focuses on the robot prototype with its motion, while the work presented in Gu et al. (2018) emphasizes more on the adhesion method.

The circular soft crawling robot proposed in Qin et al. (2018) is investigated in this study, which is a promising platforms for practical application or scientific research. This robot uses the DE materials as the robot body, which can not only provide large strain with high deformation, but also realize the similar properties of the biological muscles owing to their similarity. Besides that, four electroadhesion actuators are employed as the robot feet to provide adaptive and low-power bonding adhesion action on the ground surface, which has been described in Gu et al. (2018). In Gu et al. (2018), gave a detailed description of electroadhesion with corresponding experimental demonstrations, which shows the advantages of electroadhesion method. By comparing to the traditional adhesion mechanisms such as suction cup (Longo and Muscato, 2006), adhesive (Murphy and Sitti, 2007; Sangbae et al., 2008), magnetic adsorption (Shen et al., 2014), etc., electroadhesion has two significant advantages: (i) simple structure and easy to be manufactured; (ii) not subjected to the effect of the working surface, only requires the working surface can generate induced charges. However, due to the feature of the electrostatic force and the strength limitation of the applied voltage (electrostatic breakdown), the adhesion force caused by the electroadhesion is much smaller than the vacuum suction force or the electromagnetic force. Nevertheless, in this study, due to the light weight of the robot itself, the required frictional force is not large during its movement process. Therefore, the defect of low adhesion force can be ignored in this study, which makes electroadhesion an appropriate way. Similarly, the electroadhesion method also enables the entire robot to be fully electric-powered, which leads to a consistency with the energy source. The use of DEA and electroadhesion actuators render the robot to be light-weight and fast-response. Moreover, inspired by the bionics, the robot can achieve stable locomotion through alternating expansion/contraction of the body as well as adhesion/release of the feet.

Although the DEA-based soft robots exhibit muscle-like motions in various environments, the studies presented in Qin et al. (2018) and Gu et al. (2018) mainly focus on the robot modality which is based on the open-loop control. Only a few studies on the robot control like (Cao et al., 2018a,b) are available. In addition, there is a major practical challenge lies in the control issue due to the electromechanical coupling and viscoelasticity of the DE materials. Due to the significance of the "control" to the whole system, this study mainly aims to explore the motion control issue of the soft crawling robot for the better performance and greater application value.

Currently, the researches on both open-loop and closed-loop control are extremely limited. In Gu et al. (2015), a feed-forward control approach is proposed for a planar DEA. However, this control approach can not adjust the performance of the control outputs due to the lack of feedback information. In order to enhance the robustness of the control system, feedback control schemes have been adopted in several studies, the notable examples include the classical proportional-integral-derivative (PID) control scheme presented in Rizzello et al. (2015) and Cao et al. (2018a) and the cerebellum-inspired adaptive controller proposed in Wilson et al. (2016), Cao et al. (2018b). It should be pointed out that these previous researches on controlling DEA is primarily restricted with isolated actuators in simple geometries, and the control effect depends on model accuracy due to the model-based property (Rivera et al., 1986; Hong et al., 2014). So far, although various soft robots driven by DEA have been developed (Godaba et al., 2017; Tang et al., 2017), few studies have focused on the motion control of the DEA-based soft robots, which greatly hinders these soft robots from practical application.

The main objective of this work is to address the precise displacement tracking problem of a circular soft crawling robot via iterative learning control (ILC), which is essential to both motion control and motion planning. To our best knowledge, this is a pioneering work in the field of DEA-based soft robot with ILC, which will demonstrate the effectiveness of ILC in the motion control of DEA-based circular crawling robot. ILC, as an effective control strategy, is designed to improve the current performance of uncertain systems by fully utilizing the past control experience. Specifically, ILC is developed for systems that are able to complete some tasks over a finite time interval and perform them repeatedly. In such systems, the input and output information of past cycles, as well as the tracking objective, are used to formulate the input signal for the next iteration, hence the tracking performance could be improved iteratively. By comparing to traditional control techniques, such as PID control and fuzzy logic control, there are a number of distinct features about ILC. Primarily, ILC is designed to handle repetitive tasks. The traditional control methods cannot deal with or take advantage of the periodic nature. Under a repeatable control environment, repeating the same feedback would yield the same control performance. By incorporating learning, ILC is able to improve the control performance iteratively. Apart from this, the control objective is different. ILC tries to achieve perfect tracking during the whole operation interval, whereas most other control methods usually achieve asymptotic error convergence in the time domain. Last but not least, ILC is a partially model-free control method (Tan, 2003). As long as an appropriate learning gain is chosen, the excellent tracking performance can be achieved even when the system parameters are unknown. There is one typical situation for its application for explaining the advantages: when setting the robot in a complex environment where each area has its own terrain features, its optimal parameters are undoubtedly different in each area. In this situation, because that the ILC can adaptively adjust the parameters during the iteration, only a single set of parameters needs to be determined when adapted to the complex environment, without setting separate parameters for each type of environmental information, which really improves robot's applicability and environment adaptability.

Simultaneously, the motivation of adopting ILC for the soft robot control also comes from three aspects. Firstly, due to the action principle of the DEA, generating a desired sequence motion trajectory is essential to actuate the robot in a cluttered environment. In addition, since the DEA only performs

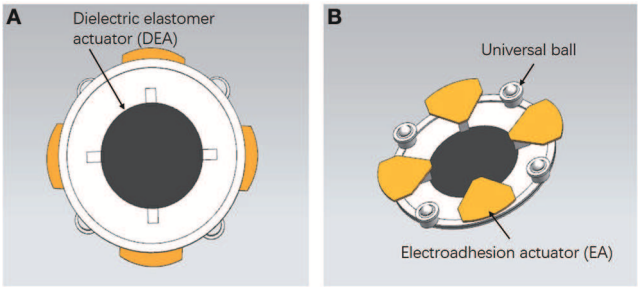

FIGURE 1 | The soft mobile robot prototype. **(A)** Top view of the soft robot. **(B)** The bottom structure of the soft robot.

open-loop control in each action cycle, for the sake of improving the performance of the robot's motion trajectory tracking, the input and output information of the DEA control system in past cycles is generally used to formulate the input signal for the next iteration which is totally repetitive tasks. Secondly, as pointed out by Cao et al. (2018a,b), one of the main reasons that deters us from controlling DEA-based soft robots is its difficulty of obtaining accurate models. Therefore, the model-free control methods can greatly reduce the workload, not to mention its excellent tracking performances. Thirdly, it has been proved that ILC is easy to be implemented. After first proposed by Arimoto et al. (2010), ILC has been extensively studied with significant progress in theory (Bien and Xu, 1998; Bristow et al., 2006), as well as wildly applied in practice, such as industrial robots (Barton and Alleyne, 2010), mobile robots (Ostafew et al., 2013), manipulators (Tayebi and Islam, 2006; Cong et al., 2017), electronic motors (Panda et al., 2008; Mohammadpour et al., 2013), as well as motion control of robotic fish (Li et al., 2016), etc.

The main contribution for this paper is that the model-free iterative learning controller is adopted to eliminated the demand of model accuracy which simplifies the difficult modeling process, and several simulations with relevant experiments are conducted to prove its effectiveness. The rest of this paper is organized as follows. Section 2 introduces the robot platform and its kinematics analysis. In section 3, the dynamical model of the soft robot is built. Section 4 presents the ILC design and its convergence analysis. Furthermore, the efficiency of the proposed ILC scheme is verified by both simulations and experiments in section 5. Finally, the conclusion is given in section 6.

2. SOFT ROBOT DESIGN

A soft crawling robot is designed and fabricated as illustrated in **Figure 1**. The robot mainly consists of a circular DEA and four electroadhesion actuators, which work together to achieve flexible 2D planar crawling. In addition, four passive omnidirectional wheels are mounted on the robot to reduce the moving frictional resistance.

2.1. Robot Body

Figure 2 illusitrates the manufacturing process of the robot body. The DEA is essentially a VHB4910 membrane sandwiched between compliant electrodes. Initially, the membrane is

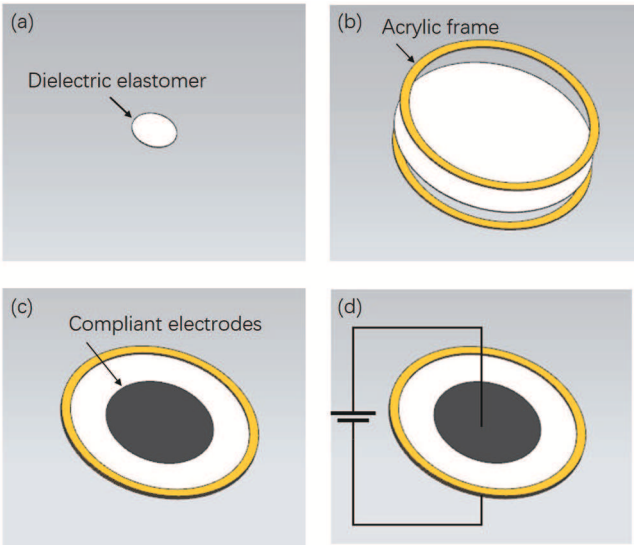

FIGURE 2 | The fabrication process of the robot body. **(a)** Initial state of the Di-electric elastomer film. **(b)** Pre-stretching processing. **(c)** Coating the electrodes. **(d)** Generating the deformation.

subjected to 4 × 4 equal-biaxial pre-stretching with the radius of 100 mm under the constraint of two annular Acrylic frames. Two compliant electrodes are smeared evenly on both surfaces of the membrane to obtain a conductive region. When the high voltage applies, the membrane will result in a thickness reduction and area expansion caused by voltage-induced Maxwell stress (Zhigang, 2010). Moreover, the membrane will restore to its original state under the action of internal elastic contraction force when the voltage is off.

With regard to the specific actuation principle, the electro-mechanical response of DEA relies primarily on the Maxwell force and blocking force, which determine its nature of stretching and contraction (Zhao et al., 2018).

As shown in **Figure 3**, the Maxwell stress perpendicular to the surface of the DE membrane is generally considered to describe the mechanical response of the electrical stimulation, which is essentially the electric field force in the electric field formed between the compliant electrodes on both sides of the membrane. Thus, the specific magnitude of the Maxwell stress can be described by:

$$\sigma_M = \varepsilon_0 \varepsilon_r E^2 = \varepsilon_0 \varepsilon_r (V/d)^2, \tag{1}$$

where ε_0 represents the vacuum dielectric constant, ε_r represents the relative dielectric constant of the material, V is the voltage applied across the membrane, and d is the distance between the two compliant electrodes.

The blocking force refers to the force required to restore the fully energized actuator in the lateral dimension, which is a resistance that needs to be overcome during the actuation. It can be calculated by:

$$\sigma_{block} = F_y / A_y = (x_0 y_0 z_0 \varepsilon_0 \varepsilon_r E^2)/(y A_y), \tag{2}$$

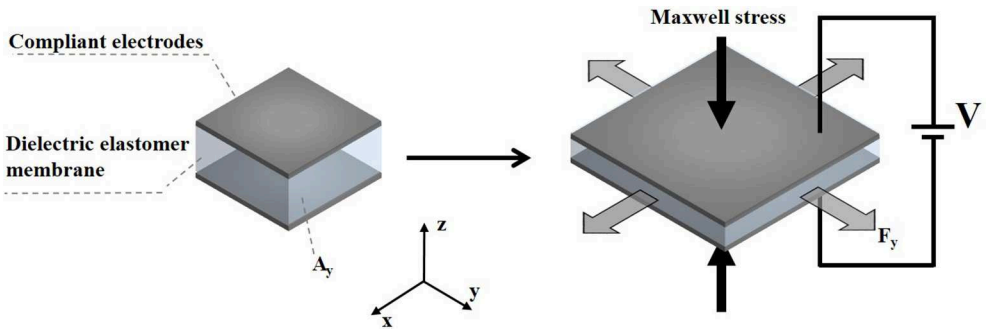

FIGURE 3 | The actuation principle of a DEA. V is the voltage applied across the membrane, A_y indicates the cross-sectional area in the y direction and F_y presents the blocking force in the y direction.

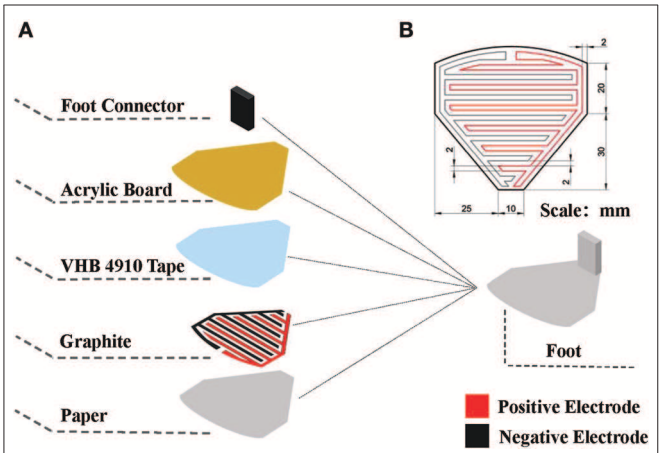

FIGURE 4 | Schematic of the robot foot. **(A)** Exploded view, **(B)** dimensions of the electrode pattern.

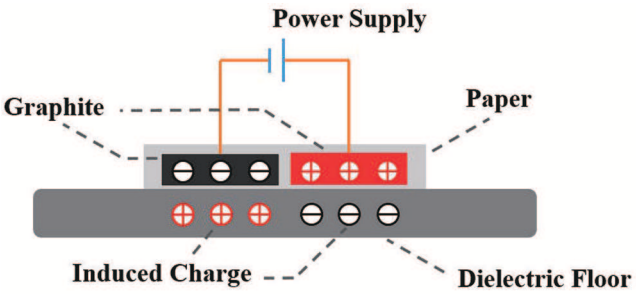

FIGURE 5 | The working principle of a EA.

where A_y indicates the cross-sectional area in the y direction.

2.2. Robot Feet

Figure 4 illustrates the composition of an electroadhesion actuator. The electrode pattern with the dimensions shown in **Figure 4B** is first designed and printed on a ordinary paper. Later on, the area enclosed by the lines is scribbled with graphite by a 2B pencil for creating a conductive region. Finally, pieces of VHB4910 membranes are used to bond the conductive layer to the Acrylic board and its foot connector. It is worth mentioning that the insulation property of the VHB layer also helps to prevent the electrodes from short-circuit via external substances.

As shown in **Figure 5**, when the electroadhesion actuator is subjected to a high voltage, the two electrodes accumulate separately positive and negative charges. Furthermore, the electric field generated by the charged electrodes causes opposite induced charges on the substrate, thereby creating an electroadhesion force (electrostatic attraction force) between the actuator and the substrate (Shintake et al., 2016). Besides, a paper layer is served as an insulating layer to prevent the inductive charges on the substrate from neutralizing the charges on the electrodes. After the absence of a voltage, the charges on the electrodes disappear as well as the electroadhesion force, thereby leading to a reversible adhesion.

2.3. Locomotion

Figure 6A shows the labeling of the four electroadhesion actuators (EAs). Due to the interaction of the four feet, the robot is able to achieve 2D motion. **Figure 6B** schematically demonstrates a periodic single-dimensional movement of this soft robot by the following actuation sequence.

At the first step of the loop, only the foot EA_1 is subjected to the voltage while all the others are not powered. thus the EA_1 adheres to the substrate. At the second step, the EA_3 and the DEA are activated simultaneously, without powering on the remaining EAs. As a result, EA_3 produces an electroadhesion force to fix itself on the substrate, and the robot body extends under the drive of DEA's expanding. Thus, the EA_1 is pushed forward. The third steps repeats the first step with the same voltage signals, causing the EA_1 to be attached on the substrate. Without the voltage induced Maxwell stress, the DEA will return to its original state. Consequently, the EA_3 is pulled toward the DEA's center and hence the entire robot moves forward. Therefore, by repeating the above actuation sequence, the soft robot will gradually move forward cycle by cycle. By reversing the actuation sequence of EA_1 and EA_3, the soft robot can move backwards.

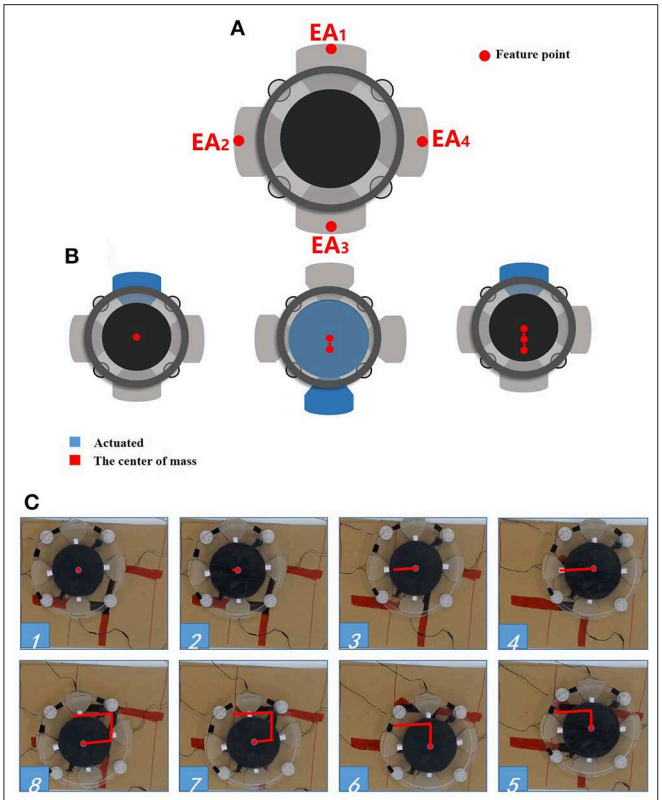

FIGURE 6 | The locomotion of the soft robot. **(A)** The feet number; **(B)** the periodic movement; **(C)** the direct tracking experiment.

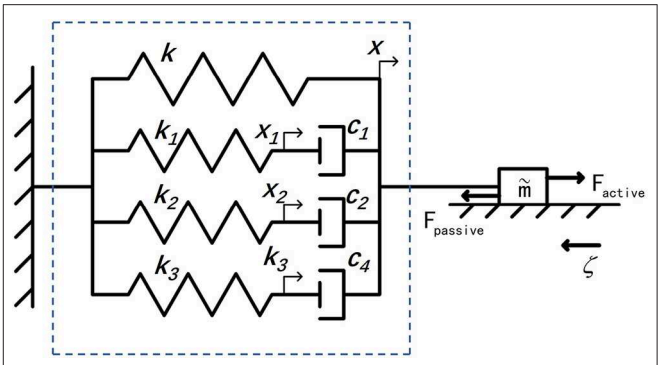

FIGURE 7 | The dynamic model of the DEA, where k, x is the stiffness and the displacement of a linear spring, respectively, x_h presents the spring deformation, k_h presents the spring stiffness, and c_h shows the viscous friction coefficient. Otherwise, F_{active} is the active driving force, $F_{passive}$ means the whole passive resistance generated by the model, ζ illustrate the frictional resistance force during the motion, and $\tilde{m}$ is the equivalent mass of the whole system.

Benefit from the isotropy brought about by the circular structure, the soft robot is able to achieve omnidirectional motion easily which is particularly suitable for unstructured environments.

Figure 6C shows a simple trajectory tracking motion in 2D plane. During the test, an external camera is used to obtain the trajectory information (the "red" line in the figure) as the feedback signals to realize the C-shaped trajectory tracking. As can be seen, the soft robot is able to track the C-shaped trajectory, which shows that the soft robot can achieve omnidirectional motion by using the appropriate sequences of the actuation.

3. KNOWLEDGE-BASED MODELING

Modeling the dynamics of the robot body is critical to the motion controller design. Due to the difficulty of the soft robot modeling, a data-driven ILC method is investigated in this study. Moreover, a knowledge-based model framework is used to build a simplified dynamic model of the DEA that can be used to export the generalization of the proposed ILC scheme.

It should be explained here that the modeling is only for DEA, not including EA, and so as the control scheme mentioned in section 4. This does not mean that the EAs is ignorable, but just because the actuation for them is relatively simple which does not require a complicated processing. Furthermore,the main motion of the robot is generated by the DEA. The EAs are play roles of alternating adhesive via sequential control. The main topic of the motion control of this study focuses on the motion trajectory tracking. Hence, the paper mainly focuses on controller design for the DEA. Thus, for its simple actuation process, we will not elaborate the EA on its modeling and control.

Consider that only the change of displacement and the driving force between the EA feet during the crawling of this soft robot are focused on in this work, the junctions between the DEA and the EA feet are selected as the feature points (see **Figure 6A**). Moreover, the change of displacement between the corresponding feature points is defined as the robot displacement. In view of the similarity between DE materials and biological muscles in terms of viscoelasticity, a simplified spring-dashpot model mentioned in Gu et al. (2017) is employed to describe the single-dimensional physical properties of the DEA. **Figure 7** shows a schematic representation of a dynamic model based on a series of spring-dashpot sets. According to the previous work pointed out in Cao et al. (2018c), a relatively simple third-order system has been used to describe this system. The static tensile force is described by a linear spring with a stiffness k. The spring-dashpot parameters include spring deformation x_h, spring stiffness k_h and viscous friction coefficient c_h $(h = 1, 2, 3)$. The model uncertainties mainly come from the equivalent mass $\tilde{m}$ of the system and the frictional resistance force ζ during the motion. Therefore, the dynamic equations can be given by

$$\tilde{m}\ddot{x} = F_{passive} + F_{active} - \zeta\, sign(\dot{x}), \tag{3a}$$

$$F_{passive} = -kx - \sum_{h=1}^{3} k_h x_h, \tag{3b}$$

$$k_h x_h = c_h(\dot{x} - \dot{x_h}), h = 1, 2, 3. \tag{3c}$$

The voltage induced compression force F_{active} can be considered as the product of an equivalent Maxwell stress and an

equivalent cross-sectional area of the actuator associated with the deformation. Since the Maxwell stress is proportional to the square of the electric field, F_{active} can be written as

$$F_{active} = g(x)V^2, \tag{4}$$

where V is the applied voltage and $g(x)$ is a function of the change of displacement x related to the deformation. Furthermore, it is found that $g(x)$ is a linear function via the experimental analysis, thus (4) can be rewritten as

$$F_{active} = (\alpha x + \beta)V^2, \tag{5}$$

where α and β are the coefficients of the first-order polynomial, the units are $N \cdot cm^{-}1 \cdot kV^{-2}$ and $N \cdot kV^{-2}$. The specific value will be obtained by the experiment.

By converting the above differential equations into a state-space model, we can have

$$\dot{X} = AX + Bu, \tag{6a}$$
$$y = CX, \tag{6b}$$

where

$$u = \frac{F_{active} + \tilde{f}}{\tilde{m}}, F_{active} \geq 0, \tag{7}$$

$$\tilde{f} = -\zeta\, sign(\dot{x}), \tag{8}$$

$$X = \begin{bmatrix} x_1 & x_2 & x_3 & x & \dot{x} \end{bmatrix}^T, \tag{9}$$

and

$$A = \begin{bmatrix} -k_1/c_1 & 0 & 0 & 0 & 1 \\ 0 & -k_2/c_2 & 0 & 0 & 1 \\ 0 & 0 & -k_3/c_3 & 0 & 1 \\ 0 & 0 & 0 & 0 & 1 \\ -k_1/\tilde{m} & -k_2/\tilde{m} & -k_3/\tilde{m} & -k/\tilde{m} & 0 \end{bmatrix}, \tag{10}$$

$$B = \begin{bmatrix} 0 & 0 & 0 & 0 & 1 \end{bmatrix}^T, \tag{11}$$

$$C = \begin{bmatrix} 0 & 0 & 0 & 1 & 0 \end{bmatrix}. \tag{12}$$

Among the model parameters, the stiffness k mainly describes the elastic properties under static conditions, α and β mainly represent the electromechanical coupling relationship, $\tilde{m}$ reflects the mass of the robot platform itself, and ζ is mainly dependent on static properties such as friction coefficient when considering only low-speed motion. The spring stiffness k_h and the viscous friction coefficient c_h determine the robot's dynamic characteristics, reflecting the viscoelasticity and creep property.

4. CONTROLLER DESIGN

In this work, the control objective is to drive the robot to follow a predefined target trajectory. To this end, the ILC scheme is designed. On the basis of the analysis presented in the previous section, the system dynamics of the robot in iteration domain is

$$X_k = AX_k + Bu_k, \tag{13a}$$
$$y_k = CX_k, \tag{13b}$$

where k is the iteration index and

$$u_k \triangleq \frac{V_k^2(\alpha x_k + \beta) - \zeta \,\mathrm{sign}(\dot{x}_k)}{\tilde{m}} \tag{14}$$

is a virtual control input to the system (the actual control input to the robot is the voltage V_k).

To facilitate the convergence analysis, it is assumed that the target trajectory y_d is generated by the following dynamical system

$$X_d = AX_d + Bu_d, \tag{15a}$$
$$y_d = CX_d. \tag{15b}$$

This is a common assumption in the area of ILC. Then, the control objective is to find a sequence of u_k such that the system output y_k can track the desired target y_d as close as possible.

4.1. ILC Design

From the modeling part, it is clear that $CB = 0$, i.e., consequently the relative degree of the system is higher than one, which motivates us to design a higher order ILC scheme. By noting the property $CAB = 1$, a D^2 type ILC law is proposed to the first-order controller (only the last iteration information is referenced in the scheme) (Yin et al., 2009)

$$V_k = \sqrt{\frac{u_k\tilde{m} + \zeta \,\mathrm{sign}(\dot{x}_k)}{\alpha x_k + \beta}}, \tag{16}$$
$$u_{k+1} = u_k + \gamma \ddot{e}_k. \tag{17}$$

where γ means the learning gain that determines the speed and effect of the iteration, as the only parameter need to be set in the whole process.

The convergence of the proposed controller is summarized in Theorem 1.

Theorem 1. *For the system (13), associated with the ILC law (17), the tracking error e_k will converge to zero as $k \to \infty$, if $\gamma \in (0, 2)$.*

Proof: Denote $e_k \triangleq y_d - y_k$, $\Delta X_k \triangleq X_d - X_k$, $\Delta u_k \triangleq u_d - u_k$. By considering the ILC law (17) and the definition of Δu_k, it gives

$$\begin{aligned} \Delta u_{k+1} &= u_d - u_{k+1} \\ &= u_d - (u_k + \gamma \ddot{e}_k) \\ &= \Delta u_k - \gamma \ddot{e}_k. \end{aligned} \tag{18}$$

Since $\Delta\dot{X}_k = A\Delta X_k + B\Delta u_k$ and $CB = 0$, we can obtain

$$\begin{aligned}\dot{e}_k &= \dot{y}_d - \dot{y}_k \\ &= C\Delta\dot{X}_k \\ &= C\left(A\Delta X_k + B\Delta u_k\right) \\ &= CA\Delta X_k \end{aligned} \tag{19}$$

which therefore implies that

$$\begin{aligned}\ddot{e}_k &= CA\Delta\dot{X}_k \\ &= CA^2\Delta X_k + CAB\Delta u_k. \end{aligned} \tag{20}$$

By substituting (20) into (18), there has

$$\begin{aligned}\Delta u_{k+1} &= (1 - \gamma CAB)\Delta u_k - \gamma CA^2\Delta X_k \\ &= (1-\gamma)\Delta u_k - \gamma CA^2\Delta X_k \end{aligned} \tag{21}$$

because $CAB = 1$.

As the solution of (13a) is

$$X_k(t) = e^{At}X_k(0) + \int_0^t e^{A(t-\tau)}Bu_k(\tau)d\tau, \tag{22}$$

then we have

$$\Delta X_k(t) = \int_0^t e^{A(t-\tau)}B\Delta u_k(\tau)d\tau, \tag{23}$$

provided that $X_d(0) = X_k(0)$. Taking norm on both sides of (23) yields

$$\|\Delta X_k(t)\| = \int_0^t e^{a(t-\tau)}b\|\Delta u_k(\tau)\|d\tau, \tag{24}$$

where $a \geq \|A\|$ and $b \geq \|B\|$. Define $\|g(t)\|_\lambda \triangleq \sup_{t\in[0,T]} e^{-\lambda t}\|g(t)\|$, then (24) gives

$$\begin{aligned}\|\Delta X_k(t)\| &\leq be^{at}\int_0^t e^{(\lambda-a)\tau}d\tau\|\Delta u_k(t)\|_\lambda \\ &= b\frac{e^{\lambda t} - e^{at}}{\lambda - a}\|\Delta u_k(t)\|_\lambda. \end{aligned} \tag{25}$$

Hence we have

$$\begin{aligned}\|\Delta X_k(t)\|_\lambda &= \sup_{t\in[0,T]} e^{-\lambda t}\|\Delta X_k(t)\| \\ &\leq b\sup_{t\in[0,T]}\frac{1 - e^{-(\lambda-a)t}}{\lambda - a}\|\Delta u_k(t)\|_\lambda \\ &\leq b\frac{1 - e^{-(\lambda-a)T}}{\lambda - a}\|\Delta u_k(t)\|_\lambda \\ &\triangleq O(\lambda^{-1})\|\Delta u_k(t)\|_\lambda \end{aligned} \tag{26}$$

for a sufficiently large $\lambda > a$.

By taking the λ-norm on both sides of (21) and applying (26), there has

$$\|\Delta u_{k+1}\|_\lambda = (|1-\gamma| + \gamma\|CA^2\|O(\lambda^{-1}))\|\Delta u_k\|_\lambda. \tag{27}$$

Since $|1-\gamma| < 1$, there exists $\delta > 0$ such that $|1-\gamma| + \delta < 1$. By selecting a sufficiently large λ, the following inequality can be satisfied

$$\gamma\|CA^2\|O(\lambda^{-1}) < \delta.$$

There convergence of $\|\Delta u_k\|_\lambda$, i.e., Δu_k, has been proven. According to the convergence of Δu_k and the inequality (26), it is obvious that $\lim_{k\to\infty}\Delta X_k = 0$. Since $e_k(t) = C\Delta X_k(t)$, the convergence of $e_k(t)$, $t \in [0, T]$, can be obtained immediately. □

5. SIMULATION AND EXPERIMENT

In order to verify the effectiveness of the proposed ILC scheme, both simulations and experiments are conducted in this section.

5.1. System Identification

To evaluate the performance of the proposed method, a preliminary evaluation through simulation is conducted so as to reduce the cost of the experiment as well as expedite the experimental process.

The previous studies of the DEA modeling are generally based on the theory of DE material (Zhu et al., 2010; Li et al., 2013; Gu et al., 2017). However, the results of these studies can not totally satisfy the control purpose because the model is described in a set of differential equations and it is quite difficult to be used in model-based controller design (which can make the controller too complex). In this subsection, a data-driven method is employed to identified the knowledge-based model the DEA as mentioned in section 3.

To obtain the specific parameter values in the framework by means of system identification, the experimental setup as shown in **Figure 8** has been developed, which consists of a EA foot (EA_3) fixed with a force sensor while the others are free, and a camera used to record the change of displacement between the feet EA_3 and EA_1.

During the identification experiment, the DEA is driven by an identification signal that is a sinusoidal voltage sweep signal with the frequencies from 0.2 to 1 Hz, the amplitude of 0.36 kV and the offset voltage of 3 kV (the minimum actuate voltage is 1.8 kv). Then, the MATLAB System Identification Toolbox is used to estimate the parameters of the dynamic model. The identification result is shown in **Figure 9A**. The identified parameters are listed in **Table 1**. In addition, the equivalent mass $\tilde{m}$ is 0.12 kg and the frictional resistance force ζ is measured to be $0.1\tilde{m}g$, where g presents the gravity acceleration.

It is also important to emphasize that the robot in this study has obvious creep property, which is a property described by the viscoelasticity subjected to changes in load response over time. The creep property is mainly manifested as: the output deformation of the material with the constant load increase gradually as time goes by. The trend is briefly that

the deformation initially increases rapidly in a short time, then gradually slows down with time passing by, and finally maintains stable. The creep response can be described by a different set of time constants, which in this model are primarily simulated by c_h/k_h $(h = 1, 2, 3)$. Therefore, another conditional constraint occurs in the identification process when considering creep characteristics: the time constants should be incremented step by step. In this way, the representation should comply with $c_1/k_1 < c_2/k_2 < c_3/k_3$. It can be found from **Table 1** that the final adjusted parameters satisfy the above constraints. Consequently the identified model meets the constraints under "viscoelasticity," which means that it has a certain physical property mapping.

After the identification, several signals with different forms (sine waves and triangle waves) and different frequencies are employed to validate the identified model, and the results are shown in **Figures 9B,C**.

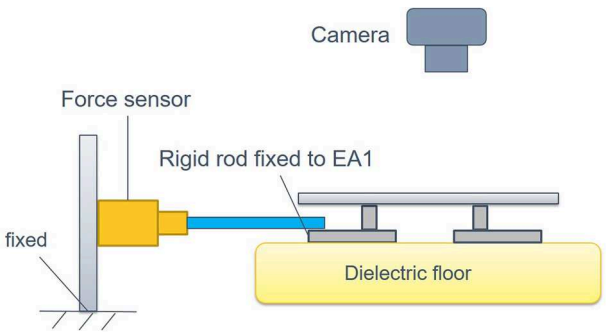

FIGURE 8 | The experiment setup for system identification. Force sensor is used to measure the magnitude of the F_active, and the camera is employed to record the displacement.

As can be observed from the model validation results, the model simulated outputs can roughly match the actual system outputs and accordingly the creep under different voltage signals can be well predicted by this model. However, the simulated outputs do not 100% match the actual output exactly (according to the measured data, the fits between the model and actual system outputs mentioned above are all greater than 85%). More specifically, there is always a slight lag in the initial stage of the response. There are mainly two reasons: (i) there is a deviation in the model identification process, especially for the linearization operation applied to the actual model. After all, the identification process has not been done very accurately, it is just a simplified model. (ii) The intrinsic viscoelasticity with other properties of the DE material will cause some model uncertainties that cannot be predicted and eliminated during the modeling process. Therefore, this deviation cannot be eliminated by barely model parameter adjustment. Such deviation can be considered as part of the model uncertainties. This further embodies the importance of the control system, which can be solved by using a robust controller to compensate the uncertainties.

Obviously, the model developed in this paper is just a simplified version compared to the actual model of the DEA.

TABLE 1 | The identified model parameters.

$\tilde{m}(kg)$		0.12	
$\zeta(N)$		$0.1\tilde{m}g$	
$k(N \cdot cm^{-1})$		3.456	
$\alpha(N \cdot cm^{-1} \cdot kV^{-2})$		3.6	
$\beta(N \cdot kV^{-2})$		-0.25	
$k_1(N \cdot cm^{-1})$	34.64	$c_1(N \cdot cm \cdot s^{-1})$	0.4
$k_2(N \cdot cm^{-1})$	15.2	$c_2(N \cdot cm \cdot s^{-1})$	5.067
$k_3(N \cdot cm^{-1})$	0.0396	$c_3(N \cdot cm \cdot s^{-1})$	12

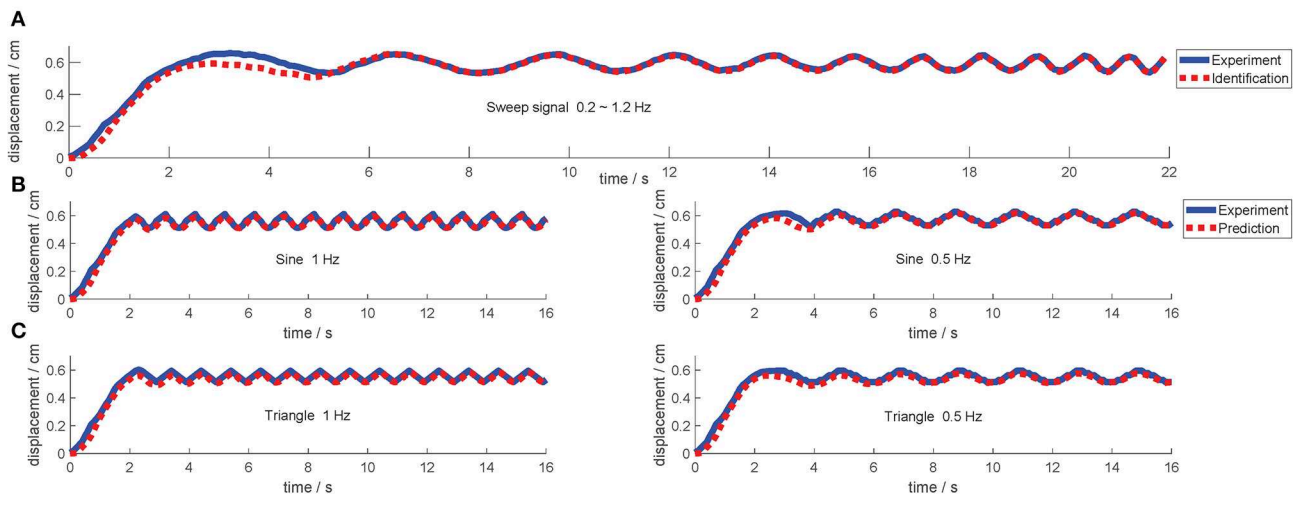

FIGURE 9 | The result of the model identification and validation. The solid line is the response output of the actual model, and the dashed line is the response output of the identified model. **(A)** The identification result applying a sweep voltage signal. **(B,C)** Are validation results applying sine voltage signal and triangle voltage signals, respectively.

The reasons why this simplified model is still acceptable in this study are as follows: (i) this is just a comparative simulation model, while its accuracy does not have much effect on the actual application (ILC works on iterative learning from zero or even unknown, instead of referring to the parameters under identified model); (ii) the excessive pursuit of model accuracy will extremely increase the model complexity and the cost, which is not the main focus in this work.

5.2. Simulation Results

After system identification, a mathematic dynamic model has been explained clearly which will then be used in simulation as the object model. Before simulating, it is necessary to emphasize here that the amplitude of the trajectory should be limited considering the displacement limitation with the physical model (mainly subject to hardware limitation with the characteristic of a high-voltage-induced breakdown, which is expected to be avoided with the method of voltage-limitation, equally to displacement-limitation). Thus, in order to maintain the consistency of the simulation with the actual situation (for subsequent physical verification), only the trajectories with the limited displacement (less than 2 cm) are appropriate to be given in this paper. Further more, the desired motion trajectory is not commonly a cumulative displacement trajectory, but a momentary displacement trajectory, that is, a single step length under the robot's movement at the current moment.

The parameters used in the simulation are given in **Table 1**. According to the dynamic model and the proposed controller, a simple trajectory (28) is first defined to verify the capability of the scheme, which only contains the "rising" curve. Significantly, in the design process, a smooth trajectory is discussed to be necessary for preventing the problems such as "high voltage breakdown" during the entire motion when the actual motion conditions are considered.

$$y_{d,S}(t) = \begin{cases} \dfrac{3t^2}{2000} & (0 \le t \le 4) \\ -\dfrac{3\,(t-20)^2}{8000} + 0.12 & (4 < t \le 20) \\ 0.12 & (t > 20) \end{cases}, \tag{28}$$

The initial input signals are set as $u_0 = 0$ and $\gamma = 0.05$. The simulation result on the this simple trajectory is shown in **Figure 10**. As can be seen, the ILC control scheme can eventually track the expected trajectory well. More specifically, its actual motion trajectory gradually approaches to the target trajectory with the number of iterations increases. After 50 iterations, the output motion trajectory almost completely reaches the desired motion trajectory.

In order to verify the generalization of the proposed ILC scheme, another simulation is carried out. The target motion trajectory is defined as (29) and **Figure 11** shows the simulation result. This trajectory is undoubtedly more complicated because it contains more basic curves such as "rising," "falling," "turning," "peak," "trough," "regress." In this way, the tracking effect of this trajectory can reflect the expected effect of almost all the remaining common curves, which makes it more representative.

$$y_{d,M}(t) = \begin{cases} \dfrac{t^2}{200} & (0 \le t \le 5) \\ -\dfrac{(t-10)^2}{200} + 0.25 & (5 < t \le 10) \\ -3\dfrac{(t-10)^2}{1000} + 0.25 & (10 < t \le 15) \\ 3\dfrac{(t-20)^2}{1000} + 0.1 & (15 < t \le 25) \\ -3\dfrac{(t-30)^2}{1000} + 0.25 & (25 < t \le 30) \\ -\dfrac{(t-30)^2}{200} + 0.25 & (30 < t \le 35) \\ \dfrac{(t-40)^2}{200} & (35 < t \le 40) \\ 0 & (t > 40) \end{cases}, \tag{29}$$

In this simulation, the initial input signals are likewise set to $u_0 = 0$ and $\gamma = 0.05$. As shown in **Figure 11**, the output of the control system can also substantially follow the desired motion trajectory very well after 50 iterations.

For specific simulation data, the MAER illustrates the convergence speed wand convergence accuracy in **Table 2**. After 30 iterations, the MAER can basically shrink to less than 2%, which shows a great efficiency.

As can be discovered from the above results, benefiting from the iterative optimization process of ILC, the control effect (trajectory tracking performance) will become better and better with the continuous repetitive experiments. Thus, under enough iterations, the performance with the ILC will undoubtedly be more excellent than other common controllers as they would remain the same response during the repetitive situation.

In summary, the simulation results indicate that the proposed ILC scheme performs well on the motion trajectory tracking of the soft robot.

5.3. Experimental Results

To verify the effectiveness and the feasibility of the proposed ILC scheme in the real-time application, experiments of motion trajectory tracking are conducted in a wooden desk with the size of 1.8 × 2 m. The experimental platform is the soft robot detailed in section 2. Each EA is actuated by an external voltage amplifier (EMCO Q101-5) which can generate a maximum voltage of 10 kV. The DEA is actuated by an adjustable amplifier (Dongwen) which could be controlled by a micro-controller. Furthermore, an embedded micro-controller (Arduino UNO) is used to receive the external sensor signals and calculate the specific execution steps to control the specific actions of the robot through internal procedures. In addition, an Opti-tracking system is adopted to capture the motion of the robot precisely as well as get accurate acceleration errors $\ddot{e}$ at every moment.

The proposed ILC controller is model-free and the feedback information is off-line. However, the comparison between the model-free control schemes can hardly reflect the specific performance quantitatively. Hence, there is no comparative analysis between different control schemes in this study.

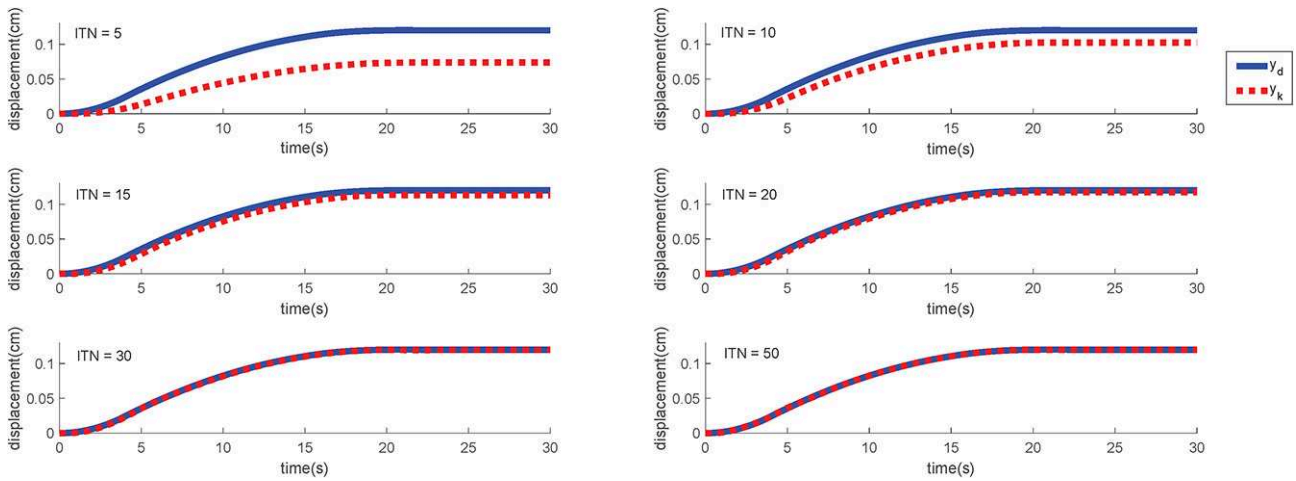

FIGURE 10 | The simulation results of S-type signal under different iterations. ITN indicates the iteration numbers.

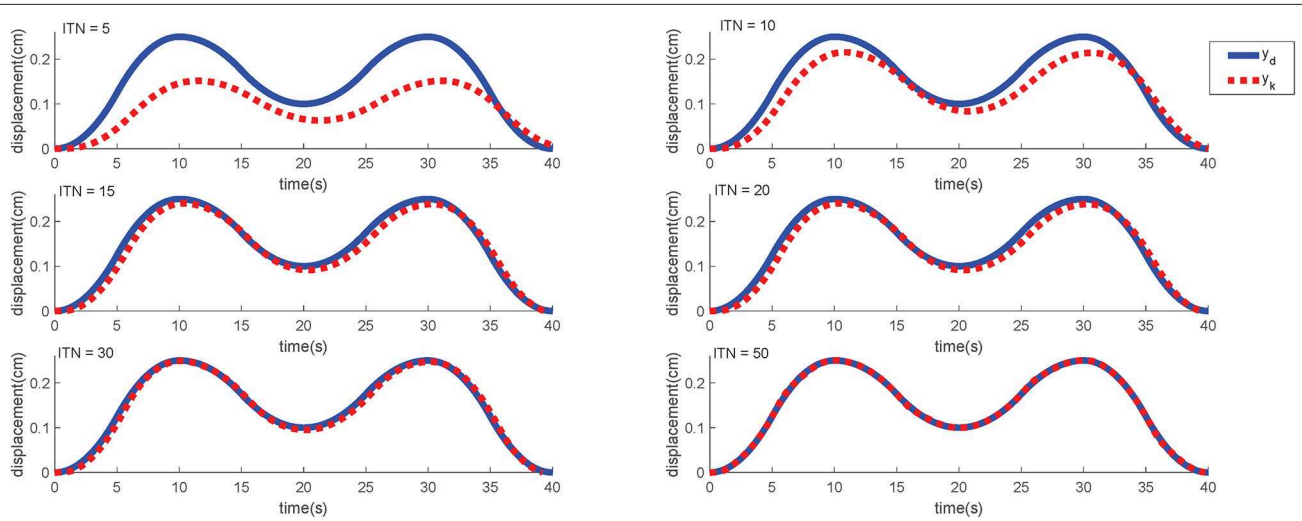

FIGURE 11 | The simulation results of M-type signal under different iterations. ITN indicates the iteration numbers.

TABLE 2 | The convergence effect during the simulation.

ITN*		5%	10%	15%	20%	30%	50%
MAER**	*S – type*	47.53	18.75	7.39	3.76	1.11	0.51
	M – type	52.28	24.78	13.26	7.17	1.78	1.42
	Experiment	75.26	49.52	29.18	9.82		

**ITN indicates the iteration numbers.*

***MAER means Maximum Absolute Error Rate, its expression is MAER* $= \frac{e_{max}}{y_{dmax}}$. e_{max} *means the max error in the current iteration,* y_{dmax} *presents the max displacement in the desired trajectory.*

Considering the cost of time and the overlapping between the above two trajectories, we only apply the more complex "M-shaped" trajectory in the experiment.

Similar to the simulation, the desired trajectory is given by (29) and the learning gain is set as $\gamma = 1$. The initial control input as the zeroth iteration is the same as that in the simulation. **Figure 12** shows the learning performance in each iteration cycle. One point should be mention here that the actual input is the voltage while the final output is displacement. Since that the voltage curves have a great relationship with the displacement curves according to the analysis in the section 3, the voltage curves would not be characterized for the sake of brevity.

As can be found from the experimental results, the motion trajectory at the first iteration has a very large tracking error from the desired trajectory. After that, the tracking error is gradually reduced under the control of the learning controller cycle-by-cycle and it can be almost eliminated to be zero after 20 iterations (the MAER is within 10% referring to **Table 2**). For the whole iterating time, it takes about 10 min to train a perfect control solution out without repetition. And for more details, we could find out that the overall trend with the motion is

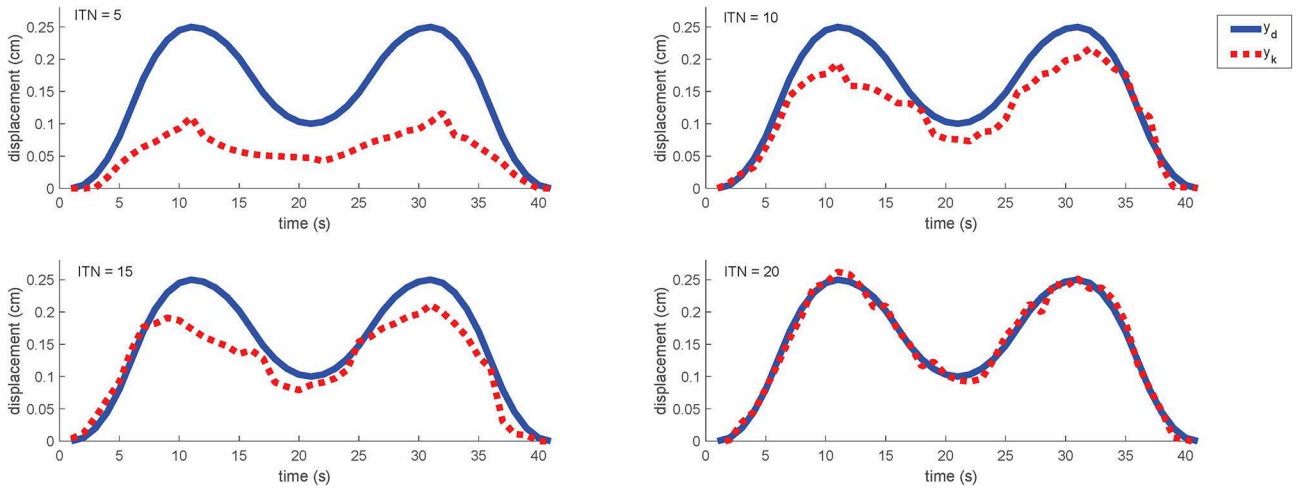

FIGURE 12 | Motion trajectory profiles in different iteration cycle and ITN indicates the iteration numbers. Sampling time is set as 1 s, and the iteration period is 40 s.

always consistent to the desired trajectory, while the optimization progress is strengthened steadily. As an online-adjusting with model-free controller (Tan, 2003), the ILC performs really good compared with other typical controllers in the consideration of adaptability and complexity. Hence, the experimental results also reveal that the proposed ILC scheme is effective for the motion trajectory tracking of the soft robot, equally it can help the system to achieve pretty good tracking performance.

6. CONCLUSION

In this study, an ILC method is proposed and applied to a DEA-based circular soft crawling robot in real-time which can achieve precise motion trajectory tracking performance. Both the simulation results and experimental results verify that the effectiveness of the ILC for the motion control of DEA-based soft robots. The main work of this study can be summarized as follows.

(i) According to the feature of DE materials, an electrically driven soft crawling robot combining the DEA with EAs referring to Qin et al. (2018) is built. It has the advantages of omnidirectional motion and periodic motion mode. This is a kind of minimalist robot unit, which can be assembled with other components in the future to realize some more complex functional robots. Furthermore, with the isotropy of the circular structure, the analysis of motion characteristics can be greatly simplified.

(ii) A knowledge-based model framework, consisting of a series of spring-dashpot sets that usually employed to simulate the model of biological muscles, is used due to the similarities between the DEA and the biological muscle. In this way, the model of the DEA not only contains the priori knowledge but also simplify the representation of the practical DEA physical model, which can reduce the difficulty of the controller design.

(iii) A partially model-free controller: ILC is employed for the motion trajectory tracking control, which can eliminate the difficulty of the accurate modeling. The periodic motion mode of the robot is fully conformed to the applicable range of the ILC controller. It is essential that the ILC scheme can help to compensate the uncertainties adaptively.

(iv) Both simulations and experiments are conducted to verify the effectiveness of the developed soft robot and the proposed control scheme. The results show that the ILC scheme can help the robot to achieve excellent motion trajectory tracking performance in the case of the imperfect model.

DATA AVAILABILITY STATEMENT

The raw data supporting the conclusions of this manuscript will be made available by the authors, without undue reservation, to any qualified researcher.

AUTHOR CONTRIBUTIONS

All authors contributed to the manuscript drafting and writing. HC developed the robot prototype, designed the controller, conducted the simulations, and experiments. XL designed and analyzed the controller. WL and JC provided the guidance and support on the system design, modeling, and integration. QR conceived and supervised this research study.

FUNDING

This work was supported by the Open Research Project of the State Key Laboratory of Industrial Control Technology, Zhejiang University, China (No. ICT1900315).

REFERENCES

Andrikopoulos, G., Nikolakopoulos, G., and Manesis, S. (2011). "A survey on applications of pneumatic artificial muscles," in *19th Mediterranean Conference on Control & Automation (MED)* (Corfu: IEEE). doi: 10.1109/MED.2011.5982983

Arimoto, S., Kawamura, S., and Miyazaki, F. (2010). Bettering operation of robots by learning. *J. Field Robot.* 1, 123–140. doi: 10.1002/rob.4620010203

Barton, K. L., and Alleyne, A. G. (2010). A norm optimal approach to time-varying ILC with application to a multi-axis robotic testbed. *IEEE Trans. Cont. Syst. Technol.* 19, 166–180. doi: 10.1109/TCST.2010.2040476

Bien, Z., and Xu, J. X. (1998). *Iterative Learning Control: Analysis, Design, Integration and Applications*. Dordrecht: Kluwer Academic Publishers.

Bristow, D., Tharayil, M., and Alleyne, A. (2006). A survey of iterative learning control. *IEEE Cont. Syst.* 26, 96–114. doi: 10.1109/MCS.2006.1636313

Cao, J., Liang, W., Ren, Q., Gupta, U., Chen, F., and Zhu, J. (2018a). "Modelling and control of a novel soft crawling robot based on a dielectric elastomer actuator," in *2018 IEEE International Conference on Robotics and Automation (ICRA)* (Brisbane), 4188–4193. doi: 10.1109/ICRA.2018.8460784

Cao, J., Liang, W., Zhu, J., and Ren, Q. (2018b). Control of a muscle-like soft actuator via a bioinspired approach. *Bioinspirat. Biomimet.* 13:066005. doi: 10.1088/1748-3190/aae1be

Cao, J., Qin, L., Liu, J., Ren, Q., Foo, C. C., Wang, H., et al. (2018c). Untethered soft robot capable of stable locomotion using soft electrostatic actuators. *Extreme Mech. Lett.* 21, 9–16. doi: 10.1016/j.eml.2018.02.004

Carpi, F., and Rossi, D. D. (2005). "Eyeball pseudo-muscular actuators for an android face," in *in Smart Structures and Materials 2005: Electroactive Polymer Actuators and Devices (EAPAD)* (San Diego, CA). doi: 10.1117/12.594026

Cong, W., Zheng, M., Wang, Z., Cheng, P., and Tomizuka, M. (2017). Robust iterative learning control for vibration suppression of industrial robot manipulators. *J. Dyn. Syst. Meas. Cont.* 140:011003. doi: 10.1115/1.4037265

Godaba, H., Li, J., Wang, Y., and Zhu, J. (2017). A soft jellyfish robot driven by a dielectric elastomer actuator. *IEEE Robot. Automat. Lett.* 1:1. doi: 10.1109/LRA.2016.2522498

Gu, G., Zou, J., Zhao, R., Zhao, X., and Zhu, X. (2018). Soft wall-climbing robots. *Sci. Robot.* 3:eaat2874. doi: 10.1126/scirobotics.aat2874

Gu, G.-Y., Gupta, U., Zhu, J., Zhu, L.-M., and Zhu, X. (2017). Modeling of viscoelastic electromechanical behavior in a soft dielectric elastomer actuator. *IEEE Trans. Robot.* 99, 1–8. doi: 10.1109/TRO.2017.2706285

Gu, G.-Y., Gupta, U., Zhu, J., Zhu, L.-M., and Zhu, X.-Y. (2015). Feedforward deformation control of a dielectric elastomer actuator based on a nonlinear dynamic model. *Appl. Phys. Lett.* 107:836. doi: 10.1063/1.4927767

Guo, S., Shi, L., Xiao, N., and Asaka, K. (2012). A biomimetic underwater microrobot with multifunctional locomotion. *Robot. Auton. Syst.* 60, 1472–1483. doi: 10.1016/j.robot.2012.07.013

Hong, X., Iplikci, S., Chen, S., and Warwick, K. (2014). A model-based pid controller for hammerstein systems using b-spline neural networks. *Int. J. Adapt. Cont. Sig. Process.* 28, 412–428. doi: 10.1002/acs.2293

Koh, J. S., and Cho, K. J. (2009). "Omegabot: biomimetic inchworm robot using sma coil actuator and smart composite microstructures (SCM)," in *IEEE International Conference on Robotics & Biomimetics* (Guilin). doi: 10.1109/ROBIO.2009.5420752

Lau, G. K., Lim, H.-T., Teo, J.-Y., and Chin, Y.-W. (2014). Lightweight mechanical amplifiers for rolled dielectric elastomer actuators and their integration with bio-inspired wing flappers. *Smart Mater. Struct.* 23, 25021–25033(13). doi: 10.1039/9781782625209

Li, T., Keplinger, C., Baumgartner, R., Bauer, S., Yang, W., and Suo, Z. (2013). Giant voltage-induced deformation in dielectric elastomers near the verge of snap-through instability. *J. Mech. Phys. Solids* 61, 611–628. doi: 10.1016/j.jmps.2012.09.006

Li, T., Li, G., Liang, Y., Cheng, T., Dai, J., Yang, X., et al. (2017). Fast-moving soft electronic fish. *Sci. Adv.* 3:e1602045. doi: 10.1126/sciadv.1602045

Li, X., Ren, Q., and Xu, J. (2016). Precise speed tracking control of a robotic fish via iterative learning control. *IEEE Trans. Indust. Electr.* 63, 2221–2228. doi: 10.1109/TIE.2015.2499719

Liu, Y., Liang, S., Liu, L., Zhen, Z., and Leng, J. (2008). "Inflated dielectric elastomer actuator for eyeball's movements: fabrication, analysis and experiments," in *Proceedings of SPIE - The International Society for Optical Engineering* (Canterbury), 6927.

Longo, D., and Muscato, G. (2006). The alicia3 climbing robot: a three-module robot for automatic wall inspection. *Robot. Automat. Mag. IEEE* 13, 42–50. doi: 10.1109/MRA.2006.1598052

Mihai Duduta, D. R. C., and Wood, R. J. (2017). "A high speed soft robot based on dielectric elastomer actuators," in *Proceedings - IEEE International Conference on Robotics and Automation* (Singapore), 4346–4351.

Mohammadpour, A., Mishra, S., and Parsa, L. (2013). "Iterative learning control for fault-tolerance in multi-phase permanent-magnet machines," in *American Control Conference* (Washington, DC), 5929–5934.

Murphy, M. P., and Sitti, M. (2007). Waalbot: an agile small-scale wall-climbing robot utilizing dry elastomer adhesives. *IEEE/ASME Trans. Mechatr.* 12, 330–338. doi: 10.1109/TMECH.2007.897277

Onal, C. D., and Rus, D. (2013). Autonomous undulatory serpentine locomotion utilizing body dynamics of a fluidic soft robot. *Bioinspir. Biomimet.* 8:026003. doi: 10.1088/1748-3182/8/2/026003

Ostafew, C. J., Schoellig, A. P., and Barfoot, T. D. (2013). "Visual teach and repeat, repeat, repeat: iterative learning control to improve mobile robot path tracking in challenging outdoor environments," in *IEEE/RSJ International Conference on Intelligent Robots & Systems* (Tokyo), 176–181. doi: 10.1109/IROS.2013.6696350

Panda, S. K., Xu, J. X., and Qian, W. (2008). "Review of torque ripple minimization in pm synchronous motor drives," in *Power & Energy Society General Meeting-conversion & Delivery of Electrical Energy in the Century* (Pittsburgh), 1–6. doi: 10.1109/PES.2008.4596931

Qin, L., Tang, Y., Gupta, U., and Zhu, J. (2018). A soft robot capable of 2d mobility and self-sensing for obstacle detection and avoidance. *Smart Mater. Struct.* 27. doi: 10.1088/1361-665X/aab393

Rivera, D. E., Morari, M., and Skogestad, S. (1986). Internal model control: pid controller design. *Indust. Eng. Chem. Process Design Dev.* 25, 2163–2163. doi: 10.1021/i200032a041

Rizzello, G., Naso, D., York, A., and Seelecke, S. (2015). Modeling, identification, and control of a dielectric electro-active polymer positioning system. *IEEE Trans. Cont. Syst. Technol.* 23, 632–643. doi: 10.1109/TCST.2014.2338356

Rolf, M., and Steil, J. J. (2012). "Constant curvature continuum kinematics as fast approximate model for the bionic handling assistant," in *IEEE/RSJ International Conference on Intelligent Robots & Systems* (Tsukuba), 3440–3446. doi: 10.1109/IROS.2012.6385596

Sangbae, K., Spenko, M., Trujillo, S., Heyneman, B., Santos, D., and Cutkosky, M. (2008). Smooth vertical surface climbing with directional adhesion. *IEEE Trans. Robot.* 24, 65–74. doi: 10.1109/TRO.2007.909786

Shen, W., Gu, J., and Shen, Y. (2014). Permanent magnetic system design for the wall-climbing robot. *Appl. Bionics Biomech.* 3, 2078–2083. doi: 10.1109/ICMA.2005.1626883

Shian, S., Bertoldi, K., and Clarke, D. R. (2015). "Use of aligned fibers to enhance the performance of dielectric elastomer inchworm robots," in *Proceedings of SPIE - The International Society for Optical Engineering* (Canterbury), 9430.

Shintake, J., Rosset, S., Schubert, B., Floreano, D., and Shea, H. (2016). Versatile soft grippers with intrinsic electroadhesion based on multifunctional polymer actuators. *Adv. Mater.* 28, 231–238. doi: 10.1002/adma.201504264

Tan, Y. (2003). Linear and nonlinear iterative learning control. *Lect. Notes Cont. Informat. Sci.* 291:xii175.

Tang, Y., Lei, Q., Li, X., Chew, C. M., and Jian, Z. (2017). "A frog-inspired swimming robot based on dielectric elastomer actuators," in *IEEE/RSJ International Conference on Intelligent Robots & Systems* (Vancouver, BC), 2403–2408.

Tayebi, A., and Islam, S. (2006). Adaptive iterative learning control for robot manipulators: experimental results. *Cont. Eng. Pract.* 14, 843–851. doi: 10.1016/j.conengprac.2005.04.013

Wang, Y., and Zhu, J. (2016). Artificial muscles for jaw movements. *Extreme Mech. Lett.* 6, 88–95. doi: 10.1016/j.eml.2015.12.007

Wilson, E. D., Assaf, T., Pearson, M. J., Rossiter, J. M., Anderson, S. R., Porrill, J., et al. (2016). Cerebellar-inspired algorithm for adaptive control of nonlinear dielectric elastomer-based artificial muscle. *J. R. Soc. Interface* 13:20160547. doi: 10.1098/rsif.2016.0547

Yeom, S. W., and Oh, I.-K. (2009). A biomimetic jellyfish robot based on ionic polymer metal composite actuators. *Smart Mater. Struct.* 18:085002. doi: 10.1088/0964-1726/18/8/085002

Yin, C., Xu, J. X., and Hou, Z. (2009). "Iterative learning control design with high-order internal model for nonlinear systems," in *IEEE Conference on Decision & Control* (Shanghai), 434–439.

Yuk, H., Kim, D., Lee, H., Jo, S., and Shin, J. H. (2011). Shape memory alloy-based small crawling robots inspired by elegans. *Bioinspirat. Biomimet.* 6:046002. doi: 10.1088/1748-3182/6/4/046002

Zhao, Z., Shuai, C., Zhang, S., Amp, I. N., Vibration, and Engineering, N. U. (2018). Dynamic behavior analysis of dielectric elastomer actuating unit. *J. Mater. Sci. Eng.* 36, 31–34. doi: 10.14136/j.cnki.issn1673-2812.2018.01.007

Zhigang (2010). Theory of dielectric elastomers. *Acta Mech. Solid. Sin.* 23, 549–578. doi: 10.1016/S0894-9166(11)60004-9

Zhu, J., Stoyanov, H., Kofod, G., and Suo, Z. (2010). Large deformation and electromechanical instability of a dielectric elastomer tube actuator. *J. Appl. Phys.* 108:77. doi: 10.1063/1.3490186

Conflict of Interest: The authors declare that the research was conducted in the absence of any commercial or financial relationships that could be construed as a potential conflict of interest.

frontiers in Robotics and AI

REVIEW
published: 19 November 2019
doi: 10.3389/frobt.2019.00114

PEDOT-Based Conducting Polymer Actuators

Faqi Hu, Yu Xue, Jingkun Xu and Baoyang Lu**

School of Pharmacy, Jiangxi Science and Technology Normal University, Nanchang, China

Conducting polymers, particularly poly(3,4-ethylenedioxythiophene) (PEDOT) and its complex with poly(styrene sulfonate) (PEDOT:PSS), provide a promising materials platform to develop soft actuators or artificial muscles. To date, PEDOT-based actuators are available in the field of bionics, biomedicine, smart textiles, microactuators, and other functional applications. Compared to other conducting polymers, PEDOT provides higher conductivity and chemical stability, lower density and operating voltages, and the dispersion of PEDOT with PSS further enriches performances in solubility, hydrophility, processability, and flexibility, making them advantageous in actuator-based applications. However, the actuators fabricated by PEDOT-based materials are still in their infancy, with many unknowns and challenges that require more comprehensive understanding for their current and future development. This review is aimed at providing a comprehensive understanding of the actuation mechanisms, performance evaluation criteria, processing technologies and configurations, and the most recent progress of materials development and applications. Lastly, we also elaborate on future opportunities for improving and exploiting PEDOT-based actuators.

Keywords: conducting polymer, PEDOT, PEDOT:PSS, actuator, artificial muscle

OPEN ACCESS

Edited by:
Guoying Gu,
Shanghai Jiao Tong University, China

Reviewed by:
Fan Wang,
Zhejiang Sci-Tech University, China
Hidenori Okuzaki,
University of Yamanashi, Japan
Kai Zhang,
Beijing Institute of Technology, China

****Correspondence:***
Jingkun Xu
xujingkun1971@yeah.net
Baoyang Lu
lby1258@163.com

Specialty section:
This article was submitted to Soft Robotics, a section of the journal Frontiers in Robotics and AI

Received: *20 July 2019*
Accepted: *16 October 2019*
Published: *19 November 2019*

Citation:
Hu F, Xue Y, Xu J and Lu B (2019) PEDOT-Based Conducting Polymer Actuators. Front. Robot. AI 6:114. doi: 10.3389/frobt.2019.00114

INTRODUCTION

Muscles are the indispensable constituents of the human body, ranging from information transfer to energy supply and transmission; thus, there is tremendous interest in their related artificial products like "artificial muscles." Nowadays so-called artificial muscles are utilized as electroactive polymer (EAP) actuators in medicine, bionics, cell biology, and microelectromechanical systems (Jager et al., 2000; Otero et al., 2012; Agrawal et al., 2019; Jayathilaka et al., 2019). The actuator is considered as a device that can achieve the conversion from external stimuli (such as electrical, thermal, optical energy) to mechanical formalization (Panda and Acharya, 2019); such devices could therefore be developed into "artificial muscles," but it is a challenging task. In the 1950s, McKibben et al. first reported a pneumatic actuator as a powertrain for artificial muscles, but such actuators were bulky and limited by the auxiliary system (Klute et al., 1999). Generators and hydraulic systems are also limited by bulky volumes, and their flexibility, strength, and overall working ability are far from those of human muscles. Subsequently, shape memory alloys (SMAs) (Huang, 2002) and electroactive ceramics (EACs) (O'Halloran et al., 2008) were used as artificial muscle materials, but they still suffered from the shortcomings of slow response speed, unpredictable movement, limited size, large brittleness, small strain capabilities, and high power consumption.

Until later, various electroactive polymers (EAPs) were used to fabricate actuating devices that could generate physical deformation under the action of the current, voltage, or electric field, and they are distinguished by their ability to convert electrical energy into mechanical energy (Bar-Cohen and Anderson, 2019). In comparison to electroactive ceramics and shape memory alloys, see Halloran's work for details (O'Halloran et al., 2008), actuators fabricated by EAPs can present lower driving potential and are easier to miniaturize. EAPs are the current promising artificial biological muscles, owing to their high resilience and fracture toughness, ability to engender large actuation strains, and inherent vibration-damping properties, which are referred to as artificial muscles in many reports (Bar-Cohen, 2000, 2002; Asplund et al., 2010). According to the deformation mechanism, EAPs can be divided into two categories (Smela, 2003; Romasanta et al., 2015; Kongahage and Foroughi, 2019; Melling et al., 2019). One is the electric field active material (also known as electronic EAPs), which is driven by electric fields or electrostatic action (Coulomb force) in dry environments. Their actuation typically requires high voltage (about 20 V μm^{-1}) (Melling et al., 2019) and specialized electronic equipment, which limits certain applications. The other current-active material is ionic EAPs driven by the mobility or diffusion of ions in solution or air environment. These are typically composed of ionic polymer gels, carbon nanotubes, ionic polymer-metal composites, and conducting polymers, which can be utilized to create soft and small actuators operating under low voltages (typically 1–7 V) (Kongahage and Foroughi, 2019). Among the ionic EAP actuators, ionic polymer metal composite (IPMC) and conductive polymer (CP) actuators have been widely studied (Kruusamäe et al., 2015). IPMCs can be driven at a voltage range (typically 1–4 V) and produce strains (about 0.5–3.3%). By contrast, CPs can be driven at a smaller voltage (typically 1-3 V) and provide a larger strain range (0.5%–12%) at the same time (Madden et al., 2004). Moreover, the more unique properties of CPs, such as holding strain under DC voltage or at open circuit, make it easy to produce consistent material and miniaturization. All these advantages make them promising materials for soft actuators (Melling et al., 2019).

Among the conducting polymers, only a few are used to design actuators. Material selection is mainly focused on polypyrrole (PPy), which has been fully studied and can be used in large-scale production (Berdichevsky and Lo, 2006; Kiefer et al., 2007). The PPy has advantages that can generate large actuation strain and stress and easily deposit dense or porous gel films in aqueous solutions or organic electrolytes (Hara and Takashima, 2004; Zainudeen et al., 2008; Temme et al., 2012). However, PPy also suffers from several drawbacks, such as high rigidity, low conductivity, ion diffusion rate, and the risk of over-oxidation (Madden et al., 2001; Temmer, 2013). Poly(3,4-ethylenedioxythiophene) (PEDOT) has been extensively studied for its high, stable, and tunable electrical conductivity (Wang, 2009). Its conductivity in the doped state is one order of magnitude higher than that of PPy and can be further improved by blending or post-treatment (Gueye, 2016). Besides, the highly stable oxidized state enables it to maintain conductivity for several months even in high temperature, and thus would considerably improve the cycling stability of actuators, which makes it an excellent choice for actuator electrode materials (Temmer, 2013). Meanwhile, the synthesis of PEDOT is simpler and more controllable either by chemical or electrochemical methods, while PPy synthesized by chemical methods is usually powder, insoluble in water or organic solvents (Joo et al., 2000; Ha et al., 2004). Also, the ease of structural modification on thiophene ring, ethylene, and dioxy group and also the main backbone can readily obtain numerous PEDOT analogues (Chen et al., 2012; Lu et al., 2013; Feng et al., 2015), derivatives (Ming et al., 2015b; Lin et al., 2017), and it-based copolymers (Lu et al., 2014; Ming et al., 2015a). In addition, dispersing PEDOT with PSS to form PEDOT:PSS aqueous solution improves the solubility, hydrophilicity, processability, and flexibility of PEDOT materials, further enriching their application in actuator areas (Lu et al., 2019; Rohtlaid, 2019; Yuk et al., 2019).

Starting with the work of Inganäs and coworkers, experiments with electrical stimulation of PEDOT film have shed light on the deformation mechanism of the freestanding polymer film, leading to the development of PEDOT actuators (Chen et al., 1996). To date, many researchers have focused their attention on the actuators fabricated by PEDOT and PEDOT:PSS and have made great effort to promote their development. PEDOT-based actuators have developed into many configurations, such as self-supporting thin films, double or three-layer composite thin films, and fiber or film micro-actuators, which can realize linear, bending, or buckling in solution or air. Plenty of studies have been devoted to blending or doping PEDOT or PEDOT:PSS electrodes with other polymers, inorganic carbon materials, or developing novel polymer electrolytes to improve the electrochemical and mechanical properties of the actuators. PEDOT-based actuators with high stress (up to 50 MPa) (Wang et al., 2017) and strain (up to 2%) (Vandesteeg et al., 2003), low voltage (typically 1–3 V) (Kotal et al., 2016), and a long cycle life (up to 10^6 cycles) (Vidal et al., 2004) have therefore been developed. While commendable advances are presented in actuators based on PEDOT and PEDOT:PSS, some inherent limitations remain as big challenges, e.g., low strain, poor cycle life, and a need for an electrolyte source, etc. Thus, a deeper understanding of the structure-performance relationship of these materials is vital for the future development of PEDOT-based actuators. In this review, we provide a brief overview of the advancements of PEDOT-based conducting polymer actuators and discuss fundamental actuation mechanisms, configurations, evaluation metrics of actuation performances, and material properties in detail. On this basis, advances in materials, manufacture technology, and application are reviewed. We also point out the remaining challenges and opportunities and hope to bring new insights for the further development of PEDOT-based actuators.

ACTUATION MECHANISMS

The key to the actuation behavior of CP's actuator depends on the volume change of polymer film electrodes during the electrochemical doping/dedoping process. When applying a

voltage, electrons will be lost or accepted in the conductive polymer chain. In order to maintain the charge neutrality in the whole structure, anions and cations in the electrolyte will migrate between the polymer matrix and the surrounding electrolyte environment, resulting in the expansion or contraction of the polymer film electrodes, causing the geometric deformation of the whole actuator (Melling et al., 2019). On the other hand, CPs like PEDPT: PSS have a porous structure and easily absorb or desorb water; thus, changing the water content can also cause the expansion or shrinkage of the polymer film. The ions doping/dedoping mechanism of p-doped polymer based on PEDOT and the moisture sorption/desorption mechanism based on PEDOT:PSS are discussed as below.

Ions Doping/Dedoping Mechanism

PEDOT is typically produced by an oxidative polymerization process. During the oxidation process, with the removal of electrons, the crosslink behavior formed between the generated polarons and dopant anions and the insertion of anions causes the PEDOT film to be swollen in the oxidized state. When a negative voltage is applied, depending on the size of the neutralized anions in the polymer chain, there are two ways of anion migration or cation migration to occur in the reduction process, which leads to shrinkage or expansion of the PEDOT film in the reduced state (Bay et al., 2001; Bund and Neudeck, 2004; Yang and Zoski, 2006).

When the dopant anion size in the PEDOT chain is small and mobile (**Figure 1A**), such as *p*-toluenesulfonic acid (PTSA), through applying a negative voltage, anions and solvent molecules can be easily expelled to maintain the neutralization of the PEDOT film, which causes the film to shrink in the reduced state. Oxidation occurred when voltage reversal, anions, and solvent molecules in the electrolyte move in, and the PEDOT film expands again in the oxidation state. The redox process is dominated by anion migration, and so it is called "anion-driven." When the dopant anions in the PEDOT chain are large and immobile (**Figure 1B**), such as polystyrene sulfonate (PSS), they become wrapped in the polymer matrix during the synthesis process and cannot leave during the reduction. At this time, cations migrate from the solution to the PEDOT chain to neutralize anions and negative charges, which causes the film to expand in the reduced state. Applying positive voltage again,

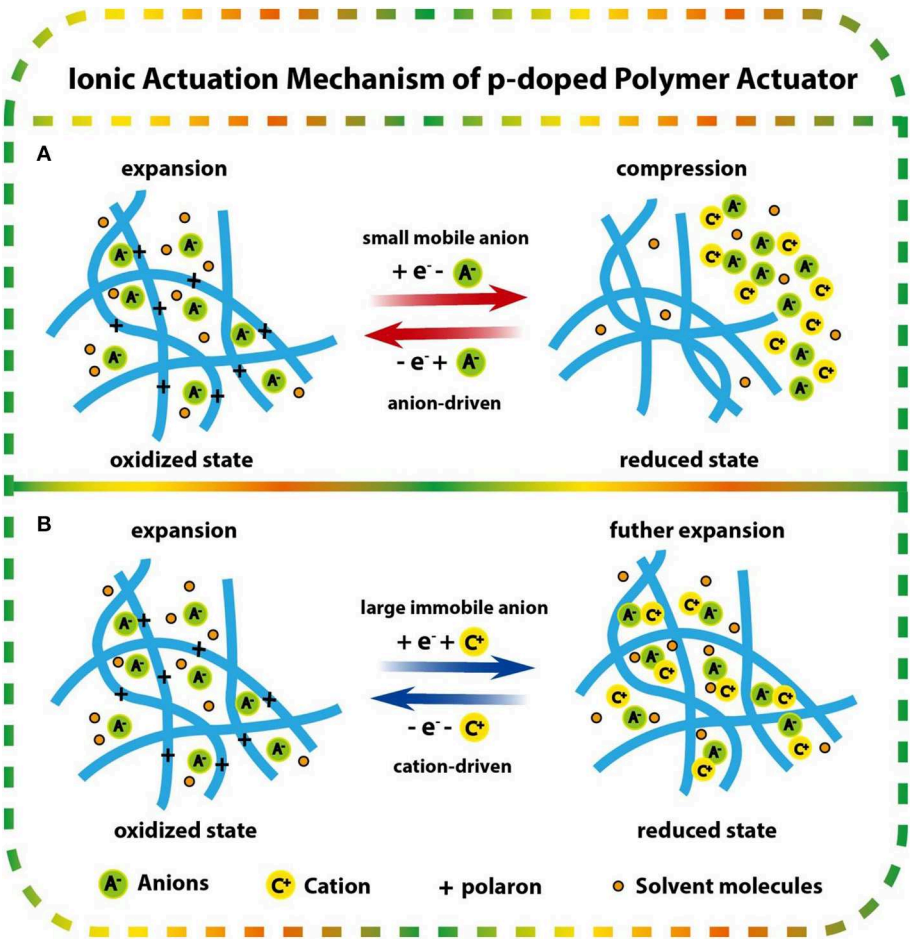

FIGURE 1 | Ionic actuation mechanism of p-doped polymer actuators: **(A)** anion transport dominated when the anion was small and highly mobile, **(B)** cation transport dominated when the anion was large and immobile.

cations are expelled and the PEDOT film shrinks in the oxidation state. The redox process is dominated by cation migration, so it is called "cation-driven."

Obviously, the type of electrolyte used in the PEDOT oxidation polymerization and actuation process has a significant effect on ion migration. It has been reported that when using molecular electrolyte solution, unless the doped anions are very large, such as with the polystyrene sulfonic acid anion (PSS^-) or dodecylbenzenesulfonic acid anion (DBS^-), the ion migration process of PEDOT actuators is mainly driven by anions. On the other hand, when using ionic liquid electrolytes diluted in organic solutions, such as 1-ethyl-3-methyl-imidazolium bis(trifluoromethyl-sulfonyl)imide (EMIBTI), the ion migration process also presents typical anion-driven characteristics. While in the neat EMIBTI, the ion migration process presents cation-driven characteristics dominated by imidazole ions (Irvin and Carberry, 2013). Moreover, the dimensional changes of the actuators not only rely on the ion flux transmission between polymer chains; the exchange of solvent molecules accompanying ion migration and the conformational change of the polymer backbone also play a role, as detailed in the works of Bund and Neudeck (2004) and Chen et al. (1996).

Moisture Sorption/Desorption Mechanism

Based on the conductivity and hydrophilicity of PEDOT:PSS and the photothermal properties of PEDOT, using them as an active layer to laminate with an inert layer fabricated actuators that can respond to stimulus such as electrical, thermal, or near infrared (NIR) light. When current or NIR light passes through the polymer film, the temperature of the film rises due to *Joule* heating, which leads to the desorption of water molecules in the film and, eventually, shrinkage. When the current is removed, the film absorbs water vaper from ambient air and expands again. When NIR light is turned off, the film is cooled and restored to its original state. The stress gradient between the active electrode layer and the inert layer drives the actuator to bend.

For example, Okuzaki et al. (Asaka and Okuzaki, 2012) first investigated the humidity sensitive PEDOT:PSS film as a soft actuator (Okuzaki et al., 2009b) whose actuation was achieved through the absorption of moisture from high pressure water vapor and which underwent constriction due to the *Joule* heat generated by the current. After that, Taccola and coworkers (Taccola et al., 2015) reported a bilayer, humidity-response actuator that was composed of an active PEDOT:PSS layer and an inert PDMS substrate, and its anisotropic motion was dependent on the stress gradient between the active and inert layer (**Figure 2**). The same mechanism was also applied by Whitesides et al. to develop actuators called "Hygroexpansive Electrothermal Paper Actuators" (Hamedi, 2016). The actuator inserted PEDOT:PSS into the paper to form a conducting path, which made full use of the conductivity of PEDOT:PSS and the hydrophilicity of paper to realize the hygroexpansive electrothermal actuation. To achieve a light stimuli response actuator, PEDOT, as a highly photothermal material, was transferred onto a PDMS film to compose a photothermally foldable bimorph (Lim, 2017). The active PEDOT films were used to capture near-infrared (NIR) light, which in turn generated thermal energy to control water desorption and caused the films shrinkage.

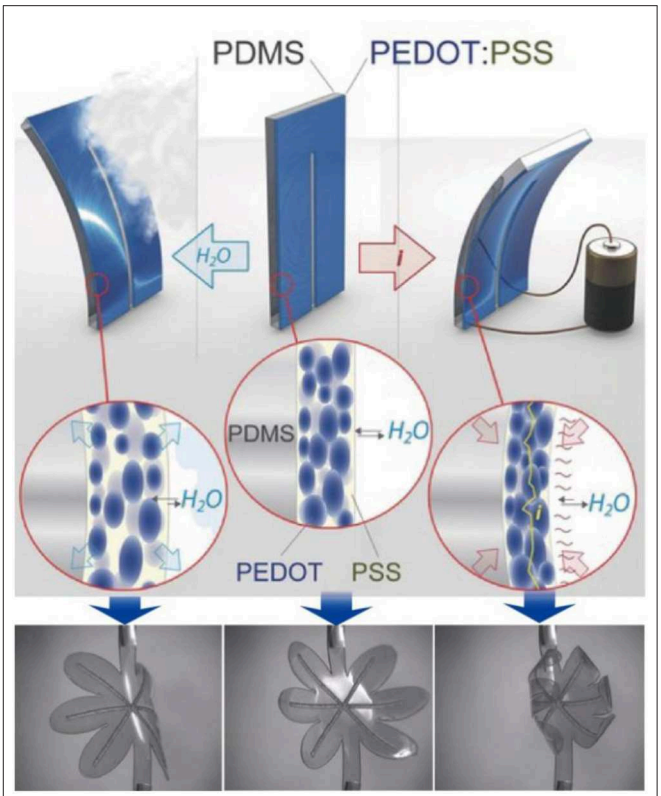

FIGURE 2 | Schematic representation of the working principle behind the PEDOT/PDMS actuator based on the sorption/desorption of environmental moisture, using the actuation movement of an electrically driven flower-shaped sample as an example. Reproduced with permission (Temmer, 2013). Copyright 2018, Wiley.

CONFIGURATIONS AND FABRICATION APPROACHES

Actuators with various configurations can realize different deformation, such as linear, bending, or folding (Takashima et al., 2005). The two main types of dimension changes of PEDOT-based actuators are linear and bending. Typically, self-supporting polymer films can realize slightly linear deformation, while multilayered structures can achieve macroscopic bending or linear deformation, which is caused by a relative differential expansion between layers and is more practical to applications (**Figures 3A,B**; Wübbenhorst and Putzeys, 2016). However, because the linear deformation is closer to the muscle deformation mode, the bending motion usually needs to be transformed into linear motion in many applications (Kaneto, 2016). One example to convert bending motion to linear motion is the use of a "three-layer" device, in which two electrode layers are made of an anion-driven film and a cation-driven

film, respectively. Both electrode films take up (or expel) ions simultaneously from the electrolyte when the voltage changes, this synergistic effect leading to linear expansion or contraction (Smela, 2008; Melling et al., 2019; **Figure 3C**). Besides, linear motion can also be achieved by using other configurations, such as sheets, hollow fibers, etc. The methods of mass-fabricating various configuration actuators are typically spin coating, spray coating, and screen-printing techniques. In recent years, the new approaches of ink jet printing or 3D printing have developed rapidly and have been used to produce some interesting applications.

Actuators Operating in Liquid Electrolytes

The configurations of PEDOT-based actuators that operate in liquid electrolytes are shown in **Figure 4**. Linear deformation in liquid electrolytes is usually realized in the form of freestanding films (**Figure 4A**), of which the operating is easier, but the strain produced by a single-layer polymer film is usually small. Zainudeen et al. (Zainudeen et al., 2008) designed actuators with two or three films by electrodepositing a PEDOT(DBS) film on a PPy(DBS) film or by sandwiching a PEDOT(DBS) film between two PPy(DBS) films, which increased the stress gradient and produced greater linear strain. Bilayer configuration is typically

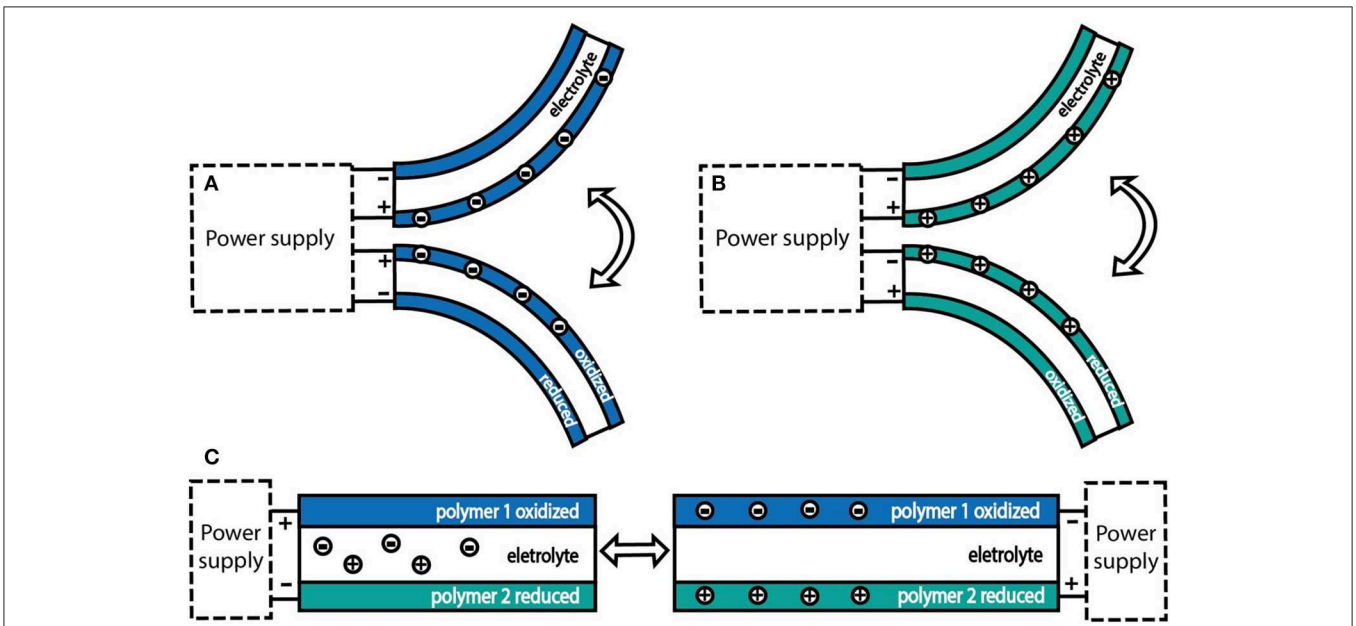

FIGURE 3 | (A) Bending trilayer actuator made using the same "anion-driven" electrode materials; **(B)** bending trilayer actuator made using the same "cation-driven" electrode materials; **(C)** a scheme for converting bending deformation into linear deformation, using one "anion-driven" electrode material and one "cation-driven" electrode material.

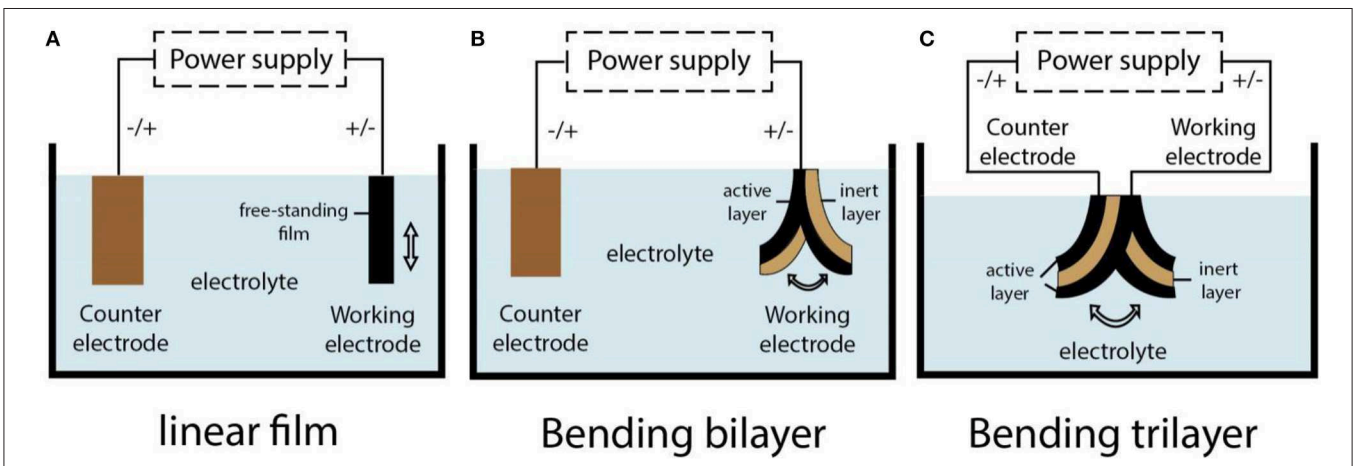

FIGURE 4 | Various configurations of the PEDOT-based actuators operating in liquid electrolytes. **(A)** A model of free-standing film actuator with linear deformation; **(B)** a model of bilayer actuator with bending deformation; **(C)** a model of trilayer actuator with bending deformation.

laminated with polymer film as an active electrode layer and a porous film as an inert layer. The porous film can accommodate ions and its volume is not affected by the stimulation. During the electrochemical redox process, the volume change of the polymer film generates a stress gradient at the interface between polymer film and inert layer, which leads to the bending deformation of the actuators (**Figure 4B**). Gaihre et al. (2013) fabricated three bilayer actuators that were comprised of PEDOT, PProDOT, and PPy film laminated with gold-coated commercial porous PVDF film, respectively, and compared their performance in different electrolytes. The result revealed that actuators operating in organic electrolyte solutions or ionic liquids existed in completely opposite driving modes. The so-called trilayer configuration was composed of two polymer films and an inert layer sandwiched between them (Poldsalu, 2018b). One conductive polymer film was connected to the working electrode and the other to the counter electrode. When the polymer film of two electrode layers had the same ion-drive mode, one layer expanded, and the other shrunk in the reduction state. Then, the actuator produced a bending deformation. Conversely, the trilayer actuator could produce linear deformation, as mentioned earlier.

Actuators Operating in Air

The ability to operate in a humid environment is one of the advantages of actuators, especially in biomedical applications that mimic the body's fluid environment. However, as the basic component of artificial muscle, it is particularly important for actuators to be able to operate in normal atmospheric environments like natural muscle. The main configurations of PEDOT-based actuators that operated in air are shown in **Figure 5**. Based on the moisture sorption/desorption

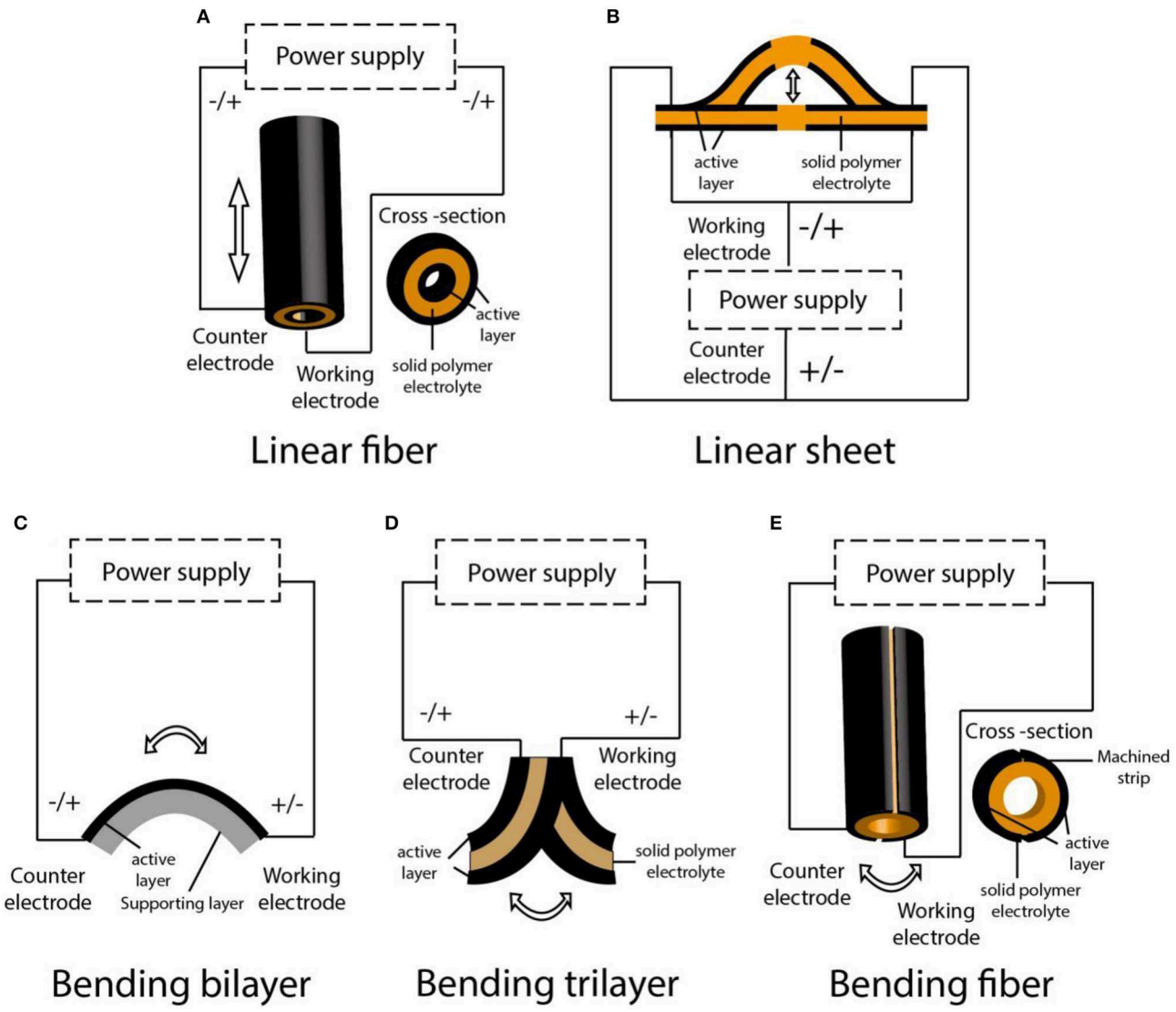

FIGURE 5 | Various configurations of the PEDOT-based actuators operating in air. **(A)** A model of tubular fiber actuator with linear deformation; **(B)** a model of buckling sheet actuator with linear deformation; **(C)** a model of bilayer actuator with bending deformation; **(D)** a model of trilayer actuator with bending deformation; **(E)** a model of tubular fiber actuator with bending deformation.

mechanism, various actuators with a bilayer structure can bend in air; for example, actuators that consist of multilayered PEDOT:PSS films and passive PDMS layers can realize a bending deformation in air (Taccola et al., 2015). Moreover, Greco et al. used PEDOT:PSS as a conductive layer to deposit over a liquid crystal elastomers film to fabricate a new bi-layered actuator that can bend in air through *Joule* heating (Greco et al., 2013; **Figure 5C**).

Currently, the main configuration of PEDOT-based actuators operating in air is a trilayer structure. To cope with the problems of electrolyte volatilization and delamination, on the one hand, the solid polymer electrolyte (SPE), based on the interpenetrating polymer networks (IPNs) containing different ionic liquids as substitute for liquid electrolytes, has been used widely as the median layer (Festin et al., 2013), in which the gelatinous ionic liquid can significantly alleviate electrolyte volatilization (Armand et al., 2009). On the other hand, a semi-IPN structure based on a polymer electrode layer and SPE layer has been introduced to design trilayer actuators. This structure embeds linear conductive polymers in the elastic interpenetrating polymer network matrix to form an integrated device similar to the traditional three-layer structure (**Figure 6**; Vidal et al., 2002). Hollow fibers based on semi-IPNs can be driven linearly in air, as reported (Plesse et al., 2008; **Figure 5A**). The driving force of the device is due to the imbalance of the surface area of PEDOT electrodes inside and outside (the ratio is 1:3). The outer electrode contains a high amount of PEDOT, which acts as the counter electrode, and can easily compensate the charge from the inner working electrode in the doping/dedoping process. Therefore, compared with the inner electrode, the change in size of the counter electrode is not obvious, and the linear actuation of the hollow fiber is dominated by the deformation of the inner working electrode. Vidal and coworkers have reported another principle for building up a one-piece linear sheet actuator (Vidal, 2006; **Figure 5B**); through a masking technique, the polymerization of EDOT is controlled to from alternating polymerized area on the IPN substrate. The deformation of PEDOT on both sides of the un-polymerized region in the same direction during the actuation process thus causes the linear buckling of the actuator. Bending motion in air can be produced with a classical trilayer or one-piece semi-IPN structure (**Figure 5D**), and the output force is usually double compared with that of bilayer or freestanding film (Bar-Cohen, 2004). Madden et al. fabricated a cylindrical IPN rod-molding with a capillary tube and chemically polymerized PEDOT as an electrode layer on its surface (Farajollahi et al., 2016a,b). Then, the laser microfabrication was used to hollow out the rod to form a tube and to process the PEDOT-penetrating layer to form two machined strips on the IPN structure, which formed two independent electrodes around the cylindrical substrate. The composition of this tubular structure is similar to a typical trilayer cantilever beam structure, which can also achieve a bending motion (**Figure 5E**).

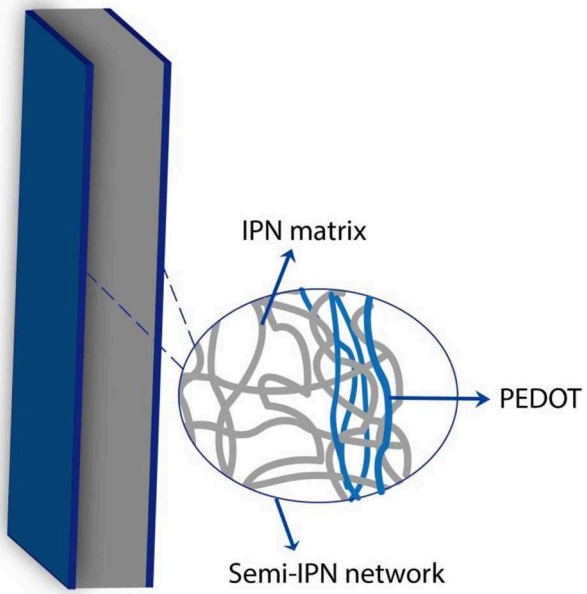

FIGURE 6 | Schematic of a PEDOT-based semi-IPN system (Illustration shown the linear PEDOT embedded in an elastomeric IPN matrix).

Fabrication Approaches

So far, the fabrication of conductive polymer actuators has been a complex and multi-step process, involving the lamination of conductive polymer electrode film with a substrate or solid electrolyte layer and the forming technology of devices. Conductive polymers can be deposited onto substrates or SPEs by chemical and electrochemical polymerization as well as through spinning, spraying, screen printing (Lee et al., 2003), and inkjet printing techniques. Among them, inkjet printing has attracted much attention in recent years due to its non-contact deposition with substrates and advantages of not requiring a mask, additives, and complex surface treatment. This high-resolution digital printing process by CAD-drawing is convenient and efficient and is expected to achieve large-scale processing (Poldsalu, 2018a,b; Shrestha et al., 2018b). At present, actuators are formed mainly on technologies such as micro-forming (Nguyen et al., 2017), mask lithography (Taccola et al., 2013), and dry etching (Maziz et al., 2015) techniques, though most of these methods have disadvantages like requiring manual fabrication, complex post-processing, or complex assembly processes. Recently, the emergence of 3D printing has brought a new approach to the manufacture of actuators, with complex structures and high resolution that can enable rapid prototyping, customized design, and production in one step (Zolfagharian et al., 2016). However, current reports on the fabrication of electroactive polymer-based soft actuators by 3D printing technology mainly focus on ionic polymer-metal composites, dielectric elastomers, piezoelectrics, etc. There are few studies in 3D printing about conducting polymers, as conducting polymers such as PEDOT and PPy are usually not soluble in any solvent, and their soluble or colloidal dispersion, such as PEDOT:PSS and PPy-(2-ethylhexyl)sulfosuccinate (PPy-DEHS), do not attain a high electrical conductivity or mechanical properties (Maziz et al.,

2016). Therefore, the doping and processing of conductive polymers and development of highly compatible dispersive conductive polymer ink may be the future direction of conductive polymer actuators for 3D printing.

PERFORMANCE EVALUATION

Based on the ionic actuation mechanism, PEDOT-based actuators undergo significant net volume changes due to ion insertion or extraction during the redox process. In order to make this mass-transfer process quick, steady, and lasting, it is necessary to understand some of the basic indicators and characterizations that determine the performance of the actuators; in turn, this will guide the selection of materials and the manufacturing of the actuators (Mirvakili and Hunter, 2018). Thus, the basic and key indicators for evaluating the device performances and material properties are listed below.

Metrics of Actuator Performances

The performance of PEDOT-based actuators can be evaluated by some basic parameters as shown in **Table 1**, in which the key parameters are stress, strain and speed (Smela, 2008). First, stress (σ) is usually described as the typical force that the actuator can exert per unit area, and the peak stress is the maximum force (also known as blocking force) at which a material can maintain its position in each cross-sectional area (Hara and Takashima, 2004). Blocking force is also an important parameter to describe the mechanical properties of actuators; generally, an actuator with high stiffness will produce higher blocking force (Wang et al., 2017), which is also an indispensable metric in many engineering applications. Next, strain (ε) represents the displacement in actuation direction based on the original length of the material. The value of it depends largely on the Young's modulus of materials used (Madden et al., 2004) and usually decreases with an increase in frequency (Wang et al., 2017), which is determined by the effective time of ion diffusion between electrolyte and electrodes. The stress and strain of PEDOT or PEDOT:PSS-based actuators can be characterized by a stress (σ) vs. strain (ε) curve obtained by a tensile mechanical testing machine, the value of which can be larger through doping electrodes with high mechanical materials (Kaneto et al., 2012). Last, strain rate (ε_r) refers to the average strain change of the actuator in unit time during the whole driving stroke. Its value reflects the driving speed, usually up to 1–10% s^{-1}, which is calculated as an average over a full bending cycle from the equation (Temmer, 2013):

$$\varepsilon_r = 4\varepsilon f$$

where the constant 4 is the number of movements (passages) of applied potential corresponding to frequency f between neutral and extreme position of the whole cycle, ε is the strain difference, and f is the frequency of applied voltage. In addition, since the tip displacement (δ) of bending actuation is related to the strain (ε), it can be measured by a laser displacement sensor or estimated by the equation (Li et al., 2014; Nguyen et al., 2018a):

$$\varepsilon = \frac{2d\delta}{L^2+\delta^2}$$

where d and L is the thickness and free length of the actuator sample, respectively. The peak to peak displacement vs. time or frequency curves reflects the displacement variation and is usually in inverse proportion (Okuzaki et al., 2014). The peak to peak displacement vs. step voltage curve demonstrates that the degree of bending deformation is affected by the applied voltage because the ionic mobility is highly dependent on the electric potential field in the polymer matrix (Gaihre et al., 2013).

Moreover, the actuation durability represents the potential of practical application and can be reflected by cycle life. As reported, PEDOT-based actuators display a desirable durability that can operate to 10^6 cycles (Vidal et al., 2004), and modifying a PEDOT electrode with high mechanical stability materials can prolong the cycle life of the actuator. Besides, the stress vs. frequency curve or strain vs. frequency curve can also reflect the cyclic stability and durability of the actuators. The scale of external stimulus needed to drive an actuator is related to the conductivity and capacitance of the material. PEDOT-based actuators can generate a motion at a lower voltage, typically about 1–3 V. Energy conversion efficiency (η) refers to the ratio of work generated to input energy, which is an important parameter to evaluate the energy utilization of the actuator, mainly depending on the electromechanical loss inside the material. PEDOT-based actuators typically have a smaller energy conversion efficiency of <1%, which is related to the elastic modulus and the output strain of actuators according to the equation (Cottinet et al., 2011):

$$\eta = \frac{0.5Y\varepsilon 2f \times Vol}{V \times I}$$

where Y is the Young's modulus, ε is the bending strain, f is the frequency of actuation, Vol is the volume of the actuator, and $V \times I$ is the electric input power. Electromechanical coupling refers to the proportion of input energy that is transformed into work; that is to say, the input energy in the actuator is partially converted into output work and the other part is stored in the actuator itself to generate internal mechanical energy. The electromechanical

TABLE 1 | Metrics of PEDOT-based actuator performances.

Property	Value	References
Stress (MPa)	Typically: 0–10 Max.: 50	Hara and Takashima, 2004; Wang et al., 2017
Strain (%)	Typically: 0–3	Vandesteeg et al., 2003; Vidal, 2006; Zainudeen et al., 2008; Li et al., 2014
Strain rate (%/s)	Typically: 10^0-10^1	Dai et al., 2010; Temmer, 2013
Life (cycle)	Typically: 10^4-10^5 Max.: 10^6	Vidal et al., 2004, Kotal et al., 2016
Potential (V)	Typically: 1–3	Kim et al., 2013; Kotal et al., 2016
Conversion Efficiency (%)	Typically: <1 Max.: 1.04	Cottinet et al., 2011; Wang et al., 2017
Electromechanical coupling	Max.: 0.1	Madden et al., 2004

coupling thus indicates the degree of energy lost inside the actuator in addition to that which is converted to work (Madden et al., 2004). Currently, however, the electromechanical coupling of PEDOT-based actuators can only reach a maximum of 0.1, which is consistent with its energy conversion efficiency.

Metrics of Material Properties

The performance of the actuator is often limited by the material used. Therefore, it is necessary to clarify the effect of the properties of materials as shown in **Table 2** used on the performance of actuators and summarize methods to improve the properties of materials; this will help to obtain high performance PEDOT-based actuators. The conductivity of the material affects the actuator response speed directly. The high electronic conductivity of PEDOT film (10^2-10^3) and high ionic conductivity of ionic liquid (10^{-3}-10^{-2}) can accelerate the ion diffusion rate between polymer film and electrolyte, thus improving the response speed and reducing actuation voltage. The electronic conductivity (σ_e) of conductive polymer electrodes can be further improved by a doping or post-treatment process. It can be measured by an in-house four-point probe, and the value can be calculated according to the Smits equation (Smits, 1958; Temmer, 2013):

$$\sigma_e = I \times (\mathbf{4.532} \times w \times V)^{-1}$$

where I is the applied constant current between the outer contacts of the probe, w is the thickness of the polymer electrode layer, and V is the measured voltage between the inner contacts. Besides, Ionic conductivity (σ_i) is essential to ensure good ion transport between conductive polymer electrodes and electrolytes, which can be measured by AC impedance spectroscopy with a VSP potentiostat (Biologic SA), and the value can be calculated from the real part resistance in the complex impedance diagram, according to the equation (Khaldi et al., 2012):

$$\sigma_i = \frac{1}{Z} \times \frac{d}{S}$$

TABLE 2 | Metrics of material properties.

Property	Value	References
Electronic conductivity (S/cm)	Typically: 10–10^3	Lee et al., 2004; Li et al., 2014
Ionic conductivity (S/cm)	Typically: 10^{-4}-10^{-3}	Vidal et al., 2003; Vidal, 2006; Wang et al., 2014
Capacitance (F/m^3)/(F/g)	Typically: 10^5-10^6 /Typically: 10–10^3	Kotal et al., 2016; Terasawa and Asaka, 2016; Poldsalu et al., 2017; Wang et al., 2017
Modulus (GPa)	Typically: 0–0.5 Max.: 15	Kim et al., 2013; Farajollahi et al., 2016a,b
Tensile strength (MPa)	Typically: 10–10^2	Madden et al., 2004; Farajollahi et al., 2016a,b
Elongation at break (%)	Typically: <50	Farajollahi et al., 2016a,b; Wang et al., 2017

where Z is the real part of the complex impedance and d and S are the thickness and the area of the sample, respectively.

Cyclic voltammograms indicated the electrode reaction properties, for instance the redox characters (redox peaks or the voltage window), capacitive characters (specific capacitance), reversibility, and stability, which can be analyzed in a CV electrochemical workstation using a three-electrode system. Specific capacitance often reported use as volume specific capacitance (C_v) and mass specific capacitance (C_m), which refers to the charge storage per unit volume or mass at a given potential difference of the electroactive electrode. The value of it implied the capacity to uptake ions in the polymer film and can be calculated from the integrated area of CV curves using these equations (Nguyen et al., 2017; Rasouli et al., 2018):

$$C_v = \int_{V_2}^{V_1} I \frac{dV}{\Delta V \times \vartheta \times V}$$

$$C_m = \int_{V_2}^{V_1} I \frac{dV}{\Delta V \times \vartheta \times S}$$

where ΔV is the potential window, V_1 and V_2 are the lowest and the highest values, ϑ is the scan rate, and V or S is the volume or weight taken of the one polymer electrode of the actuators. Typically, polymer electrode materials with large specific capacitance will bring larger stress and strain to the actuator. By increasing the porosity of the material properly, the charge capacity in the polymer film will be increased and the specific capacitance can be improved (Terasawa and Asaka, 2016).

To expound the mechanical properties of the electrode films, the stress vs. strain curves can be obtained by a tensile test with a mechanical tester, which can calculate the parameters, including the Young's modulus (E, slope of the straight line of the stress-strain curve), tensile strength (σ_b, maximum stress that the specimen can withstand before tensile fracture), and elongation at break (e, maximum strain rate that the specimen can withstand before tensile fracture). The electrode materials with lower Young's modulus, higher tensile strength, and elongation at break are conducive to the output of high stress and strain of actuators (Farajollahi et al., 2016a,b). In addition, conductive polymers as charge storage elements will form a double electric layer on its surface during ion diffusion, in which charge is injected and transferred. Reducing the polymer film thickness, therefore, will shorten the charge injection time. Similarly, reducing the spectator layer thickness will decrease the ion diffusion distance (the thickness of actuator typically $<200\,\mu m$). Both of these in turn narrow the response time of actuators, while the output stress will be affected (Smela, 2008). Moreover, the type and ion size of the electrolyte will affect the peak strain and stress of actuators. Large ions inserted into the polymer film may cause a greater strain charge ratio, which is beneficial to produce larger peak strains. Aqueous electrolytes generally have higher ionic conductivity than organic or ionic liquid electrolytes, which helps shorten the response time. When ionic liquids are used as electrolyte materials, the high ion concentration and large ion radius in the double layer of the polymer film surface are also conducive to large peak strain and stress (Doebbelin et al., 2010).

ACTUATOR MATERIALS

As previously mentioned, the properties of the electrode and electrolyte materials used greatly affect actuator performance. Doping with inorganic nanocarbon materials, small organic molecules or other high-molecule polymers can improve the electrochemical and mechanical properties of PEDOT or PEDOT:PSS electrodes, thus helping to improve the output stress and strain, durability, and energy conversion effectiveness of actuators. The construction of a solid polymer electrolyte with both ionic conductivity and mechanical stability facilitates the stable operation of the actuator in air.

Electrode Materials

Pure PEDOT or PEDOT:PSS

Properly increasing the porosity in the polymer film can increase the charge density within the film, which make the electrochemical redox reaction occur quickly in the films. However, the pure PEDOT:PSS film forms too many high-porosity structures in aqueous solution, so it cannot cause deformation by ion doping under electrical stimulation (Anquetil et al., 2004). Pure PEDOT:PSS film or fiber can be subjected to local joule heating for the desorption of water in the film under the action of an electric field, resulting in linear deformation. Its strain increases with the rise of doped PSS content and relative humidity (up to 7%) (Okuzaki et al., 2009a, 2013). Besides, the PEDOT:PSS microfiber can produce more than 20 MPa stress in <0.5 s and has a cycle life up to 10^4 cycles. This actuation mode requires high environmental humidity, and the operation is complicated (Zhou et al., 2016). It has been reported that pure PEDOT films obtained by electrochemical polymerization in an aqueous solution have linear deformation, which possesses higher stress (maximum 2.1 MPa) and strain (maximum 2%), but lower conductivity (only 8 S/cm) (Vandesteeg et al., 2003). Therefore, studies on doped pure PEDOT or PEDOT:PSS with other functional materials used them as an active electrode layer, in order to obtain bilayer or trilayer actuators with better performance.

Composite With Nanocarbon Materials

Pure PEDOT or PEDOT:PSS films can be doped with additives to improve electrical conductivity, capacitance, and mechanical properties. Nano-carbon materials, including carbon nanotubes, graphene, and activated carbon aerogels, have good electrical conductivity, mechanical rigidity, and chemical stability, which can be used as ideal additives for electrode materials. The single-walled carbon nanotube (SWCNT)-doped PEDOT:PSS electrode shows a synergistic effect of electrostatic double-layer capacitance and faraday capacitance, so that the composite electrode has a larger specific capacitance than the pure PEDOT:PSS electrode (from 22 to 244 F/g). Meanwhile, single-walled carbon nanotubes form highly entangled mesoporous networks in the composite polymer film, which increases the Young's modulus of the electrode film (from 102 to 214 MPa), and corresponding actuators are also proven to produce output stress three times higher than the undoped ones (Terasawa and Asaka, 2016). Carboxylic multi-walled carbon nanotubes (MWCNTs) have also been reported to improve the conductivity and mechanical properties of PEDOT:PSS electrodes. The PEDOT:PSS electrode with 30% carboxylic MWCNTs has an electrical conductivity that is one order of magnitude larger than the original electrode (from 4.64 to 153.75 S/cm) and output strain increases to 0.64%. The tensile modulus increases by eight times that of its original value (from 127.64 to 918.27 MPa), which makes the energy conversion efficiency as high as 1.04% (Wang et al., 2017). This is because the highly conductive MWCNTs network in the polymer matrix increases the electrical conductivity and mechanical strength, and the π-π interaction between MWCNTs and the PEDOT chain as well as the hydrogen bonding between MWCNTs and PSS chain causes the charge to be transferred from the PEDOT chain to the MWCNTs, which is beneficial to ion migration and promotes the conversion efficiency of electrical energy to mechanical energy. Heteroatom sulfur and nitrogen-doped reduced graphene oxide have a larger specific surface area, better ion transport performance, and mechanical properties. The composite electrode obtained after doping with PEDOT:PSS has a higher capacitance and conductivity (up to 505 F/g, 767 S/cm), and the mechanical flexibility and stability increase under bending deformation. The constructed trilayer actuator has a maximum bending strain of 4.5 times higher than that of an undoped one at the voltage of 1 V, and the durability is improved (remain 96% strain after 18,000 cycles; Kotal et al., 2016). The addition of activated carbon aerogel particles in PEDOT:PSS is beneficial to ion transmission and large elastic modulus of the electrode, which increases the specific capacitance and output stress while interfering with the PEDOT:PSS structure, resulting in a decrease in strain caused by the pure Faraday current in the polymer film. Therefore, the mixed electrode is suitable for the actuator requiring high stress (Poldsalu et al., 2017).

Composite With Other Polymers

PEDOT or PEDOT:PSS films composite with other polymers can significantly improve their mechanical property. For instance, the electrochemical polymerization of PPy(DBS) film and the electrodeposition of PEDOT(DBS) on its surface to form the actuator with double-layer composite film exhibits electrochemical characteristics similar to that of pure PPy film in electrolyte, and its strain in a high scan rate between reduced state and oxidation state is improved effectively (up to 3%) without any delamination phenomenon (Zainudeen et al., 2008). Moreover, the double-network hydrogels based on PEDOT:PSS hydrolyzed partially to realize bending motion in an aqueous electrolyte with a pH $>$ 4.7 by electrical stimulation (the strain up to 66% in 120 s). In the double-network hydrogels, poly(acrylamide) (PAAm), as the first network converts the amide group into a carboxyl group through hydrolysis and ionization, makes the matrix negatively charged and can respond to electrical stimulation. The semi-IPN hydrogel based on PEDOT:PSS serves as the second network, in which the conductive PEDOT phase and PSS polyelectrolyte phase improve the electronic and ionic conductivity of the hydrogels, respectively. Besides, the PEDOT phase forms clusters when compression fractures, which can disperse local stress and increase the mechanical strength of double-network hydrogels (Dai et al., 2010).

Modification by Organic Small Molecules

The conductivity of PEDOT:PSS electrode film can also be improved by modifying it using an organic solvent. Doping of PEDOT:PSS film with polar solvent DMSO (volume ratio: 4:1) can promote the separation of the PEDOT chain and PSS chain in the polymer matrix so that the conductivity of the PEDOT:PSS film at room temperature increases to 43 S/cm. The doped electrode laminated with an active PVDF layer can be used to prepare a bimorph actuator that can run stably under a high frequency electric field (Lee et al., 2004). It has been reported that electrode films with high conductivity and stretchability can be obtained by doping (50%wt) xylitol with PEDOT:PSS films and subsequently exposing it to heat treatment. First, the doped xylitol can form hydrogen bonds with PSS chains to weaken the hydrogen bonds between the PSS chains, thus reducing the viscosity between colloidal particles. Next, it can function similar to a plasticizer to enhance the flexibility and stretchability of the film. Meanwhile, it also has the additional ability to increase carrier mobility between colloidal particles and improve the conductivity of thin films (up to 407 S/cm), and the constructed trilayer actuator can generate 0.15% strain under the stimulation of 2 V voltage (Li et al., 2014).

Solid Polymer Electrolyte Materials

The development of high-performance electrode materials can be used in a variety of configurations, including self-supporting polymer films, bilayers, trilayers etc. As for trilayer actuators, to achieve stable operation in air requires an appropriate electrolyte layer. In addition to the development of high-performance electrode materials, therefore, the development and modification of electrolyte materials and the optimization of ion migration in the separation layer is also important for the development of high-performance actuators. Traditional solid electrolyte materials used commercial poly (vinylidene fluoride) (PVDF) porous film soaked with ionic liquid. Its porosity ensures the ionic conductivity and its relatively large Young's modulus (∼70 MPa) ensures mechanical stability, though its size tailoring is restricted (Schmidt et al., 2006; Gaihre et al., 2013). Synthesized composite solid-polymer electrolyte materials with adjustable ion conductivity and mechanical properties are therefore of great significance in practical applications of actuators.

IPN Based on Polyethylene Oxide

Ionic conductive polymer polyethylene oxide (PEO) is often used to form an interpenetrating polymer network, with mechanically strong polymers such as polycarbonate (PC), polybutadiene (PB), nitrile butadiene (NBR), and polytetrahydrofuran (PTHF) as a separation layers, and soak with ionic liquid to form solid polymer electrolyte materials (Cho M. et al., 2007; Cho M. S. et al., 2007; Plesse et al., 2007). The PEO is an ionic conductive polymer in which the oxygen atom can form coordination bonds with the metal cation in the electrolyte to promote ion pair separation, facilitate ion transmission, and improve ion conductivity. However, it also has significant disadvantages, such as a high degree of crystallization at room temperature and the fact that ion transport mainly occurs in the amorphous region of the polymer; reducing the crystallinity of PEO is therefore conducive to ion migration. Vidal et al. introduced short poly (ether oxide) side chains into the PEO network, which significantly reduced the crystallinity of PEO, thus increasing the volume available for ion migration, and improved the ionic conductivity of the branched PEO network to 5×10^{-4} S/m (Vidal et al., 2003). Since both PEO and PC networks contain ether oxygen units, the two networks have good compatibility, and are thus conducive to the formation of interpenetrating networks. On the other hand, due to the interaction between the ethylene oxide unit of PEO and dioxyethylene unit of EDOT, the PEO network has an affinity to the monomer EDOT. The composite PEO/PC film was soaked in EDOT solution and the polymerization of PEDOT within it to obtain an integrated semi-IPN actuator with a conductivity of 10 S/m (Vidal et al., 2003). Moreover, the PEO formed interpenetrating networks with NBR or PTHF, and their ionic conductivity could reach 10^{-3} S/m after soaking in the ionic solution (Plesse et al., 2011). The actuator with PEO/NBR/PEDOT configuration could achieve 2.4% strain at 2 V voltage (Vidal, 2006).

Natural Macromolecule Cellulose

As an electroactive material, cellulose has advantages of light weight, biodegradation, and operation under low voltage. Using cellulose electroactive material containing a lithium chloride solution as an intermediate layer electrolyte, PEDOT:PSS forms a nanometer coating on both sides, which can improve the durability of the trilayer actuator and significantly reduce (90%) energy loss (Mahadeva and Kim, 2009). Bacterial cellulose is produced by all sorts of bacteria and has higher chemical purity and crystallinity, tensile strength and stiffness, and an improved ultra-fine network structure compared with plant cellulose. The freeze-dried bacterial cellulose forms a porous structure with high strength and high Young's modulus (15 GPa); it can absorb a large amount of ionic liquid and has enhanced electrochemical and mechanical properties, and it is thus suitable for use as an ion exchange film. The trilayer actuator composed of PEDOT:PSS electrodes and the freeze-dried bacterial cellulose can produce a displacement of 1.5 mm at 1 V voltage (Kim et al., 2013). In another example, polyvinyl alcohol (PVA) is also a water-soluble, biodegradable, and biocompatible polymer. Gelatinous bacterial cellulose cannot be dispersed in water but can be converted and decomposed into individual nanofibers by the oxidation of TEMPO. By crosslinking PVA with oxidized bacterial cellulose, hydrogen bonds were formed through interaction with hydroxyl groups in PVA and cellulose, and thus the composite film is obtained. Compared with pure oxidized bacterial cellulose film, the crystallinity and stiffness of composite film is reduced, and the ionic conductivity of composite film is increased by 20%, which increased the maximum bending displacement of the actuator by 2.3 times its original value (Wang et al., 2014).

APPLICATIONS

Bionics and Biomedicine Applications

So far, PEDOT-based actuators have been widely used in bionics or biomedicine, intelligent textiles, microactuators, and functional applications. Actuators that work within the field of

bionics or biomedicine are interesting and meaningful. A semi-IPN trilayer actuator with a PEDOT and PEO/NBR host matrix was integrated into a biomimetic vision system by Vidal and coworkers (Festin et al., 2011). In this system, the position of the micro-camera is controlled by a closed loop formed by a trilayer actuator excited by a pulse-width modulation signal and a visual perception board. The function of actuators on both sides of the micro-imager—to adjust the imaging position—was similar to that of the ciliary body in the eye. The same group also reported a new application of PEO/NBR/PEDOT semi-IPN films, which was integrated into a biomimetic perception system as an artificial tentacle to imitate the tactile perception of a rat tentacle (Festin et al., 2014). The artificial tentacle consisted of a PMMA fiber and two semi-IPN films where one acted as an actuator to derive the tentacle movement and another as a sensor to sense and collect real time deformation during the actuation process. What's more, continuous progress in the development of hybrid muscle was generated by combining skeletal muscle and artificial structures. Kim et al. Kim et al. (2016) developed a hybrid muscle powered by C_2C_{12} skeletal muscle cells based on the PEDOT/MWCNT hydrophilic sheet to achieve biomimetic actuation, which was controlled by electric field stimulation and presented flexible movement and physical durability in solution. The PEDOT/MWCNT sheet has excellent biocompatibility, mechanical stability, and shape adjustability, which make it ideal as a platform for culturing a variety of cells to form mixed muscles in the field of biomedicine and is expected to be used as a patch for artificial organs or biosensors.

Textiles and Wearable Applications

When used in textiles and other wearable applications, the actuator generates mechanical motion, sound, or substance release (such as thermal energy) upon receipt of electronic signals. With the development of smart electronic textiles, great advances have been made in the actuator for wearable applications such as textile-capacitive touch sensors, wearable heaters and artificial muscles etc. For the electronic textiles, an essential component is electrically conducting yarns. Wet spinning PEDOT:PSS fiber has played an important role in the development of electronic textiles due to its inherent electrical conductivity and charge-storage capability. The wet spinning process, with a novel and one-step route, eliminated the need for post-spinning treatment with organic solvent such as ethylene glycol, as was reported by Wallace and co-workers. From this, fibers can be imparted enhanced electrical conductivity and redox cycling properties (Jalili et al., 2011). Lund et al. also developed conducting silks; they used PEDOT:PSS as ink to coated over mulberry silk yarns and post-treated them in a dimethyl sulfoxide (DMSO) or ethylene glycol (EG) solvent, which improved their conductivity to the highest level for coated fiber: 70 S cm^{-1}(**Figure 7A**). They also produced a woven band that could serve as a capacitive touch-sensitive textile keyboard using dyed PEDOT:PSS-conducting yarns, which connected with a liquid crystal display that displayed messages when pressing the PEDOT:PSS textile area (Lund et al., 2018; **Figure 7B**). Similarly, the coating of fabrics with a PEDOT-PPy layer was synthesized by a chemical electrochemistry method to form textile actuators, and the strain can be improved 53-fold that of pure fabrics. This makes it possible to integrate them into textiles and garments to assist walking, and there is great potential for development in driving intelligent prostheses and the applications of soft robots (Maziz et al., 2017). Moreover, as we know, electrical impulses in the human heart can be detected by placing electrodes at specific points around the human heart. To this end, Kimura et al. presented a foldable textile based on PEDOT:PSS and poly(vinyl alcohol) (PVA)-blended fiber as a flexible electrode that has enhanced conductivity and mechanical strength to detect human heartbeats (Miura et al., 2014). This will provide a platform to realize integrated, wearable electronics.

Microapplications

In recent years, the rapid development in the production of actuators that operate in air or solutions has been demonstrated on a micro scale. Various types of microactuators have

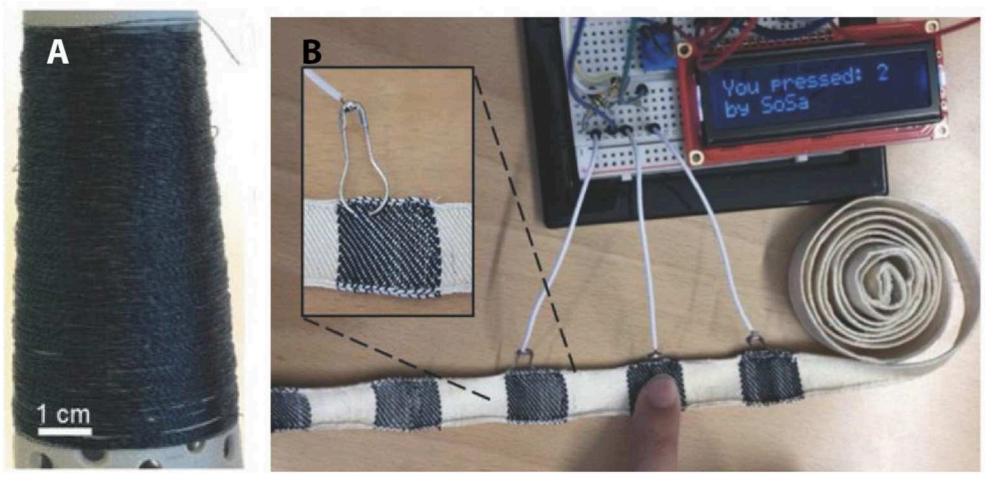

FIGURE 7 | (A) Photograph of a yarn bobbin with 100+ m of dyed yarn; **(B)** photograph of the textile capacitive touch sensor with key number 2 activated. The insert shows the safety pin electrical connection. **(A,B)** Reproduced with permission (Terasawa and Asaka, 2016). Copyright 2018, Wiley.

been applied in many fields such as mechanics, chemistry, biomedicine, etc. (Jager et al., 2000). Among several smart electroactive materials, conducting polymers have attracted much attention because of their ability for miniaturization, which improves the electrochemical and mechanical properties of microactuators, such as speed and stress output. Taccola et al. fabricated a bilayer microactuator that operated in solution with the structure of PEDOT:PSS coated with SU8 photoresist. This was patterned by lithography technology to form microfingers that can bend in the electrochemical redox process (Taccola et al., 2013). A PEDOT-based microactuator that can work in air was reported in the early years. Composed of SPE with an IPN structure and PEDOT electrodes interpenetrated on both sides, the plasma dry etching technique was used successfully on the extremely thin (12 μm) conductive microactuator film (Khaldi et al., 2011). In order to overcome the shortcomings of manual operation in some steps of microactuator production, Maziz and coworkers reported a top-down integration process to micro-fabricate soft, conducting polymer actuators to achieve continuity in direct synthesis, patterning, and operation (Maziz et al., 2016). Through this innovative and sequential layer stacking, the trilayer microstructures were fabricated by using two PEDOT electrodes by vapor-phase polymerization and the PEO/NBR semi-interpenetrating polymer network as the intermediate SPE layer. These materials have been successfully patterned using photolithography and reactive ion etching techniques and are easily scalable for the simultaneous batch-production of microactuators with hundreds of electromechanical structures (Nguyen et al., 2018b).

Other Functional Applications

Various functional applications have been realized by many PEDOT-based actuators with different configurations. Lee et al. fabricated a flexible organic film speaker using PEDOT:PSS (DMSO) as an electrode and PVDF as an active layer by using the screen printing method, which showed a flat and stable sound pressure level over 400 Hz (Lee et al., 2003). Ikushima et al. prepared a micro autofocus lens actuator by using trilayer-bending PEDOT:PSS (PEO)/PVDF/ PEDOT:PSS

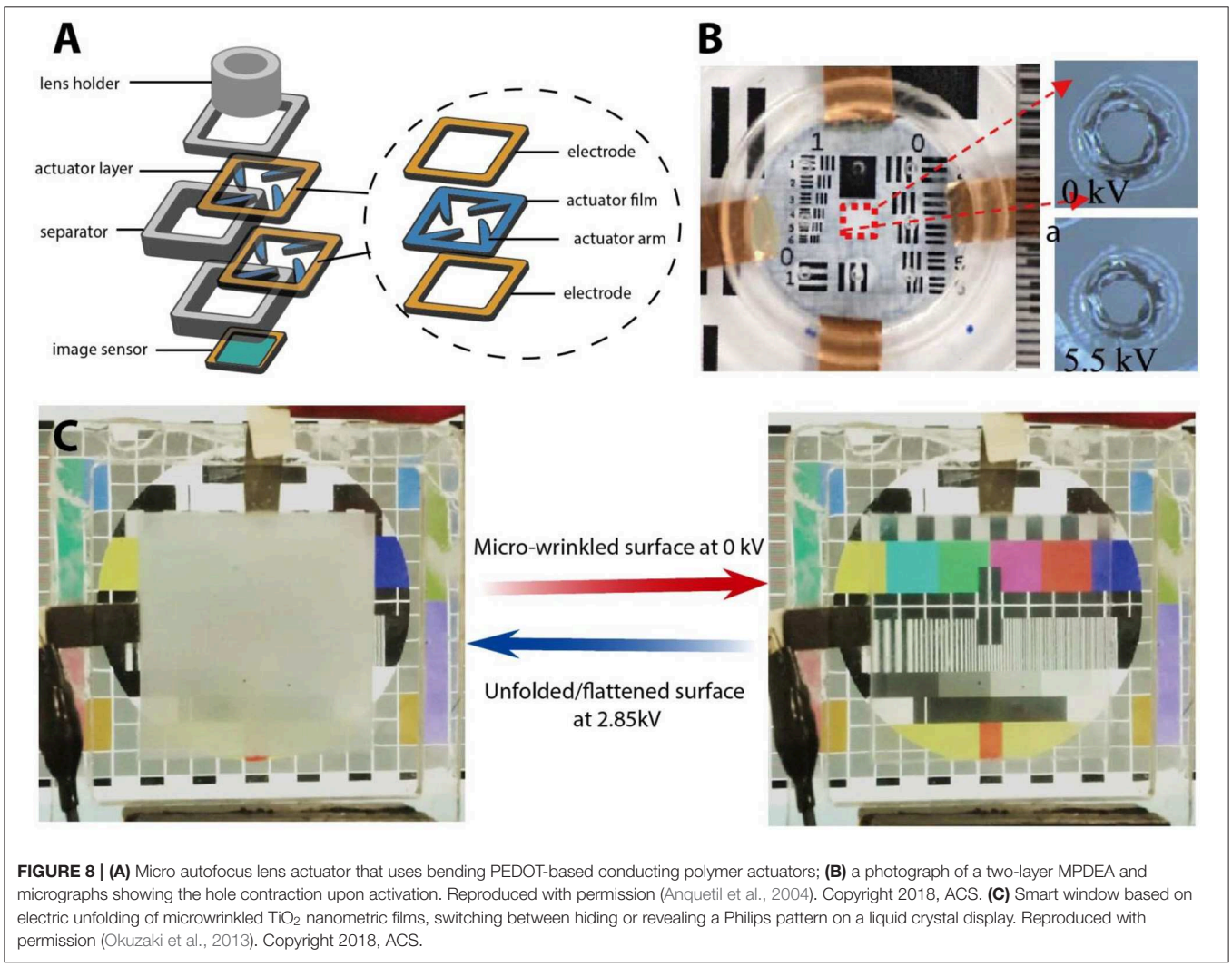

FIGURE 8 | (A) Micro autofocus lens actuator that uses bending PEDOT-based conducting polymer actuators; **(B)** a photograph of a two-layer MPDEA and micrographs showing the hole contraction upon activation. Reproduced with permission (Anquetil et al., 2004). Copyright 2018, ACS. **(C)** Smart window based on electric unfolding of microwrinkled TiO_2 nanometric films, switching between hiding or revealing a Philips pattern on a liquid crystal display. Reproduced with permission (Okuzaki et al., 2013). Copyright 2018, ACS.

(PEO) actuators and simply drip-coating PEDOT:PSS (PEO) solution onto the treated PVDF membrane; they designed the tests to inspect the actuator's use in micro autofocus lenses, showing that the actuators can operate stably for more than a million cycles (Ikushima et al., 2010; **Figure 8A**). PEDOT or PEDOT:PSS can be combined with other electroactive polymers such as a dielectric elastomer to design actuator with new features to accommodate new applications. Shrestha et al. developed a transparent and adjustable sound-absorption material based on a micro-perforated dielectric elastomer actuator with an inkjet-printed PEDOT:PSS electrode, which can adjust the absorption spectrum while transmitting light. Such a transparent absorber is thus suitable for noise absorption on window glass (Shrestha et al., 2018b; **Figure 8B**). Moreover, a smart window based on small-strain microwrinkling/unfolding to switch between frosted and clear was created by sandwiching a dielectric elastomer actuator between a pair of thin, microwrinkled TiO_2/PEDOT:PSS film electrodes (Shrestha et al., 2018a). This all-solid-state smart window was durable and high-performance at a low cost and low power, which exceeded even that which was reported by a commercial polymer-dispersed liquid crystal smart window, as shown in **Figure 8C**.

CONCLUSION AND OUTLOOK

The high conductivity of PEDOT and the soluble processability and flexibility of its dopant, PEDOT:PSS, means actuators based on them are able to provide a large driving strain at low voltage while also being lightweight, of high durability, and of low cost. The PEDOT-based conductive polymer actuators attracted the attention of researchers back in 1996 and have since made great progress in actuator applications owing to its admirable intrinsic properties. This feature article has provided an overview of the basic actuation mechanisms, performance evaluation criteria, configurations, processing technologies, recent development of materials, and applications of PEDOT-based actuators. However, although many studies have shifted the actuators from principle verification to practical applications, there are still many scientific and technical challenges to overcome before widespread commercialization can occur.

Further developments on both the device materials and applications of soft actuators as artificial muscles may revolve around the wearable themes. To be incorporated into wearable and flexible electronics, the selection of material should have enough strength, structural rigidity, and flexibility, and it should be able to provide a sufficient amount of actuating force; in particular, it should possess comfortability and biocompatibility. Conducting hydrogels based on PEDOT:PSS may become potential applications in future development. The trilayer PEDOT-based actuators are the main configurations that produce significant deformation, but the fact that they work in the air causes certain problems, one of which is that the ionic liquid will leave the device over time and will be substituted by the environment molecules. Hence, it is important to add an appropriate encapsulation layer to protect the electrolyte's solvent from evaporation or the ionic medium from being lost when the device is in operation (Rinne et al., 2019; Takalloo et al., 2019). Moreover, actuator applications in the future should be energy saving and environmentally friendly; a new study presented of an autonomously powered actuator that can bend reversibly in both directions and is driven by glucose and O_2 only (Mashayekhi Mazar et al., 2019) provided a perfect demonstration of future applications. Finally, developing compatible inks to use in 3D printing technology for the mass production of actuators will provide a powerful impetus to their commercial applications.

AUTHOR CONTRIBUTIONS

This study was conceived and designed by JX and BL. The paper was drafted, written by FH and revised, approved by BL and YX.

FUNDING

This work was supported by the National Natural Science Foundation of China (51763010, 51963011), the Innovation Driven 5511 Project of Jiangxi Province (20165BCB18016), the Key Research & Development Project of Jiangxi Province (20171BBH80007), and the Science Foundation for Excellent Youth Talents in Jiangxi Province (20162BCB23053). FH thanks Jiangxi Science & Technology Normal University for a Postgraduate Innovation Program grant (YC2019-X16).

REFERENCES

Agrawal, R., Koteswarapavan, C., Kaushik, N., and Matre, P. (2019). Smart actuators for innovative biomedical applications: an interactive overview. *Appl. Microbiol. Bioeng.* 101–119. doi: 10.1016/B978-0-12-815407-6.00007-1

Anquetil, P. A., Rinderknecht, D., Vandesteeg, N. A., Madden, J. D., and Hunter, I. W. (2004). Large strain actuation in polypyrrole actuators. Smart Structures and Materials 2004: Electroactive Polymer Actuators and Devices (EAPAD). *Int. Soc. Opt. Photon.* 5385, 380–387. doi: 10.1117/12.540141

Armand, M., Endres, F., MacFarlane, D. R., Ohno, H., and Scrosati, B. (2009). Ionic-liquid materials for the electrochemical challenges of the future. *Nat. Mater.* 8, 621–629. doi: 10.1038/nmat2448

Asaka, K., and Okuzaki, H. (2012). Soft actuators. *Stretchable Electron.* 305–324. doi: 10.1002/9783527646982.ch13

Asplund, M., Nyberg, T., and Inganäs, O. (2010). Electroactive polymers for neural interfaces. *Polym. Chem.* 1, 1374–1391. doi: 10.1039/c0py00077a

Bar-Cohen, Y. (2000). Electroactive polymers as artificial muscles: capabilities, potentials and challenges. *Robotics* 188–196. doi: 10.1061/40476(299)24

Bar-Cohen, Y. (2002). Electroactive polymers: current capabilities and challenges. Smart Structures and Materials 2002: Electroactive Polymer Actuators and Devices (EAPAD). *Int. Soc. Opt. Photon.* 4695, 1–7. doi: 10.1117/12.475159

Bar-Cohen, Y. (2004). *Electroactive Polymer (EAP) Actuators as Artificial Muscles: Reality, Potential, and Challenges*. Bellingham, WA: SPIE Press. doi: 10.1117/3.547465

Bar-Cohen, Y., and Anderson, I. A. (2019). Electroactive polymer (EAP) actuators-background review. *Mech. Soft Mater.* 1:5. doi: 10.1007/s42558-019-0005-1

Bay, L., Jacobsen, T., Skaarup, S., and West, K. (2001). Mechanism of actuation in conducting polymers: osmotic expansion. *J. Phys. Chem. B* 105, 8492–8497. doi: 10.1021/jp003872w

Berdichevsky, Y., and Lo, Y. H. (2006). Polypyrrole nanowire actuators. *Adv. Mater.* 18, 122–125. doi: 10.1002/adma.200501621

Bund, A., and Neudeck, S. (2004). Effect of the solvent and the anion on the doping/dedoping behavior of poly (3, 4-ethylenedioxythiophene) films studied with the electrochemical quartz microbalance. *J. Phys. Chem. B* 108, 17845–17850. doi: 10.1021/jp0469721

Chen, S., Lu, B., Duan, X., and Xu, J. (2012). Systematic study on chemical oxidative and solid-state polymerization of poly (3, 4-ethylenedithiathiophene). *J. Polym. Sci. A Polym. Chem.* 50, 1967–1978. doi: 10.1002/pola.25971

Chen, X., Xing, K. Z., and Inganäs, O. (1996). Electrochemically induced volume changes in poly (3, 4-ethylenedioxythiophene). *Chem. Mater.* 8, 2439–2443. doi: 10.1021/cm9600034

Cho, M., Seo, H., Nam, J., Choi, H. R., Koo, I. G., and Lee, Y. (2007). High ionic conductivity and mechanical strength of solid polymer electrolytes based on NBR/ionic liquid and its application to an electrochemical actuator. *Sensors Actuators B Chem.* 128, 70–74. doi: 10.1016/j.snb.2007.05.032

Cho, M. S., Seo, H. J., Nam, J. D., Choi, H. R., Koo, J. C., and Lee, Y. (2007). An electroactive conducting polymer actuator based on NBR/RTIL solid polymer electrolyte. *Smart Mater. Struct.* 16, S237–S242. doi: 10.1088/0964-1726/16/2/S06

Cottinet, P. J., Souders, C., Labrador, D., Porter, S., Liang, Z., Wang, B., et al. (2011). Nonlinear strain–electric field relationship of carbon nanotube buckypaper/Nafion actuators. *Sensors Actuators A Phys.* 170, 164–171. doi: 10.1016/j.sna.2011.06.013

Dai, T., Qing, X., Zhou, H., Shen, C., Wang, J., and Lu, Y. (2010). Mechanically strong conducting hydrogels with special double-network structure. *Synth. Met.* 160, 791–796. doi: 10.1016/j.synthmet.2010.01.024

Doebbelin, M., Marcilla, R., Pozo-Gonzalo, C., and Mecerreyes, D. (2010). Innovative materials and applications based on poly(3,4-ethylenedioxythiophene) and ionic liquids. *J. Mater. Chem.* 20, 7613–7622. doi: 10.1039/c0jm00114g

Farajollahi, M., Sassani, F., Naserifar, N., Fannir, A., Plesse, C., Nguyen, G. T., et al. (2016a). Characterization and dynamic charge dependent modeling of conducting polymer trilayer bending. *Smart Mater. Struct.* 25:115044. doi: 10.1088/0964-1726/25/11/115044

Farajollahi, M., Woehling, V., Plesse, C., Nguyen, G. T., Vidal, F., Sassani, F., et al. (2016b). Self-contained tubular bending actuator driven by conducting polymers. *Sens. Actuat. A* 249, 45–56. doi: 10.1016/j.sna.2016.08.006

Feng, Z., Mo, D., Wang, Z., Zhen, S., Xu, J., Lu, B., et al. (2015). Low-potential electrosynthesis of a novel nitrogen analog of PEDOT in an ionic liquid and its optoelectronic properties. *Electrochim. Acta* 160, 160–168. doi: 10.1016/j.electacta.2015.02.054

Festin, N., Maziz, A., Plesse, C., Teyssié, D., Chevrot, C., and Vidal, F. (2013). Robust solid polymer electrolyte for conducting IPN actuators. *Smart Mater. Struct.* 22:104005. doi: 10.1088/0964-1726/22/10/104005

Festin, N., Plesse, C., Chevrot, C., Teyssié, D., Pirim, P., and Vidal, F. (2011). Conducting IPN actuators for biomimetic vision system. Electroactive Polymer Actuators and Devices (EAPAD). *Int. Soc. Opt. Photon.* 7976:79760K. doi: 10.1117/12.877634

Festin, N., Plesse, C., Pirim, P., Chevrot, C., and Vidal, F. (2014). Conducting IPN actuator/sensor for biomimetic vibrissa system. Electroactive Polymer Actuators and Devices (EAPAD). *Int. Soc. Opt. Photon.* 9056:90562A. doi: 10.1117/12.2047644

Gaihre, B., Ashraf, S., Spinks, G. M., Innis, P. C., and Wallace, G. G. (2013). Comparative displacement study of bilayer actuators comprising of conducting polymers, fabricated from polypyrrole, poly(3,4-ethylenedioxythiophene) or poly(3,4-propylenedioxythiophene). *Sensors Actuators A Phys.* 193, 48–53. doi: 10.1016/j.sna.2012.12.007

Greco, F., Domenici, V., Desii, A., Sinibaldi, E., Zupancic, B., Zalar, B., et al. (2013). Liquid single crystal elastomer/conducting polymer bilayer composite actuator: modelling and experiments. *Soft Matter.* 9, 11405–11416. doi: 10.1039/c3sm51153g

Gueye, M. N. (2016). Structure and dopant engineering in PEDOT thin films: practical tools for a dramatic conductivity enhancement. *Chem. Mater.* 28, 3462–3468. doi: 10.1021/acs.chemmater.6b01035

Ha, Y.-H., Nikolov, N., Pollack, S. K., Mastrangelo, J., Martin, B. D., and Shashidhar, R. (2004). Towards a transparent, highly conductive Poly (3, 4-ethylenedioxythiophene). *Adv. Funct. Mater.* 14, 615–622. doi: 10.1002/adfm.200305059

Hamedi, M. M. (2016). Electrically activated paper actuators. *Adv. Funct. Mater.* 26, 2446–2453. doi: 10.1002/adfm.201505123

Hara, S. Z. T., and Takashima, W. (2004). Artificial muscles based on polypyrrole actuators with large strain and stress induced electrically. *Polym. J.* 36:151. doi: 10.1295/polymj.36.151

Huang, W. (2002). On the selection of shape memory alloys for actuators. *Mater. Des.* 23, 11–19. doi: 10.1016/S0261-3069(01)00039-5

Ikushima, K., John, S., Ono, A., and Nagamitsu, S. (2010). PEDOT/PS bending actuators for autofocus micro lens applications. *Synth. Met.* 160, 1877–1883. doi: 10.1016/j.synthmet.2010.07.003

Irvin, J. A., and Carberry, J. R. (2013). Dominant ion transport processes of ionic liquid electrolyte in poly(3,4-ethylenedioxythiophene). *J. Poly. Sci. B Polym. Phys.* 51, 337–342. doi: 10.1002/polb.23229

Jager, E. W., Smela, E., and Inganäs, O. (2000). Microfabricating conjugated polymer actuators. *Science* 290, 1540–1545. doi: 10.1126/science.290.5496.1540

Jalili, R., Razal, J. M., Innis, P. C., and Wallace, G. G. (2011). One-step wet-spinning process of poly(3,4-ethylenedioxythiophene):poly(styrenesulfonate) fibers and the origin of higher electrical conductivity. *Adv. Funct. Mater.* 21, 3363–3370. doi: 10.1002/adfm.201100785

Jayathilaka, W. A. D. M., Qi, K., Qin, Y., Chinnappan, A., Serrano-García, W., Baskar, C., et al. (2019). Significance of nanomaterials in wearables: a review on wearable actuators and sensors. *Adv. Mater.* 31:e1805921. doi: 10.1002/adma.201805921

Joo, J., Lee, J. K., Lee, S. Y., Jang, E. J. Oh., and Epstein, A. J. (2000). Physical characterization of electrochemically and chemically synthesized polypyrroles. *Macromolecules* 33, 5131–5136. doi: 10.1021/ma991418o

Kaneto, K. (2016). Research trends of soft actuators based on electroactive polymers and conducting polymers. *J. Phys. Conf. Ser.* 704:012004. doi: 10.1088/1742-6596/704/1/012004

Kaneto, K., Takayanagi, K., Tominaga, K., and Takashima, W. (2012). How to improve electrochemomechanical strain in conducting polymers. Electroactive Polymer Actuators and Devices (EAPAD). *Int. Soc. Opt. Photon.* 8340:83400K. doi: 10.1117/12.917879

Khaldi, A., Plesse, C., Soyer, C., Cattan, E., Vidal, F., Legrand, C., et al. (2011). Conducting interpenetrating polymer network sized to fabricate microactuators. *Appl. Phys. Lett.* 98:164101. doi: 10.1063/1.3581893

Khaldi, A., Plesse, C., Soyer, C., Chevrot, C., Teyssié, D., Vidal, F., et al. (2012). "Patterning process and actuation in open air of micro-beam actuator based on conducting IPNs," in *Electroactive Polymer Actuators and Devices (EAPAD). International Society for Optics and Photonics, Vol. 8340*. doi: 10.1117/12.915086

Kiefer, R., Kilmartin, P. A., Bowmaker, G. A., Cooney, R. P., and Travas-Sejdic, J. (2007). Mixed-ion linear actuation of PPy and PEDOT in propylene carbonate-triflate electrolytes. Electroactive Polymer Actuators and Devices (EAPAD). *Int. Soc. Opt. Photon.* 6524:65240U. doi: 10.1117/12.715089

Kim, S. S., Jeon, J. H., Kee, C. D., and Oh, I. K. (2013). Electro-active hybrid actuators based on freeze-dried bacterial cellulose and PEDOT: PSS. *Smart Mater. Struct.* 22:085026. doi: 10.1088/0964-1726/22/8/085026

Kim, T. H., Kwon, C. H., Lee, C., An, J., Phuong, T. T. T., Park, S. H., et al. (2016). Bio-inspired hybrid carbon nanotube muscles. *Sci. Rep.* 6:26687. doi: 10.1038/srep26687

Klute, G. K., Czerniecki, J. M., and Hannaford, B. (1999). "McKibben artificial muscles: pneumatic actuators with biomechanical intelligence," in *IEEE/ASME International Conference on Advanced Intelligent Mechatronics* (Atlanta, GA), 221–226.

Kongahage, D., and Foroughi, J. (2019). Actuator materials: review on recent advances and future outlook for smart textiles. *Fibers* 7:21. doi: 10.3390/fib7030021

Kotal, M., Kim, J., Kim, K. J., and Oh, I. K. (2016). Sulfur and nitrogen co-doped graphene electrodes for high-performance ionic artificial muscles. *Adv. Mater.* 28, 1610–1615. doi: 10.1002/adma.201505243

Kruusamäe, K., Punning, A., Aabloo, A., and Asaka, K. (2015). Self-sensing ionic polymer actuators: a review. *Actuators* 4, 17–38. doi: 10.3390/act4010017

Lee, C. S., Joo, J., Han, S., and Koh, S. K. (2004). Multifunctional transducer using poly (vinylidene fluoride) active layerand highly conducting poly (3,4-ethylenedioxythiophene) electrode: actuator and generator. *Appl. Phys. Lett.* 85, 1841–1843. doi: 10.1063/1.1784890

Lee, C. S., Kim, J. Y., Lee, D. E., Joo, J., Wagh, B. G., Han, S., et al. (2003). Flexible and transparent organic film speaker by using highly conducting PEDOT/PSS as electrode. *Synth. Met.* 139, 457–461. doi: 10.1016/S0379-6779(03)00199-1

Li, Y., Tanigawa, R., and Okuzaki, H. (2014). Soft and flexible PEDOT/PSS films for applications to soft actuators. *Smart Mater. Struct.* 23:074010. doi: 10.1088/0964-1726/23/7/074010

Lim, H. (2017). Construction of a photothermal Venus flytrap from conductive polymer bimorphs. *Npg Asia Mater.* 9:e399. doi: 10.1038/am.2017.101

Lin, K., Chen, S., Lu, B., and Xu, J. (2017). Hybrid π-conjugated polymers from dibenzo pentacyclic centers: precursor design, electrosynthesis and electrochromics. *Sci. China Chem.* 60, 38–53. doi: 10.1007/s11426-016-0298-2

Lu, B., Yuk, H., Lin, S., Jian, N., Qu, K., Xu, J., et al. (2019). Pure PEDOT: PSS hydrogels. *Nat. Commun.* 10:1043. doi: 10.1038/s41467-019-09003-5

Lu, B., Zhang, S., Qin, L., Chen, S., Zhen, S., and Xu, J. (2013). Electrosynthesis of poly (3, 4-ethylenedithiathiophene) in an ionic liquid and its electrochemistry and electrochromic properties. *Electrochim. Acta* 106, 201–208. doi: 10.1016/j.electacta.2013.05.068

Lu, B., Zhen, S., Zhang, S., Xu, J., and Zhao, G. (2014). Highly stable hybrid selenophene-3, 4-ethylenedioxythiophene as electrically conducting and electrochromic polymers. *Polym. Chem.* 5, 4896–4908. doi: 10.1039/c4py00529e

Lund, A., Darabi, S., Hultmark, S., Ryan, J. D., Andersson, B., Ström, A. (2018). Roll-to-roll dyed conducting silk yarns: a versatile material for E-textile devices. *Adv. Mater. Technol.* 3:1800251. doi: 10.1002/admt.201800251

Madden, J. D., Madden, P. G., and Hunter, I. W. (2001). Polypyrrole actuators: modeling and performance. Smart Structures and Materials 2001: Electroactive Polymer Actuators and Devices. *Int. Soc. Opt. Photon.* 4329, 72–83. doi: 10.1117/12.432688

Madden, J. D., Vandesteeg, N. A., Anquetil, P. A., Madden, P. G., Takshi, A., Pytel, R. Z., et al. (2004). Artificial muscle technology: physical principles and naval prospects. *IEEE J. Ocean. Eng.* 29, 706–728. doi: 10.1109/JOE.2004.833135

Mahadeva, S. K., and Kim, J. (2009). Effect of polyelectrolyte nanocoating on the performance and durability of cellulose electro-active paper actuator. *J. Nanosci. Nanotechnol.* 9, 5757–5763. doi: 10.1166/jnn.2009.1241

Mashayekhi Mazar, F., Martinez, J. G., Tyagi, M., Alijanianzadeh, M., Turner, A. P. F., and Jager, E. W. H. (2019). Artificial muscles powered by glucose. *Adv. Mater.* 31:1901677. doi: 10.1002/adma.201901677

Maziz, A., Concas, A., Khaldi, A., Stålhand, J., Persson, N. K., and Jager, E. W. H. (2017). Knitting and weaving artificial muscles. *Sci. Adv.* 3:e1600327. doi: 10.1126/sciadv.1600327

Maziz, A., Plesse, C., Soyer, C., Cattan, E., and Vidal, F. (2015). High speed electromechanical response of ionic microactuators. Electroactive Polymer Actuators and Devices (EAPAD). *Int. Soc. Opt. Photon.* 9430:94300O. doi: 10.1117/12.2085516

Maziz, A., Plesse, C., Soyer, C., Cattan, E., and Vidal, F. (2016). Top-down approach for the direct synthesis, patterning, and operation of artificial micromuscles on flexible substrates. *ACS Appl. Mater. Interfaces* 8, 1559–1564. doi: 10.1021/acsami.5b09577

Melling, D., Martinez, J. G., and Jager, E. W. H. (2019). Conjugated polymer actuators and devices: progress and opportunities. *Adv. Mater.* 31:1808210. doi: 10.1002/adma.201808210

Ming, S., Zhen, S., Lin, K., Zhao, L., Xu, J., and Lu, B. (2015b). Thiadiazolo [3, 4-c] pyridine as an acceptor toward fast-switching green donor-acceptor-type electrochromic polymer with low bandgap. *ACS Appl. Mater. Interfaces* 7, 11089–11098. doi: 10.1021/acsami.5b01188

Ming, S., Zhen, S., Liu, X., Lin, K., Liu, H., Zhao, Y., et al. (2015a). Chalcogenodiazolo [3, 4-c] pyridine based donor-acceptor-donor polymers for green and near-infrared electrochromics. *Polym. Chem.* 6, 8248–8258. doi: 10.1039/c5py01321f

Mirvakili, S. M., and Hunter, I. W. (2018). Artificial muscles: mechanisms, applications, and challenges. *Adv. Mater.* 30:1704407. doi: 10.1002/adma.201704407

Miura, H., Fukuyama, Y., Sunda, T., Lin, B., Zhou, J., Takizawa, J., et al. (2014). Foldable textile electronic devices using all-organic conductive fibers. *Adv. Eng. Mater.* 16, 550–555. doi: 10.1002/adem.201300461

Nguyen, N. T., Dobashi, Y., Soyer, C., Plesse, C., Nguyen, G. T., Vidal, F., et al. (2018a). Nonlinear dynamic modeling of ultrathin conducting polymer actuators including inertial effects. *Smart Mater. Struct.* 27:115032. doi: 10.1088/1361-665X/aae456

Nguyen, N. T., Plesse, C., Vidal, F., Soyer, C., Grondel, S., Madden, J. D., et al. (2017). Microfabricated PEDOT trilayer actuators: synthesis, characterization, and modeling. Electroactive Polymer Actuators and Devices (EAPAD). *Int. Soc. Opt. Photon.* 10163:101631K. doi: 10.1117/12.2260431

Nguyen, T. N., Rohtlaid, K., Plesse, C., Nguyen, G. T. M., Soyer, C., Grondel, S., et al. (2018b). Ultrathin electrochemically driven conducting polymer actuators: fabrication and electrochemomechanical characterization. *Electrochim. Acta* 265, 670–680. doi: 10.1016/j.electacta.2018.02.003

O'Halloran, A., O'malley, F., and McHugh, P. (2008). A review on dielectric elastomer actuators, technology, applications, and challenges. *J. Appl. Phys.* 104:071101. doi: 10.1063/1.2981642

Okuzaki, H., Hosaka, K., Suzuki, H., and Ito, T. (2013). Humido-sensitive conducting polymer films and applications to linear actuators. *React. Funct. Polym.* 73, 986–992. doi: 10.1016/j.reactfunctpolym.2012.10.013

Okuzaki, H., Suzuki, H., and Ito, T. (2009a). Electrically driven PEDOT/PSS actuators. *Synth. Met.* 159, 2233–2236. doi: 10.1016/j.synthmet.2009.07.054

Okuzaki, H., Suzuki, H., and Ito, T. (2009b). Electromechanical properties of poly (3, 4-ethylenedioxythiophene)/poly (4-styrene sulfonate) films. *J. Phys. Chem. B* 113, 11378–11383. doi: 10.1021/jp902845x

Okuzaki, H., Takagi, S., Hishiki, F., and Tanigawa, R. (2014).Ionic liquid/polyurethane/PEDOT:PSS composites for electro-active polymer actuators. *Sensors Actuators B Chem.* 194, 59–63. doi: 10.1016/j.snb.2013.12.059

Otero, T. F., Martinez, J. G., and Arias-Pardilla, J. (2012). Biomimetic electrochemistry from conducting polymers. A review. *Electrochim. Acta* 84, 112–128. doi: 10.1016/j.electacta.2012.03.097

Panda, S., and Acharya, B. (2019). "Electronic applications of conducting polymer nanocomposites," in *Proceedings of the Third International Conference on Microelectronics, Computing and Communication Systems* (Singapore: Springer), 211–220.

Plesse, C., Khaldi, A., Wang, Q., Cattan, E., Teyssié, D., Chevrot, C., et al. (2011). Polyethylene oxide-polytetrahydrofurane-PEDOT conducting interpenetrating polymer networks for high speed actuators. *Smart Mater. Struct.* 20:124002. doi: 10.1088/0964-1726/20/12/124002

Plesse, C., Vidal, F., Gauthier, C., Pelletier, J. M., Chevrot, C., Teyssie, D., et al. (2007). Poly(ethylene oxide)/polybutadiene based IPNs synthesis and characterization. *Polymer* 48, 696–703. doi: 10.1016/j.polymer.2006.11.053

Plesse, C., Vidal, F., Teyssié, D., and Chevrot, C. (2008). Conducting IPN fibers: a new design for linear actuation in open air. *Adv. Sci. Technol.* 61, 53–58. doi: 10.4028/www.scientific.net/AST.61.53

Poldsalu, I. (2018a). Mechanical and electro-mechanical properties of EAP actuators with inkjet printed electrodes. *Synth. Met.* 246, 122–127. doi: 10.1016/j.synthmet.2018.10.009

Poldsalu, I. (2018b). Thin ink-jet printed trilayer actuators composed of PEDOT:PSS on interpenetrating polymer networks. *Sensors Actuators B Chem.* 258, 1072–1079. doi: 10.1016/j.snb.2017.11.147

Poldsalu, I., Hajro, M., Tamm, T., Uibu, M., Peikolainen, A. L., Kiefer, R., et al. (2017). Inkjet-printed hybrid conducting polymer-activated carbon aerogel linear actuators driven in an organic electrolyte. *Sensors Actuators B Chem.* 250, 44–51. doi: 10.1016/j.snb.2017.04.138

Rasouli, H., Naji, L., and Hosseini, M. G. (2018). The influence of electrodeposited conducting polymer electrode structure on the actuation performance of muscle-like ionic actuators. *Sensors Actuators A Phys.* 279, 204–215. doi: 10.1016/j.sna.2018.05.041

Rinne, P., Põldsalu, I., Johanson, U., Tamm, T., Põhako-Esko, K., Punning, A., et al. (2019). Encapsulation of ionic electromechanically active polymer actuators. *Smart Mater. Struct.* 28:074002. doi: 10.1088/1361-665X/ab18c0

Rohtlaid, K. (2019). Poly(3,4-ethylenedioxythiophene): poly(styrene sulfonate)/polyethylene oxide electrodes with improved electrical and electrochemical properties for soft microactuators and microsensors. *Adv. Electron. Mater.* 5:1800948. doi: 10.1002/aelm.201800948

Romasanta, L. J., Lopez-Manchado, M. A., and Verdejo, R. (2015). Increasing the performance of dielectric elastomer actuators: a review from the materials perspective. *Prog. Polym. Sci.* 51, 188–211. doi: 10.1016/j.progpolymsci.2015.08.002

Schmidt, V. H., Lediaev, L., and Polasik, J. (2006). Piezoelectric actuators employing PVDF coated with flexible PEDOT-PSS polymer electrodes. *IEEE Trans. Dielectr. Electr. Insul.* 13, 1140–1148. doi: 10.1109/TDEI.2006.1714940

Shrestha, M., Asundi, A., and Lau, G.-K. (2018a). Smart window based on electric unfolding of microwrinkled TiO_2 nanometric films. *ACS Photon.* 5, 3255–3262. doi: 10.1021/acsphotonics.8b00486

Shrestha, M., Lu, Z., and Lau, G. K. (2018b). Transparent tunable acoustic absorber membrane using inkjet-printed PEDOT:PSS thin-film compliant electrodes. *ACS Appl. Mater. Interfaces* 10, 39942–39951. doi: 10.1021/acsami.8b12368

Smela, E. (2003). Conjugated polymer actuators for biomedical applications. *Adv. Mater.* 15, 481–494. doi: 10.1002/adma.200390113

Smela, E. (2008). Conjugated polymer actuators. *MRS bulletin.* 33, 197–204. doi: 10.1557/mrs2008.45

Smits, F. M. (1958). Measurement of sheet resistivities with the four-point probe. *Bell Syst. Tech. J.* 37, 711–718. doi: 10.1002/j.1538-7305.1958.tb03883.x

Taccola, S., Greco, F., Mazzolai, B., Mattoli, V., and Jager, E. W. H. (2013). Thin film free-standing PEDOT:PSS/SU8 bilayer microactuators. *J. Micromech. Microeng.* 23:117004. doi: 10.1088/0960-1317/23/11/117004

Taccola, S., Greco, F., Sinibaldi, E., Mondini, A., Mazzolai, B., and Mattoli, V. (2015). Toward a new generation of electrically controllable hygromorphic soft actuators. *Adv. Mater.* 27, 1668–1675. doi: 10.1002/adma.201404772

Takalloo, S., Fannir, A., Nguyen, G. T. M., Plesse, C., Vidal, F., and Madden, J. D. W. (2019). Evaluating performance of wet unencapsulated PEDOT trilayer actuators operating in air and water. *Multifunct. Mater.* 2:014003. doi: 10.1088/2399-7532/ab0a9a

Takashima, W., Kanamori, K., Pandey, S. S., and Kaneto, K. (2005). Patternable bi-ionic actuator: an example of new functionality of actuation, folding and unfolding of electrochemical spring. *Sensors Actuators B Chem.* 110, 120–124. doi: 10.1016/j.snb.2005.01.018

Temme, R., Must, I., Kaasik, F., Aabloo, A., and Tamm, T. (2012). Combined chemical and electrochemical synthesis methods for metal-free polypyrrole actuators. *Sensors Actuators B Chem.* 166–167, 411–418. doi: 10.1016/j.snb.2012.01.075

Temmer, R. (2013). In search of better electroactive polymer actuator materials: PPy versus PEDOT versus PEDOT-PPy composites. *Smart Mater. Struct.* 22:104006. doi: 10.1088/0964-1726/22/10/104006

Terasawa, N., and Asaka, K. (2016). High-performance PEDOT:PSS/single-walled carbon nanotube/ionic liquid actuators combining electrostatic double-layer and faradaic capacitors. *Langmuir* 32, 7210–7218. doi: 10.1021/acs.langmuir.6b01148

Vandesteeg, N., Madden, P. G. A., Madden, J. D., Anquetil, P. A., and Hunter, I. W. (2003). Synthesis and characterization of EDOT-based conducting polymer actuators. Smart Structures and Materials 2003: Electroactive Polymer Actuators and Devices (EAPAD). *Int. Soc. Opt. Photon.* 5051, 349–357. doi: 10.1117/12.484418

Vidal, F. (2006). Conducting IPN actuators: from polymer chemistry to actuator with linear actuation. *Synth. Met.* 156, 1299–1304. doi: 10.1016/j.synthmet.2006.09.012

Vidal, F., Plesse, C., Teyssié D., and Chevrot, C. (2004). Long-life air working conducting semi-IPN/ionic liquid based actuator. *Synth. Met.* 142, 287–291. doi: 10.1016/j.synthmet.2003.10.005

Vidal, F., Popp, J. F., Chevrot, C., and Teyssie, D. (2002). Actuators based on conducting poly (3, 4-ethylenedioxythiophene)/PEO semi-IPN. Smart Structures and Materials 2002: Electroactive Polymer Actuators and Devices (EAPAD). *Int. Soc. Opt. Photon.* 4695, 95–103. doi: 10.1117/12.475153

Vidal, F., Popp, J. F., Plesse, C., Teyssié, D. (2003). Feasibility of conducting semi-interpenetrating networks based on a poly (ethylene oxide) network and poly (3, 4-ethylenedioxythiophene) in actuator design. *J. Appl. Polym. Sci.* 90, 3569–3577. doi: 10.1002/app.13055

Wang, D., Lu, C., Zhao, J., Han, S., Wu, M., and Chen, W. (2017). High energy conversion efficiency conducting polymer actuators based on PEDOT:PSS/MWCNTs composite electrode. *RSC Adv.* 7, 31264–31271. doi: 10.1039/C7RA05469F

Wang, F., Kim, S. S., Kee, C. D., Shen, Y. D., and Oh, I. K. (2014). Novel electroactive PVA-TOCN actuator that is extremely sensitive to low electrical inputs. *Smart Mater. Struct.* 23:074006. doi: 10.1088/0964-1726/23/7/074006

Wang, Y. (2009). Research progress on a novel conductive polymer–poly(3,4-ethylenedioxythiophene) (PEDOT). *J. Phys. Conf. Ser.* 152:012023. doi: 10.1088/1742-6596/152/1/012023

Wübbenhorst, M., Zhang, X., and Putzeys, T. (2016). *Electromechanically Active Polymers: A Concise Reference*. doi: 10.1007/978-3-319-31530-0

Yang, N., and Zoski, C. G. (2006). Polymer films on electrodes: investigation of ion transport at poly(3,4-ethylenedioxythiophene) films by scanning electrochemical microscopy. *Langmuir* 22, 10338–10347. doi: 10.1021/la061167u

Yuk, H., Lu, B., and Zhao, X. (2019). Hydrogel bioelectronics. *Chem. Soc. Rev.* 48, 1642–1667. doi: 10.1039/C8CS00595H

Zainudeen, U. L., Careem, M. A., and Skaarup S. (2008). PEDOT and PPy conducting polymer bilayer and trilayer actuators. *Sensors Actuators B Chem.* 134, 467–470. doi: 10.1016/j.snb.2008.05.027

Zhou, J., Mulle, M., Zhang, Y., Xu, X., Li, Q., Han, F., et al. (2016). High-ampacity conductive polymer microfibers as fast response wearable heaters and electromechanical actuators. *J. Mater. Chem. C* 4, 1238–1249. doi: 10.1039/C5TC03380B

Zolfagharian, A., Z. Kouzani, A., Yang Khoo, S., Ali Amiri Moghadam, A., Gibson, I., and Kaynak, A. (2016). Evolution of 3D printed soft actuators. *Sensors Actuators A Phys.* 250, 258–272. doi: 10.1016/j.sna.2016.09.028

Conflict of Interest: The authors declare that the research was conducted in the absence of any commercial or financial relationships that could be construed as a potential conflict of interest.

frontiers in Robotics and AI

ORIGINAL RESEARCH
published: 21 November 2019
doi: 10.3389/frobt.2019.00126

Jellyfish-Inspired Soft Robot Driven by Fluid Electrode Dielectric Organic Robotic Actuators

*Caleb Christianson[1], Christopher Bayag[2], Guorui Li[3], Saurabh Jadhav[2], Ayush Giri[4], Chibuike Agba[4], Tiefeng Li[3] and Michael T. Tolley[2]**

[1] Department of Nanoengineering, University of California, San Diego, La Jolla, CA, United States, [2] Mechanical and Aerospace Engineering, University of California, San Diego, La Jolla, CA, United States, [3] School of Aeronautics and Astronautics, Institute of Applied Mechanics, Zhejiang University, Hangzhou, China, [4] Department of Mechanical Engineering, Howard University, Washington, DC, United States

Robots for underwater exploration are typically comprised of rigid materials and driven by propellers or jet thrusters, which consume a significant amount of power. Large power consumption necessitates a sizeable battery, which limits the ability to design a small robot. Propellers and jet thrusters generate considerable noise and vibration, which is counterproductive when studying acoustic signals or studying timid species. Bioinspired soft robots provide an approach for underwater exploration in which the robots are comprised of compliant materials that can better adapt to uncertain environments and take advantage of design elements that have been optimized in nature. In previous work, we demonstrated that frameless DEAs could use fluid electrodes to apply a voltage to the film and that effective locomotion in an eel-inspired robot could be achieved without the need for a rigid frame. However, the robot required an off-board power supply and a non-trivial control signal to achieve propulsion. To develop an untethered soft swimming robot powered by DEAs, we drew inspiration from the jellyfish and attached a ring of frameless DEAs to an inextensible layer to generate a unimorph structure that curves toward the passive side to generate power stroke, and efficiently recovers the original configuration as the robot coasts. This swimming strategy simplified the control system and allowed us to develop a soft robot capable of untethered swimming at an average speed of 3.2 mm/s and a cost of transport of 35. This work demonstrates the feasibility of using DEAs with fluid electrodes for low power, silent operation in underwater environments.

Keywords: dielectric elastomer actuators, artificial muscles, soft robotics, bioinspired robotics, jellyfish swimming

OPEN ACCESS

Edited by:
Herbert Shea,
École Polytechnique Fédérale de Lausanne, Switzerland

Reviewed by:
Zhenshan Bing,
Technical University of Munich, Germany
Jun Shintake,
University of Electro-Communications, Japan

***Correspondence:**
Michael T. Tolley
tolley@ucsd.edu

Specialty section:
This article was submitted to Soft Robotics, a section of the journal Frontiers in Robotics and AI

Received: *21 July 2019*
Accepted: *06 November 2019*
Published: *21 November 2019*

Citation:
Christianson C, Bayag C, Li G, Jadhav S, Giri A, Agba C, Li T and Tolley MT (2019) Jellyfish-Inspired Soft Robot Driven by Fluid Electrode Dielectric Organic Robotic Actuators. Front. Robot. AI 6:126. doi: 10.3389/frobt.2019.00126

INTRODUCTION

Robots are being used in increasing numbers for underwater exploration and environmental monitoring (Dunbabin and Marques, 2012) and will continue to serve as a valuable data collection tool for scientists (Wynn et al., 2014). However, traditional robots introduce their own risks. Since robots are typically made from rigid materials that can move quickly, they pose inherent danger when operating near fragile structures and creatures and may become lodged in confined spaces. Additionally, underwater robots are usually driven by propellers or jet thrusters, which generate considerable noise and vibration. This additional noise is especially problematic when studying elusive animals or when studying underwater acoustics. Lastly, they consume a large amount of

power, requiring considerable batteries or a tether. Recent work by Jaffe et al. demonstrated the deployment of low power profiling floats to study the conditions of large regions of the ocean as they change over time (Jaffe et al., 2017), however the floats only have a buoyancy control and aren't capable of lateral swimming.

The growing field of soft robotics presents a promising approach to designing robots that make them more adaptable to their environments (Calisti et al., 2011; Onal and Rus, 2013; Bauer et al., 2014; Rus and Tolley, 2015; Yuk et al., 2017; Shintake et al., 2018), facilitating safer interactions with fragile objects and creatures, and can enable silent, low power locomotion (Li et al., 2017; Christianson et al., 2018b). Many soft robots are driven either pneumatically or hydraulically by pressurizing and depressurizing fluidic actuators to generate propulsion (Marchese et al., 2014; Katzschmann et al., 2018; Aubin et al., 2019). However, soft robots powered by fluidic actuators require bulky, rigid pumps that consume considerable power.

In this work, we developed a low power, silent, soft, jellyfish-inspired robot driven by fluid electrode dielectric organic robotic actuators (FEDORAs). We used a mechanical model to determine optimal dimensions and validated it with experimental data. Considering fluid dynamic analyses of jellyfish locomotion, we hypothesized that the system would have an optimal driving frequency that maximizes speed and minimizes cost of transport (COT), which we tested experimentally. To enable untethered propulsion, we designed a waterproof, untethered power supply for driving the robot. These efforts resulted in a silent, low-power, untethered soft swimming robot capable of jellyfish-inspired locomotion, comprised of actuators with a maximum deflection of 10 mm, maximum force of 6.1 mN, and maximum work output of 16 μJ. A tethered version swam at a maximum speed of 1.8 mm/s and had a COT of 260. The untethered robot achieved an average speed of 3.2 mm/s with a COT of 35. The layout of the rest of the paper is as follows: in section Background we give an overview of jellyfish locomotion, previous work on jellyfish-inspired robots, and dielectric elastomer actuators; section Robot Design describes the design of our robot; section Experimental Design discusses our experimental design; in section Results we provide our results; and we end with a discussion of the work and our conclusions.

BACKGROUND

Jellyfish Locomotion

In terms of cost of transport (COT), the jellyfish is the most efficient animal at locomotion. COT relates the energy required to move a unit mass a unit distance:

$$COT = \frac{E}{mgd} = \frac{P}{mgv} \tag{1}$$

where E is the input energy, m is the mass of the animal, g is the standard acceleration due to gravity, d is the distance traveled, P is the input power, and v is the animal's velocity. The COT for Aurelia aurita is reported to be between 0.2 and 0.9 (Gemmell et al., 2013). Jellyfish have a thin layer of muscles on the underside of their bell, which they contract to eject a volume of fluid from within their bell. The ejected fluid propels the jellyfish forward. The jellyfish then releases the contraction on their muscles and the elasticity of the jellyfish restores the bell to its initial volume. In other words, the jellyfish primarily expends energy during the contraction phase in which energy not transferred to the fluid can be stored in the elastic structure, and the stored energy can be recovered during the relaxation phase of the swimming cycle. This approach of passive relaxation enables the jellyfish to achieve such high efficiency. Jellyfish swim the fastest and the most efficiently at or near their resonant frequency, based on the stiffness and dimensions of their bell (Hoover and Miller, 2015). The pulse frequency at which jellyfish swim is also inversely proportional to their mass, and they reduce their pulse frequency as they grow to reduce the energetic cost of driving a large mass at a high frequency (McHenry, 2003).

Actuation for Jellyfish-Inspired Robots

Recently, an untethered jellyfish-inspired soft robot was developed using hydraulic actuators (Frame et al., 2018). One challenge with fluidic actuators is that they necessitate either a pump or piston for pressurizing the chambers, which often draw a considerable amount of power, are most efficient when driven continuously instead of in intermittent pulses, and are made from rigid materials. Nawroth et al. presented a tissue-engineered jellyfish-inspired robot that used cardiac myocytes (heart cells) for actuation (Nawroth et al., 2012). This approach resulted in a completely soft, jellyfish-inspired robot, but led to many fabrication and storage challenges commensurate with implementing biological tissues into a robotic actuator. Several jellyfish-inspired robots have been developed with actuators based on shape memory alloys (SMAs) (Villanueva et al., 2011; Tadesse et al., 2012) and ionic polymer-metal composites (IPMCs) (Yeom and Oh, 2009), but SMAs are challenged by slow response speeds and IPMCs require encapsulation. Ren et al. developed a small scale soft robot that employed an external field to actuate magnetic lappets (Ren et al., 2019). Their work demonstrated the ability to effectively swim and transport cargo, but required an external field for propulsion. Recently, Cheng et al. demonstrated an untethered soft robotic jellyfish that was powered by dielectric elastomer actuators (DEAs) that swam with a maximum speed of 1 cm s^{-1} (Cheng et al., 2019). While the work of Cheng et al. was the first demonstration of an untethered jellyfish-inspired robot powered by DEAs, their work relies upon a prestretched membrane and hydrogel electrodes. Previously, we demonstrated that the performance of soft, swimming robots based on DEAs may be possible with a simpler and more compliant design by implementing prestrain-free membranes and electrodes comprised of a conductive fluid (Christianson et al., 2018a,b).

Overview of DEAs

DEAs provide an energy efficient method of achieving deformations with high strains for soft robots (Pelrine et al., 2000). Recent efforts on jellyfish-inspired robots driven by dielectric elastomer actuators include those by Godaba et al. in which they developed a pressurized DEA membrane that expanded to eject a volume of water from within a 3D printed

shell (Godaba et al., 2016) and a soft, multi-lobed flapping robot developed by Shintake et al. (2016). DEAs are a type of smart material consisting of a dielectric polymer membrane with two conductive electrodes on either side (Carpi et al., 2015). A high voltage is applied through the electrodes across the membrane. As charges accumulate on either side of the membrane, the attraction of opposite charges compresses the film in thickness while repulsion of like charges on the surfaces expands the film in area. If the actuator is laminated to a flexible but inextensible strain-limiting layer, the actuator will curve toward the inextensible layer as it lengthens. One of the benefits of DEAs is that they are energy efficient and have a reported electromechanical conversion efficiency of 90% (Pelrine et al., 2000). Energy loss occurs due to current leakage through the dielectric as well as viscoelastic losses from the material (Chiang Foo et al., 2012). Practically, additional energy is lost when the actuators are discharged, as there are typically energy losses in removing the charges from the actuator (in the worst case they are shunted to ground).

The dielectric film in a DEA is typically either a silicone or acrylic based elastomer (e.g., polydimethylsiloxane—PDMS—or the acrylic adhesive VHB from 3M). The compliant, conductive electrodes can be made from a variety of materials, including thin films of deposited metals; conductive hydrogels; or carbon-based electrodes that are either in a dry powder form, suspended in a silicone grease, or dispersed in an elastomeric matrix. Deposited metals feature high conductivity but their stiffness precludes them from most practical DEA applications and they typically require a deposition in a cleanroom environment or other costly fabrication approaches. Conductive hydrogels are transparent, conductive, and compliant, but they need to be encapsulated to avoid dehydration, impart some non-negligible stiffness, and require some effort to fabricate (Keplinger et al., 2013; Li et al., 2017). Carbon-based electrodes are the most widely used materials for compliant electrodes in DEAs due to their low cost, high compliance, and ease of prototyping, but also need to be encapsulated to prevent smearing under mechanical abrasion. The silicone oil in carbon grease is also reported to disperse through the dielectric membrane, affecting the properties and lifetime of the actuators.

We recently reported that water makes an excellent conductive electrode, especially for underwater applications (Christianson et al., 2017, 2018a,b). Five key advantages of using water for compliant electrodes in a DEA are that fluid electrodes (1) impart no additional stiffness to the structure and are fully compliant to deformations of the actuator; (2) eliminate the need for an external encapsulation layer, reducing the overall stiffness and complexity of fabrication; (3) can be transparent; (4) are inexpensive and straightforward to manufacture; and (5) can be loaded with dyes or other solutions for visual communication or other applications. Previously, we developed an eel-inspired swimming robot that used a series of bimorph fluid electrode dielectric organic robotic actuators (FEDORAs) to undulate through the water at a maximum speed of 1.9 mm/s (Christianson et al., 2018b). In addition, while many DEAs rely upon being prestrained and having a rigid or semi-rigid frame to maintain that strain, prestrained actuators demonstrate a number of disadvantages, including the need to use a rigid frame, the challenge of rupturing the film during prestrain, and the impractability during many applications, especially in soft robotics where compliance is advantageous (Opris, 2018).

ROBOT DESIGN

Description of Overall Design

The overall design is based on an axisymmetric array of unimorph actuators, as shown in **Figure 1**. The outer surface of the robot is an active dielectric elastomer actuator, which expands in area when we apply a voltage to it. To apply the voltage, we implement fluid electrodes—one electrode is a thin film of fluid that is encapsulated underneath the dielectric elastomer, and the other electrode is provided by the surrounding, grounded fluid that the robot is immersed in. A second layer of dielectric elastomer encapsulates the inner fluid electrode. A flexible but

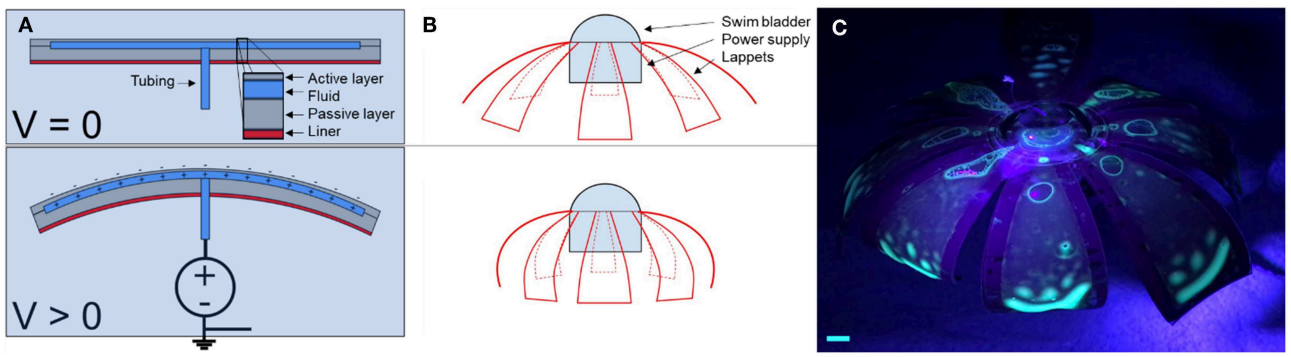

FIGURE 1 | Working principle and fluorescence image of the jellyfish-inspired robot. **(A)** The FEDORAs comprise two elastomeric layers that encapsulate a conductive fluid. When we applied a voltage to the internal fluid electrode w.r.t. the surrounding fluid, Maxwell forces induced a pressure on the dielectric membrane, causing it to lengthen and thin, which resulted in bending toward the inextensible layer. **(B)** To achieve untethered swimming, we designed an axisymmetric array of FEDORAs and attached a waterproof high voltage power supply. A swim bladder provided buoyancy control. When the power supply was on, the electrostatic forces caused the lappets of the robot to bend downward, generating a net thrust upwards. **(C)** Screen captures from **Video 3**, in which we demonstrated the transparency of the dielectric membrane and fluid electrodes by adding a fluorescent dye to the fluid which we stimulated with an ultraviolet light. Scale bar is 1 cm.

inextensible film serves as a strain-limiting layer and provides a small prestrain to the dielectric elastomer. We establish electric contact between the inner fluid electrode and a power supply through a silicone tube with a fluid that provides a conducting path. When we apply a voltage through the fluid across the dielectric elastomer, the elastomer expands in area and the bell of the jellyfish-inspired robot contracts. This contraction accelerates fluid around the edge of the bell, enabling forward propulsion of the robot.

Design of the Unimorph Actuators

Each actuator comprises four layers—the active dielectric elastomer, the fluid electrode, the passive dielectric elastomer, and the strain-limiting layer, as shown in **Figure 1**. We designed the unimorph actuator using the optimization results for bending of a multilayer electro-active polymer presented by Balakrisnan et al. (2015), which are based on the tri- and multi-layer analytical models by Benslimane et al. and Devoe et al., respectively (DeVoe and Pisano, 1997; Benslimane et al., 1999). The analytical model predicts the performance of the unimorph actuator as a function of the layer thickness and stiffness of the material. We employed this analytical model to optimize the actuator design for achieving maximum curvature and the desired block force required to produce sufficient thrust underwater. For the unimorph actuator, a large deformation (change in curvature) upon actuation is required to propel the jellyfish by displacing a large quantity of fluid in a single actuation cycle. Additionally, the unimorph actuator is required to generate thrust to overcome the drag generated during each pulse of the actuation cycle. Hence, the blocking force that the unimorph actuator can produce should be sufficient to generate the desired thrust. The unimorph actuator design presented in this paper can be approximated to the trilayer configuration consisting of a mechanically invisible fluid layer at the center.

For generating higher force, the passive layer should have a large relative thickness as compared to the active layer of the unimorph structure. However, a large thickness of the passive layer significantly reduces the change in curvature and deformation of the unimorph structure upon actuation. The minimal thickness and high relative modulus of the passive layer help to achieve maximum curvature in the case of a bilayer structure. Hence, as a compromise between this conflicting relationship for achieving both high force and large deflections, we used a passive layer with matched thickness relative to the active layer and an additional liner with significantly high stiffness that acts as reinforcement for the passive layer. This additional reinforcing layer provides the desired stiffness for the passive layer with minimal change in its thickness and enables us to optimize the design to achieve the desired block force and deformation.

We selected the dielectric elastomer layers from among commercially available materials and electronic components to maximize the strain of actuation. We chose an acrylic-based elastomer for the dielectric layers due to its high actuation response, self-adhesion, and prevalence in DEA research (for comparison with other work). We found four thicknesses for commercially available acrylic elastomers and selected the one that would provide the largest strain at the maximum voltage that we could achieve with a commercially available high voltage power supply (EMCO Q101) without suffering breakdown. We used the analytical mechanical model described by Balakrisnan et al. to determine the optimal thickness of the passive dielectric layer that would maximize work. While a passive layer that matches the thickness of the active layer should achieve the highest deflection, a thicker passive will provide greater force. Thus, we needed to select the thickness that would provide the greatest total work. We also used the same model to predict the increase in work that could be achieved by an additional, stiffer, strain-limiting layer.

Additionally, DEAs are known to have improved performance when they are prestrained, however, prestrained DEAs typically require a rigid frame to maintain that strain. Alternatively, we imparted the strain-limiting layer with some initial curvature to apply a prestrain to the DEAs (**Figure 2B**). The acrylic elastomer is shipped on a thin polyethylene liner. When the liner is peeled off of the elastomer, the liner undergoes plastic deformation and exhibits some curvature. When we reapplied the liner with its initial curvature to the elastomer, the layer provided a small initial prestrain to the actuators, which increased their performance.

To generate the axisymmetric design for the jellyfish, we designed a hemisphere in CAD with eight segments or lappets. To enable fabrication of a 3D body using laminate fabrication techniques, we flattened the hemisphere onto a planar projection and used layer-by-layer manufacturing to the assemble the structure, as shown in **Figure 2**. Fabrication details are provided in Materials and Methods and in **Figure 3**.

Design of Untethered System

The untethered system needed to provide a high voltage signal to the inner fluid electrode with respect to the surrounding grounded fluid. To accomplish this, we attached a battery to a timing circuit that generated a low voltage square wave signal, as shown in **Figure 4**. The output of the timer powered a voltage regulator, which then triggered an LED and the high voltage DC/DC convertor. We connected the high voltage output of the HVDC convertor by wire to the internal fluid electrode and immersed the low voltage lead in the surrounding fluid to serve as a ground electrode. In these experiments we used tap water for the fluid electrodes, which we previously found to be sufficiently conductive for actuation (Christianson et al., 2018a,b). We placed a discharge resistor with a high impedance across the high voltage and ground leads to enable passive recovery of the actuators. Since the discharge resistor was in parallel with the actuator and power supply, a low impedance resistor would have reduced the discharge time while a high impedance resistor reduced the power loss, through the resistor during charging. For a power supply with a fixed output power, a higher impedance discharge resistor connected in parallel with the actuator results in a higher operating output voltage across the actuator.

To provide buoyancy control, we assembled a swim bladder out of two layers of an acrylic elastomer using a similar fabrication approach as what was used for the actuators (see materials and methods). A tube was inserted in between the elastomer layers and we injected air with a syringe through a

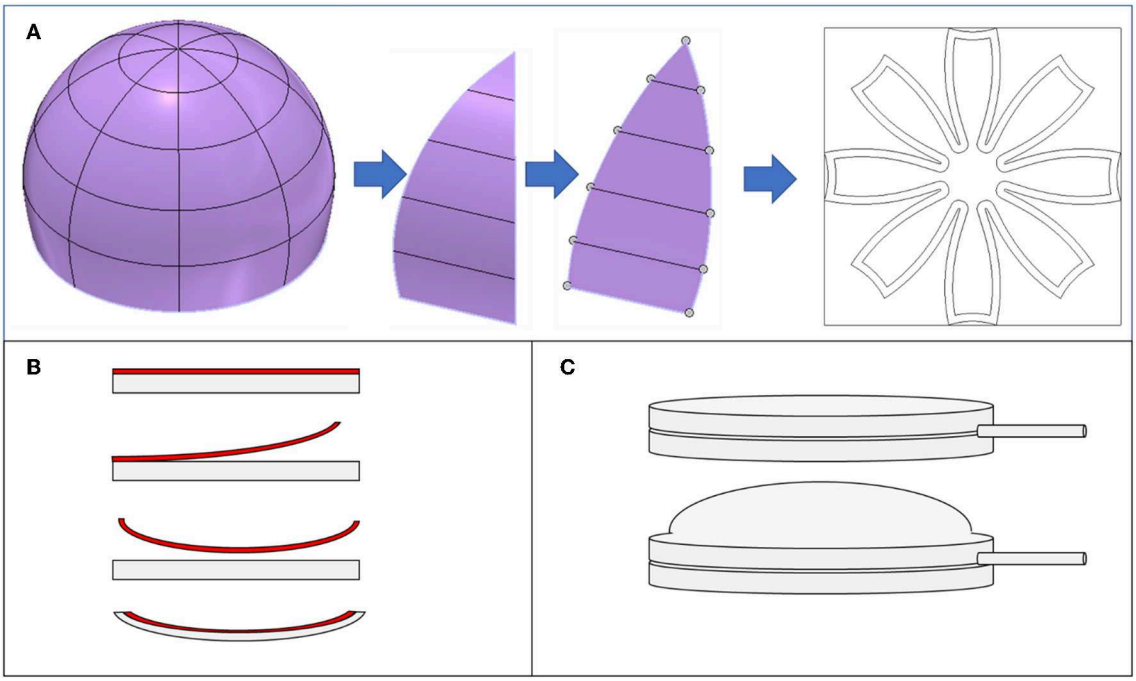

FIGURE 2 | Design of lappets, application of prestrain, and swim bladder. **(A)** Lappets were designed in CAD by segmenting a hemisphere into eight lappets. The lappets were flattened into 2D and then arranged in an axisymmetric array to generate the design for the jellyfish-inspired robot. **(B)** The acrylic elastomer (gray) came affixed to a polyethylene liner (red). When the liner was removed, it exhibited some curvature. When we reapplied the liner to the elastomer, the elastomer was prestrained slightly by the liner and demonstrated a similar curvature. **(C)** The swim bladder was made from two layers of an acrylic elastomer that were adhered to each other at the outer border. A silicone tube was inserted between the layers and pneumatic pressure was applied through the tube to inflate it, providing buoyancy for the jellyfish-inspired robot.

small tube to pressurize the swim bladder. The swim bladder was affixed to the upper surface of the jellyfish to provide buoyancy control. This configuration also has the benefit of reducing the risk of pull-in instability due to local deformation of the high voltage wire underneath.

EXPERIMENTAL DESIGN

Measure Deflection and Force as a Function of Frequency for Different Actuator Configurations

To determine optimal configurations for the actuators, we measured their maximum deflection and blocked force, as shown in **Figure 5**. Using the same lateral geometry for each actuator (50.8 mm in width, 76.2 mm in length, with a passive border of 8 mm), we tested actuators with a passive layer thickness of 0.5, 1, and 1.5 mm. We tested the impact of an inextensible strain-limiting layer (the polyethylene backing that the acrylic elastomer is initially affixed to) on actuation. Each test begins with the liner applied (as supplied by the manufacturer), then we measure the actuator again after removing the liner. The acrylic elastomer was rolled up in a tube. When we remove the liner from the elastomer, the liner exhibits a curvature in the opposite direction as the curvature it had when it was on the tube. When we re-apply the liner to the elastomer, the elastomer is prestrained and curls slightly due to the curvature of the liner (**Figure 2**). We suspended the actuators in water and applied a constant, fixed voltage (7 kV) and measured the maximum deflection. To determine the maximum blocked force, we placed a strip of spring steel with known dimensions adjacent to the actuator and measured the deflection of both the spring steel and actuator when we applied a voltage. Using Euler-Bernoulli beam theory, we calculated the corresponding force at this actuator displacement:

$$F = \frac{6yEI}{(3l - a)a^2} \tag{2}$$

where y is the deflection at the tip of a beam with length l, EI is the flexural rigidity of the beam, and a is the position along the length of the beam where the force was applied. Assuming a linear relationship between force and displacement, we extrapolated to find the blocked force. The area under the curve is calculated as the work output of the actuator. We then compared the work output for three thicknesses of passive layer (0.5, 1, and 1.5 mm) and three conditions of the inextensible backing (backing on, backing removed, and backing reapplied).

Measure Speed for Tethered Design

To determine the maximum speed as a function of frequency, we attached the robot to a high voltage power supply and drove it at a fixed frequency. The robot was suspended by its silicone tubing which was affixed to a float to maintain a constant vertical

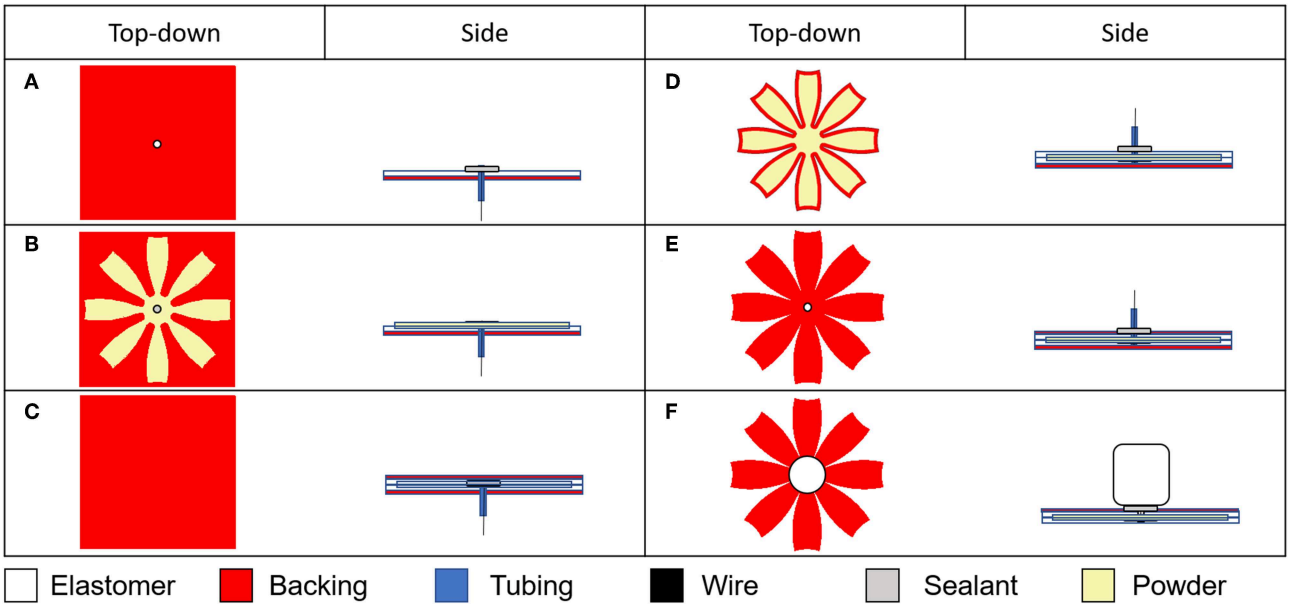

FIGURE 3 | Fabrication process for FEDORA jellyfish. **(A)** We prepared the back layer of the elastomer by cutting it to size and creating a hole in the center of the sheet where we inserted a silicone tube and sealede the tube to the elastomer with a silicone glue. For the untethered case, we threaded a thin, flexible wire through the tubing to reduce the risk of an air in the tube causing an open circuit. **(B)** We used a mask to apply a passivating powder to the lower elastomer layer and then **(C)** encased the powder with the dielectric elastomer layer. **(D)** We removed the backing layer, sealed the underside of the tube with silicone glue, and trimmed the excess material from the actuator through all layers using a laser cutter. After the sealing agent has cured, we injected the fluid electrode through the tubing using a syringe. **(E)** We reapplied the backing layer to the under (tubing) side of the actuator. **(F)** We connected the inner fluid electrode to the driving electronics, removed the backing layer from the dielectric elastomer layer, and applied a passivating agent to the outside of the dielectric elastomer to prevent unintended self-adhesion. For the tethered case, we electrically connected the high voltage power supply to the inner fluid electrode via a metallic syringe tip. For the untethered case, we sealed the tubing shut using a nylon cable tie and electrically connected the power supply to the exposed wire. We then affixed and sealed the electronics to the robot using a silicone glue.

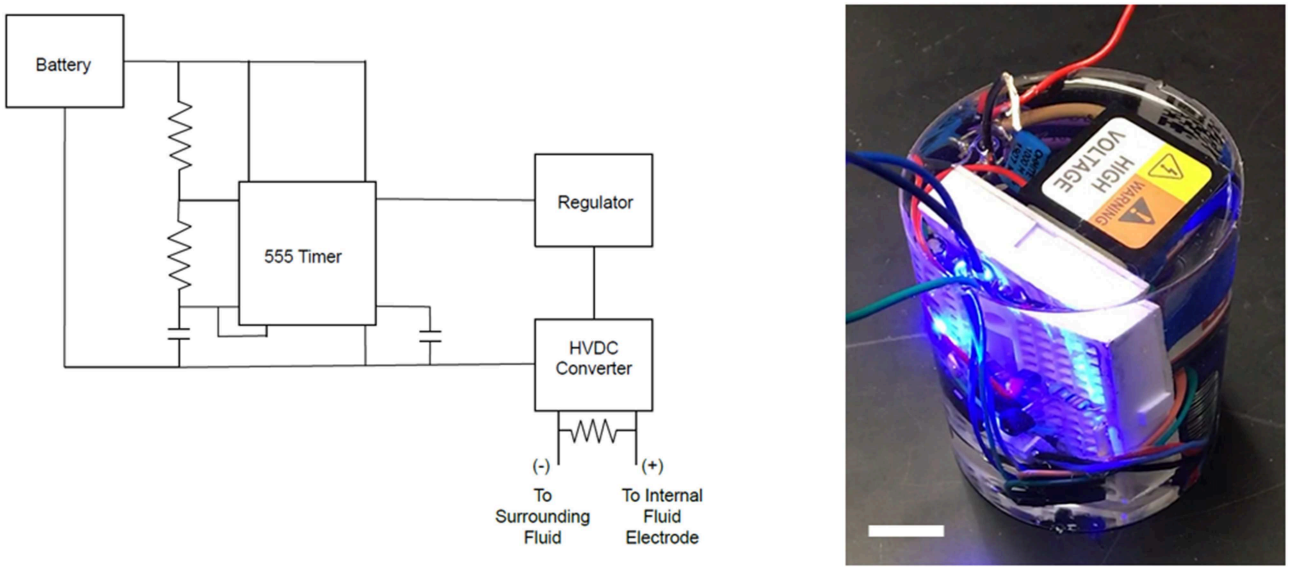

FIGURE 4 | Untethered power supply. **Left**: schematic. A battery powered a 555 timer which we designed to provide a square wave output signal at a desired frequency and duty cycle. We connected the output of the timer to a voltage regulator that provides a consistent maximum voltage to the dc/high voltage dc (HVDC) convertor. The high voltage output of the HVDC convertor was connected to the inner fluid electrode and the ground output is connected to the surrounding fluid. **Right**: photo of power supply encased in silicone with its LED illuminated. Scale bar is 1 cm.

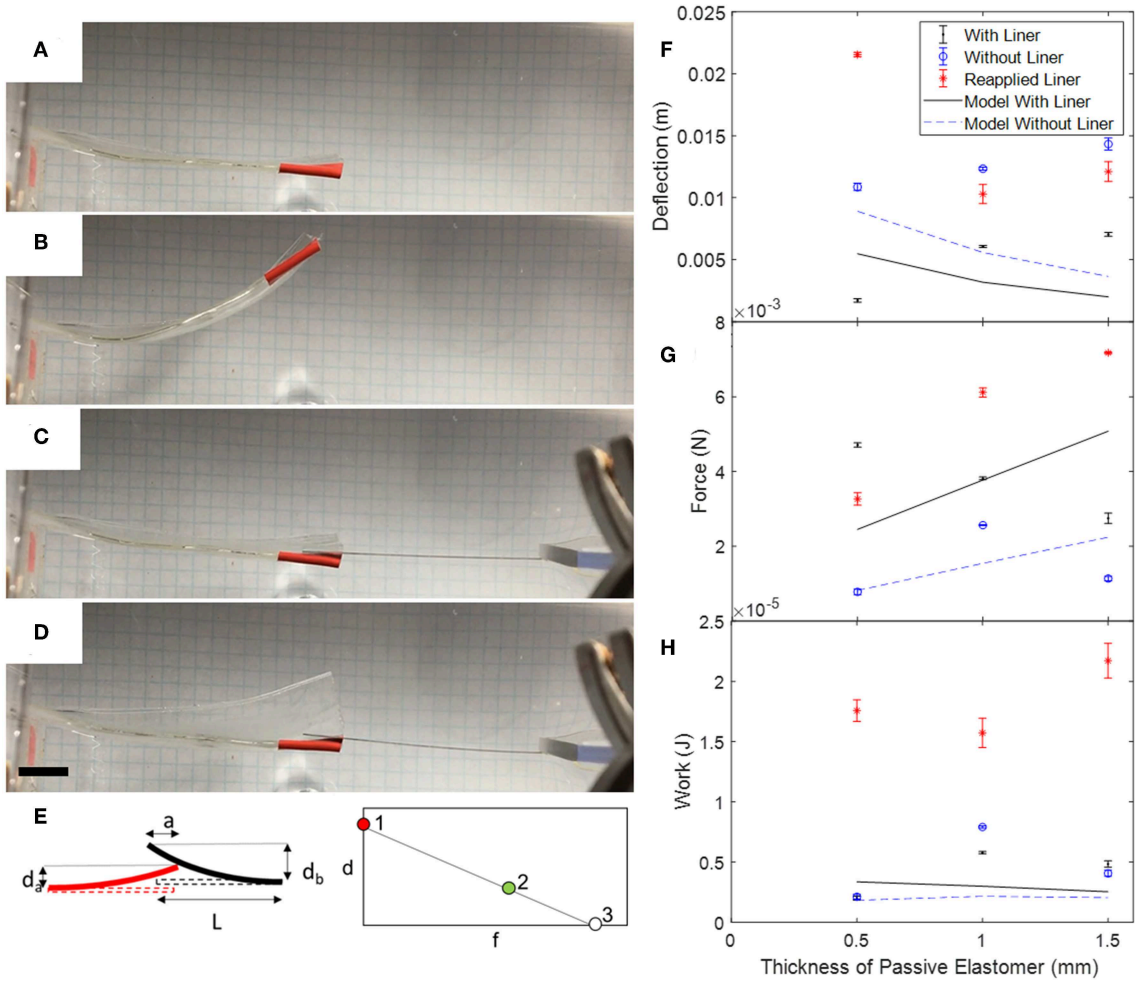

FIGURE 5 | Static tests of unimorph FEDORAs to determine deflection, force, and work as a function of the thickness of the passive layer. Left column: deflection was taken as the difference of the position of the tip when the voltage was off **(A)** and on **(B)**. Tape (red) was applied to the tip as a visual marker to help with tracking. To measure blocked force, we placed a beam of spring steel with length L next to the tip of the actuator **(C)** and measured the deflection of the beam (d_b) and actuator (d_a) when the voltage is on **(D)** as shown in the schematic **(E)**. The beam overlapped the tip of the actuator a distance a. We used Euler-Bernoulli beam theory to calculate the force that the actuator imparted on the beam (Equation 2). To estimate the blocked force, we plotted the displacement at no force (1) and the calculated force at a small displacement (d_a, 2) and assumed a linear relation between the force and displacement and extrapolated to determine the blocked force (3). Right column: comparison of analytical model and experimental results for **(F)** deflection, **(G)** blocked force, and **(H)** work as a function of the thickness of the elastomeric passive layer. Error bars are the standard deviation from three actuations for each actuator configuration. Scale bar is 1 cm.

position. A wire connected the fluid electrode to the high voltage electronics. Overhead video provided a record of the lateral position of the robot with respect to time and the videos were analyzed using Tracker (Brown, 2019).

Estimated Power Consumption and Cost of Transport

To estimate the mechanical power required to deform the actuator, we followed an approach described previously (Christianson et al., 2018b) which calculates the electrical input power to be $P_{electrical} = C_{act}V^2f$, based on the capacitance when the actuator is actuated (C_{act}), the applied voltage (V), and driving frequency (f). To find C_{act}, we measured the capacitance of the actuator in the rest state directly using an LCR meter and calculated the expected value of C_{act} based on the change in area and thickness that is predicted from Pelrine's equation and Hooke's law (Pelrine et al., 2000). To calculate the maximum input power as a "worst-case" value for cost of transport calculations, we used the maximum output power of the high voltage direct current (HVDC) power converters, which provide 0.5 watts. At a duty cycle of 50%, the average electrical power from the HVDC convertors to the actuators was 0.25 W. We then calculated the cost of transport using Equation (1) (Paschal et al., 2017).

Measure Speed for Untethered Swimming

To determine the ability of the robot to swim untethered, we sealed the wireless power supply to the robot and attached a

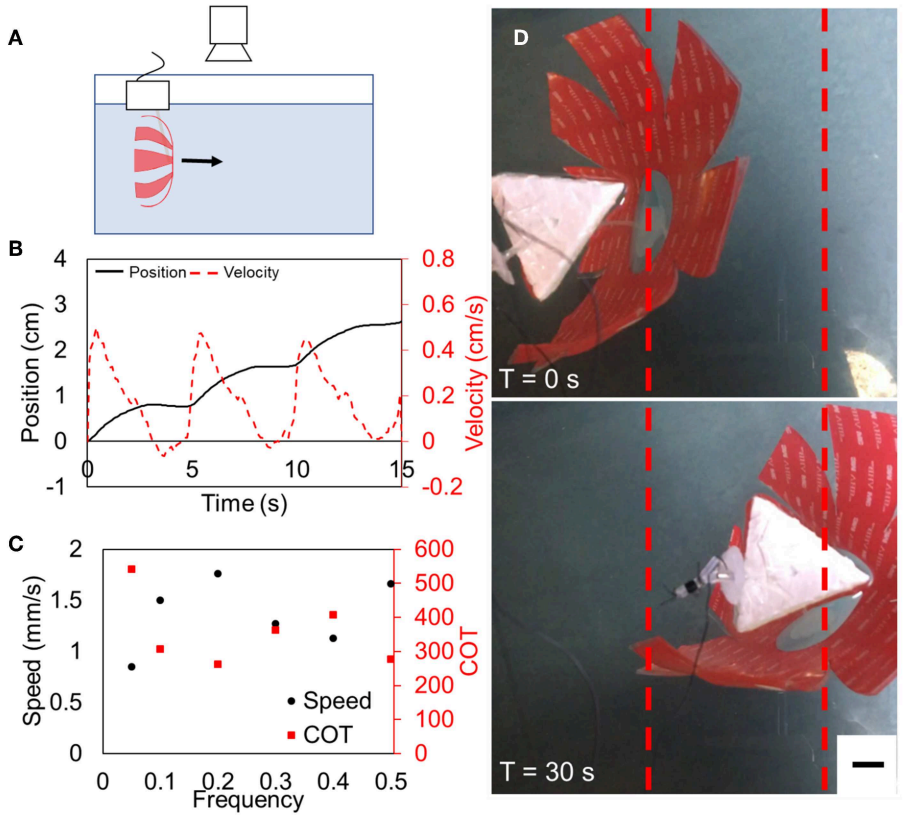

FIGURE 6 | Tethered FEDORA jellyfish swimming results. **(A)** Schematic of experimental setup. **(B)** Representative example of position and velocity as a function of time for three actuation cycles. **(C)** Speed and cost of transport as functions of frequency, demonstrating a maximum speed of 1.8 mm/s and a corresponding COT of 260. **(D)** Still frames taken from swimming tests at the beginning of the test (top) and after 30 s (bottom). Scale bar is 1 cm.

pneumatic swim bladder to the top of it. We tuned the bladder so that the overall structure was slightly negatively buoyant, placed the robot at the bottom of a tank of water, and actuated it at a fixed frequency. We used video to record the position of the robot with respect to time as the robot swam to the top of the tank of water.

RESULTS

Deflection, Blocked Force, and Work of Unimorph Actuators

As the thickness of the passive layer increased from 0.5 to 1.5 mm, the deflection also increased (**Figure 5**). For each thickness of passive layer, the deflection increased when the liner was removed. When the liner was reapplied, the deflection decreased, except in the case when the passive layer was the same thickness as the active layer. The model predicted that the deflection would be greater for the actuator without a liner vs. with a liner, and that the deflection would decrease as the thickness of the passive layer increased. The greatest deflection that we measured was 2.2 cm for the actuator with 0.5 mm thick active and passive elastomer layers and the reapplied liner.

When the actuators were tested with the liner still affixed, the blocked force decreased as the thickness of the passive layer increased. The model predicted that the actuators with the liner would have a greater blocked force than the actuators without a liner and that the blocked force increased as the thickness of the passive layer increased. The maximum blocked force was 7.2 mN for the 0.5/1.5 mm layers and the reapplied liner.

For actuators without an inextensible layer, the model predicted that a peak value of work exists when the passive layer is twice that of the active layer. In contrast, when there was an inextensible layer, the work decreased as the thickness of the passive layer increased. The experimental results for the two cases of the as-prepared liner and actuator without liner agreed with the trend predicted by the model for the case without a liner. However, the actuators with reapplied liners showed the opposite trend. We calculated the maximum work to be 22 μW for the 0.5/1.5 mm layers and reapplied liner.

Tethered Swimming Performance

The motion of the robot was approximately sinusoidal with propulsion and coast phases, which we found to be qualitatively similar to the motion of jellyfish. Representative tethered swimming is shown in **Video 1**. The maximum average speed of the tethered robot was 1.8 mm/s at a driving frequency of 0.2 Hz, as shown in **Figure 6**, with an instantaneous peak speed of 5 mm/s during contraction. The electrical input power P at

0.2 Hz was 0.25 W and corresponding COT was 260 (**Table 1**). We measured the swimming speed and calculated the COT for actuation frequencies between 0.05 and 0.5 Hz. While the results shown in **Figure 6C** suggest that there might be a second harmonic and additional extrema in speed and COT at a driving frequency above 0.5 Hz, empirical results demonstrated that the peak swimming speed was below 0.5 Hz and a thorough investigation of performance at higher frequencies is reserved for future work.

Untethered Swimming Performance

The untethered jellyfish-inspired robot was driven at 0.2 Hz and the average speed over the first three cycles was 3.2 mm/s, as shown in **Figure 7** and **Video 2**, and the peak instantaneous speed was 7.1 mm/s. For a bell margin diameter of 16.3 cm, this corresponds to an average swimming speed of 0.02 BL/s. After three cycles, the upward velocity increased which was likely coupled with a positive change in buoyancy as the pressure on the swim bladder decreased. The COT for the untethered jellyfish was 35, due to the increase in velocity and mass of the robot compared to the tethered case. For this test, we used a battery with a capacity of 180 mAh. The HVDC convertor consumed an average of 0.25 W to power the FEDORAs. At an average power input of 0.25 W and an average speed of 3.2 mm/s, we estimate that a 180 mAh battery would provide enough power for 2.7 h of actuation.

TABLE 1 | COT comparison for tethered and untethered swimming.

	Average input power (W)	Mass (kg)	Average speed (mm/s)	COT
Tethered	0.25	0.055	1.8	260
Untethered	0.25	0.23	3.2	35

DISCUSSION

As discussed in section Design of the Unimorph Actuators, the model predicts maximum deflection for a unimorph actuator that behaves as a simple bilayer—i.e., for the case where both layers have the same thickness and modulus. However, when we use FEDORAs without a liner, both dielectric elastomer layers (top and bottom) should experience some strain, proportional to their thickness. In the case where the passive layer is thicker than the active layer, then the strain in the active layer should dominate. Interestingly, we still observed deflection for the case when both layers had the same thickness. This result may be due to our fabrication approach in which a passivating powder is applied to the passive layer which imparts some additional stiffness in the thickness direction of the passive layer, imparting the asymmetry necessary for bending.

As the model is unable to account for prestrain, we were unable to use it to predict the performance of the actuator when we reapplied the liner. The model successfully predicted that the deflection would be greater for an actuator without an inextensible layer and that the force would be greater with the inextensible layer. We also observed the trend that the work of the actuator without a liner would be the greatest when the thickness of the passive layer was twice that of the active layer. However, the trends of how the force and deflection scale with the thickness of the passive layer disagreed with our experimental results. This may be due to the model not taking Maxwell stress on the passive elastomer into account or that there is additional prestrain in the device due to the manufacturing process.

We used the unimorph results to guide our design of the jellyfish-inspired robot. We selected the combination of layer thicknesses that would result in maximizing work for a fully elastomeric robot (0.5 mm thick DEA and 1 mm thick passive layer). To further increase the work, we also used the reapplied liner. Our experimental unimorph results suggest that we may

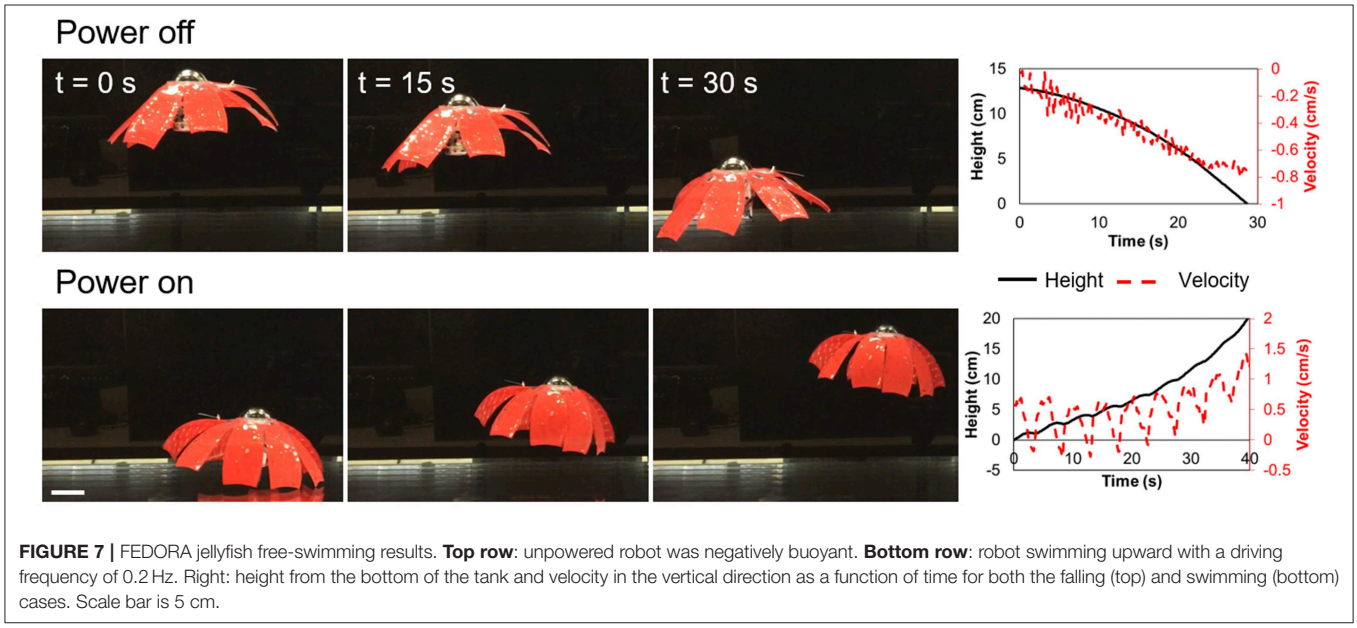

FIGURE 7 | FEDORA jellyfish free-swimming results. **Top row**: unpowered robot was negatively buoyant. **Bottom row**: robot swimming upward with a driving frequency of 0.2 Hz. Right: height from the bottom of the tank and velocity in the vertical direction as a function of time for both the falling (top) and swimming (bottom) cases. Scale bar is 5 cm.

be able to further increase the actuation of our jellyfish-inspired robot by using a thicker passive elastomer layer, but a full comparison between the performance of robots with different thicknesses of the passive layer is reserved for future work.

One challenge with this approach is that prestrain-free DEAs are incapable of providing large forces and thus high-speed propulsion. The maximum tethered and untethered speeds that we measured were 1.8 and 3.2 mm/s, respectively, which may be insufficient for applications in high flow, high speed environments. The speed of our untethered jellyfish is ∼3× slower than that of jellyfish of similar mass and the COT of our untethered jellyfish was ∼10× greater than that of a jellyfish with a similar mass (Gemmell et al., 2013). The development and employment of sensors, programmability, and lateral control is reserved for future work.

CONCLUSION

In this work, we developed a completely soft jellyfish-inspired robot in which all the components—aside from the driving electronics—were flexible or stretchable. The high voltage electrode is encapsulated within a dielectric membrane, ensuring that it is safe for use around animals. As with our previous work using fluid electrodes (Christianson et al., 2018a,b), the FEDORAs actuate completely silently as opposed to traditional ROVs that rely on propeller or jet propulsion, enabling stealthy locomotion. We demonstrate that a flexible but inextensible layer can apply a non-negligible prestrain for DEAs, creasing the performance of the actuators. Many DEAs employ prestrain to improve their performance, but this approach typically requires a rigid frame to maintain that prestrain during actuation. By using an inextensible layer with an initial curvature, we were able to more than double the work output of our actuators without employing a rigid frame. Additionally, we developed a waterproof power supply and demonstrated untethered swimming of our jellyfish-inspired robot. The onboard power supply obviates the need for a tether or external magnetic or electric field. This proof-of-concept prototype demonstrates the feasibility of using FEDORAs for driving bioinspired swimming robots for underwater applications where low power and silent locomotion are important.

MATERIALS AND METHODS

We used VHB 4905 (3M) for the 0.5 mm thick dielectric elastomers, VHB 4910 for the 1 mm thick elastomers, and a laminate of the two for 1.5 mm thick layers. Caster sugar was used as the passivating powder and dish soap was used as a passivating liquid. An EMCO Q101 high voltage power convertor was used as a voltage amplifier in all experiments.

DATA AVAILABILITY STATEMENT

The data generated for this study is available upon request.

AUTHOR CONTRIBUTIONS

CC and MT conceived of the project and wrote the initial draft of the paper. CC, CB, GL, AG, and CA fabricated the devices and performed the experiments. CC analyzed the data. SJ helped with modeling and design. TL and MT provided guidance for the project. All authors helped with editing the paper.

FUNDING

This work was funded by the Office of Naval Research (ONR) grants N000141712062 and N00014-18-1-2277. CC was supported by National Science Foundation Graduate Research Fellowship grant number DGE-1144086.

SUPPLEMENTARY MATERIAL

The Supplementary Material for this article can be found online at: https://www.frontiersin.org/articles/10.3389/frobt.2019.00126/full#supplementary-material

REFERENCES

Aubin, C. A., Choudhury, S., Jerch, R., Archer, L. A., Pikul, J. H., and Shepherd, R. F. (2019). Electrolytic vascular systems for energy-dense robots. *Nature* 571, 51–57. doi: 10.1038/s41586-019-1313-1

Balakrisnan, B., Nacev, A., and Smela, E. (2015). Design of bending multi-layer electroactive polymer actuators. *Smart Mater. Struct.* 24:045032. doi: 10.1088/0964-1726/24/4/045032

Bauer, S., Bauer-Gogonea, S., Graz, I., Kaltenbrunner, M., Keplinger, C., and Schwödiauer, R. (2014). 25th anniversary article: a soft future: from robots and sensor skin to energy harvesters. *Adv. Mater.* 26, 149–162. doi: 10.1002/adma.201303349

Benslimane, M., Gravesen, P., West, K., Skaarup, S., and Sommer-Larsen, P. (1999). "Performance of polymer-based actuators: the three-layer model," in *Smart Structures and Materials 1999: Electroactive Polymer Actuators and Devices*, Vol. 3669, ed Y. Bar-Cohen (Newport Beach, CA: SPIE), 87–97. doi: 10.1117/12.349667

Brown, D. (2019). *Tracker Video Analysis*. Available online at: http://physlets.org/tracker/

Calisti, M., Giorelli, M., Levy, G., Mazzolai, B., Hochner, B., Laschi, C., et al. (2011). An octopus-bioinspired solution to movement and manipulation for soft robots. *Bioinsp. Biomimet.* 6:036002. doi: 10.1088/1748-3182/6/3/036002

Carpi, F., Anderson, I., Bauer, S., Frediani, G., Gallone, G., Gei, M., et al. (2015). Standards for dielectric elastomer transducers. *Smart Mater. Struct.* 24:105025. doi: 10.1088/0964-1726/24/10/105025

Cheng, T., Li, G., Liang, Y., Zhang, M., Liu, B., Wong, T. W., et al. (2019). Untethered soft robotic jellyfish. *Smart Mater. Struct.* 28:015019. doi: 10.1088/1361-665X/aaed4f

Chiang Foo, C., Cai, S., Jin Adrian Koh, S., Bauer, S., and Suo, Z. (2012). Model of dissipative dielectric elastomers. *J. Appl. Phys.* 111:034102. doi: 10.1063/1.3680878

Christianson, C., Goldberg, N., Cai, S., and Tolley, M. T. (2017). Fluid electrodes for submersible robotics based on dielectric elastomer actuators. *Electr. Polym. Actuat. Dev.* XIX:101631O. doi: 10.1117/12.2257201

Christianson, C., Goldberg, N. N., Deheyn, D. D., Cai, S., and Tolley, M. T. (2018b). Translucent soft robots driven by frameless fluid electrode dielectric elastomer actuators. *Sci. Robot.* 3:eaat1893. doi: 10.1126/scirobotics.aat1893

Christianson, C., Goldberg, N. N., and Tolley, M. T. (2018a). Elastomeric diaphragm pump driven by fluid electrode dielectric elastomer actuators (FEDEAs). *Electr. Polym. Actuat. Dev.* XX:21. doi: 10.1117/12.2294557

DeVoe, D. L., and Pisano, A. P. (1997). Modeling and optimal design of piezoelectric cantilever microactuators. *J. Microelectromech. Syst.* 6, 266–270. doi: 10.1109/84.623116

Dunbabin, M., and Marques, L. (2012). Robots for environmental monitoring: significant advancements and applications. *IEEE Robot. Autom. Magaz.* 19, 24–39. doi: 10.1109/MRA.2011.2181683

Frame, J., Lopez, N., Curet, O., and Engeberg, E. D. (2018). Thrust force characterization of free-swimming soft robotic jellyfish. *Bioinspir. Biomimet.* 13:064001. doi: 10.1088/1748-3190/aadcb3

Gemmell, B. J., Costello, J. H., Colin, S. P., Stewart, C. J., Dabiri, J. O., Tafti, D., et al. (2013). Passive energy recapture in jellyfish contributes to propulsive advantage over other metazoans. *Proc. Natl. Acad. Sci. U.S.A.* 110, 17904–17909. doi: 10.1073/pnas.1306983110

Godaba, H., Li, J., Wang, Y., and Zhu, J. (2016). A soft jellyfish robot driven by a dielectric elastomer actuator. *IEEE Robot. Autom. Lett.* 1, 624–631. doi: 10.1109/LRA.2016.2522498

Hoover, A., and Miller, L. (2015). A numerical study of the benefits of driving jellyfish bells at their natural frequency. *J. Theor. Biol.* 374, 13–25. doi: 10.1016/j.jtbi.2015.03.016

Jaffe, J. S., Franks, P. J. S., Roberts, P. L. D., Mirza, D., Schurgers, C., Kastner, R., et al. (2017). A swarm of autonomous miniature underwater robot drifters for exploring submesoscale ocean dynamics. *Nat. Commun.* 8, 1–8. doi: 10.1038/ncomms14189

Katzschmann, R. K., DelPreto, J., MacCurdy, R., and Rus, D. (2018). Exploration of underwater life with an acoustically controlled soft robotic fish. *Sci. Robot.* 3:eaar3449. doi: 10.1126/scirobotics.aar3449

Keplinger, C., Sun, Y. J., Foo, C. C., Rothemund, P., Whitesides, G. M., and Suo, Z. (2013). Stretchable, transparent, ionic conductors. *Science* 341, 984–987. doi: 10.1126/science.1240228

Li, T., Li, G., Liang, Y., Cheng, T., Dai, J., Yang, X., et al. (2017). Fast-moving soft electronic fish. *Sci Adv.* 3:e1602045. doi: 10.1126/sciadv.1602045

Marchese, A. D., Onal, C. D., and Rus, D. (2014). Autonomous soft robotic fish capable of escape maneuvers using fluidic elastomer actuators. *Soft Robot.* 1, 75–87. doi: 10.1089/soro.2013.0009

McHenry, M. J. (2003). The ontogenetic scaling of hydrodynamics and swimming performance in jellyfish (*Aurelia aurita*). *J. Exp. Biol.* 206, 4125–4137. doi: 10.1242/jeb.00649

Nawroth, J. C., Lee, H., Feinberg, A. W., Ripplinger, C. M., McCain, M. L., Grosberg, A., et al. (2012). A tissue-engineered jellyfish with biomimetic propulsion. *Nat. Biotechnol.* 30, 792–797. doi: 10.1038/nbt.2269

Onal, C. D., and Rus, D. (2013). Autonomous undulatory serpentine locomotion utilizing body dynamics of a fluidic soft robot. *Bioinspir. Biomimet.* 8:026003. doi: 10.1088/1748-3182/8/2/026003

Opris, D. M. (2018). Polar elastomers as novel materials for electromechanical actuator applications. *Adv. Mater.* 30:1703678. doi: 10.1002/adma.201703678

Paschal, T., Shintake, J., Mintchev, S., and Floreano, D. (2017). Development of bio-inspired underwater robot with adaptive morphology capable of multiple swimming modes. *IEEE Int. Conf. Intell. Robots Syst.* 2017, 4197–4202. doi: 10.1109/IROS.2017.8206281

Pelrine, R., Kornbluh, R., Pei, Q., and Joseph, J. (2000). High-speed electrically actuated elastomers with strain greater than 100%. *Science* 287, 836–839. doi: 10.1126/science.287.5454.836

Ren, Z., Hu, W., Dong, X., and Sitti, M. (2019). Multi-functional soft-bodied jellyfish-like swimming. *Nat. Commun.* 10:2703. doi: 10.1038/s41467-019-10549-7

Rus, D., and Tolley, M. T. (2015). Design, fabrication and control of soft robots. *Nature* 521, 467–475. doi: 10.1038/nature14543

Shintake, J., Cacucciolo, V., Floreano, D., and Shea, H. (2018). Soft robotic grippers. *Adv. Mater.* 30:1707035. doi: 10.1002/adma.201707035

Shintake, J., Shea, H., and Floreano, D. (2016). Biomimetic underwater robots based on dielectric elastomer actuators. *IEEE/RSJ Int. Conf. Intell. Robots Syst* 2, 4957–4962. doi: 10.1109/IROS.2016.7759728

Tadesse, Y., Villanueva, A., Haines, C., Novitski, D., Baughman, R., and Priya, S. (2012). Hydrogen-fuel-powered bell segments of biomimetic jellyfish. *Smart Mater. Struct.* 21:045013. doi: 10.1088/0964-1726/21/4/045013

Villanueva, A., Smith, C., and Priya, S. (2011). A biomimetic robotic jellyfish (robojelly) actuated by shape memory alloy composite actuators. *Bioinspir. Biomimet.* 6:036004. doi: 10.1088/1748-3182/6/3/036004

Wynn, R. B., Huvenne, V. A., Le Bas, T. P., Murton, B. J., Connelly, D. P., Bett, B. J., et al. (2014). Autonomous underwater vehicles (AUVs): their past, present and future contributions to the advancement of marine geoscience. *Marine Geol.* 352, 451–468. doi: 10.1016/j.margeo.2014.03.012

Yeom, S. W., and Oh, I. K. (2009). A biomimetic jellyfish robot based on ionic polymer metal composite actuators. *Smart Mater. Struct.* 18:085002. doi: 10.1088/0964-1726/18/8/085002

Yuk, H., Lin, S., Ma, C., Takaffoli, M., Fang, N. X., and Zhao, X. (2017). Hydraulic hydrogel actuators and robots optically and sonically camouflaged in water. *Nat. Commun.* 8, 1–12. doi: 10.1038/ncomms14230

Conflict of Interest: The authors declare that the research was conducted in the absence of any commercial or financial relationships that could be construed as a potential conflict of interest.

frontiers in Robotics and AI

BRIEF RESEARCH REPORT
published: 22 November 2019
doi: 10.3389/frobt.2019.00127

Sensitivity Improvement of Highly Stretchable Capacitive Strain Sensors by Hierarchical Auxetic Structures

Jun Shintake, Toshiaki Nagai and Keita Ogishima*

Department of Mechanical and Intelligent Systems Engineering, School of Informatics and Engineering, University of Electro-Communications, Chofu, Japan

Highly stretchable sensors that can detect large strains are useful in deformable systems, such as soft robots and wearable devices. For stretchable strain sensors, two types of sensing methods exist, namely, resistive and capacitive. Capacitive sensing has several advantages over the resistive type, such as high linearity, repeatability, and low hysteresis. However, the sensitivity (gauge factor) of capacitive strain sensors is theoretically limited to 1, which is much lower than that of the resistive-type sensors. The objective of this study is to improve the sensitivity of highly stretchable capacitive strain sensors by integrating hierarchical auxetic structures into them. Auxetic structures have a negative Poisson's ratio that causes increase in change in capacitance with applied strains, and thereby improving sensitivity. In order to prove this concept, we fabricate and characterize two sensor samples with planar dimensions 60 mm × 16 mm. The samples have an acrylic elastomer (3M, VHB 4905) as the dielectric layer and a liquid metal (eutectic gallium-indium) for electrodes. On both sides of the sensor samples, hierarchical auxetic structures made of a silicone elastomer (Dow Corning, Sylgard 184) are attached. The samples are tested under strains up to 50% and the experimental results show that the sensitivity of the sensor with the auxetic structure exceeds the theoretical limit. In addition, it is observed that the sensitivity of this sensor is roughly two times higher than that of a sensor without the auxetic structure, while maintaining high linearity ($R^2 = 0.995$), repeatability ($\geq 10^4$ cycles), and low hysteresis.

Keywords: stretchable, capacitive, strain sensors, auxetic structures, soft robotics, wearable devices

OPEN ACCESS

Edited by:
Herbert Shea,
École Polytechnique Fédérale de Lausanne, Switzerland

Reviewed by:
Surya Girinatha Nurzaman,
Monash University Malaysia, Malaysia
Janno Torop,
University of Tartu, Estonia

****Correspondence:***
Jun Shintake
shintake@uec.ac.jp

Specialty section:
This article was submitted to Soft Robotics, a section of the journal Frontiers in Robotics and AI

Received: *24 July 2019*
Accepted: *08 November 2019*
Published: *22 November 2019*

Citation:
Shintake J, Nagai T and Ogishima K (2019) Sensitivity Improvement of Highly Stretchable Capacitive Strain Sensors by Hierarchical Auxetic Structures. Front. Robot. AI 6:127. doi: 10.3389/frobt.2019.00127

INTRODUCTION

Highly stretchable strain sensors, which detect large strains, are an important element for sensing deformations of compliant systems, to assess their status and performance control. These soft matter-based systems include robots and wearable devices (Polygerinos et al., 2017; Rich et al., 2018; Shintake et al., 2018a), with applications in exploration (Katzschmann et al., 2018), manipulation (Shintake et al., 2016), virtual reality (Suzuki et al., 2016), and human monitoring (Bartlett et al., 2016) to name a few. Researchers have developed highly stretchable strain sensors using various materials and fabrication methods, as summarized in a review article by Amjadi et al. (2016).

There are mainly two types of sensing modes available for highly stretchable strain sensors: resistive and capacitive modes. Resistive sensing is based on the piezo-resistive effect where strain causes deformation of the electrodes, and subsequent change in their electrical resistivity.

Capacitive sensing relies on changes in capacitance between a pair of electrodes, sandwiching a dielectric material. Strain changes the area of the electrodes and the thickness of the dielectric material, resulting in a variation of the capacitance. As discussed in the literature on strain sensors (Amjadi et al., 2016; Shintake et al., 2018b), although the resistive-type strain sensors exhibit high sensitivity (gauge factor, GF), they have large hysteresis and a non-linear response. On the other hand, the capacitive-type strain sensors show small hysteresis and a linear response, thus making them a promising solution for the soft matter-based systems.

However, the sensitivity of capacitive strain sensors is low [theoretically 1 (Amjadi et al., 2016; Shintake et al., 2018b)], which renders them useless for certain applications, for instance, when a high resolution is required in a fixed system specification. So far, only a few studies have reported improvement in sensitivity of the capacitive strain sensors. Nur et al. have developed a sensor with electrodes made from wrinkled gold films and have shown sensitivity of 3.05 with maximum strain of 140% (Nur et al., 2018). Xu et al. have demonstrated that a nano composite membrane consisting of ionic hydrogels and silver nano fibers, exhibits a large change of the capacitance between the electrodes, placed at the edges of the membrane (Xu et al., 2019). In their study, the sensitivity is reported to be 165 with maximum strain of 1,000%. While these studies are successful in improving the sensitivity, they suggest opportunities for further developments. For example, fabrication of wrinkled gold films requires pre-stretch of the substrate and metal deposition, which can be difficult to carry out due to its need for a specialized setup; whereas, hydrogels can suffer from evaporation of aquatic contents that can change their sensing behavior.

In this paper, we describe a method to improve the sensitivity of stretchable capacitive strain sensors. Our approach is to mechanically program the deformation behavior of the sensors by integrating hierarchical auxetic structures into them. Auxetics are a type of meta-material, that exhibit a negative Poisson's ratio (Liu and Hu, 2010; Ren et al., 2018). When integrated into the sensors, auxetic structures increase the amount of change in the capacitance with applied strains, thus leading to a higher sensitivity. For this study, we have fabricated a prototype strain sensor where, the auxetic structure forms an elastomeric layer, and the entire fabrication is done by layer-by-layer process in a room environment. Thus, the structure of our sensor and its fabrication process are relatively simpler, compared to the other studies. The materials used, are elastomers and a liquid metal, which have almost negligible water content, and provide a stable sensor response. Using this prototype, we demonstrate, that the sensitivity of the capacitive strain sensor can be improved by roughly two times, while maintaining the original characteristics, such as high linearity, repeatability, and low hysteresis.

SENSITIVITY OF CAPACITIVE STRAIN SENSORS

Generally, the structure of highly stretchable capacitive strain sensors is similar to that of a parallel plate capacitor, i.e., it consists of a soft dielectric layer sandwiched between two compliant electrodes, as represented in **Figure 1A**. With no strain applied, the capacitance of the sensor in the initial state can be expressed as

$$C_0 = \varepsilon_0 \varepsilon_r \frac{l_{e0} w_{e0}}{h_{d0}}, \tag{1}$$

where, ε_0 is the permittivity of free space, ε_r the relative permittivity of the dielectric layer, l_{e0} the initial length of the electrode, w_{e0} the initial width of the electrode, and h_{d0} is the initial thickness of the dielectric layer. Upon the application of uniaxial strain, the electrodes of the sensor elongate, their surface area increases and the thickness of the dielectric layer decreases. This leads to changes in the capacitance. Assuming the Poisson's ratio for the dielectric layer and for the electrodes to be the same, the capacitance of the sensor under uniaxial strain can be written as,

$$C = \varepsilon_0 \varepsilon_r \frac{l_{e0}(1+\varepsilon)\, w_{e0}\,(1-\varepsilon \nu_2)}{h_{d0}\,(1-\varepsilon \nu_3)}, \tag{2}$$

where, ε is the strain in the loading (length) direction and ν_2 and ν_3 are the Poisson's ratio in the width direction and the thickness direction, respectively. Assuming, that the materials used in the sensor are incompressible, like elastomers (i.e., $\nu_2 = \nu_3 \approx 0.5$), Equation (2) becomes

$$C = C_0\,(1+\varepsilon)\,. \tag{3}$$

Equation (3) suggests that the response of the sensor is proportional to the applied strain. The sensitivity (gauge factor, GF) of the sensor is obtained as

$$GF = \frac{C - C_0}{C_0 \varepsilon} = 1. \tag{4}$$

Thus, Equation (4) indicates that the sensitivity of capacitive strain sensors with normal configuration is equal to 1.

MATERIALS AND METHODS

As discussed above, when the principal strain is applied, the capacitance of the sensor gets larger due to the increase in electrode area and decrease in the thickness of the dielectric layer, as represented in **Figure 1A**. The Poisson's ratio of the sensor structure is normally close to 0.5, which reduces the width of the electrode and essentially limits the sensitivity theoretically to 1. In this study, the idea is to integrate auxetic structures into the sensor architecture for improving its sensitivity. In the proposed sensor configuration illustrated in **Figure 1B**, auxetic structures are attached on both sides of the sensor. Under application of the principal strain, the negative Poisson's ratio of the auxetic structures causes the width to be increased during sensor deformation, unlike the normal sensors (**Figure 1A**) where the width reduces in a similar situation. This means that ν_2 in Equation (2) takes a negative value and no longer equals ν_3. The increased rate of the width change causes increased electrode

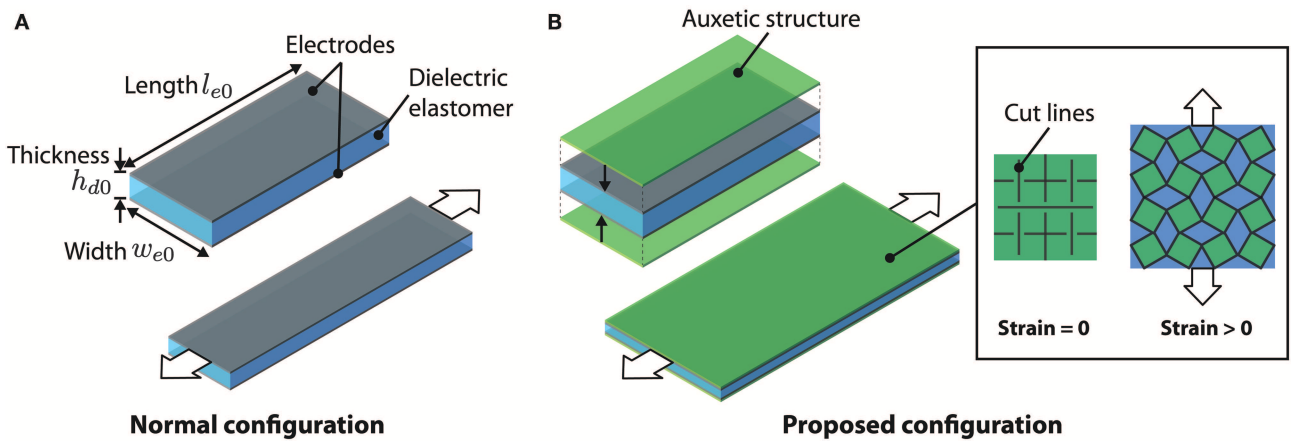

FIGURE 1 | (A) Schematics of capacitive-type stretchable strain sensor. **(B)** Schematics of the senor with the hierarchical auxetic structure proposed in this study.

area expansion and subsequent thickness reduction, therefore affecting the capacitive change, and results in high sensitivity.

As for the geometry of the auxetic structure, we employed the hierarchical design described in the study by Tang et al. (2015). The deformation of this geometry is depicted in **Figure 1B** inset. When stretched, the segments in the auxetic structure rotate, resulting in an extension perpendicular to the direction of the applied strain. This deformation characteristic leads to an increase in the width of the sensor instead of the normal decrease in width. Apart from the reasons mentioned above, we chose this design as it exhibits a constant negative Poisson's ratio until 70% of linear strain.

The focus of this paper is to prove the aforementioned concept through the characterization of a physical sensor sample. The sensor sample is composed of several layers comprising of the dielectric, electrodes, and auxetic structures, respectively. **Figure 2** details the fabrication process that is done in three parts: (1) fabrication of the base sensor, (2) fabrication of the auxetic structure, and (3) assembling of these parts. We used a 0.5 mm-thick acrylic elastomer layer (3M, VHB 4905) as the dielectric and the structure of the base sensor, a silicone elastomer (Dow Corning, Sylgard 184) as the auxetic structure, and a liquid metal [eutectic gallium-indium (EGaIn)] (Dickey et al., 2008; Dickey, 2017) for the electrodes. These materials were integrated layer-by-layer. It can be seen in the figure that in the base sensor, the liquid metal is encapsulated by the acrylic elastomer layers.

Figures 2A–E show the fabrication process of the base sensor. (**Figure 2A**) First, a sheet of the acrylic layer for the dielectric was cut using a laser-engraving machine, and a conductive tape was placed on both sides of the layer. (**Figure 2B**) Then, additional acrylic layers that created a hollow space corresponding to the electrode shape, were attached. Bonding of the layers was assured by their intrinsic stiction. (**Figure 2C**) After this, EGaIn was filled manually in the hole and (**Figure 2D**) sealed with another acrylic layer. (**Figure 2E**) The steps (**Figures 2B–D**) were repeated on the other side of the dielectric layer, and the base sensor was complete. The inset picture in **Figure 2E** shows one of the fabricated sensors.

Figures 2F–H show the fabrication process of the auxetic structure. (**Figure 2F**) First, the silicone elastomer was mixed with a curing agent in the weight ratio of 10:1, and this mixture was poured into a mold made from an acrylic plate. The mixture was then cured in an oven at 60°C for 2 h, which formed a membrane of thickness 1.0 mm. (**Figure 2G**) Subsequently, a silicone adhesive film (Taiyo Wire Cloth, Polysil) was attached onto the membrane. (**Figure 2H**) Finally, the whole sheet was cut using the laser-engraving machine, and the auxetic structure parts were fabricated.

Figures 2I,J show the assembling process. (**Figure 2I**) The auxetic structures were attached on both sides of the base sensor. (**Figure 2J**) Holders made of an acrylic plate were placed. The inset picture in **Figure 2J** shows one such fabricated sensor that is ready to be tested. The effective length of the sensor where the electrodes overlap was 40 mm, with the outline dimensions of 60 mm × 16 mm.

In order to investigate the effect of auxetic structure on the improvement of sensitivity, we performed the characterization on a fabricated prototype. In the characterization, two different sensor samples were prepared. One was a sensor with the auxetic structure, and the other was without the auxetic structure. Each sample was attached to a linear motorized stage (Zaber, X-LRT-1500) and up to 50% of strain was applied with 5% steps for capacitance measurement by an LCR meter (TEXIO, LCR6000). With the same setup, repeatability of the sensor response was characterized by applying cyclic strain of 50% (strain speed 25%/s). **Supplementary Video 1** shows the sensor being tested under repeated strain. In the characterization, we put our focus on exploring sensitivity as well as other characteristics such as linearity and hysteresis. The sensitivity of the sensor was calculated using Equation (4).

RESULTS AND DISCUSSIONS

First, we visually observed the deformation behavior of the sensor samples before starting the characterization. As can be seen in

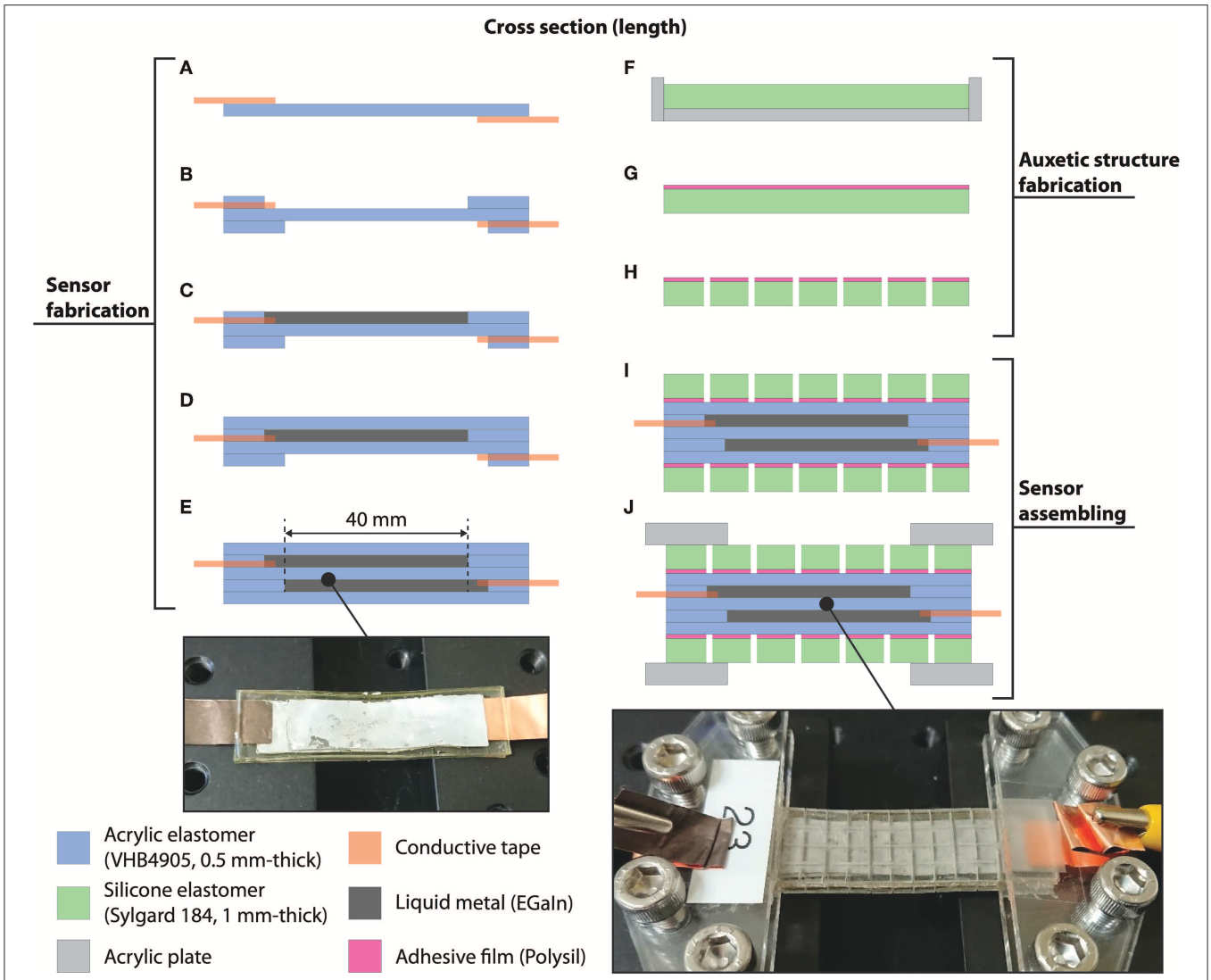

FIGURE 2 | Fabrication process of the sensor sample. **(A–E)** Fabrication of the base sensor. **(A)** A sheet of the acrylic layer is cut and a conductive tape is placed on both sides of the layer. **(B)** Additional acrylic layers with the electrode shape are attached. **(C)** EGaIn is filled and **(D)** sealed with another acrylic layer. **(E)** Repeating the steps **(B–D)** on the other side. **(F–H)** Fabrication of the auxetic structure. **(F)** The silicone elastomer is poured into a mold and cured. **(G)** A silicone adhesive film is attached onto the silicone elastomer. **(H)** The whole sheet is cut. **(I,J)** Assembling of the parts. **(I)** The auxetic structures are attached on both sides of the base sensor. **(J)** Holders are placed.

Figures 3A,B, the presence of the auxetic structure makes the electrodes wider with stretching, which is obvious, especially when 50% strain is applied. We then assessed the sensitivity of the sensors. The initial capacitance value of the sensors right after the fabrication was 32.9 pF for the sensor with the auxetic structure and 32.6 pF for the sensor without the auxetic structure, respectively. As plotted in **Figure 4A**, the sample with the auxetic structure exhibited larger capacitance change compared to the one with normal configuration. The larger change in capacitance indicates a higher sensitivity, which essentially validates the concept of this study.

Moreover, the sensor with the auxetic structure still holds the original characteristics of capacitive sensing, such as high linearity ($R^2 = 0.995$) and small hysteresis (3.5%). Here, the hysteresis was evaluated as the drift error in the sensor reading at 0% strain, measured before and after the stretch cycles. The two parameters, linearity and hysteresis, are not directly linked to the sensitivity but are important in strain sensors; non-linearity can make the calibration of the device more complex and difficult, whereas large hysteresis results in the irreversible sensing performance (Amjadi et al., 2016). In Equation (2), our sensor should possess a negative value of Poisson's ratio ν_2 in the width direction, due to the auxetic structure property and also $\nu_2 \neq \nu_3$. This changes the form of Equation (3) and predicts the sensor response to be non-linear. The reason why the result shows linearity could be the change of ν_2 with the

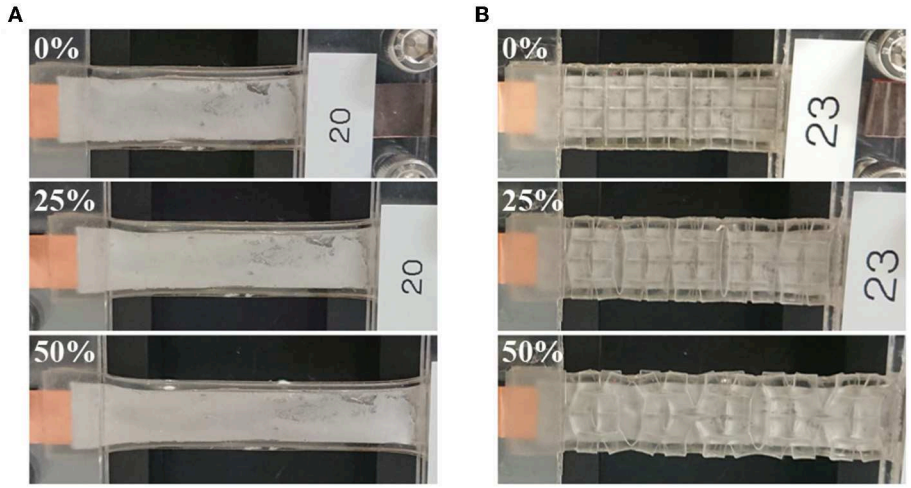

FIGURE 3 | Deformation of the fabricated sensors at the applied strain of 0, 25, and 50% (top view). **(A)** Sensor without the auxetic structure and **(B)** sensor with the auxetic structure.

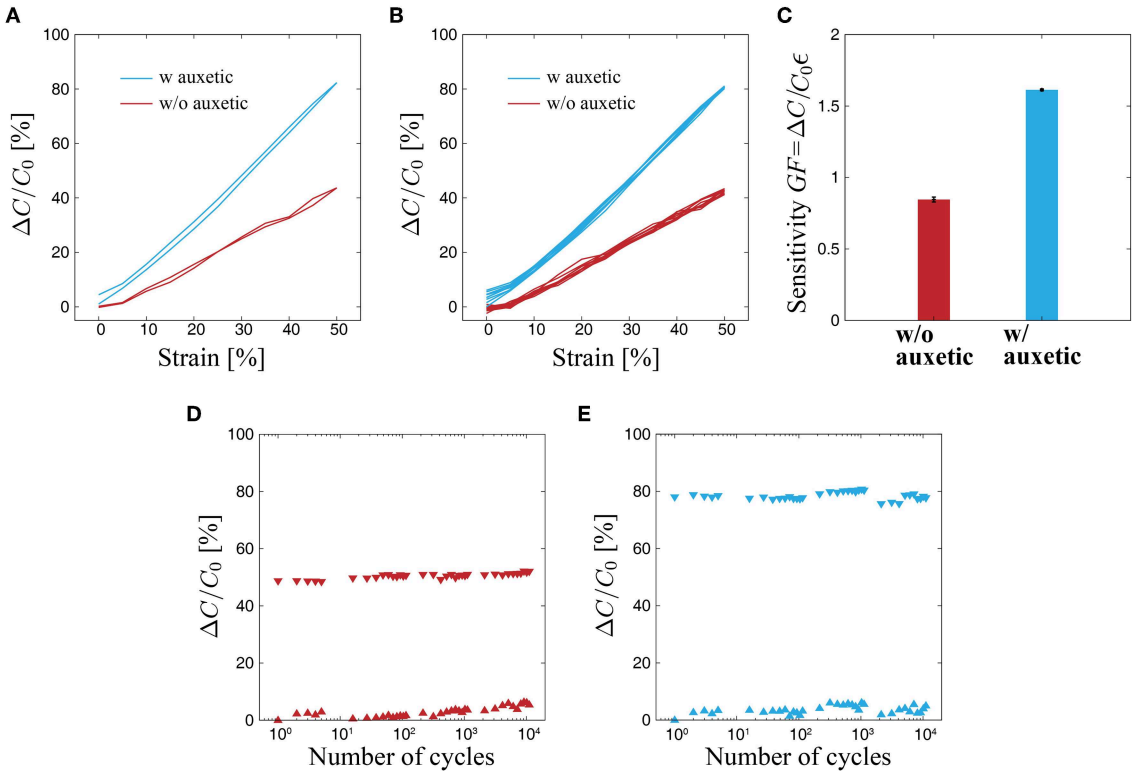

FIGURE 4 | Characterization results of the fabricated sensors. **(A)** Capacitive change as a function of the applied strain for one cycle. **(B)** Capacitive change as a function of the applied strain for five cycles. **(C)** Calculated sensitivity of the sensors. **(D)** Response of the sensor without the auxetic structure for 11,135 cycles. **(E)** Response of the sensor with the auxetic structure for 11,135 cycles.

applied strain. In the proposed configuration, ν_2 is considered a constant regardless of the amount of the strain. However, because the entire deformation of the sensor is determined from the structural interaction between the auxetic structures and other parts, the Poisson's ratio ν_2 may dynamically change with strain, thus resulting in a linear response.

The performance of the sensor was maintained for additional cycles, as shown in **Figure 4B**. Based on this result, we calculated

the sensitivity GF. The obtained value was 1.61 ± 0.01 for the sensor with the auxetic structure, and 0.86 ± 0.02 for that without the auxetic structure, thus indicating that it increased by 1.9 times for the former sensor (**Figure 4C**). The sensitivity 1.61 obtained in this study is lower than those reported in the other studies: 3.05 (Nur et al., 2018) and 165 (Xu et al., 2019). However, the current design of the sensor is only to validate the concept of this study and it can potentially be optimized for achieving better performance. Moreover, our method also allows implementation of various auxetic geometries available in the literature (Liu and Hu, 2010; Ren et al., 2018), which could further improve sensitivity.

We also characterized the repeatability and robustness of the sensor for a larger number of strain cycles. We applied more than 11,000 strain cycles (50%) to the sensor samples. The result is plotted in **Figures 4D,E**. As can be seen, both sensors exhibited excellent repeatability and durability, which implies that the presence of the auxetic structure does not influence the repeatability of the sensor response, and maintains high robustness successfully.

To summarize, we have described a method to improve the sensitivity of highly stretchable strain sensors by integrating auxetic structures. The proposed sensor configuration uses the negative Poisson's ratio of auxetic structures that increases the width of the sensor in response to the principal strain in the length direction, unlike the normal sensor configuration where the width reduces. The deformation characteristics of the sensor causes larger capacitive change and improved sensitivity. Through the characterization, we have shown that the fabricated sensors exhibit improved sensitivity, roughly two times of the normal sensors. Aside from higher sensitivity, the sensors also show linearity, low hysteresis, repeatability, and durability. The results validate the feasibility of the use of the auxetic structures for highly stretchable strain sensors and thus contribute to their further development. Lastly, our ongoing work is to further improve the sensitivity by optimizing the geometry of the sensors and to understand their mechanical behavior with the aid of analytical and numerical modeling. As demonstrated in many studies for example in Bartlett et al. (2016), Nur et al. (2018), and Shintake et al. (2018b), strain sensors are able to detect bending deformations when placed on the surface of the target object. Therefore, applications of our sensor will also include soft robotic systems that undergo large bending deformations such as grippers, mobile robots, and wearable devices.

DATA AVAILABILITY STATEMENT

The raw data supporting the conclusions of this manuscript will be made available by the authors, without undue reservation, to any qualified researcher.

AUTHOR CONTRIBUTIONS

JS and KO designed the experiments. KO and TN collected and processed data. Data interpretation was performed by JS and TN. JS wrote the manuscript. All authors have read and approved the final manuscript.

FUNDING

This work was supported by the Japanese Ministry of Education, Culture, Sports, Science and Technology (MEXT) through the Leading Initiative for Excellent Young Researchers (LEADER).

ACKNOWLEDGMENTS

The authors would like to thank Dr. Tilo H. Yang for helpful discussions.

SUPPLEMENTARY MATERIAL

The Supplementary Material for this article can be found online at: https://www.frontiersin.org/articles/10.3389/frobt.2019.00127/full#supplementary-material

Supplementary Video 1 | Deformation of the fabricated sensor.

REFERENCES

Amjadi, M., Kyung, K.-U., Park, I., and Sitti, M. (2016). Stretchable, skin-mountable, and wearable strain sensors and their potential applications: a review. *Adv. Funct. Mater.* 26, 1678–1698. doi: 10.1002/adfm.201504755

Bartlett, M. D., Markvicka, E. J., and Majidi, C. (2016). Rapid fabrication of soft, multilayered electronics for wearable biomonitoring. *Adv. Funct. Mater.* 26, 8496–8504. doi: 10.1002/adfm.201602733

Dickey, M. D. (2017). Stretchable and soft electronics using liquid metals. *Adv. Mater.* 29, 1–19. doi: 10.1002/adma.201606425

Dickey, M. D., Chiechi, R. C., Larsen, R. J., Weiss, E. A., Weitz, D. A., Whitesides, G. M., et al. (2008). Eutectic gallium-indium (EGaIn): a liquid metal alloy for the formation of stable structures in microchannels at room temperature**. *Adv. Funct. Mater.* 18, 1097–1104. doi: 10.1002/adfm.200701216

Katzschmann, R. K., DelPreto, J., MacCurdy, R., and Rus, D. (2018). Exploration of underwater life with an acoustically controlled soft robotic fish. *Sci. Robot.* 3:eaar3449. doi: 10.1126/scirobotics.aar3449

Liu, Y., and Hu, H. (2010). A review on auxetic structures and polymeric materials. *Sci. Res. Essays* 5, 1052–1063. Available online at: https://academicjournals.org/journal/SRE/article-abstract/27EF13219060

Nur, R., Matsuhisa, N., Jiang, Z., Nayeem, M. O. G., Yokota, T., and Someya, T. (2018). A highly sensitive capacitive-type strain sensor using wrinkled ultrathin gold films. *Nano Lett.* 18, 5610–5617. doi: 10.1021/acs.nanolett.8b02088

Polygerinos, P., Correll, N., Morin, S. A., Mosadegh, B., Onal, C. D., Petersen, K., et al. (2017). Soft robotics: review of fluid-driven intrinsically soft devices; manufacturing, sensing, control, and applications in human-robot interaction. *Adv. Eng. Mater.* 19, 1–22. doi: 10.1002/adem.201700016

Ren, X., Das, R., Tran, P., Ngo, T. D., and Xie, Y. M. (2018). Auxetic metamaterials and structures: a review. *Smart Mater. Struct.* 27:023001. doi: 10.1088/1361-665X/aaa61c

Rich, S. I., Wood, R. J., and Majidi, C. (2018). Untethered soft robotics. *Nat. Electron.* 1, 102–112. doi: 10.1038/s41928-018-0024-1

Shintake, J., Cacucciolo, V., Floreano, D., and Shea, H. (2018a). Soft robotic grippers. *Adv. Mater.* 30:1707035. doi: 10.1002/adma.201707035

Shintake, J., Piskarev, E., Jeong, S. H., and Floreano, D. (2018b). Ultrastretchable strain sensors using carbon black-filled elastomer composites and comparison of capacitive versus resistive sensors. *Adv. Mater. Technol.* 3, 1–8. doi: 10.1002/admt.201700284

Shintake, J., Rosset, S., Schubert, B., Floreano, D., and Shea, H. (2016). Versatile soft grippers with intrinsic electroadhesion based on multifunctional polymer actuators. *Adv. Mater.* 28, 231–238. doi: 10.1002/adma.201504264

Suzuki, K., Yataka, K., Okumiya, Y., Sakakibara, S., Sako, K., Mimura, H., et al. (2016). Rapid-response, widely stretchable sensor of aligned MWCNT/elastomer composites for human motion detection. *ACS Sensors* 1, 817–825. doi: 10.1021/acssensors.6b00145

Tang, Y., Lin, G., Han, L., Qiu, S., Yang, S., and Yin, J. (2015). Design of hierarchically cut hinges for highly stretchable and reconfigurable metamaterials with enhanced strength. *Adv. Mater.* 27, 7181–7190. doi: 10.1002/adma.201502559

Xu, H., Lv, Y., Qiu, D., Zhou, Y., Zeng, H., and Chu, Y. (2019). An ultra-stretchable, highly sensitive and biocompatible capacitive strain sensor from an ionic nanocomposite for on-skin monitoring. *Nanoscale* 11, 1570–1578. doi: 10.1039/C8NR08589G

Conflict of Interest: The authors declare that the research was conducted in the absence of any commercial or financial relationships that could be construed as a potential conflict of interest.

frontiers in Robotics and AI

REVIEW
published: 05 December 2019
doi: 10.3389/frobt.2019.00129

A Compact Review of IPMC as Soft Actuator and Sensor: Current Trends, Challenges, and Potential Solutions From Our Recent Work

Muyu Hao [1], Yanjie Wang [1,2], Zicai Zhu [3], Qingsong He [4], Denglin Zhu [1,2] and Minzhou Luo [1,2]*

[1] School of Mechanical and Electrical Engineering, Hohai University, Changzhou, China, [2] Jiangsu Key Laboratory of Special Robot Technology, Hohai University, Changzhou, China, [3] Jiangsu Provincial Key Laboratory of Bionic Functional Materials, Nanjing University of Aeronautics and Astronautics, Nanjing, China, [4] School of Mechanical Engineering, Xi'an Jiaotong University, Xi'an, China

Recently, attempts have been made to develop ionic polymer–metal composite (IPMC), which is garnering growing interest for ionic artificial muscle, as a soft actuator and sensor due to its inherent properties of low weight, flexibility, softness, and particularly, its efficient transformation of electrical energy into mechanical energy, with large bending strain response under a low activation voltage. In this paper, we focused on several current deficiencies of IPMC that restrict its application, such as non-standardized preparation steps, relaxation under DC voltage, solvent evaporation, and poor output force. Corresponding solutions to overcome the abovementioned problems have recently been proposed from our point of view and developed through our research. After a brief introduction to the working mechanism of IPMC, we here investigate the key factors that influence the actuating performance of IPMC. We also review the optimization strategies in IPMC actuation, including those for preparation steps, additive selection for a thick casting membrane, solvent substitutes, water content, encapsulation, etc. With consideration of the role of the interface electrode, its effects on the performance of IPMC are revealed based on our previous work. Finally, we also discuss IPMCs as potential sensors theoretically and experimentally. The elimination of the deficiencies of IPMC will promote its applications in soft robotics.

Keywords: IPMC, relaxation effect, solvent evaporation, output force, soft robotics

OPEN ACCESS

Edited by:
Guoying Gu,
Shanghai Jiao Tong University, China

Reviewed by:
Yingxiang Liu,
Harbin Institute of Technology, China
Ilkwon Oh,
Korea Advanced Institute of Science & Technology (KAIST), South Korea

***Correspondence:**
Yanjie Wang
yjwang@hhu.edu.cn

Specialty section:
This article was submitted to Soft Robotics, a section of the journal Frontiers in Robotics and AI

Received: *04 September 2019*
Accepted: *08 November 2019*
Published: *05 December 2019*

Citation:
Hao M, Wang Y, Zhu Z, He Q, Zhu D and Luo M (2019) A Compact Review of IPMC as Soft Actuator and Sensor: Current Trends, Challenges, and Potential Solutions From Our Recent Work. Front. Robot. AI 6:129. doi: 10.3389/frobt.2019.00129

INTRODUCTION

In recent years, with developments in the field of soft robotics, new demands have emerged that actuators and sensors for use in such robotics must be flexible and miniaturized. Ionic polymer–metal composites (IPMC) have been studied as promising smart materials for use as actuators and sensors in soft robotics and other industrial applications during the last two decades (Tiwari and Garcia, 2011; Bhandari et al., 2012; Kim, 2013). As a kind of electroactive polymer (EAP), IPMC has some distinct advantages for use in soft robotics. Its advantageous features include but are not limited to low weight, flexibility, softness, and especially, efficient transformation of electrical energy to mechanical energy, with a large bending strain response to low activation voltage (1∼3 V), low power consumption, rapid response, mechanical and chemical

tolerance and stability, ease of miniaturization, and so on. Due to the above characteristics, IPMC can be used as soft actuators in soft robotics, especially microrobots and underwater robots. Additionally, IPMC can also convert mechanical energy into electrical energy. Because of its self-sensing capacity, it has some favorable properties for use in the sensing field, as well.

Many potential uses for IPMC have already been proposed by researchers (Bonomo et al., 2005; Shahinpoor and Kim, 2005). Mojarrad used IPMC for the propeller of a biomimetic robotic underwater propulsion system (Mojarrad and Shahinpoor, 1997). A snake-like swimming robot using an IPMC actuator/sensor was proposed by Kamamichi et al. (2006). In 2007, Guo et al. used IPMC as part of the actuators developed for a jellyfish-like underwater microrobot (Guo et al., 2007). Krishen studied the application of IPMC for space missions (Krishen, 2009). In 2015, Shen et al. developed a biomimetic underwater vehicle with IPMC sensors (Shen et al., 2015). Palmre et al. fabricated a bio-inspired IPMC actuator as an active fin that was capable of bending and twisting (Palmre et al., 2012). As soft actuators, as well as for use in robotics, IPMCs also have applications in optical systems, such as an auto-focus compact camera module and a tilting actuator for an endoscope (Kim et al., 2012; Tsai et al., 2012). Additionally, Tripathi et al. developed an IPMC actuator that was used as a prototype for an active catheter-guidewire maneuvering application (Tripathi et al., 2019). In 2018, an IPMC-based refreshable braille display application was reported (Feng and Hou, 2018). Recently, Chang et al. designed a drug-release device using IPMC for biomedical applications (Chang X.L. et al., 2018). However, there still are some inherent challenges, such as relaxation under direct current (DC) voltage, poor output force, solvent evaporation, and non-standardized preparation steps, that restrict IPMC use in the sensing and actuating fields, and there is still a large amount of room for improvement (Jung et al., 2003; Lee et al., 2005). In recent years, to overcome these unfavorable factors, a series of solutions have been proposed for its further application in soft robotics. Optimizing and improving the preparation steps will make the surface electrode layers more homogeneous, so that a sample with uniform performance can be obtained. To overcome the problem of relaxation, some efforts had been made to adjust the water content of water-based IPMC or replace the water with other non-volatile solvents (such as ionic liquids), and so on. In the past 5 years, research regarding IPMC for soft robotics applications has aroused widespread interest in various fields, including materials science, physical chemistry, chemistry, polymer science, electrical engineering, nanoscience, and applied physics, as shown in **Figure 1**.

This paper intends to review and discuss the effects of these solutions on the relief of the inherent defects of IPMC, considering the optimization of the surface electrode, polymer membrane, electrode interface, and so on. This review consists of three sections as follows. After the working mechanism of IPMC has been introduced, the methods for optimizing IPMC actuating performance are discussed, including the optimization of the preparation steps, relaxation elimination, and output force enhancement. Finally, the use of IPMCs as sensors is briefly discussed.

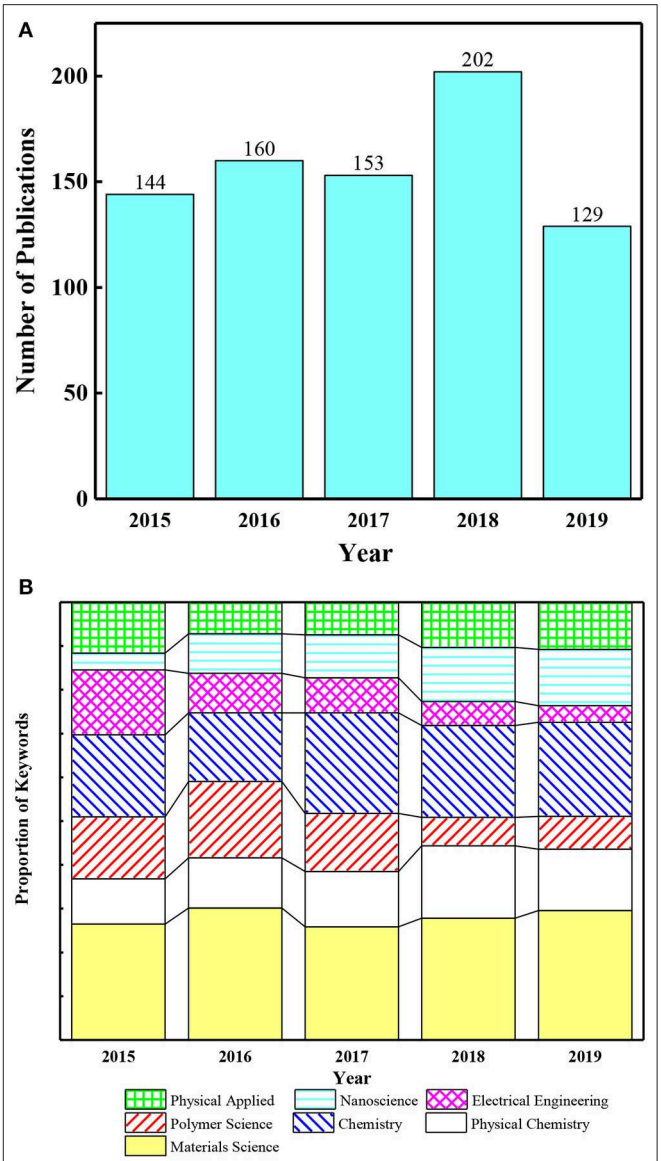

FIGURE 1 | (A) Number of publications during the last 5 years (data from WOS to August 2019). **(B)** Recent research hotspots in IPMC.

WORKING MECHANISM OF IPMC

Generally, IPMC consists of three layers, specifically a thin electrolyte membrane with two noble metal electrode layers on either side, so that the structure of IPMC is like a sandwich. The actuating mechanism of IPMC is shown in **Figure 2**. Due to their similar chemical structures and properties, Nafion, Flemion, Aciplex, etc. are the most used materials for the base membrane of IPMC. A conductive electrode layer is plated on each side of the base membrane using noble metal salts or a mixture of such salts, including gold, platinum, palladium, etc. When an electric field is applied to the IPMC, the cations, together with water molecules, will move toward the cathode. Due to the anisotropic concentration distributions of cations and water molecules, strain

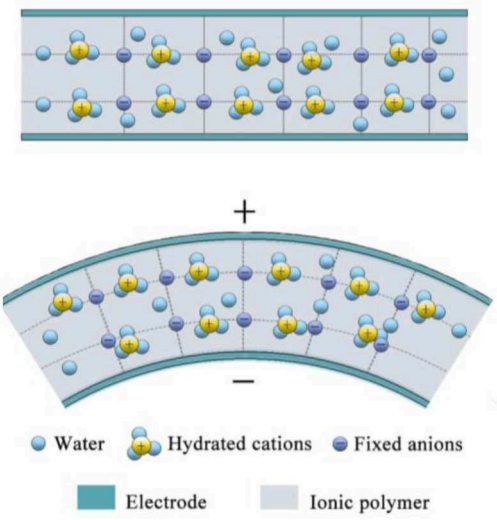

FIGURE 2 | Ionic polymer–metal composite (IPMC) sensing under bending deformation (Wang et al., 2019) (reprinted with permission).

will be generated near the cathode of the IPMC, and the IPMC will bend toward the anode (Shahinpoor, 2003; Schmidt-Rohr et al., 2008). Likewise, when mechanical deformation or another stimulus is applied to IPMC, ion migration will occur due to the strain gradient inside the IPMC and will then result in a potential difference on both sides of the IPMC. According to the above depiction, there are actually four components to constructing IPMC, namely the mid-layer, cations, solvents, and electrode layers. Many researchers have therefore devoted themselves to improving the performance of IPMC by optimizing these components.

OPTIMIZATION STRATEGIES IN IPMC ACTUATION

Preparation Steps

Generally, the current state-of-the-art IPMC manufacturing techniques incorporate four steps: pretreatment (surface roughening), the initial compositing process [typically, impregnation-reduction (IR) and reductant permeation (RP)], the surface electroding process (typically, physical deposition and electroplating), and ion exchange. Each step involves many factors that affect IPMC performance, so optimization of the key factors is necessary (Takenaka et al., 1982; Millet et al., 1995; Kim and Kim, 2008; Hamburg et al., 2016). In 2012, Chang et al. proposed an effective method for preparing Pd-type IPMC (Chang et al., 2012). The overall preparation process was divided into three crucial steps, namely pretreatment, impregnation-reduction plating (IRP), and autocatalytic plating (ACP), and several specific procedures were focused on and improved, including the addition of a reducing agent and the time consumed. In terms of IPMC's own physical properties, its surface resistivity, bending stiffness, and dielectric coefficient will exert an influence its performance. In 2014, Wang et al. studied the physical and electromechanical properties of IPMC actuators and the effects of processing parameters on that performance (Wang et al., 2014c). They fabricated several IPMC samples with different features by combining certain crucial processing steps such as pretreatment, impregnation-reduction, and chemical plating. The formation mechanism of the surface and interface electrode in the processing steps was revealed, together with the effects of physical parameters on the performance of IPMC. Pretreatment provided a rough landscape, which increased the depth of electrode penetration and decreased the bending stiffness. The impregnation-reduction process mainly forms a granular penetration electrode between the mid-layer and the electrode layer. Due to the broad dispersion zone of penetrated electrode nanoparticles, the double-layer capacitance of IPMC was improved. Compared to a sample without roughening and chemical plating, the IPMC sample after roughening and chemical plating showed better performance, displaying a maximum of 10 mm under 1.7 V DC.

Furthermore, in 2016, Wang et al. performed a series of detailed experiments and revealed how the sandblasting method affected the surface and interfacial electrodes (Wang et al., 2016). Sandblasting is a convenient and controllable roughening method for treating the mid-layer without causing chemical damage. By changing the sandblasting time and powder size, a variety of surface profiles can be obtained on Nafion, and the corresponding parameters of the IPMC based on it, such as its surface resistance, equivalent modulus, and capacitance, can be optimized.

Relaxation Elimination

When a DC voltage is applied to IPMC using water as a solvent, there is a corresponding rapid increase in deformation and then its slow reversal even beyond the initial position, which is called the relaxation effect of IPMC. The presence of relaxation will bring serious instability to IPMC actuators, which is unfavorable for the application of IPMC actuators in soft robotics. Currently, two methods have been developed to overcome the relaxation of IPMC: adjusting the water content and using an ionic liquid as a solvent (Bennett and Leo, 2004).

The water content of IPMC is a key factor affecting the relaxation. Wang et al. revealed the effects of dehydration on the electromechanical parameters of Au-type and Pd-type IPMCs (Wang et al., 2014b). The morphological evolution of surface electrodes depends on the water content of IPMC. Moreover, the physical parameters of IPMC, such as its stiffness, surface resistance, and capacitance, that are related to water content play an important role in the actuation process, which provides a way of understanding the effects of water content on the deformation mechanism of IPMC. The maximum deformation of IPMC without relaxation can be obtained by encapsulating IPMC at fixed water content (W3) (Barramba et al., 2007).

Output Force Enhancement

Traditionally, Nafion 117 has been the most-used base membrane of IPMC, the thickness of which is around 180 μm. Due to the thinness of Nafion 117, the output force of the IPMC is lower than 10 mN, which will restrict IPMC use where a large output

force is needed. Apparently, an effective way to improve the output force is to fabricate IPMC with a thicker base membrane. (Kim and Shahinpoor, 2002) fabricated IPMC with a thicker membrane through solution casting. An IPMC actuator with 1.12-mm thickness, 4-mm width, and 30-mm length can output 4.5 gf under 3 V DC. In 2011, He et al. studied the performance of IPMCs with various thicknesses (He et al., 2011). Under 3.5 V, with thickness increases from 0.22 to 0.42 mm and 0.80 mm, the deformation decreased by 26.1 and 47.3%, respectively, and the output force increased by 100.6 and 13.8%, respectively. The results indicated that as the thickness of the Nafion membrane increased, the output force of the IPMC was enhanced.

Another feasible method to improve the output force of IPMC is by doping additives into the polymer membrane (Oh and Jung, 2008; Yip et al., 2012). By doping water-soluble sulfonated multi-walled carbon nanotubes (sMWCNT) into the Nafion matrix, Ru et al. developed a new kind of IPMC actuator that has higher bending deformation and output force under low driving voltage; the output force can reach 14.37 mN when 3 V DC is applied (Ru et al., 2016). Wang et al. fabricated polymer membrane with different additives by solution casting, and analyzed the respective effects of doping with ethylene glycol (EG), dimethyl sulfoxide (DMSO), N,N0-dimethyl formamide (DMF), and N-methyl formamide (NMF) (Wang et al., 2014a). The EG-based IPMC actuator had better electromechanical properties at a 2 V DC voltage, with 1.5 mN output force and 4.0 mm tip deformation. Additionally, Nemat-Nasser et al. tried to improve the output force by altering the base membrane and movable cations (Nemat-Nasser et al., 2006). Furthermore, Ma et al. prepared IPMC with various additives to optimize the output force of IPMC (Ma et al., 2009).

Besides the methods mentioned above, some novel structures have been designed to increase the output force (Konyo et al., 2004; Zolfagharian et al., 2016). In 2018, Chang et al. developed IPMC actuators with single-layered electrodes, which led to distinct S-shaped deformation with large displacement and high output force (Chang L. et al., 2018).

Effects of Interfacial Electrodes on IPMC Actuation

IPMC consists of an ionomer layer with metal electrode layers on either side. Between the ionomer layer and the surface electrode layer, there is an interfacial layer, which plays an important role in the performance of the IPMC. In particular, it has been clearly shown that the actuation capability of IPMC depends strongly on a high interfacial surface area between the metal and polymer because capacitance is directly related to the actuation performance of IPMC (Wang et al., 2017).

So far, the interfacial electrode of IPMC has been classified into two types, namely, dendritic and granular electrodes. Asaka et al. developed a structure of dendritic interfacial electrodes based on Au-type IPMC (Fujiwara et al., 2000). Chen et al. and Kim et al., respectively, proposed platinum and palladium granular interfacial structures (Shahinpoor and Kim, 2002). Their capacitance values are 1.5, 0.22, and 0.34 mF/cm^2, respectively. The capacitance of the gold dendritic interfacial electrodes is 7 and 4 times as high as that of other structures. With an increase in the capacitance of interfacial surface electrodes, the electromechanical properties of IPMC can be effectively improved.

Recently, several methods have aimed at realizing the formation of a high interface surface area, including impregnation-reduction (IR), reductant permeation (RP), solution casting, and a direct assembly process. By combining the impregnation electroplating step (IEP) with the impregnation-reduction (IR) step, dendritic interfacial electrodes (DIEs) of palladium, platinum, silver, and copper inside an ionomer for IPMC can be obtained (Noh et al., 2002; Kim and Shahinpoor, 2003). DIEs are conducive to improvements in performance in IPMC actuation by reducing the metal consumption and increasing the surface area. In the initial research, DIEs were only formed by repeated IR with an Au complex.

Wang et al. proposed a rapid, facile, and efficient method to achieve the formation of Pd, Pt, Ag, and Cu DIEs inside the polymer membrane (Wang et al., 2017). Taking the Pd DIEs as an example, the main preparation steps are as follows. Firstly, the surface of the Nafion membrane should be roughened, which will increase the surface area and is favorable for the IR process of a Pd complex. The IR step is then performed after the palladium ion exchanging process. The reduction reaction occurs near the inner surfaces of the membrane, and the palladium atoms will grow along the thickness direction. The final step is to electroplate the membrane-containing palladium complex. As the reaction goes on, the palladium particles gradually grow up to become the main branches, then secondary branches are generated, and so on. The maximum depth of Pd DIEs can almost reach through to contact from either side of the ionic polymer. Because of the DIEs, the actuation performance of IPMC is effectively improved. This enhancement in the actuating performance of IPMC means that it will work better for actuators in soft robotics.

IPMC as a Sensor

After external stimulus is exerted on IPMC, an electrical response will be generated according to the ion migration mechanism inside the IPMC (Bahramzadeh and Shahinpoor, 2011). When IPMC is used as a sensor in soft robotics, it can realize the perception of deformation, velocity, pressure, humidity, and even location-sensing through the distributed IPMC structure. Recently, many researchers have devoted themselves to researching and optimizing its sensing performance. Yamakita et al. proposed a system with IPMC sensor/actuator integration (Yamakita, 2006). Shahinpoor et al. reported the output voltage at 2 mV of an IPMC cantilever (40×5 mm) under 1-mm bending deformation (Shahinpoor et al., 1998). Konyo et al. developed an IPMC cantilever as a velocity sensor with a sensitivity of 9–12 mV/(m/s) (Konyo et al., 2004).

The main deficiency that restricts IPMC use as sensors is its low electrical response. To increase the output voltage, Zhu et al. proposed a novel IPMC sensor design with a 3×3 array that was achieved by solution casting (**Figure 3**) (Zhu et al., 2016a). Two different voltage responses were generated when pressure was

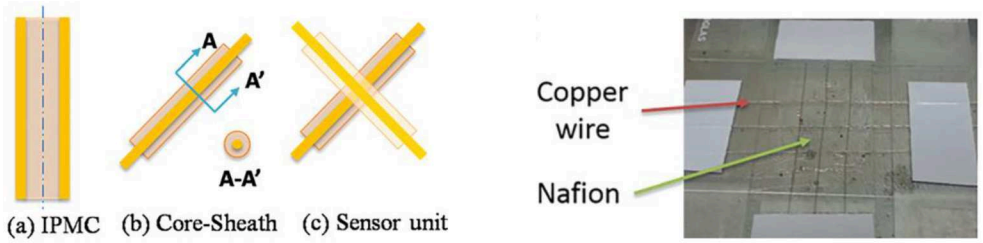

FIGURE 3 | Conceptual design of an ionic polymer pressure sensor derived from the IPMC structure (Zhu et al., 2016a). In (b), the core is a single electrode wire, and the sheath is a Nafion membrane. (a) IPMC, (b) core-sheath, and (c) sensor unit **(Left)**. Image of the 3 × 3 ionic sensor network **(Right)** (reprinted with permission).

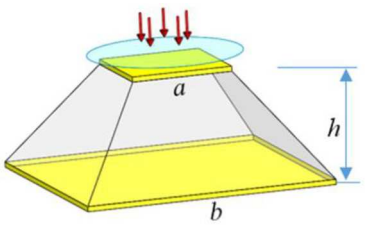

FIGURE 4 | IPMC pressure sensor with a gradient shape (Zhu et al., 2019) [reproduced from Zhu et al. (2019) with the permission of AIP Publishing].

applied to the IPMC array. Due to this design with a symmetrical structure, the output voltage reached up to 25 mV.

Subsequently, Zhu et al. studied the influence of the ambient humidity on Au-type IPMC under various humidity environments (Zhu et al., 2016b). According to the results, the response was seriously affected by humidity. In contrast to traditional strip-shaped IPMC sensors, Lei et al. presented a novel tube-shaped IPMC sensor that can respond to all stimuli perpendicular to the tube axis (Hong et al., 2016). Recently, Zhu et al. proposed a new ionic polymer pressure sensor with a gradient shape, fabricated by the casting method (**Figure 4**). The maximum response was much higher than that of the traditional strip-shaped IPMC (Zhu et al., 2019).

Additionally, Zhu et al. investigated the effects of different cations on the electrical responses of IPMC sensors at different ambient humidities (Zhu et al., 2016c). Volpini et al. established a predictive model to explain the dynamic compression-sensing response (Volpini et al., 2017). In 2017, Gudarzi designed an IPMC dynamic pressure sensor based on the streaming potential hypothesis and then presented charge current-generation mechanisms that operate due to the external pressure in both compression and shear modes (Gudarzi et al., 2017a,b). Considering the effect of the dimensions of the IPMC sensors, Wang et al. estimated the sensing performance of IPMC with various thicknesses, widths, and lengths (Wang et al., 2019).

CONCLUSIONS AND REMARKS

As a soft transducer, IPMC has great potential in soft robotics, with the advantages of low weight, softness, flexibility, low power consumption, and self-sensing capacity. There are still some deficiencies, such as in its output force, relaxation, etc. that limit the application of IPMC in soft robotics.

Among the preparation steps of IPMC, there are still some pretreatment problems that need to be solved. Currently, the pretreatment methods of the base membrane mainly include sandpapering, chemical corrosion, plasma etching, and sandblasting. The membrane surface obtained by sandpapering is non-uniform and can be affected by human factors. Although chemical corrosion and plasma etching can result in a uniform surface, the molecular structure of the membrane surface is easy to break. Meanwhile, the surface uniformity of the base membrane is also hard to control with sandblasting. Therefore, a novel method to roughen the Nafion membrane still needs to be investigated to create a more uniform surface. The existing methods for eliminating relaxation also still have some disadvantages. Although using ionic liquids as the solvent can relieve relaxation, the response speed will decrease. Controlling the water content seems to be a better way to eliminate relaxation, but even a little variation in water content will lead to a large difference in performance. Additionally, difficulties arise with IPMC encapsulation at a specific water content. On the one hand, with a decrease in water content, the response speed will drop. On the other hand, due to the added encapsulation layer, the actuation of the IPMC will be weakened. Therefore, a compromise balance relation between relaxation elimination and maximizing performance needs to be achieved. To enhance the output force of IPMC, increasing the thickness of IPMC is a convenient approach. There are two ways to make the base membrane thicker: multilayer integration by hot pressing and solution casting. However, multilayers are easy to separate by long-term use, while casting a thick membrane will decrease the deformation and response rate. To improve the response rate of IPMC, Zhu et al. employed a high voltage pulse as the electric excitation signal for a short time in the early stage, by which the deformation attenuation of the thick IPMC could be avoided (Zhu et al., 2018).

In short, the existing solutions from our group have only partially relieved the deficiencies of IPMC, and these problems are not completely solved. Considering the favorable properties of IPMC, actuators and sensors in soft robotics made of this material will have promising prospects in the

near future, and much research still needs to be done for its wide application.

AUTHOR CONTRIBUTIONS

MH: thoughts, writing–original draft. YW, ZZ, QH, DZ, and ML: discussion and investigation. YW: project administration. YW and ZZ: writing–review and editing.

FUNDING

This research was supported by the National Natural Science Foundation of China (51975184 and 91748124), the Fundamental Research Funds for the Central Universities (2019B21514), and the Foundation (2017B21114) of Jiangsu Key Laboratory of Special Robot Technology, P.R. China. The authors gratefully acknowledge this support.

REFERENCES

Bahramzadeh, Y., and Shahinpoor, M. (2011). Dynamic curvature sensing employing ionic-polymer–metal composite sensors. *Smart Mater. Struct.* 20:094011. doi: 10.1088/0964-1726/20/9/094011

Barramba, J. O., Silva, J. O., and Branco, P. J. C. (2007). Evaluation of dielectric gel coating for encapsulation of ionic polymer–metal composite (IPMC) actuators. *Sens. Actu. A Phys.* 140, 232–238. doi: 10.1016/j.sna.2007.06.035

Bennett, M. D., and Leo, D. J. (2004). Ionic liquids as stable solvents for ionic polymer transducers. *Sensors & Actuators A Physical* 115, 79–90. doi: 10.1016/j.sna.2004.03.043

Bhandari, B., Lee, G. Y., and Ahn, S. H. (2012). A review on IPMC material as actuators and sensors: fabrications, characteristics and applications. *Int. J. Precision Eng. Manuf.* 13, 141–163. doi: 10.1007/s12541-012-0020-8

Bonomo, C., Fortuna, L., Giannone, P., and Graziani, S. (2005). A method to characterize the deformation of an IPMC sensing membrane. *Sens. Actu. A Phys.* 123, 146–154. doi: 10.1016/j.sna.2005.03.012

Chang, L., Chen, H., Zhu, Z., and Li, B. (2012). Manufacturing process and electrode properties of palladium-electroded ionic polymer–metal composite. *Smart Materials and Structures* 21, 065018. doi: 10.1088/0964-1726/21/6/065018

Chang, L., Yu, L., Li, C., Niu, Q., Hu, Y., Lu, P., et al. (2018). Ionic polymer with single-layered electrodes: a novel strategy for ionic actuator design. *Smart Mater. Struct.* 27:105046. doi: 10.1088/1361-665X/aae00a

Chang, X. L., Chee, P. S., Lim, E. H., and Chong, W. C. (2018). Radio-frequency enabled ionic polymer metal composite (IPMC) actuator for drug release application. *Smart Materials and Structures* 28, 015024. doi: 10.1088/1361-665X/aaefd3

Feng, G.-H., and Hou, S.-Y. (2018). Investigation of tactile bump array actuated with ionic polymer–metal composite cantilever beams for refreshable braille display application. *Sens. Actu. A Phys.* 275, 137–147. doi: 10.1016/j.sna.2018.04.007

Fujiwara, N., Asaka, K., Nishimura, Y., Oguro, K., and Torikai, T., et al. (2000). Preparation of gold? Solid polymer electrolyte composites as electric stimuli-responsive materials. *Chem. Mater.* 12, 1750–1754. doi: 10.1021/cm9907357

Gudarzi, M., Smolinski, P., and Wang, Q. M. (2017a). Bending mode ionic polymer-metal composite (IPMC) pressure sensors. *Measurement* 103, 250–257. doi: 10.1016/j.measurement.2017.02.029

Gudarzi, M., Smolinski, P., and Wang, Q. M. (2017b). Compression and shear mode ionic polymer-metal composite (IPMC) pressure sensors. *Sens. Actu. A Phys.* 260, 99–111. doi: 10.1016/j.sna.2017.04.010

Guo, S., Shi, L., Ye, X. A., and Li, L. (2007). New jellyfish type of underwater microrobot," in *International Conference on Mechatronics and Automation* (2007). doi: 10.1109/ICMA.2007.4303595

Hamburg, E., Zondaka, Z., Punning, A., Johanson, U., and Aabloo, A. (2016). Some electrochemical aspects of aqueous ionic polymer-composite actuators. *Electroactive Polymer Actuators and Devices (EAPAD)* 2016, 2016:979815. doi: 10.1117/12.2219031

He, Q., Min, Y., Song, L., Ding, H., Zhang, X., and Dai, Z. (2011). experimental study and model analysis of the performance of IPMC membranes with various thickness. *J. Bionic Eng.* 8, 77–85. doi: 10.1016/S1672-6529(11)60001-2

Hong, L., Sharif, M., and Tan, X. (2016). Dynamics of omnidirectional IPMC sensor: experimental characterization and physical modeling. *IEEE/ASME Trans. Mech.* 21, 601–612. doi: 10.1109/TMECH.2015.2468080

Jung, K., Nam, J., and Choi, H. (2003). Investigations on actuation characteristics of IPMC artificial muscle actuator. *Sensors & Actuators A* 107, 183–192. doi: 10.1016/S0924-4247(03)00346-7

Kamamichi, N., Yamakita, M., Asaka, K., Kozuki, T., and Luo, Z.-W. et al. (2006). "A snake-like swimming robot using IPMC actuator/sensor[C]," in *IEEE International Conference on Robotics & Automation* (Orlando, FL). doi: 10.1109/IROS.2005.1545485

Kim, C., Yang, H., Park, N. C., Kim, S.-J., and Park, Y. P. (2012). An auto-focus lens actuator using ionic polymer metal composites: design, fabrication and control. *Int. J. Prec. Eng. Manuf.* 13, 1883–1887. doi: 10.1007/s12541-012-0247-4

Kim, K. J. (2013). Recent advances in ionic polymer–metal composite actuators and their modeling and applications. *Prog. Polym. Sci.* 38, 1037–1066. doi: 10.1016/j.progpolymsci.2013.04.003

Kim, K. J., and Shahinpoor, M. (2002). A novel method of manufacturing three-dimensional ionic polymer–metal composites (IPMCs) biomimetic sensors, actuators and artificial muscles. *Polymer* 43, 797–802. doi: 10.1016/S0032-3861(01)00648-6

Kim, K. J., and Shahinpoor, M. (2003). Ionic polymer–metal composites: II. Manufacturing techniques. *Smart Mater. Struct.* 12:65. doi: 10.1088/0964-1726/12/1/308

Kim, S. M., and Kim, K. J. (2008). Palladium buffer-layered high performance ionic polymer–metal composites. *Smart Mater. Struct.* 17, 035011. doi: 10.1088/0964-1726/17/3/035011

Konyo, M., Konishi, Y., Tadokoro, S., and Kishima, T. (2004). Development of velocity sensor using ionic polymer-metal composites. *Proc. SPIE— Int. Soc. Opt. Eng.* 5385, 307–318. doi: 10.1117/12.540266

Krishen, K. (2009). Space applications for ionic polymer-metal composite sensors, actuators, and artificial muscles. *Acta Astronaut.* 64, 1160–1166. doi: 10.1016/j.actaastro.2009.01.008

Lee, J. H., Lee, J. H., Nam, J.-D., Choi, H., Jung, K., Jeon, J. W., et al. (2005). Water uptake and migration effects of electroactive ion-exchange polymer metal composite (IPMC) actuator. *Sensors & Actuators A Physical* 118, 98–106. doi: 10.1016/j.sna.2004.07.001

Ma, C. H., Yu, T. L., Lin, H.-L., and Huang, Y.-T. (2009). Morphology and properties of Nafion membranes prepared by solution casting. *Polymer* 50, 1764–1777. doi: 10.1016/j.polymer.2009.01.060

Millet, P., Andolfatto, F., and Durand, R. (1995). Preparation of solid polymer electrolyte composites: investigation of the precipitation process. *Journal of applied electrochemistry* 25, 233–239. doi: 10.1007/BF00262961

Mojarrad, M., and Shahinpoor, M. (1997). "Biomimetic robotic propulsion using polymeric artificial muscles[C]," in *IEEE International Conference on Robotics & Automation* (Albuquerque, NM).

Nemat-Nasser, S., Zamani, S., and Tor, Y. (2006). Effect of solvents on the chemical and physical properties of ionic polymer-metal composites. *J. Appl. Phys.* 99, 51–191. doi: 10.1063/1.2194127

Noh, T. G., Tak, Y., Nam, J. D., and Hyoukryeol, C. (2002). Electrochemical characterization of polymer actuator with large interfacial area. *Electrochim. Acta* 47, 2341–2346. doi: 10.1016/S0013-4686(02)00089-0

Oh, I.-K., and Jung, J.-Y. (2008). Biomimetic nano-composite actuators based on carbon nanotubes and ionic polymers. *J. Intell. Mater. Syst. Struct.* 19, 305–311. doi: 10.1177/1045389X07083125

Palmre, V., Hubbard, J. J., Fleming, M., Pugal, D., Kim, S., Kim, K. J., et al. (2012). An IPMC-enabled bio-inspired bending/twisting fin for underwater applications. *Smart Mater. Struct.* 22:014003. doi: 10.1088/0964-1726/22/1/014003

Ru, J., Wang, Y., Chang, L., Chen, H., and Li, D. (2016). Preparation and characterization of water-soluble carbon nanotube reinforced Nafion

membranes and so-based ionic polymer metal composite actuators. *Smart Mater. Struct.* 25:095006. doi: 10.1088/0964-1726/25/9/095006

Schmidt-Rohr, K., and Chen, Q.Schmidt-Rohr, K., and Chen, Q. (2008). Parallel cylindrical water nanochannels in Nafion fuel-cell membranes. *Nat. Mater.* 7, 75–83. doi: 10.1038/nmat2074

Shahinpoor, M. (2003). Mechanoelectrical phenomena in ionic polymers. *Mathematics and Mechanics of Solids* 8, 281–288. doi: 10.1177/1081286503008003003

Shahinpoor, M., Bar-Cohen, Y., Xue, T., Harrison, J. S., and Smith, J. G. (1998). Some experimental results on ionic polymer-metal composites (IPMC) as biomimetic sensors and actuators. *Smart Struct. Mater.* 1998, 251–267. doi: 10.1117/12.316870

Shahinpoor, M., and Kim, K. J. (2002). Novel ionic polymer–metal composites equipped with physically loaded particulate electrodes as biomimetic sensors, actuators and artificial muscles. *Sens. Actu. A Phys.* 96, 125–132. doi: 10.1016/S0924-4247(01)00777-4

Shahinpoor, M., and Kim, K. J. (2005). Ionic polymer–metal composites: IV. Industrial and medical applications. *Smart Mater. Struct.* 14, 197–214. doi: 10.1088/0964-1726/14/1/020

Shen, Q., Wang, T., and Kim, K. J. (2015). A biomimetic underwater vehicle actuated by waves with ionic polymer-metal composite soft sensors. *Bioinspir. Biomim.* 10:055007. doi: 10.1088/1748-3190/10/5/055007

Takenaka, H., Torikai, E., Kawami, Y., and Wakabayashi, N. (1982). Solid polymer electrolyte water electrolysis. *Int. J. Hydrogen Energy* 7, 397–403. doi: 10.1016/0360-3199(82)90050-7

Tiwari, R., and Garcia, E. (2011). The state of understanding of ionic polymer metal composite architecture: a review. *Smart Mater. Struct.* 20:083001. doi: 10.1088/0964-1726/20/8/083001

Tripathi, A., Chattopadhyay, B., and Das, S. (2019). Cost-effective fabrication of ionic polymer based artificial muscles for catheter-guidewire maneuvering application. *Microsyst. Technol.* 25, 1129–1136. doi: 10.1007/s00542-018-4152-3

Tsai, S. A., Wei, H. C., and Su, G. D. (2012). Polydimethylsiloxane coating on an ionic polymer metallic composite for a tunable focusing mirror. *Appl. Opt.* 51, 8315–8323. doi: 10.1364/AO.51.008315

Volpini, V., Bardella, L., Rodella, A., Cha, Y., and Porfiri, M. (2017). Modelling compression sensing in ionic polymer metal composites. *Smart Mater. Struct.* 26:035030. doi: 10.1088/1361-665X/26/3/035030

Wang, J., Wang, Y., Zhu, Z., Wang, J., He, Q., and Luo, M. (2019). The effects of dimensions on the deformation sensing performance of ionic polymer-metal composites. *Sensors* 19:2104. doi: 10.3390/s19092104

Wang, Y., Chen, H., Wang, Y., Lu, B., Chang, L., Zhu, Z., et al. (2014a). Influence of additives on the properties of casting nafion membranes and SO-based ionic polymer–Metal composite actuators. *Polymer Eng. Sci.* 54, 818–830. doi: 10.1002/pen.23634

Wang, Y., Chen, H., Wang, Y., Zhu, Z., and Li, D. (2014b). Effect of dehydration on the mechanical and physicochemical properties of gold-and palladium-ionomeric polymer-metal composite (IPMC) actuators. *Electrochim. Acta* 129, 450–458. doi: 10.1016/j.electacta.2014.02.114

Wang, Y., Liu, J., Zhu, Y., Zhu, D., and Chen, H. (2017). Formation and characterization of dendritic interfacial electrodes inside an ionomer. *ACS Appl. Mater. Interfaces* 9, 30258–30262. doi: 10.1021/acsami.7b08012

Wang, Y., Zhu, Z., Chen, H., Luo, B., Chang, L., Wang, Y., et al. (2014c). Effects of preparation steps on the physical parameters and electromechanical properties of IPMC actuators. *Smart Materials and Structures* 23, 125015. doi: 10.1088/0964-1726/23/12/125015

Wang, Y., Zhu, Z., Liu, J., Chang, L., and Chen, H. (2016). Effects of surface roughening of Nafion 117 on the mechanical and physicochemical properties of ionic polymer–metal composite (IPMC) actuators. *Smart Materials and Structures* 25, 085012. doi: 10.1088/0964-1726/25/8/085012

Yamakita, M. (2006). "Integrated design of IPMC actuator/sensor," in *IEEE International Conference on Robotics & Automation* (Orlando, FL). doi: 10.1109/ROBOT.2006.1641973

Yip, J., Ding, F., Yick, K.-L., MarcusYuen, C. W., Lee, T.-T., and Choy, W.-H., et al. (2012). Tunable carbon nanotube ionic polymer actuators that are operable in dry conditions. *Sens. Actu. B Chem.* 162, 76–81. doi: 10.1016/j.snb.2011.12.038

Zhu, Z., Bian, C., Ru, J., Bai, W., and Chen, H. (2018). Rapid deformation of IPMC under a high electrical pulse stimulus inspired by action potential. *Smart Mater. Struct.* 28:01LT01. doi: 10.1088/1361-665X/aadc38

Zhu, Z., He, X., He, Q., Fang, X., Hu, Q., and Chen, H. (2019). Ionic polymer pressure sensor with gradient shape based on ion migration. *J. Appl. Phys.* 125:024901. doi: 10.1063/1.5058100

Zhu, Z., Horiuchi, T., Kruusamäe, K., Chang, L., and Asaka, K. (2016b). Influence of ambient humidity on the voltage response of ionic polymer–metal composite sensor. *J. Phys. Chem. B* 120, 3215–3225. doi: 10.1021/acs.jpcb.5b12634

Zhu, Z., Horiuchi, T., Takagi, K., Takeda, J., Chang, L., and Asaka, K. (2016c). Effects of cation on electrical responses of ionic polymer-metal composite sensors at various ambient humidities. *J. Appl. Phys.* 120, 57–69. doi: 10.1063/1.4961732

Zhu, Z., Wang, Y., Hu, X., Sun, X., Chang, L., and Lu, P. (2016a). An easily fabricated high performance ionic polymer based sensor network. *Appl. Phys. Lett.* 109:073504. doi: 10.1063/1.4961529

Zolfagharian, A., Kouzani, A. Z., Khoo, S. Y., Moghadam, A. A. A., Gibson, I., and Akif, K (2016). Evolution of 3D printed soft actuators. *Sens. Act. A Phys.* 250, 258–272. doi: 10.1016/j.sna.2016.09.028

Conflict of Interest: The authors declare that the research was conducted in the absence of any commercial or financial relationships that could be construed as a potential conflict of interest.

frontiers in Robotics and AI

ORIGINAL RESEARCH
published: 13 December 2019
doi: 10.3389/frobt.2019.00133

Self-Sensing Control for Soft-Material Actuators Based on Dielectric Elastomers

*Thorben Hoffstadt and Jürgen Maas**

Mechatronic System Laboratory, Institute of Machine Design and Systems Technology, Technische Universität Berlin, Berlin, Germany

Due to their energy density and softness that are comparable to human muscles dielectric elastomer (DE) transducers are well-suited for soft-robotic applications. This kind of transducer combines actuator and sensor functionality within one transducer so that no external senors to measure the deformation or to detect collisions are required. Within this contribution we present a novel self-sensing control for a DE stack-transducer that allows to control several different quantities of the DE transducer with the same controller. This flexibility is advantageous e.g., for the development of human machine interfaces with soft-bodied robots. After introducing the DE stack-transducer that is driven by a bidirectional flyback converter, the development of the self-sensing state and disturbance estimator based on an extended Kalman-filter is explained. Compared to known estimators designed for DE transducers supplied by bulky high-voltage amplifiers this one does not require any superimposed excitation to enable the sensor capability so that it also can be used with economic and competitive power electronics like the flyback converter. Due to the behavior of this converter a sliding mode energy controller is designed afterwards. By introducing different feed-forward controls the voltage, force or deformation can be controlled. The validation proofs that both the developed self-sensing estimator as well as the self-sensing control yield comparable results as previously published sensor-based approaches.

Keywords: dielectric elastomers, self-sensing, control, soft material actuator, extended Kalman filter, stack-actuator, flyback-converter

OPEN ACCESS

Edited by:
Herbert Shea,
École Polytechnique Fédérale de Lausanne, Switzerland

Reviewed by:
Senentxu Lanceros-Mendez,
University of Minho, Portugal
Janno Torop,
University of Tartu, Estonia

***Correspondence:**
Jürgen Maas
juergen.maas@tu-berlin.de

Specialty section:
This article was submitted to Soft Robotics, a section of the journal Frontiers in Robotics and AI

Received: *06 September 2019*
Accepted: *18 November 2019*
Published: *13 December 2019*

Citation:
Hoffstadt T and Maas J (2019) Self-Sensing Control for Soft-Material Actuators Based on Dielectric Elastomers. Front. Robot. AI 6:133. doi: 10.3389/frobt.2019.00133

1. INTRODUCTION

Entirely soft-bodied robots exploit the full potential of robotic systems in terms of safe human-machine-interactions and, thus, are in the scope of research. However, novel mechanical designs in conjunction with smart and soft materials as well as innovative approaches for modeling and the development of control strategies to handle such a highly sophisticated robot species are necessary (Navarro et al., 2013; Robla-Gomez et al., 2017). Due to their behavior that resembles human muscles, dielectric elastomers (DEs) are a promising approach that could pave the way for soft-bodied robots. As a DE transducer consists of a very thin, elastomeric dielectric film covered with compliant electrodes, its behavior can be described by a shape varying capacitor.

By applying a voltage v_p to the electrodes of the DE transducer with permittivity $\varepsilon_0 \cdot \varepsilon_r$ and thickness d the resulting electrostatic pressure

$$\sigma_{el} = \varepsilon_0 \cdot \varepsilon_r \cdot \left(\frac{v_p}{d}\right)^2 \quad (1)$$

compresses the elastomer. This pressure is used to operate a DE transducer in actuator mode. However, if the change of the transducer's capacitance is detected that is caused by its deformation, a simultaneous operation as sensor is enabled. If the deformation dependency of the capacitance is known, the mechanical transducer state can be determined. By exploiting this self-sensing capability, soft and smart transducers can be realized that do not require additional external sensors and, thus, can be comparably easy integrated into various applications not limited to soft robotics.

For various types of DE transducers different approaches to control their displacement or force (Maas et al., 2011; Sarban and Jones, 2012; Rizzello et al., 2015; Wilson et al., 2016; Hoffstadt and Maas, 2017, 2018b) or to use them for active vibration attenuation (Dubois et al., 2008; Kaal and Herold, 2011; Sarban, 2011) have been presented previously. Within these approaches the control variables are directly measured with external sensors, so that the DE transducer is only operated as actuator. Due to the additional sensor, these controls are referred to as sensor-based control schemes.

Within this paper, the focus is given on the development of a model-based self-sensing control for DE transducers that allows to control the voltage, force and deformation of the transducer without measuring any mechanical quantities. **Figure 1** gives an overview of the overall developed control circuit.

As shown in the center and on the right hand side of **Figure 1** the terminal voltage v_{DE} and current i_{DE} have to be measured to enable the combined actuator-sensor-operation. In order to determine the mechanical state based on these measurement quantities adequate self-sensing algorithms are required. Anderson et al. (2012) summarizes different approaches for this purpose. The goal of most self-sensing algorithms is to identify the capacitance of the DE transducer in a first step and afterwards estimate the deformation and force based on a model or experimentally obtained information about the deformation dependency of the capacitance. For almost all approaches the driving voltage v_{DE} is superimposed with a harmonic excitation that is used for the sensor functionality.

Chuc et al. (2008) and Jung et al. (2008) published first frequency domain based approaches by experimentally identifying changes of the electrical impedance of a DE transducer under deformation when it is excited by a harmonic voltage v_{DE}. Beside the capacitance C_p they also considered losses in the polymer and the electrode by adding the resistances R_s and R_p, respectively, see **Figure 1**.

In Hoffstadt et al. (2014) another model-based identification algorithm in the frequency domain is presented that estimates the electrical parameters of a DE transducer by evaluating the amplitudes of and the phase shift between the superimposed terminal voltage and current. Furthermore, it was shown that the behavior of a DE transducer can be sufficiently modeled by neglecting the parallel resistance R_p representing losses in the dielectric, if the DE transducer is excited with a comparable high frequency.

The extended Kalman-filter introduced in Hoffstadt and Maas (2018a) estimates the strain of a DE transducer without any superimposed excitation so that it can be used independent of the utilized power electronics. Other approaches in the time domain estimate the charge q_p of the capacitance C_p. Under further consideration of the measured voltage v_{DE} the capacitance $C_p \approx q_p/v_{DE}$ can be determined (Matysek et al., 2011; Gisby et al., 2013).

Rizzello et al. (2017) developed a self-sensing algorithm based on the recursive least squares (RLS) method. For this purpose, he takes into account the equivalent circuit diagram with three parameters (see **Figure 1**). In a first step, the parameters of a discrete transfer function describing the behavior of the considered circuit are estimated. As these parameters depend on the electrical parameters, they can be calculated afterwards. For the identification a harmonic excitation signal is superimposed.

Although several self-sensing approaches have been developed only a few closed-loop self-sensing controller designs have been published, so far. Gisby et al. (2011) controls the deformation of a single-layer circular DE transducer by using the already mentioned self-sensing approach (Gisby et al., 2013). Here, the terminal voltage is PWM generated. While the deformation of the DE transducer mainly depends on the mean of this voltage, the included higher harmonics are used to enable the sensor functionality. The manually adjusted proportional gain controller yields comparable low dynamics and accuracy. Therefore, Rosset et al. (2013) extends this controller to a PI-controller, using the same self-sensing approach (Gisby et al., 2013). Here, the parameters of the controller are optimized for one particular operating point of the nonlinear control plant. The derived controller is used to control an optical grid.

Rizzello et al. (2016) systematically combines his RLS-based self-sensing approach (Rizzello et al., 2017) with his robust position controller (Rizzello et al., 2015) to control the deformation of a DE membrane actuator. For the combined actuator-sensor-operation the required driving voltage determined by the controller is superimposed with a harmonic excitation with a high frequency of 1 kHz and an amplitude of 75 V. Compared to the sensor-based control (Rizzello et al., 2015) almost no drawbacks in terms of the accuracy are observed, while the bandwidth of the closed-loop self-sensing control is reduced due to the dynamics of the parameter identification.

Within the referenced publications costly and bulky high-voltage amplifiers were used to feed the DE transducer. However, due to the capacitive behavior of DE transducers voltage-fed current sources are well suited instead of high-voltage amplifiers (Eitzen et al., 2011a). Here, compact and efficient driving electronics can be realized when using switched-mode operated topologies like the bidirectional flyback converter. This converter allows not only to supply the DE transducer with a certain voltage but also to recover the energy stored in the DE transducer when discharging it.

Under consideration of the properties of the bidirectional flyback converter and the DE transducer, we previously published sensor-based position and force controls in Hoffstadt and Maas

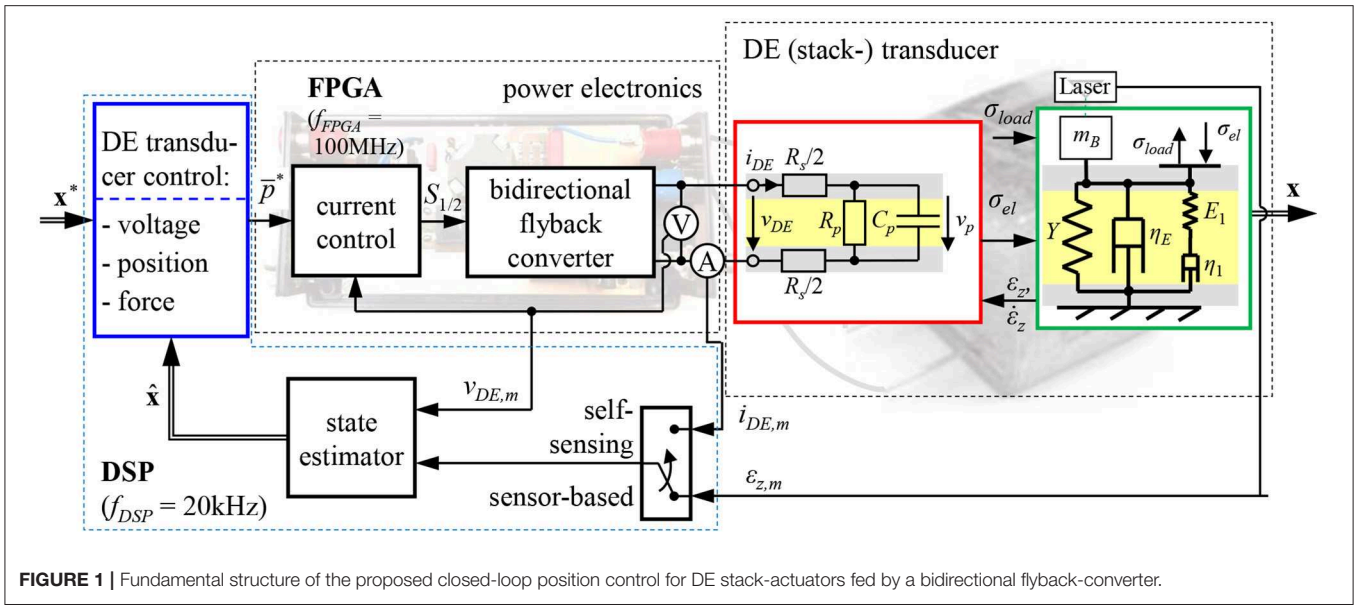

FIGURE 1 | Fundamental structure of the proposed closed-loop position control for DE stack-actuators fed by a bidirectional flyback-converter.

(2017, 2018b) that use the directly measured deformation as feedback-signal, cf. **Figure 1**. Within this publication we extend them to a self-sensing controller that is able to universally control the voltage, force or deformation of the DE transducer by just measuring the terminal voltage v_{DE} and current i_{DE}. For this purpose, in the following section 2 the considered control plant comprising a DE stack-transducer (Maas et al., 2015) fed by a bidirectional flyback converter (Eitzen et al., 2011b; Hoffstadt and Maas, 2016) is introduced and modeled. The design of the novel self-sensing state and disturbance estimator is presented in section 3. Due to the non-linear behavior of the control plant an extended Kalman-filter (EKF) is used for this purpose (Welch and Bishop, 2001). The developed estimator does not require any superimposed excitation. The subsequently presented controller design (Hoffstadt and Maas, 2017, 2018b) is based on the sliding mode control approach (DeCarlo et al., 1988) as this is well suited for the considered control plant and its characteristic behavior. The self-sensing estimator and control are experimentally validated in section 5. Finally, section 6 summarizes the developed approaches and the result.

2. MODEL OF THE DE TRANSDUCER SYSTEM

Figure 2A shows a schematic representation of the considered DE stack-transducer with N layers. This multilayer design is used to scale the deformation Δz in z-direction, as one single layer has an initial thickness of only $d_0 = 50\ \mu$m. Details about the design and the manufacturing were published by Maas et al. (2015). The static strain-force-behavior is shown in **Figure 2B**. The transducer generates higher tensile forces F_{act} at smaller strains $\varepsilon_z = \Delta z/z_0$, with $z_0 = N \cdot d_0$. By increasing the initial electric field strength $E_0 = v_{\mathrm{DE}}/d_0$ the electrostatic pressure according to Equation (1) increases so that higher forces and strains are obtained. The blocking-force $F_{\mathrm{act}}(\varepsilon_z = 0)$ and the no-load strain $\varepsilon_z(F_{\mathrm{act}} = 0)$ represent two characteristic points of the strain-force behavior.

An analytical model for this transducer is published in Hoffstadt and Maas (2015). In **Figure 2** the modeled results of the static strain-force behavior are compared with measurement results and a finite element analysis (FEA) published by Kuhring et al. (2015). The analytical model is based on the structure shown on the right of **Figure 1**. The actuator tension σ_{act} is given by the force equilibrium:

$$\sigma_{\mathrm{act}} = \beta \cdot \sigma_{\mathrm{el}} - \sigma_{\mathrm{elast}} - \eta_E \cdot \dot{\varepsilon}_z - E_1 \cdot \varepsilon_{E_1}, \text{ with } \beta = \frac{A_{\mathrm{e}}}{A}. \quad (2)$$

Here, σ_{elast} is the elastic material tension that is calculated using the Neo-Hookean approach with the Young's modulus Y to consider the hyperelastic, non-linear material behavior:

$$\sigma_{elast} = \frac{Y}{3} \cdot \left(\frac{1}{1-\varepsilon_z} - (1-\varepsilon_z)^2 \right). \quad (3)$$

Beside this reversible elastic behavior, viscoelastic properties are taken into account with the viscosity η_E and the Maxwell element with stiffness E_1 and viscosity η_1. Furthermore, with the area ratio β it is considered that the electrostatic pressure σ_{el} acts only on the area A_{e} covered with electrode, while all other tensions are assumed to homogeneously act on the whole transducer area A in z-direction. Instead of applying Equation (1) for the electrostatic pressure σ_{el}, here it is determined depending on the energy $U_{\mathrm{c,diel}}$ in the electric field of the capacitance C_p:

$$\beta \cdot \sigma_{\mathrm{el}} = \frac{2}{V} \cdot U_{\mathrm{c,diel}}. \quad (4)$$

The bidirectional flyback converter control proposed in Hoffstadt and Maas (2016) enables three discrete input states in terms of

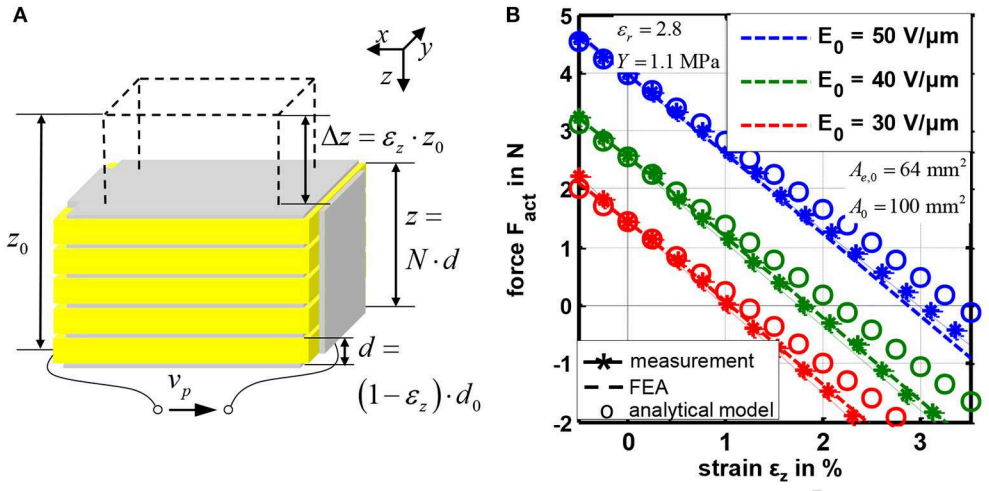

FIGURE 2 | Schematic design **(A)** and static strain-force characteristics **(B)** of the considered silicone-based DE stack-actuators.

the feeding power $\bar{p}$. Beside an off-state, the DE can be charged and discharged with almost constant power depending on the characteristic energy increment $\Delta U_{\max}$ transfered during every switching period T_S of the converter:

$$\bar{p} = \begin{cases} +\bar{p}_{\max} = +\frac{\Delta U_{\max}}{T_S}, & \text{charging} \\ 0, & \text{off-state} \\ -\bar{p}_{\max} = -\frac{\Delta U_{\max}}{T_S}, & \text{discharging} \end{cases}$$
$$\text{with } \Delta U_{\max} = \frac{1}{2} \cdot L_m \cdot I_{m,\max}. \tag{5}$$

The energy increment $\Delta U_{\max}$ depends on the magnetizing inductance L_m of the converter and the magnetizing current $I_{m,\max}$ adjusted by its inner control. Under further consideration of losses p_{Re} dissipated in the electrode material the power $\bar{p}' = \bar{p} - p_{Re}$ feeds the capacitance of the DE transducer. With this, the electromechanically coupled behavior of a DE transducer can be modeled based on a power balance yielding the state space representation

$$\dot{\mathbf{x}} = \begin{bmatrix} \dot{\varepsilon}_z \\ \frac{V}{m_B \cdot z_0^2} \cdot \frac{\sigma_{act} - \sigma_{load}}{1-\varepsilon_z} \\ \dot{\varepsilon}_z - \frac{E_1}{\eta_1} \cdot \varepsilon_{E_1} \\ -2 \cdot U_{c,diel} \cdot \left(\frac{\dot{\varepsilon}_z}{1-\varepsilon_z} + \frac{1}{\tau_p} \right) \end{bmatrix} + \begin{bmatrix} 0 \\ 0 \\ 0 \\ 1 \end{bmatrix} \cdot \bar{p}', \tag{6}$$
$$\text{with } \mathbf{x} = \begin{bmatrix} \varepsilon_z \\ \dot{\varepsilon}_z \\ \varepsilon_{E_1} \\ U_{c,diel} \end{bmatrix}.$$

Beside the strain ε_z and the energy $U_{c,diel}$ the state vector $\mathbf{x}$ includes the velocity $\dot{\varepsilon}_z$ as well as the strain ε_{E_1} of the stiffness E_1 of the Maxwell element. Depending on the supplied input power $\bar{p}'$ and an external load σ_{load} the inner states of the DE transducer with volume V and accelerated mass m_B can be calculated with Equation (6).

For the subsequently developed self-sensing state estimator models describing the strain dependency of the electrical transducer parameters are required, too. The series resistance R_s mainly comprises losses in the contacting of the DE transducer and electrodes that are applied on the initial area $A_{e,0}$ of every layer. It was shown Hoffstadt et al. (2016) that this resistance is almost constant in the relevant range of deformation. In contrast, the capacitance C_p for the N layers connected in parallel is given by:

$$C_p = N \cdot \varepsilon_0 \cdot \varepsilon_r \cdot \frac{A_{e,0}}{d_0} \cdot \frac{1}{(1-\varepsilon_z)^\kappa} = C_{p,0} \cdot \frac{1}{(1-\varepsilon_z)^\kappa} \tag{7}$$

The change of the initial capacitance $C_{p,0}$ also depends on the factor κ. In case of an absolutely homogeneous deformation without constraints, $\kappa = 2$ would apply. However, due to a passive area around A_e that is required for insulation purposes, as well as due to stiff mechanical interfaces applied on the top and/or bottom of the transducer, here the factor is slightly decreased to $\kappa = 1.85$.

In analogy, the strain dependency of the parallel resistance R_p reads as follows:

$$R_p = \frac{1}{N} \cdot \rho_p \cdot \frac{d_0}{A_{e,0}} \cdot (1-\varepsilon_z)^\kappa = R_{p,0} \cdot (1-\varepsilon_z)^\kappa. \tag{8}$$

This resistance represents losses in the dielectric with the specific resistance ϱ_p.

Although C_p and R_p vary with the strain ε_z the resulting time constant τ_p is independent of the strain:

$$\tau_p = R_p \cdot C_p = \varepsilon_0 \cdot \varepsilon_r \cdot \rho_p = \text{const.} \tag{9}$$

3. EKF-BASED SELF-SENSING ALGORITHM

In Hoffstadt and Maas (2018a) we already published a self-sensing estimator based on a discrete, extended Kalman-filter that estimates the strain of the DE transducer without superimposed excitation. However, for the closed-loop operation beside the inner states of the transducer also the disturbance σ_{load} has to be estimated. For example, this load tension might result from a collision of an external device or human with a soft-bodied robot equipped with DE transducers. Therefore, a new and extended approach based on Equation (6) is applied here. As mentioned above, the goal is to determine the electromechanical state of the DE transducer based on the measured terminal voltage ν_{DE} and the current i_{DE}. However, in Equation (6) the energy $U_{\text{c,diel}}$ represents the electrical state. Therefore, a modification of the model is required to design the self-sensing estimator.

For this purpose, the change of the charge q_{p} on the capacitance C_{p} is taken into account. It can be calculated under consideration of the current i_{DE} and the leakage current $\nu_{\text{p}}/R_{\text{p}} = q_{\text{p}}/\tau_{\text{p}}$, see **Figure 1**:

$$\dot{q}_{\text{p}} = i_{\text{DE}} - \frac{\nu_{\text{p}}}{R_{\text{p}}} = i_{\text{DE}} - \frac{1}{\tau_{\text{p}}} \cdot q_{\text{p}}, \text{ with } q_{\text{p}} = C_{\text{p}} \cdot \nu_{\text{p}}. \tag{10}$$

As the charge depends on the measured current and the invariant time constant τ_{p} from Equation (9), it is used as input variable u_{qv} in the following. Furthermore, if instead of the energy $U_{\text{c,diel}}$ the charge q_{p} is considered, the electrostatic pressure can be expressed by:

$$\beta \cdot \sigma_{\text{el}} = \frac{2}{V} \cdot U_{\text{c,diel}} = \frac{q_{\text{p}}^2}{V \cdot C_{\text{p}}(\varepsilon_z)}, \text{ with } U_{\text{c,diel}} = \frac{1}{2} \cdot \frac{q_{\text{p}}^2}{C_{\text{p}}(\varepsilon_z)}. \tag{11}$$

Additionally, the voltage ν_{p} across C_{p} depends on the terminal voltage ν_{DE} reduced by the voltage drop $R_{\text{s}} \cdot i_{\text{DE}}$ across the series resistance R_{s} that is assumed to be constant here:

$$\nu_{\text{p}} = \frac{q_{\text{p}}}{C_{\text{p}}(\varepsilon_z)} = \nu_{\text{DE}} - R_{\text{s}} \cdot i_{\text{DE}}. \tag{12}$$

This voltage will be used as output variable y_{qv} afterwards.

Beside the mechanical states included in $\mathbf{x}$ and Equation (6) the external load σ_{load} has to be estimated as disturbance, too. As it represents an unknown disturbance it is assumed (according to Isermann and Munchhof, 2011) that it is constant during one sample time T of the discrete EKF implemented on a DSP. By applying $\dot{\sigma}_{\text{load}} = 0$ in combination with Equations (10)–(12) a fourth order system can be established for the estimation:

$$\begin{aligned} \dot{\mathbf{x}}_{qv} = \mathbf{f}_{qv}\left(\mathbf{x}_{qv}, u_{qv}\right) &= \begin{bmatrix} \dot{\varepsilon}_z \\ \gamma_1 \cdot \frac{\sigma_{\text{act}}(q_p) - \sigma_{\text{load}}}{1-\varepsilon_z} \\ \dot{\varepsilon}_z - \frac{E_1}{\eta_1} \cdot \varepsilon_{E_1} \\ 0 \end{bmatrix}, \\ \text{with } \mathbf{x}_{qv} = \begin{bmatrix} \varepsilon_z \\ \varepsilon_z \\ \varepsilon_{E_1} \\ \sigma_{\text{load}} \end{bmatrix}, \ \gamma_1 &= \frac{V}{m_{\text{B}} \cdot z_0^2} \text{ and} \\ y_{qv} = g_{qv}\left(\mathbf{x}_{qv}, u_{qv}\right) &= \frac{(1-\varepsilon_z)^{\kappa}}{C_{\text{p,0}}} \cdot q_{\text{p}} = \nu_{\text{p}} = \nu_{\text{DE,m}} - R_{\text{s}} \cdot i_{\text{DE,m}}. \end{aligned} \tag{13}$$

According to Adamy (2014) the observability of the nonlinear system (13) is given if the determinant of the observability matrix $\mathbf{Q}_{\text{B},qv}$ is not zero. This matrix can be calculated under consideration of the Lie derivatives $L^i_{\mathbf{f}_{qv}} g_{qv}$, with $i = 0, ..., 3$:

$$\mathbf{Q}_{\text{B},qv}\left(\mathbf{x}_{qv}, u_{qv}\right) = \begin{bmatrix} \frac{\partial L^0_{\mathbf{f}_{qv}} g_{qv}(\mathbf{x}_{qv}, u_{qv})}{\partial \mathbf{x}_{qv}} \\ \frac{\partial L^1_{\mathbf{f}_{qv}} g_{qv}(\mathbf{x}_{qv}, u_{qv})}{\partial \mathbf{x}_{qv}} \\ \frac{\partial L^2_{\mathbf{f}_{qv}} g_{qv}(\mathbf{x}_{qv}, u_{qv})}{\partial \mathbf{x}_{qv}} \\ \frac{\partial L^3_{\mathbf{f}_{qv}} g_{qv}(\mathbf{x}_{qv}, u_{qv})}{\partial \mathbf{x}_{qv}} \end{bmatrix} = \begin{bmatrix} \frac{\partial g_{qv}(\mathbf{x}_{qv}, u_{qv})}{\partial \mathbf{x}_{qv}} \\ \frac{\partial L^1_{\mathbf{f}_{qv}} g_{qv}(\mathbf{x}_{qv}, u_{qv})}{\partial \mathbf{x}_{qv}} \\ \frac{\partial L^2_{\mathbf{f}_{qv}} g_{qv}(\mathbf{x}_{qv}, u_{qv})}{\partial \mathbf{x}_{qv}} \\ \frac{\partial L^3_{\mathbf{f}_{qv}} g_{qv}(\mathbf{x}_{qv}, u_{qv})}{\partial \mathbf{x}_{qv}} \end{bmatrix} \tag{14}$$

Beside material parameters that are different from zero, the determinant of $\mathbf{Q}_{\text{B},qv}$ depends on the charge q_{p} and the strain ε_z:

$$\begin{aligned} \det\left(\mathbf{Q}_{\text{B},qv}\left(\mathbf{x}_{qv}, u_{qv}\right)\right) = q_{\text{p}}^4 \cdot \frac{\gamma_1^2 \cdot \kappa^4 \cdot E_1^2}{\eta_1 \cdot C_{\text{p}}^4(\varepsilon_z) \cdot (1-\varepsilon_z)^6} \neq 0, \\ \text{for } \varepsilon_z < 1 \text{ and } q_{\text{p}} \neq 0. \end{aligned} \tag{15}$$

The strain ε_z is always smaller than one, and thus does not influence the observability. However, the uncharged state with $q_{\text{p}} = 0$ is not observable. In contrast for example to piezoelectric materials, this is due to the fact that the DE materials do not contain inherent dipoles causing a charge separation under deformation. Instead, a DE transducer has to be electrically pre-charged so that a current flow or change of voltage can be detected when it is deformed. Furthermore, the restricted observability for $q_p = 0$ is not only a drawback of the proposed approach. All referenced self-sensing methods have the same issue, but the usually superimposed voltage excitations ensure that this operating point does not occur. As this superimposed excitation is not required for the EKF-based estimator a certain amount of charge $q_{\text{p,min}}$ is always applied, here.

This results in the structure of the EKF-based self-sensing state and disturbance estimator shown in **Figure 3**. As the EKF will be implemented on a DSP its discrete implementation according to Welch and Bishop (2001) is applied. Using the external estimation of the charge by filtering the measured current $i_{\text{DE,m}}$ has the advantage, that the state vector $\mathbf{x}_{qv}$ only includes mechanical states that have to be estimated with the EKF. Furthermore, the parameterization effort increases significantly

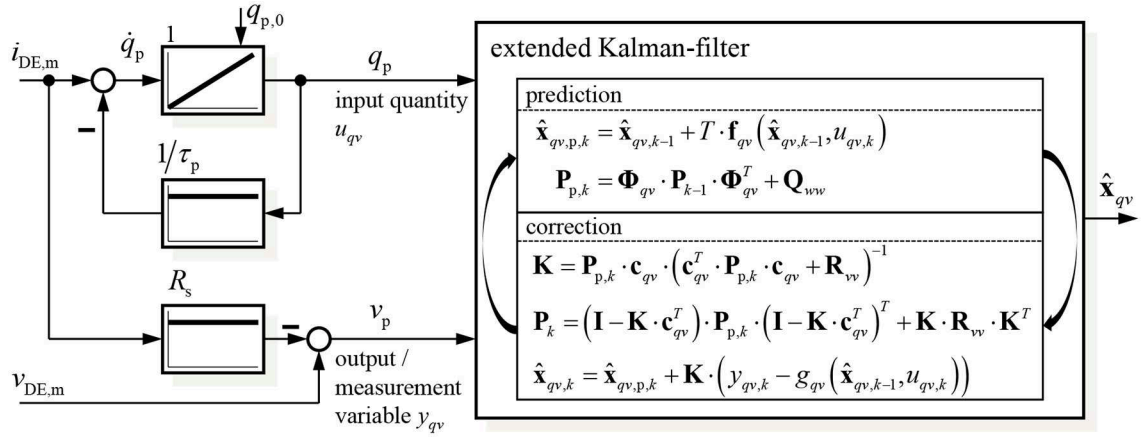

FIGURE 3 | Structure of the proposed self-sensing state and disturbance estimator based on an extended Kalman-filter.

with increasing system order so that it is meaningful to use a system with order $n = 4$ instead of $n = 5$.

For the implementation of the Kalman-filter algorithm according to **Figure 3** the system (13) has to be linearized in the predicted state $\hat{\mathbf{x}}_{qv,\mathrm{p},k}$:

$$\mathbf{A}_{qv,k} = \left.\frac{\partial \mathbf{f}_{qv}\left(\mathbf{x}_{qv}, u_{qv}\right)}{\partial \mathbf{x}_{qv}}\right|_{\hat{\mathbf{x}}_{qv,\mathrm{p},k}, u_{qv,k}} = \begin{bmatrix} 0 & 1 & 0 & 0 \\ a_{qv,21} & \frac{-\gamma_1 \cdot \eta_\mathrm{E}}{1-\hat{\varepsilon}_{z,\mathrm{p}}} & \frac{-\gamma_1 \cdot E_1}{1-\hat{\varepsilon}_{z,\mathrm{p}}} & \frac{-\gamma_1}{1-\hat{\varepsilon}_{z,\mathrm{p}}} \\ 0 & 1 & -\frac{E_1}{\eta_1} & 0 \\ 0 & 0 & 0 & 0 \end{bmatrix}, \tag{16}$$

$$\text{with } a_{qv,21} = \frac{\gamma_1}{1-\hat{\varepsilon}_{z,\mathrm{p}}} \cdot \left[\frac{\hat{\sigma}_{\mathrm{act,p}}\left(u_{qv,k}\right) - \hat{\sigma}_{\mathrm{load,p}}}{1-\hat{\varepsilon}_{z,\mathrm{p}}} - \frac{d\hat{\sigma}_{\mathrm{elast,p}}}{d\hat{\varepsilon}_{z,\mathrm{p}}} - \frac{d\hat{\sigma}_{\mathrm{el,p}}}{d\hat{\varepsilon}_{z,\mathrm{p}}}\right],$$

$$\text{and } \frac{d\hat{\sigma}_{\mathrm{el,p}}}{d\hat{\varepsilon}_{z,\mathrm{p}}} \overset{(11)}{\underset{(7)}{=}} -\frac{\kappa \cdot q_\mathrm{p}^2 \cdot \left(1-\hat{\varepsilon}_{z,\mathrm{p}}\right)^{\kappa-1}}{V \cdot C_{\mathrm{p},0}}.$$

Based on this the discrete transition matrix Φ_{qv} can be approximated by (Ifeachor and Jervis, 2002):

$$\Phi_{qv} \approx \mathbf{I} + \mathbf{A}_{qv,k} \cdot T, \tag{17}$$

where $\mathbf{I}$ represents the unity matrix of order $n = 4$. The output vector $\mathbf{c}_{qv,k}^T$ is calculated by the jacobian of the output function g_{qv} in Equation (13) with respect to the state vector $\mathbf{x}_{qv}$:

$$\mathbf{c}_{qv,k}^T = \left.\frac{\partial g_{qv}\left(\mathbf{x}_{qv}, u_{qv}\right)}{\partial \mathbf{x}_{qv}}\right|_{\hat{\mathbf{x}}_{qv,rmp,k}, u_{qv,k}} = \left[-\frac{\kappa \cdot \left(1-\hat{\varepsilon}_{z,p}\right)^{\kappa-1}}{C_{\mathrm{p},0}} \cdot u_{qv,k} \;\; 0 \;\; 0 \;\; 0\right]. \tag{18}$$

With these information the predicted state $\hat{\mathbf{x}}_{qv,\mathrm{p},k}$ and the related covariance matrix $\mathbf{P}_{\mathrm{p},k}$ can be determined in the prediction step (denoted by the index p) of the algorithm shown in **Figure 3**. In the following correction the Kalman matrix $\mathbf{K}$ and covariance matrix $\mathbf{P}_k$ are calculated to update the estimated state vector $\hat{\mathbf{x}}_{qv,k}$. The covariance matrices of the measurement and system noise $\mathbf{R}_{vv}$ and $\mathbf{Q}_{ww}$, respectively, will be parameterized in the validation section 5. With the information, included in the state vector $\mathbf{x}_{qv,k}$ and Equation (4) to calculate the energy $U_{\mathrm{c,diel}}$ based on the charge q_p, all state variables in $\mathbf{x}$ from Equation (6) as well as the load σ_{load} can be determined.

4. SELF-SENSING SLIDING MODE CONTROL

The considered control plant modeled with Equation (6) has a strongly non-linear behavior. Furthermore, the bidirectional flyback converter allows to supply discrete feeding powers $\bar{p}$ so that it can be described by the three-point switch in Equation (5). Due to these properties the design of a variable structure control is well suited. In Hoffstadt and Maas (2017) a position controller based on the model (6) was introduced that uses the sliding mode control (SMC), for this purpose. Additionally, a SMC force controller was published in Hoffstadt and Maas (2018b). In the following it will be shown that this controller cannot be used to solely control the force F_{act} of the DE transducer but also the strain ε_z and the voltage v_p by applying different feed-forward structures to one and the same controller. This flexibility makes the approach advantageous for sophisticated applications like in soft robotics. The detailed design of the controller shown in **Figure 4** can be found in Hoffstadt and Maas (2018b) and will be summarized in the following.

In case of the SMC a static setpoint state vector $\mathbf{x}^*$ has to be defined including setpoints for every state variable. Under consideration of the static force equilibrium

$$\lim_{t\to\infty} \sigma_{\mathrm{act}}(t) = \beta \cdot \sigma_{\mathrm{el}} - \sigma_{\mathrm{elast}} \overset{(4)}{=} \frac{2}{V} \cdot U_{\mathrm{c,diel}} - \sigma_{\mathrm{elast}} \overset{!}{=} \sigma_{\mathrm{load}} \tag{19}$$

resulting from Equation (2) setpoints for the energy $U_{\mathrm{c,diel}}^*$ can be derived. On the one hand, the energy can be calculated depending

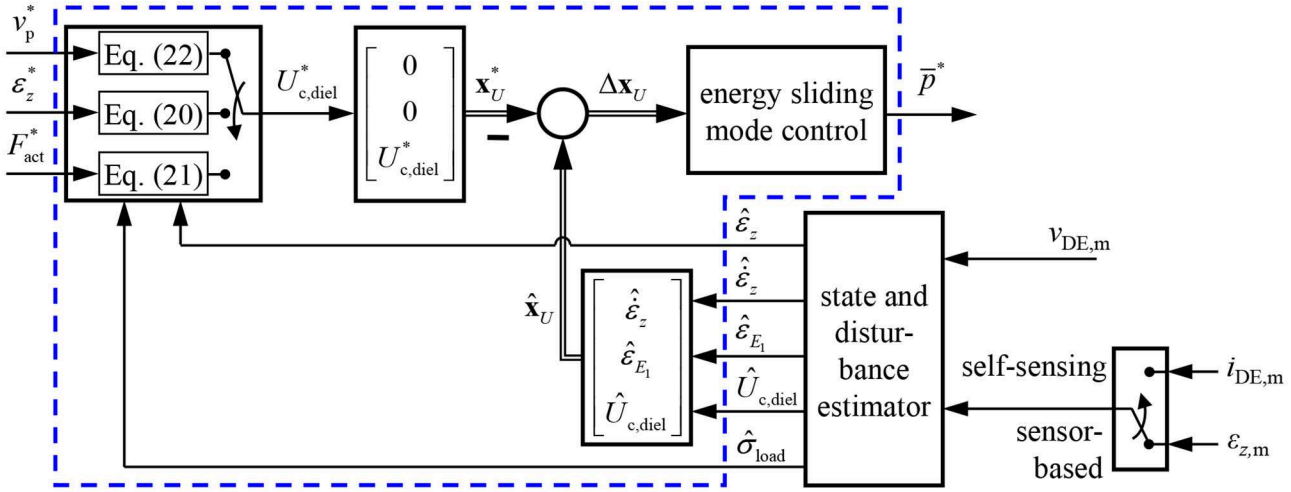

FIGURE 4 | Detailed structure of the controller (blue box in **Figure 1**) including a feed-forward structure to either control the voltage, strain or force and a three-point controller with hysteresis and adaption of the inner flyback converter control.

on a setpoint strain ε_z^*:

$$U_{\mathrm{c,diel}}^*\left(\varepsilon_z^*\right) = \frac{V}{2}\cdot\left(\sigma_{\mathrm{elast}}\left(\varepsilon_z^*\right) + \sigma_{\mathrm{load}}\right). \tag{20}$$

To achieve this strain the electrostatic pressure caused by the energy according to Equation (4) has to compensate the elastic material tension $\sigma_{\mathrm{elast}}(\varepsilon_z^*)$ given by Equation (3) as well as the influence of the disturbance σ_{load}. On the other hand, if the DE transducer should generate a certain force $F_{\mathrm{act}}^* = A\cdot\sigma_{\mathrm{act}}$ the corresponding energy $U_{\mathrm{c,diel}}^*$ is given by:

$$\begin{aligned} U_{\mathrm{c,diel}}^*\left(F_{\mathrm{act}}^*\right) &= \frac{V}{2}\cdot\left(\frac{F_{\mathrm{act}}^*}{A\left(\varepsilon_z\right)} + \sigma_{\mathrm{elast}}\left(\varepsilon_z\right)\right), \\ \text{with } \sigma_{\mathrm{load}} &= \frac{F_{\mathrm{act}}^*}{A\left(\varepsilon_z\right)} \text{ and } A\left(\varepsilon_z\right) = \frac{A_0}{1-\varepsilon_z}. \end{aligned} \tag{21}$$

In this case, the influence of the elastic deformation has to be compensated, i.e., the energy has to be increased with increasing strain ε_z (see **Figure 2B**).

Beside these approaches, the energy $U_{\mathrm{c,diel}}^*$ can be also determined depending on a setpoint voltage v_{p}^* across the capacitance $C_{\mathrm{p}}(\varepsilon_z)$ in Equation (7):

$$U_{\mathrm{c,diel}}^*\left(v_{\mathrm{p}}^*\right) = \frac{1}{2}\cdot C_{\mathrm{p}}\left(\varepsilon_z\right)\cdot v_{\mathrm{p}}^{*2}. \tag{22}$$

With Equations (20)–(22) three approaches exist to define a setpoint value for the energy $U_{\mathrm{c,diel}}^*$. For the system (6) also a setpoint for the strain ε_z^* is required, while the other two state variables are zero during steady state $\dot{\varepsilon}_z = \varepsilon_{E_1} = 0$, respectively. However, especially if the force or voltage should be controlled by applying Equations (21) or (22), they should be independent of the strain, i.e., that no setpoint ε_z^* can be defined in this case. To overcome this issue, the control design is based on a reduced system (23) with $\dot{\varepsilon}_z$, ε_{E_1} and $U_{\mathrm{c,diel}}$ as state variables while the strain ε_z together with the load tension σ_{load} is considered to be a disturbance, here:

$$\dot{\mathbf{x}}_U = \begin{bmatrix} \ddot{\varepsilon}_z \\ \dot{\varepsilon}_{E_1} \\ \dot{U}_{\mathrm{c,diel}} \end{bmatrix} = \underbrace{\begin{bmatrix} \frac{V}{m_{\mathrm{B}}\cdot z_0^2}\cdot\frac{\sigma_{\mathrm{act}}-\sigma_{\mathrm{load}}}{1-\varepsilon_z} \\ \dot{\varepsilon}_z - \frac{E_1}{\eta_1}\cdot\varepsilon_{E_1} \\ -2\cdot U_{\mathrm{c,diel}}\cdot\left(\frac{\dot{\varepsilon}_z}{1-\varepsilon_z} + \frac{1}{\tau_{\mathrm{p}}}\right) \end{bmatrix}}_{\mathbf{f}_U(\mathbf{x}_U,\mathbf{z})} + \underbrace{\begin{bmatrix} 0 \\ 0 \\ 1 \end{bmatrix}}_{\mathbf{b}_U}\cdot\bar{p}', \tag{23}$$

with $\mathbf{z} = \begin{bmatrix} \varepsilon_z \\ \sigma_{\mathrm{load}} \end{bmatrix}$.

In this case, the setpoint state vector reads as:

$$\dot{\mathbf{x}}_U^* = \begin{bmatrix} 0 & 0 & U_{\mathrm{c,diel}}^* \end{bmatrix}^T. \tag{24}$$

4.1. Design of the Sliding Mode

The control operation with a SMC is characterized by two phases. During the sliding mode the system is led toward its setpoint $\mathbf{x}^*$ on the switching function $S(\Delta\mathbf{x}) = S(\mathbf{x}-\mathbf{x}^*) = 0$. Within the reaching phase it is ensured, first, that this switching function is reached from any arbitrary initial state. According to DeCarlo et al. (1988) one comparable simple approach for the design of the switching function is obtained if the system is in standard canonical form (denoted by the index R). To determine a corresponding transformation matrix $\mathbf{T}$, the system (23) has to be linearized yielding the system matrix $\mathbf{A}_U$ for the estimated state $\hat{\mathbf{x}}_U$:

$$\mathbf{A}_U = \left.\frac{\partial\mathbf{f}_U\left(\mathbf{x}_U,\mathbf{z}\right)}{\partial\mathbf{x}_U}\right|_{\mathbf{x}_U=\hat{\mathbf{x}}_U} = \begin{bmatrix} \frac{-\gamma_1\cdot\eta_{\mathrm{E}}}{1-\hat{\varepsilon}_z} & \frac{-\gamma_1\cdot E_1}{1-\hat{\varepsilon}_z} & \frac{\gamma_1\cdot 2/V}{1-\hat{\varepsilon}_z} \\ 1 & -\frac{E_1}{\eta_1} & 0 \\ -\frac{2\cdot\hat{U}_{\mathrm{c,diel}}}{1-\hat{\varepsilon}_z} & 0 & -\frac{2\cdot\hat{\dot{\varepsilon}}_z}{1-\hat{\varepsilon}_z} - \frac{2}{\tau_{\mathrm{p}}} \end{bmatrix}. \tag{25}$$

As the system behaves linear concerning the input u, the constant input vector $\mathbf{b}_U$ is already given in Equation (23). With

these information the following transformation matrix $\mathbf{T}$ can be derived as proposed by Kalman (1960):

$$\mathbf{T} = -\frac{V}{2} \cdot \frac{1-\hat{\varepsilon}_z}{\gamma_1} \cdot \begin{bmatrix} 0 & -1 & 0 \\ -1 & \frac{E_1}{\eta_1} & 0 \\ t_{31} & t_{32} & -\frac{2}{V} \cdot \frac{\gamma_1}{1-\hat{\varepsilon}_z} \end{bmatrix} \tag{26}$$

$$\text{with } t_{31} = \frac{E_1}{\eta_1} + \frac{\gamma_1 \cdot \eta_E}{1-\hat{\varepsilon}_z} \text{ and } t_{32} = \frac{E_1}{\eta_1} \cdot \left(\frac{\gamma_1 \cdot \eta_1}{1-\hat{\varepsilon}_z} - \frac{E_1}{\eta_1} \right).$$

For the considered single input single output (SISO) system a linear switching function is defined:

$$\begin{aligned} S(\Delta\mathbf{x}_\mathrm{R}) &= \mathbf{c}^T \cdot \Delta\mathbf{x}_{\mathrm{R},U} = \begin{bmatrix} c_1 & c_2 & c_3 \end{bmatrix} \cdot \mathbf{T} \cdot \left(\hat{\mathbf{x}}_U - \mathbf{x}_U^* \right), \\ &\text{with } \Delta\mathbf{x}_{\mathrm{R},U} = \mathbf{T} \cdot \left(\hat{\mathbf{x}}_U - \mathbf{x}_U^* \right). \end{aligned} \tag{27}$$

During the sliding mode $S(\Delta\mathbf{x}_\mathrm{R}) = 0$ as well as $\dot{S}(\Delta\mathbf{x}_\mathrm{R}) = 0$ applies. This behavior is obtained by the equivalent input (DeCarlo et al., 1988)

$$\begin{aligned} u_\mathrm{eq} &= -\left(\mathbf{c}^T \cdot \mathbf{b}_{\mathrm{R},U} \right)^{-1} \cdot \mathbf{c}^T \cdot \mathbf{A}_{\mathrm{R},U} \cdot \Delta\mathbf{x}_{\mathrm{R},U}, \\ &\text{with } \mathbf{A}_{\mathrm{R},U} = \mathbf{T} \cdot \mathbf{A}_U \cdot \mathbf{T}^{-1} \text{ and } \mathbf{b}_{\mathrm{R},U} = \mathbf{T} \cdot \mathbf{b}_U. \end{aligned} \tag{28}$$

With this input the dynamics during the sliding mode only depend on the coefficients c_i, with $i = 1, 2, 3$, of the switching function in Equation (27):

$$\begin{aligned} \Delta\dot{\mathbf{x}}_{\mathrm{R},U} &= \mathbf{A}_{\mathrm{R},U} \cdot \Delta\mathbf{x}_{\mathrm{R},U} + \mathbf{b}_{\mathrm{R},U} \cdot u_\mathrm{eq} \\ &= \left[\mathbf{I} - \mathbf{b} \cdot \left[\mathbf{c}^T \cdot \mathbf{b} \right]^{-1} \cdot \mathbf{c}^T \right] \cdot \mathbf{A}_{\mathrm{R},U} \cdot \Delta\mathbf{x}_{\mathrm{R},U} \\ &= \begin{bmatrix} 0 & 0 & 0 \\ 0 & 0 & 1 \\ 0 & -\frac{c_1}{c_3} & -\frac{c_2}{c_3} \end{bmatrix} \cdot \Delta\mathbf{x}_\mathrm{R} = \begin{bmatrix} 0 & \mathbf{0}^T \\ \mathbf{0} & \tilde{\mathbf{A}}_1 \end{bmatrix} \cdot \Delta\mathbf{x}_{\mathrm{R},U}. \end{aligned} \tag{29}$$

An other characteristic property of the SMC approach is that during the sliding mode the system order n is reduced by the number of inputs p (here $p = 1$). Thus, the dynamics during the sliding mode can be defined by a pole placement under consideration of $\tilde{\mathbf{A}}_1$. For a second order element with damping coefficient D and cut-off frequency ω_g this results in:

$$\begin{aligned} \det\left(s \cdot \mathbf{I} - \tilde{\mathbf{A}}_{1,U} \right) &= s^2 + \frac{c_2}{c_3} \cdot s + \frac{c_1}{c_3} \overset{!}{=} s^2 + 2 \cdot D \cdot \omega_\mathrm{g} \cdot s + \omega_\mathrm{g}^2 \\ &\text{with } c_3 = 1, \Rightarrow\ c_1 = \omega_\mathrm{g}^2,\ c_2 = 2 \cdot D \cdot \omega_\mathrm{g}. \end{aligned} \tag{30}$$

4.2. Reachability

To reach this sliding mode a proper controller function $u\left(\Delta\mathbf{x}_{\mathrm{R},U}\right)$ has to be determined and parametrized under consideration of the properties of the feeding power electronics. One approach to prove the reachability is based on an investigation of the Laypunov function $V\left(\Delta\mathbf{x}_{\mathrm{R},U}\right) = 1/2 \cdot S^2\left(\Delta\mathbf{x}_{\mathrm{R},U}\right)$. To ensure stable steady-state behavior the time derivate of the Lyapunov function has to be negative:

$$\dot{V}\left(\Delta\mathbf{x}_{\mathrm{R},U}\right) = S\left(\Delta\mathbf{x}_{\mathrm{R},U}\right) \cdot \dot{S}\left(\Delta\mathbf{x}_{\mathrm{R},U}\right) \overset{!}{<} 0. \tag{31}$$

The derivative of the switching function is given by:

$$\begin{aligned} \dot{S}\left(\Delta\mathbf{x}_{\mathrm{R},U}\right) &= \mathbf{c}^T \cdot \mathbf{T} \cdot \left(\mathbf{A}_U \cdot \Delta\mathbf{x}_U + \mathbf{b}_U \cdot u\left(\Delta\mathbf{x}_{\mathrm{R},U}\right) \right) \\ &= \zeta_1 \cdot \Delta\dot{\varepsilon}_z + \zeta_2 \cdot \Delta\varepsilon_{E1} + \zeta_3 \cdot \Delta U_\mathrm{c,diel} + u\left(\Delta\mathbf{x}_{\mathrm{R},U}\right), \text{ with} \end{aligned} \tag{32}$$

$$\begin{aligned} \zeta_1 = \frac{V}{2 \cdot \gamma_1} \Bigg(& \omega_\mathrm{g}^2 - 2 \cdot D \cdot \omega_\mathrm{g} \cdot \left(\gamma_1 \cdot \eta_\mathrm{E} + \frac{E_1}{\eta_1} \right) \\ & + \gamma_1^2 \cdot \eta_\mathrm{E}^2 + \gamma_1 \cdot E_1 \cdot \left(\frac{\eta_\mathrm{E}}{\eta_1} - 1 \right) + \frac{E_1^2}{\eta_1^2} \Bigg), \end{aligned} \tag{33a}$$

$$\begin{aligned} \zeta_2 = \frac{V \cdot E_1}{2 \cdot \gamma_1 \cdot \eta_1} \cdot \Bigg(& \omega_\mathrm{g}^2 + 2 \cdot D \cdot \omega_\mathrm{g} \cdot \left(\gamma_1 \cdot \eta_1 - \frac{E_1}{\eta_1} \right) \\ & - 2 \cdot \gamma_1 \cdot E_1 - \gamma_1^2 \cdot \eta_\mathrm{E} \cdot \eta_1 + \frac{E_1^2}{\eta_1^2} \Bigg) \text{ and} \end{aligned} \tag{33b}$$

$$\zeta_3 = 2 \cdot D \cdot \omega_\mathrm{g} - \frac{2}{\tau_\mathrm{p}} - \frac{E_1}{\eta_1} - \gamma_1 \cdot \eta_\mathrm{E}, \text{ for } \hat{\mathbf{x}}_U = \mathbf{0}. \tag{33c}$$

The coefficients ζ_1, ζ_2 and ζ_3 depend on material parameters as well as the damping ratio D and cut-off frequency ω_g. These two controller parameters are chosen in such a way that the influence of the state variables $\Delta\dot{\varepsilon}_z$ and $\Delta\varepsilon_{E_1}$ on Equation (32) vanishes. By solving $\zeta_1 = 0$ and $\zeta_2 = 0$ the following parameters result:

$$\omega_{\mathrm{g},0} = \sqrt{\gamma_1 \cdot E_1 \cdot \frac{\eta_1 + \eta_\mathrm{E}}{\eta_1}} \text{ and} \tag{34a}$$

$$D_0 = \frac{1}{2} \cdot \sqrt{\frac{\left(E_1 + \gamma_1 \cdot \eta_1 \cdot \eta_\mathrm{E} \right)^2}{\gamma_1 \cdot E_1 \cdot \eta_1 \cdot (\eta_1 + \eta_\mathrm{E})}}. \tag{34b}$$

According to Equation (5) the input power $\bar{p}$ supplied by the bidirectional flyback converter can be described by a three-point controller. However, for the design of the SMC the off-state with $\bar{p} = 0$ can be neglected in a first step. Under consideration $\bar{p} = \pm\bar{p}_\mathrm{max}$ a two-point controller is defined:

$$u\left(\Delta\mathbf{x}_{\mathrm{R},U}\right) = \mathrm{sgn}\left(S\left(\Delta\mathbf{x}_{\mathrm{R},U}\right) \right) \cdot \varrho. \tag{35}$$

The parameter $\varrho = \pm\bar{p}_\mathrm{max}$ will be chosen so that the reachability is ensured.

By inserting Equations (34), (34b), and (35) into Equation (32) the time derivative of the switching function simplifies to:

$$\begin{aligned} \dot{S}\left(\Delta\mathbf{x}_{\mathrm{R},U}\right) &= -\frac{2}{\tau_\mathrm{p}} \cdot \Delta U_\mathrm{c,diel} + u\left(\Delta\mathbf{x}_{\mathrm{R},U}\right) \\ &= \frac{2}{\tau_\mathrm{p}} \cdot U_\mathrm{c,diel}^* + \mathrm{sgn}\left(S\left(\Delta\mathbf{x}_{\mathrm{R},\varepsilon}\right) \right) \cdot \varrho. \end{aligned} \tag{36}$$

The control parameter ϱ is determined by applying a case-by-case analysis to satisfy Equation (31):

$$\begin{aligned} \text{I.: } S\left(\Delta\mathbf{x}_{\mathrm{R},U}\right) > 0,\ &\Rightarrow\ u\left(\Delta\mathbf{x}_{\mathrm{R},U}\right) = +\varrho, \\ &\Rightarrow\ \dot{S}\left(\Delta\mathbf{x}_{\mathrm{R},U}\right) = \frac{2}{\tau_\mathrm{p}} \cdot U_\mathrm{c,diel}^* + \varrho \overset{!}{<} 0, \\ \text{II.: } S\left(\Delta\mathbf{x}_{\mathrm{R},U}\right) < 0,\ &\Rightarrow\ u\left(\Delta\mathbf{x}_{\mathrm{R},U}\right) = -\varrho, \\ &\Rightarrow\ \dot{S}\left(\Delta\mathbf{x}_{\mathrm{R},U}\right) = \frac{2}{\tau_\mathrm{p}} \cdot U_\mathrm{c,diel}^* - \varrho \overset{!}{>} 0. \end{aligned} \tag{37}$$

As the energy $U^*_{\mathrm{c,diel}}$ will always be equal to or larger than zero, both inequalities are solved by choosing:

$$\varrho = -\bar{p}'_{\max} \quad \Rightarrow \quad \bar{p}'_{\max} > \frac{2}{\tau_{\mathrm{p}}} \cdot U^*_{\mathrm{c,diel}}. \tag{38}$$

Especially during steady state the introduced two-point controller will permanently switch between the positive and negative input power $\pm\bar{p}_{\max}$. To avoid this chattering, the controller is extended to a three-point controller with hysteresis, as already shown in **Figure 4**:

$$\bar{p}^* = \begin{cases} +\bar{p}_{\max}, & \text{for } S\left(\Delta\mathbf{x}_{\mathrm{R},U}\right) \leq -\delta_S \text{ or } -\delta_S < S\left(\Delta\mathbf{x}_{\mathrm{R},U}\right) < 0 \wedge \dot{S}\left(\Delta\mathbf{x}_{\mathrm{R},U}\right) > 0 \\ 0, & \text{else} \\ -\bar{p}_{\max} & \text{for } S\left(\Delta\mathbf{x}_{\mathrm{R},U}\right) \geq \delta_S \text{ or } 0 < S\left(\Delta\mathbf{x}_{\mathrm{R},U}\right) < \delta_S \wedge \dot{S}\left(\Delta\mathbf{x}_{\mathrm{R},U}\right) < 0 \end{cases}. \tag{39}$$

On the one hand, the off-state of the flyback converter is now taken into account, while on the other hand the hysteresis with threshold δ_S will significantly reduce the switching frequency in closed-loop operation. In **Figure 4** an output limitation is also depicted that switches off the control, when the energy $\hat{U}_{\mathrm{c,diel}}$ exceeds a maximum value $U_{\mathrm{c,diel,max}}$. Furthermore, to improve the steady state behavior the inner control of the flyback converter is adapted. Depending on the absolute value of the switching function $|S(\Delta\mathbf{x}_{\mathrm{R},U})|$, the maximum magnetizing current $I^*_{m,\max}$ and thus the feeding power $\bar{p}$ according to Equation (5) is varied. This ensures, that for large control deviations corresponding to large values of $|S(\Delta\mathbf{x}_{\mathrm{R},U})|$ the maximum feeding power is supplied for achieving the maximum dynamics. In contrast, for small control deviations the power is reduced for a higher accuracy by also adapting the hysteresis threshold δ_S. Further details can be found in Hoffstadt and Maas (2017, 2018b).

5. EXPERIMENTAL VALIDATION

5.1. Test Setup for the Experimental Validation

Figure 5 schematically depicts the test setup used for the experimental validation of the self-sensing estimator and the self-sensing control. It consists of a bidirectional flyback converter that supplies the DE transducer with voltages up to 2.5 kV (Hoffstadt and Maas, 2016). The voltage $v_{\mathrm{DE,m}}$ is measured with the voltage probe TT-SI 9010 from Testec, while the current $i_{\mathrm{DE,m}}$ is determined by the voltage drop across the shunt resistance R_{is} =1 kΩ. Details about the utilized DE transducers can be found in Maas et al. (2015). If no-load scenarios are investigated in the following, the displacement of the DE transducer is directly

TABLE 1 | Parameters of the utilized silicone based DE stack-transducer and the self-sensing controller.

Y	η_{E}	E_1	η_1	V	m_{B}	$N \cdot d_0 = z_0$	τ_{p}
1.08 MPa	490 Pa·s	155 kPa	1.7 kPa·s	1.4 cm^3	0.5 g	9.6 mm	24 s
$C_{\mathrm{p,0}}$	R_s	R_{vv}	ω_{g}	D	$I_{\min}$	$I_{\max}$	δ_S
6 nF	135 kΩ	4 V^2	2.430 rad/s	3	4 A	8 A	$4 \cdot \Delta U_{\max}$

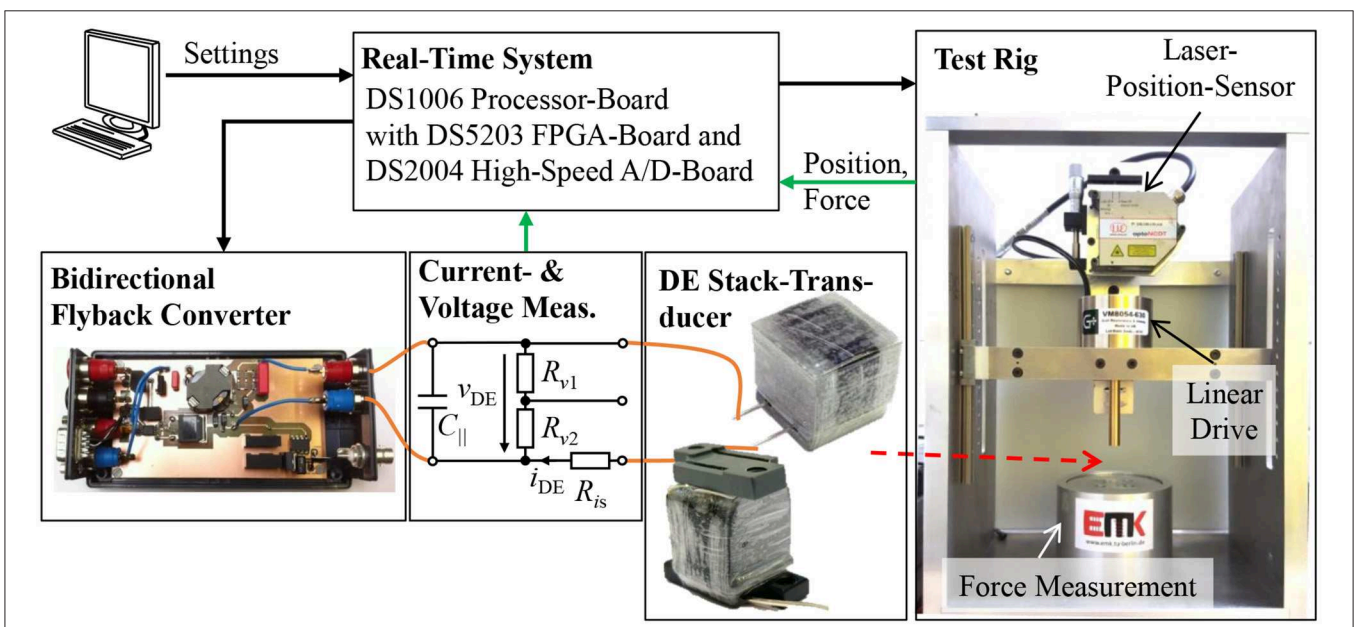

FIGURE 5 | Test setup for the experimental validation comprising a bidirectional flyback converter, a voltage and current measurement, a DE stack-transducer and a test rig with linear drive, while the data logging and the different controls are implemented on the real-time system.

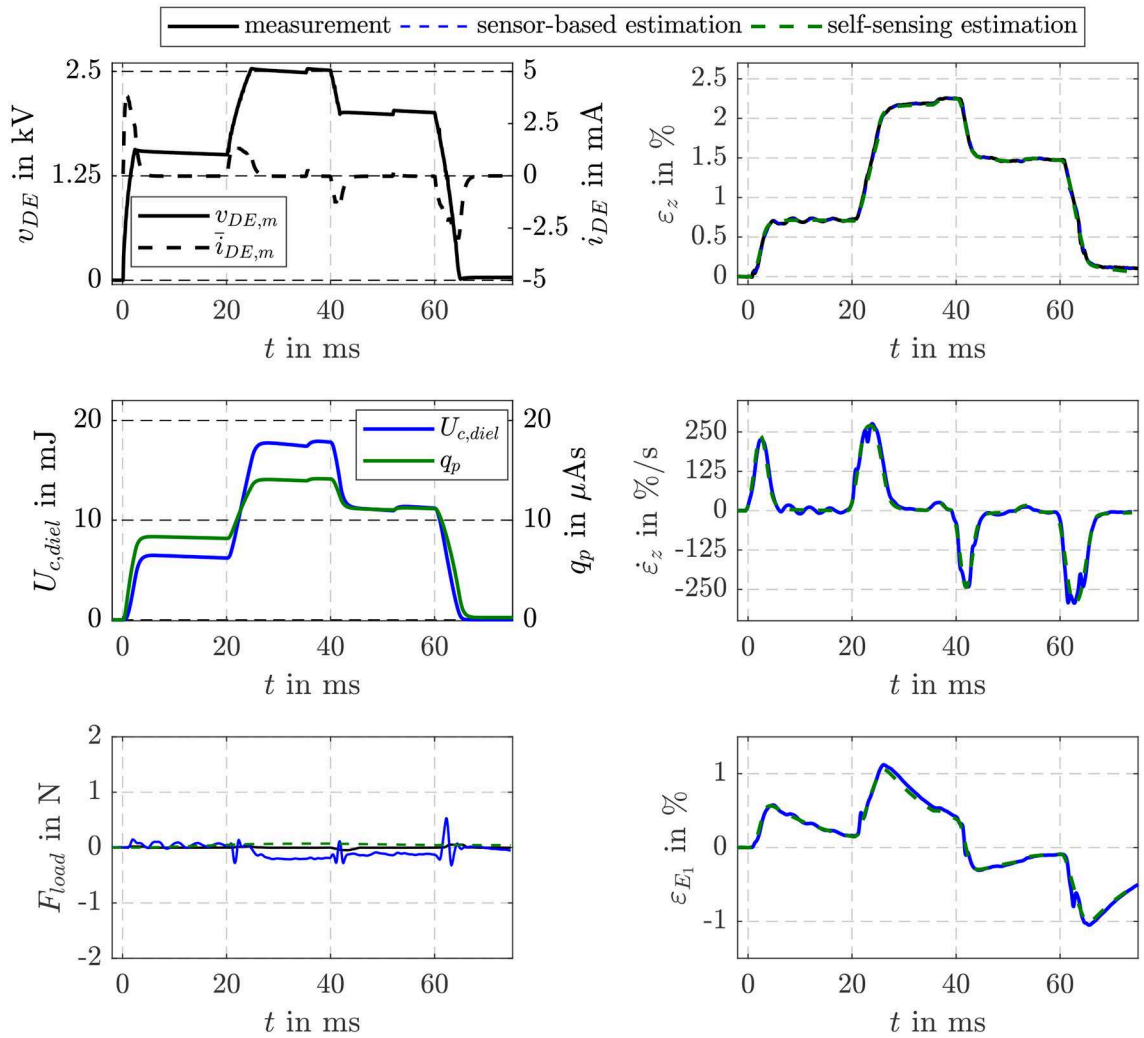

FIGURE 6 | Comparison of the EKF-based estimation results of the proposed self-sensing filter with a sensor-based filter for the no-load scenario.

measured with the laser sensor OptoNCDT ILD 2300 from Micro-Epsilon. To apply loads to the DE transducer the test rig on the right hand side of **Figure 5** will be used. It consists of a force measurement with the force sensor 9217A from Kistler and a voice coil linear drive VM8054-630 from Geeplus. The DE transducer can be attached between the force measurement and the linear drive. Via the voice coil load profiles with high dynamics can be applied to the DE transducer, while the resulting actuator force $F_{\mathrm{act,m}}$ is measured. Here, the same laser sensor as for the no-load scenarios measures the displacement of the rigidly coupled voice coil and DE transducer.

The proposed self-sensing algorithm and the energy control are implemented on the DSP of a real-time system from dSPACE operating with a sample rate of $f_{\mathrm{DSP}} = 20$ kHz. The system contains also a fast FPGA board. On this board the control of the flyback converter and the signal conditioning for the measured voltage and current $v_{\mathrm{DE,m}}$ and $i_{\mathrm{DE,m}}$ are performed.

5.2. Validation of the EKF-Based Self-Sensing Algorithm

Before the closed-loop self-sensing operation is investigated, the estimation results obtained with the suggested self-sensing approach are compared to results estimated with the sensor-based observer introduced in Hoffstadt and Maas (2017, 2018b). The parameters of the silicone based DE stack-transducer with $N = 192$ layers are listed in **Table 1**. This table also includes parameters for the controller used in the following section.

Figure 6 compares the estimation results of the proposed self-sensing approach with the sensor-based estimator. The voltage controlled bidirectional flyback converter supplies the DE stack-transducer stepwise with voltages of v_{DE} =1.5, 2.5, and 2 kV, respectively. The charge q_{p} determined by filtering the measured current $i_{\mathrm{DE,m}}$ according to Equation (10) is used as input for the self-sensing filter, while the sensor-based estimator uses the energy $U_{\mathrm{c,diel}}$ as input.

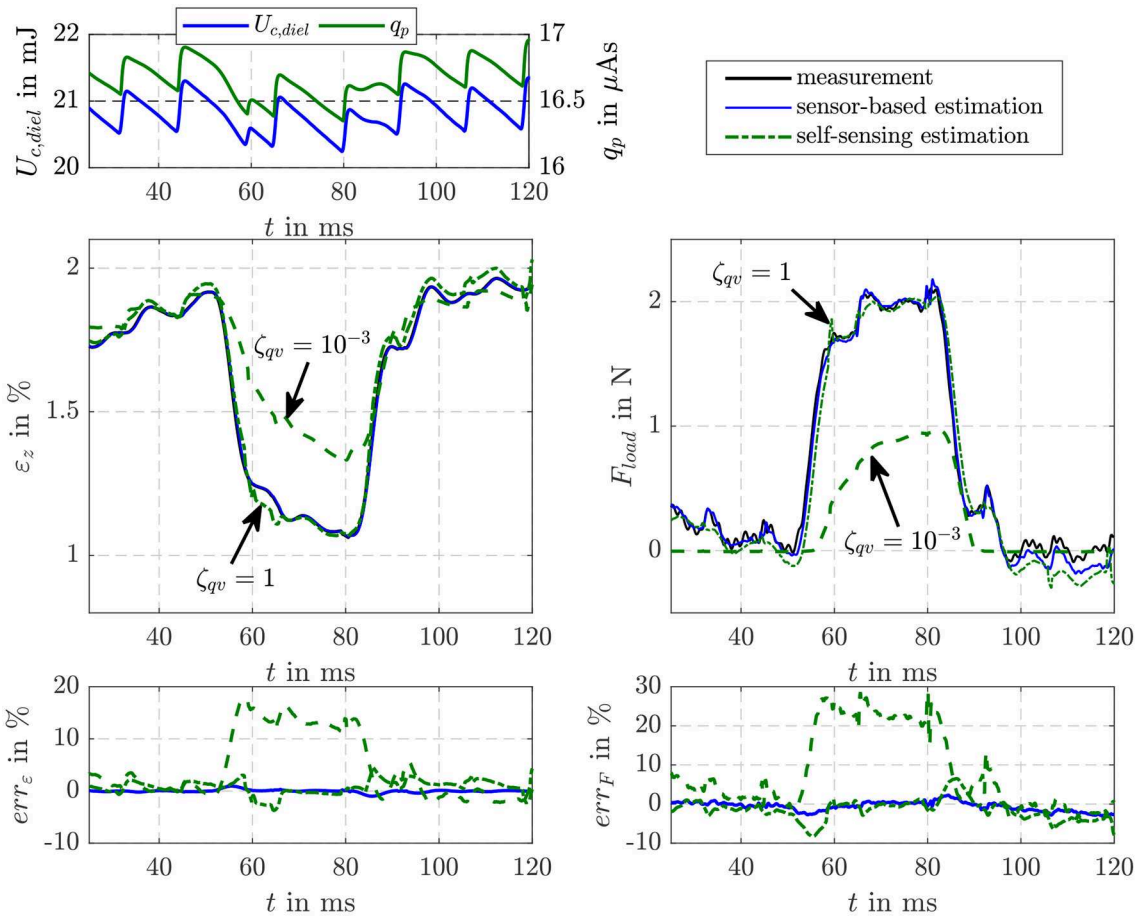

FIGURE 7 | Comparison of the EKF-based estimation results of the proposed self-sensing filter with a sensor-based filter when a load force is applied to the DE transducer.

The measurement noise $R_{vv} = 4\ \mathrm{V}^2$ required for the implementation of the EKF can be determined experimentally. For this, the output function g_{qv} in Equation (13) and the properties of the voltage probe and current measurement via the shunt have to be taken into account. One of the main issues when designing an EKF is to find an appropriate choice of $\mathbf{Q}_{ww}$. Here, the numerical optimization approach presented by Powell (2002) is used to minimize the error between simulated and estimated state variables by varying the entries of the symmetric matrix $\mathbf{Q}_{ww}$. For the system introduced in section 3 this optimization yields:

$$\mathbf{Q}_{ww,qv} = \zeta_{qv} \cdot \begin{bmatrix} 4,8 \cdot 10^{-8} & -1,7 \cdot 10^{-9} & -2,2 \cdot 10^{-8} & -9,3 \cdot 10^{-4} \\ -1,7 \cdot 10^{-9} & 4,9 \cdot 10^{-5} & 1,5 \cdot 10^{-4} & 4,4 \cdot 10^{-1} \\ -2,2 \cdot 10^{-8} & 1,5 \cdot 10^{-4} & 1,6 \cdot 10^{-9} & -1,7 \cdot 10^{-5} \\ -9,3 \cdot 10^{-4} & 4,4 \cdot 10^{-1} & -1,7 \cdot 10^{-5} & 7,6 \cdot 10^{4} \end{bmatrix}. \tag{40}$$

The entries represent in a certain way the uncertainty of the model (13) to describe the dynamics of the state variables. While all entries of the matrix are comparable small, the one in the fourth row and column is very large. This is due to the unknown dynamics of the load tension that is considered with $\dot{\sigma}_{\mathrm{load}} = 0$ in Equation (13). As the dynamics of the state estimation can be adjusted by the absolute values of the entries in $\mathbf{Q}_{ww}$ the scaling factor ζ_{qv} is introduced. It gives the opportunity to adjust a compromise between sufficient dynamics, reliable state estimation and noise suppression.

In **Figure 6** the no-load scenario with $F_{\mathrm{load}} = A \cdot \sigma_{\mathrm{load}} = 0$ is considered. As can be seen in the comparison of the measured and estimated strains ε_z in the top right plot, almost no deviations between the approaches in terms of dynamics and accuracy occur. Due to parameter deviations the sensor-based filter estimates small load forces especially during transient operation. For the self-sensing filter with $\zeta_{qv} = 10^{-3}$ a comparable small factor is applied here. With this negligible deviations in the estimated load force occur without affecting the estimation results of the state variables shown on the right.

Figure 7 compares the estimation results obtained when a load force of $F_{\mathrm{load}} = 2$ N is stepwise applied to the DE stack-transducer with the force controlled voice coil actuator. When the tensile load is applied the strain of the DE transducer reduces

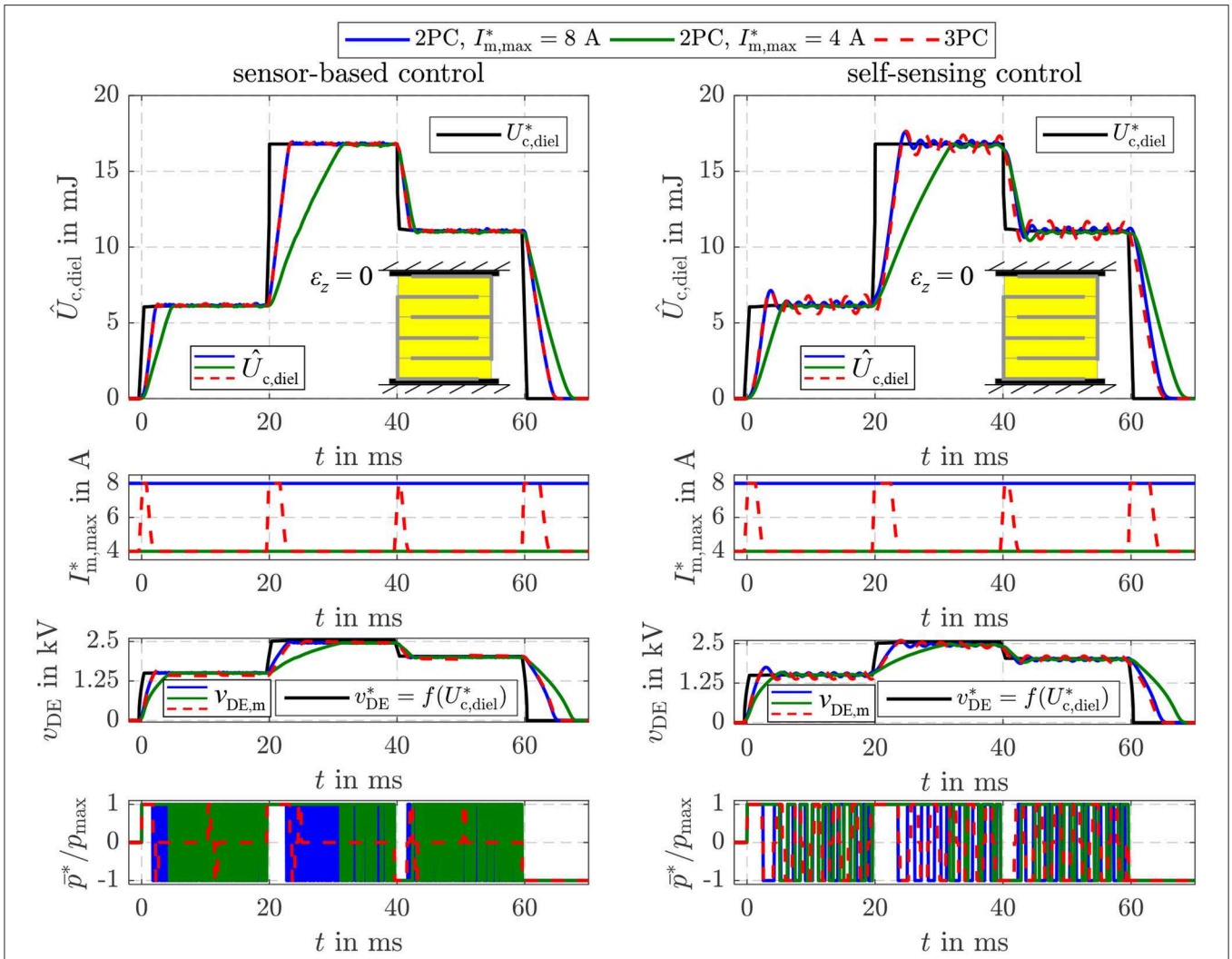

FIGURE 8 | Comparison of the sensor-based and self-sensing sliding mode energy control. In both cases two-point controllers (2PC) with $I^*_{\mathrm{m,max}} = 8$ A and $I^*_{\mathrm{m,max}} = 4$ A as well as the three-point controller (3PC) with hysteresis and adaption of the inner flyback converter control are considered.

from $\varepsilon_z \approx 1.9\%$ to $\varepsilon_z \approx 1.1\%$. In voltage controlled operation this causes a reduction of charge and energy as can be seen in the top left plot. The saw tooth profile in the charge q_{p} and energy $U_{\mathrm{c,diel}}$ is caused by the voltage control of the flyback converter that is based on a hysteresis controller. The sensor-based filter estimates the strain as well as the load force with errors less than $|err_\varepsilon| \leq 1\%$ and $|err_F| \leq 4\%$, respectively. For the self-sensing filter two parameterization with $\zeta_{qv} = 10^{-3}$ and $\zeta_{qv} = 1$ are investigated. While with $\zeta_{qv} = 10^{-3}$ the strain and force are estimated with errors below $|err_\varepsilon| \leq 1\%$ before the load is applied and after it is released, the dynamics of the estimation is not sufficient to consider the influence of the load correctly. In contrast, with $\zeta_{qv} = 1$ the influence of the load is accurately estimated. However, with this setting the noise suppression especially for charge states below $q_{\mathrm{p}} \leq 5\ \mu$As is not sufficient. Therefore, for the following investigations of the self-sensing control the scaling factor is switched from $\zeta_{qv} = 10^{-3}$ to $\zeta_{qv} = 1$ if the charge exceed $q_{\mathrm{p}} \leq 5\ \mu$As. This ensures an accurate estimation of the inner transducer states at low charge states as well as an accurate detection of a load force and its influence on the states.

5.3. Validation of the Self-Sensing Control

The parameters of the sliding mode energy controller designed in section 4 are listed in **Table 1**. The damping coefficient $D = 3$ and cut-off frequency $\omega_{\mathrm{g}} = 2.430$ rad/s were determined with Equation (34). The hysteresis threshold $\delta_S = 4 \cdot \Delta U_{\max}$ for the three-point controller in Equation (39) is set to a multiple of the energy increment $\Delta U_{\max}$ transfered during one switching period T_{S} of the flyback converter. **Figure 8** compares the closed-loop operation of the sensor-based controller published in Hoffstadt and Maas (2018b) and the proposed self-sensing controller. First of all, no feed-forward control approaches as suggested in Equations (20)–(22) are considered. Instead, three setpoint steps for the energy $U^*_{\mathrm{c,diel}}$ are applied that correspond to voltages of

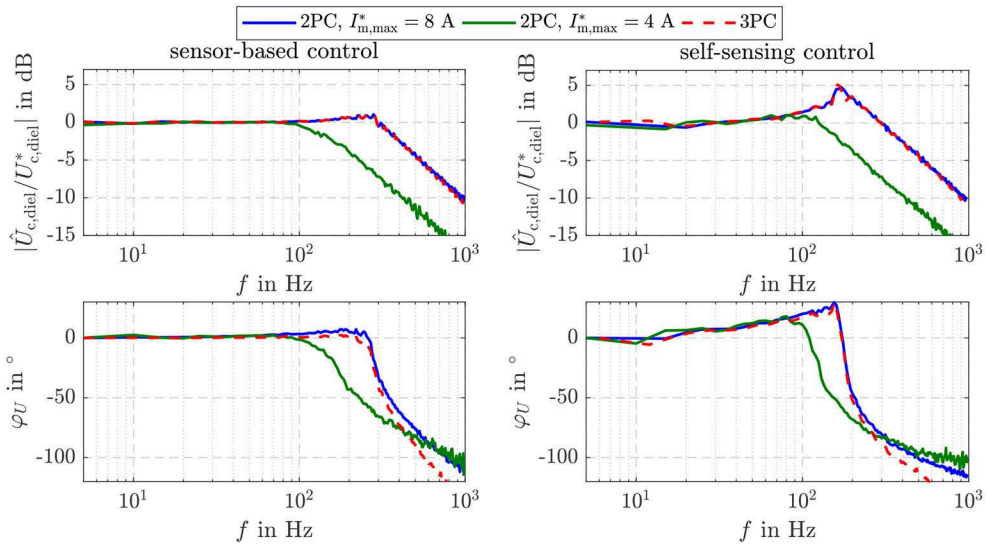

FIGURE 9 | Bandwidth of the sensor-based and self-sensing sliding mode energy control for the three investigated controller settings.

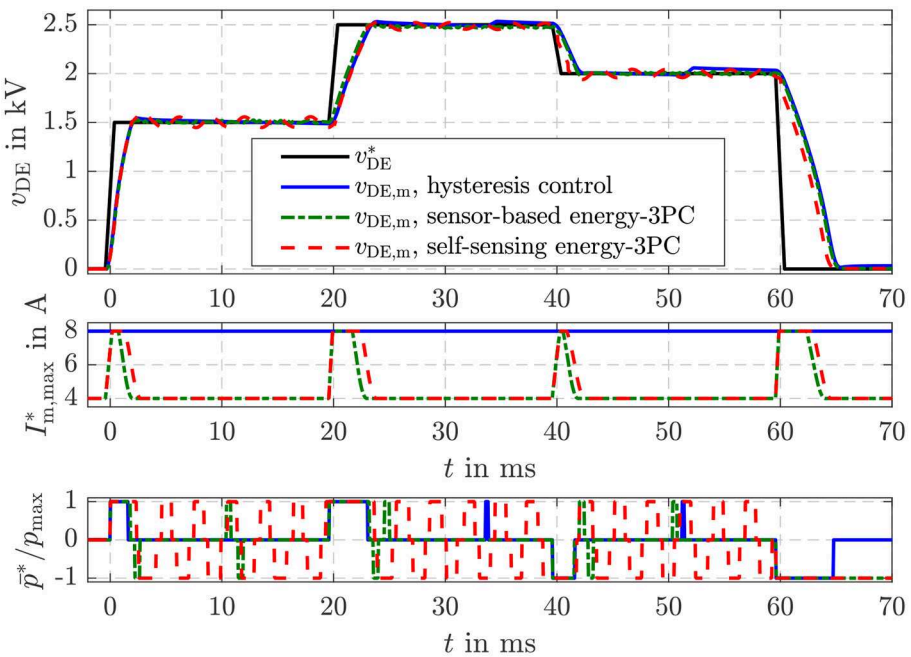

FIGURE 10 | Comparison of a simple hysteresis voltage control with the sensor-based and self sensing energy three-point controller using a voltage feed-forward control.

v_{DE} = 1.5 kV, 2.5 kV and 2 kV for the silicone based DE-stack-transducer, respectively. For both, the sensor-based and the self-sensing control two-point controllers (2PC) according to Equation (35) with $I^*_{m,max}$ = 8 A and $I^*_{m,max}$ = 4 A are investigated as well as the three-point controller (3PC) with hysteresis and adaption of the inner flyback converter control from Equation (39) and **Figure 4**. The DE stack-transducer is attached between the force measurement and the blocked voice coil so that it cannot deform ($\varepsilon_z = 0$) to avoid disturbances.

Via the setpoint $I^*_{m,max}$ for the current control of the flyback converter its feeding power is adjusted according to Equation (5). Due to the reduced power it takes a longer time to adjust the setpoint energies with the two-point controller with $I^*_{m,max} = 4$ A compared to the one with $I^*_{m,max} = 8$ A. In contrast, the reduced feeding power results in a higher accuracy during steady state. The standard deviation for the time interval between 50 and 60 ms increases from 0.03 mJ (2PC, $I^*_{m,max}$ = 4 A) to 0.05 mJ (2PC, $I^*_{m,max} = 8$ A) for the sensor-based control and from 0.1 to

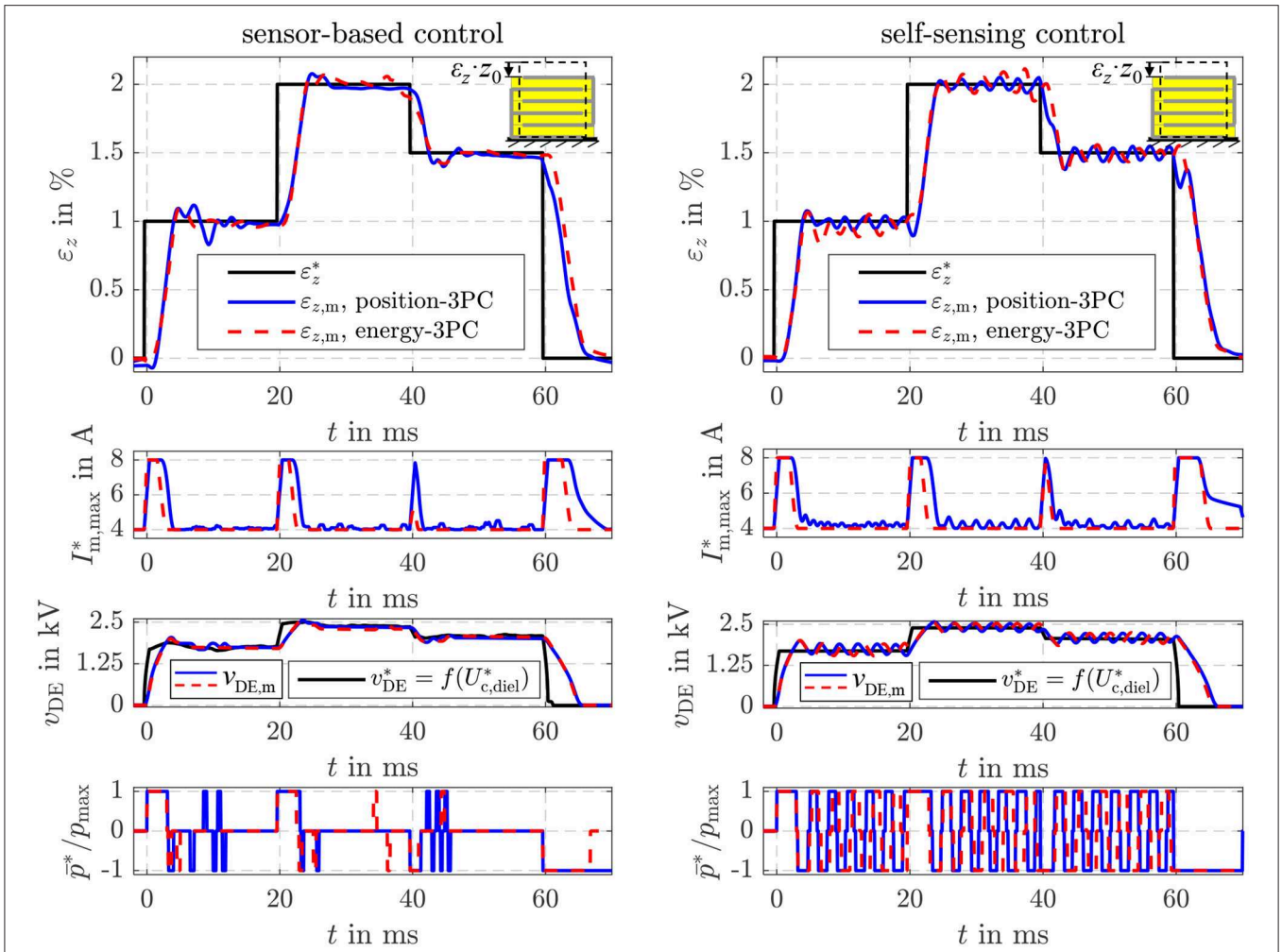

FIGURE 11 | Comparison of the sensor-based and self-sensing energy control with position feed-forward control and an explicit sliding mode position control.

0.3 mJ for the self-sensing control, respectively. The adaptive three-point controller with hysteresis combines the advantageous of the two mentioned two-point controllers by automatically choosing the maximum current $I^*_{\mathrm{m,max}} = 8$ A right after setpoint steps and reducing this current to $I^*_{\mathrm{m,max}} = 4$ A at steady state. This fundamental behavior applies for both the sensor-based and self-sensing control. Although the dynamics of both approaches are comparable, a small oscillation around the setpoint can be observed in case of the self-sensing control that results in the higher standard deviation.

Furthermore, it can be seen that the two-point controllers permanently switch between the maximum charging and discharging power $\bar{p} = \pm\bar{p}_{\max}$ during steady state. By extending the controller to a three-point controller with hysteresis, the switching frequency can be significantly reduced by more than 80% in case of the sensor-based control and 30% in case of the self-sensing control.

Figure 9 depicts the comparison of the bandwidth of the introduced controller settings. For this purpose, the small signal behavior is considered. A harmonic setpoint $U^*_{\mathrm{c,diel}}$ with increasing frequency, an offset of $\bar{U}_{\mathrm{c,diel}} = 12$ mJ and an amplitude of $U_{\mathrm{c,diel,amp}} = 2$ mJ is applied. The sensor-based two-point controller with $I^*_{\mathrm{m,max}} = 8$ A and the three-point controller have a high -3 dB cut-off frequency of about 400 Hz. This is also obtained with the self-sensing control. However, disruptive amplitude peaks of about 5 dB result in the already observed oscillation. By reducing the feeding power $\bar{p}$ with $I^*_{\mathrm{m,max}} = 4$ A, the cut-off frequency is reduced to 200 Hz, while the amplitude peaks are suppressed.

5.4. Energy Control With Voltage Feed-Forward Control

By applying Equation (22) for the feed-forward control depicted in **Figure 4** the voltage v_{p} across the capacitance C_{p} can be controlled. In **Figure 10** the results of the sensor-based and self-sensing energy three-point controller are compared to the behavior obtained with the hysteresis voltage control for the bidirectional flyback converter suggested in Hoffstadt and Maas (2016).

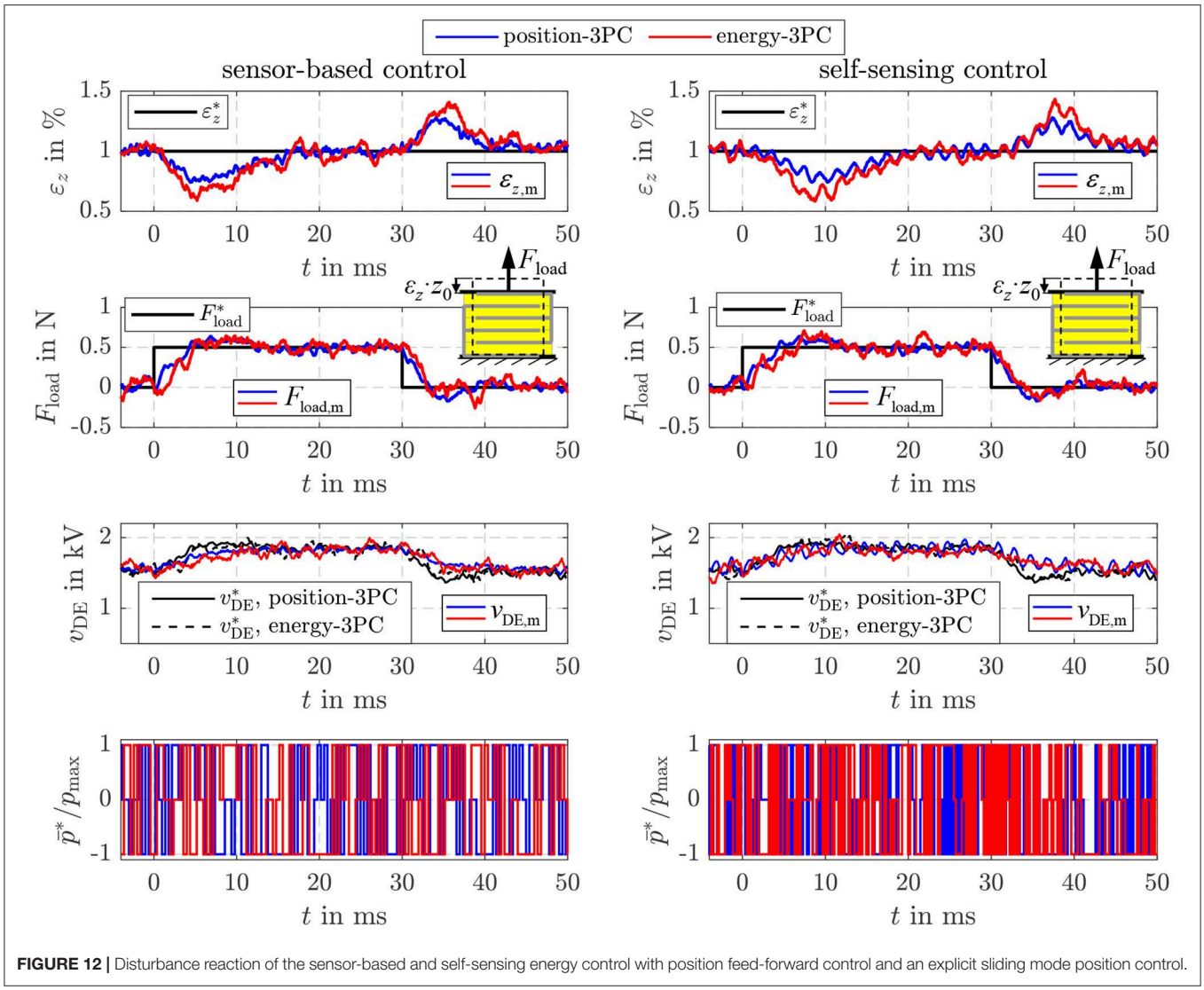

FIGURE 12 | Disturbance reaction of the sensor-based and self-sensing energy control with position feed-forward control and an explicit sliding mode position control.

For the hysteresis voltage control a threshold of $\Delta v_{\mathrm{DE}} = 30$ V was chosen. If the control deviation $|v_{\mathrm{DE}}^* - v_{\mathrm{DE,m}}|$ exceeds this threshold the control activates the flyback converter to charge or discharge the DE transducer. Afterwards the converter is turned into idle state again. The three-point controller suggested here behaves more or less the same. The only difference is that with the controller settings from **Table 1** a threshold of $v_{\mathrm{p}} \approx 16$ V results. This smaller threshold increases on the one hand the steady state accuracy. However, the switching frequency is on the other hand a bit higher compared to the simple hysteresis voltage control. Concerning the sensor-based and self-sensing energy control a comparable behavior as shown and explained in **Figure 8** can be observed here, too.

5.5. Energy Control With Position Feed-Forward Control

If the setpoint energy $U_{\mathrm{c,diel}}^*$ of the control structure in **Figure 4** is determined with Equation (20) the proposed energy control can be used to adjust a certain strain ε_z^*, although the strain is not part of the state vector $\mathbf{x}_U$. To compensate the influence of a disturbance, the estimated load $\hat{\sigma}_{\mathrm{load}}$ is considered in Equation (20). In contrast, an explicit position control based on the model (6) was derived in Hoffstadt and Maas (2017). **Figure 11** shows the comparison of the explicit (Position-3PC) and energy-based position control (Energy-3PC) for the no-load case of the DE stack-transducer. Both approaches are realized as sensor-based and self-sensing control with the adaptive three-point controller from Equation (39).

The explicit and energy-based position control show comparable dynamics and accuracy for both the sensor-based and the self-sensing control. The different setpoints are adjusted within a few milliseconds. By increasing the strain setpoint ε_z^* the energy $U_{\mathrm{c,diel}}^*$ also increases according to Equation (20). Instead of the energy, the voltage v_{DE} is depicted in **Figure 11** as it is measured directly and can be interpreted more intuitively. With Equation (22) a relationship between the voltage $v_{\mathrm{p}} \approx v_{\mathrm{DE}}$ is given. As the no-load case is considered here, for a constant setpoint of the strain

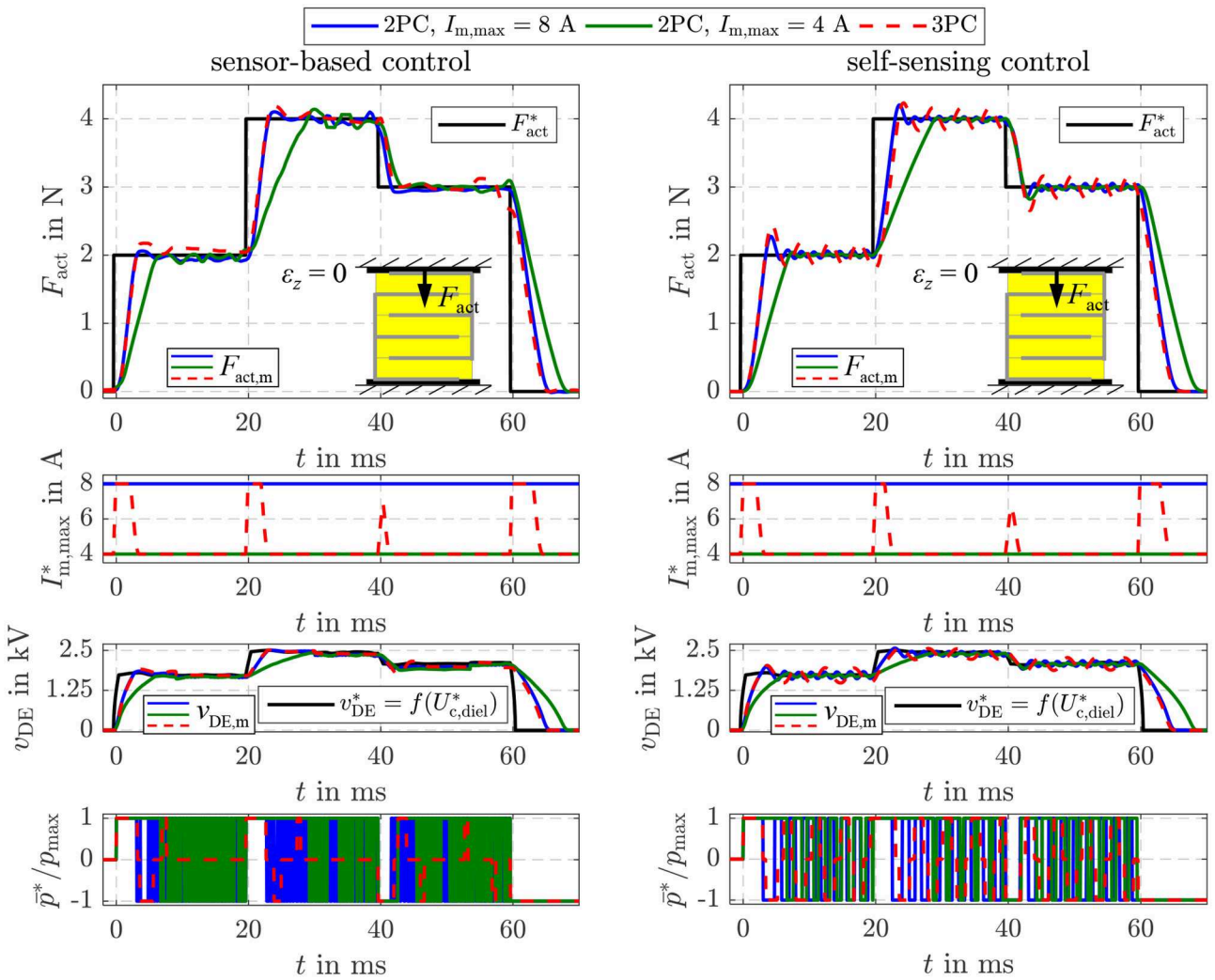

FIGURE 13 | Comparison of the sensor-based and self-sensing sliding mode energy control with force feed-forward control. In both cases two-point controllers (2PC) with $I^*_{\mathrm{m,max}} = 8$ A and $I^*_{\mathrm{m,max}} = 4$ A as well as the three-point controller (3PC) with hysteresis and adaption of the inner flyback converter control are considered.

ε^*_z a constant setpoint for the energy $U^*_{\mathrm{c,diel}}$ or the voltage results, respectively.

In addition, **Figure 12** depicts the disturbance reaction of the different position control approaches. For this purpose, a tensile load force of $F^*_{\mathrm{load}} = 0.5$ N is applied by the linear drive of the test rig in **Figure 5**, while the setpoint strain is constantly set to $\varepsilon^*_z = 1\%$. Right after the load is applied, the strain deviates from its setpoint due to the influence of the disturbance. However, the load is estimated with the sensor-based as well as the self-sensing EKF. According to Equation (20) the setpoint energy $U^*_{\mathrm{c,diel}}$, or voltage v^*_{DE}, respectively, is increased to compensate the influence of the disturbance $\hat{\sigma}_{\mathrm{load}}$. In **Figure 12** this behavior can be seen in the response of the corresponding voltage v_{DE} in the third subplot. This compensates the influence of the disturbance within approx. 15 ms. In case of the energy-based position control a slightly higher control deviation can be observed after the load steps. This is mainly due to the fact, that the energy control only reacts on control deviations of the energy $U_{\mathrm{c,diel}}$, while the explicit position control considers the control deviation of the strain ε_z directly.

5.6. Energy Control With Force Feed-Forward Control

Beside the two validated approaches, Equation (21) offers the opportunity to realize a force feed-forward control under consideration of the current elastic material tension $\sigma_{\mathrm{elast}}(\hat{\varepsilon}_z)$ based on the proposed energy control as already depicted in **Figure 4**. As for the previous two approaches, the controller settings are the same as listed in **Table 1**. However, in **Figure 13** also the two-point controller with $I_{\mathrm{m,max}} = 8$ A and $I_{\mathrm{m,max}} = 4$ A is considered again. The deformation of the DE stack-transducer is blocked in this case to investigate the control behavior caused by setpoint steps without any disturbance. In general, a comparable behavior to the pure energy control in **Figure 8** can

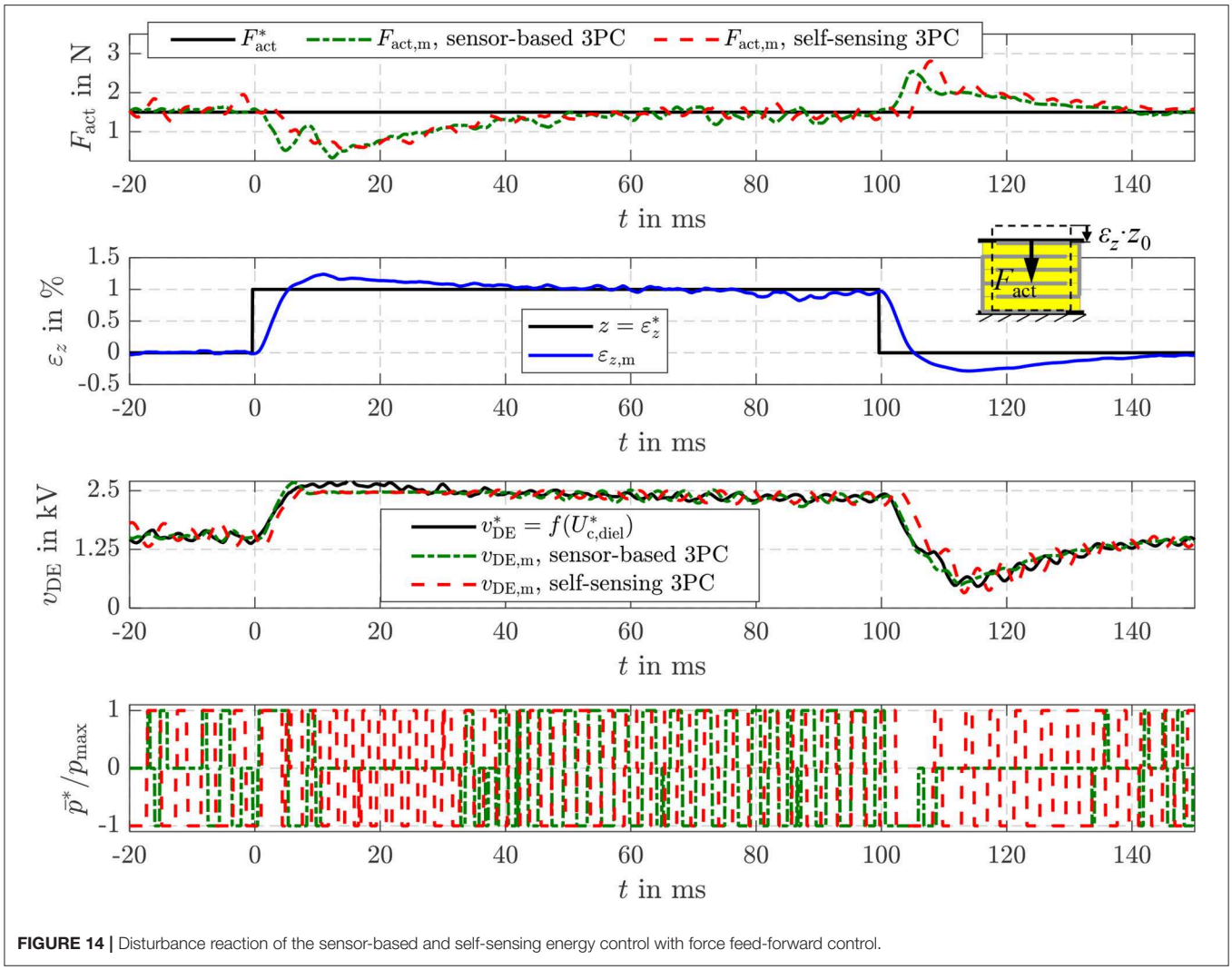

FIGURE 14 | Disturbance reaction of the sensor-based and self-sensing energy control with force feed-forward control.

be observed here, too. According to Equation (21) a constant energy setpoint $U^*_{c,diel}$ is obtained for a certain force F^*_{act} and $\varepsilon_z = 0$. In comparison to the two-point controllers the adaptive three-point controller from Equation (39) ensures the highest possible dynamics by the maximum current $I_{m,max} = 8$ A during transient operation as well as good steady state accuracy with significantly reduced switching frequency by reducing the current to $I_{m,max} = 4$ A. The self-sensing control adjusts the different setpoint forces with dynamics that are absolutely comparable to the sensor-based control.

In **Figure 14** also the disturbance reaction of the energy-based force control is shown. In this case a variable strain ε_z adjusted by the position-controlled linear drive acts as a disturbance. The stepwise change of the strain to $\varepsilon^*_z = 1\%$ causes a reduction of the force F_{act} in the first moment. However, by increasing the setpoint energy $U^*_{c,diel}$, or voltage v^*_{DE}, respectively, according to Equation (21) the influence is compensated comparable to the behavior observed for the disturbance reaction of the energy-based position control in **Figure 12**. The sensor-based control offers a marginal better control quality what is caused by the slightly higher dynamics of the sensor-based state and disturbance estimation.

The investigation of the pure energy control in **Figures 8**, **9** as well as of the different feed-forward controls in the **Figures 10**–**14** proved that both high dynamics and good steady state accuracy are obtained with the proposed self-sensing control approach. The developed self-sensing EKF estimates not only the inner states of the DE transducer but also an external load tension. In case of the position feed-forward control this allows to compensate the influence of a disturbance load. In contrast, if the force feed-forward control is applied the elastic material tension caused by a deformation of the DE transducer is reliably compensated. Furthermore, extensions to an adaptive three-point controller enabled a reduction of the switching frequency of up to 80% to increase the energy efficiency without reducing the bandwidth of about 400 Hz and the steady state accuracy.

6. CONCLUSION

DE transducer combine high energy densities and multi-functional operation modes. Multilayer topologies like the DE stack-actuator considered here have also high force densities with considerable absolute deformations so that they are well-suited to be used as active skins or as end effector in soft-robotic applications. But, beside the transducer design also appropriate control and sensing algorithms are required to enable the combined actuator-sensor-operation in closed loop operation without external sensors to measure mechanical states. The design of such a self-sensing state and disturbance estimator as a universal energy control that uses the information from a novel self-sensing estimator were addressed within this contribution.

For this purpose, in section 2 the control plant comprising a DE stack-transducer fed by a bidirectional flyback converter and its model to describe the electormechanically coupled behavior was summarized. To characterize the electrical behavior the model includes the energy $U_{\mathrm{c,diel}}$ as one state variable. Based on this model subsequently a self-sensing state and disturbance estimator was developed that estimates the mechanical state of the transducer as well as an external load force by just measuring the terminal voltage and current. Due to the non-linear system behavior an EKF was used for this purpose. It allows to estimate the transducer state without any superimposed voltage excitation as used for other self-sensing approaches. The validation results have shown that almost no confinements in terms of dynamics and accuracy compared to the sensor-based estimator are obtained. The sensor-based estimator requires a measurement of the terminal voltage and the displacement.

The developed energy control uses the information provided by the self-sensing EKF for closed loop operation. Due to the behavior of the bidirectional flyback converter, that either charges or discharges a DE transducer with almost constant power when enabled, the sliding mode control approach was applied. By controlling the energy in the capacitance of the DE transducer it is possible to control the voltage, force or displacement of the transducer by using different feed-forward control structures. The setpoint energy required to achieve a certain actuator force or displacement was obtained under consideration of the static force equilibrium included in the derived model. Within the validation it was shown that a precise control of the voltage, force and displacement with high dynamics and a bandwidth of up to 400 Hz is achieved with this approach. The step response as well as the disturbance reaction yield comparable dynamics and accuracy for both the sensor-based and self-sensing control.

Although here a DE stack-transducer was considered, the developed self-sensing EKF and control approach can also be applied to other topologies well-suited for soft robotic applications like DE-based minimum energy structures or membrane actuators. The utilized bidirectional flyback converter represents an efficient and competitive converter topology and can also be used to supply any kind of DE transducer. In case of soft-bodied robots equipped with DE transducers and the mentioned converter the suggested self-sensing control approach can be used to control the impedance of the robot by applying the proposed force and displacement feed-forward controls in combination with a human-machine-interface model. If under consideration of the utilized test setup a charge of at least $q_{\mathrm{p}} = 5\ \mu\mathrm{As}$ is applied, the proposed self-sensing filter can also detect collisions or interactions. This could be used e.g., in human machine interfaces or active skins, so that the control can react on these events. While for these applications the force and displacement control are most important, the voltage control could be used to avoid exceeding limitations that would cause a damage of the transducer.

DATA AVAILABILITY STATEMENT

The raw data supporting the conclusions of this manuscript will be made available upon request to JM (juergen.maas@tu-berlin.de).

AUTHOR CONTRIBUTIONS

The research results included in this contribution are the outcome of TH's Ph.d. thesis that was supervised by JM.

REFERENCES

Adamy, J. (2014). *Nichtlineare Systeme und Regelungen, 2nd Edn*. Berlin: Springer Vieweg.

Anderson, I. A., Gisby, T. A., McKay, T. G., O'Brien, B. M., and Calius, E. P. (2012). Multi-functional dielectric elastomer artificial muscles for soft and smart machines. *J. Appl. Phys.* 112:041101. doi: 10.1063/1.4740023

Chuc, N. H., Thuy, D. V., Park, J., Kim, D., Koo, J., Lee, Y., et al. (2008). A dielectric elastomer actuator with self-sensing capability. *Proc. SPIE* 6927:69270V. doi: 10.1117/12.777900

DeCarlo, R. A., Zak, S. H., and Matthews, G. P. (1988). Variable structure control of nonlinear multivariable systems: a tutorial. *Proc. IEEE* 76, 212–232. doi: 10.1109/5.4400

Dubois, P., Rosset, S., Niklaus, M., Dadras, M., and Shea, H. (2008). Voltage control of the resonance frequency of dielectric electroactive polymer (deap) membranes. *J. Microelectromech. Syst.* 17, 1072–1081. doi: 10.1109/JMEMS.2008.927741

Eitzen, L., Graf, C., and Maas, J. (2011a). "Bidirectional high voltage dc-dc converters for energy harvesting with dielectric elastomer generators," in *IEEE Energy Conversion Congress & Exposition (ECCE'11)* (Arizona).

Eitzen, L., Graf, C., and Maas, J. (2011b). "Cascaded bidirectional flyback converter driving deap transducers," in *37th Annual Conference of the IEEE Industrial Electronics Society IECON-2011*, (Melbourne), 1226–1231. doi: 10.1109/IECON.2011.6119484

Gisby, T. A., O'Brien, B. M., and Anderson, I. A. (2013). Self sensing feedback for dielectric elastomer actuators. *Appl. Phys. Lett.* 102:193703. doi: 10.1063/1.4805352

Gisby, T. A., O'Brien, B. M., Xie, S. Q., Calius, E. P., and Anderson, I. A. (2011). Closed loop control of dielectric elastomer actuators (SPIE). *SPIE Proc.* 7976. doi: 10.1117/12.880711

Hoffstadt, T., Griese, M., and Maas, J. (2014). Online identification algorithms for integrated dielectric electroactive polymer sensors and self-sensing concepts. *Smart Mater. Struct.* 23:1–13. doi: 10.1088/0964-1726/23/10/104007

Hoffstadt, T., and Maas, J. (2015). Analytical modeling and optimization of deap-based multilayer stack-transducers. *Smart Mater. Struct.* 24:1–14. doi: 10.1088/0964-1726/24/9/094001

Hoffstadt, T., and Maas, J. (2016). Sensorless bcm control for a bidirectional flyback-converter. *IEEE IECON 2016* 42, 3600–3605. doi: 10.1109/IECON.2016.7793842

Hoffstadt, T., and Maas, J. (2017). Adaptive sliding-mode position control for dielectric elastomer actuators. *IEEE/ASME Trans. Mechatr.* 22, 2241–2251. doi: 10.1109/TMECH.2017.2730589

Hoffstadt, T., and Maas, J. (2018a). Model-based self-sensing algorithm for dielectric elastomer transducers based on an extended Kalman filter. *Mechatronics* 50, 248–258. doi: 10.1016/j.mechatronics.2017.09.013

Hoffstadt, T., and Maas, J. (2018b). Sensorless force control for dielectric elastomer transducers. *J. Intell. Mater. Syst. Struct.* 30. doi: 10.1177/1045389X17754255

Hoffstadt, T., Meier, P., and Maas, J. (2016). "Modeling approach for the electrodynamics of multilayer de stack-transducers," in *ASME 2016 Conference on Smart Materials, Adaptive Structures and Intelligent Systems V001T02A015* (Florence).

Ifeachor, E. C., and Jervis, B. W. (2002). *Digital Signal Processing: A Practical Approach, 2nd Edn*. Harlow: Prentice Hall.

Isermann, R., and Munchhof, M. (2011). *Identification of Dynamical Systems: An Introduction With Applications*. Advanced textbooks in control and signal processing. Berlin; London: Springer.

Jung, K., Kim, K. J., and Choi, H. R. (2008). A self-sensing dielectric elastomer actuator. *Sens. Actuat. A* 143, 343–351. doi: 10.1016/j.sna.2007.10.076

Kaal, W., and Herold, S. (2011). Electroactive polymer actuators in dynamic applications. *IEEE/ASME Trans. Mechatr.* 16, 24–32. doi: 10.1109/TMECH.2010.2089529

Kalman, R. E. (1960). Contributions to the theory of optimal control. *Boletin de la Sociedad* 5, 102–119

Kuhring, S., Uhlenbusch, D., Hoffstadt, T., and Maas, J. (2015). Finite element analysis of multilayer deap stack-actuators. *Proc. SPIE* 9430:94301L. doi: 10.1117/12.2085121

Maas, J., Graf, C., and Eitzen, L. (2011). Control concepts for dielectric elastomer actuators. *Proc. SPIE* 7976:79761H. doi: 10.1117/12.879938

Maas, J., Tepel, D., and Hoffstadt, T. (2015). Actuator design and automated manufacturing process for deap-based multilayer stack-actuators. *Meccanica* 50, 2839–2854. doi: 10.1007/s11012-015-0273-2

Matysek, M., Haus, H., Moessinger, H., Brokken, D., Lotz, P., and Schlaak, H. F. (2011). Combined driving and sensing circuitry for dielectric elastomer actuators in mobile applications (SPIE). *SPIE Proc.* 7976:1–11. doi: 10.1117/12.879438

Navarro, S. E., Marufo, M., Ding, Y., Puls, S., Goger, D., Hein, B., et al. (2013). "Methods for safe human-robot-interaction using capacitive tactile proximity sensors," in *2013 IEEE/RSJ International Conference*, 1149–1154. doi: 10.1109/IROS.2013.6696495

Powell, T. D. (2002). Automated tuning of an extended kalman filter using the downhill simplex algorithm. *J. Guid. Cont. Dyn.* 25, 901–908. doi: 10.2514/2.4983

Rizzello, G., Naso, D., York, A., and Seelecke, S. (2015). Modeling, identification, and control of a dielectric electro-active polymer positioning system. *IEEE Trans. Control Syst. Technol.* 23, 632–643. doi: 10.1109/TCST.2014.2338356

Rizzello, G., Naso, D., York, A., and Seelecke, S. (2016). Closed loop control of dielectric elastomer actuators based on self-sensing displacement feedback. *Smart Mater. Struct.* 25:035034. doi: 10.1088/0964-1726/25/3/035034

Rizzello, G., Naso, D., York, A., and Seelecke, S. (2017). A self-sensing approach for dielectric elastomer actuators based on online estimation algorithms. *IEEE/ASME Trans. Mechatr.* 22, 728–738. doi: 10.1109/TMECH.2016.2638638

Robla-Gomez, S., Becerra, V. M., Llata, J. R., Gonzalez-Sarabia, E., Torre-Ferrero, C., and Perez-Oria, J. (2017). Working together: a review on safe human-robot collaboration in industrial environments. *IEEE Access* 5, 26754–26773. doi: 10.1109/ACCESS.2017.2773127

Rosset, S., O'Brien, B. M., Gisby, T., Xu, D., Shea, H. R., and Anderson, I. A. (2013). Self-sensing dielectric elastomer actuators in closed-loop operation. *Smart Mater. Struct.* 22:104018. doi: 10.1088/0964-1726/22/10/104018

Sarban, R. (2011). *Active vibration control using DEAP transducers*. (Dissertation). University of Southern Denmark, Sønderborg, Denmark.

Sarban, R., and Jones, R. W. (2012). Physical model-based active vibration control using a dielectric elastomer actuator. *J. Intell. Mater. Syst. Struct.* 23, 473–483. doi: 10.1177/1045389X11435430

Welch, G., and Bishop, G. (2001). *An Introduction to the Kalman Filter*. Chapel Hill: University of North Carolina.

Wilson, E. D., Assaf, T., Pearson, M. J., Rossiter, J. M., Anderson, S. R., Porrill, J., et al. (2016). Cerebellar-inspired algorithm for adaptive control of nonlinear dielectric elastomer-based artificial muscle. *J. R. Soc. Interface* 13:1–15. doi: 10.1098/rsif.2016.0547

Conflict of Interest: The authors declare that the research was conducted in the absence of any commercial or financial relationships that could be construed as a potential conflict of interest.

frontiers in Robotics and AI

ORIGINAL RESEARCH
published: 20 December 2019
doi: 10.3389/frobt.2019.00140

Ionic Actuators as Manipulators for Microscopy

Indrek Must, Pille Rinne, Friedrich Krull, Friedrich Kaasik, Urmas Johanson and Alvo Aabloo*

Intelligent Materials and Systems Lab, Institute of Technology, University of Tartu, Tartu, Estonia

Non-destructive handling of soft biological samples at the cellular level is becoming increasingly relevant in life sciences. In particular, spatially dense arrangements of soft manipulators with the capability of *in situ* monitoring via optical and electron microscopes promises new and exciting experimental techniques. The currently available manipulation technologies offer high positioning accuracy, yet these devices significantly grow in complexity in achieving compliance. We explore soft and compliant actuator material with a mechanical response similar to gel-like samples for perspective miniaturized manipulators. First, we demonstrate three techniques for rendering the bulk sheet-like electroactive material, the ionic and capacitive laminate (ICL), into a practical manipulator. We then show that these manipulators are also highly compatible with electron optics. Finally, we explore the performance of an ICL manipulator in handling a single large cell. Intrinsic compliance, miniature size, simple current-driven actuation, and negligible interference with the imaging technologies suggest a considerable perspective for the ICL in spatially dense arrays of compliant manipulators for microscopy.

Keywords: manipulators, ionic and capacitive laminates, ionic liquids, vacuum, compliant actuation, SEM

OPEN ACCESS

Edited by:
Stefan Seelecke,
Saarland University, Germany

Reviewed by:
Giuseppe Puglisi,
Politecnico di Bari, Italy
Okan Ozdemir,
Dokuz Eylül University, Turkey

****Correspondence:***
Indrek Must
indrekm@ut.ee

Specialty section:
This article was submitted to Soft Robotics, a section of the journal Frontiers in Robotics and AI

Received: *20 July 2019*
Accepted: *03 December 2019*
Published: *20 December 2019*

Citation:
Must I, Rinne P, Krull F, Kaasik F, Johanson U and Aabloo A (2019) Ionic Actuators as Manipulators for Microscopy. Front. Robot. AI 6:140. doi: 10.3389/frobt.2019.00140

INTRODUCTION

Precise biomedical applications often involve manipulation of soft and fragile objects: gel-like substances or delicate samples of biological origin. Biological systems on any scale (from viruses and cells to organs) create mechanical cues in response to mechanical forces being applied to them (Krieg et al., 2019), implying immense importance of scalable and compliant manipulation techniques for mechanobiology studies. Highly repeatable manipulators are commercially available at nanometer-scale positioning accuracy, rendering closed-loop systems that do not require human intervention for positioning, such as the atomic force microscope (AFM), the leading platform for mechanobiological research (Castillo et al., 2009; Alsteens et al., 2017). In addition to piezoelectric actuators, as in AFM instruments, thermoelectric and electrostatic actuators prevail among the miniaturized contact-based manipulators. Actuators linked to microelectromechanical systems (MEMS) enable cellular- and subcellular-level manipulation (Verotti et al., 2017).

Compliance is one of the essential characteristics of both hard and soft robotic systems. Conventional (industrial) hard robots made of rigid materials (e.g., metal) can be engineered to be compliant toward softer biological subjects (such as humans) mainly thanks to their highly sensitive sensors and high-precision control algorithms. However, in case of grave malfunction, these systems could cause serious damage, creating the need for intrinsically soft devices (Polygerinos et al., 2017). In soft robotics, the compliance of the robot (e.g., a manipulator) is sometimes achieved by matching Young's moduli of its constituent materials (Majidi, 2014; Rus and Tolley, 2015; Coyle et al., 2018). Moreover, soft robotic systems bioinspired by vertebrates, where the properties of

constituent materials span several magnitudes of moduli (from soft tissue to bone) (Yang et al., 2018) can still be considered compliant thanks to the seamless integration.

The soft (biological) samples are often widely distributed cellular structures with their characteristic dimensions and mechanical properties varying widely between specimens and in time. Consequently, scalable and compliant manipulators are favored for biomaterial manipulation, whereas the absolute positional accuracy can be of secondary importance. Moreover, if a large number of semi-independent actuators are involved, then the feedback-loop-based systems (as in AFM instruments) start to increase in complexity exponentially. Furthermore, in some cases, larger biological systems (above 100 μm) than just a single cell need to be characterized (e.g., when the mechanical properties also depend on the interactions with the extracellular matrix). In such cases, much larger probes than the standard AFM probe are needed for accurate characterization (Andolfi et al., 2019). The intrinsic compliance, miniaturizaibility, and excellent scalability of soft manipulators enabled by shape-morphing materials can enable new *in situ* methods for cellular-level manipulation (Jager et al., 2000b). Electromechanically active actuators have been demonstrated in scale relevant to microscopy studies (Jager et al., 2000a). However, rendering the morphing materials into practical manipulators still poses numerous challenges—in particular, concerning the useful/relevant device configurations, their cycling stability in various operating environments, and their possible interference with the *in situ* visualization techniques.

We explore the application of gel-like actuators in the manipulation of soft samples. As biological (gel-like) samples commonly exhibit viscoelastic properties (Muñoz and Albo, 2013), the viscoelasticity can be considered relevant for the living organisms in physical interactions with the environment. Therefore, also manipulators that exhibit viscoelastic properties also could be beneficial for enhanced contact with soft samples. Instead of using an additional viscoelastic joint between an actuator and the contact point to the sample, we propose actuators that are viscoelastic thanks to their mobile liquid phase component. Liquid-containing compliant manipulators are known to minimize sample damage and enable advanced physical interaction modes specific to soft bodies (Polygerinos et al., 2017). Indeed, also soft fluid-containing electroactive actuators demonstrate intrinsic viscoelasticity (Vunder et al., 2012). Such electroactive laminate achieves the advantages of fluidic actuators on a scale that is already challenging to fabricate using soft lithography.

We demonstrate μm- to mm-scale manipulators based on ionic and capacitive laminates (ICLs). ICLs have an exclusive set of desirable properties for this purpose. Their soft and compliant nature has made ICL materials appealing to various biomimetic soft robotics applications (Must et al., 2015; Hines et al., 2017). ICL is composed of two polarizable electrodes separated by an ion-conductive open-pore network gel layer. Upon applying a potential difference between the electrodes, the anions and cations in the liquid phase of the gel are electrostatically attracted to the positively and negatively polarized electrodes, respectively. As a consequence of this charging, the ions of the electrolyte

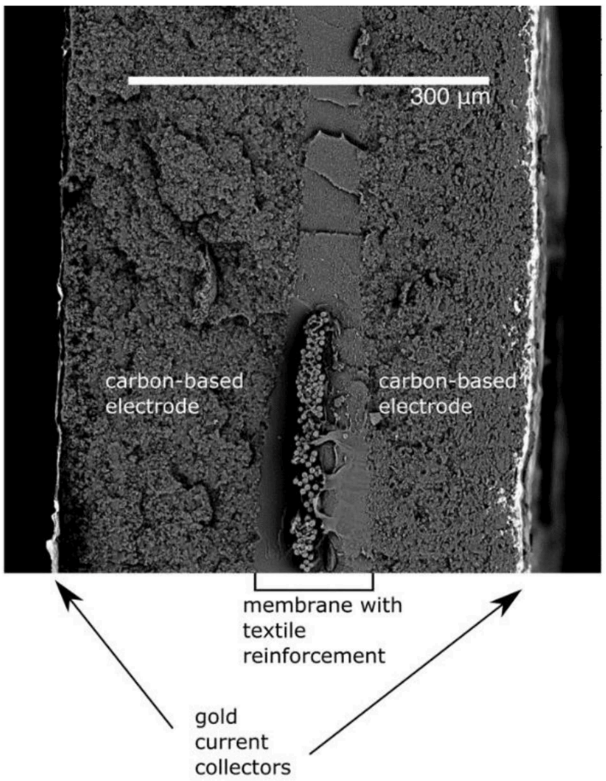

FIGURE 1 | Cryofractured cross-section of ICL.

(e.g., ionic liquid) inside the gel get displaced toward the respectively polarized electrodes. Since the anions and cations of the electrolyte differ in size, mobility, and physicochemical properties, a swelling ratio imbalance results in the composite. This, in turn, causes the laminar actuator to bend toward the positively polarized electrode typically. See **Figure 1** for a detailed description of the actuator structure.

The mobile electrified liquid phase incorporated within the gel network gives the actuator a viscous response in addition to the elastic component. In the context of manipulation, the resulting viscoelastic property is beneficial: the elastic response of the actuator promises a good match for *in situ* manipulation under optical as well as electron microscopes while the viscous response contributes to compliance and provides an intrinsic cutout of high frequencies for noise cancellation. Importantly, the electrostatically driven non-electrochemical processes in ICLs have shown to result in very high cycling stability and lifetime (Kaasik et al., 2017). Contrary to solvent-based electrolytes, ionic liquids as ICL electrolytes and gel-swelling agents allow operation of the actuators in the air as well as in a vacuum, thanks to the negligible vapor pressure of ionic liquids. Low-voltage non-magnetic and non-thermal activation excludes interference with the electron optics of scanning electron microscopes, also enabling *in situ* SEM observation. Despite the listed favorable properties of the basic ICL material, rendering the laminate into practical manipulators still poses several challenges that are

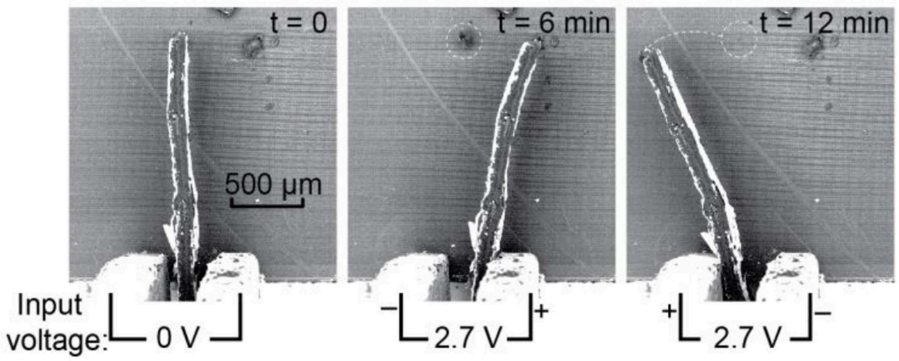

FIGURE 2 | *In situ* scanning electron micrographs of a miniaturized ICL actuator used directly as a manipulator; displacement of small objects on the SEM stage surface is demonstrated.

addressed here by suggesting possible configurations in relevant case studies.

MATERIALS AND METHODS

Fabrication of ICL Actuators

The ICL material is a three-layer composite with an ion-conductive membrane sandwiched between two electron-conductive electrodes—a structure that is similar to the electrical double-layer capacitors. The material used for the preparation of manipulators in this study was fabricated using an industrially scalable ICL manufacturing method that has been previously described in detail elsewhere (Kaasik et al., 2017). In short, fine textile with inert fibers [e.g., silk fabric (11.5 g/m^2, Esaki) or glass fiber fabric (18 g/m^2, Storm RC World)] was fastened and tautened onto a frame. Then the membrane solution was applied to the fabric using a brush. After the evaporation of solvents, an open-pore ion-conductive polymeric gel membrane was formed. Then, electrodes were sprayed on both sides of the membrane using an airbrush (Iwata). Finally, gold leaf (Giusto Manetti Battiloro 24K transfer leaves) current collectors were glued on the laminate using a rolling method similar to what has been previously described elsewhere (Must et al., 2015). The final thickness of the composite is very well tunable. In the comparative performance study introduced in section Tool Attachment—Bending Stiffness Matching, a 150–160 µm thick laminate was used. The actuator material was prepared at room temperature and at a relative humidity between 65 and 75%.

The cross-section of the structure of the prepared material is presented in **Figure 1**. The thickness of the imaged actuator exceeds that of actuators prepared for manipulation. Therefore, all the layers are visible from the cryofractured cross-section.

The prepared bulk material can be cut into various shapes to obtain functional manipulators. However, this basic manufacturing procedure can also be modified to integrate various probes and sensors directly into the active material. In section Manipulator Concepts and Their Fabrication, we will describe four manipulator concepts, from the simplest to more advanced ones, that are all based on the same ICL material described above. As the four concepts share most of the manufacturing steps, the corresponding descriptions in sections below cover only the necessary modifications to the main ICL preparation procedure to obtain the more advanced manipulator.

Manipulator Concepts and Their Fabrication

A Cantilevered Actuator Directly as a Manipulator

In the simplest embodiment, the ICL can be cut into a cantilever and used to apply force to an object via direct contact with the actuator's side or the electrode area. This configuration can be useful in applications where manipulators are needed for extremely confined spaces. Since the ICL thickness is controllable in the manufacturing process, and its other dimensions are easily miniaturizable in the cutting and shaping stages; therefore the final dimensions of the actuator/manipulator could even span less than a few cubic millimeters per manipulator. **Figure 2** shows the *in situ* scanning electron micrographs of an ICL actuator moving objects on the SEM stage surface.

Active Tweezers

In a more complicated embodiment, two cantilevered ICL actuators can be stacked together and operated in opposite phases, forming soft grippers. The conceptual drawing in the open and closed configuration is given in **Figures 3A,B**, respectively. Typically, this type of actuator material bends toward the positive terminal (although deviations to this general rule exist). Therefore, when positive conventional current is applied to the inward-facing electrodes in respect to the outward-facing electrodes, the distance between the tips of the actuators gets shorter, upon reversing the potential or current, the distance between the tips increases. Alternatively, a longer ICL actuator could also be clamped in the middle to achieve similar gripping-type behavior.

The gripper used in this study was fabricated as described in section Fabrication of ICL Actuators (silk as the base material) with the following modifications. Two 5.0 × 1.2 × 0.15 mm^3 (length × width × thickness) pieces of ICL (in red) were cut and

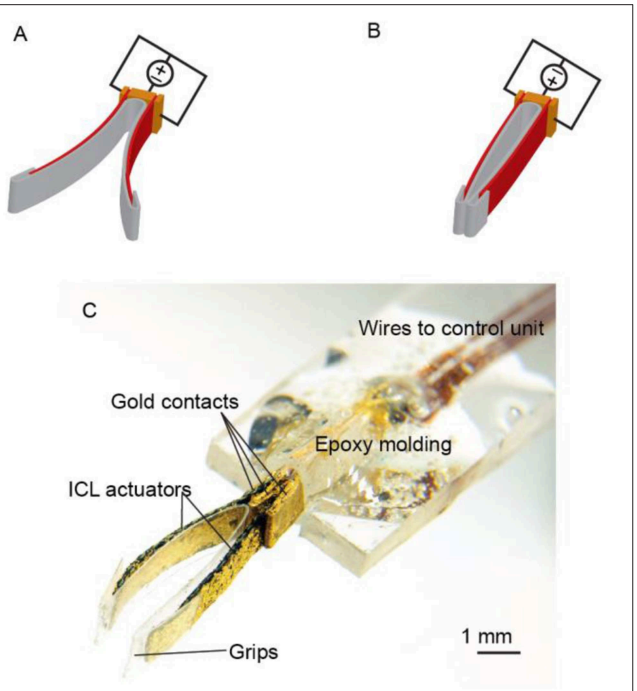

FIGURE 3 | Electroactive tweezers based on ICL actuators. **(A,B)** Tweezers in the open and closed positions, respectively. **(C)** Photograph of the final device.

clamped face-to-face between three gold contacts (in orange), as shown in **Figures 3A,B**. The inward-facing electrodes, as well as the outward-facing electrodes of the ICL actuators, were commutated together. The gripper arms were lined with a single piece of 30-μm polypropylene foil (in gray) to minimize cross-contamination between the ICL and possibly liquid-containing samples, and to define the contact area better. The final gripper assembly is depicted in **Figure 3C**.

An Active Probe

The next case study considers an ICL actuator with a flexible and conductive probe integrated into the material already during fabrication. For example, various probes and tubes can be integrated into the material in the final step during the current collector attachment. We designed an ICL with an integral wire probe that bends along with the actuator. This can be considered a two-in-one manipulator configuration, where the free end of the cantilevered probe can manipulate a sample mechanically to measure its mechanical properties, and simultaneously, various integrated sensors could be used to evaluate the electrical, electrochemical, and chemical properties of the same sample. **Figures 4A,B** show the manipulator concept, depicted in the not contacted and contacted state, respectively.

The main challenge with this approach is to select and attach such a probe that a sufficient deflection magnitude is still maintained in the ICL actuator after the integration. The probe's mechanical properties should not interfere with the actuation, whereas it should still be functional as a probe (e.g., sufficiently conductive for conductivity measurements). We chose to integrate a very fine gold-coated tungsten wire (diameter: 30 μm), as illustrated in **Figures 4C,D**.

The fabrication of this manipulator proceeded as described in section Fabrication of ICL Actuatorswith silk as the supporting structure and with the following modifications. In the current collector attachment step, a 2 × 5 cm piece of the composite was fastened on a metal rod ($d = 3$ cm) using tape, and the first current collector was attached to one side of the laminate as usual. Then, the actuator was removed from the rod and turned over. About 6 cm long gold-coated tungsten wires (diameter: 30 μm) were cut and tightly fastened over the composite on the rod using tape (**Figure 4E**). After that, the current collector was attached on the top of the wires as usual (**Figure 4F**). After removing the composite from the rod, it was carefully cut into smaller samples using a scalpel and a metallic ruler aligned with the probe wires (**Figure 4G**).

The microscope accessory was completed by attaching the manipulator to a custom holder inside a plastic Petri dish that facilitated the probing of liquid samples, as shown in **Figures 4H,I**. A suitable contact pressure to the actuator was maintained using a spring-loaded pin. The tip of the probe wire was finally shaped (e.g., bent), as needed. For conductivity measurements, a counter electrode was fixed on the bottom of the dish, and the sample in question was placed on top of it.

An Active Pipette, Also Functioning as a Tool-Positioner

The most involved approach for preparing ICL-probe assemblies is integrating the probe (e.g., wire or tubing) already in the early stages of the composite preparation. For example, we integrated inert, flexible non-conductive PTFE, PET, or polyimide tubes into the membrane of the actuator. Inspired by the proboscis of a mosquito, the ICL-tube assembly can behave as an active pipette tip for depositing or extracting liquids to/from desired areas, as schematically shown in **Figures 5A,B**, yet preserving compliance to soft tissues. Moreover, if some of the supporting fibers of the ICL membrane have been replaced with tubes, these now hollow fibers could be used for inserting other probes or sensors (e.g., the same conductivity probe introduced in the previous section) into the actuator. This would enable fast and easy switching between tools or sensors during an experiment.

The fabrication of an active capillary manipulator started with the integration of a capillary tube into the supporting fabric structure to achieve the centermost position for the tube. One fiber bundle was first removed from the glass fabric and then replaced with a tube (e.g., PTFE: 254 μm inner diameter, 76 μm wall thickness; polyimide: 127 μm inner diameter, 20 μm wall thickness; or PET: 300 μm inner diameter, 3.8 μm wall thickness) (**Figure 5C**). The fabrication then proceeded, as described in section Fabrication of ICL Actuators. The scanning electron micrograph in **Figure 5D** confirms the central location of the tube. **Figure 5E** shows the micrograph of the capillary tube woven in-between the glass fiber bundles. A metallic wire has been inserted into the tube for better visualization. **Figure 5F** gives a snapshot of the fabrication process after the attachment of the gold current collector, showing the elevated surface feature that reveals the location of the capillary tube. **Figure 5G** shows

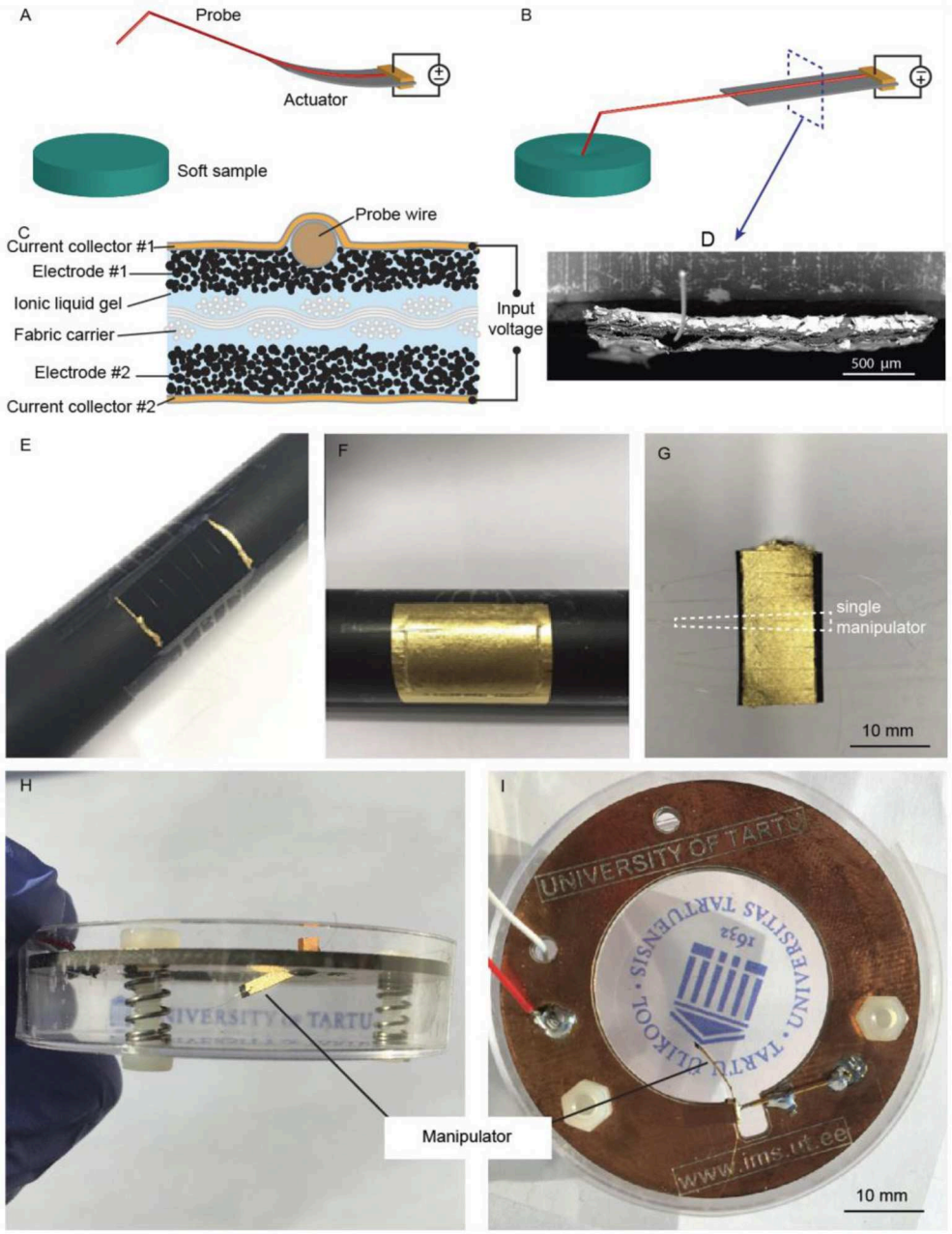

FIGURE 4 | The electroactive probe manipulator concept, shown in **(A)** not contacted and **(B)** contacted mode. **(C)** Schematic and **(D)** SEM image of the cross-section of the ICL manipulator, showing the location of the wire probe. Snapshots recalled from the fabrication: **(E)** metal wires were placed on the electrode surface; **(F)** metal wires were fixed in place under the gold current collector; and, finally, **(G)** the manipulators were formed by cutting. Photographs of the **(H)** side and **(I)** top view the final device.

the finished active pipette tip. The final assembly was attached to gold electrical terminals from its base and equipped with a visually distinguishable marker at its tip for displacement detection via video recognition, as shown in **Figure 5H**. **Figure 5I** and **Supplementary Video 1** show an active pipette with PI tubing dispensing droplets of aqueous methylene green solution into different locations on a microscope slide.

Microscopy

Hitachi TM3000 scanning electron microscope was used at 15 keV acceleration voltage to visualize the probing of soft samples in vacuum. The actuator was fastened between gold clamps commutated to a DC power supply.

The cross-sections of actuators were visualized with the same Hitachi TM3000 scanning electron microscope. Samples for SEM

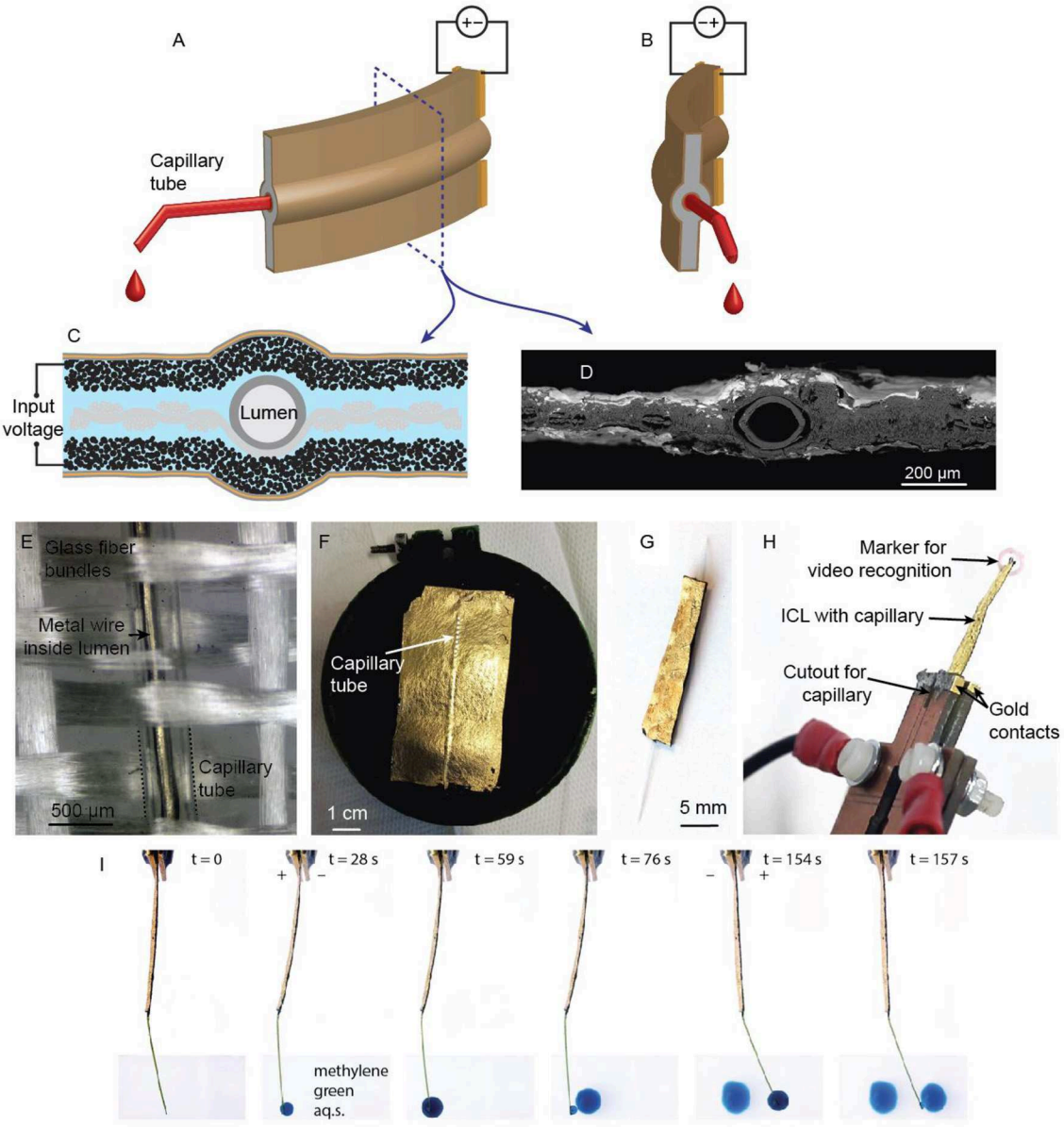

FIGURE 5 | (A,B) the concept of an active pipette for positioning fluids in oppositely polarized states. **(C)** The cross-section diagram and **(D)** an SEM micrograph of the mosquito proboscis-inspired ICL-pipette assembly, showing the arrangement of the capillary tube in the center of the laminate. **(E)** A macro photograph of the glass fiber cloth with an interwoven capillary tube before application of the membrane. **(F)** The active pipette after application of electroactive layers; the elevated strip indicates the location of the capillary tube. **(G)** The finished active pipette. **(H)** The active pipette in its holder, showing the gold contacts and a marker attached for video recognition. **(I)** Deposition of methylene green dye by an electrically steerable ICL-pipette.

micrographs were first cryofractured using liquid nitrogen to obtain clearer cross-sections and then taped on a metal sample holder with their cross-sections facing up. The samples, together with the sample holder, were sputtered with 5 nm of gold using a Leica EM ACE600 sputter coater to obtain more detailed SEM micrographs.

5x and 10x objectives were used for optical microscopy.

Displacement Characterization

The actuation of active tweezers was characterized by post-processing the recorded videos with video recognition implemented in the Vision Development module in LabView, National Instruments. Digital templates were created of visually distinctive areas (edge and surface defects from intentionally rough cutting, or visual markers attached for the detection purpose) and tracked frame-by-frame using the grayscale value pyramid pattern-matching algorithm.

The influence of various integrated probes was comparatively studied on samples from the same batch with different integrated probes (**Figure 6C**). The displacement detection method for this comparative study was done as previously described in detail elsewhere (Punning et al., 2014). In brief, the actuator's (free length: 18 mm) displacement was video recorded, and the

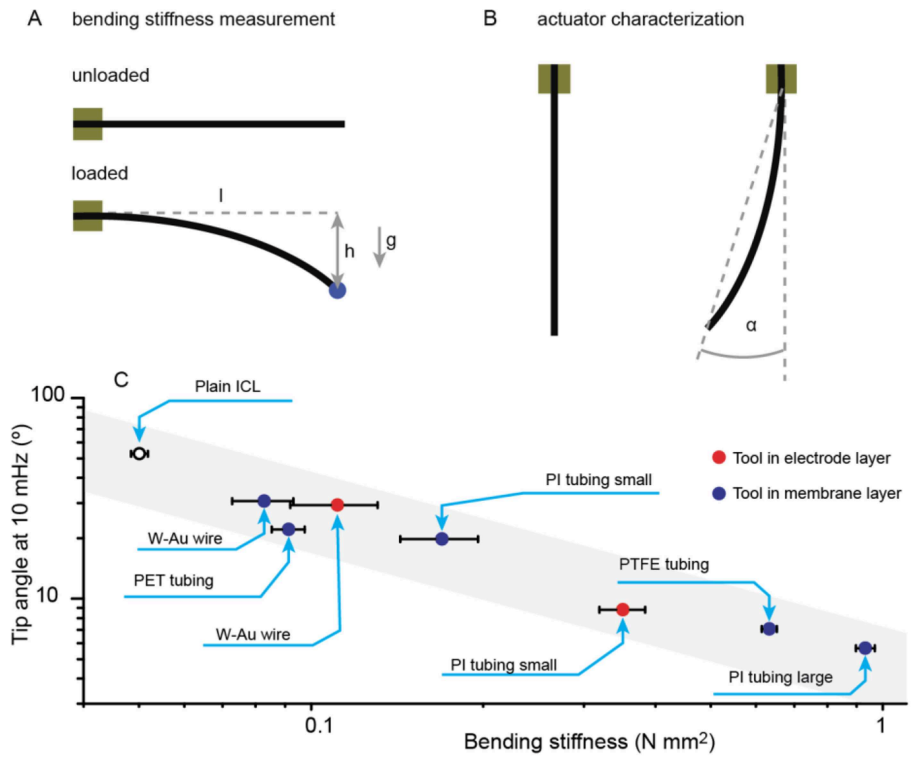

FIGURE 6 | (A) bending stiffness measurement setup; **(B)** bending angle definition; **(C)** Manipulator deflection with ±2 V 10 mHz triangular input signal for ICLs carrying denoted tools vs. their bending stiffness.

actuator's tip angle, defined in **Figure 6B**, was extracted by post-processing in LabView.

Electrical Characterization

Electrical driving signals were generated, and impedances registered using IVIUM CompactStat and Princeton Applied Research Parstat 2273 electrochemical workstations. All electrical measurements were done using electrochemically inactive gold contacts.

The measurement setup for the comparative performance study (**Figure 6B**) has been previously described elsewhere in detail (Punning et al., 2014). In the comparative study, we used triangular voltage waves (cyclic voltammetry) to drive the actuators. The electrochemical aspects of the material and its capacitive nature have been described in detail elsewhere (Kaasik et al., 2017).

Mechanical Characterization

The mechanical characterization of non-homogeneous multilayer composite materials with integrated probes is not straightforward. For example, tensile testing in the same direction as the reinforcement fibers is expected to be dominated mostly by the mechanical properties of the fibers (characteristic values in the GPa range) and not by the bulk active material itself (characteristic values in the MPa range). Since bending performance is the most important characteristic of this type of actuators, it is most reasonable to use bending stiffness (the actuator's resistance to bending deformation) to characterize and compare different manipulator configurations. Bending stiffness is a function of Young's modulus and the area moment of inertia of the sample.

The bending stiffness of the bare ICL material and the ICL-probe assemblies was characterized using the end-loaded cantilever beam configuration. The actuators were fastened between clamps, and different weights were attached on the tip of the cantilever. The resulting deflection was measured from the video. See **Figure 6A** for a description of the measurement setup.

The bending stiffness (**BS**) of different manipulator assemblies was calculated using the following formula for end-loaded cantilever beams:

$$BS = \frac{m \times g \times l^3}{3 \times h},$$

where m is the mass of the added load (in blue in **Figure 6A**; 7.4 and 50.9 mg loads were used), g is the gravitational acceleration (9.8 m s^{-2}), l is the free length of the cantilever beam (18 mm), and h is the measured deflection in the cantilever beam due to the added load.

Samples for Probing

Capelin eggs for manipulation experiments were purchased from the local supermarket. In the conductive probing experiment, a drop of 1-ethyl-3-methylimidazolium trifluoromethanesulfonate ([EMIM][OTf]) ionic liquid was used.

RESULTS AND DISCUSSION

The considered manipulator concepts suggest pathways to transfer the ICL actuators from simple configurations suitable for material characterization toward practical arrangements as microscope accessories. Modifications in various stages of the ICL fabrication enable us to manufacture considerably different functional manipulators. Both electronically conductive (i.e., the metal wire), and non-conductive and inert (i.e., the capillary tube) tools can be integrated into the ICL electrode or membrane during the ICL manufacturing.

Tool Attachment—Bending Stiffness Matching

In the presented active manipulator concepts, the ICL was used to bend a supplementary component; thus, matching the ICL actuator bending stiffness to its supplement is essential for effective operation. In general, the supplementary components increase the bending stiffness of the manipulator, effectively creating a load for the actuator. **Figure 6C** compares the actuation performance of ICL manipulators carrying various tools. Indeed, the ICL without a tool attached yielded the largest bending angle; and the general trend shows a linear decrease of actuation magnitude in the log-log-scale. Consequently, it is possible to estimate the bending magnitude of the manipulator by knowing the bending stiffness of the actuator and the tool.

In general, the position of the textile base material determines the location of the ICL's neutral layer, which is the layer with zero strain on bending. However, ICL manipulators were manufactured with tools placed in two locations: in the membrane layer in the center of the laminate, and close to one side of the laminate. In the former case, the tool location coincides with the textile reinforcement; thus, the bending stiffnesses of the tool and the ICL are expected to be additive. Indeed, **Figure 6C** shows most of the manipulators with tools placed within the membrane following a uniform linear trend. Minor deviations from it could be caused by the part of the electrode deposited on top of the non-conductive and inert tubing that renders this part of the composite electromechanically inactive due to blocked ion flux. Indeed, **Figure 6C** shows that the manipulator carrying the extremely soft but wide and flat PET tubing yielded actuation performance lower than expected due to a significant decrease in the actuator's effective surface area. Slightly better performance is even achieved with a gold-coated tungsten wire probe integrated into the actuator, although the mechanical properties of metal wire are orders of magnitude stiffer.

The placement of the tool on the surface of the laminate potentially affects the bending performance due to a shift in the location of the neutral layer toward the electrode carrying the tool. Therefore, for more predictable actuation behavior in both directions, it is advisable to attach probes already in the neutral layer (i.e., in the textile). However, from the manufacturing point of view, the ease of attaching probes only in the final manufacturing stage might be a more significant advantage in some cases.

Driving Considerations, Performance, and Stability

The ICL actuator is a capacitive device very similar to electrical double-layer capacitors (EDLC). The defining difference is that the swelling and contraction of electrodes upon the application of an electric signal that drives the bending motion in ICLs is seen as a disadvantage in EDLC-s. The actuation in the ICL is proportional to the charge stored in it (Kaasik et al., 2017). Indeed, in a capacitive system, input current directly determines the actuation speed, whereas the charge (i.e., the integral of current) determines the distance traveled if all other parameters are kept unchanged. Very typically, the three-layer bending type actuators have previously been controlled using voltage steps, sine or triangular waves in the two-electrode configuration. In the following sections, we will explore the capability of efficiently using current as the process parameter, as small current levels can generally be controlled more precisely than variations in large voltage levels (e.g., microvolt-level voltage variations in an ICL charged to the open-circuit potential of hundreds of mV). Therefore, charge-driven energy-storing actuators, such as the ICLs, prevail in applications that require slow and uniform actuation speeds. However, the electrochemical stability windows of components used in the ICL preparation (i.e., material parameter) as well as the internal resistance of the ICL manipulator (i.e., device parameter) need to be considered in the current-driven mode.

Precision control of the ICL using current signals is demonstrated using the tweezer configuration. The ICL tweezer gap, as shown in **Figure 7A** (microscope image in **Figure 7B**) formed at the distance of 5.1 mm from the tweezer's base and varied from zero (tweezers closed) to ∼2 mm in the experiments, demonstrating a practically sufficient shape variation in the miniaturized scale. **Figure 7C** shows the active tweezer gap modulation upon applying a 1-Hz square-wave current of 3 mA. The tweezer gap followed an almost ideal triangular pattern, following the course of the charge stored in the capacitive device. The peak-to-peak amplitude of actuation was $86 \pm 17\,\mu m$ ($n = 90$). **Figure 7D** shows that current levels varied over more than two orders of magnitude during actuation and resulted in a well-defined, close-to-proportional control of the ICL manipulator speed. For practical considerations, the behavior of the manipulator at low current levels (i.e., low speed) is particularly noteworthy. **Figure 7E** demonstrates the control of ICL tweezers at a rate of only $590\,nm\,s^{-1}$ by applying a 10-μA input current; the ICL terminal voltage spanned by 0.21 V only. The superimposed drift of the tweezer gap in **Figure 7E** is characteristic of soft manipulators with a viscous component and can be considered as an advantage for compliantly manipulating soft samples (see also section Compliant Manipulation of Soft Objects). Moreover, this drift ($55\,nm\,s^{-1}$) was much smaller than that imposed by the current actuation signal. Consequently, the ICL manipulator matches well with the typical *in situ* microscopy methods, offering actuation control at fast as well as at slow rates.

The excellent stability of ICL tweezers is further demonstrated in **Figures 8A,B**. In 350 cycles at 0.1 Hz rectangular current of 500 μA, the tweezer gap was modulated by $188 \pm 15\,\mu m$. No pronounced pattern that could be attributed to the degradation

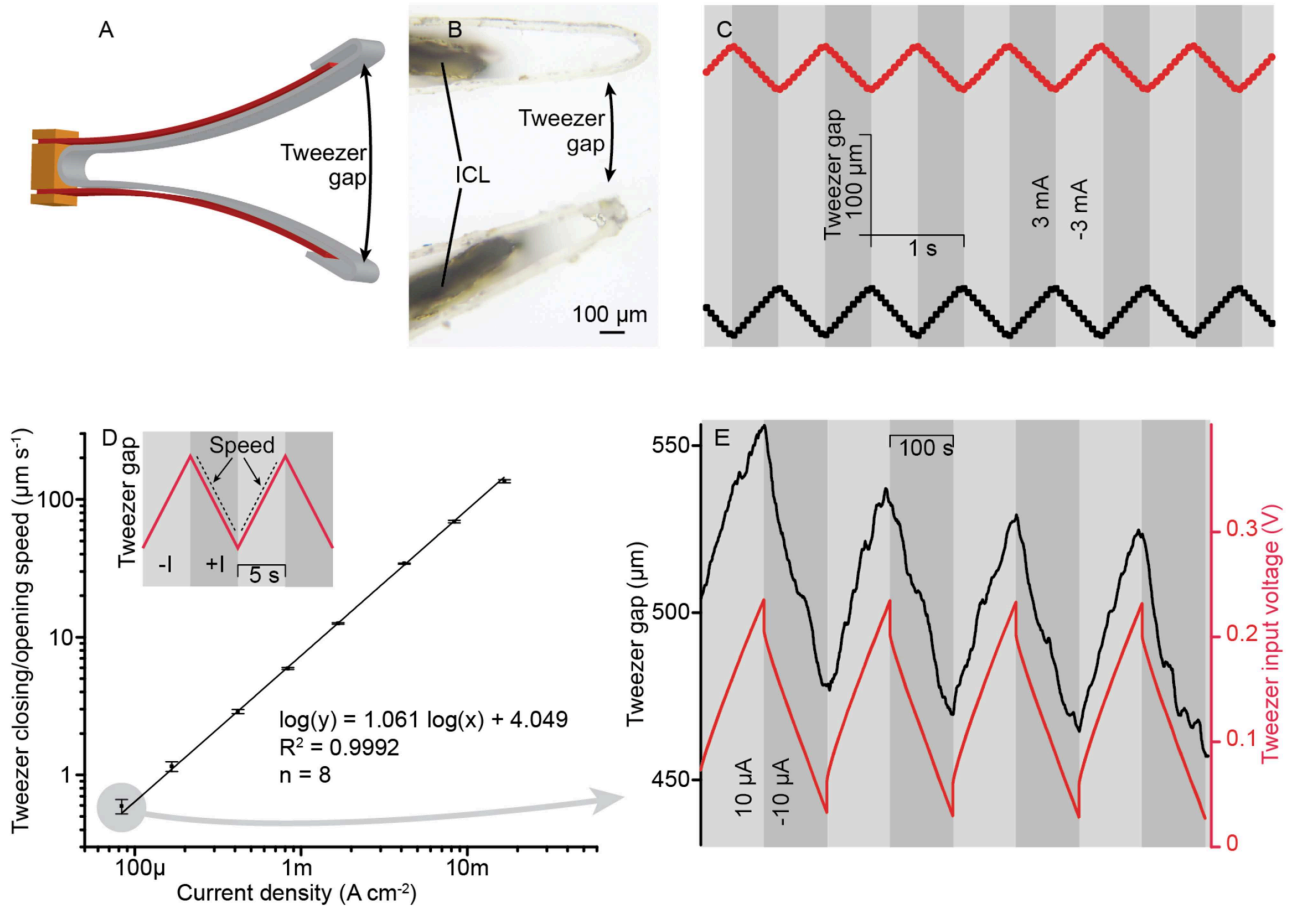

FIGURE 7 | (A) Tweezer gap used as the performance metric for the electroactive tweezers. **(B)** Microscope image of the tweezer arm tips showing the grips as contact points. **(C)** The position of tweezer arm tips upon applying a 1-Hz square wave at ±3 mA amplitude. **(D)** The tweezer closing/opening speed in an unobstructed mode at a range of current densities. **(E)** The typical response curve of the electroactive tweezers upon applying an extremely small current, ±10 µA.

of the material was observed (the dotted line represents a guide for the eye).

Further advantages of using current to control the speed of the manipulator are highlighted in **Figure 8A**. The tweezer's terminal voltage consists of the voltage drop at the equivalent series resistance (ESR), denoted as U_{ESR}, and the voltage drop at the electric double-layer at the electrodes denoted as U_{EDL}. In the particular current density value, U_{ESR} was larger than U_{EDL}. Moreover, the ESR value decreased noticeably (5.5%) during cycling, possibly due to water absorption by the ionic liquid electrolyte and by Joule heating. However, using current as the feedback parameter ensured a uniform triangular actuation pattern throughout the lifetime experiment, deterring possible dependence on the ESR variations and the current density level.

Compliant Manipulation of Soft Objects

The viscoelastic properties of the ICL material imply that the actuator's shape at zero position, i.e., the position with zero charge injected, is tunable and that it also adjusts further according to the applied load. **Figure 9** demonstrates the recovery behavior of the ICL laminate in response to applying and removing a load in the gravitational field. As typical for viscoelastic materials that exhibit both elastic and viscous properties, the removal of the load first results in quick elastic recovery that is followed by a slower recovery at a continuously decreasing rate. Depending on the applied load, the viscous recovery might result in permanent deformation that can be useful for preshaping the material into, for example, custom gripper arms. Moreover, this behavior is very beneficial in case of compliant handling of soft samples; the manipulator remains operational after contact thanks to the elastic deformation component, but is safe to the object thanks to the viscous deformation component. The ICL adjusts itself to a new shape without the need for active control loops, preventing the build-up of a high loading pressure. The viscoelastic property is generally considered a disadvantage due to loss of positional accuracy. However, a large number of potential biomaterial manipulation cases require the application of a differential mechanical stimulus (e.g., a gentle touch), whereas referencing to an absolute position may be of secondary importance.

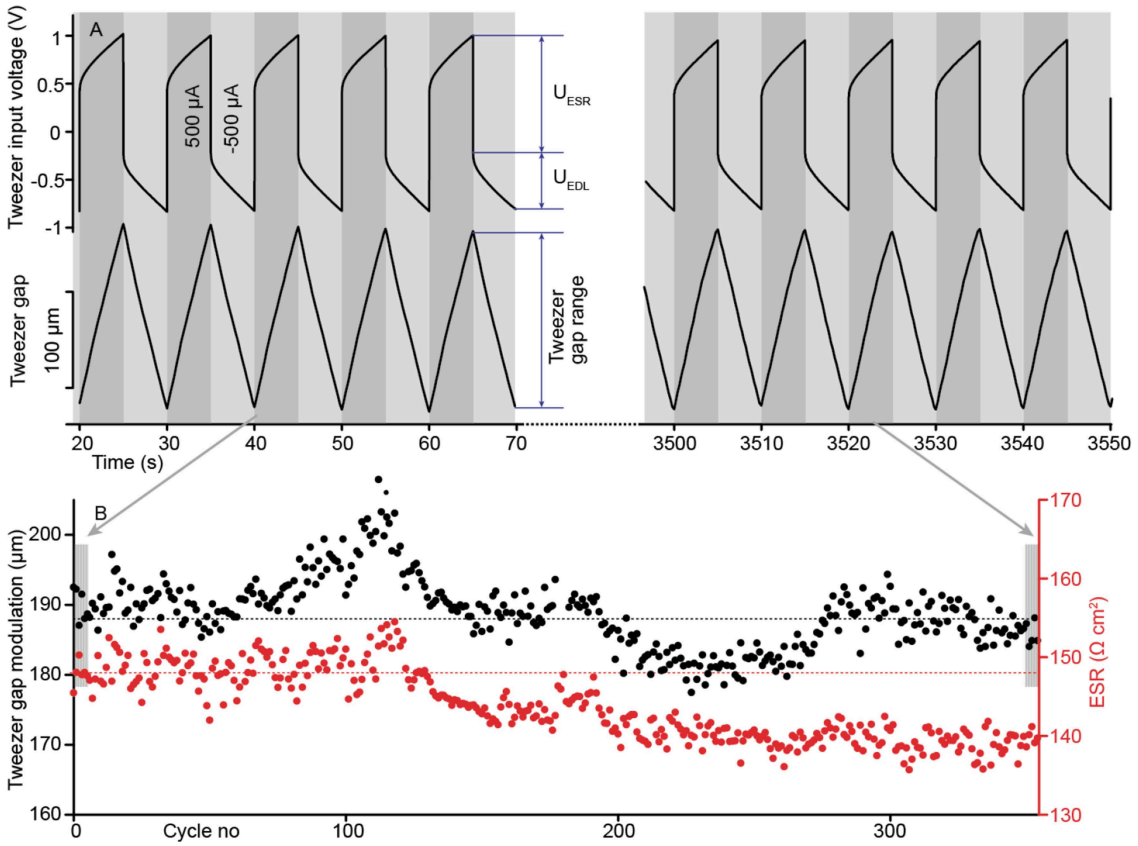

FIGURE 8 | (A) Repeatable pattern of the tweezer gap and the corresponding transient voltage, showing the contribution of the equivalent series resistance (ESR). **(B)** Tweezer lifetime and ESR during 350 actuation cycles.

The intrinsically soft ICL manipulator is particularly well-suited for probing soft samples, offering the necessary safety margin and conforming to samples of non-uniform geometries. **Figures 10A,B** demonstrate the ICL-based active tweezers gripping a large cell, a single capelin egg. The ICL provides the intrinsic safety for such manipulation: the tweezers can grasp a highly delicate object and squeeze it with minimum risk of damage thanks to the compliant nature of the soft actuator.

The electroactive tweezer arms were used to manipulate a delicate capelin egg as follows. First, the sample was attached to the grips at zero charge; the gripped load adjusted itself in time so that the contact pressure approached zero. Then, a differential load was applied by injecting charge to the ICL to clamp the capelin egg with the tweezers. **Figures 10C,D** depict the mechanical squeezing of a capelin egg between the tweezer arms (see also **Supplementary Video 2**). The gap distance (**Figure 10C**) adjusted itself according to the sample size, and the compliant nature of the ICL material prevented the build-up of possible large stresses upon a possible (spontaneous) change in the sample geometry. The tweezer gap distance modulated by ∼200 µm, indicating compliant and soft deformation applied to the capelin egg sample (**Figure 10D**).

Manipulator Operation in Vacuum

The ICL includes a liquid electrolyte essential to its working principle. This raises the question—are the ICL manipulators stable in the vacuum chamber of conventional SEM instruments? A simple biological sample (a human hair) was manipulated in the SEM vacuum chamber to prove that the ICL material can also be used to probe samples in the vacuum environment. **Figure 11** shows the highly miniaturized setup of a soft ICL manipulator and a soft sample, accommodated in an extremely confined space in the SEM chamber (2 mm longest dimension). Moreover, as the ICL is conductive, it is not subjected to the charging effects, unlike the non-conductive hair (see also **Supplementary Video 3**). Indeed—charging effects were observed in case of the hair, expressed as the bending of the electron beam upon passing near the charged hair in **Figure 11**, whereas no deflection of the electron beam was noticed in case of the conductive ICL. As the driving voltages for the ICL material are orders-of-magnitude lower than the acceleration voltage of the electron beam used in SEM, also no interference by the actuating voltage to the electron beam was registered during the operation of an ICL that was fully exposed to the electron beam. This is a clear advantage over the electrostatically-driven actuators, such as comb drives and dielectric elastomers that rely on high actuation

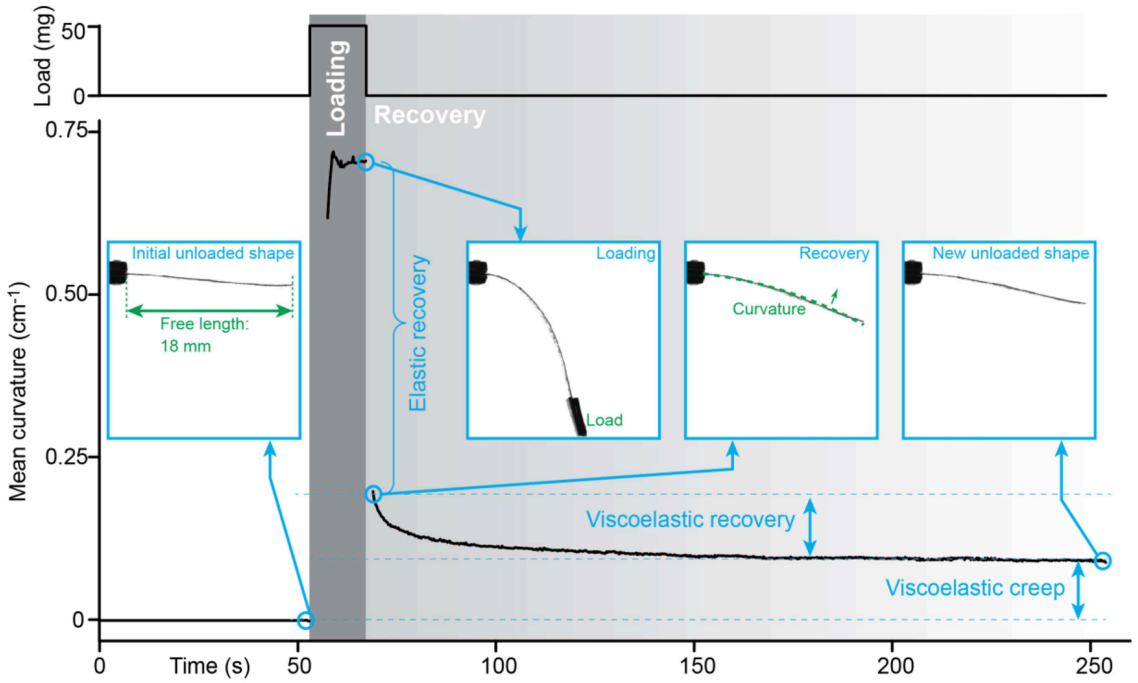

FIGURE 9 | Viscoelastic component in an ICL laminate, evidenced by the inelastic recovery of an ICL post-loading.

voltage levels (in kilovolts) that can interact and interfere with the electron beam if used in a similar configuration as the ICL probe introduced here.

Simultaneous Electrical and Mechanical Probing

The integration of conductive probes or sensors into the ICL opens up the possibility to characterize the mechanical and electrical properties of a sample (even simultaneously). As the current and voltage levels to drive an ICL are small, the interference from the actuation signal to the conductivity measurements is considered to be negligible. The possibility to measure the electrical properties of various samples was evaluated with the wire-carrying manipulator by probing a conductive sample—a drop of ionic liquid (**Figures 12A,B**). **Figure 12C** illustrates the probe and the droplet under a microscope. The surface tension force, as evidenced by the formation of a meniscus upon contact with the sample, did not significantly interfere with the actuation of the probe tip. The ICL-actuated probe tip was highly responsive under magnification, crossing the field-of-view in a few seconds, again showing that the ICL can fully cover the speed range relevant to most common micrographic techniques.

Moreover, the electrical properties of the assembly were tested using a simple continuity test. The actuation of the ICL manipulator (measured using a laser distance meter at 5 mm from the manipulator's base) reversibly created contact between the integrated probe and the liquid sample, as schematically shown in **Figure 12D**. The registered continuity data and the cantilever actuation is shown in **Figure 12E**. Combining the electrical measurement capabilities with the high-precision control introduced in more detail with active tweezers and the miniaturizability shown in the SEM probing section could be, for example, crucial for spatially dense manipulation scenarios of unknown and complicated samples.

CONCLUSIONS

The ICLs have previously been demonstrated primarily for their actuation capability. We have explored how small changes in the manufacturing process can render these materials useful for prospective technologies of miniaturized manipulators. We have shown that ionic-liquid-based ICLs can be operated in air or in a vacuum, enabling probing of biological or other samples under an optical as well as a scanning electron microscope. The latter is enabled by the non-evaporative nature of ionic liquids and by the negligible interference from actuators to the electron optics.

The application-based design of ICL manipulators is an essential step ahead—instead of just characterizing the actuating material, we modified the ICL assembly procedure to construct practically relevant devices, i.e., a manipulator for interacting with soft (biological) samples. We explored four different manipulator configurations and demonstrated the integration of various tools—a simple cantilever probe, a needle probe, a capillary tube, and tweezer arms that are then steered by the ICL actuator.

The capillary tube integrated into the ICL's textile base demonstrates new application possibilities that

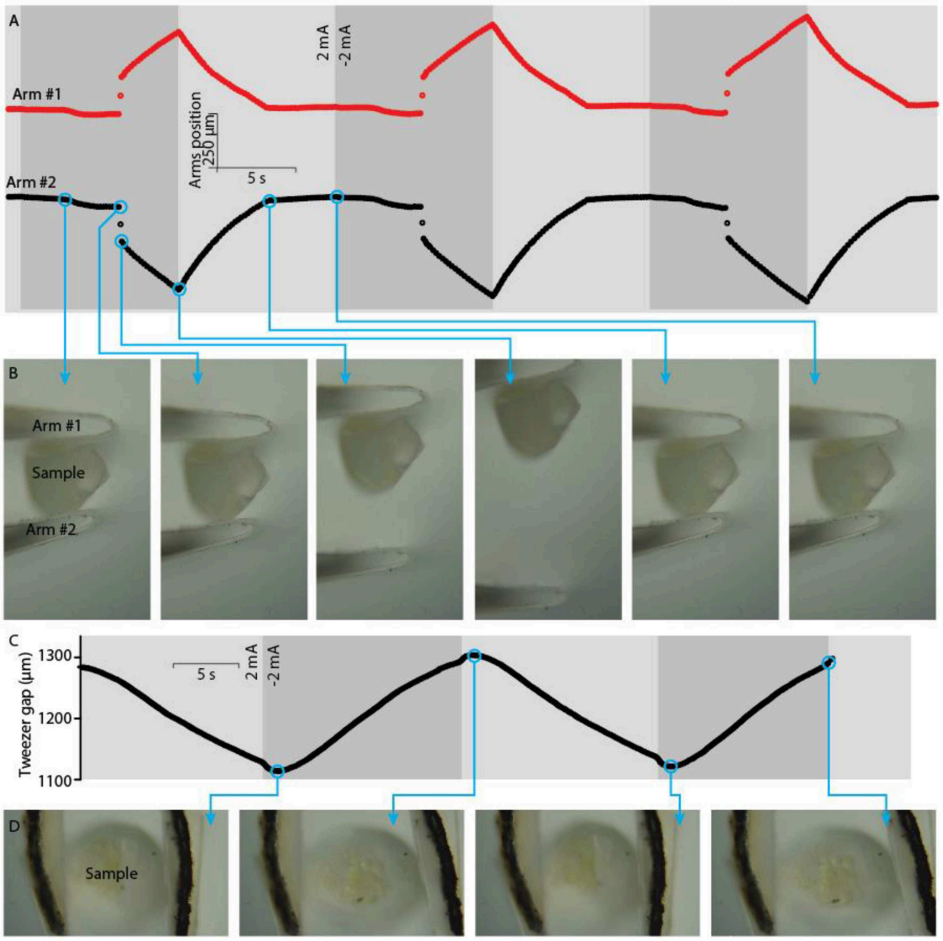

FIGURE 10 | Manipulation of a soft biological sample, a capelin egg. **(A)** Positions of tweezer arm tips while repetitive clamping-releasing of a capelin egg, and **(B)** optical micrographs corresponding to the indicated time steps. **(C)** Position of tweezer arms while squeezing a capelin egg, and **(D)** the corresponding optical micrographs.

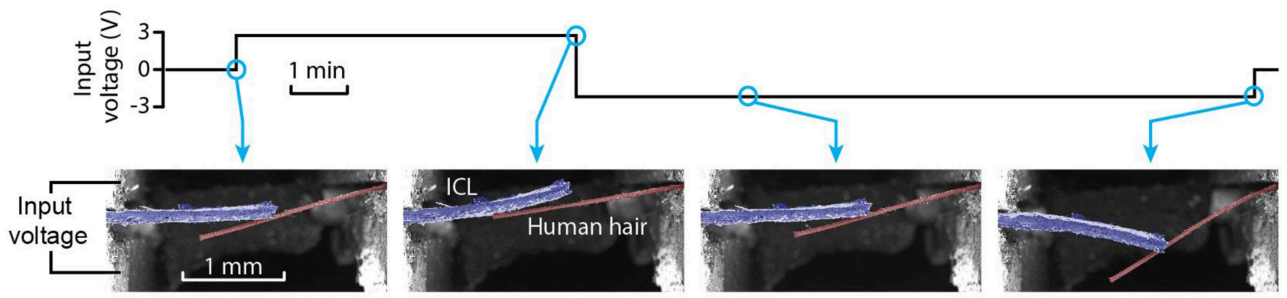

FIGURE 11 | Image sequence of an ICL actuator (false-colored in blue) probing human hair (false-colored in brown) in a vacuum.

take advantage of the uniform and widely distributed nature of textiles that have a well-defined structure in the mm-scale, but span in meters in two dimensions. The integration of fluidics in a self-morphing flexible textile platform is an essential step toward new health and care applications.

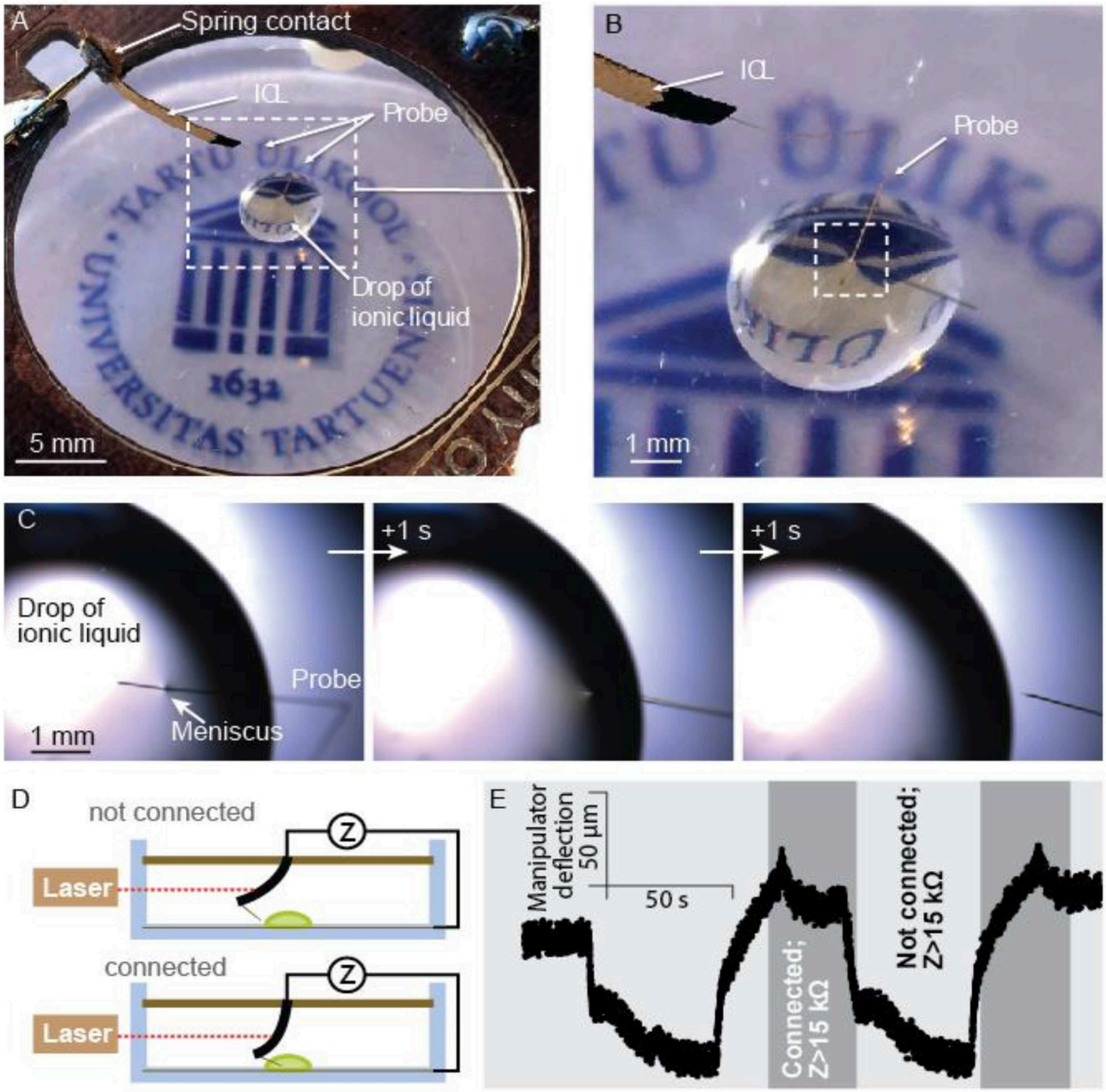

FIGURE 12 | (A) The ICL manipulator probing a drop of liquid, and **(B)** closeup of the same. **(C)** A sequence of micrographs upon breaking the contact in-between the liquid sample and the probe. **(D)** Schematic description of the continuity measurement setup, and **(E)** probe's displacement at 5 mm from the contacts and formation and loss of electrical contact to the sample monitored by EIS (1 kHz, 5 mV_{RMS}) between the integrated probe and a counter electrode (W/Au wire) on the bottom of the Petri dish.

However, the biocompatibility of the actuators is of crucial importance when probing living tissues, cells, or other biological samples. ICL does offer actuation at relatively low potentials, thus providing a high safety margin in terms of electrical control. However, the choice of ICL constituent materials has, to date, been driven primarily by their impact on the composite actuation performance, consequently reaching to harmful substances (e.g., carbon nanotubes or some ionic liquids), and little research has so far been focused on the safety and biocompatibility of ICL materials. There have been attempts to encapsulate ICL materials with biocompatible passive layers. However, every passive addition to the active material reduces its maximum achievable deflection. Therefore, further development is suggested in the field of efficient encapsulation methods to enable safe probing of various samples in liquid, vacuum, or air without compromising the actuation performance to a large degree.

DATA AVAILABILITY STATEMENT

All datasets generated for this study are included in the article/**Supplementary Material**.

AUTHOR CONTRIBUTIONS

IM designed and analyzed the active tweezer, performed data analysis, participated in writing, and revising of the

manuscript. PR did the comparative characterization of manipulator concepts, designed and analyzed the probe manipulator, performed data analysis, participated in writing, and revising of the manuscript. FKr designed, prepared, and analyzed the active pipette tip. FKa performed the vacuum manipulation study. UJ took part in the discussions and revised the manuscript. AA took part in the discussions.

FUNDING

This research was partially funded by the institutional research funding (IUT-20-24) of the Estonian Ministry of Education and Mobilitas Pluss Returning Researcher Grant MOBTP47 and by the European Union through the European Regional Development Fund.

ACKNOWLEDGMENTS

The Authors would like to thank Janno Torop, Teet Tilk, and Maris Nuhkat for their help in preparing the set-ups.

SUPPLEMENTARY MATERIAL

The Supplementary Material for this article can be found online at: https://www.frontiersin.org/articles/10.3389/frobt.2019.00140/full#supplementary-material

Supplementary Video 1 | Demonstration of an active, ICL-driven pipette for positioning liquids.

Supplementary Video 2 | Squeezing of a soft sample, a single capelin egg, using ICL tweezers.

Supplementary Video 3 | *In situ* bending of a biological sample—a human hair—using an ICL manipulator in the vacuum of the SEM chamber.

REFERENCES

Alsteens, D., Gaub, H. E., Newton, R., Pfreundschuh, M., Gerber, C., and Müller, D. J. (2017). Atomic force microscopy-based characterization and design of biointerfaces. *Nat. Rev. Mater.* 2:17008. doi: 10.1038/natrevmats.2017.8

Andolfi, L., Greco, S. L. M., Tierno, D., Chignola, R., Martinelli, M., Giolo, E., et al. (2019). Planar AFM macro-probes to study the biomechanical properties of large cells and 3D cell spheroids. *Acta Biomater.* 94, 505–513. doi: 10.1016/j.actbio.2019.05.072

Castillo, J., Dimaki, M., and Svendsen, W. E. (2009). Manipulation of biological samples using micro and nano techniques. *Integr. Biol.* 1, 30–42. doi: 10.1039/B814549K

Coyle, S., Majidi, C., LeDuc, P., and Hsia, K. J. (2018). Bio-inspired soft robotics: material selection, actuation, and design. *Extrem. Mech. Lett.* 22, 51–59. doi: 10.1016/j.eml.2018.05.003

Hines, L., Petersen, K., Lum, G. Z., and Sitti, M. (2017). Soft actuators for small-scale robotics. *Adv. Mater.* 29:1603483. doi: 10.1002/adma.201603483

Jager, E. W., Inganäs, O., and Lundström, I. (2000b). Microrobots for micrometer-size objects in aqueous media: potential tools for single-cell manipulation. *Science* 288, 2335–2338. doi: 10.1126/science.288.5475.2335

Jager, E. W., Smela, E., and Inganäs, O. (2000a). Microfabricating conjugated polymer actuators. *Science* 290, 1540–1545. doi: 10.1126/science.290.5496.1540

Kaasik, F., Must, I., Baranova, I., Põldsalu, I., Lust, E., Johanson, U., et al. (2017). Scalable fabrication of ionic and capacitive laminate actuators for soft robotics. *Sensors Actuators B Chem.* 246, 154–163. doi: 10.1016/j.snb.2017.02.065

Krieg, M., Fläschner, G., Alsteens, D., Gaub, B. M., Roos, W. H., Wuite, G. J. L., et al. (2019). Atomic force microscopy-based mechanobiology. *Nat. Rev. Phys.* 1, 41–57. doi: 10.1038/s42254-018-0001-7

Majidi, C. (2014). Soft robotics: a perspective—current trends and prospects for the future. *Soft Robot.* 1, 5–11. doi: 10.1089/soro.2013.0001

Muñoz, J. J., and Albo, S. (2013). Physiology-based model of cell viscoelasticity. *Phys. Rev. E* 88:012708. doi: 10.1103/PhysRevE.88.012708

Must, I., Kaasik, F., Poldsalu, I., Mihkels, L., Johanson, U., Punning, A., et al. (2015). Ionic and capacitive artificial muscle for biomimetic soft robotics. *Adv. Eng. Mater.* 17, 84–94. doi: 10.1002/adem.201400246

Polygerinos, P., Correll, N., Morin, S. A., Mosadegh, B., Onal, C. D., Petersen, K., et al. (2017). Soft robotics: review of fluid-driven intrinsically soft devices; manufacturing, sensing, control, and applications in human-robot interaction. *Adv. Eng. Mater.* 19:e201700016. doi: 10.1002/adem.201700016

Punning, A., Kim, K. J., Palmre, V., Vidal, F., Plesse, C., Festin, N., et al. (2014). Ionic electroactive polymer artificial muscles in space applications. *Sci. Rep.* 4:6913. doi: 10.1038/srep06913

Rus, D., and Tolley, M. T. (2015). Design, fabrication and control of soft robots. *Nature* 521, 467–475. doi: 10.1038/nature14543

Verotti, M., Dochshanov, A., and Belfiore, N. P. (2017). A comprehensive survey on microgrippers design: mechanical structure. *J. Mech. Des.* 139:060801. doi: 10.1115/1.4036351

Vunder, V., Punning, A., and Aabloo, A. (2012). Mechanical interpretation of back-relaxation of ionic electroactive polymer actuators. *Smart Mater. Struct.* 21:115023. doi: 10.1088/0964-1726/21/11/115023

Yang, G.-Z., Bellingham, J., Dupont, P. E., Fischer, P., Floridi, L., Full, R., et al. (2018). The grand challenges of Science Robotics. *Sci. Robot.* 3:eaar7650. doi: 10.1126/scirobotics.aar7650

Conflict of Interest: The authors declare that the research was conducted in the absence of any commercial or financial relationships that could be construed as a potential conflict of interest.

frontiers in Robotics and AI

ORIGINAL RESEARCH
published: 10 January 2020
doi: 10.3389/frobt.2019.00150

Modeling and Design Optimization of a Rotational Soft Robotic System Driven by Double Cone Dielectric Elastomer Actuators

Sophie Nalbach[1,2,3]*, *Rukmini Manoz Banda*[2,3], *Sipontina Croce*[4], *Gianluca Rizzello*[2,3], *David Naso*[4] and *Stefan Seelecke*[1,2,3]

[1] Center for Mechatronics and Automation Technologies (ZeMA) gGmbH, Saarbrücken, Germany, [2] Department of Systems Engineering, Saarland University, Saarbrücken, Germany, [3] Department of Material Science and Engineering, Saarland University, Saarbrücken, Germany, [4] Department of Electrical and Information Engineering, Polytechnic University of Bari, Bari, Italy

Dielectric elastomers (DEs) consist of highly compliant electrostatic transducers which can be operated as actuators, by converting an applied high voltage into motion, and as sensors, since capacitive changes can be related to displacement information. Due to large achievable deformation (on the order of 100%) and high flexibility, DEs appear as highly suitable for the design of soft robotic systems. An important requirement for robotic systems is the possibility of generating a multi degree-of-freedom (MDOF) actuation. By means of DE technology, a controllable motion along several directions can be made possible by combining different membrane actuators in protagonist-antagonist configurations, as well as by designing electrode patterns which allow independent activation of different sections of a single membrane. However, despite several concepts of DE soft robots have been presented in the recent literature, up to date there is still a lack of systematic studies targeted at optimizing the design of the system. To properly understand how different parameters influence the complex motion of DE soft robots, this paper presents an experimental study on how geometry scaling affects the performance of a specific MDOF actuator configuration. The system under investigation consists of two cone DE membranes rigidly connected along the outer diameter, and pre-compressed out-of-plane against each other via a rigid spacer. The electrodes of both membranes are partitioned in four sections that can be activated separately, thus allowing the desired MDOF actuation feature. Different prototypes are assembled and tested to study the influence of the inner radius as well as the length of the rigid spacer on the achievable motion range. For the first experimental study presented here, we focus our analysis on a single actuation variable, i.e., the rotation of the rigid spacer about a fixed axis. A physics-based model is then developed and validated based on the collected experimental measurements. A model-based investigation is subsequently performed, with the aim of studying the influence of the regarded parameters on the rotation angle. Finally, based on the results of the performed study, a model-based optimization of the prototype geometry is performed.

Keywords: dielectric elastomer, soft robot, multi-DOF, double cone actuator, simulation

OPEN ACCESS

Edited by:
Federico Carpi,
University of Florence, Italy

Reviewed by:
Hyouk Ryeol Choi,
Sungkyunkwan University,
South Korea
Andrew T. Conn,
University of Bristol, United Kingdom

***Correspondence:**
Sophie Nalbach
sophie.nalbach@imsl.uni-saarland.de

Specialty section:
This article was submitted to Soft Robotics, a section of the journal Frontiers in Robotics and AI

Received: *30 August 2019*
Accepted: *16 December 2019*
Published: *10 January 2020*

Citation:
Nalbach S, Banda RM, Croce S, Rizzello G, Naso D and Seelecke S (2020) Modeling and Design Optimization of a Rotational Soft Robotic System Driven by Double Cone Dielectric Elastomer Actuators. Front. Robot. AI 6:150. doi: 10.3389/frobt.2019.00150

INTRODUCTION

In recent years, the idea of human-robot cooperation, in which robots support human workers by undertaking exhausting or harmful subtasks of their work, is becoming more and more relevant. If robots operating with high force levels have to share the same working environment with humans, it is of fundamental importance that they do not cause harm to the users. A potential way of addressing this problem consists of designing soft robots in which conventional metal parts are replaced by highly compliant materials (Albu-Schaffer et al., 2008; Laschi et al., 2017). Ideally, these soft materials must be able to sustain the structure of the robot, as well as to provide actuation and sensing capabilities. Most of the current solutions to this problem are based on a combination of flexible structures, e.g., springs, pneumatic actuators, electric motors (Robinson et al., 1999; Pratt and Krupp, 2004; Pan et al., 2015). A viable alternative for the design of soft robots is represented by smart materials like shape memory alloys (Laschi et al., 2012; Cianchetti et al., 2015; Villoslada et al., 2015), shape memory polymers (Shen et al., 2016), or electro-active polymers (Shintake et al., 2015; Godaba et al., 2016). Among those materials, dielectric elastomers (DEs) represent a class of electro-active polymers which appear to be particularly suitable for soft robotics applications. This is due to a unique combination of features such as large deformations, high flexibility, lightweight, low power consumption, and self-sensing (Carpi et al., 2008).

A DE consists of a stretchable elastomer membrane that is sandwiched between two compliant electrodes. By applying high voltage to this soft capacitive structure, the charges distributing on the electrodes lead to a voltage-induced stress in the material typically referred to as Maxwell stress. The Maxwell stress, denoted by σ_M, can be quantified as follows

$$\sigma_M = -\varepsilon_0 \varepsilon_r E^2 = \varepsilon_0 \varepsilon_r \left(\frac{v}{z}\right)^2, \tag{1}$$

where ε_0 and ε_r denote the vacuum permittivity and the DE relative permittivity, respectively, E is the electric field in the DE material, v is the voltage applied between the electrodes, and z is the DE membrane thickness. As a result of the Maxwell stress, the DE membrane reacts with a reduction in thickness and, due to the incompressibility of the material, with an expansion of surface area (see **Figure 1A**). Both effects can be used to create the motion of an actuator.

To generate a stroke out of this surface change, a pre-load force must be applied to the DE membrane. This pre-stress can be realized in many different ways, e.g., via a linear spring (He et al., 2010), a bi-stable spring (Hodgins et al., 2013), a permanent magnet (Loew et al., 2018), or also another DE membrane (Cao et al., 2019). The working principle of a DE actuator (DEA) is shown in **Figure 1B**, in which the biasing element (i.e., a linear spring) creates a one-dimensional stroke when the membrane surface increases due to a voltage. The resulting stroke can be used in applications like pumps (Loverich et al., 2006; Carpi et al., 2010), valves (Goulbourne et al., 2004; Giousouf and Kovacs, 2013), or positioners (Jordan and McCarthy, 2011; Hau et al., 2012).

While most of current DE actuator applications operate by performing a one-dimensional stroke only, robotic systems usually require a multi-degree of freedom (MDOF) motion. Different possibilities to realize this motion via DE transducers have been presented in the literature. One common approach is based on converting the in-plane elongation of rolled DEAs into complex motions via the actuator design. In this way, it is possible to move fingers (Jung et al., 2006), legs (Nguyen et al., 2014b), or wings (Lau et al., 2014) of soft robots. Another option consists of exploiting the bending motion of DEAs, which can be realized with rolled actuators (Pei et al., 2004a,b) as well as planar ones (Kofod et al., 2007; Shian et al., 2015a,b). Due to the flexibility and adaptability of DE material, also complex types of bio-inspired motion can be realized, e.g., the swimming of a jellyfish (Godaba et al., 2016) or crawling of worms (Jung et al., 2007). As an alternative way, a MDOF actuation can be generated by patterning several electrodes on a DE membrane (e.g., via screen printing), in such a way that each one of them can be activated individually. Among the different types of MDOF DE configurations presented in the literature, the so-called double cone DEA (DC-DEA) design has been adopted by a number of authors. More specifically, a DC-DEA consists of two circular out-of-plane DEAs pre-stressed against each other. By dividing the electrode of one membrane into two or more segments, the axis of the actuator can be moved in many different ways. An example of DC-DEA with electrodes partitioned in two segments is shown in **Figure 2**. Depending on which combination of electrode segments is activated, vertical, horizontal, or rotational motion can be achieved, see **Figure 2B**. A VHB based actuator with four segments on each membrane is presented by Conn and Rossiter (2012). Stroke along different

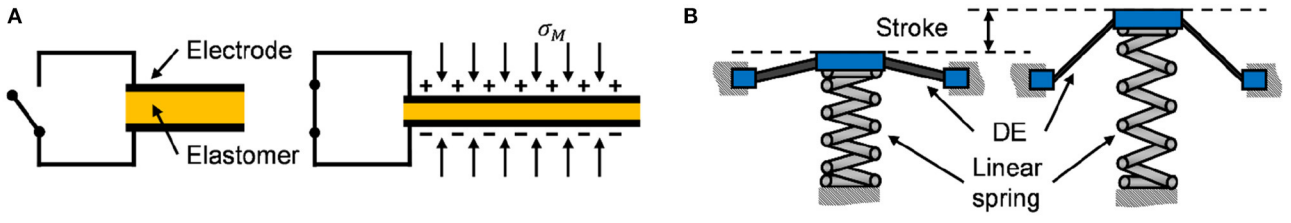

FIGURE 1 | Structure of compliant capacitor and working principle of DE under high voltage activation **(A)**, and example of stroke generation via pre-stressed DEAs **(B)**.

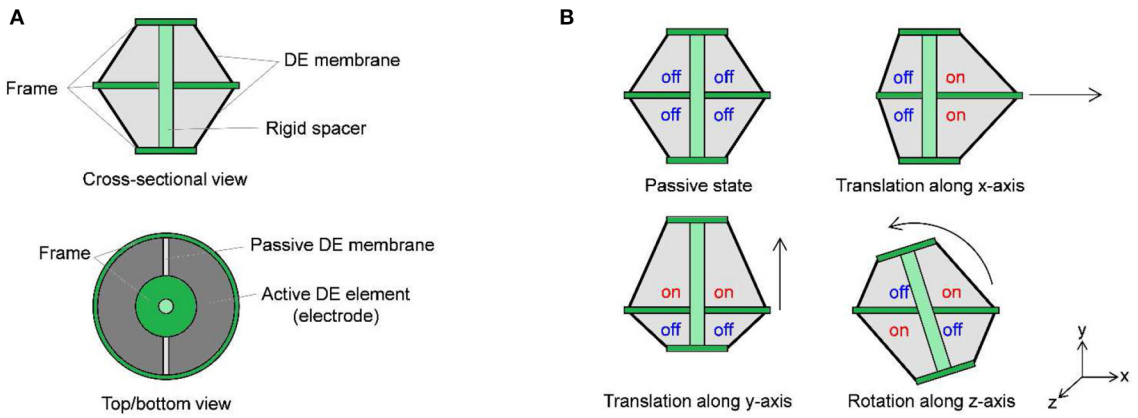

FIGURE 2 | Principle of MDOF motion creation with segmented DE membrane: system cross-sectional and top/bottom views **(A)**, and possible actuation modes **(B)**.

directions, force and moment outputs, as well as the frequency response are characterized by the authors. Choi et al. (2003) designed a MDOF actuator consisting of two DE membranes with four segments each, and illustrated the potential of the DC-DEA for soft robotic systems by building a hexapod robot out of several of similar actuators (Nguyen et al., 2014a). A similar principle is also used by Branz and Francesconi (2016) for developing a DC-DEA with two membranes, segmented into two parts. A finite element model of the system is also developed and experimentally validated. In Cao and Conn (2018), an analytical model has been presented to describe the deformation profile of a DC-DEA. By means of the above model, the authors investigated the effects of geometry and material pre-stretch on the actuator stroke and work output. A dynamic model of a double cone DE vibrissal system, based on combining hyperelasticity theory and Euler-Bernoulli beam equations, is presented in Conn et al. (2012). The model is shown to predict experimental results of the given system in terms of both stroke and deflection.

From the above examples, it can be concluded that many types of DC-DEAs have currently been developed for different applications, each one designed with different materials, configurations, and geometrical parameters. However, there is still a lack of systematic studies on how the different design parameters determine the actuator behavior, e.g., in terms of motion or force range. We remark that, while modeling and design are generally well-understood for simple (i.e., single degree of freedom) DE systems, up to now the literature on MDOF DE actuators lacks systematic experimental studies as well as accurate analytical modeling tools. Once better knowledge on system modeling and characterization is made available, it will allow for better design, optimization, and control of future soft robotics applications, i.e., a tentacle arm which uses many DC-DEAs as modular elements.

The aim of this paper is to understand the relationship between DC-DEA geometry and resulting actuation performance. The overall goal of our research is to use DC-DEAs as constitutive modules for a soft tentacle arm robots. Since the rotational degree of freedom represents the most relevant actuation mode for such application, the relationship between geometry and rotation performance must be properly understood first. Following this goal, in this work we focus on modeling and design optimization of the DC-DEA rotational degree of freedom. To systematically study the effects of geometry on actuator performance, different prototypes are manufactured by changing the inner radius of the membrane as well as the length of the spacer between the two membranes. For each one of them, the maximum rotation angle is examined. The collected data are subsequently used to develop a dynamic model of the soft robotic structure. The presented model shares some similarities with to the one in Conn et al. (2012). However, to obtain a systematic description of the structure non-linearities and electro-mechanical coupling in a control-oriented fashion, a different approach based on the Euler-Lagrange framework is pursued in our work. A control-oriented model is preferred over a finite element one, since it allows for fast parameter identification and numerical simulations. Furthermore, it also provides a framework for the development of future control algorithms. The developed model is then calibrated and used to perform a theoretical parametric study. Based on the results of the numerical simulations, an optimized prototype with improved rotation angle is manufactured. These investigations will provide a basic understanding of the actuator element that is necessary for the development of future robot arms.

The remainder of this paper is organized as follows. In section Design of the MDOF DE Actuation Module, the design of the DE membranes as well as of the overall MDOF actuator is described. In section System Modeling, the simulation model is presented. The experimental setup is presented in section Experimental Characterization and Model Validation, together with the results of the angle measurement and the validation of the simulation model. After that, a parameter simulation is used to optimize the DEAs geometry in terms of the maximum rotation angle, and the performance of the resulting prototype are evaluated in section Actuator Optimization. Finally, section Conclusions provides a final discussion and discusses possible future research directions of the presented work.

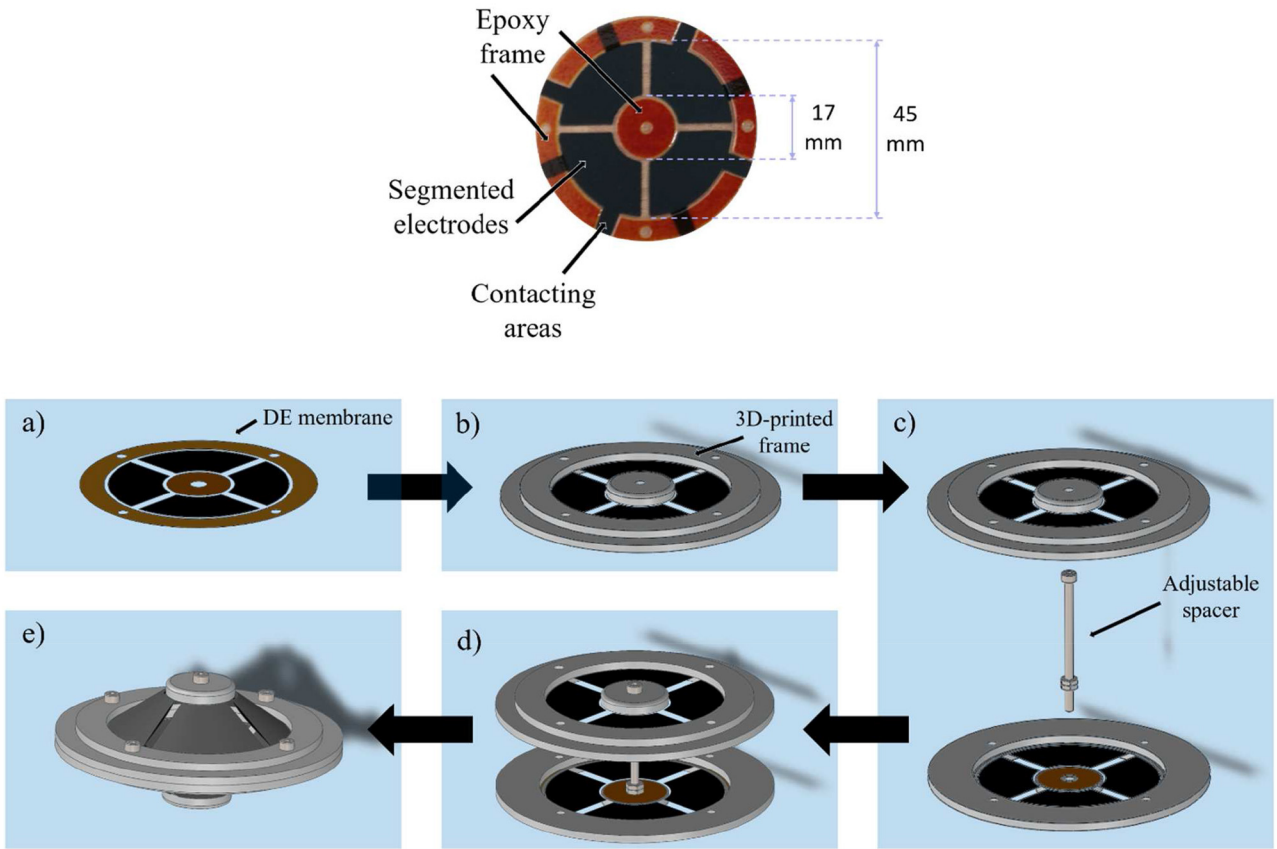

FIGURE 3 | Upper part: picture of the screen printed DE membrane with epoxy frame (orange parts). Lower part: mounting of the DC-DEA, DE membrane **(a)**, adding of 3D-printed frame **(b)**, placing of rigid spacer **(c)**, connecting at inner actuator part **(d)**, and outer actuator diameter **(e)**.

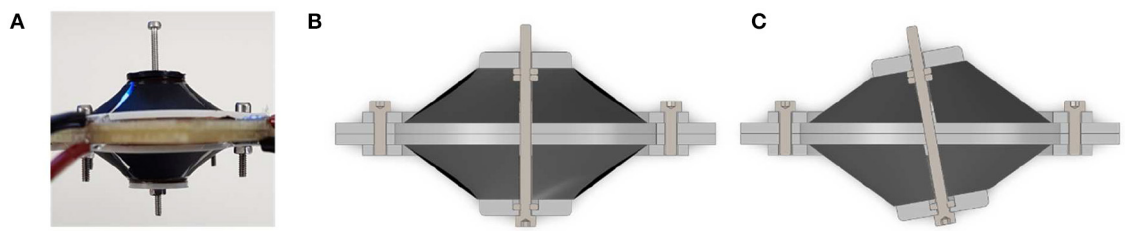

FIGURE 4 | Picture of assembled actuator with $r_i = 8.5$ mm and adjustable start deflection d **(A)**, CAD section view of actuator assembly without exitation voltage **(B)**, and with excitating the opposite membranes to create a rotational motion **(C)**.

DESIGN OF THE MDOF DE ACTUATION MODULE

To generate the desired MDOF actuation, a DC-DEA is chosen in this work. The system consists of two circular out-of-plane DE membranes pre-stressed against each other via a rigid spacer. A picture of the adopted circular DE membrane is shown in **Figure 3**, upper part. For the considered design, outer and inner diameters are equal to 45 and 17 mm, respectively. Carbon black electrodes are screen-printed on a 50 µm silicone membrane (Wacker Elastosil 2030), bi-axially pre-stretched by 10%. The active electrode area of each DE membrane is divided into four equal segments, which can be activated independently. To allow the membrane to deform out-of-plane, an epoxy frame is applied at both outer and inner circumferences (orange parts in **Figure 4**). It is pointed out that the overall membrane design is similar to other actuators presented in literature (e.g., Choi et al., 2003; Conn and Rossiter, 2012; Branz and Francesconi, 2016). Differently from the mentioned works, however, the DE material adopted in our paper is silicone, rather than VHB. As a result, it is expected that it provides different performance in terms of maximum stretch and viscoelastic losses.

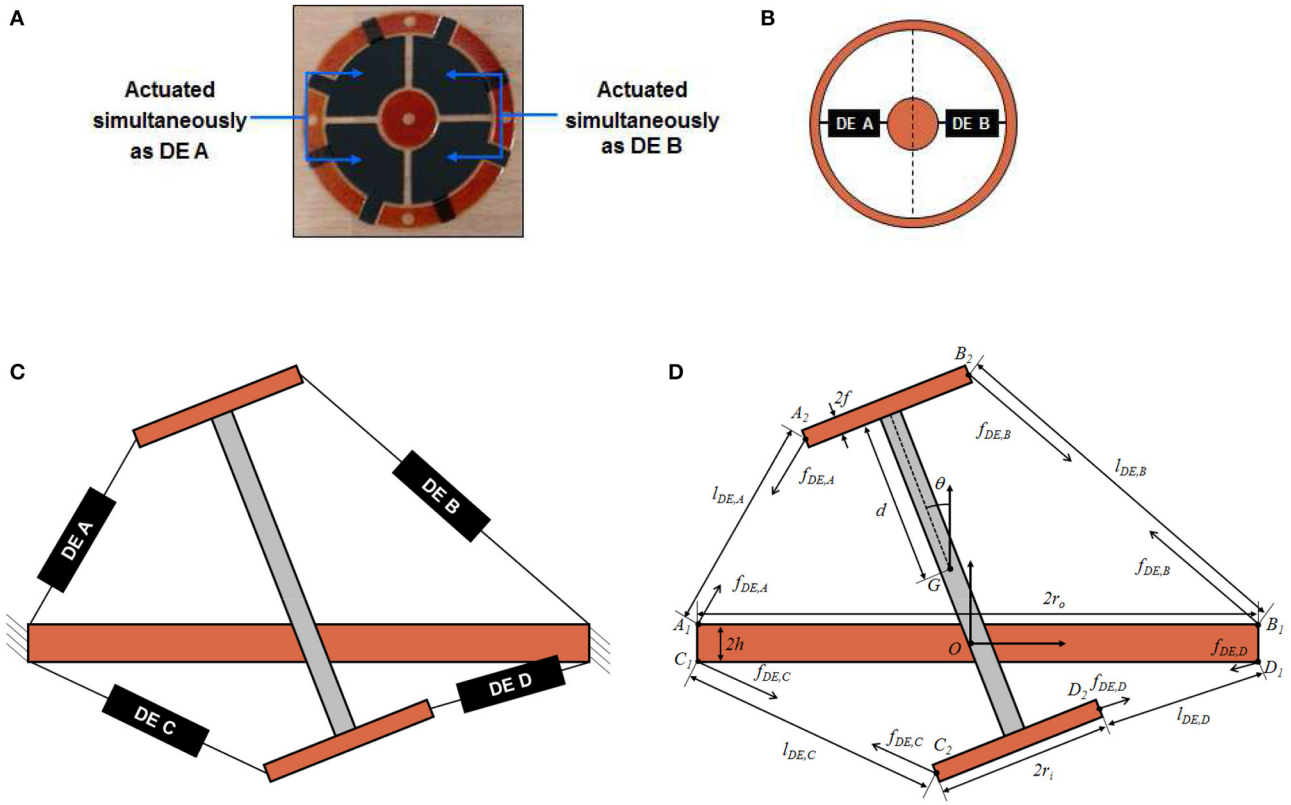

FIGURE 5 | Circular DE membrane activation for in-plane rotation, upper view **(A)**, and equivalent lumped representation **(B)**. Cross-sectional sketch of DC-DEA **(C)**, and equivalent structure model which highlights all geometrical parameters **(D)**.

To assemble the whole system, 3D-printed circular frames are added at both outer and inner diameters of the membrane (lower part of **Figures 3a,b**). After that, a rigid spacer is implemented by means of a screw placed between the actuator halves (**Figure 3c**), and then the two inner parts of both membranes are rigidly connected via the spacer (**Figure 3d**). Finally, the two outer diameters are joined together with a rigid ring element which, in turn, is connected to a fixed frame (**Figure 3e**). Due to the flexibility of the DE membranes, the rigid spacer is allowed to move with respect to the rigid outer frame (see **Figure 4**). **Figure 4** shows also the rigid connector in details, and also highlights the screw which allows to modify the spacer length.

When pre-strained out of plane by the rigid spacer, each DE membrane is subject to a radial pre-loading force which depends on the system geometry (i.e., inner diameter, outer diameter, rigid spacer length), as well as by the type of DE material. For the considered cone DE geometries, the existence of such a pre-load is fundamental for the generation of an actuation stroke. Without electrical activation, and provided that gravitational effects are negligible compared to DE elasticity (due to the lightweight structure), the pre-load forces induced by each segment onto the rigid spacer are approximately the same. As a result, at equilibrium the rigid spacer rests in the middle of the two membranes, directed orthogonally to the plane containing the outer rigid frames. By applying high voltage to an electrode segment, the corresponding membrane portion tends to increase its surface as a consequence of the Maxwell stress. This effect creates a mismatch between pre-loading forces, which results into the rigid spacer moving to a new equilibrium configuration. Depending on which combinations of DE segments are activated simultaneously, different actuation modes can be achieved, similarly to **Figure 2B**. Note, however, that in this case the existence of eight independent actuation variables (four for each membrane) makes it possible to control 5 degrees of freedom (translation along three axes and rotation along two axes) of the rigid spacer, allowing to also achieve more complex motion patterns than simple in-plane translation and rotation.

SYSTEM MODELING

To better understand the relationship between system geometry and actuation performance, a control-oriented model of the DC-DEA is developed in this section. Since in this work we primarily focus on the in-plane rotation angle, the model is restricted to the in-plane motion, implying that only four independent actuation variables exist (corresponding to pairs of adjacent electrode segments). To this end, we consider the sketch of the DC-DEA shown in **Figure 5A**. Each pair of adjacent DE segments is represented by an equivalent lumped DE element, placed in the

middle of the corresponding membrane segment (see **Figure 5B**). Based on this equivalent representation of the DE membranes, a cross-sectional view of the complete DC-DEA is shown in **Figure 5C**. Note that four equivalent membranes appear in this picture, labeled as DE A (upper-left), DE B (upper-right), DE C (lower-left), and DE D (lower-right), respectively.

It is assumed that the deformation state of each membrane can be completely described by the distance between the points connecting the equivalent DE element and the rigid parts of the structure (i.e., inner circle and outer frame in **Figure 5B**). As a result, the force provided by each DE is assumed to be a function of the distance between those points, as well as the applied voltage. We point out that this kind of simplifying assumption is common when modeling single-DOF cone DE membrane in a control-oriented fashion (Rizzello et al., 2015). This modeling choice is therefore needed in order to treat each DE membrane as a lumped element.

Based on the above considerations, each DE element can be replaced with an equivalent force, acting along the line connecting the membrane attachment points. A sketch of the resulting system is then shown in **Figure 5D**. The relevant geometric quantities appearing in **Figure 5D** are listed in the following:

- r_i: DE membrane inner radius;
- r_o: DE membrane outer radius;
- d: half length of the rigid spacer;
- h: half thickness of the frame connecting the two membranes;
- f: half thickness of the frame connecting the rigid spacer to the inner frame of each membrane;
- O: origin of a fixed right-handed reference frame, attached to the geometric center of the frame connecting the two membranes, and oriented such that the y-axis is orthogonal to the ground;
- $K_1 = [K_{1x}\ K_{1y}]^T$, $K \in \{A, B, C, D\}$: position of attachment point between DE membrane K and outer frame connected to a fixed reference, measured with respect to the frame having origin in O;
- $K_2 = [K_{2x}\ K_{2y}]^T$, $K \in \{A, B, C, D\}$: position attachment point between DE membrane K and inner frame connected to the rigid spacer, measured with respect to the frame having origin in O;
- $G = [G_x\ G_y]^T$: position of the center of mass of the rigid spacer, measured with respect to the frame having origin in O;
- θ: rotation angle of the rigid spacer with respect to its center of mass;
- $l_{DE,K}$, $K \in \{A, B, C, D\}$: equivalent length of DE membrane K.

Based on the above discussion, DE membranes and structure can be treated as two interconnected systems. In the following, independent models are developed for both structure and DEs. Afterwards, a proper interconnection among those parts if performed, leading to an electro-mechanically coupled model of the complete system.

Structure Model

To model the structure, a Lagrangian approach is pursued in this work (Goldstein et al., 2002). The goal is to develop a general modeling framework which can be used for both system analysis, simulation, and control. Note that the only moving part of the system is the rigid spacer, which can be considered as an unconstrained rigid body. For the in-plane motion case, only three independent variables are necessary to describe the system configuration, which are conveniently chosen as G_x, G_y, and θ. The overall system Lagrangian, denoted by $\mathcal{L}$, is given as a function of the independent variables as follows

$$\mathcal{L} = \frac{1}{2} m \left(\dot{G}_x^2 + \dot{G}_y^2 \right) + \frac{1}{2} I \dot{\theta}^2 - mgG_y. \tag{2}$$

The terms appearing on the right-hand side of (2) represent the translational kinetic energy of the spacer, the rotational kinetic energy of the spacer, and the negated gravitational potential energy of the spacer, respectively. Quantities m and I resent the rigid spacer mass and moment of inertia with respect to the center of mass, respectively. Based on (2), the equations of motion are given as follows

$$\frac{d}{dt}\frac{\partial \mathcal{L}}{\partial \dot{G}_x} - \frac{\partial \mathcal{L}}{\partial G_x} = \tau_{Gx} \ \rightarrow \ m\ddot{G}_x = \tau_{Gx}, \tag{3}$$

$$\frac{d}{dt}\frac{\partial \mathcal{L}}{\partial \dot{G}_y} - \frac{\partial \mathcal{L}}{\partial G_y} = \tau_{Gy} \ \rightarrow \ m\ddot{G}_y + mg = \tau_{Gy}, \tag{4}$$

$$\frac{d}{dt}\frac{\partial \mathcal{L}}{\partial \dot{\theta}} - \frac{\partial \mathcal{L}}{\partial \theta} = \tau_{\theta} \ \rightarrow \ I\ddot{\theta} = \tau_{\theta}, \tag{5}$$

where τ_{Gx}, τ_{Gy}, and τ_{θ} represents the generalized forces. Note that, while G_x and θ are only affected by the corresponding generalized forces, an additional contribution due to gravity can be observed in the equation describing the dynamics of G_y.

DE Membranes Model

The DE membranes model relates the force of each DE, denoted as $f_{DE,K}$ in **Figure 5D**, to the corresponding membranes lengths $l_{DE,K}$ and applied voltage $v_{DE,K}$, for $K \in \{A, B, C, D\}$. In principle, modeling of the DE behavior is challenging due to the large deformation, strong non-linearities, and rate-dependent effects exhibited by the material. To keep the mathematical complexity of the model sufficiently simple, we assume that the force of membrane K only depends on deformation and voltage of the same membrane, thus neglecting neighboring effects among different segments of the same DE. As a result, the overall model of the four DE membranes can be expressed as four independent models in the following form

$$f_{DE,K} = f_{DE,K}\left(l_{DE,K}, v_{DE,K}\right), \ \ K \in \{A, B, C, D\}. \tag{6}$$

By using the results in Rizzello et al. (2015), DE length $l_{DE,K}$, force $f_{DE,K}$, and voltage $v_{DE,K}$ can be normalized into radial stretch $\lambda_{DE,K}$, true radial stress $\sigma_{DE,K}$, and true electric field $E_{DE,K}$, as follows

$$\lambda_{DE,K} = \frac{l_{DE,K}}{r_o - r_i}, \tag{7}$$

$$\sigma_{DE,K} = \frac{2\lambda_{DE,K}}{\pi z_0 \left(r_0^2 - r_i^2\right)} f_{DE,K}, \tag{8}$$

$$E_{DE,K} = \frac{\lambda_{DE,K}}{z_0} v_{DE,K}, \tag{9}$$

where z_0 is the thickness of the cone DE membrane in undeformed configuration. Since the model description is based on true radial stress and true electric field, rather than on nominal ones, it allows to predict how those quantities change according to the current membrane geometry and deformation. Once these quantities are available, a constitutive DE material model can be expressed, in first approximation, as follows (Rizzello et al., 2015)

$$\sigma_{DE,K} = \sum_{i=1}^{N} \left(\beta_i \lambda_{DE,K}^{\alpha_i} - \gamma_i \lambda_{DE,K}^{-\alpha_i} \right) - \varepsilon_0 \varepsilon_r E_{DE,K}^2 + \eta_{v0} \dot{\lambda}_{DE,K}, \tag{10}$$

where α_i, β_i, γ_i, $i = 1,\ldots, N$, are constitutive parameters describing a modified N-th order Ogden model, and η_{v0} represents a viscoelastic damping coefficient. Clearly, the same material parameters will be used to describe each one of the four membranes. Note that Equation (10) is described in terms of radial stretch only, since for cone DEAs undergoing homogeneous deformations it is typically to assume that a constant circumferential stretch (Rizzello et al., 2015) (pure-shear assumption).

Overall System Model

Independent models for both structure and DE membranes were developed in the previous section. On the one hand, the structure model expressed by Equations (3)–(5) receives generalized forces τ as input, and returns Lagrangian parameters q as outputs, where

$$q = \begin{bmatrix} G_x & G_y & \theta \end{bmatrix}^T, \tag{11}$$

$$\tau = \begin{bmatrix} \tau_{Gx} & \tau_{Gy} & \tau_\theta \end{bmatrix}^T. \tag{12}$$

On the other hand, the DE model given by Equations (6)–(10) makes use of DE lengths l_{DE} and DE voltages v_{DE} to compute the DE forces f_{DE}, where

$$l_{DE} = \begin{bmatrix} l_{DE,A} & l_{DE,B} & l_{DE,C} & l_{DE,D} \end{bmatrix}^T, \tag{13}$$

$$v_{DE} = \begin{bmatrix} v_{DE,A} & v_{DE,B} & v_{DE,C} & v_{DE,D} \end{bmatrix}^T, \tag{14}$$

$$f_{DE} = \begin{bmatrix} f_{DE,A} & f_{DE,B} & f_{DE,C} & f_{DE,D} \end{bmatrix}^T. \tag{15}$$

Since both models are expressed in terms of a different set of force-displacement coordinates, a direct interconnection between the two is not possible. However, suitable coordinate transformations can be introduced to relate θ to l_{DE} and f_{DE} to τ, respectively, so that a consistent coupling among the two subsystems can be effectively achieved.

As a first step, we determine the relationship between θ and l_{DE} by means of a kinematic model. Based on **Figure 5D**, the coordinates of points A_1, A_2, B_1, B_2, C_1, C_2, D_1, D_2 with respect to fixed origin O can be computed as functions of q, as follows:

$$A_1 = \begin{bmatrix} -r_o \\ h \end{bmatrix}, \tag{16}$$

$$A_2(q) = \begin{bmatrix} G_x - (d+f)\sin\theta - r_i\cos\theta \\ G_y + (d+f)\cos\theta - r_i\sin\theta \end{bmatrix}, \tag{17}$$

$$B_1 = \begin{bmatrix} r_o \\ h \end{bmatrix}, \tag{18}$$

$$B_2(q) = \begin{bmatrix} G_x - (d+f)\sin\theta + r_i\cos\theta \\ G_y + (d+f)\cos\theta + r_i\sin\theta \end{bmatrix}, \tag{19}$$

$$C_1 = \begin{bmatrix} -r_o \\ -h \end{bmatrix}, \tag{20}$$

$$C_2(q) = \begin{bmatrix} G_x + (d+f)\sin\theta - r_i\cos\theta \\ G_y - (d+f)\cos\theta - r_i\sin\theta \end{bmatrix}, \tag{21}$$

$$D_1 = \begin{bmatrix} r_o \\ -h \end{bmatrix}, \tag{22}$$

$$D_2(q) = \begin{bmatrix} G_x + (d+f)\sin\theta + r_i\cos\theta \\ G_y - (d+f)\cos\theta + r_i\sin\theta \end{bmatrix}. \tag{23}$$

The overall kinematic model is then given as follows

$$l_{DE}(q) = \begin{bmatrix} l_{DE,A}(q) \\ l_{DE,B}(q) \\ l_{DE,C}(q) \\ l_{DE,D}(q) \end{bmatrix} = \begin{bmatrix} \|A_2(q) - A_1\| \\ \|B_2(q) - B_1\| \\ \|C_2(q) - C_1\| \\ \|D_2(q) - D_1\| \end{bmatrix}, \tag{24}$$

where $||P_2 - P_1||$ denotes the Euclidean distance between points P_2 and P_1. The complete expression for Equation (24) is rather complex, and thus it is omitted for conciseness.

Once the kinematic model in Equation (24) is available, the principle of virtual works can be used to relate DE forces to generalized forces in an energy consistent way. In particular, since the structure is assumed to be a conservative system, the principle of virtual works implies that

$$f_{DE}^T \delta l_{DE} + \tau^T \delta q = 0. \tag{25}$$

By using Equation (24), and by defining the Jacobian as a 4×3 matrix function as follows

$$J(q) = \frac{\partial l_{DE}(q)}{\partial q} = \begin{bmatrix} \frac{\partial l_{DE,A}(q)}{\partial G_x} & \frac{\partial l_{DE,A}(q)}{\partial G_y} & \frac{\partial l_{DE,A}(q)}{\partial \theta} \\ \frac{\partial l_{DE,B}(q)}{\partial G_x} & \frac{\partial l_{DE,B}(q)}{\partial G_y} & \frac{\partial l_{DE,B}(q)}{\partial \theta} \\ \frac{\partial l_{DE,C}(q)}{\partial G_x} & \frac{\partial l_{DE,C}(q)}{\partial G_y} & \frac{\partial l_{DE,C}(q)}{\partial \theta} \\ \frac{\partial l_{DE,D}(q)}{\partial G_x} & \frac{\partial l_{DE,D}(q)}{\partial G_y} & \frac{\partial l_{DE,D}(q)}{\partial \theta} \end{bmatrix}, \tag{26}$$

Equation (25) can be rewritten as

$$\left(f_{DE}^T J(q) + \tau^T \right) \delta q = 0. \tag{27}$$

To let (27) hold for any independent change of q, the following must be true

$$\tau = -J^T(q) f_{DE}. \tag{28}$$

Equation (28) represents the desired transformation equation.

A causal representation of the complete model can be obtained by combining Equations (3)–(10), (24), (26), and (28). The resulting model considers v_{DE} as independent input, and

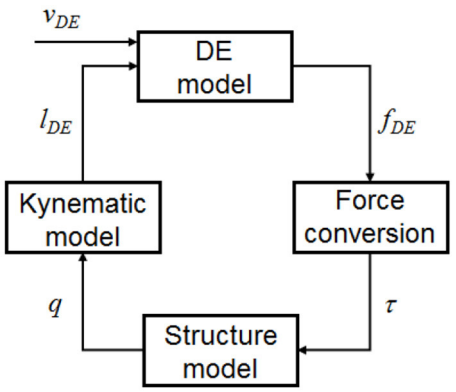

FIGURE 6 | Conceptual block diagram representation of the complete DC-DEA model.

permits to compute q (as well as any other internal variable) as resulting outputs. A conceptual block diagram representation of the overall model, including corresponding coupling terms and transformation equations, is provided in **Figure 6**. For concluding this section, we point out that the DE model in Equation (10) requires not only l_{DE} as mechanical input, but also its time derivative (due to the presence of the stretch rate term). Despite this issue, a causal interconnection between the two dynamic blocks can still be obtained if we consider that

$$\dot{l}_{DE}\left(q,\dot{q}\right) = J\left(q\right)\dot{q}, \tag{29}$$

and that both q and its time derivative are outputs of the structure model. Performing a velocity dependent interconnection based on Equation (29) is straightforward, and does not violate causality during the implementation. Nevertheless, this additional coupling term is not reported explicitly in **Figure 6**, since this figure is intended to represent a conceptual scheme rather than an accurate simulation block diagram.

EXPERIMENTAL CHARACTERIZATION AND MODEL VALIDATION

Experimental characterization of the prototype is performed in this section. Note that the actuator possess many degree of freedom, therefore the characterization of its performance can be achieved in many different ways. For this work we choose to investigate and to validate the simulation model based on the rotational motion, which is described by the rotation angle θ. Since the maximum rotation angle of a single DC-DEA is an important parameter for determining the overall bending of a tentacle arms, it is chosen as the main quantity to be investigated in this work. Data on rotation angle are collected for different geometries, and are subsequently used to calibrate and validate the model developed in section System Modeling.

Experimental Setup and Test Procedure

The aim of this first investigations is the analysis of the achievable rotation angle. A LabView script is used to record a video of the moving actuator as well as to control the actuation. With the NI USB-6343 Multifunction I/O device, a signal between 0 and 10 V is generated and sent to a precision high voltage amplifier (UltraVolt® HVA series 4HVA24-P1) that scales it up to 4 kV. A low-pass filtered step signal is implemented in LabVIEW to precisely control the speed and amplitude of the actuation. After recording a video of the actuator motion with a camera (Pulnix TMC-1405GE), the rotation angle is measured with the help of the edge detection algorithm implemented in Matlab. To improve the accuracy of the rotation angle measurement, the axis of the spacer actuator is extended with an additional rigid element (see **Figure 7**).

In order to obtain a rotational motion, the opposite electrodes are activated with the same amount of high voltage, as shown in **Figure 7**. The non-activated electrodes are always kept at 0 V, to ensure as much symmetry as possible during the rotation.

The excitation signal that is given to the activated membranes is chosen as a step signal, which starts from 0 V and transitions to a high voltage level which depends on the specific geometry. More specifically, to ensure repeatable conditions among the different actuators and also to operate below the breakdown strength of the adopted silicone material, the voltage amplitude is chosen so that when the rigid spacer is not displaced (i.e., $q = 0$) the electric field equals $E_{DE,Max} = 80$ V/μm WackerChemie. An estimation of the voltage required to generate a desired electric field, given a specific actuator geometry, can be obtained by combining Equations (7), (9), (16), (17), and (24), i.e.,

$$v_{DE,Max} = \frac{z_0}{\sqrt{1+\left(\frac{d+f-h}{r_o-r_i}\right)^2}} E_{DE,Max}. \tag{30}$$

Parameter Variation

To study the effect of geometrical parameters on the actuator performance, several prototypes with different values of rigid spacer length and inner radius of the circular DE membrane are designed. The variation of the rigid spacer is implemented by a screw that connects the two rigid inner parts of the membranes (**Figure 4**). In this way, the value of d (i.e., the half of the rigid spacer length) can be varied from 4 to 14 mm with increments of 1 mm. For testing different values of inner radius, three different types of DE membranes are manufactured, having values of r_i of 8.5, 12.5, and 16.5 mm, while r_o is kept constant at 22.5 mm (see **Figure 8**). Different combinations of d and r_i are subsequently tested. The excitation voltage is chosen for each case based on equation (30), with $E_{DE,Max}$ = 80 V/μm.

The steady-state rotation angles measured for all of the designed actuators are shown in **Figure 9**. It can be clearly noted that decreasing leads r_i to a larger rotation angle, at least in the investigated range. Concerning the spacer length, a general decrease in angle is observed for increasing values of d. The maximum achieved angle among all the manufactured actuators equals 2.2 degrees, and corresponds to $r_i = 8.5$ mm and $d = 9$ mm.

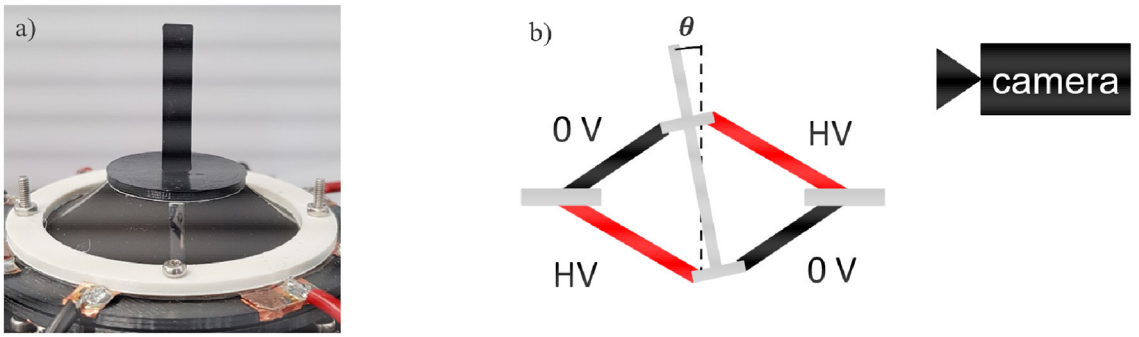

FIGURE 7 | Picture **(a)** and schematic structure **(b)** of the experimental setup for the characterization of the DC-DEA rotation angle.

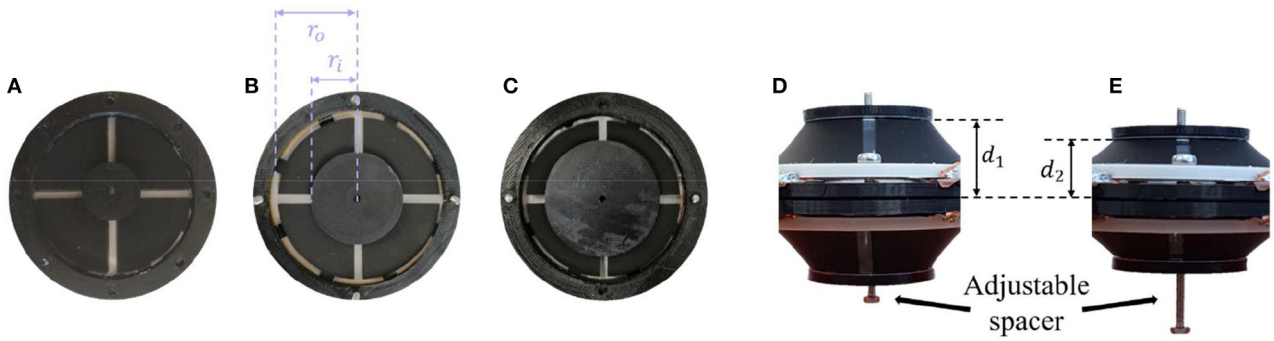

FIGURE 8 | Assembled DE membranes with different inner radii of $r_i = 8.5$ mm **(A)**, $r_i = 12.5$ mm **(B)**, and $r_i = 16.5$ mm **(C)**, and different spacer length d_1 **(D)** and d_2 **(E)**.

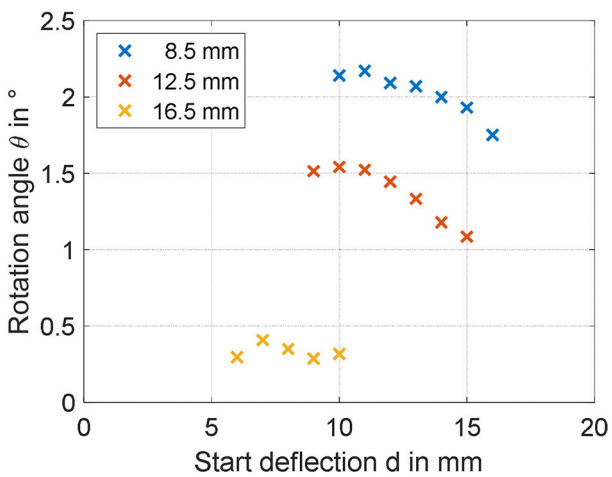

FIGURE 9 | Experimental identification of geometry dependencies on maximum rotation angle for r_i of 8, 12.5, and 16.5 mm.

TABLE 1 | System parameters used for the simulations.

Parameter	Value	Unit	Status
r_o	22.5	mm	Known
h	2	mm	Known
f	0	mm	Known
g	9.807	m/s^2	Known
ε_0	8.854	pF/m	Known
ε_r	2.8	–	Identified
α_i	[2, 4]	–	Identified
β_i	[1.707, −0.023]	MPa	Identified
γ_i,	[1.298, −0.955]	MPa	Identified
η_{v0}	0.2	MPa·s	Identified

Validation of the Simulation Model

By inspecting the results in **Figure 9**, it can be expected that the maximum angle can be increased by reducing both r_i and d. To better quantify the effect of both parameters, the simulation model developed in section System Modeling is calibrated based on the collected steady-state measurements. Some of the system parameters can be measured or estimated with sufficiently high accuracy, i.e., the geometrical and inertial ones, and are reported in **Table 1**. Values of m and I differ for each experiment, and are not explicitly reported for conciseness. More specifically, among the many experiments, m ranges within 2.5 and 9.1 g, while I varies within 0.17 and 2.14 kg·mm^2. The parameters which need to be identified represent the DE constitutive parameters, i.e., α_i, β_i, γ_i, $i = 1,\ldots, N$, ε_r, and η_{v0}.

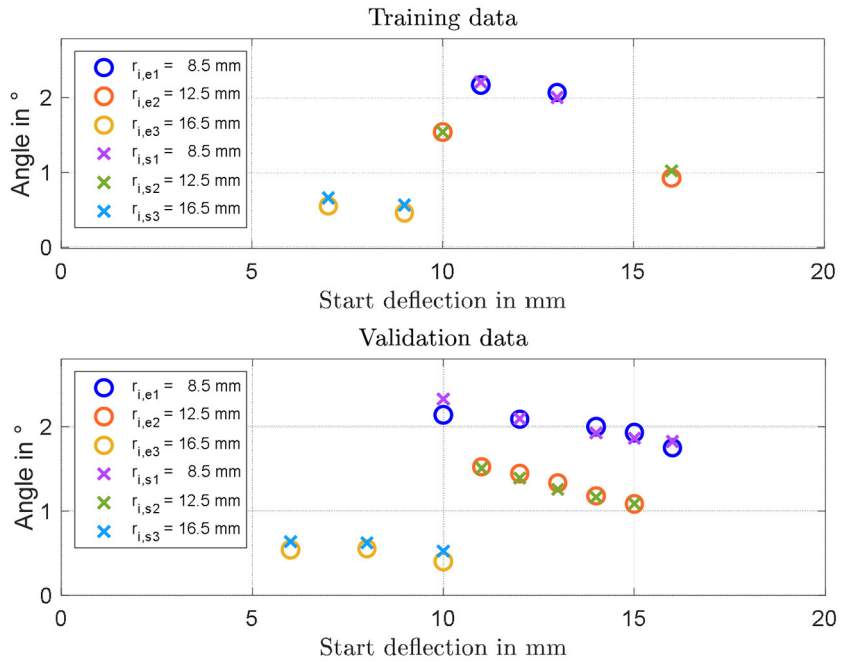

FIGURE 10 | Results of model identification and calibration **(Upper part)**, and experimental validation **(Lower part)**. In each figure, circles represent experiments and crosses represent model predictions.

Among those parameters, ε_r is selected equal to 2.8 according to the material producer datasheet, while the other ones are calibrated based on a non-linear least square method. For identification purpose, the 19 performed experiments, each one corresponding to a different DC-DEA geometry, are split into a training set and a validation set. The training set consists of six randomly selected experiments, 2 for each r_i, which are used to calibrate all the unknown model parameters. The result of this calibration is shown in the upper part of **Figure 10**. After calibration, the remaining 13 experiments are used for the model validation purpose. The results of the validation are shown in **Figure 10**, lower part. It can be seen that the simulation model well-predicts the rotation angle of the DC-DEA for each of the considered geometries, despite the calibration being performed only with 30% of the collected data. As a result, we conclude that the developed model permits a satisfactory extrapolation of results. In **Figure 10**, measured data are reported as circles, while calibration (upper part) and validation data (lower part) are represented as crosses. Finally, the stress-stretch curves of the optimized DE material model is shown in **Figure 11**, for both $E = 0$ V/μm and $E = 80$ V/μm.

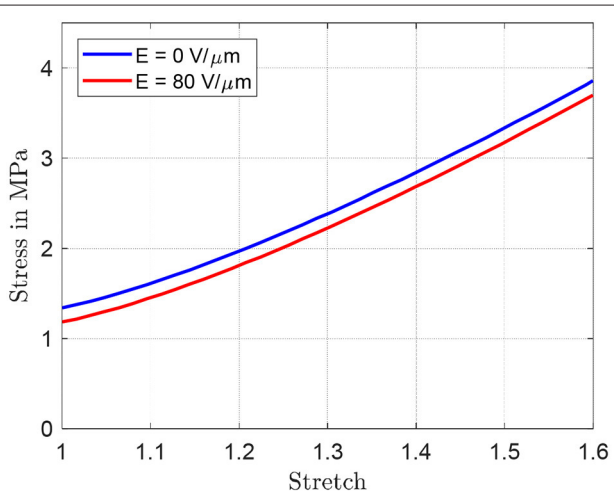

FIGURE 11 | Optimized DE material model.

ACTUATOR OPTIMIZATION

The validation procedure described in the previous section highlighted the ability of the developed model in predicting the steady-state response for different geometrical configurations. This fact will be used in the present section to perform a parameter study which, in turn, will be exploited to optimize the design of the structure for achieving high rotation angle. Torque performance is not considered in here, since in this study we are mostly interested in kinematic optimization of soft tentacle arms.

Parameter Study

The simulation model characterized in section Validation of the Simulation Model is here used to study the effect the two investigated parameters. The range of both inner radius and start

deflection is extended with respect to the previous measurements, to see for which values of parameters the rotation angle can be increased in a meaningful way. **Figure 12** shows the results of the simulation for values of r_i ranging from 2 to 7 mm, and d varying between 4 and 18 mm. Since from studies conducted in section Experimental Characterization and Model Validation, it is observed that the value of m has a low impact on the steady performance, no gravitational force is considered for this study, making the resulting actuator motion completely symmetric. From **Figure 12**, it is clearly visible that the rotation angle can be significantly affected by changing the geometry of the actuator. According to the model, a smaller start deflection in combination with a small inner radius increases the rotation angle of the actuator in the range around 10 degrees. Rotational actuator motions in this range allows to significantly improve the effectiveness of the considered actuator for different application scenarios. As a final remark, note that the start deflection defines both the moment lever arm and the pre-stress in the material at the same time. This relationship is highly complex to quantify, due to both structure and DE material non-linearities. It is reasonable to assume that the maximum observable in **Figure 12** represents indeed the optimal trade-off between all those effects, which leads to the maximum resulting rotation angle θ.

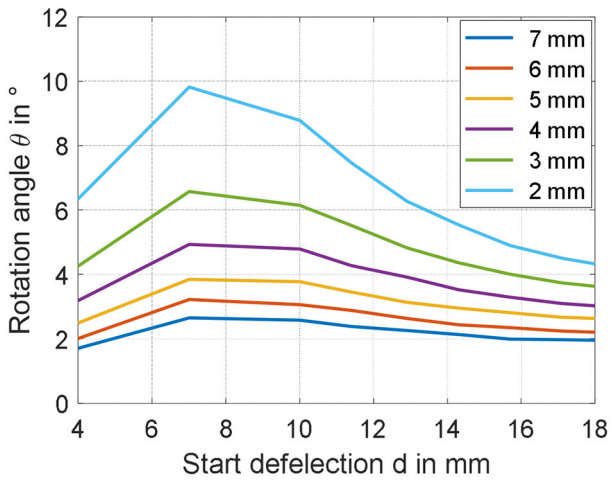

FIGURE 12 | Parameter studies showing the appreciable increase of the rotation angle by decreasing the inner radius r_i as well as the start deflection d.

Optimized Actuator Design

Based on the results of the previous sections, novel prototypes are realized and tested. According to the results in **Figure 12**, the rotation angle can be maximized by reducing the inner radius r_i as much as possible, and by setting the spacer parameter $d = 7$ mm. For practical manufacturability, a compromise value of 2 mm is selected for r_i. Corresponding to this inner radius, three different values of d are tested, i.e., 4 mm (corresponding to the smallest possible spacer length), 7 mm (corresponding to the theoretical maximum angle), and 10 mm (assuming also a value for θ near the maximum). To manufacture membranes having inner radius equal to 2 mm, a novel DE membrane lacking the epoxy frame in the middle is screen-printed (**Figure 13A**). The resulting DC-DEAs are then assembled according to the required geometries, with one example shown in **Figure 13B** (i.e., for $d =$ 10 mm).

Once again, the axis of the rigid spacer is extended to measure the rotation angle generated by the application of a filtered step voltage, given by Equation (30) with $E_{DE,Max} =$ 80 V/μm. The obtained angles are shown in **Figure 14** (upper part), marked as yellow crosses, and equal 7.47 degrees for $d = 4$ mm, 9.60 degrees for $d = 7$ mm, and 6.62 degrees for $d = 10$ mm, respectively. Compared to previous experiments, in which the maximum rotation angle was of 2.2 degrees, a significant improvement can be appreciated. In particular, the 9.60 degrees rotation observed for $d = 7$ mm is sufficiently close to the model prediction, of about 9.80 degrees (error of 2%). Lower, bust still overall satisfactory accuracy is observed for $d = 4$, in which the experimental measurement of 7.47 degrees is sufficiently closed to the simulated angle of 6.35 degrees (error of 15%). For the start deflection of $d = 10$ mm, however, the measured rotation angle of 6.62 deviates from the predicted value

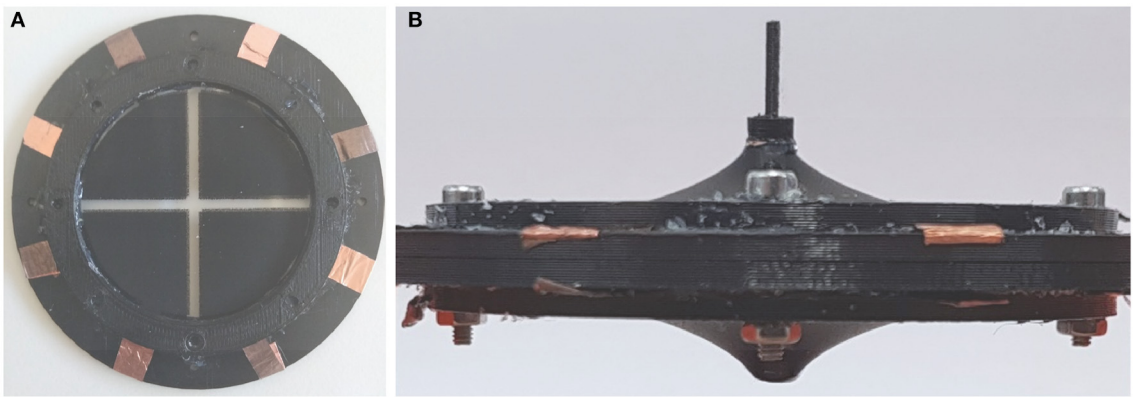

FIGURE 13 | Adapted DE membrane **(A)** and optimized actuator with $r_i = 2$ mm and $d = 10$ mm **(B)**.

of about 8.80 degrees of a more significant amount (error of 25%). The reasons for those inaccuracies may be due to several factors, which are discussed in the following.

First, we point out that the gravity force has been neglected when performing the analysis in section Parameter Study. While it can be safely neglected for the calibration and validation experiments, in which the DE pre-stretch is sufficiently high, this may not be true for the optimized geometries corresponding to barely stretched membranes, i.e., for $d = 4$ mm. Another possible reason for the observed inaccuracy is the unavoidable deviation of the membrane from the ideal cone shape, which is particularly critical for small r_i and large d. For the optimized design, this fact is especially true for the two actuators with $d = 10$ mm, and is also clearly visible in **Figure 13**, where the shape of the membrane is more curved instead of cone-shaped. Despite modeling of such a behavior has already been investigated in the literature, the resulting constitutive relationships are based on spatially-dependent differential equations which appear as unsuitable for our scope (He et al., 2010). Better accuracy could be potentially achieved by employing a more accurate, yet more complex, dynamic model describing the DE material which also accounts for membrane necking in a control-oriented fashion, e.g., an extension of the work in (Rizzello et al., 2018) for cone-shaped geometries. Finally, to understand even more the potential reasons for the observed inaccuracy, both measured and predicted angles are plotted as a function of maximum DE radial stretch λ_1 in unacted condition, instead of d. The maximum DE radial stretch is computed by combining Equations (7) and (16)–(24), and is based on the current geometric parameters d and r_i as well as on the maximum simulated angle. The resulting plot is shown in **Figure 14**, lower part. As it can be observed, the last set of designs lie in a region of low stretch, in which no calibration and validation data are available. As a result, we conclude that despite the model is capable of accurately predict the effect of different geometries in the calibration stretch range, some issues arise when trying to extrapolate the results. It can be foreseen that the improvement of the calibration process, with additional data for lower stretches, can lead to better model predictions.

Despite the issues pointed out above, it can be noted that the error between predicted and measured angles never exceeds 25% for all of the considered optimized designs. Furthermore, it can be observed that the value of the angle is increased of about 4 times compared to the initial designs. As a result, we deduce that performance improvement is still successfully achieved.

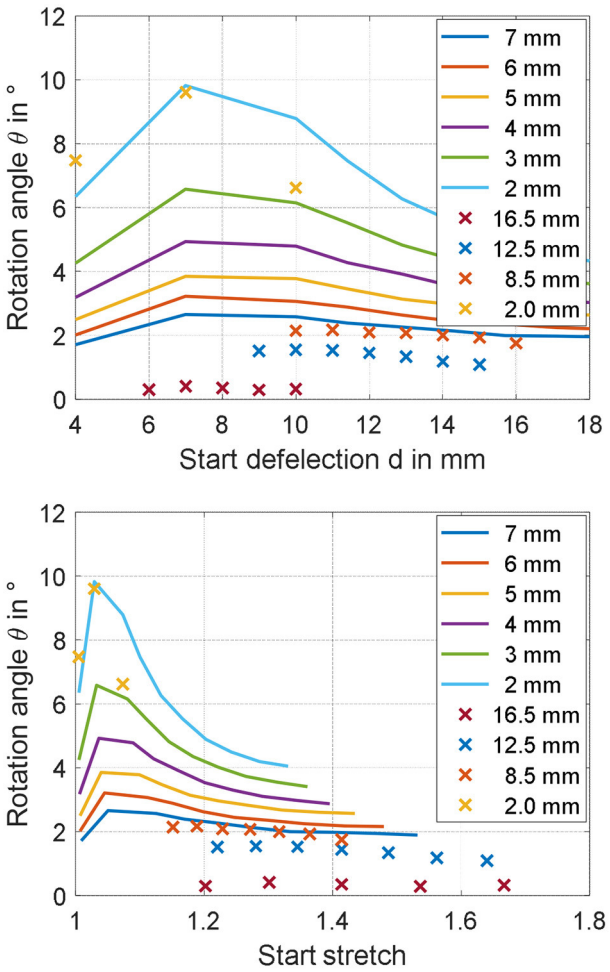

FIGURE 14 | Predicted (continuous lines) and measured (crosses) rotation angles for different r_i, represented as functions of start deflection d **(Upper part)**, and material stretch λ_1 **(Lower part)**.

CONCLUSIONS

In this work, characterization, modeling, and design optimization of a multi degree-of-freedom dielectric elastomer actuator system for soft robotic applications has been presented. The performed investigation has shown the influence of geometrical scaling on the motion behavior of the DE actuator, expressed in terms of in-plane rotation angle. A control-oriented model has been developed and validated based on the collected data, and has shown a good capability in predicting the achieved angle for different geometrical configurations. The maximum angle achieved with the first set of DC-DEAs is 2.2 degrees, corresponding to the smallest of the three radii (8.5 mm) and a start deflection of 9 mm. Based on the developed model, the effect of geometry on actuation performance have been investigated. As a result of this numerical analysis, an optimized DC-DEA is then assembled. The optimized actuator has been designed with $r_i = 2$ mm and $d = 7$ mm, and has allowed to achieve a maximum angle of 9.60 degrees with an error between simulations and experiments of 2%. It has been observed, however, that for some of the theoretical optimal geometries the model fails in providing accurate predictions. An error of 15% for $d = 4$ mm, and an error of 25% of $d = 10$ mm, is observed, respectively. This is mostly due to some simplifying assumptions made when developing the model, as well as due to limitation in the data calibration set. Therefore, for future works, more extensive modeling efforts and experimental campaigns will be required for achieving a more accurate scaling prediction. Despite this fact, the first attempt to improve the performance via model-based predictions presented in this paper has led to an overall positive outcome, since the

overall maximum angle has been increased from the original value of 2.2 degrees up to 9.60 degrees. As a final remark, we point out that the obtained angle appears smaller than the ones typically obtained by other authors dealing with DC-DEAs, which is typically larger than 10 degrees (usually in the range between 20 and 30 degrees). While most of the authors have used VHB acrylic-based DE materials, in our work we have performed one of the first attempts to develop, model, and optimize a silicone-based DE soft robot. Despite performance comparisons between silicone and VHB materials for DEs are normally conducted for simple actuator configurations, the high non-linearity of the presented structure makes it difficult to quantitatively foresee how such performance difference is reflected into rotational DC-DEA motion. For evaluation purpose, we point out that a comparison between different DE materials for a modified DC-DEA design has been presented by Ghilardi et al. (2017). The amount of rotation angle they obtained with silicone is of about 8 degrees for 3.9 kV, corresponding to 89 V/μm. Such a performance appears as consistent with the results obtained in our experiments. We also point out that, while silicone is characterized by a smaller stretch than other elastomers, it also exhibit many attractive characteristics over VHB which include higher bandwidth, smaller viscoelastic loss, less sensitivity to temperature and humidity, and improved manufacturability. Investigating whether it is possible to achieve motion performance comparable to VHB acrylic DEs while keeping all the advantages of silicone DEs will be one of the major challenges of future research.

Among the next fundamental steps, the design of a DC-DEA module with a larger value of r_o will also be considered. In this way, the resulting actuator will have a smaller ratio between inner and outer radii, thus potentially allowing to further increase the rotation angle even more. Additionally, more complex DEA robotic structures will also be considered for the further optimization of the rotation angle. As an example, the rigid spacer can be replaced by an elastic spacer, like a linear spring or even a bi-stable element. Furthermore, other than the in-plane rotation angle, also the translational motion in x- and y-direction, as well as the out-of-plane rotation, will be considered and included in the model. In this way, the design of the DC-DEA can be properly optimized for applications which differ from soft tentacle arms, and thus require more complex actuation patterns. Motion and forces in all three spatial directions will be evaluated with suitable measurement equipment, and then optimized regarding the geometry as well as the properties of the DE and the applied spacer. Finally, with the aid an adapted simulation model, control of the full 3D motion in space will be achieved.

DATA AVAILABILITY STATEMENT

The datasets generated for this study are available on request to the corresponding author.

AUTHOR CONTRIBUTIONS

SN and RB: experimental results and manufacturing. SC: modeling and simulation results. GR: modeling and paper revision. DN and SS: paper revision.

FUNDING

The authors gratefully acknowledge the support of the Deutsche Forschungsgemeinschaft (DFG, German Research Foundation) through Priority Program SPP 2100 Soft Material Robotic Systems (Projects: SE704/6-1, RI3030/1-1).

REFERENCES

Albu-Schaffer, A., Eiberger, O., Grebenstein, M., Haddadin, S., Ott, C., Wimbock, T., et al. (2008). "Soft robotics," in *IEEE Robotics and Automation Magazine,* Vol. 15, 20–30. doi: 10.1109/MRA.2008.927979

Branz, F., and Francesconi, A. (2016). Modelling and control of double-cone dielectric elastomer actuator. *Smart Mater. Struct.* 25, 1–10. doi: 10.1088/0964-1726/25/9/095040

Cao, C., Burgess, S., and Conn, A. T. (2019). Toward a dielectric elastomer resonator driven flapping wing micro air vehicle. *Front. Robot.* 5:137. doi: 10.3389/frobt.2018.00137

Cao, C., and Conn, A. T. (2018). Performance optimization of a conical dielectric elastomer actuator. *Actuators* 7:32. doi: 10.3390/act7020032

Carpi, F., De Rossi, D., Kornbluh, R., Pelrine, R., and Sommer-Larsen, P. (2008). *Dielectric Elastomers as Electromechanical Transducers: Fundamentals, Materials, Devices, Models and Applications of an Emerging Electroactive Polymer Technology.* Amsterdam: Elsevier.

Carpi, F., Menon, C., and De Rossi, D. (2010). Electroactive elastomeric actuator for all-polymer linear peristaltic pumps. *IEEE/ASME Trans. Mechatr.* 15,460–470. doi: 10.1109/TMECH.2009.2028884

Choi, H. R., Jung, K. M., Kwak, J. W., Lee, S. W., Kim, H., Jeon, J. W., et al. (2003). "Multiple degree-of-freedom digital soft actuator for robotic applications," in *Proceedings of SPIE-The International Society for Optical Engineering*, 5051. doi: 10.1117/12.484385

Cianchetti, M., Calisti, M., Margheri, L., Kuba, M., and Laschi, C. (2015). Bioinspired locomotion and grasping in water: the soft eight-arm OCTOPUS robot. *Bioinsp. Biomim.* 10, 1–19. doi: 10.1088/1748-3190/10/3/035003

Conn, A. T., Pearson, M. J., Pipe, A. G., Welsby, J., and Rossiter, J. (2012). "Dielectric elastomer vibrissal system for active tactile sensing," in *Electroactive Polymer Actuators and Devices (EAPAD)* Vol. 8340:83400F. doi: 10.1117/12.915425

Conn, A. T., and Rossiter, J. (2012). Towards holonomic electro-elastomer actuators with six degrees of freedom. *Smart Mater. Struct.* 21:035012. doi: 10.1088/0964-1726/21/3/035012

Ghilardi, M., Boys, H., Busfiled, J., and Carpi, F. (2017). "Double cone dielectric elastmer-driven positioning system," in *EuroEAP17.*

Giousouf, M., and Kovacs, G. (2013). Dielectric elastomer actuators used for pneumatic valve technology. *Smart Mater. Struct.* 22:104010. doi: 10.1088/0964-1726/22/10/104010

Godaba, H., Li, J., Wang, Y., and Zhu, J. (2016). A soft jellyfish robot driven by a dielectric elastomer actuator. *IEEE Robot. Autom. Lett.* 1, 624–631. doi: 10.1109/LRA.2016.2522498

Goldstein, H., Poole, C., and Safko, J. (2002). *Classical Mechanics. AAPT.* New York, NY: Addison-Wesley.

Goulbourne, N. C., Frecker, M. I., and Mockensturm, E. (2004) Electro-elastic modeling of a dielectric elastomer diaphragm for a prosthetic blood pump. *Smart Struct Mater.* 2004, 122–133. doi: 10.1117/12.539818

Hau, S., Rizzello, G., Hodgins, M., York, A., Seelecke, S., and Hau, S. (2012). Design and control of a high-speed positioning system based on dielectric elastomer membrane actuators. *IEEE/ASME Trans. Mechatr.* 26, 25–31. doi: 10.1109/TMECH.2017.2681839

He, T., Cui, L., Chen, C., and Suo, Z. (2010). Nonlinear deformation analysis of a dielectric elastomer membrane–spring system. *Smart Mater. Struct.* 19:085017. doi: 10.1088/0964-1726/19/8/085017

Hodgins, M., York, A., and Seelecke, S. (2013). Experimental comparison of bias elements for out-of-plane DEAP actuator system. *Smart Mater. Struct.* 22:094016. doi: 10.1088/0964-1726/22/9/094016

Jordan, G., and McCarthy, D. (2011). Actuated micro-optical submount using a dielectric elastomer actuator. *IEEE/ASME Trans. Mechatr.* 16, 98–102. doi: 10.1109/TMECH.2010.2089991

Jung, K., Koo, J. C., Do Nam, J., Lee, Y. K., and Choi, H. R. (2007). Artificial annelid robot driven by soft actuators. *Bioinsp. Biomim.* 2, S42–S49. doi: 10.1088/1748-3182/2/2/S05

Jung, M. Y., Nguyen, C. H., Kim, J. W., Koo, I. M., Jung, K. M., Lee, Y. K., et al. (2006). Fabrication and characterization of linear motion dielectric elastomer actuators. *Smart Struct. Mater. 2006 Electroact. Polym. Actuators Devices.* 6168:616824. doi: 10.1117/12.658145

Kofod, G., Wirges, W., Paajanen, M., and Bauer, S. (2007). Energy minimization for self-organized structure formation and actuation. *Appl. Phys. Lett.* 90, 1–4. doi: 10.1063/1.2695785

Laschi, C., Cianchetti, M., Mazzolai, B., Margheri, L., Follador, M., and Dario, P. (2012). Soft robot arm inspired by the octopus. *Adv. Robot.* 26, 709–727. doi: 10.1163/156855312X626343

Laschi, C., Rossiter, J., Iida, F., Cianchetti, M., and Margheri, L. (eds.). (2017). *Soft Robotics: Trends, Applications and Challenges,* Vol. 17. Cham: Springer International Publishing. doi: 10.1007/978-3-319-46460-2

Lau, G. K., Lim, H. T., Teo, J. Y., and Chin, Y. W. (2014). Lightweight mechanical amplifiers for rolled dielectric elastomer actuators and their integration with bio-inspired wing flappers. *Smart Mater. Struct.* 23:025021. doi: 10.1088/0964-1726/23/2/025021

Loew, P., Rizzello, G., and Seelecke, S. (2018). A novel biasing mechanism for circular out-of-plane dielectric actuators based on permanent magnets. *Mechatronics* 56, 48–57. doi: 10.1016/j.mechatronics.2018.10.005

Loverich, J. J., Kanno, I., and Kotera, H. (2006). Concepts for a new class of all-polymer micropumps. *Lab. Chip* 6, 1147–1154. doi: 10.1039/b605525g

Nguyen, C. T., Phung, H., Nguyen, T. D., Lee, C., Kim, U., Lee, D., et al. (2014a). "Biomimetic printable hexapod robot driven by soft actuator," in *2014 11th International Conference on Ubiquitous Robots and Ambient Intelligence (URAI)* (Kuala Lumpur), 189–190. doi: 10.1109/URAI.2014.7057528

Nguyen, C. T., Phung, H., Nguyen, T. D., Lee, C., Kim, U., Lee, D. H., et al. (2014b). A small biomimetic quadruped robot driven by multistacked dielectric elastomer actuators. *Smart Mater. Struct.* 23:065005. doi: 10.1088/0964-1726/23/6/065005

Pan, Y., Guo, Z., Yu, H., Chen, G., and Huang, S. (2015). Human–robot interaction control of rehabilitation robots with series elastic actuators. *IEEE Trans. Robot.* 31, 1089–1100. doi: 10.1109/TRO.2015.2457314

Pei, Q., Pelrine, R., Rosenthal, M. A., Stanford, S., Prahlad, H., and Kornbluh, R. D. (2004b). "Recent progress on electroelastomer artificial muscles and their application for biomimetic robots," in *Proceedings: Smart Structures and Materials 2004: Electroactive Polymer Actuators and Devices (EAPAD)*, Vol. 5385 (San Diego, CA). doi: 10.1117/12.540462

Pei, Q., Rosenthal, M., Stanford, S., Prahlad, H., and Pelrine, R. (2004a). Multiple-degrees-of-freedom electroelastomer roll actuators. *Smart Mater. Struct.* 13, N86–N92. doi: 10.1088/0964-1726/13/5/N03

Pratt, J. E., and Krupp, B. T. (2004). "Series elastic actuators for legged robots," in *Proceedings Volume 5422, Unmanned Ground Vehicle Technology VI* (Orlando, FL). doi: 10.1117/12.548000

Rizzello, G., Hodgins, M., Naso, D., York, A., and Seelecke, S. (2015). Modeling of the effects of the electrical dynamics on the electromechanical response of a DEAP circular actuator with a mass–spring load. *Smart Mater. Struct.* 24:094003. doi: 10.1088/0964-1726/24/9/094003

Rizzello, G., Loew, P., Naso, D., and Seelecke, S. (2018). Analytical modeling of clamped dielectric elastomer strip membranes exhibiting necking effect. *IFAC-PapersOnLine* 51:119. doi: 10.1016/j.ifacol.2018.03.119

Robinson, D. W., Pratt, J. E., Paluska, D. J., and Pratt, G. A. (1999). "Series elastic actuator development for a biomimetic walking robot," in *1999 IEEE/ASME International Conference on Advanced Intelligent Mechatronics* (Atlanta, GA). doi: 10.1109/AIM.1999.803231

Shen, Q., Trabia, S., Stalbaum, T., Palmre, V., Kim, K., and Oh, I. K. (2016). A multiple-shape memory polymer-metal composite actuator capable of programmable control, creating complex 3D motion of bending, twisting, and oscillation. *Sci. Rep.* 6:24462. doi: 10.1038/srep24462

Shian, S., Bertoldi, K., and Clarke, D. R. (2015a). Dielectric Elastomer Based 'grippers' for Soft Robotics. *Adv. Mater.* 27, 6814–6819. doi: 10.1002/adma.201503078

Shian, S., Bertoldi, K., and Clarke, D. R. (2015b). Use of aligned fibers to enhance the performance of dielectric elastomer inchworm robots. *Electroact. Polym. Actuators Devices* 9430:94301P. doi: 10.1117/12.2084140

Shintake, J., Schubert, B., Rosset, S., Shea, H., and Floreano, D. (2015). "Variable stiffness actuator for soft robotics using dielectric elastomer and low-melting-point alloy," in *IEEE/RSJ International Conference on Intelligent Robots and Systems (IROS)* (Hamburg), 1097–1102. doi: 10.1109/IROS.2015.7353507

Villoslada, A., Flores, A., Copaci, D., Blanco, D., and Moreno, L. (2015). High-displacement flexible Shape Memory Alloy actuator for soft wearable robots. *Rob. Auton. Syst.* 73, 91–101. doi: 10.1016/j.robot.2014.09.026

WackerChemie AG. *Neue Perspektiven Und Innovative Anwendungen Mit Elastosil ®Film Hauchdünne Siliconfolie.* Tech. Datasheet, 1–4. Available online at: https://www.wacker.com/h/medias/7091-DE.pdf

Conflict of Interest: The authors declare that the research was conducted in the absence of any commercial or financial relationships that could be construed as a potential conflict of interest.

frontiers in Robotics and AI

ORIGINAL RESEARCH
published: 10 January 2020
doi: 10.3389/frobt.2019.00146

Electrically-Driven Soft Fluidic Actuators Combining Stretchable Pumps With Thin McKibben Muscles

Vito Cacucciolo [1†], Hiroyuki Nabae [2†], Koichi Suzumori [2] and Herbert Shea [1]*

[1] Soft Transducers Laboratory (LMTS), Institute of Microengineering, School of Engineering, École Polytechnique Fédérale de Lausanne (EPFL), Neuchâtel, Switzerland, [2] Suzumori-Endo Laboratory, Department of Mechanical Engineering, Tokyo Institute of Technology, Tokyo, Japan

Soft wearable robots could provide support for lower and upper limbs, increase weight lifting ability, decrease energy required for walking and running, and even provide haptic feedback. However, to date most of wearable robots are based on electromagnetic motors or fluidic actuators, the former being rigid and bulky, the latter requiring external pumps or compressors, greatly limiting integration and portability. Here we describe a new class of electrically-driven soft fluidic muscles combining thin, fiber-like McKibben actuators with fully Stretchable Pumps. These pumps rely on ElectroHydroDynamics, a solid-state pumping mechanism that directly accelerates liquid molecules by means of an electric field. Requiring no moving parts, these pumps are silent and can be bent and stretched while operating. Each electrically-driven fluidic muscle consists of one Stretchable Pump and one thin McKibben actuator, resulting in a slender soft device weighing 2 g. We characterized the response of these devices, obtaining a blocked force of 0.84 N and a maximum stroke of 4 mm. Future work will focus on decreasing the response time and increasing the energy efficiency. Modular and straightforward to integrate in textiles, these electrically-driven fluidic muscles will enable soft smart clothing with multi-functional capabilities for human assistance and augmentation.

Keywords: soft robotics, soft actuators, soft wearables, soft fluidic actuators, wearable robots, stretchable pumps, thin McKibben muscles, artificial muscles

OPEN ACCESS

Edited by:
Federico Carpi,
University of Florence, Italy

Reviewed by:
Ilkwon Oh,
Korea Advanced Institute of Science & Technology (KAIST), South Korea
Daniel Bruch,
Saarland University, Germany

***Correspondence:**
Vito Cacucciolo
vito.cacucciolo@epfl.ch

†These authors have contributed equally to this work

Specialty section:
This article was submitted to Soft Robotics, a section of the journal Frontiers in Robotics and AI

Received: *13 October 2019*
Accepted: *12 December 2019*
Published: *10 January 2020*

Citation:
Cacucciolo V, Nabae H, Suzumori K and Shea H (2020) Electrically-Driven Soft Fluidic Actuators Combining Stretchable Pumps With Thin McKibben Muscles. Front. Robot. AI 6:146. doi: 10.3389/frobt.2019.00146

INTRODUCTION

Soft wearables for human assistance and augmentation can provide muscle support for lower and upper limbs (Galiana et al., 2012; Asbeck et al., 2014; Natali et al., 2019), decrease the metabolic cost of running and walking (Kim et al., 2019), provide haptic feedback (Hinchet et al., 2018; Takahashi et al., 2019). They should be comfortable to wear and discretely integrated into clothing, however most development on wearable robots has been carried out to date using electromagnetic motors. It is becoming clear that intrinsically soft actuators are required for fully-integrated soft wearables. Of the different classes of soft actuators, soft fluidic actuators are the most widely adopted for wearables, due to their robustness, simple fabrication, and high energy density. These actuators generally consist of a chamber inflated with a pressurized fluid. Examples include bellows-shaped pneumatic actuators ("pneu-nets") (Mosadegh et al., 2014; Yap et al., 2015), fiber-reinforced fluidic actuators (Polygerinos et al., 2014; Cacucciolo et al., 2016), and McKibben actuators (Wehner et al., 2013).

A recent development in McKibben actuators is devices with very small diameter (inner diameter of order 1 mm), called Thin McKibben Muscles (TMMs) for their similarity with mammal's muscles (Kurumaya et al., 2017). TMMs are highly flexible even when pressurized, unlike conventional McKibben actuators, which drastically stiffen with pressurization. TMMs filaments can be bundled together to multiply the contracting force (**Figure 1**). Such TMMs have been demonstrated in a wide variety of wearable devices for human support and assistance and have been successfully knitted into textiles (Koizumi et al., 2018; Abe et al., 2019).

TMMs have a limitation that is common to all soft fluidic actuators: they require an external pump or compressor to drive the pressurized fluid. Such pumps are generally rigid, noisy and bulky components that cannot be integrated with the actuator, preventing untethered and portable operations. To overcome this limitation, Cacucciolo et al. have recently developed a class of all-soft-matter electrically-driven pumps (Cacucciolo et al., 2019). These 1 g-weighted Stretchable Pumps are solid-state and pump the liquid using a physical mechanism called EHD (ElectroHydroDynamics), where the liquid molecules are directly accelerated by an electric field, without moving mechanical components (**Figure 2**). These pumps can be largely bent, stretched and twisted while operating, allowing straightforward integration into wearables. The authors demonstrated these pumps in a wearable thermal regulation device and in self-contained bending fluidic actuators.

In this work, we describe the first integration of Stretchable Pumps with thin McKibben Muscles. The two devices together weight 2 g, are slender (maximum radial size 4 mm for the muscle and cross section of 1.5 × 10 mm for the pump), and can be largely bent or twisted (**Figure 3**). We measured a blocked force of 0.84 N and a maximum contracting stroke of 4 mm (corresponding to 2.2% of the muscle length). The result is an electrically-driven fluidic muscle for integration in soft wearables and active textiles.

This paper is organized as follows. In section Materials and Methods we describe the design and fabrication of the TMM and of the Stretchable Pumps, their integration and the characterization experiments. Section Results reports the characterization of the TMM and of the TMM integrated with the pump, in terms of force vs. contraction ratio (defined as stroke over initial muscle length) and response time. We then present a demo where we repeatedly lift a 2 g weight, equivalent to the weight of the Stretchable Pump—TMM ensemble. In section Discussion we discuss the results, limitations and future developments.

MATERIALS AND METHODS

The TMM (Thin McKibben Muscles) used in this study are a modified version of the devices developed by the authors in previous works (Kurumaya et al., 2017; Koizumi et al., 2018; Suzumori et al., 2018; Abe et al., 2019). To enable operation of the TMMs using Stretchable Pumps instead of industrial pressure source required lowering the TMM actuation pressure from 100 to 200 kPa to 10–20 kPa, resulting in LPTMMs (Low Pressure Thin McKibben Muscles). The decrease in actuating pressure was achieved by decreasing the wall thickness of the inner tube. However, it becomes more challenging to obtain tubes of uniform thickness when the thickness values become too low. As a tradeoff, we selected a tube with a wall thickness of 0.15 mm.

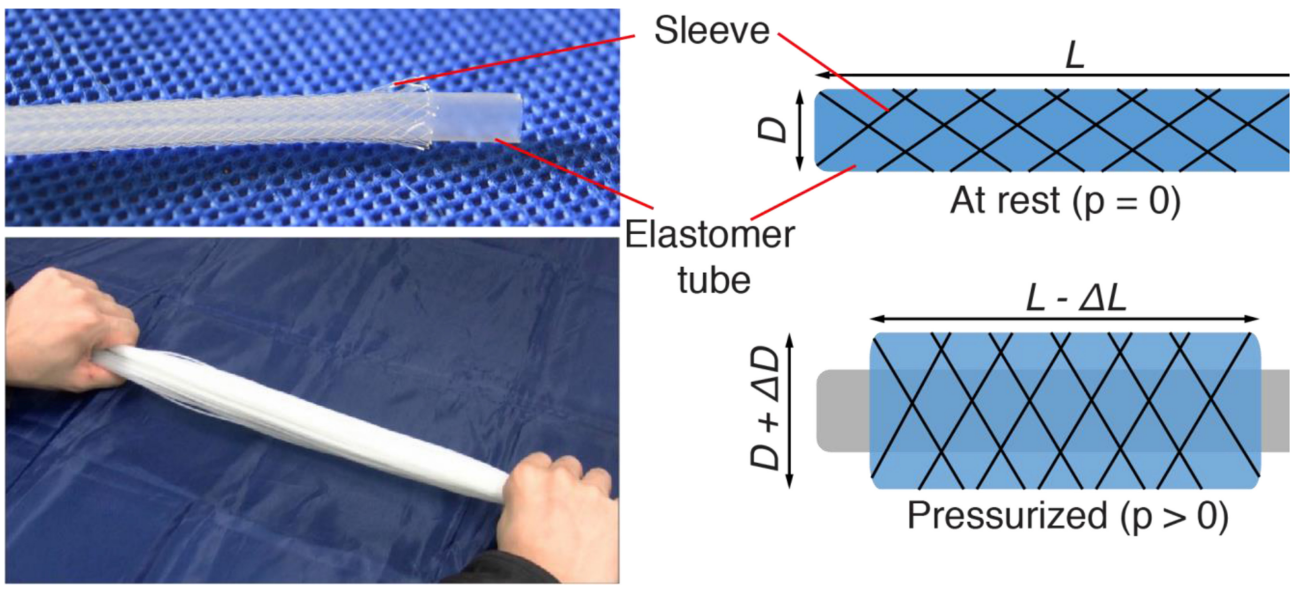

FIGURE 1 | Thin McKibben muscles (Kurumaya et al., 2017). Each filament is composed of an elastomer tube and an external sleeve. When the tube is pressurized, the sleeve drives the deformation into a axial contraction and radial expansion. A number of filaments can be arranged together in bundles to provide high contraction force.

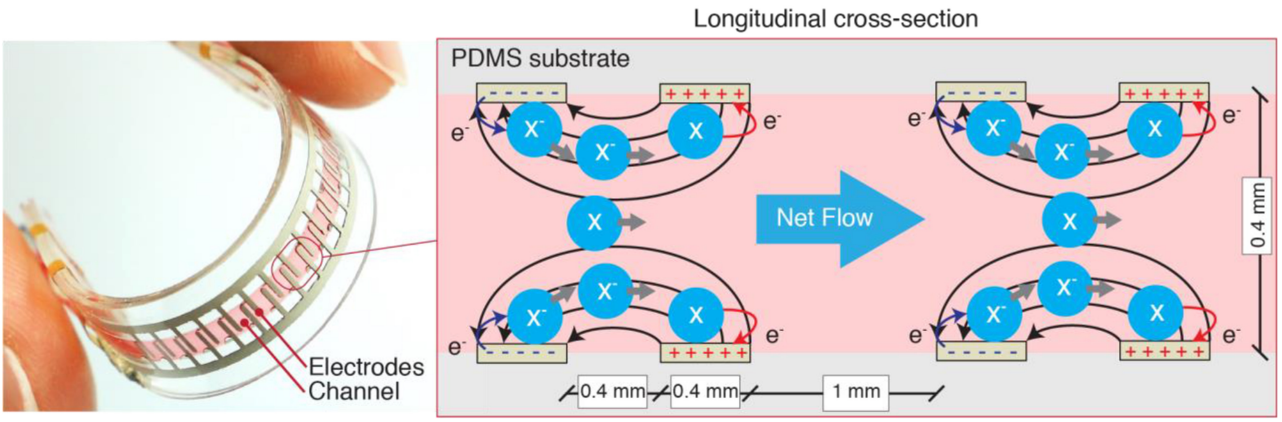

FIGURE 2 | Schematics of the Stretchable Pumps (Cacucciolo et al., 2019) used in this study, based on ElectroHydroDynamics. The electrodes are made of a stretchable silver ink. The top and bottom PDMS substrates are each 400 μm-thick. The pump generates continuous flow with no moving parts.

FIGURE 3 | Integration of a Stretchable Pump with a thin McKibben Muscle. When the voltage is turned on, the pump accelerates the fluid by EHD (ElectroHydroDynamics) and drives it into the muscle, causing its contraction. A negative voltage generates opposite flow, with fluid being driven out of the muscle, leading to its relaxation. The result is an electrically-driven soft fluidic muscle.

The Stretchable Pumps used in this study are based on the design and fabrication of the Ag pumps (i.e., the pump with silver electrodes) presented in Cacucciolo et al. (2019). **Figure 2** shows a picture of a Stretchable Pump (left) and the schematic diagram of the working principle (right). The channel and the electrodes backing are made of 400 μm-thick Polydimethylsiloxane (Dow Corning Sylgard 184). The interdigitated electrodes are realized by casting a commercial stretchable silver ink (Chimet Ag 520 EI) through a 23 μm-thick BoPET (biaxially-oriented polyethylene terephthalate) mask. The laser-cut channel layer is bonded to the electrode layers using silicone adhesives.

The integration of the Stretchable Pumps with the LPTMMs is achieved by connecting the pump's outlet tube to the actuator's inlet tube through a fluidic connector (**Figure 3**). We measured

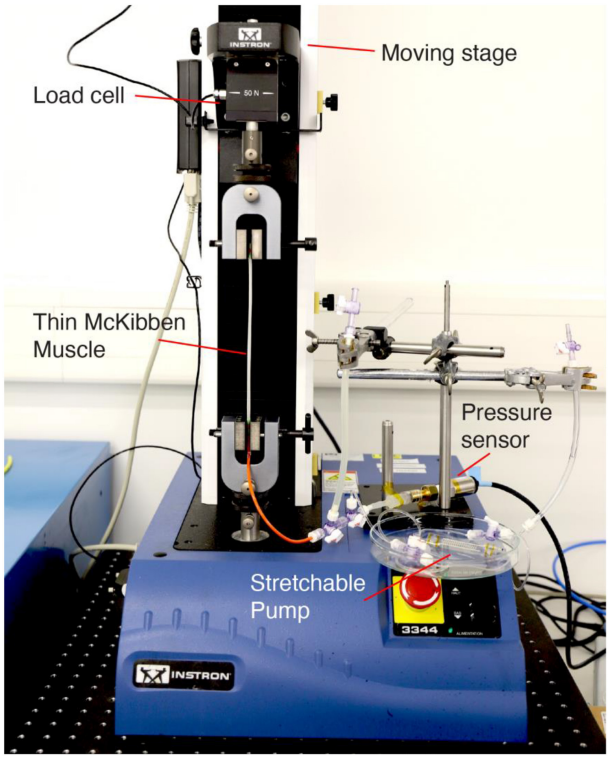

FIGURE 4 | Testing apparatus composed of a pull tester with a load cell and a motorized stage, a pressure sensor, the Stretchable Pump and the LPTMM actuator.

the LPTMM force and displacement by using a pull-tester (Instron Universal Testing System). One end of the actuators is mechanically clamped to the fixed side of the pull-tester, while the other end is clamped to the motorized stage through a load cell (**Figure 4**). The voltage to the Stretchable Pump is provided by an EMCO CB 101 power supply, with voltage and current measurement outputs. An H-Bridge circuit is used to reverse the polarity of the voltage in order to invert the pump flow direction. The pressure output from the pump is recorded using a pressure sensor (SSI Technologies, P51 MediaSensor^{TM}).

The load-lifting demo consists of two Stretchable Pumps connected in series between a reservoir and one LPTMM actuator (**Figure 5**). The free-end of the actuator is connected to a plastic disk weighting two grams. The displacement of the disk is recorded using a digital camera at 50 fps and measured using an image processing software (Kinovea).

RESULTS

Sections Characterization of Volume vs. Pressure for the LPTMMs and Characterization of Force and Contraction Ratio for the LPTMMs present the characterization of the LPTMMs driven by a pressure generator, while section Characterization of Force and Contraction Ratio for the LPTMMs Driven by Stretchable Pumps. Section Weight-Lifting Demo includes an experiment where one LPTMM driven by two Stretchable Pumps cyclically lift up a weight.

Characterization of Volume vs. Pressure for the LPTMMs

In sections Characterization of Volume vs. Pressure for the LPTMMs and Characterization of Force and Contraction Ratio for the LPTMMs, we first characterized the LPTMMs using a pressure generator (Fluigent MFCS^{TM}) before connecting them to the Stretchable Pumps. The aim of the first tests was to characterize the LPTMMs as fluidic loads, in terms of pressure vs. volume. To subtract the influence of the fluidic circuit (tubes, valves, connectors) and of the eventual air trapped into the system, we first conducted the experiment without the LPTMM. We removed these results from those taken with the LPTMM to obtain the net characteristic of the LPTMM. The results are summarized in **Table 1**. We measured a pressure—volume characteristics of 0.24 kPa/µl when pressurizing or depressurizing the system. We therefore need 83 µl of liquid to reach a pressure of 20 kPa. This result can be merged with the pressure—flow-rate characteristic of the pump to predict the pump flow-rate required to obtain a given response of the actuator.

Characterization of Force and Contraction Ratio for the LPTMMs

Figure 6 shows the typical characteristic curve of LPTMMs at 50 kPa. For a given pressure, a LPTMM behaves as a non-linear spring. We performed this measurement by mounting the LPTMM in a pull tester. We apply the pressure with the actuator at its rest length $L_0 = 180$ mm (length corresponding to ambient pressure) and measure its first contraction force F_{FC} . The pull tester then gradually decreases the length of the actuator until reaching a zero contraction force. The branch on the left of **Figure 6**. represents the behavior of the actuator during this first phase. The contraction value ΔL at zero force represents the free contraction of the actuator at that given pressure. It follows one full cycle of elongation back to the initial length L_0, at maximum force (blocked force F_B) and then shrinking back until zero force, at maximum elongation. After the first contraction, the actuator always follows the same cycle, showing very high repeatability (maximum standard deviation of 0.0312 N among five trials). The reasons for the lower force values at the first contraction are related to the sliding between the inner chamber and outer sleeve of the LPTMMs and related friction each time the soft muscles are fully depressurized and pressurized again (Kurumaya et al., 2017; Koizumi et al., 2018; Abe et al., 2019).

Figure 7 shows the force vs. pressure results for the LPTMMs. As expected for McKibben muscles, the curve is almost linear and there is very little hysteresis (Kurumaya et al., 2017; Koizumi et al., 2018; Abe et al., 2019). We measured a force vs. pressure characteristic of 0.0424 N/kPa. The measured force in **Figure 7**. corresponds to the contraction force at the first pressurization. It is lower than the blocked force that the LPTMM can achieve after being contracted and stretched again, as shown in **Figure 6**.

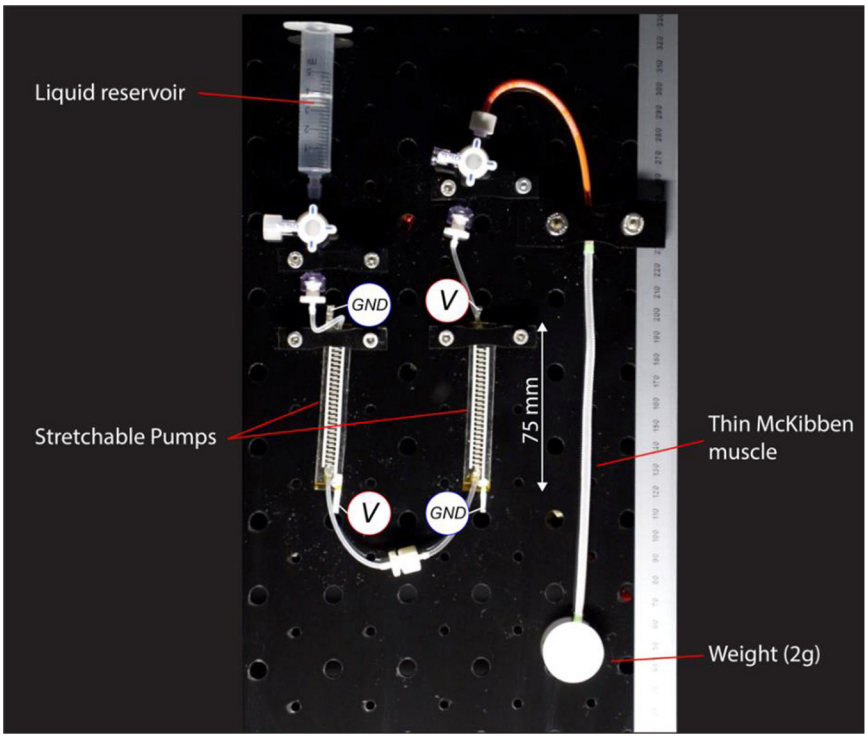

FIGURE 5 | Schematics of the weight-lifting experiments (**Supplementary Video 1**). Two Stretchable Pumps are connected in series to one LPTMM lifting a 2 g weight.

TABLE 1 | Pressure—Volume characteristic of the thin McKibben muscles and of the fluidic circuit.

	Pressure—volume slope [kPa/μl]	
	Pressurizing	**Depressurizing**
Fluidic circuit	0.70	−0.65
Fluidic circuit + muscle	0.18	−0.18
Muscle only	0.24	−0.24

Figure 8 presents the characteristic curves of LPTMM at different pressures. We removed the left branches corresponding to the first pressurization for clarity. The area below each of these curves represents the energy per unit length of the LPTMM. As expected, higher pressures lead to both higher blocked forces and higher free contraction values, leading to higher energy. We can notice that, unlike the contraction force at initial pressurization (**Figure 7**), the maximum blocked force shown in **Figure 8** increases less than linearly with the pressure, possibly due to the stiffening of the inner tube elastomer and due to friction between the inner tube and the outer sleeve.

Characterization of Force and Contraction Ratio for the LPTMMs Driven by Stretchable Pumps

We measure force and contraction ratio of a Stretchable Pump connected to a LPTMM using the same set-up described for the characterization of LPTMMs (sections Characterization of Volume vs. Pressure for the LPTMMs and Characterization of Force and Contraction Ratio for the LPTMMs). The Stretchable Pump replaces the pressure generator. The pump is activated using a DC voltage source. When the voltage is turned on, the pump moves the liquid from a reservoir to the LPTMM. The main difference between the pressure generator and the Stretchable Pump is that the former imposes a constant pressure regardless of volume change in the LPTMM, while the pumps pressure depends on flow-rate. As a consequence, the dynamics

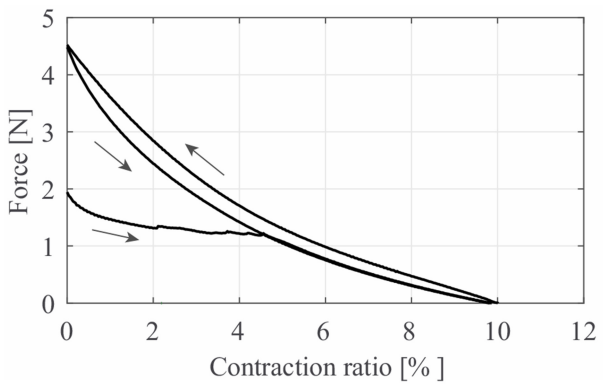

FIGURE 6 | The typical quasi-static characteristic curve of thin McKibben muscles, obtained using a pressure generator. The curve branch on the bottom left applies only to the first actuation cycle after pressurization. After, the actuator consistently follows the cycle on the right.

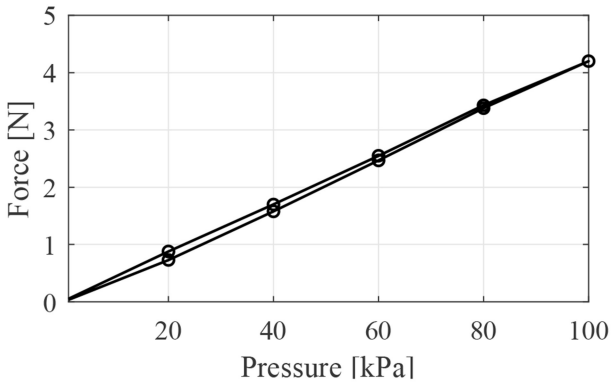

FIGURE 7 | Force vs. pressure response curve of one thin McKibben muscle obtained using a pressure generator.

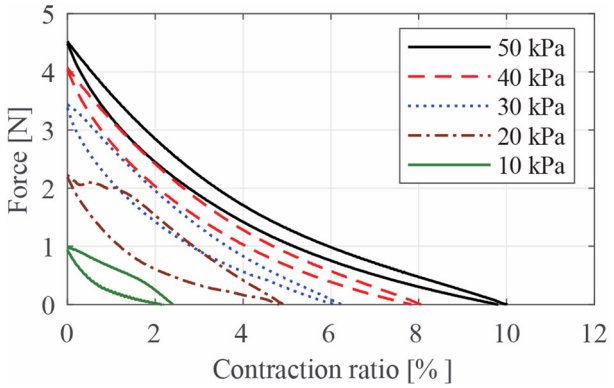

FIGURE 8 | Quasi-static characteristic curves of the thin McKibben muscle used in this study, obtained using a pressure generator.

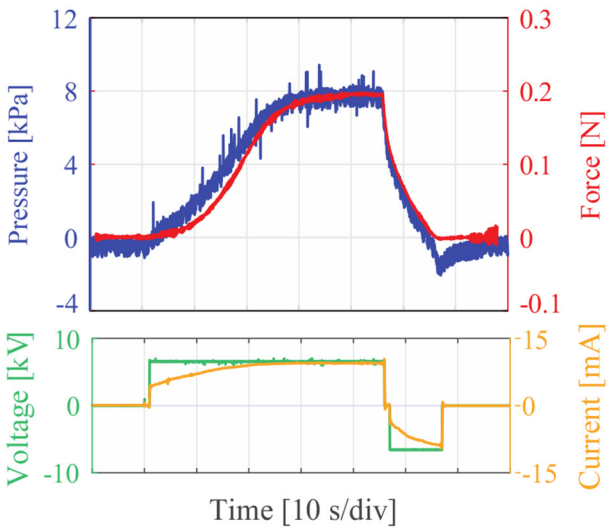

FIGURE 9 | Response curve of one Stretchable Pump and one thin McKibben muscle to a voltage step.

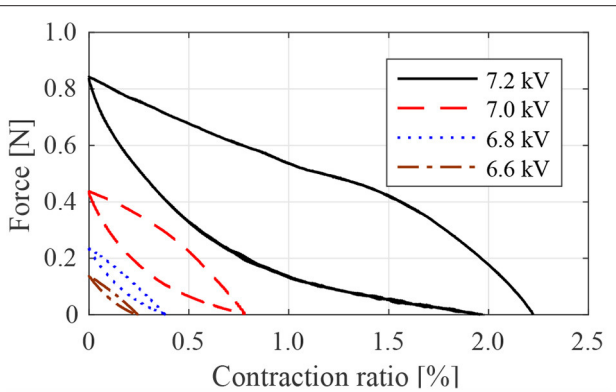

FIGURE 10 | Quasi-static characteristic curves of one thin McKibben muscle activated with one Stretchable Pump, at different values of the applied voltage.

of the Stretchable Pumps will influence the characteristic curves of the LPTMM.

We measure the dynamic response to a 7 kV voltage step of a Stretchable Pump connected to a LPTMM. The pressure response gives a good approximation of the dynamics of the Stretchable Pump. The time required to achieve the maximum pressure here is determined by both: (1) the intrinsic dynamics of the Stretchable Pumps that use FC-40 as dielectric liquid, (2) the fluidic characteristics of the LPTMM (section Characterization of Volume vs. Pressure for the LPTMMs), since at higher flow rate values of the Stretchable Pumps correspond lower pressure values. The generated force replicates closely the pressure profile, consistent with the data presented in **Figure 9**. The force here is the first contraction force (see section Characterization of Force and Contraction Ratio for the LPTMMs).

We then measure the force vs. contraction ratio of the LPTMM driven by a Stretchable Pump (**Figure 10**). The **Figure 11** speed of the motorized stage on the pull-tester is programmed to 0.1 mm/s. The maximum force measured is 0.84 N and the maximum contraction ratio is 2.2%, corresponding to a stroke of 4 mm. The hysteresis between the loading and unloading curve is due to both the intrinsic quasi-static characteristic of the LPTMM (**Figure 8**) and the dynamics of the Stretchable Pumps. In particular, in the case of unloading (actuator shortens), the volume of the muscle increases, therefore its pressure decreases until enough liquid gets pushed inside the muscle chamber by the pump. In addition to the LPTMM hysteresis, the shape of the unloading curve is then determined by: (1) the speed of contraction of the muscle, (2) the volume vs. contraction of the muscle, (3) the volume vs. pressure curve of the LPTMM (section Characterization of Volume vs. Pressure for the LPTMMs and **Table 1**), (4) the pressure vs. flow-rate characteristic of the pump. In the loading path (actuator elongates), the volume of the muscle decreases, so the liquid moves from the muscle to the reservoir through the pump and the tubing, while the pump keeps pushing the liquid in the opposite direction. This effect, in combination with the fluidic impedance encountered by the fluid, generates part of the overpressure observed in the loading cycle.

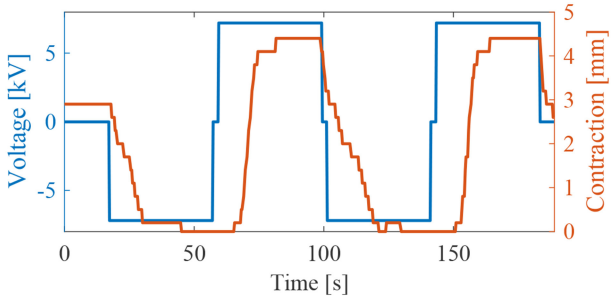

FIGURE 11 | Results of the weight lifting experiment (**Figure 5**). Contraction of the thin McKibben muscle activated by two Stretchable Pumps at 7.2 kV.

Weight-Lifting Demo

We tested the ability of the Stretchable Pumps to drive the LPTMM to repeatedly lift up a small disk weighing 2 g. We connected two Stretchable Pumps in series to double their output pressure. **Figure 5** shows the experimental set-up, lying in a vertical plane. When a positive voltage is applied to the pumps, they push the liquid from the reservoir to the LPTMM, which contracts and lifts the weight. When the voltage is reversed, the pumps drive the liquid from the LPTMM back into the reservoir, relaxing the actuator, and lowering the weight. We measured a total displacement $\Delta x = 4.4$ mm from $V = -7.2$ kV to $V = 7.2$ kV.

DISCUSSION

In this work, we demonstrated the first integration of Thin McKibben Muscles and Stretchable Pumps to realize electrically-driven soft fluidic muscle fibers that are flexible and stretchable. Each of these muscles weighs 2 g and realizes a blocked force of 0.84 N and a maximum stroke of 4 mm.

Although these results are outstanding compared to other electrically-driven soft actuators, to employ these devices in wearable soft exoskeletons requires further improving their performance. The force and stroke can be both enhanced by connecting the muscles in bundles or by braiding them into active textiles (Koizumi et al., 2018; Abe et al., 2019). We expect major improvements of the performance of the Stretchable Pumps by optimizing the geometry and material of the electrode, and by tuning the electrical properties of the liquids.

The relatively high voltage required to drive the EHD soft pumps (5–8 kV) might raise concerns about safety and size of the power supply. These concerns have been addressed in a previous work on Stretchable Pumps where the authors demonstrate untethered operation using a palm sized battery-driven power supply weighting 18 g (Cacucciolo et al., 2019). Each of these portable power supplies is limited to a current output of 100 μA, widely below the human safety threshold (1–10 mA) but large enough to power up to 6 Stretchable Pumps at the same time. Nonetheless, some applications would benefit from reducing the driving voltage. Strategies to reduce the voltage include reducing the electrodes spacing and searching for combinations of electrodes and liquid materials showing higher EHD performance at lower fields.

A major limitation of these devices in their current form is the response time. We estimated a force rise time of 14 s and a fall time of 6.6 s, with 10 and 90% reference levels, in response to a voltage step of 6.8 kV (**Figure 9**). The response time of the system composed by pump and muscles depends from: (1) the flow-rate of the pumps; (2) the response time of the actuator; (3) the response time of the pump. From **Table 1**, we can estimate that 80 μl of fluid are required for a pressure of 20 kPa. Given that from earlier work (Cacucciolo et al., 2019) the maximum flow rate of the pump is Q_M =100 μl/s, we can roughly estimate a time of the order of 1 s to reach the target pressure and force. The mechanical response time of the actuator is significantly shorter than 1 s, so it is not a limiting factor in this configuration. The results in **Figure 9** confirm that there is no noticeable delay between the pressure applied by the pump and the force generated by the actuator. The most critical factor limiting the response time of the system is the EHD response time of the FC-40 liquid used for the Stretchable Pumps in these experiments. This liquid was chosen for its high breakdown voltage and good compatibility with PDMS, however **Figure 9** shows how the time for the pressure to reach its maximum value is significantly larger than 1 s. Liquids with sub-second EHD response times have been already demonstrated for Stretchable Pumps in the authors' earlier work (Cacucciolo et al., 2019), but they have limited compatibility with PDMS. Future work will focus on finding liquid/elastomer combinations featuring long-term compatibility and fast responses.

Energy efficiency is a critical and often overlooked aspect in novel soft actuators. We estimated the efficiency of the pump η_p by dividing the average output power generated by the pump (product of average flow-rate $\overline{Q}$ and average pressure $\overline{p}$) by the total electrical power (the product of voltage V and average electrical current $\overline{I}$ from the power supply).

By using data from the weight lifting experiment (**Figure 5** and **Supplementary Video 1**), we computed the average flow-rate $\overline{Q} = 80$ μl/s, the ratio of the displaced volume during a single lifting event (1100 μl) divided by the lifting time (t_l = 14 s). To obtain the average pressure, we assumed for simplicity a linear variation of pressure vs. time between the start and the end of the lifting, i.e., between 0 and a maximum pressure p_M ($\overline{p} = 0.5\ p_M$). We computed p_M from pressure characterization data of the same pumps used in the weight lifting experiments using the same voltage of 7.2 kV. $p_M = 19$ kPa is the average value over 1 s acquisition at 10 kHz, after the pressure reached a steady state value. The voltage is constant $V = 7.2$ kV and the current, $\overline{I} = 17$ μA is the average of data recorded during the lifting phase of the weight lifting experiment (14 s at 10 kHz).

The resulting pump energy efficiency is $\eta_p = \left(\overline{Q} * \overline{p}\right) / \left(V * \overline{I}\right)$ = 0.75 mW/120 mW = 0.65%. We can also compute the efficiency η_s of the entire system composed of the soft pump and the soft muscle. η_s is the ratio between the gain in potential energy for the $m = 2$ g disk weight during a single lifting event (displacement $\Delta x = 4.4$ mm) and the electrical energy used during a single lifting. $\eta_s = (m\ g\ \Delta x) / (V * \overline{I} * t_l) = 0.0052\%$. The low efficiency of the soft pump η_p, in line with other novel soft actuators, is due to both losses in the EHD phenomenon itself (e.g., leakage currents, liquid circulation) and losses in the drive electronics.

Future work will aim at increasing the soft pump energy efficiency η_p through a deeper understanding of EHD, the use of new modeling tools to optimize the pump design and the selection of better materials. Future strategies to enhance the efficiency η_s include using more pump modules per soft muscle and adopting antagonistic configurations to reuse the elastic energy stored in the muscle during each cycle.

CONCLUSION

This work demonstrated electrically-driven soft fluidic muscles in the form of thin fibers. The characterization of the devices shows values of force and stroke compatible with wearable applications (up to 0.8 N and 4 mm for each 2 g fiber actuator), while response time and energy efficiency require further optimization. These actuators are flexible, stretchable, modular and completely silent, opening up a path to a new class of fully integrated and comfortable wearables for human assistance and augmentation.

DATA AVAILABILITY STATEMENT

The datasets generated for this study are available on request to the corresponding author.

AUTHOR CONTRIBUTIONS

VC, HN, KS, and HS conceived the project. VC and HN designed, fabricated, characterized the devices, analyzed the data, and wrote the paper. KS and HS contributed to data interpretation. All authors provided feedback and agree with the final version of the manuscript.

FUNDING

We acknowledge financial support by JSPS KAKENHI Grant-in-Aid for Scientific Research on Innovative Areas Science of Soft Robot project under Grant Number JP18H05465.

SUPPLEMENTARY MATERIAL

The Supplementary Material for this article can be found online at: https://www.frontiersin.org/articles/10.3389/frobt.2019.00146/full#supplementary-material

Supplementary Video 1 | This video shows the system lifting a 2 g weight. Two Stretchable Pumps are connected in series to drive one LPTMM.

REFERENCES

Abe, T., Koizumi, S., Nabae, H., Endo, G., Suzumori, K., Sato, N., et al. (2019). Fabrication of '18 Weave' muscles and their application to soft power support suit for upper limbs using thin McKibben muscle. *IEEE Robot. Automat. Lett.* 4, 2532–2538. doi: 10.1109/LRA.2019.2907433

Asbeck, A. T., Rossi, S. M. M. D., Galiana, I., Ding, Y., and Walsh, C. J. (2014). Stronger, smarter, softer: next-generation wearable robots. *IEEE Robot. Automat. Mag.* 21, 22–33. doi: 10.1109/MRA.2014.2360283

Cacucciolo, V., Renda, F., Poccia, E., Laschi, C., and Cianchetti, M. (2016). Modelling the nonlinear response of fibre-reinforced bending fluidic actuators. *Smart Mater. Struct.* 25:105020. doi: 10.1088/0964-1726/25/10/105020

Cacucciolo, V., Shintake, J., Kuwajima, Y., Maeda, S., Floreano, D., and Shea, H. (2019). Stretchable pumps for soft machines. *Nature* 572, 516–519. doi: 10.1038/s41586-019-1479-6

Galiana, I., Hammond, F. L., Howe, R. D., and Popovic, M. B. (2012). "Wearable soft robotic device for post-stroke shoulder rehabilitation: identifying misalignments," in *2012 IEEE/RSJ International Conference on Intelligent Robots and Systems* (Vilamoura). doi: 10.1109/IROS.2012.6385786

Hinchet, R., Vechev, V., Shea, H., and Hilliges, O. (2018). "DextrES: wearable haptic feedback for grasping in VR via a thin form-factor electrostatic brake," in *Proceedings of the 31st Annual ACM Symposium on User Interface Software and Technology* (New York, NY), 901–912. doi: 10.1145/3242587.3242657

Kim, J., Lee, G., Heimgartner, R., Revi, D. A., Karavas, N., Nathanson, D., et al. (2019). Reducing the metabolic rate of walking and running with a versatile, portable exosuit. *Science* 365, 668–672. doi: 10.1126/science.aav7536

Koizumi, S., Kurumaya, S., Nabae, H., Endo, G., and Suzumori, K. (2018). Braiding thin mckibben muscles to enhance their contracting abilities. *IEEE Robot. Automat. Let.* 3, 3240–3246. doi: 10.1109/LRA.2018.2851025

Kurumaya, S., Nabae, H., Endo, G., and Suzumori, K. (2017). Design of thin McKibben muscle and multifilament structure. *Sensors Actua A Phys.* 261, 66–74. doi: 10.1016/j.sna.2017.04.047

Mosadegh, B., Polygerinos, P., Keplinger, C., Wennstedt, S., Shepherd, R. F., Gupta, U., et al. (2014). Pneumatic networks for soft robotics that actuate rapidly. *Adv. Funct. Mater.* 24, 2163–2170. doi: 10.1002/adfm.201303288

Natali, C. D., Poliero, T., Sposito, M., Graf, E., Bauer, C., Pauli, C., et al. (2019). Design and evaluation of a soft assistive lower limb exoskeleton. *Robotica* 37, 2014–2034. doi: 10.1017/S0263574719000067

Polygerinos, P., Wang, Z., Galloway, K. C., Wood, R. J., and Walsh, C. J. (2014). Soft robotic glove for combined assistance and at-home rehabilitation. *Robot. Autonomous Syst.* 73, 135–143. doi: 10.1016/j.robot.2014.08.014

Suzumori, K., Seita, S., Wakimoto, S., Kouno, K. (2018). *Mckibben Artificial Muscle*. US20180252244A1.

Takahashi, N., Takahashi, H., and Koike, H. (2019). "Soft exoskeleton glove enabling force feedback for human-like finger posture control with 20 degrees of freedom," in *2019 IEEE World Haptics Conference (WHC)* (Tokyo), 217–222. doi: 10.1109/WHC.2019.8816142

Wehner, M., Quinlivan, B., Aubin, P. M., and Martinez-Villalpando,E., Baumann, M., et al. (2013). "A lightweight soft exosuit for gait assistance," in *2013 IEEE International Conference on Robotics and Automation* (Karlsruhe), 3362–3369. doi: 10.1109/ICRA.2013.6631046

Yap, H. K., Lim, J. H., Nasrallah, F., Goh, J. C. H., and Yeow, R. C. H. (2015). "A soft exoskeleton for hand assistive and rehabilitation application using pneumatic actuators with variable stiffness," in *2015 IEEE International Conference on Robotics and Automation (ICRA)* (Seattle, WA), 4967–4972. doi: 10.1109/ICRA.2015.7139889

Conflict of Interest: VC and HS declare financial interest in form of a patent application.

The remaining authors declare that the research was conducted in the absence of any commercial or financial relationships that could be construed as a potential conflict of interest.

frontiers in Robotics and AI

ORIGINAL RESEARCH
published: 15 January 2020
doi: 10.3389/frobt.2019.00152

Self-Assembled 3D Actuator Using the Resilience of an Elastomeric Material

Naoki Hashimoto[1]*, *Hiroki Shigemune*[1,2]*, *Ayato Minaminosono*[2], *Shingo Maeda*[2] and *Hideyuki Sawada*[1]

[1] Department of Applied Physics, Waseda University, Tokyo, Japan, [2] Division of Mechanical Engineering, Shibaura Institute of Technology, Tokyo, Japan

Self-folding technologies have been studied by many researchers for applications to various engineering fields. Most of the self-folding methods that use the physical properties of materials require complex preparation, and usually take time to complete. In order to solve these problems, we focus on the elasticity of a material, and propose a model for forming a 3D structure using its characteristics. Our proposed model achieves high-speed and high-precision self-folding with a simple structure, by attaching rigid frames to a stretchable elastomer. The self-folded structure is applied to introduce a self-assembled actuator by exploiting a dielectric elastomer actuator (DEA). We develop the self-assembled actuator driven with the voltage application by attaching stretchable electrodes on the both side of the elastomer. We attempt several experiments to investigate the basic characteristics of the actuator. We also propose an application of the self-assembled actuator as a gripper based on the experimental results. The gripper has three joints with the angle of 120°, and successfully grabs objects by switching the voltage.

Keywords: soft robotics, dielectric elastomer actuator, self-folding method, self-assembled actuator, gripper

OPEN ACCESS

Edited by:
Gianluca Rizzello, Saarland University, Germany

Reviewed by:
Massimo Mastrangeli, Delft University of Technology, Netherlands
Wenzeng Zhang, Tsinghua University, China

***Correspondence:**
Naoki Hashimoto
hashimoto@sawada.phys.waseda.ac.jp
Hiroki Shigemune
hshige@shibaura-it.ac.jp

Specialty section:
This article was submitted to Soft Robotics, a section of the journal Frontiers in Robotics and AI

Received: *16 September 2019*
Accepted: *20 December 2019*
Published: *15 January 2020*

Citation:
Hashimoto N, Shigemune H, Minaminosono A, Maeda S and Sawada H (2020) Self-Assembled 3D Actuator Using the Resilience of an Elastomeric Material. Front. Robot. AI 6:152. doi: 10.3389/frobt.2019.00152

INTRODUCTION

A technology of "origami" that creates a 3D structure by folding a flat sheet such as a paper and a metal plate has been studied by many researchers. In recent years, new techniques related to origami have been widely studied in the field of engineering. By folding a large sheet into a small piece, the sheet object is hardly carried to different places to be extended into complex 3D structures. For example, space structures (Torisaka et al., 2016), solar cell arrays (Natori et al., 2013), protein origami (Dobson, 2003), and folding of insect wings (Saito et al., 2017) are the successful applications of origami studies.

On the other hand, the research on self-folding mechanism has been actively conducted by utilizing physical properties of materials. Examples of such prior studies are found in heat-shrinkable polymer (Liu et al., 2012, 2017; Felton et al., 2014) and paper (Shigemune et al., 2016, 2017).

We focus on an elastomeric material, and introduce a self-folding mechanism that utilizes the resilience of the material. Elastomers have several properties such as being capable of large deformations of several hundreds percent, superior processability, and high compatibility with living organisms in terms of stretchablity. Furthermore, it can also be applied to an actuator by designing conductive electrode.

Dielectric Elastomer Minimum Energy Structures (DEMES) (Araromi et al., 2015) is a device that forms a 3D structure, in which the elastic energy of the elastomer and the folding energy of the flexible frame are minimized. This structure shows large deformation by the voltage application, and enables the manufacture of lightweight and flexible actuators. However, the research mainly focuses on obtaining larger displacements with the Dielectric Elastomer Actuator, and it has difficulty to form precise self-folded structures. Mintchev et al. introduced a 3D structure formation method by combining a rigid frame with a flexible elastomeric material (Mintchev et al., 2017). This structure displays both high load bearing and high resilience characteristics. The research focuses on reducing the impact on the device from the outside, and is not intended for the use as an actuator.

In this research, we propose a self-folding method using the characteristics of the elastomeric material. Our proposed mechanism uses the resilience of the elastomer for assembly, therefore the total system can be untethered. This assembly does not require external stimuli, and the assembling time is much shorter than the other methods. The self-folded structure can naturally introduce a self-assembled electric actuator called a Dielectric Elastomer Actuator (DEA), by applying stretchable electrodes to the elastomer. We demonstrate the potential ability of the self-assembled actuator by applying it as a gripper.

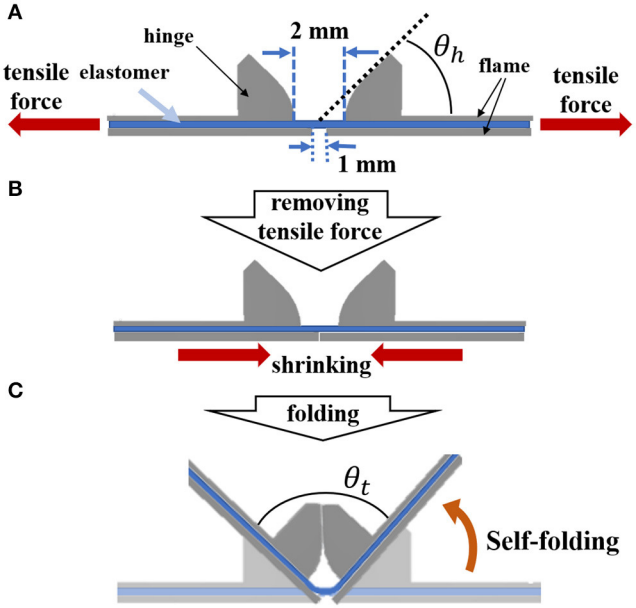

FIGURE 1 | Mechanism of forming a 3D structure. **(A)** Attach two hinged and non-hinged frames to both sides of the pre-stretched elastomer. **(B)** When the tensile force is removed, the elastomer shrinks and the non-hinge frames collide, which has a shorter distance between the frames. **(C)** The contraction force of the elastomer produces a 3D structure, and the folding angle θ_t is determined by the angle θ_h of the hinge.

MECHANISM

Self-Folding Model Using an Elastomer and Rigid Frames

We propose a model that automatically forms a 3D structure using the resilience of an elastomer by pasting multiple rigid frames on both sides of a pre-stretched elastomer, as shown in **Figure 1**. First, we prepare a pre-strained elastomer using a rigid frame, and attach two hinged frames on a folding side and two frames without a hinge on the other side of the folding side. At this time, the distance between the hinge frames on the folding side is made wider than the frames on the other side (**Figure 1A**). Next, when the tensile force applied to the elastomer is removed by taking off from the rigid frame, the restoring force of the elastomer causes contraction, and the frames with shorter intervals come in contact with each other to restrict folding toward the side (**Figure 1B**). Then, the sheet bends toward the hinge frames with the remained gap (**Figure 1C**). The folding direction can be controlled in this way.

A method similar to the proposed method, in which hard frames are spaced apart and self-folding using the thermal contraction of the shape memory polymer, has already been studied (Tolley et al., 2014). In this method, the folding angle is controlled by adjusting the distance between the frames fixed on both sides of the shape memory polymer. On the other hand, the folding angle in our method can be adjusted by the different approach. The minimum bending angle can be designed in advance by attaching a hinge to the frame to constrain the bending angle. Furthermore, our method uses the shrinkage of the elastomer, and the time required for structure formation is much shorter than the thermal effect.

As shown in **Figure 1**, a target folding angle θ_t after self-folding can be arbitrarily determined by the size of the angle θ_h of the hinge portion of the frame, which can be expressed by Equation (1).

$$\theta_t = 2\theta_h, \tag{1}$$

When assembling a 3D structure using two frames with the same hinge angle θ_h, the θ_h should be set to half the θ_t.

Activation of Dielectric Elastomer Actuator

An elastomer film is sandwiched by the frames to self-fold. A self-assembled actuator is fabricated by applying carbon nanotube (CNT) electrodes on both sides of the elastomer. In order to drive the 3D structure introduced in section self-folding model using an elastomer and rigid frames, we employ a Dielectric Elastomer Actuator (DEA). **Figure 2** shows the structure of DEA, in which a dielectric elastomer is sandwiched by stretchable electrodes to work as a capacitor. DEA has advantages of its simple and lightweight structures, being compatible with low energy consumption and fast response time (Plante and Dubowsky, 2007). In order to greatly deform the electrode part of DEA, the application of pre-strain is necessary. Pelrine showed that the maximum amount of deformation in the area of the elastomer when voltage is applied increases when the acrylic elastomer is properly pre-strained (Pelrine et al., 2000). DEA is applied for

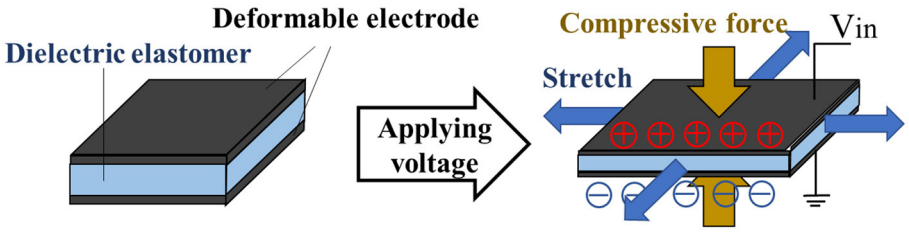

FIGURE 2 | Structure and principle of DEA. When voltage is applied to the elastomer having deformable electrodes attached to both sides, it extends in the horizontal direction.

a versatile gripper (Shintake et al., 2016), a deformable motor (Minaminosono et al., 2019), and a balloon speaker (Hosoya et al., 2019) by exploiting its characteristics. Conversely, there are also studies that use DEA without pre-stretching the elastomer (Duduta et al., 2016). In such cases, however, it is necessary to reduce the thickness of the electrode sufficiently or to form a multilayer structure.

In this study, we use CNT powder as the stretchable electrodes. The application of voltage to the electrodes generates electrostatic attraction between the electrodes, which results in the elastomer being compressed and deformed in the horizontal direction. The compressive force $p(N/m^2)$ due to this electrostatic attraction can be expressed by Equation (2) (Wissler and Mazza, 2007).

$$p = \varepsilon_0 \varepsilon_r \frac{V^2}{z^2}, \tag{2}$$

where, ε_0 is the permittivity of vacuum($\varepsilon_0 = 8.854 \times 10^{-12}$F/m), ε_r is the relative permittivity of elastomer, V is the applied voltage, and z is the distance between electrodes. According to Equation (2), by using an elastomer with a high dielectric constant and a thin film thickness as a material of DEA, larger compressive force and large deformation can be generated. The compressive force also increases in proportion to the square of the applied voltage (O'Hallorana et al., 2008).

The self-assembled actuator not only automatically forms a 3D structure, but also maintains the pre-strain of the elastomer to be activated as the DEA. The pre-strained elastomer extends by applying voltage toward the applied CNT electrodes. **Figure 3** shows a self-assembled actuator fabricated by attaching electrodes to a 3D structure fabricated by self-folding. When a voltage is applied to the electrode, the expansion of DEA is converted toward displacement in the direction to open the hinge.

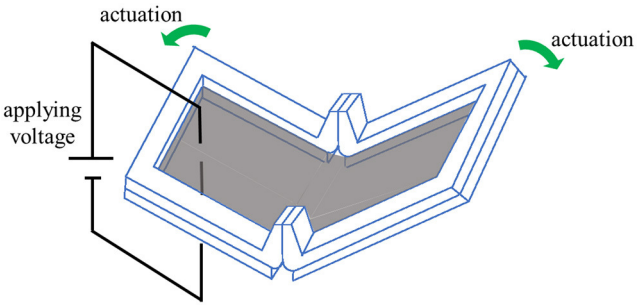

FIGURE 3 | Appearance of self-assembled actuator and mechanism of actuation. The gray area represents an area which the electrode is attached. The electrode is attached to both sides of the elastomer. When a voltage is applied to the electrodes, the actuator is driven in the opening direction.

FABRICATION

Frame

Two types of frames were designed to realize self-folding with the proposed model. A 3D-CAD (Auto CAD) was employed for designing, and the fabrication was conducted by a 3D printer (AGILISTA-3200; KEYENCE, Tokyo, Japan). **Figure 4** shows the design data and the photos of the frames. When designing the frame, the following two points were taken into consideration. The first point is to attach a hinge to determine the folding angle. The hinges of the frame A limit the folding due to the shrinkage of the elastomer by colliding with each other, and contribute to the determination of the folding angle. The length of the side of frame B was designed to be slightly longer than that of frame A so that it would collide first when the elastomer contracted. As a result, the entire structure folds in the direction of frame A. In this way, the frame A plays a role in determining the folding angle, and the frame B plays a role in determining the direction of folding. The second point is to fix the pre-stretch of the elastomer at the part where the electrode is applied to make DEA. As explained in section activation of dielectric elastomer actuator, a pre-strained DEA is greatly deformed. In our preliminary experiment, we discovered that 300% pre-strain should be uniformly applied for the best performance by using an acrylic elastomer (VHB 4905-J; 3M Company, Saint Paul, Minnesota, United States).

3D Structure Fabricated by Self-Folding

Figure 5 shows the fabrication process of a 3D structure using our proposed mechanism. First, we prepare a 300% pre-stretched elastomer, and attach two frames (frames A and B) to each side of the elastomer (**Figure 5A**). The distance between frames B should be shorter than the distance between frames A. In this experiment, the interval between frames A was set to 2 mm, and that between frames B was set to 1 mm (**Figure 5B**). By removing the elastomer from the frame, a 3D structure

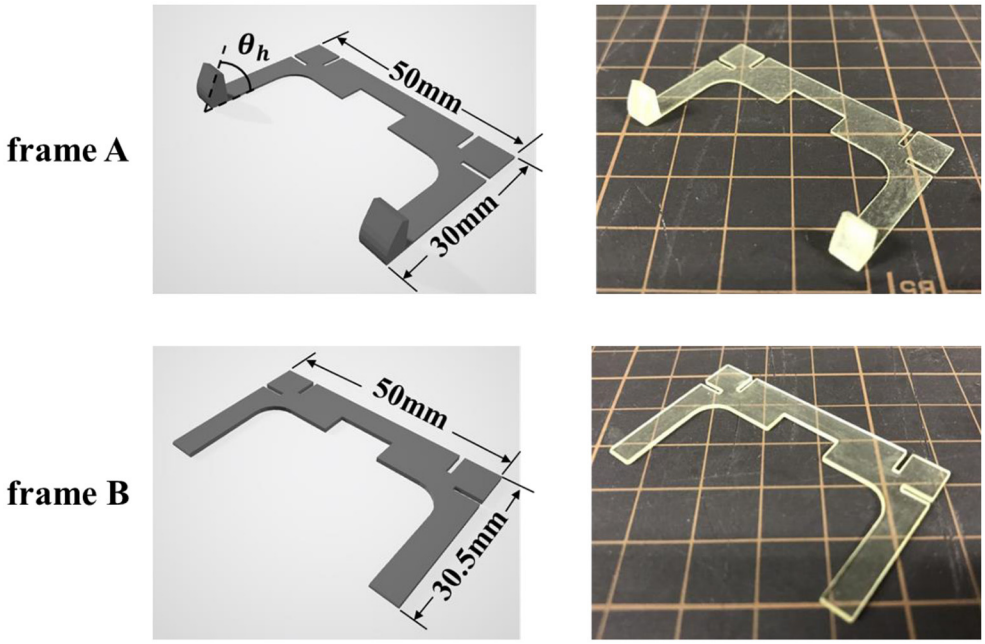

FIGURE 4 | Frame data designed in CAD software and actual printed frame. In order to realize the self-folding described in **Figure 1**, the length of the short side of frame B was designed to be 0.5 mm longer than that of frame A. The thickness of each frame is 0.5 mm. Here, the case of $\theta_h = 60$ is shown as an example of the frame A.

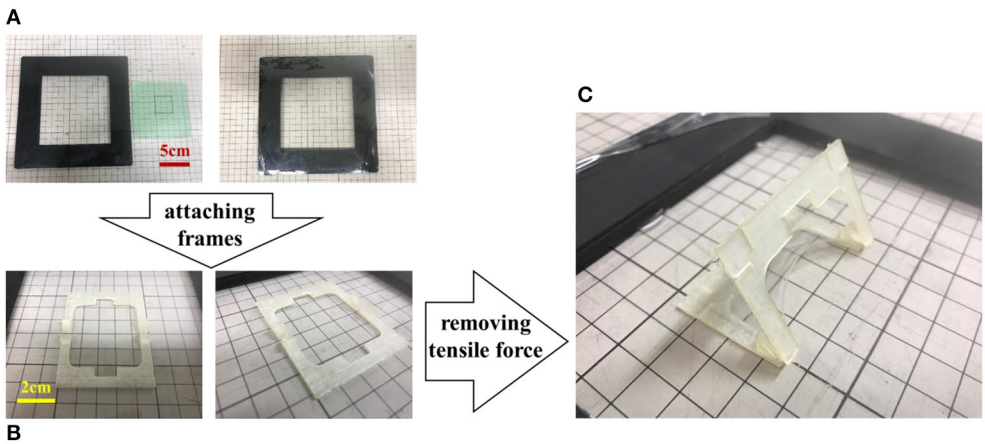

FIGURE 5 | Process of fabricating a self-folding prototype. **(A)** Elastomer is fixed with 300% pre-strain. **(B)** Frames are attached to both sides of the elastomer. **(C)** A 3D structure is spontaneously formed using the resilience of the elastomer. Self-folding is completed in about 1 s.

is spontaneously formed using the resilience of the elastomer (**Figure 5C**). Self-folding is completed in about 1 second after the tensile force of the elastomer is removed. A video recording the process of creating the self-folded structure is attached as **Supplementary Material**.

Figure 6 shows a side view of the hinge part of frame A. The surface where the hinges contact with each other is flat, and the surface close to the bottom is partly curved as shown in the figure. In this way, Frame A not only determines the folding angle, but also plays a role in helping the smooth operation when the voltage is applied to the self-assembled actuator. All four types of frames A with different angles θ_h are designed so that the distance from the intersection of the extension lines of the flat part of the hinge and the bottom to the bottom of the frame becomes 2 mm.

Figure 7 shows the difference in bending when the gap between frames A is changed. Here, the point P_C is the point where the extension lines of the planar parts of the hinges of the two Frame A intersect. **Figure 7A** shows the case where the point P_C is above the plane where Frame B exists. In this state, when the tensile force applied to the elastomer is removed, self-folding

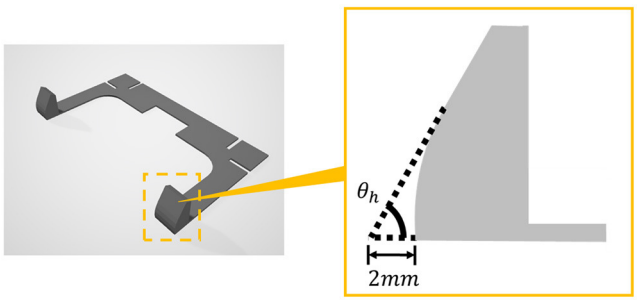

FIGURE 6 | The structure of Frame A and enlarged view of hinge part. Hinge part is rounded as shown in the right figure so as not to impede the drive of the structure by applying voltage.

occurs due to the contraction of the elastomer, and the frame A is fixed in a state where the plane parts are in contact with each other and the frame B is separated. **Figure 7B** shows the case where the point P_C is on the plane where Frame B exists. When the tensile force is removed, the frame A is fixed in a state where the plane parts are in contact with each other and the frames B are also in contact with each other. **Figure 7C** shows the case where point P_C is below the plane where Frame B exists. When the tensile force is removed, the frames A touch each other with a line instead of a face as shown in the figure, and the frames B are fixed in contact with each other. As shown in **Figure 3**, when the voltage is applied to the self-assembled actuator, the actuator is driven to open. When the frame B is in the state (a) where the frames B are separated from each other, the operation is not disturbed by the frame and it can be said that the operation works best. When the interval between frames A is 2 mm and the interval between frames B is 1 mm, the state is as shown in **Figure 7A**.

Self-Assembled Actuator

A self-assembled actuator is fabricated by attaching electrodes to the fabricated 3D structure. The actuator works by applying voltage to the electrodes as shown in **Figure 8**. The actuator displaces to increase folding angle. In this study, the self-assembled actuator is fabricated by brushing multi-walled carbon nanotubes (MWCNTs) on the elastomer part of the 3D structure as proposed in our previous study (Shigemune et al., 2018).

EXPERIMENTS

Accuracy of Self-Folded Angle Based on a Designed Angle θ_d

Experimental Condition

In order to verify the accuracy of the proposed model, we conducted an experiment to investigate the relationship between the hinge angle θ_h and the actual folding angle θ_m. **Figure 9** shows four prototypes of 3D structure achieved by self-folding. The four prototypes i to iv with a target angle θ_t of 60°, 90°, 120°, and 140° were designed and fabricated, by using two frames A with the hinge angle θ_h of 30°, 45°, 60°, and 70°, respectively. We fabricated five samples for each prototype i to iv to measure the self-folded angle θ_m shown in **Figure 9.** We measured the angles by using the image analysis software (Kinovea) referring to the photos taken parallel to the ground.

Results and Discussions

Table 1 shows the results of the experiment. The self-folded angles had small difference within 2 degrees from the initial designs i, ii, and iii. Prototype iv showed a larger difference of 14.08° to the opening direction. The standard deviation became larger when the self-folded angle was obtuse.

From the results, we found that the self-folded angle is highly affected by the gravity caused by the weight of the frames and the elastomer. The self-folded angle is determined by the balance between the tension of the elastomer and the gravity applied to the elastomer.

Figure 10 shows the relationship between the tension and gravity acting in the direction perpendicular to the tangent at a certain point of the elastomer. In Prototype i, when the target angle θ_t is acute, the direction of the tensile force to self-fold and the direction of the gravity faces in the same direction (**Figure 10a**). Therefore, the folding angle θ_m is stable near the target angle, because folding is limited by the hinge. Even if the design angle θ_t is a right angle as in Prototype ii, the directions of tension and gravity do not oppose each other (**Figure 10b**). The self-folded angle with Prototype ii also becomes stable as Prototype i. The small difference occurred in the acute angle, because the 3D structure was slightly curved by thinning the frame to reduce weight of the frame.

On the other hand, when the target angle θ_t is obtuse, as in the prototype iii and iv, the difference occurs in the opening direction, because the gravity pushes the self-folded structure to the ground direction (**Figures 10c,d**). The reason why the standard deviation is large and the bending angle is not stable is also considered to be the opposite direction of tension and gravity.

We found that to designing the folding angle is feasible with the effect of the gravity. By further reducing the weight of the frame by changing the material, the influence of gravity will be reduced.

Displacement Measurement of the Self-Assembled Actuator Under DC Voltage Application

Experimental Condition

When voltage is applied to the self-assembled actuator, the elastomer extends to increase the folding angle. We measured the angular displacement ϕ_m with the application of different voltage. Each prototype was initially given a voltage of 1 kV, and then voltage was increased by 1 kV. Since the actuator was broken with 6 kV of voltage, we set the maximum voltage 5 kV. Experiments for each prototype was performed four times. In each trial, voltage was applied for at least 8 s to observe the response of the actuators. We used image analysis software (Kinovea) to measure the angle.

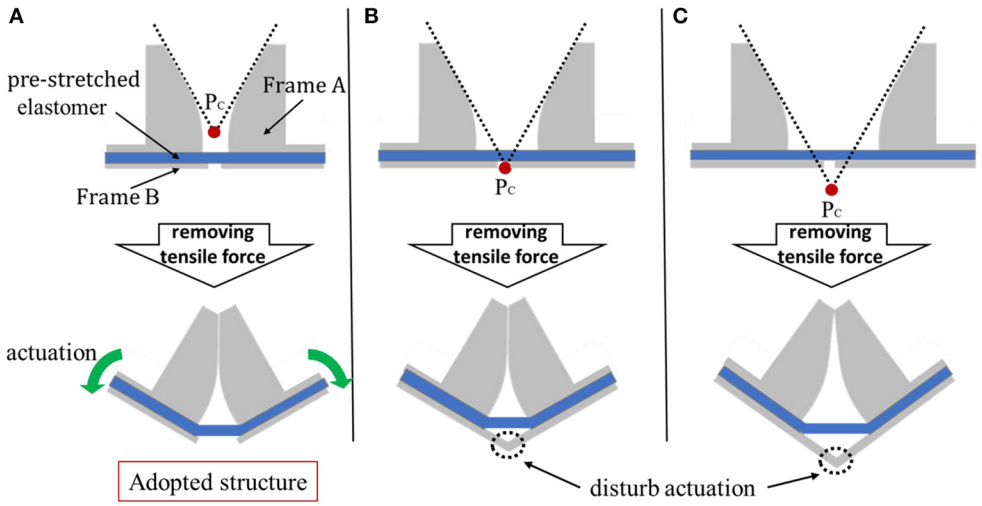

FIGURE 7 | Three examples of relationship between gaps and self-folding between frames A. In this research, in order to optimize the operation of the actuator, we designed the distance between frames A to be 2 mm and that of B to be 1 mm as shown in **(A)**. **(A)** The case where point Pc is above the plane where Frame B exists. This structure was adopted in this research. **(B)** The case where the point Pc is on the plane where Frame B exists. In this state, the actuator does not operate when voltage is applied. **(C)** The case where point Pc is below the plane where Frame B exists. As in case B, the actuator does not operate.

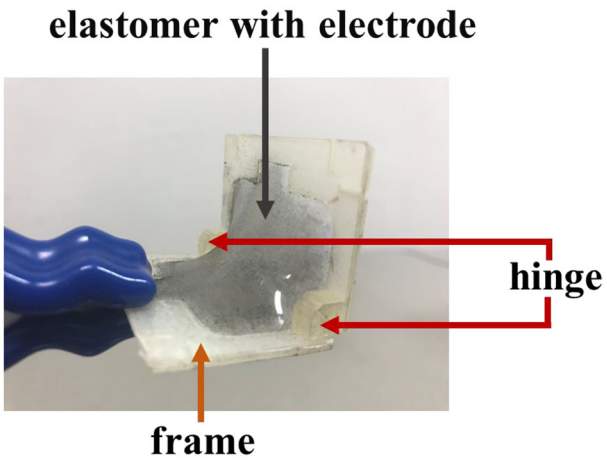

FIGURE 8 | Appearance of the self-assembled actuator.

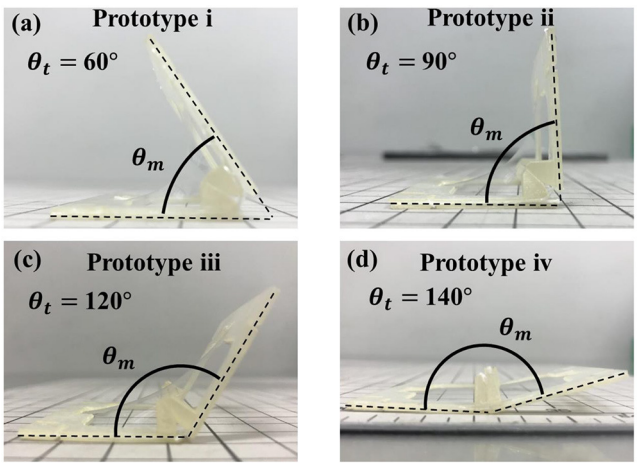

FIGURE 9 | Four prototypes with different target angles θ_t to measure self-folding angles θ_m. **(a)** The state of target angle $\theta_t = 60°$. **(b)** The state of target angle $\theta_t = 90°$. **(c)** The state of target angle $\theta_t = 120°$. **(d)** The state of target angle $\theta_t = 140°$.

Results and Discussions

Figure 11 shows the relationship between the applied voltage and the angular displacement for the prototypes i∼iv. One of the results out of four trials are shown. The reference angle for starting measurement is the angle at which the three-dimensional structure is formed by self-folding and the angle is fixed. In this experiment, it was considered that the angle change was sufficiently completed after 8 s, so the angle after 8 s from the start of voltage application was defined as the value when the actuation end. The greater voltage was applied, the greater folding angle was obtained. The maximum angle around 6° was obtained by applying 5 kV of voltage to prototype iii. In prototype iv, since it was broken when 5 kV was applied, the data with applying 1∼4 kV of voltage was plotted in the graph.

TABLE 1 | Measurement results of self-folded angle θ_m.

	i (60°)	ii (90°)	iii (120°)	iv (140°)
Average of θ_m (degree)	59.09	88.91	121.89	154.08
Error from θ_t (degree)	−0.91	−1.09	1.89	14.08
Standard deviation	0.85	0.87	5.49	5.78

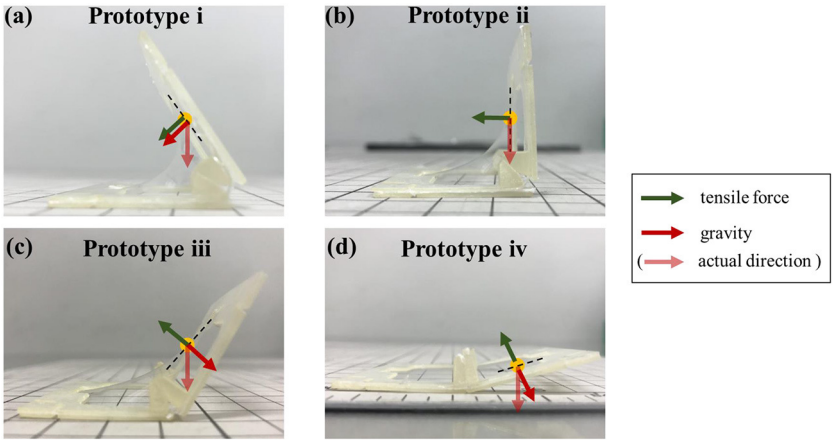

FIGURE 10 | Tension and gravity acting on each prototype. **(a)** In prototype i, the direction of the tensile force to self-fold and the direction of the gravity faces in the same direction. **(b)** In prototype ii, the directions of tension and gravity do not oppose each other. **(c,d)** As in the prototype iii and iv, when the target angle θ_t is obtuse, the directions of tension and gravity oppose each other.

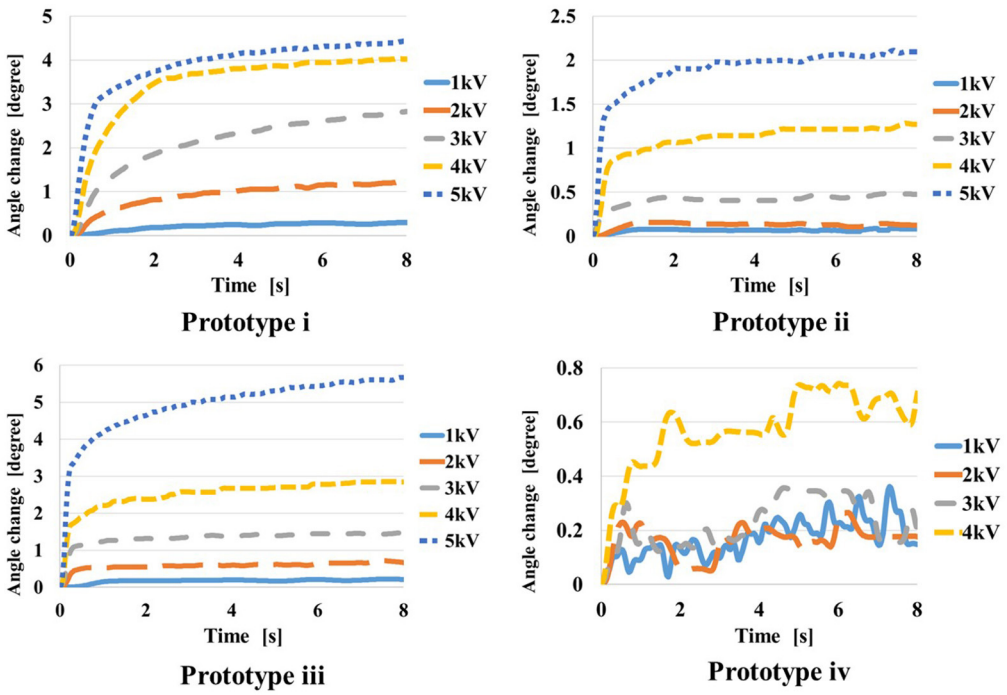

FIGURE 11 | Result of applying DC voltage to each prototype.

Figure 12 shows the temporal response of angular displacements when 5 kV is applied to prototypes i to iv. **Table 2** shows the results of the angular displacements after 8 s from the voltage application. For each prototype, 4 trials were performed and the average and the variance are shown. In each trial, small variance is found, however expected actuation is obtained by the application of voltage. The angular displacement increases in the order of prototype iii, i, ii.

When voltage is applied, the elastomer expands, so the balance between gravity and tension changes, and the contribution of gravity increases. This change in balance is considered to be greater when tension and gravity work in opposite directions, that is, when the folding angle is obtuse. Because the direction of opening coincides with the direction of gravity. The reason why the change in the prototype iv is small is thought to be because it was greatly affected by gravity at the time of self-folding, and the change in force balance

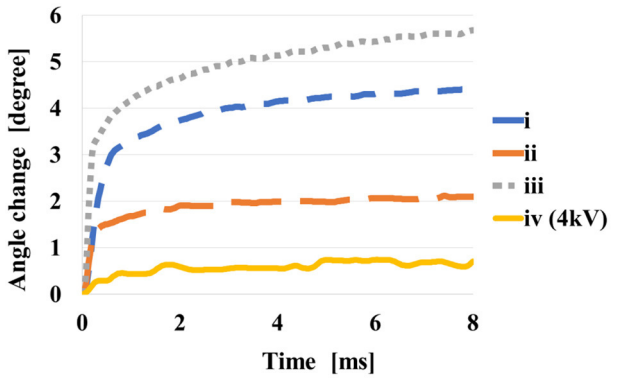

FIGURE 12 | Comparison of four prototypes at the applying voltage of 5 kV.

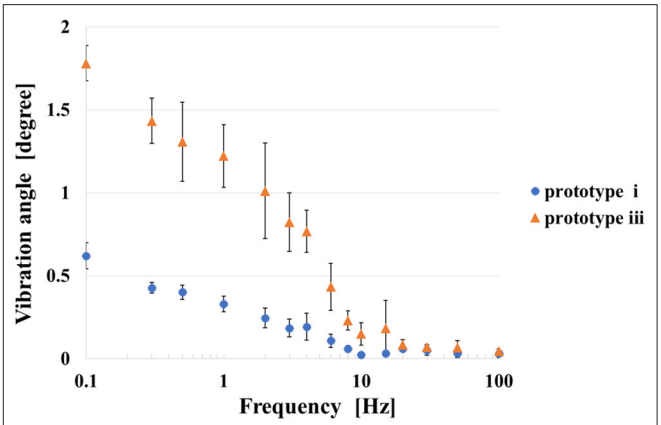

FIGURE 13 | Result of applying 5 kV AC voltage to prototype (i) and (iii).

TABLE 2 | Measurement results of angular displacement by applying DC voltage.

		i (60°)	ii (90°)	iii (120°)
Angular displacement (degree)	Trial 1	4.44	2.09	5.67
	Trial 2	3.11	3.02	5.12
	Trial 3	4.43	2.15	4.89
	Trial 4	3.97	2.09	5.67
	Average	3.98	2.54	5.17
	Variance	0.29	0.18	0.08

by voltage applying was not so large. It can be considered that the structure of the prototype iii is most affected by this effect. From this experiment, we consider the shape of the prototype iii is suit to obtain larger displacement as the actuator.

In addition, the response relaxations are found in **Figures 9**, **10**. These relaxations are considered to be caused by the viscosity of the elastomer. The acrylic elastomer (VHB 4905-J) used in this experiment is known to have the characteristics of higher viscosity and lower elasticity than silicon elastomer. Michel et al., show that the viscosity in acrylic elastomers can be minimized by pre-straining those (Michel et al., 2009). According to an experiment introduced by Shigemune et al., when 2 kV DC voltage was applied to an acrylic elastomer with 300% pre-strain, it took about 3,000 s to relax the strain (Shigemune et al., 2018). In our proposed mechanism, the elastomer is fixed with 300% pre-strain, so the viscosity can be kept small. Furthermore, since the motion direction of the self-assembled actuator is amplified by the effect of the gravity, the relaxation time is shorter than the previous study. Therefore, our proposed mechanism has the structure that can enhance the response of the elastomer by voltage application. In this experiment, the angular displacement in 8 s from the start of voltage application was recorded. Although the angular displacement gradually increases after 8 s, the figures properly show the response of the actuator to voltage application.

Displacement Measurement of the Self-Assembled Actuator Under AC Voltage Application

Experimental Condition

We conducted an experiment to investigate the response characteristics of the self-assembled actuators. We applied rectangular waves of 15 patterns of frequencies (0.1, 0.3, 0.5, 1.0, 2.0, 3.0, 4.0, 6.0, 8.0, 10.0, 15.0, 20.0, 30.0, 50.0, 100 Hz) to prototypes i and iii for 20 s. We selected prototypes i and iii, since the prototypes showed better performance with the DC voltage application. Difference between the maximum value and the minimum value of the angle between 5 and 20 s is plotted. This experiment was also performed four times for each prototype.

Results and Discussions

Figure 13 shows the results of the experiment. The plot in the figure represents the average of four trials, and the error bar represents the standard deviation of the four data. The angular displacement decreases as increasing the applied frequency. According to the result, the self-assembled actuator could respond to the rectangular wave with frequency up to 10 Hz. The standard deviation increases around 1 to 10 Hz. The prototype iii, which has the structure in which tension and gravity work in opposite directions, has a larger angular displacement than the prototype i when a voltage of the same frequency is applied.

Force Measurement of the Self-Assembled Actuator

Experimental Condition

We measured the force generated by the self-assembled actuator. The experimental environment is shown in **Figure 14**. We fixed the self-assembled actuator to the base, and connected the load cell at the tip of the actuator with a string. At this time, the string was set to remain taut. When a voltage is applied to the actuator, the actuator is driven toward the opening direction to pull the string. In this experiment, Prototype iii that showed the best performance in Experiments 4.2 and 4.3 was used. We

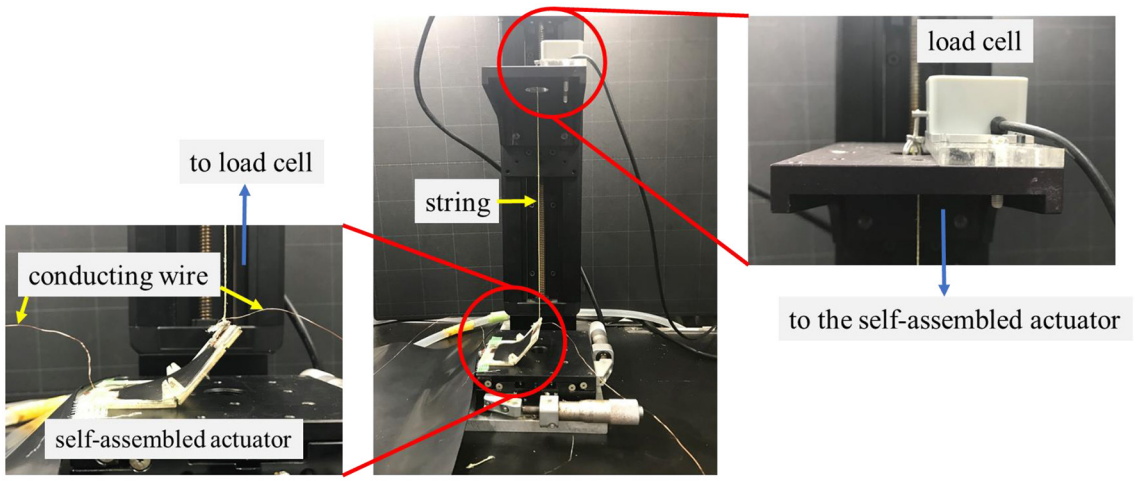

FIGURE 14 | The experimental environment for measuring the force generated by the self-assembled actuator. When a voltage is applied to the actuator, the string connected to the load cell is pulled downward. That force is recorded by the load cell.

TABLE 3 | Measurement results of the force generated by the actuator.

	Trial 1	Trial 2	Trial 3	Trial 4	Average
Driving force (N)	0.63	0.65	0.62	0.76	0.66

measured the force generated with applying voltage of 5 kV for four times.

Results and Discussions

Table 3 shows the results of the experiment. The average force of the four actuators was 0.66 N. Since the average weight of the four prototypes used in the experiment was 3.30 g, the gravity applied to the entire actuator is approximately 0.0033 [kg] $\times$9.8 [m/s] $=$ 0.032 [N]. Therefore, the effect of gravity is negligible compared to the force generated by the actuators. By considering the generated force, the actuator mechanism has great potential to be applied for various applications including a gripper which is demonstrated at later section.

APPLICATION FOR A GRIPPER

Design and Concept

Based on the experimental results, we attempted to apply the self-assembled actuator for a gripper. In order to achieve a large gripper operation by applying voltage, we select the self-folded angle 120° referring to the results described above.

Figure 15 shows the concept of a self-assembled gripper. The gripper has a structure, in which three joints are connected in series. Among the joints, an elastomer with electrodes is fixed at two places on both sides, and when voltage is applied, the joints are actuated in the direction of opening. The gripper achieves the gripping of an object by switching the voltage. The gripper opens while switching ON, and closes while switching OFF. The gripper keeps closing while switching OFF, therefore the device does not consume energy to grab an object.

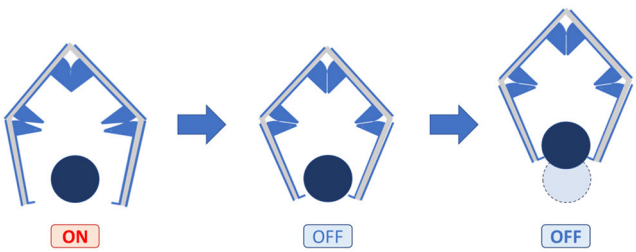

FIGURE 15 | Concept of self-folded gripper. The left and right joints open when a voltage is applied, and close when the voltage is removed.

Figure 16 shows the blueprint of the gripper and the appearance of the frame used. Based on the results of Experiments 4.2 and 4.3, the hinge angle was designed as shown in the figure. Frame A_1 has a claw hook at tips to make it easier to grab.

Figure 17 shows the process of making a gripper. **Figure 17A** shows a state in which frames are pasted on an elastomer given pre-strain of 300% as shown in **Figure 16**. When the elastomer outside the frame in the state (a) is removed, the gripper structure is formed (**Figure 17B**). Finally, the CNT electrode is attached to the elastomer to complete the gripper (**Figure 17C**).

The gripper can hold various objects by changing the design of the frame according to the shape of the object. Since the gripper has a flexible joint, it can hold the object even if its size slightly changes.

Performance

We verified the performance of the gripper by letting grab an object. The gripper grabs an object, and manually transfers to another position. **Figure 18** shows the procedures of the attempt.

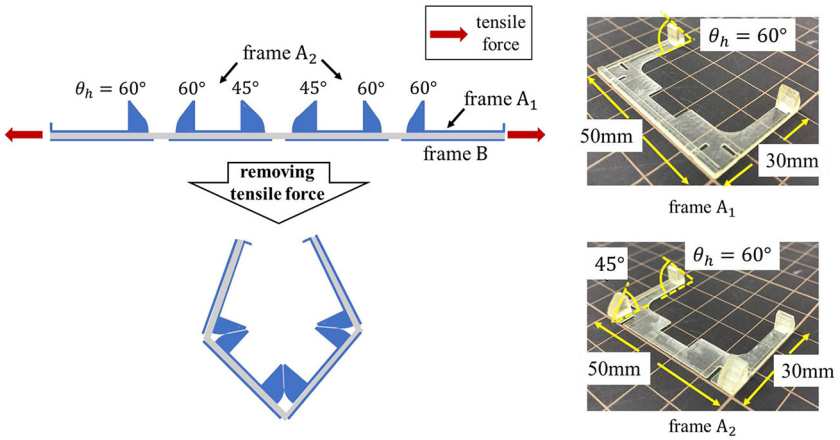

FIGURE 16 | Blueprint of the gripper and appearance of frames A_1 and A_2.

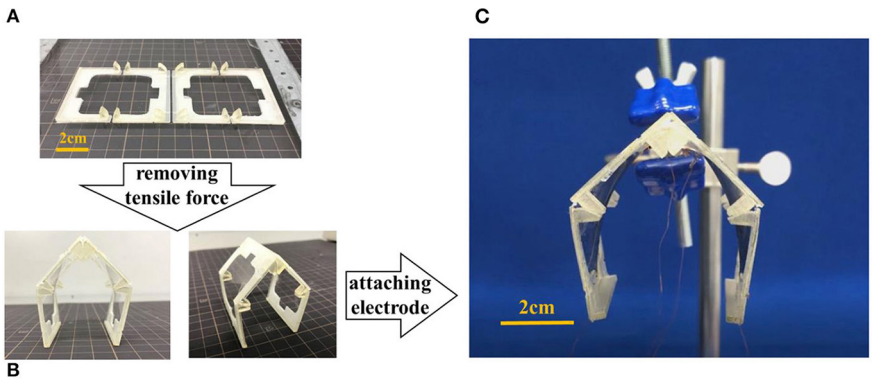

FIGURE 17 | The structure of the gripper. The center joint was designed to be 90°, and the left and right joints were designed to be 120°. **(A)** Frames are pasted on an elastomer given pre-strain of 300%. **(B)** When the elastomer outside the frame is removed, the gripper structure is formed. **(C)** Appearance of the gripper.

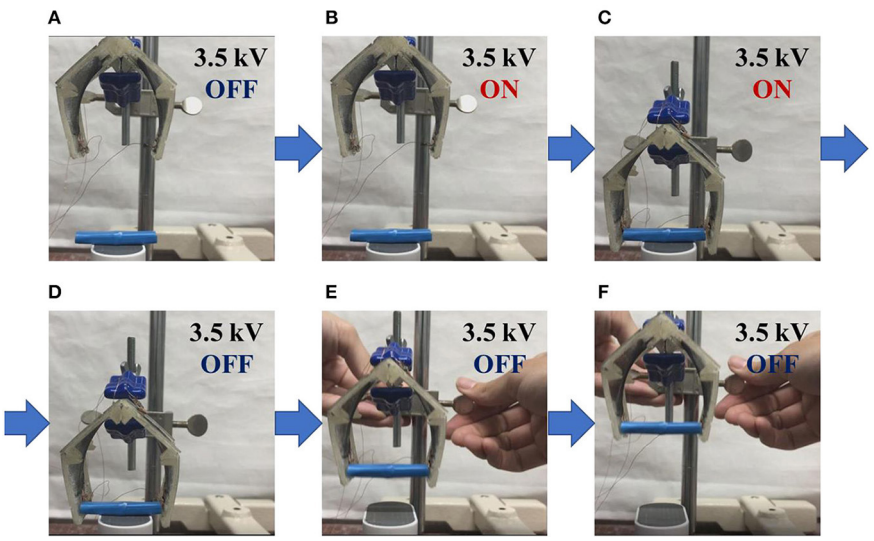

FIGURE 18 | Demonstration to grip an object. The gripper achieves in gripping the object by switching the voltage. **(A)** Initially, the gripper is closed. **(B)** When voltage is applied, the gripper opens. **(C)** Move the open gripper closer to the object. **(D)** When the voltage is turned off, the gripper grips the object. **(E,F)** The object can be lifted by moving the gripper.

In this experiment, an object with a length of 47.0 mm and a weight of 0.65 g was employed. In the state of (a), no voltage was applied to the electrode and the gripper was closed. When a voltage was applied, the gripper was in the open state (b). The gripper approaches to the object (c), then the voltage is turned off to grasp the object (d). The gripper successfully grasps the object with the length was 36.7 mm and weight up to 3.28 g.

CONCLUSION

In this research, we proposed a self-assembled actuator using an elastomeric material and a rigid frame. We evaluated accuracy of the self-folding actuators, and carried out an experiment to investigate the performance of the self-assembled actuator by applying DC and AC voltage. We attempted to apply the actuator for a self-assembled gripper, and achieved to grab an object with the length of 36.7 mm and the weight of 3.28 g. The 3D structure formation by self-folding was limited by the hinge when the design angle was obtuse, so the standard deviation of data was small. On the other hand, when the design angle was acute, the folding angle was determined by the balance between tension and gravity, so the standard deviation of data was relatively large. When DC voltage was applied, the folding angle suitable for the largest displacement was 120°. When AC voltage was applied, the prototypes were confirmed to respond at frequencies below 10 Hz. In the future work, we try to assemble much complex structures using multiple hinges. Complex self-assembled actuators will realize flexible locomotion by utilizing its flexible joints.

DATA AVAILABILITY STATEMENT

The datasets generated for this study are available on request to the corresponding author.

AUTHOR CONTRIBUTIONS

All authors made an intellectual contribution to this paper and acknowledged the publication. In particular, NH designed and fabricated the devices, designed the experimental setup, analyzed the data, contributed to data interpretation, and wrote the paper. HSh designed the concept of the project, contributed to data interpretation, and wrote the paper. AM designed the experimental setup and wrote the paper. HSa and SM provided advice to fundamentals of the research and wrote the paper.

FUNDING

This work was supported by JSPS KAKENHI Grant Nos. 18H05473, 18H05895, and 19K20377, and the Waseda University Grant for Special Research Projects (Project No. 2018S-125).

SUPPLEMENTARY MATERIAL

The Supplementary Material for this article can be found online at: https://www.frontiersin.org/articles/10.3389/frobt.2019.00152/full#supplementary-material

Supplementary Video | This video shows the process of fabricating a self-folding prototype shown in **Figure 5**.

REFERENCES

Araromi, O. A., Gavrilovich, I., Shintake, J., Rosset, S., Richard, M., Gass, V., et al. (2015). Rollable multisegment dielectric elastomer minimum energy structures for a deployable microsatellite gripper. *IEEE/ASME Trans. Mechatron.* 20, 438–446. doi: 10.1109/TMECH.2014.2329367

Dobson, C. M. (2003). Protein folding and misfolding. *Nature* 426, 884–890. doi: 10.1038/nature02261

Duduta, M., Wood, R. J., and Clarke, D. R. (2016). Multilayer dielectric elastomers for fast, programmable actuation without prestretch. *Adv. Mater.* 28, 8058–8063. doi: 10.1002/adma.201601842

Felton, S., Tolley, M., Demaine, E., Rus, D., and Wood, R. (2014). A method for building self-folding machines. *Science* 345:644. doi: 10.1126/science.1252610

Hosoya, N., Masuda, H., and Maeda, S. (2019). Balloon dielectric elastomer actuator speaker. *Appl. Acoust.* 148, 238–245. doi: 10.1016/j.apacoust.2018.12.032

Liu, Y., Boyles, J. K., Genzer, J., and Dickey, M. D. (2012). Self-folding of polymer sheets using local light absorption. *Soft Matter* 8, 1764–1769. doi: 10.1039/C1SM06564E

Liu, Y., Shaw, B., Dickey, M. D., and Genzer, J. (2017). Sequential self-folding of polymer sheets. *Sci. Adv.* 3:e1602417. doi: 10.1126/sciadv.1602417

Michel, S., Zhang, X. Q., Wissler, M., Löwe, C., and Kovacs, G. (2009). A comparison between silicone and acrylic elastomers as dielectric materials in electroactive polymer actuators. *Poly. Int.* 59, 391–399. doi: 10.1002/pi.2751

Minaminosono, A., Shigemune, H., Okuno, Y., Katsumata, T., Hosoya, N., and Maeda, S. (2019). A deformable motor driven by dielectric elastomer actuators and flexible mechanisms. *Front. Robot. AI* 6:1. doi: 10.3389/frobt.2019.00001

Mintchev, S., Shintake, J., and Floreano, D. (2017). Bioinspired dual-stiffness origami. *Sci. Robot.* 3:eaau0275. doi: 10.1126/scirobotics.aau0275

Natori, M. C., Katsumata, N., Yamakawa, H., Sakamoto, H., and Kishimoto, N. (2013). "Conceptual model study using origami for membrane space structures," *International Design Engineering Technical Conferences and Computers and Information in Engineering Conference, Volume 6B: 37th Mechanisms and Robotics Conference* (ASME). doi: 10.1115/DETC2013-13490

O'Hallorana, A., O'Malley, F., and McHugh, P. (2008). A review on dielectric elastomer actuators, technology, applications, and challenges. *J. Appl. Phys.* 104:071101. doi: 10.1063/1.2981642

Pelrine, R., Kornbluh, R., Pei, Q., and Joseph, J. (2000).High-speed electrically actuated elastomers with strain greater than 100%. *Science* 287, 836–839. doi: 10.1126/science.287.5454.836

Plante, J. S., and Dubowsky, S. (2007). On the performance mechanisms of dielectric elastomer actuators. *Sens. Actuat. A* 137, 96–109. doi: 10.1016/j.sna.2007.01.017

Saito, K., Nomura, S., Yamamoto, S., Niiyama, R., and Okabe, Y. (2017). Investigation of hindwing folding in ladybird beetles by artificial elytron transplantation and microcomputed tomography. *Proc. Natl. Acad. Sci. U.S.A.* 114, 5624–5628. doi: 10.1073/pnas.1620612114

Shigemune, H., Maeda, S., Cacucciolo, V., Iwata, Y., Iwase, E., Hashimoto, S., et al. (2017). Printed paper robot driven by electrostatic actuator.

IEEE Robot. Automat. Lett. 2, 1001–1007. doi: 10.1109/LRA.2017.2658942

Shigemune, H., Maeda, S., Hara, Y., Hosoya, N., and Hashimoto, S. (2016). Origami robot: a self-folding paper robot with an electrothermal actuator created by printing. *IEEE/ASME Trans. Mechatron.* 21, 2746–2754. doi: 10.1109/TMECH.2016.2593912

Shigemune, H., Sugano, S., Nishitani, J., Yamauchi, M., Hosoya, N., Hashimoto, S., et al. (2018). Dielectric elastomer actuators with carbon nanotube electrodes painted with a soft brush. *MDPI Actuat.* 7:51. doi: 10.3390/act7030051

Shintake, J., Rosset, S., Schubert, B., Floreano, D., and Shea, H. (2016). Versatile soft grippers with intrinsic electroadhesion based on multifunctional polymer actuators. *Adv. Mater.* 28, 231–238. doi: 10.1002/adma.201504264

Tolley, M. T., Felton, S. M., Miyashita, S., Aukes, D., Rus, D., and Wood, R. J. (2014). Self-folding origami: shape memory composites activated by uniform heating. *Smart Mater. Struct.* 23:094006, doi: 10.1088/0964-1726/23/9/094006

Torisaka, A., Satoh, Y., Akita, T., Natori, M. C., Yamakawa, H., and Miyashita, T. (2016). "Membrane space structure with sterical support of booms and cables," *3rd AIAA Spacecraft Structures Conference* (American Institute of Aeronautics and Astronautics Inc, AIAA). doi: 10.2514/6.2016-1217

Wissler, M., and Mazza, E. (2007).Electromechanical coupling in dielectric elastomer actuators. *Sens. Actuat. A* 138, 384–393. doi: 10.1016/j.sna.2007.05.029

Conflict of Interest: The authors declare that the research was conducted in the absence of any commercial or financial relationships that could be construed as a potential conflict of interest.

frontiers in Robotics and AI

ORIGINAL RESEARCH
published: 11 February 2020
doi: 10.3389/frobt.2020.00009

A Worm-Like Biomimetic Crawling Robot Based on Cylindrical Dielectric Elastomer Actuators

Sascha Pfeil[1]*, *Markus Henke*[2,3], *Konrad Katzer*[4,5], *Martina Zimmermann*[4,5] and *Gerald Gerlach*[1]

[1] Faculty of Electrical and Computer Engineering, Institute of Solid State Electronics, Technische Universität Dresden, Dresden, Germany, [2] Faculty of Electrical and Computer Engineering, Institute of Semiconductors and Microsystems, Technische Universität Dresden, Dresden, Germany, [3] PowerOn Ltd., Auckland, New Zealand, [4] Fraunhofer Institute for Material and Beam Technology IWS, Dresden, Germany, [5] Faculty of Mechanical Science and Engineering, Institute for Material Science, Technische Universität Dresden, Dresden, Germany

In recent years the field of soft robotics has gained a lot of interest both in academia and industry. In contrast to rigid robots, which are potentially very powerful and precise, soft robots are composed of compliant materials like gels or elastomers (Rich et al., 2018; Majidi, 2019). Their exclusive composition of nearly entirely soft materials offers the potential to extend the use of robotics to fields like healthcare (Burgner-Kahrs et al., 2015; Banerjee et al., 2018) and advance the emerging domain of cooperative human-machine interaction (Asbeck et al., 2014). One material class used frequently in soft robotics as actuators are electroactive polymers (EAPs). Especially dielectric elastomer actuators (DEAs) consisting of a thin elastomer membrane sandwiched between two compliant electrodes offer promising characteristics for actuator drives (Pelrine et al., 2000). Under an applied electric field, the resulting electrostatic pressure leads to a reduction in thickness and an expansion in the free spatial directions. The resulting expansion can reach strain levels of more than 300% (Bar-Cohen, 2004). This paper presents a bioinspired worm-like crawling robot based on DEAs with additional textile reinforcement in its silicone structures. A special focus is set on the developed cylindrical actuator segments that act as linear actuators.

Keywords: biomimetics, cylindrical DEA, dielectric elastomer actuators, textile reinforcement, soft robotics, *in-situ* pre-stretch, linear actuators, inflatable actuators

OPEN ACCESS

Edited by:
Stefan Seelecke,
Saarland University, Germany

Reviewed by:
Ioannis Andrea Ieropoulos,
University of the West of England, United Kingdom
Deepak Trivedi,
General Electric, United States

***Correspondence:**
Sascha Pfeil
sascha.pfeil@tu-dresden.de

Specialty section:
This article was submitted to Soft Robotics, a section of the journal Frontiers in Robotics and AI

Received: *06 September 2019*
Accepted: *20 January 2020*
Published: *11 February 2020*

Citation:
Pfeil S, Henke M, Katzer K, Zimmermann M and Gerlach G (2020) A Worm-Like Biomimetic Crawling Robot Based on Cylindrical Dielectric Elastomer Actuators. Front. Robot. AI 7:9. doi: 10.3389/frobt.2020.00009

1. INTRODUCTION

Soft robotics are an emerging field for academic and industrial research. In order to adapt the conventional robotic architecture to changing requirements in both industrial and service robotics, there is a currently change from continuously running assembly lines to more adaptive ones (Zhong et al., 2017). The trend is to develop the handling of one and the same product to more adaptive fabrication techniques that can handle changing products in real-time. Especially in e-commerce applications there is a strong demand for more flexible robots (Liang et al., 2015). The second big driver in industry is the introduction of so-called collaborative robots, or cobots (Romero et al., 2016). In future factories workers and robots will co-exist and collaborate as colleagues. This close collaboration introduces a risk of injuries and accidents caused by the robots. To prevent this and to increase the psychological acceptance of cobots as colleagues, it is advantageous to introduce soft robotic structures where possible.

Before soft, collaborative robotic systems will be widely used, it is necessary to develop materials, processes and components that are soft. Such parts can resemble all sub-components that are necessary to build up conventional robots, such as sensors, actuators, signal processors, and the structure itself. Within the recent years many major breakthroughs on these fields have been made by scientists and engineers all over the world, resulting in the world's first entirely soft, fully functional robot, the octobot, in 2016 (Wehner et al., 2016). Even though the octobot was a world's first, many scientists work on sensors and actuators that are soft and flexible, but can be controlled electrically. Such concepts include electroactive polymers (Bar-Cohen, 2004), especially dielectric elastomers (DEs) (Carpi et al., 2008) or HASEL actuators (Kellaris et al., 2018). DEs have been proven as multi-functional (Anderson et al., 2012) and can be used as signal-generators (O'Brien and Anderson, 2012; Henke et al., 2018) and -processors (Wilson et al., 2016, 2017) for self-controlled, untethered robots (Cao et al., 2017; Henke et al., 2017, 2019). Due to their wide range of applications, there is a focus on electroactive driven soft robotics since end of the 1990s (Pelrine et al., 1998).

Beyond these efforts in the field of soft robotics there is also a trend to make such robots self-sustainable. A core-aspect for self-sustainability is energy autonomy. Different approaches deal with energy harvesting to overcome the need of external power supplies for robotic concepts. Aghakhani and Basdogan (2018) showed a concept to convert mechanical energy into electrical energy by using piezoelectric patches. Also the use of electroactive polymers to generate electrical energy is possible as shown by McKay et al. (2011) or Mathew and Koh (2018). These developments pave the way for fully autonomous robots like the Row-Bot presented by Philamore et al. (2015).

Worm-like robotic concepts based on different soft materials are already implemented. Often these robotic concepts use peristaltic motion with a small number of segments that can contract axially and expand in radial direction (Dario et al., 2004; Omori et al., 2009; Seok et al., 2010). Another approach to achieve forward motion is to use a method of anchored crawling. This method clamps the ends of an actuator element to the ground, which allows the robot to move forward. An actuator element located between the lockable ends ensures the forward motion by expanding in axial direction like in Chowdhury et al. (2017) or Joey et al. (2019). In this paper we present a robot that inherits two features that have been rarely used in the field of soft robotics until now. The first one is the concept to use DEAs in large area complex geometries. In the presented case the actuators are not applied in the well established planar geometry but in a cylindrical shape. This means that the planar DEAs are wrapped around a cylindrical inner holding structure, providing the shape for the actuators. The second innovative feature is to use a textile material as reinforcement structure for the inner silicone parts. Due to miniaturization the used materials become very unstable and fragile. Also the inner structures have to take up some external forces and the forces generated by the DEAs themselves. These forces can possibly lead to undefined deformations and changes of the aspired cylindrical geometry. In the presented concept a textile material consisting of parallel oriented carbon fibers, coated in an styrene-butadiene rubber system is used to ensure the shape consistency. The textile reinforcement enhances the stiffness in the supporting areas of the robot. Due to the reinforcement a miniaturization of the system is possible while the structures still can handle the existing forces without collapsing or breaking. Finally, the movement of the cylindrical DEA elements is limited in a way that they act as linear actuators in length direction. This paper is mainly about the development, description, and the characterization of these cylindrical DEA elements.

2. METHODS

2.1. Robotic Concept

The aim of the robotic concept is to develop a biomimetic structure that is driven by customized actuator segments of a cylindrical shape. These segments act as the core part of the robot. The whole robotic setup is inspired by the biological role-model of inchworms. They consist (besides many other body parts) of an inner muscular structure with longitudinal oriented muscles and an outer structure with ring muscles, generating the forward movement (Edwards and Bohlen, 1996). In the developed robotic concept the cylindrical actuator segments serve the function of force generation for the movement. The cylindrical actuator segments consist of rolled up DEAs around an inner holding structure. The robot consists of three cylindrical DEAs as actuator segments on the circumference of the inner-holding structure. Their ground electrode is continuously connected to all three actuator elements so it only needs one electrical connection for the ground electrode at the foot-end of the robot. The activation of the single elements then is realized by switching the high voltage electrodes of each actuator element. The inner holding structure is made of a soft silicone mixture *Dow Corning Sylgard 184* © and designed in a way to serve different needs. First, it gives the cylindrical shape to the DEAs. This becomes necessary since the only 100 μm *Elastosil 2030* © dielectric membrane of the DEAs would collapse under its own weight without an additional holding structure. Second, the inner holding structure limits the degrees of freedom for the actuation and ensures a mainly longitudinal expansion. Its geometry is constructed to predominantly elongate in length direction when an internal gas pressure is applied (see **Figure 1**). Third, it sets the robot to a certain operating point and gives a well defined shape for both the DEAs and the whole setup. In the presented stage of development a pressure pump is used to provide the internal gas pressure. In later developments a pneumatic valve can be used to prevent the compressed air from outflowing. Since the compressed air mainly serves shaping purposes it could also be replaced by another medium. Even approaches toward self-sustainability by eliminating the use of an external pressure pump are possible. As presented by Onal et al. (2017), an integrated pressure generator could be used to provide the internal gas pressure.

In contrast to established DEA concepts, the developed actuator segments are non-planar and controlled in their movement direction to act as linear actuators. The fabrication of the inner holding structure itself is done in a cast process.

Therefore, a cast mold is designed to cast the silicone mixture to a half of the desired geometry. The silicone is cast around a textile material consisting of SGL's *Sigrafil C T50-4.4/255-E100* © fiber with a grammage of 200 $\frac{g}{m^2}$ coated with a low-viscosity *Lefasol VL 90/1* © styrene-butadiene rubber (SBR) system by Lefatex. The textile material is added as an additional stiffening in the supporting rings of the inner structure. It ensures the needed mechanical stability to take up the existing forces due to the application of the additional features for the robotic concept. **Figure 2** shows the concept of a single half structure with integrated textile material and the full concept for the inner holding structure consisting of two half structures attached to each other. The dimensions of the inner holding structure are shown in **Figure 3**. The dimensions are decreased to a point that takes the miniaturization to a limit under common laboratory conditions without special production technologies.

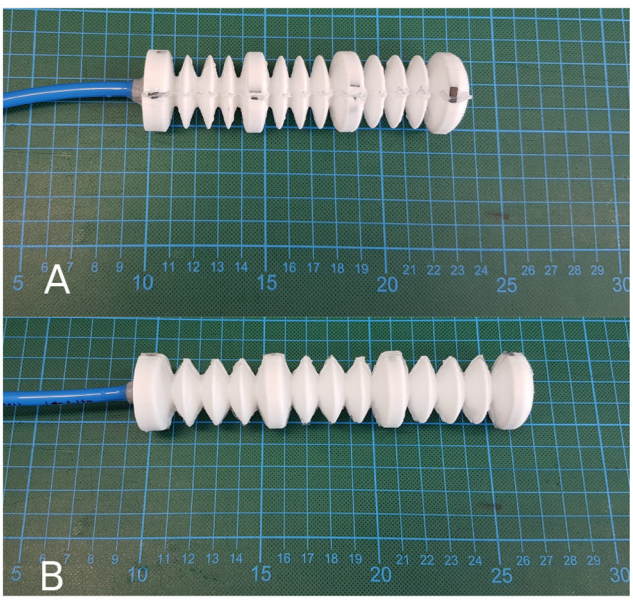

FIGURE 1 | Inner holding structure. **(A)** without applied gas pressure in initial state, **(B)** with an applied gas pressure of 80 mbar.

Below these dimensions some advanced fabrication technologies would become necessary in order to maintain produceability. The mechanical dimensions of the robot, including its weight and the outer diameter at the tips of the gripper rings are summed up in **Table 1**. The other functional parts of the robot serve the generation of a forward motion. Namely these are the hook-like gripper rings. Their function is to generate a directional adjusted friction to allow an easy forward movement and to stick to the underlying surface in backward direction. The design of the grippers follows the idea of using hooks to prevent backward movement by anchoring in the ground. The forward movement remains unaffected by this as the geometry allows the anchoring to be released in the forward direction. The movement itself follows the concept of anchored crawling. The three actuator segments are switched with a phase shift of 120° between each other, performing a square waveform of the voltage. **Figure 4** illustrates the time behavior of the electrical signals on each DEA for an exemplary switching frequency of 4 Hz. The switching to an electrical active state leads to an expansion of the actuator elements. In the realized concept the actuators elongate with a time overlap between each other. A further function of the gripper rings is to ensure a gap between the outer DEA electrodes and the surface on which the robot is moving in order not to destroy the DEAs. **Figure 5** shows the full robotic concept with the previously described elements. The movement itself follows a simple concept of consecutively activating the single actuator segments to generate a forward motion of the robot.

2.2. Theory: Cylindrical Actuation

In order to get an assessment of the generated force that expands the actuator segments of the presented robot, some general electromechanical considerations are made. In comparison to the typical planar DEA setups, the cylindrical geometry of the presented crawling robot requires some considerations adapted to the geometrical conditions. First of all, the use of cylindrical coordinates is advisable to describe the behavior. Besides the change to cylindrical coordinates, some physical assumptions are made. The electrodes on the inner and outer radius are assumed as neglectable thin and perfectly conductive. Also the electrical voltage and therefore the electrical field is assumed as oriented exclusively in radial direction of $\vec{e}_\rho$ between the electrodes. Due to the use of an inner holding structure the

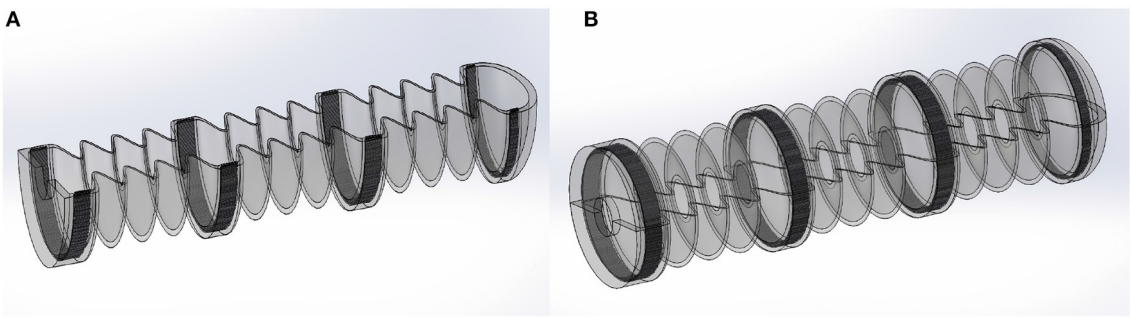

FIGURE 2 | Concept of inner holding structure. **(A)** single half as it is cast with integrated textile material at supporting positions, **(B)** full inner holding structure assembled from two similar cast halfs.

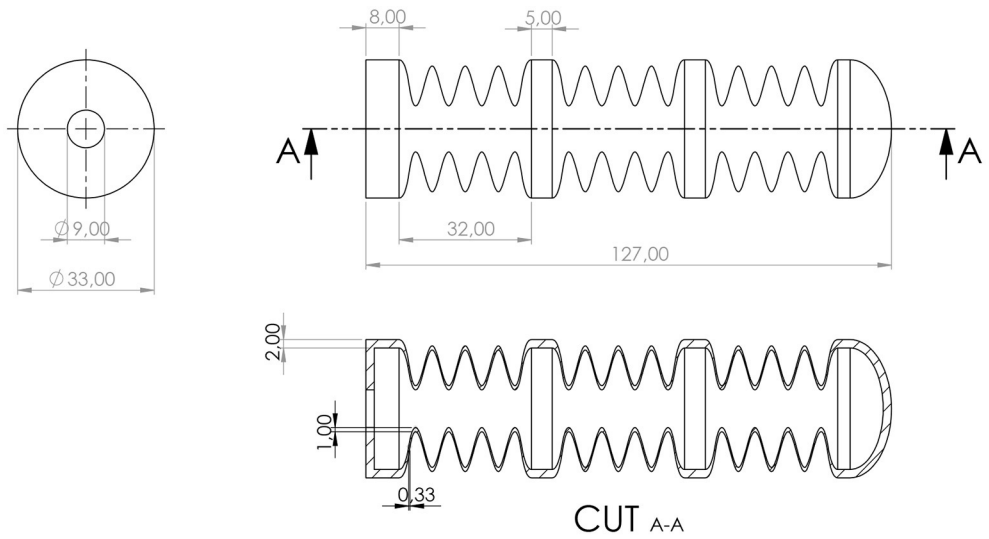

FIGURE 3 | Construction of the inner holding structure with dimensions.

TABLE 1 | Overview of the mechanical parameters and values of the robot.

	Setup value
Weight	29.08 g
Length	127 mm
Outer diameter	49.5 mm
Gait	Anchored crawling

free spatial directions for the expansion of the actuators are limited. While pure cylindrical actuators would mainly expand in radial direction (Carpi et al., 2009), the presented crawling robot expands in longitudinal direction to achieve a forward motion. The limitation of the free spatial directions to expand is ensured by the inflatable inner holding structure. The DEAs are attached to the circumference of the inner holding structure so that the expansion is limited by the mechanical behavior of the inner structure. The inner radius r_i is fixed and does not change. The applied charge Q on the outer electrode leads to an electric field between the electrodes that moves the outer electrode toward the inner electrode. The dielectric material itself is assumed as isotropic and homogeneous. Under these assumptions we derive an expression for the electrical generated maxwell pressure. Using this pressure description as a connection between the electrical and the mechanical behavior, we can describe the generated force of the actuator segments. The generated maxwell pressure on the electrodes can be described using some analytical descriptions for electrodynamics. According to Süße (2006) and Eringen and Maugin (2012), the maxwell stress tensor can be written as:

$$\vec{T} = \vec{E} \otimes \vec{E} + \vec{B} \otimes \vec{B} - \frac{1}{2} \cdot \epsilon_0 (E^2 + B^2) \tag{1}$$

which is equivalent to

$$\vec{T} = \epsilon(\vec{E} \cdot \vec{E^T} - \frac{1}{2} \cdot \mathrm{I} \cdot |E|^2) + \frac{1}{\mu}(\vec{B} \cdot \vec{B^T} - \frac{1}{2} \cdot \mathrm{I} \cdot |B|^2). \tag{2}$$

with the electrical field strength E, the dielectric permittivity ϵ, the magnetic field strength B, the magnetic permeability μ, and the unit matrix I. Due to the quasi electrostatic case, we can assume the magnetic field strength as zero which simplifies the equation for the maxwell stress tensor to:

$$\vec{T} = \epsilon(\vec{E} \cdot \vec{E^T} - \frac{1}{2} \cdot \mathrm{I} \cdot |E|^2). \tag{3}$$

Figure 6 shows the principle geometry conditions for the cylindrical actuator. The first step toward an expression for the maxwell stress is to describe the electric field, caused by the charge distribution σ_A, which contains the charge Q over the area of the cylinder wall A.

$$\vec{E} = \frac{Q}{\epsilon A} = \frac{\sigma_A}{\epsilon} \cdot \vec{e}_{\rho,\phi,z} \tag{4}$$

The derived equation for the electric field can be inserted into Equation (2).

$$\vec{T} = \epsilon[\begin{pmatrix} E_\rho \\ E_\phi \\ E_z \end{pmatrix} \cdot (E_\rho; E_\phi; E_z) - \frac{1}{2} \begin{pmatrix} 1 & 0 & 0 \\ 0 & 1 & 0 \\ 0 & 0 & 1 \end{pmatrix} \cdot E^2] \tag{5}$$

$$\vec{T} = \frac{\epsilon}{2} \begin{pmatrix} E^2 & 0 & 0 \\ 0 & -E^2 & 0 \\ 0 & 0 & -E^2 \end{pmatrix} \tag{6}$$

Using the expression for the maxwell stress tensor, we can calculate the force impact on the cylindrical wall.

$$\vec{F} = \iint_A \vec{T} \cdot d\vec{A} \tag{7}$$

The differential area element $d\vec{A}$ comprises of

$$d\vec{A} = r_o d\phi dz \cdot \vec{e}_\rho \tag{8}$$

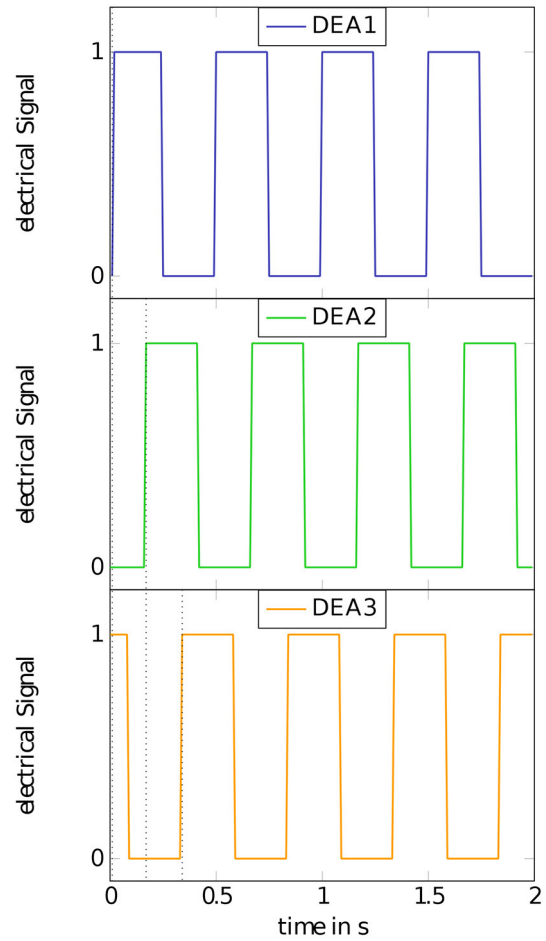

FIGURE 4 | Concept of consecutively switching of the actuator segments. The three DEAs are switched with a phase shift of 120° between each other, performing a square waveform of the voltage.

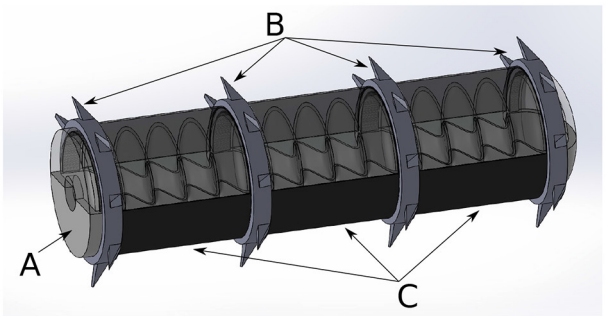

FIGURE 5 | Full robotic concept with, **(A)** inflatable inner holding structure, **(B)** gripping segments with hooks on circumference, and **(C)** cylindrical actuator segments based on dielectric elastomer actuators.

in cylindrical coordinates. The force can be written as

$$\vec{F} = \frac{\epsilon \cdot \sigma_A^2}{2\epsilon^2} r_o \int_0^l \int_0^{2\pi} d\phi dz. \tag{9}$$

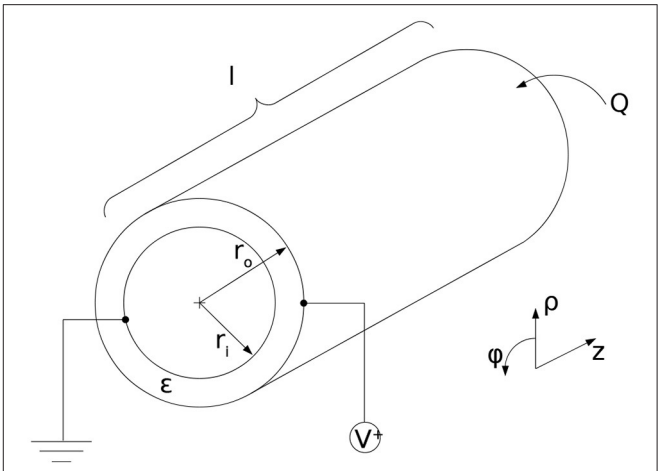

FIGURE 6 | Geometrical conditions for the cylindrical dielectric elastomer actuator with radii r_i and r_o, length l, applied voltage V and charge Q.

After solving the integral, the final expression for the force impact on the cylindric wall is

$$F = \frac{\sigma_A^2}{2\epsilon} \cdot 2\pi r_o l \tag{10}$$

$$F = \frac{\sigma_A^2}{2\epsilon} \cdot A. \tag{11}$$

In order to derive an equation consisting of practical useable values, the expression of the force can be reformulated. To get an expression that depends on the applied voltage V instead of the charge distribution σ_A, a consideration of the electric potential Φ in radial direction is necessary. In general, the potential can be expressed as

$$\Phi_o = \Phi_i - \int_{r_i}^{r_o} E(r) dr. \tag{12}$$

With Equation (4) for the electric field from above the potential is

$$\Phi_o = \Phi_i - \frac{Q}{2\epsilon\pi l} \cdot \int_{r_i}^{r_o} \frac{1}{r} dr \tag{13}$$

$$\Phi_o = \Phi_i - \frac{Q}{2\epsilon\pi l} \cdot ln(\frac{r_o}{r_i}). \tag{14}$$

Using a description for the applied voltage as a difference of electric potentials

$$V = \Phi_o - \Phi_i = \frac{Q}{2\epsilon\pi l} \cdot ln(\frac{r_i}{r_o}) \tag{15}$$

we can derive an expression for the charge Q by converting the equation for the voltage

$$Q = \frac{V 2\epsilon\pi l}{ln(\frac{r_i}{r_o})}. \tag{16}$$

Using this formulation the charge distribution σ_A can be described as

$$\sigma_A = \frac{Q}{A} = \frac{V \cdot 2\epsilon\pi l}{ln(\frac{r_i}{r_o})2\pi r_o l} = \frac{V \cdot 2\epsilon}{ln(\frac{r_i}{r_o})r_o} \tag{17}$$

which leads to an expression for the force of

$$F = \frac{\epsilon V^2 \pi l}{ln^2(\frac{r_i}{r_o})r_o}. \tag{18}$$

For the further use, we need a description as stress component. Therefore, a division by the area A leads to the final expression for the stress component $\sigma_{maxwell}$ in radial direction due to an electric charge on the electrode:

$$\sigma_{\text{maxwell}} = \frac{F}{A} = \frac{\epsilon V^2}{ln^2(\frac{r_i}{r_o})2r_o^2}. \tag{19}$$

Due to the assumed incompressibility of the silicone material, the derived description for the radial stress component also acts in the other free spatial directions. In this case the maxwell pressure $\sigma_{maxwell}$ also acts on the wall thickness of the cylinder and causes a length dilatation. The area over the wall thickness can be calculated by the following expression.

$$A_{\text{wall}} = \pi(r_o^2 - r_i^2) \tag{20}$$

The force generated by a single actuator segment can than be calculated by the following equation.

$$F = \sigma_{\text{maxwell}} \cdot A_{\text{wall}} \tag{21}$$

$$F = \frac{\epsilon V^2}{ln^2(\frac{r_i}{r_o})2r_o^2} \cdot \pi(r_o^2 - r_i^2) \tag{22}$$

For the given dimensions of the crawling robot of $r_o = 16.55$ mm, $r_i = 16.5$ mm, and a dielectric permittivity ϵ of $2.8 * 0.8854 * 10^-11 \frac{A \cdot s}{V \cdot m}$ the generated force for an applied voltage of $3,000V$ equals $0.313\ N$. **Figure 7** shows the force curves for different voltages applied to 50 and 100 μm thin dielectric membranes.

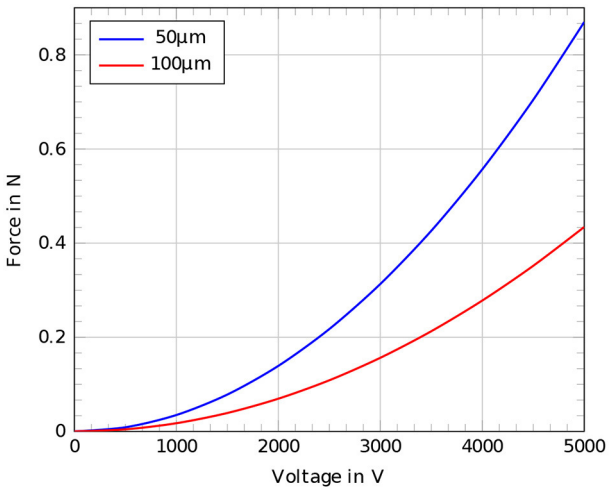

FIGURE 7 | Comparison of the estimated forces according to the analytical derived expression for voltages up to 5,000 V, red: 100μm dielectric membrane, blue: 50 μm dielectric membrane.

3. MEASUREMENTS AND EXPERIMENTAL SETUP

The characterization of the robotic concept is a crucial task to validate the mechanical behavior of the demonstrator. Therefore, displacement measurements were done to evaluate the extension of the robot. Two demonstrators were used for different test scenarios. To evaluate the behavior of the robotic concept and the single actuator segments, different measurements were performed to characterize the setup. All of the measurements were carried out on a fully built up robot including all the previously described functional parts. For the following measurements two different versions of the robot were used: a version consisting of a 50 μm *Elastosil 2030* © dielectric membrane and a version consisting of a 100 μm *Elastosil 2030* © dielectric membrane. To ensure a well-defined setting of the pressure, a microfluidic pressure pump "Elveflow AF1-P-1600" with a pressure stability of 1 mbar and a power consumption of maximum 15 W according to the datasheet (Elveflow, 2019) was used for all the measurements. The actuators were driven with a high voltage source *Peta-pico-Voltron* delivering output voltages of up to 5 kV and output currents of maximum 220 μA according to Schlatter et al. (2018). Except for the characterization of the crawling movement, a DIC system from GOM, ARAMIS 5M was used to perform camera based displacement measurements. The used camera has a resolution of 2,448 × 2,050 pixels with a focal length of 50 mm. The frame rate was set to a maximum of 15 Hz. After a calibration with a ceramic calibration target, the system was able to detect length differences of a few micrometers. The subset size was set to 19 pixels and the distance to 15 pixels.

3.1. Crawling Movement

After building up a demonstrator for pre-testing and characterization of single actuator segments, an adapted full working demonstrator was built. As it turned out, 50 μm thin dielectric membranes in the introduced production method for the DEAs were too fragile to be used. Hence, the membrane thickness was increased to 100 μm. For the testing of the full demonstrator, video captures were taken of the crawling robot acting on 3,000 V supply voltage and 40 mbar inner gas pressure (see **Table 2**). It turned out that the hook-like ring elements are not sufficient for the crawling on common plane grounds like wood or plastics. Therefore, the ground was slightly tilted by an angle of 1°. At this slightly tilting the robot began to move forward. There was still an observable

backwards slippage that was not measured. To not only observe forward gliding due to its own weight no further tilting was applied. To eliminate the influence of the weight force of the feed lines, they were held up using some mountings. Under these conditions the crawling robot got partly enough grip to the surface to move forward. Though the forward movement was not continuous, a few cycles were observed and the displacement was averaged.

3.2. Passive Mechanical Behavior

To evaluate the passive mechanical behavior of the robot, the robotic setup consisting of the more reliably 100 μm dielectric membrane was used. The observed actuator segment was not electrically activated to evaluate the pure passive elongational behavior for different internal gas pressures p_{gas}. The pressure values were set from 0 to 110 mbar in 10 mbar steps. For each pressure value the displacement was captured to receive the pressure-dependent elongational behavior of a single actuator segment.

3.3. Elongation Measurement

Despite the deficient suitability of the robotic setup with 50 μm thin dielectric membranes for a fully operational concept, displacement measurements for a single actuator segment were performed on this structure. The images were captured from a distance of about 1 m to the demonstrator. Marker points with a speckle pattern for the DIC-measurement were adhered to the circumference of the hook-like gripping segments of the robot. To evaluate the elongation of a single actuator segment, the front end segment of the robot was chosen for displacement measurements. The robot was introduced to air pressures at 20, 40, 60, and 80 mbar. Each pressure setting was tested at different voltages of 2,000, 3,000, and 3,500 V. The displacement was captured for every single operating point using the DIC system. **Figure 8** shows two example images for the described measurement in the initial and in the activated state.

TABLE 2 | Overview of characteristic parameters and values used for the characterization of the robot.

	Setup value
Switching frequency	2 Hz
Voltage	3 kV
Pneumatic pressure	40 mbar
Power consumption	$< 3 \times 0.66$ W

3.4. Force Detection

Regardless of the previous experiments, additional measurements were done concerning the voltage-dependent force generated by a cylindrical DEA to expand a segment. The force measurements were performed on the previously mentioned fully working robotic setup with a 100 μm dielectric membrane. These measurements were performed on a Zwick-Roell Z050 tensile testing machine with a force transducer of $F_{max} = 100$ N. To take up the robot and to measure the generated force of a single actuator segment, some customized mountings were fabricated. These mountings ensure to take up the generated force along the whole circumference of the ring muscle and to translate them in a linear direction to the force transducer without an angular displacement. The worm-like robot is fixed in two of these mountings and slightly pre-stretched. **Figure 9** shows the general measurement setup for the force measurement and the concept of the customized mountings.

To measure exclusively the generated force without any impact of the weight of the robot or geometrical variations, the setup is pre-loaded with a force F_{pre} of 1.89 N. In this state the setup is fixed in the tensile testing machine on a defined position and can not move beyond that position. In the case of the performed measurements the defined position was at an elongation of 4.776 mm in length direction. The activation of the clamped actuator segment leads to a decreased measured force F_m because of the limited freedom of movement. The generated force F can be described as:

$$F = F_{\text{pre}} - F_m \tag{23}$$

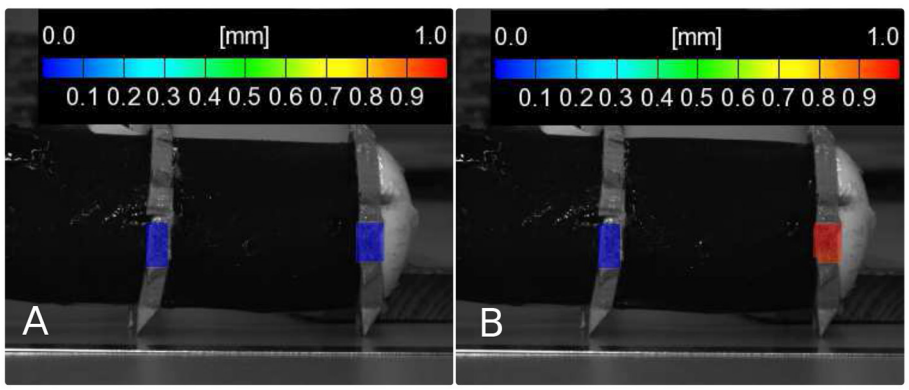

FIGURE 8 | Image for the DIC measurement of the single actuator segment with an applied gas pressure of 60 mbar, **(A)** in the initial state, **(B)** with an applied voltage of 3,500 V.

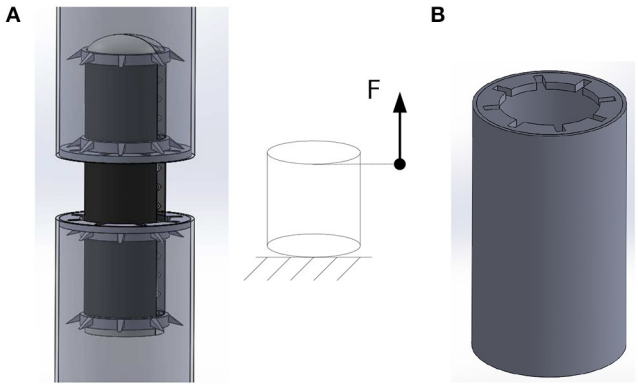

FIGURE 9 | Concept for the force measurement. **(A)** Measurement setup with applied forces to pre-stretch to a working point. **(B)** Construction to take up one end of the cylindrical actuator segment and lock in the hooks to enable an exclusively linear measurement without angular displacement.

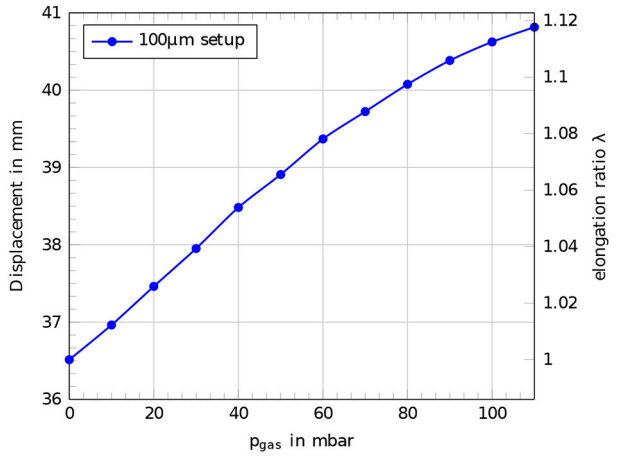

FIGURE 10 | Passive mechanical behavior of a single actuator segment of the robotic concept with a 100 μm dielectric membrane. Displacement and elongation ratio λ for different applied internal gas pressures p_{gas}.

4. RESULTS AND DISCUSSION

The full robotic concept consisting of a 100 μm dielectric membrane was not performing a continuous forward motion with enough generated grip on the hook-like grippers. Therefore, only an averaged measurement of the forward motion was performed. At a switching frequency of 2 Hz with an applied voltage of 3,000 V the robot moved 7 mm in forward direction after 30 cycles, meaning a displacement of 0.23 mm per switching cycle and a velocity of 28 $\frac{\text{mm}}{\text{min}}$.

The passive mechanical behavior of a single cylindrical actuator segment followed a linear behavior for lower internal gas pressures p_{gas} up to 60 mbar. Beyond 60 mbar the structure became stiffer in a way that the expansion for a further increasing of the internal gas pressure became lower and the displacement curve flattened in higher pressure ranges. **Figure 10** shows the displacement curve as a function of the internal gas pressure p_{gas} for a robotic setup with a 100 μm dielectric membrane.

The measurements for the active behavior of a single cylindrical actuator segment were performed on a robotic setup with 50 μm dielectric membranes. By electrical activation of the cylindrical DEAs, the displacement is increasing in every case with an increasing voltage on the electrodes. Also an increasing internal gas pressure p_{gas} leads to an increasing displacement until a point where the whole structure becomes stiffer. The optimum operation point can be assumed in the range around 60 mbar. Beyond this pressure the whole structure becomes stiffer and the actuation is reduced. A maximum deflection of 1.05 mm was recorded for an internal gas pressure of 60 mbar and an applied voltage of 3,500 V on the electrodes of the cylindrical DEA. **Figure 11** shows the results of the measurements for the active elongation behavior.

The force measurements were performed on a robotic setup consisting of a 100 μm dielectric membrane. The results

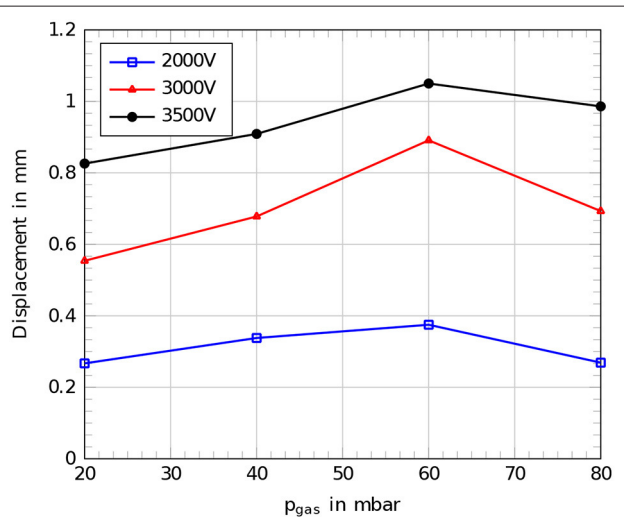

FIGURE 11 | Comparison of measured displacements for the setup with a 50 μm dielectric membrane at different internal gas pressures p_{gas} for different applied voltages, blue: 2,000 V, red: 3,000 V, black: 3,500 V.

followed the expected values from the theoretical calculation with a maximum offset of 0.144 N. Also a quadratic fitting between the measured values resulted in good conformity to the expected curve from the theoretical calculation. A generated maximum of 0.29 N was detected for an applied voltage of 5,000 V. The applied pre-loading force F_{pre} of 1.89 N led to an elongation of 4.7 mm of the measured actuator segment which corresponds to an internal gas pressure of 100 mbar. **Figure 12** shows the results of the force measurement with a comparison to the expected values from theory and a quadratic fit of the measured values. The offset to the theoretical force curve can be explained by the imperfection of the fabricated

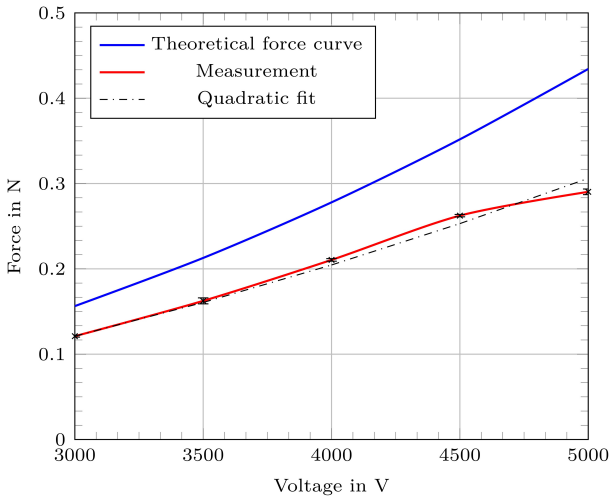

FIGURE 12 | Generated force of a single actuator segment of the robotic concept with a 100 μm dielectric membrane with comparison to the theoretical values (blue) and an additional quadratic fitting of the measured values.

cylindrical actuator segments. The DEAs can not be assumed as perfectly cylindrical since they are built by wrapping the dielectric membrane around the inner structure. This fabrication method inevitably leads to a seam where the edges of the membrane need to overlap. To avoid electrical shortcuts and to increase reliability, there was no coating of an outer electrode attached in the area above the seam. Both features, the non-fully cylindrical coating of an outer electrode and the overlap of the dielectric membrane lead to deviations from the expected behavior.

5. CONCLUSION

The presented robotic concept shows sufficient capabilities of expanding cylindrical actuator elements based on DEAs as robotic drives and to use them as linear actuators. The direction of expansion is successfully limited in longitudinal direction by attaching the cylindrical DEAs to the circumference of an inner holding structure. In the presented implementation and geometry, relative elongations of up to 2.4 % and generated forces of 0.29 N were achieved. The achieved velocity of 28 $\frac{\text{mm}}{\text{min}}$ is not optimal since backward slippage occurred. By optimizing the gripper design the velocity could easily be improved. As shown in the theoretical considerations, the use of thinner dielectric membranes leads to higher generated forces at similar operating voltages. Additionally, thinner membranes lead to a softer expected mechanical behavior of the setup, which leads to higher expected elongations. Therefore, it seems to be advisable to use as thin dielectric membranes as possible. The proceedings of this work showed that the use of thinner dielectric membranes to produce cylindrical DEAs however leads to some additional challenges. In case of the manufacturing and handling of the robotic setup with common laboratory equipment, soon a limit of handling capability is reached. The used 50 μm dielectric membranes tend to develop cracks more easily than the later used 100 μm dielectric membranes. Also the positioning and the application itself is far more challenging for thinner membranes. A main source for possible flaws is generated through the manufacturing process itself. The implemented fabrication strategy leads to an overlap of the membrane that stiffens the actuator segment along the seam. Also the area directly above the seam could not be coated with an electrode to prevent electrical shortcuts between the electrodes. A possible way to overcome these effects is to produce a dielectric membrane in the form of a sleeve. The sleeve geometry would avoid overlap and mechanical in homogenities. Some preliminary experiments on fabricating a dielectric membrane in such a fully cylindrical geometry were done. Therefore, a silicone mixture *Dow Corning Sylgard 184* © was put into a rotating heated rod and cured under constant rotation. Afterwards the cured sleeve was released from the rod for further processing. Because of some restrictions according the handling of such a sleeve no demonstrator was built using this technique. The sleeve tended to collapse during handling and to stick to itself. Also a further application of electrodes would be by far more challenging since the sleeve has to be turned inside out after one electrode is applied to manufacture the other electrode. Besides the challenges the use of sleeve dielectric membranes is definitely an advisable approach to improve the concept of the introduced cylindrical linear actuators for future developments. Beyond possible improved fabrication methods, the operating point for the linear actuators should be set to its optimum. As the results for the elongation under electrical activation suggest, there is an optimal operating point at a certain internal gas pressure. To find this optimum point, some measurements of the passive mechanical behavior should be done under a higher resolution. With more substeps for the applied internal gas pressure, the point of decreasing slope can be narrowed. Afterwards the electrical activated measurements can be performed around this point to find an optimum operating point for a maximum elongation. The presented concept of cylindrical linear actuators based on DEAs shows promising capabilities to act as driving elements for soft robotics. A wide range of applications is possible since the mechanical properties of the used materials fit for a lot of applications where rigid robotics are self-excluding. Therefore, fields like aerospace engineering or human-machine interaction in health care emerge beyond the presented use as a drive for soft robotic concepts.

DATA AVAILABILITY STATEMENT

All datasets generated for this study are included in the article/supplementary material.

AUTHOR CONTRIBUTIONS

SP contributed the majority of the text, developed the constructions, built up the demonstrators, and did the theoretical

calculations. MH contributed support for the conception, the layout for the soft structures, and provided help with the experimental setups. KK contributed the majority of the measurements and did the conception for the measurements in accordance with SP and also contributed main parts for the text according the measurements. MZ and GG contributed scientific support and coordination as well as recommendations for the typesetting.

FUNDING

The authors thank for the provided funding through the German Research Foundation. The work contributed to this publication was fully funded by the DFG (German Research Foundation), project number 380321452-GRK2430. Open Access Funding was provided by the Publication Fund of the Dresden University of Technology.

REFERENCES

Aghakhani, A., and Basdogan, I. (2018). "Multiple piezo-patch energy harvesters on a thin plate with respective AC-DC conversion," in *Active and Passive Smart Structures and Integrated Systems XII, Vol. 10595* (Denver, CO: International Society for Optics and Photonics), 105951B. doi: 10.1117/12.2296831

Anderson, I. A., Gisby, T. A., McKay, T. G., O'Brien, B. M., and Calius, E. P. (2012). Multi-functional dielectric elastomer artificial muscles for soft and smart machines. *J. Appl. Phys.* 112:041101. doi: 10.1063/1.4740023

Asbeck, A. T., De Rossi, S. M., Galiana, I., Ding, Y., and Walsh, C. J. (2014). Stronger, smarter, softer: next-generation wearable robots. *IEEE Robot. Autom. Mag.* 21, 22–33. doi: 10.1109/MRA.2014.2360283

Banerjee, H., Tse, Z. T. H., and Ren, H. (2018). Soft robotics with compliance and adaptation for biomedical applications and forthcoming challenges. *Int. J. Robot. Autom.* 33, 69–80. doi: 10.2316/Journal.206.2018.1.206-4981

Bar-Cohen, Y. (2004). "Electroactive Polymer (EAP) Actuators as Artificial Muscles: Reality," in *Potential, and Challenges, SPIE-Society of Photographic Instrumentation Engineers* (Bellingham, WA).

Burgner-Kahrs, J., Rucker, D. C., and Choset, H. (2015). Continuum robots for medical applications: a survey. *IEEE Trans. Robot.* 31, 1261–1280. doi: 10.1109/TRO.2015.2489500

Cao, J., Qin, L., Lee, H. P., and Zhu, J. (2017). "Development of a soft untethered robot using artificial muscle actuators," in *Electroactive Polymer Actuators and Devices (EAPAD) 2017, Vol. 10163* (Portland, OR: International Society for Optics and Photonics), 101631X. doi: 10.1117/12.2260375

Carpi, F., de Rossi, D. E., Kornbluh, R., Pelrine, R., and Sommer-Larsen, P., (eds.). (2008). *Dielectric Elastomers as Electromechanical Transducers: Fundamentals, Materials, Devices, Models and Applications of an Emerging Electroactive Polymer*. Amsterdam: Elsevier.

Carpi, F., Menon, C., and De Rossi, D. (2009). Electroactive elastomeric actuator for all-polymer linear peristaltic pumps. *IEEE/ASME Trans. Mechatron.* 15, 460–470. doi: 10.1109/TMECH.2009.2028884

Chowdhury, A., Ansari, S., and Bhaumik, S. (2017). "Earthworm like modular robot using active surface gripping mechanism for peristaltic locomotion," in *Proceedings of the Advances in Robotics* (New Delhi: ACM), 54.

Dario, P., Ciarletta, P., Menciassi, A., and Kim, B. (2004). Modeling and experimental validation of the locomotion of endoscopic robots in the colon. *Int. J. Robot. Res.* 23, 549–556. doi: 10.1177/0278364904042204

Edwards, C. A., and Bohlen, P. J. (1996). *Biology and Ecology of Earthworms, Vol. 3*. Columbus, OH: Springer Science & Business Media.

Elveflow (2019). *Product Catalog PC19-0618*. datasheet Elveflow AF1-P-1600. Available online at: https://www.elveflow.com/?wpdmdl=19181

Eringen, A. C., and Maugin, G. A. (2012). *Electrodynamics of Continua I: Foundations and Solid Media*. New York, NY: Springer Science & Business Media.

Henke, E.-F. M., Schlatter, S., and Anderson, I. A. (2017). Soft dielectric elastomer oscillators driving bioinspired robots. *Soft Robot.* 4, 353–366. doi: 10.1089/soro.2017.0022

Henke, E.-F. M., Wilson, K., and Anderson, I. (2018). Modeling of dielectric elastomer oscillators for soft biomimetic applications. *Bioinspir. Biomimet.* 13:046009. doi: 10.1088/1748-3190/aac911

Henke, E. F. M., Wilson, K. E., Slipher, G. A., Mrozek, R. A., and Anderson, I. A. (2019). "Artificial muscle logic devices for autonomous local control," in *Robotic Systems and Autonomous Platforms*, eds S. M. Walsh and M. S. Strano (Cambridge: Woodhead Publishing), 29–40.

Joey, Z. G., Calderón, A. A., Chang, L., and Pérez-Arancibia, N. O. (2019). An earthworm-inspired friction-controlled soft robot capable of bidirectional locomotion. *Bioinspir. Biomimet.* 14:036004. doi: 10.1088/1748-3190/aae7bb

Kellaris, N., Gopaluni Venkata, V., Smith, G. M., Mitchell, S. K., and Keplinger, C. (2018). Peano-hasel actuators: muscle-mimetic, electrohydraulic transducers that linearly contract on activation. *Sci. Robot.* 3, 1–10. doi: 10.1126/scirobotics.aar3276

Liang, C., Chee, K., Zou, Y., Zhu, H., Causo, A., Vidas, S., et al. (2015). "Automated robot picking system for e-commerce fulfillment warehouse application," in *The 14th IFToMM World Congress* (Taipei).

Majidi, C. (2019). Soft-matter engineering for soft robotics. *Adv. Mater. Technol.* 4:1800477. doi: 10.1002/admt.201800477

Mathew, A. T., and Koh, S. J. A. (2018). "Maximum energy output of a two-phased self-priming dielectric elastomer generator," in *2018 IEEE/ASME International Conference on Advanced Intelligent Mechatronics (AIM)* (Auckland:IEEE), 1366–1371. doi: 10.1109/AIM.2018.8452325

McKay, T. G., O'Brien, B. M., Calius, E. P., and Anderson, I. A. (2011). Soft generators using dielectric elastomers. *Appl. Phys. Lett.* 98:142903. doi: 10.1063/1.3572338

O'Brien, B. M., and Anderson, I. A. (2012). An artificial muscle ring oscillator. *IEEE/ASME Trans. Mechatron.* 17, 197–200. doi: 10.1109/TMECH.2011.2165553

Omori, H., Nakamura, T., and Yada, T. (2009). An underground explorer robot based on peristaltic crawling of earthworms. *Indust. Robot* 36, 358–364. doi: 10.1108/01439910910957129

Onal, C. D., Chen, X., Whitesides, G. M., and Rus, D. (2017). "Soft mobile robots with on-board chemical pressure generation," in *Robotics Research*, eds H. I. Christensen, O. Khatib (Cambridge:Springer), 525–540.

Pelrine, R., Kornbluh, R., and Kofod, G. (2000). High-strain actuator materials based on dielectric elastomers. *Adv. Mater.* 12, 1223–1225. doi: 10.1002/1521-4095(200008)12:16<1223::AID-ADMA1223>3.0.CO;2-2

Pelrine, R. E., Kornbluh, R. D., and Joseph, J. P. (1998). Electrostriction of polymer dielectrics with compliant electrodes as a means of actuation. *Sens. Actuat. A Phys.* 64, 77–85. doi: 10.1016/S0924-4247(97)01657-9

Philamore, H., Rossiter, J., Stinchcombe, A., and Ieropoulos, I. (2015). "Row-bot: an energetically autonomous artificial water boatman," in *2015 IEEE/RSJ International Conference on Intelligent Robots and Systems (IROS)* (Hamburg: IEEE), 3888–3893.

Rich, S. I., Wood, R. J., and Majidi, C. (2018). Untethered soft robotics. *Nat. Electron.* 1:102. doi: 10.1038/s41928-018-0024-1

Romero, D., Stahre, J., Wuest, T., Noran, O., Bernus, P., Fast-Berglund, Å., et al. (2016). "Towards an operator 4.0 typology: a human-centric perspective on the fourth industrial revolution technologies," in *International Conference on Computers and Industrial Engineering (CIE46) Proceedings* (Tianjin).

Schlatter, S., Illenberger, P., and Rosset, S. (2018). Peta-pico-voltron: an open-source high voltage power supply. *HardwareX* 4:e00039. doi: 10.1016/j.ohx.2018.e00039

Seok, S., Onal, C. D., Wood, R., Rus, D., and Kim, S. (2010). "Peristaltic locomotion with antagonistic actuators in soft robotics," in *2010 IEEE International Conference on Robotics and Automation* (Anchorage, AK:IEEE), 1228–1233. doi: 10.1109/ROBOT.2010.5509542

Süße, R. (2006). *Theoretische Grundlagen der Elektrotechnik 2*. Ilmenau: Teubner.

Wehner, M., Truby, R. L., Fitzgerald, D. J., Mosadegh, B., Whitesides, G. M., Lewis, J. A., et al. (2016). An integrated design and fabrication strategy for entirely soft, autonomous robots. *Nature* 536, 451–455. doi: 10.1038/nature 19100

Wilson, K. E., Henke, E.-F. M., Slipher, G. A., and Anderson, I. A. (2016). Rubbery logic gates. *Extreme Mech. Lett.* 9, 188–194. doi: 10.1016/j.eml.2016. 07.001

Wilson, K. E., Henke, E.-F. M., Slipher, G. A., and Anderson, I. A. (2017). "Rubbery computing," in *Proc. SPIE, Vol. 10163*, ed Y. Bar-Cohen (Portland, OR).

Zhong, R. Y., Xu, X., Klotz, E., and Newman, S. T. (2017). Intelligent manufacturing in the context of industry 4.0: a review. *Engineering* 3, 616–630. doi: 10.1016/J.ENG.2017.05.015

Conflict of Interest: MH was employed by the company PowerOn Ltd.

The remaining authors declare that the research was conducted in the absence of any commercial or financial relationships that could be construed as a potential conflict of interest.

frontiers in Robotics and AI

ORIGINAL RESEARCH
published: 15 December 2020
doi: 10.3389/frobt.2020.510757

Dielectric Elastomer Actuator Driven Soft Robotic Structures With Bioinspired Skeletal and Muscular Reinforcement

M. Franke[1]*, *A. Ehrenhofer*[2], *S. Lahiri*[1], *E.-F. M. Henke*[1,3], *T. Wallmersperger*[2] and *A. Richter*[1]

[1] Institute of Semiconductors and Microsystems (IHM), Technische Universität Dresden, Dresden, Germany, [2] Institute of Solid Mechanics, Technische Universität Dresden, Dresden, Germany, [3] PowerOn Ltd., Auckland, New Zealand

Natural motion types found in skeletal and muscular systems of vertebrate animals inspire researchers to transfer this ability into engineered motion, which is highly desired in robotic systems. Dielectric elastomer actuators (DEAs) have shown promising capabilities as artificial muscles for driving such structures, as they are soft, lightweight, and can generate large strokes. For maximum performance, dielectric elastomer membranes need to be sufficiently pre-stretched. This fact is challenging, because it is difficult to integrate pre-stretched membranes into entirely soft systems, since the stored strain energy can significantly deform soft elements. Here, we present a soft robotic structure, possessing a bioinspired skeleton integrated into a soft body element, driven by an antagonistic pair of DEA artificial muscles, that enable the robot bending. In its equilibrium state, the setup maintains optimum isotropic pre-stretch. The robot itself has a length of 60 mm and is based on a flexible silicone body, possessing embedded transverse 3D printed struts. These rigid bone-like elements lead to an anisotropic bending stiffness, which only allows bending in one plane while maintaining the DEA's necessary pre-stretch in the other planes. The bones, therefore, define the degrees of freedom and stabilize the system. The DEAs are manufactured by aerosol deposition of a carbon-silicone-composite ink onto a stretchable membrane that is heat cured. Afterwards, the actuators are bonded to the top and bottom of the silicone body. The robotic structure shows large and defined bimorph bending curvature and operates in static as well as dynamic motion. Our experiments describe the influence of membrane pre-stretch and varied stiffness of the silicone body on the static and dynamic bending displacement, resonance frequencies and blocking forces. We also present an analytical model based on the Classical Laminate Theory for the identification of the main influencing parameters. Due to the simple design and processing, our new concept of a bioinspired DEA based robotic structure, with skeletal and muscular reinforcement, offers a wide range of robotic application.

Keywords: dielectric elastomer actuator, soft robot, modelling and simulation, bimorph actuation, anisotropy, skeleton, silicone, pre-stretch

OPEN ACCESS

Edited by:
Guoying Gu,
Shanghai Jiao Tong University, China

Reviewed by:
Jun Shintake,
The University of Electro-Communications, Japan
Ioannis Georgilas,
University of Bath, United Kingdom

***Correspondence:**
M. Franke
markus.franke@tu-dresden.de

Specialty section:
This article was submitted to Soft Robotics, a section of the journal Frontiers in Robotics and AI

Received: *07 November 2019*
Accepted: *23 October 2020*
Published: *15 December 2020*

Citation:
Franke M, Ehrenhofer A, Lahiri S, Henke E-FM, Wallmersperger T and Richter A (2020) Dielectric Elastomer Actuator Driven Soft Robotic Structures With Bioinspired Skeletal and Muscular Reinforcement. Front. Robot. AI 7:510757. doi: 10.3389/frobt.2020.510757

INTRODUCTION

Biological evolution has revealed versatile motion types and structures culminating in the skeletal and muscular systems of vertebrate animals (Marshall, 1980). The effective, stable, and powerful interactions between skeleton, antagonistic muscles, ribbons, and joints have inspired researchers to transfer that ability into technical motion for artificial muscles or actuators in robotic systems (Bar-Cohen, 2016). However, replacing muscles and tissues by technical polymer materials is challenging, especially providing large strokes and generating high force output, while creating entirely soft devices. Furthermore, a smart integrated actuation system is needed, which typically consumes a significant amount of energy or consists of hard materials, as can be seen in the hydraulically driven autonomous soft robotic fish for 3D swimming (Katzschmann et al., 2016). Also fully soft actuator systems have been developed, e.g., a microfluidically and pneumatically driven autonomous working Octobot (Wehner et al., 2016) or a pneumatically driven multigait soft robot (Shepherd et al., 2011). These systems lack a stabilizing skeleton reinforcement and suffer from an obvious low movement speed. In the case of a given Octobot construction, the movement is inherent at a certain level of chemical concentration and cannot immediately be changed as the catalytical chemical decomposition of hydrogen peroxide produces a defined gaseous volume and leads to the tentacle movement. Furthermore, the reaction is quite sensitive to temperature changes and can decrease the precision of the displacement. The interaction and control of the system which commonly uses electrical signals is complicated. Also, in oscillatory operation, thermal influences on actuation and breakdown of DEAs have to be considered (Kleo et al., 2020).

Therefore, a direct electrical control of robotic actuation is preferred and can be achieved by dielectric elastomers (DE), which already have shown promising capabilities as artificial muscles for driving versatile biomimetic structures (Gu et al., 2017). For instance, DE are applied in a bimorph actuator (Goh and Lau, 2010), a fishtail (Berlinger et al., 2018), a transparent swimming soft robot (Christianson et al., 2018) or a caterpillar (Henke et al., 2017). They can simultaneously act as dielectric elastomer actuators generating large strokes and as sensors monitoring themselves (Henke et al., 2017). However, to generate significant amounts of stroke and force for actuation, membrane type actuators have to be pre-stretched to operate at their optimum work point (Kofod, 2008). Further advantages of pre-stretching the DE membrane are removing of electromechanical instabilities and enhancing breakdown field strength (Gu et al., 2017). However, it is difficult to integrate pre-stretched membranes in entirely soft robotic structures as instantaneous deformation occurs (Rosset et al., 2014; Araromi et al., 2015).

In this contribution, we present a simple, novel way to integrate DEAs, made of pre-stretched membranes, into soft robotic structures without any undesired bending. The robot possesses a bioinspired skeleton, integrated in a soft silicone body, for stabilizing the structural integrity and defining the degrees of freedom. This movement is stimulated by two antagonistic DEA artificial muscles made of isotropic pre-stretched membranes that are bonded to the body element. This allows a bimorph-bending curvature in the desired direction. The arrangement of this DEA pair allows a precise displacement in static mode and large and fast displacements in dynamic mode, due to resonance effects. In this study we investigated the influence of the pre-stretch value of the DE membranes and the stiffness of the silicone body material on the static and dynamic displacement of a bimorph-type bioinspired robot. Furthermore, the applicable blocking force of the robotic structure and the achievable maximum velocity and acceleration are estimated.

MECHANISM

DEA Operation Principle

DEAs possess a soft plate capacitor structure consisting of a flexible elastomer membrane, usually made of silicone or acrylic membranes, which are sandwiched between two compliant, conductive electrodes (see **Figure 1**) (Pelrine et al., 1998). To achieve reliable electrode flexibility, many different concepts and fabrication processes have been developed, wherein carbon-based materials like pure carbon powder, carbon grease or carbon-silicone-composites are most commonly used (Rosset and Shea, 2013). Application of high voltages, typically within the range of 1–5 kV, charges the compliant electrodes and generates a compression of the DEA membrane with an initial film thickness h_0 due to the Coulomb forces. Due to its incompressibility, the polymer membrane gets compressed in z-direction with a certain thickness decrease h and expands in its lateral dimensions simultaneously. The elastic behavior of the DEAs causes a reversible reconfiguration of the initial shape and initial film thickness after discharging the electrodes (Kofod, 2008).

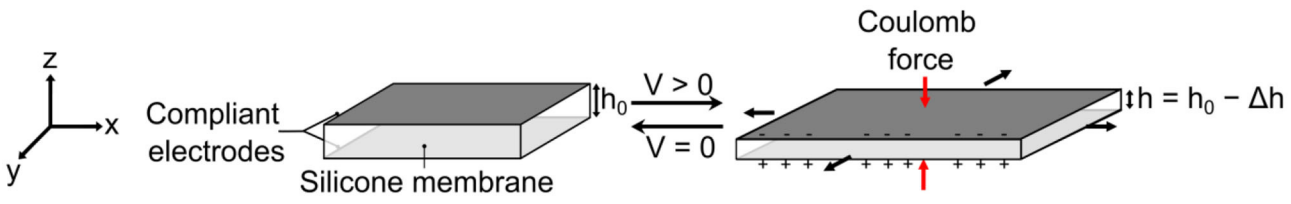

FIGURE 1 | Working principle of a DEA, showing a voltage induced charging of the electrodes of the DEA capacitor structure. Coulomb forces lead to an attraction of the compliant electrodes and reduction of the initial film thickness $\mathbf{h_0}$ and an aerial expansion simultaneously.

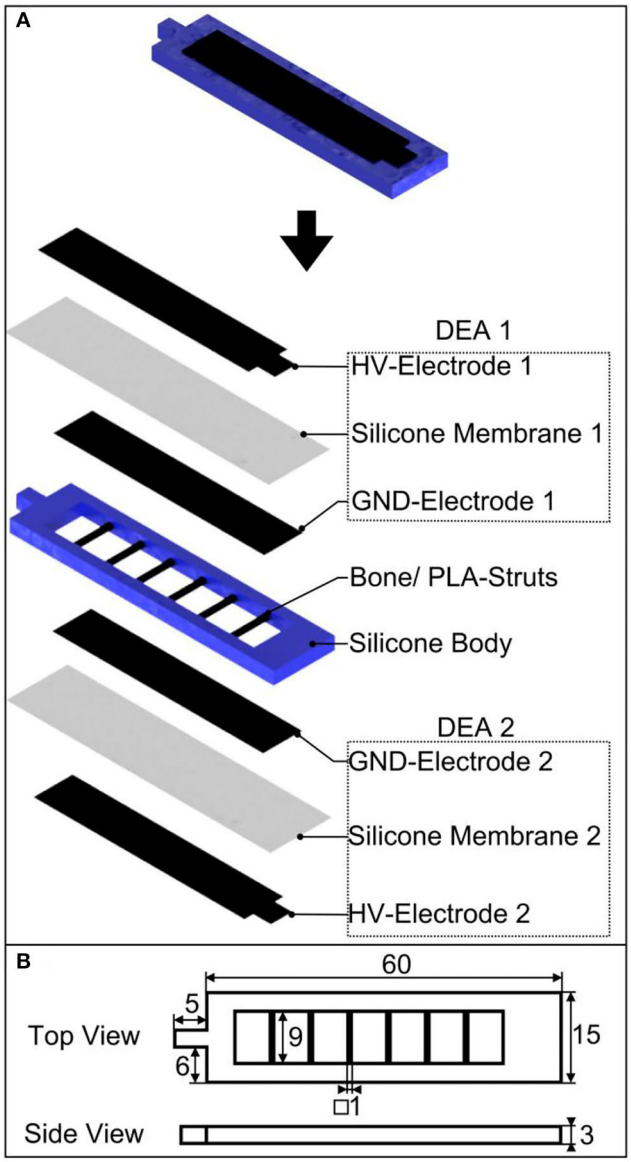

FIGURE 2 | Bioinspired soft robotic structure with an antagonistically working DEA artificial muscle pair and integrated bones for anisotropic bending stiffness; **(A)** design and setup as exploded representation, **(B)** geometric dimensions in mm.

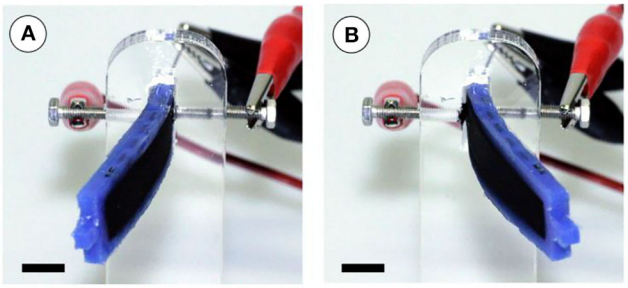

FIGURE 3 | Working principle of the soft robotic structure with two antagonistically working DEA muscles during dynamic testing. In **(A)** the right DEA is activated and the robot bends left. In **(B)** the left DEA is activated and the robot bends right (scale bar is 10 mm).

To achieve maximum performance, DEAs have to be pre-stretched (Kofod, 2008). Please note that the term λ^{pre} is used to denote the initial tensile deformation of the DEA, before it is added to the backbone structure. The same effect can also be called pre-strain with the according definition of technical strain $\varepsilon^{\mathrm{pre}} = \lambda^{\mathrm{pre}} - 1$. The pre-stretch of the actuators plays a significant role in the overall behavior of the DEA structure. This has several reasons: pre-stretching of the membrane reduces its thickness and, thus, scales the Maxwell stress, and the compression force. This effect scales quadratically with the DEA thickness. From the mechanical point of view, the role of buckling instability has to be considered as well: In active-passive composite setups for actuation purposes—e.g., when the passive material is used as a stiffening backbone—the active material is mostly in a constrained setup (Ehrenhofer and Wallmersperger, 2020). In such setups, an elongation of a thin structure, i.e., a structure with one or more dimensions much smaller than the primary direction(s), leads to buckling instabilities (Biot, 1963). Pre-tension of a DEA strip—in the current setup realized by pre-stretching the membrane—circumnavigates this problem. However, the pre-stretch must be accordingly high so that throughout the actuation, the applied stress is always lower than the pre-stress, or buckling will occur.

Design and Setup

The soft robotic structure presented in the current work, comprises a multilayer setup, which is schematically shown in **Figure 2A**. The setup consists of two DEA artificial muscles on the top and bottom of a soft silicone body. Both DEA membranes possess the same defined equibiaxial pre-stretch (λ_{pre}), covered with compliant electrodes, where the outer electrode represents the high voltage (HV) electrode and the inner one the ground (GND) electrode. The GND electrodes are fixed toward the central body element and connected to the same ground potential. The silicone body itself is flexible, with integrated stiff PLA struts, allowing anisotropic bending stiffness of the entire soft robotic structure, resulting in high flexibility in the longitudinal direction and a high bending stiffness in the transverse direction simultaneously. **Figure 2B** depicts the geometric dimensions of the overall structure.

Bending Mechanism and Analytical Modeling

Figure 3 depicts the deflection of the structure during testing, to illustrate the working principle of the soft robotic structure. Both DEA artificial muscles cover the silicone body and possess the same defined pre-stretch. In the equilibrium state, the bending moments, which are generated by both DEA muscles and applied to the silicone body, are balanced and the structure

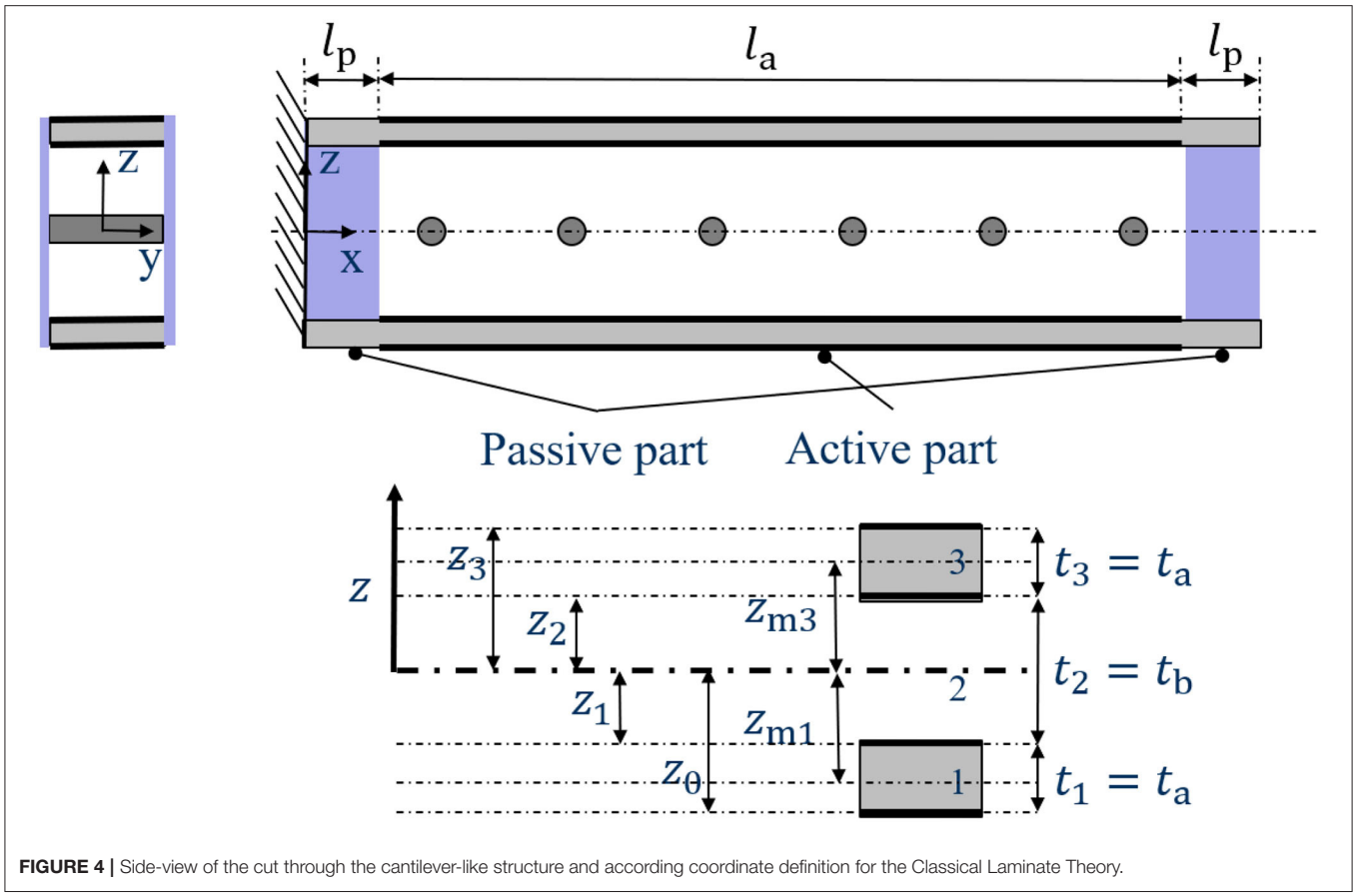

FIGURE 4 | Side-view of the cut through the cantilever-like structure and according coordinate definition for the Classical Laminate Theory.

stays straight. When the DEAs operate antagonistically, bending of the structure occurs in the opposite direction of the activated DEA. The reason for this behavior is the superposition of the (tensile) pre-stretch with the actuation strain that follows through lateral contraction in the activated membrane. This results in less force and, thus, less bending moment applied to the silicone body by the activated DEA. Depending on which DEA is activated, the robotic structure bends reversibly to the left or right direction. This allows a static or dynamic bending as can be seen in **Supplementary Video SM1**. A better view and explanation of the bending behavior is given by **Figure 3A**, in which the right DEA is activated and the robot is displaced to the left direction. Instead in **Figure 3B**, the left actuator is activated and the robot is displaced to the right.

The description of the layered system, for design purposes, can be achieved through different approaches. In the current work, we focus on (i) the analytical description using the two-dimensional Classical Laminate Theory (Reddy, 2003) and (ii) the full three-dimensional description. Both approaches have in common that the actuation of the DEA layers is realized by using the Temperature-Expansion-Model (Ehrenhofer et al., 2016, 2018).

In the current modeling approach, the actuation strain of the DEA is implemented using the analogy to thermal expansion, i.e., the area strain $\varepsilon_{xx} = \varepsilon_{yy} = \varepsilon_{\text{in-plane}}$ is modeled with thermal expansion strain $\varepsilon^{\text{therm}}$ and realizes following relation:

$$\varepsilon_{\text{in-plane}} \hat{=} \varepsilon^{\text{therm}} = \alpha\, \Theta. \tag{1}$$

Here, α is a (pseudo-)thermal expansion coefficient and Θ a stimulus-difference (normalized to a reference value). Thus, the elongation of the plate-like (i.e., l_x, $l_y \gg l_z$) DEA in x-y-plane due to the compression in z-direction, caused by the electrostatic force, is replicated. The adequate definition of $\varepsilon^{\text{therm}}$ can be implemented in the context of the 3D continuum mechanical formulation as well as in simplified 2D and 1D theories.

Note that in the derivation of 2D theories, like plate or shell descriptions, the z-direction is assumed as the neutral direction. In combination with the thinness-criterion, this leads to the assumption of plane stress state (Reddy, 2003). Since the main criteria of these theories are violated in DEA structures, 2D theories must be applied with extreme caution. This is also valid for the use of 1D theories like Bernoulli beam theory, in which a one-dimensional stress state is assumed. Layered composite shell structures require more complex assumptions, which makes the analytical solution process more difficult, even calling for specialized discretization methods (Kulikov and Carrera, 2008). In those cases, a full three-dimensional modeling approach, solved by using the Finite-Element-Method, might be more efficient.

Note that the applied material model for the analytical description with CLT is linear. The underlying assumption is that for composite setups designed for bending purposes, small strains can lead to large strokes. This is due to the effect of active-passive stiffness pairing, i.e., both material and geometrical parameters play a role in the levering effect (Ehrenhofer and Wallmersperger, 2020). This is also known from simple bimetal strips where very small temperature changes and small thermal expansion coefficients lead to large tip displacement, nevertheless. From the viewpoint of modeling, a Young's modulus (elastic modulus) is gained through a linearization at a working point, e.g., the pre-stretched DEA.

Description Using the Classical Laminate Theory

The Classical Laminate Theory is a common approach for multilayer composite systems (Reddy, 2003). It is based on the description of every lamina as a homogenized structure with possible direction dependent properties. It is valid for a certain set of prerequisites: small deformations, linear elasticity, constant layer thickness, Bernoulli hypothesis and ideal connection of the layers. The derivation of the expression for the curvature is shown in the **Modeling Appendix**. The curvature of the bending of the composite is derived there.

The actual 1D setup in x-direction (side-view according to **Figure 4**) is needed to derive the bending line and the respective tip displacement for comparison to the experimental values. The bending line is separated into three parts, whereas the only active part is in the middle.

The tip displacement, i.e., the displacement of the right side when the composite system is fixed on the left side, is derived as

$$\begin{aligned} w_{\mathrm{Tip}} &= w\left(x = l_a + 2\,l_p\right) \\ &= \frac{3\,l_a\,E_a\,\left(t_a + t_b\right)\left(\alpha_1\Theta_1 - \alpha_3\Theta_3\right)\,\left(l_a + 2\,l_p\right)}{8\,E_a t_a^3 + 24\,E_a\,t_a^2\,t_p + 24\,E_a\,t_a t_b^2 + E_b t_b^3}. \end{aligned} \quad (2)$$

The derivation of Equation (2) can be found in the **Modeling Appendix** (**Supplementary Material 1**). Here, for $i = a, p$ with active (a) and passive (p), the material and geometry parameters are the lengths l_i, layer thicknesses t_i and Young's moduli E_i. The expansion strains $\alpha_i\ \Theta_i$ for the active layers 1 and 3 include pre-strain and actuation. Equation (2) is only valid for small deformations, i.e., a total tip displacement of generally less than half the beam height. The scope of the analytical approach is therefore very narrow; however, it can be used to identify the crucial parameters in the system. For the description of the complete bending process, a three-dimensional model is needed.

The developed model, based on the CLT, is now applied with the experimental values. As can be seen in the Equation (2), the pre-strains in the DEAs (layer 1 and 3) cancel out in $\alpha_1\Theta_1 - \alpha_3\Theta_3 = \left(\varepsilon_1^{\mathrm{pre}} + \varepsilon_1^{\mathrm{actuation}}\right) - \left(\varepsilon_3^{\mathrm{pre}} + \varepsilon_3^{\mathrm{actuation}}\right)$ and only the difference between the actuation strains remains. However, the pre-strain still plays a role in the layer thickness. The actuation strain in height direction is

$$\varepsilon_{zz}^{\mathrm{actuation}}\,(V) = -\epsilon_0\epsilon_r \frac{V^2}{E_{\mathrm{ELASTOSIL}}\,t^2_{\mathrm{ELASTOSIL,\,pre-stretched}}} \quad (3)$$

where $\epsilon_0 = 8.854 \cdot 10^{-12}\,\frac{\mathrm{As}}{\mathrm{Vm}}$ is the vacuum permittivity, $\epsilon_r = 2.8$ the relative permittivity between the electrodes, and $\mathrm{E_{ELASTOSIL}}$ the Young's modulus of the ELASTOSIL membrane (experimental values are shown in section DEA). There is no stiffening effect of the electrodes due to the described fabrication process: The pre-strain is only applied to the ELASTOSIL membrane, then the electrodes are added. In Equation (3), the thickness of the ELASTOSIL membrane $t_{\mathrm{ELASTOSIL,\,pre-stretched}}$ depends on the multiaxial in-plane pre-stretch $\lambda_x = \lambda_y = \lambda^{\mathrm{pre}}$ via volume constancy ($\lambda_x\lambda_y\lambda_z = 1$)

$$t_{\mathrm{ELASTOSIL,\,pre-stretched}} = t_{\mathrm{ELASTOSIL},0}\,\frac{1}{(\lambda^{\mathrm{pre}})^2} \quad (4)$$

with the initial membrane thickness of $t_{\mathrm{ELASTOSIL},0} = 100\ \mu m$. Thus, the actuation strain $\varepsilon_{zz}^{\mathrm{actuation}}\,(V)$, which depends on the voltage $V = 0 \ldots 5$ kV can be calculated.

The actuation strain in z-direction is now transformed to in-plane strain. Please note that the actuation strain equally contributes to strains in x- and y-direction, therefore $\lambda_{x,\mathrm{act}} = \lambda_{y,\mathrm{act}} = \lambda_{\mathrm{in-plane,act}}$, which leads to

$$\lambda_{x,\mathrm{act}}\lambda_{y,\mathrm{act}}\lambda_{z,\mathrm{act}} = \lambda^2_{\mathrm{in-plane,act}}\lambda_{z,\mathrm{act}} = 1 \quad (5)$$

$$\begin{aligned} \varepsilon_3^{\mathrm{actuation}} &= \varepsilon_{xx}^{\mathrm{actuation}} = \lambda_{\mathrm{in-plane,act}} - 1 = \frac{1}{\sqrt{\lambda_{z,\mathrm{act}}}} - 1 \\ &= \frac{1}{\sqrt{\varepsilon_{zz}^{\mathrm{actuation}} + 1}} - 1 \end{aligned} \quad (6)$$

With the described simulation parametrization, the following static tip displacement of the robot according to Equation (2) can be calculated, and is compared with the experimental data, see **Figure 8**. Here, $E_a = E_{\mathrm{ELASTOSIL}}$ because, as explained above, the electrodes do not play a role in the pre-strain and actuation strain. For the Young's modulus of the passive material E_p, different experimental values for the different materials are inserted, see section Investigation of the Materials Young's Moduli.

FABRICATION

DEA

The fabrication process of the DEAs is described in **Figures 5A–D**. In order to prepare the DEAs, commercially available 100 µm thick silicone elastomer membranes (ELASTOSIL 2030 by Wacker Chemie AG, Germany) are fixed in an in-house made pre-stretching device using magnetic clamping (**Figure 5A**) and pre-stretched to the desired equibiaxial values of $\lambda_{\mathrm{pre}} = 1.1$, 1.3, 1.5, and 1.7, respectively. After pre-stretching, the silicone membrane is fixed to an acrylic frame using an adhesive RTV silicone (RS PRO Silicone) (**Figure 5B**). The compliant electrodes are fabricated by aerosol deposition, using

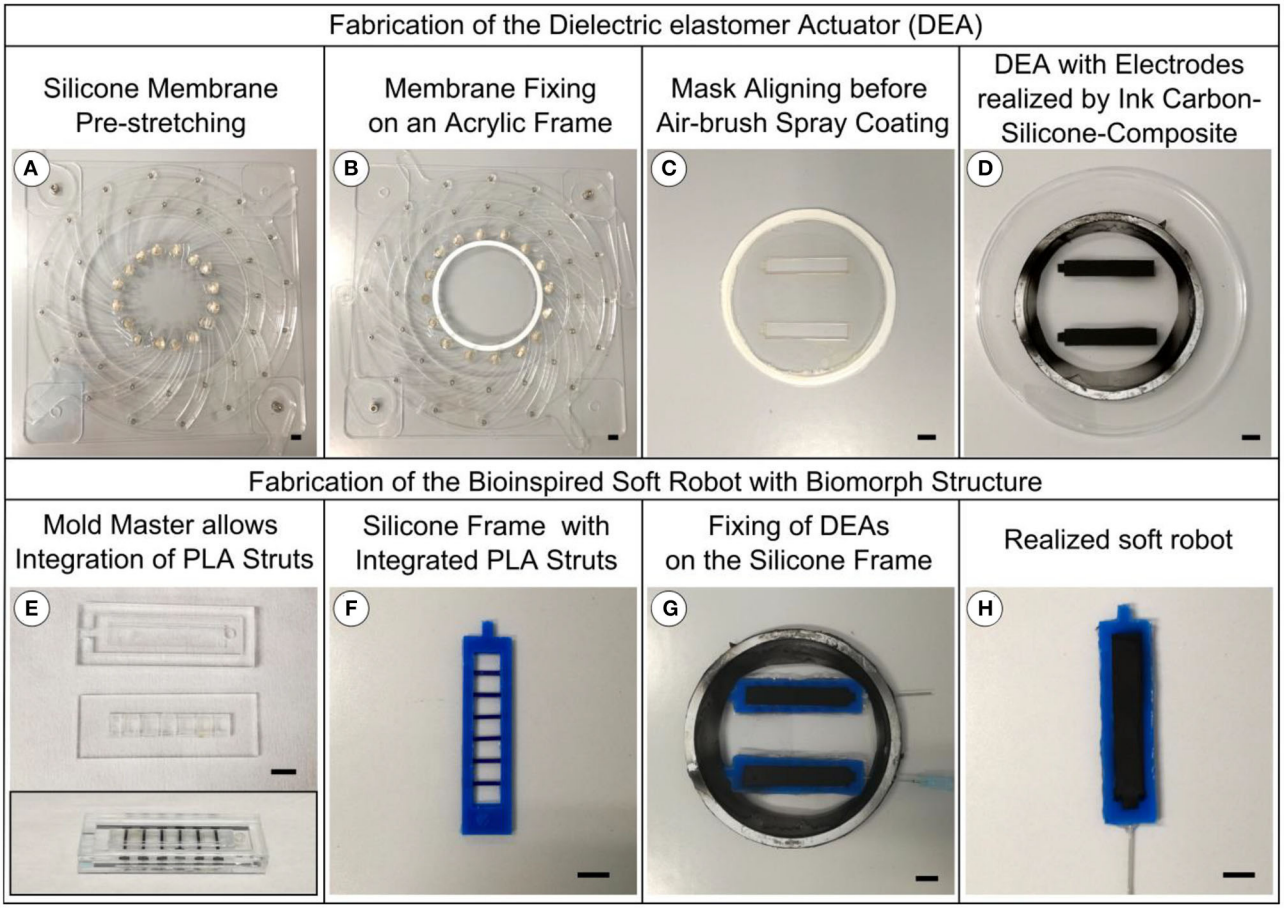

FIGURE 5 | Fabrication process of the DEA and the bioinspired soft robotic structure. **(A)** Pre-stretching of the silicone membrane. **(B)** Fixing the silicone membrane to an acrylic frame using an adhesive RTV silicone. **(C)** Shadow masks for processing the compliant electrodes by aerosol deposition, using an air-brush, on the top and bottom side of the silicone membranes. **(D)** Finalized DEA membrane. **(E)** Acrylic mold, including the bone elements, for injection molding the silicone body. **(F)** Silicone body with integrated bone elements. **(G)** Bonding of the silicone body on top of the previously prepared DEA membrane, still fixed on an acrylic frame, by an adhesive RTV silicone. Afterwards, a second DEA membrane is bonded on top of the body. **(H)** Finalized soft robotic structure. Scale bar is 10 mm.

TABLE 1 | Young's moduli of the applied silicone materials.

Material	E_i in *kPa*
ELASTOSIL 2030	1400.4 ± 33.4
Ecoflex 00-10	36.53 ± 1.45
Moldstar 30	805 ± 17.1
Sylgard 184	1301.1 ± 27.5

an air-brush and shadow masks (**Figure 5C**), on the top and bottom side of the silicone membranes. The ink is produced by mixing carbon black powder (Vulcan XC72, Cabot, CA, USA) with a two-component silicone elastomer rubber (Ecoflex 00-10 by Kaupo, Germany). To adjust the viscosity, Heptane is used as a solvent (Ashby et al., 2019). After applying the ink, the electrodes are cured at 40°C for 12 h. **Figure 5D** shows the finalized DEA membrane.

Soft Robotic Structure

The fabrication process of the soft bimorph structure is shown in **Figures 5E–H**. The silicone body is injection molded in an acrylic mold, including the bone elements, consisting of 3D printed PLA struts (**Figure 5E**). In order to study the influence of different Young's moduli on the static and dynamic behavior of the entire system, three different silicones, with different Young's moduli are used: Ecoflex 00-10 (Kaupo, Germany), Moldstar 30 (Kaupo, Germany), and Sylgard 184 (Dow Corning, USA). The two-component silicone materials are processed consecutively by sufficient A:B-mixing (A:B = 1:1 Ecoflex 00-10 and Moldstar 30, A:B = 10:1 Sylgard 184), degassing, injection into the mold, and finally heat curing at 60°C for 12 h. The resulting silicone body with integrated bone elements (**Figure 5F**) is firstly bonded on top of the previously prepared DEA membranes, still fixed on an acrylic frame, by the adhesive RTV silicone (**Figure 5G**). Afterwards, a second DEA membrane is bonded on top of the structure by the same process. The GND contacts are realized by a cannula that is pierced through the silicone body. After curing

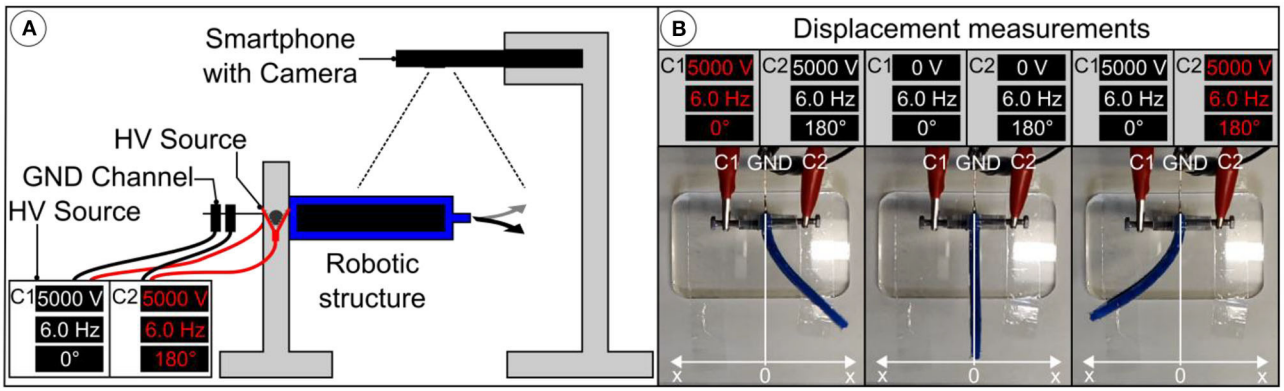

FIGURE 6 | Measurement of the displacement while running in static or dynamic mode. **(A)** Scheme of the experimental setup. **(B)** Video frames showing the left and right displacement x at maximum in dynamic mode depending on the voltage and frequency. Note that both actuators of the bimorph robotic structure are working 180° phase shifted while the activated one shows the red colored channel C1 or C2.

the RTV silicone, the bodies are cut out of the acrylic frames. **Figure 5H** depicts a final structure.

High Voltage Supply

The high voltage signals, driving the two DEAs 180° phase-shifted, are supplied by the open-source low-current high voltage power supply: Peta-pico-Voltron, previously presented by Schlatter et al. (2018). The high voltage power supply has three separately working channels able to provide 5 kV, either continuous, or as square waves with a frequency range between 1 mHz and 1 kHz. The channels can be run simultaneously and phase-shifted.

EXPERIMENTS

Investigation of the Materials Young's Moduli

To investigate the Young's modulus of the DEA membrane material ELASTOSIL 2030 and the silicone support structure materials Ecoflex 00-10, Moldstar 30 and Sylgard 184 tensile testing experiments are conducted. Ecoflex 00-10, Moldstar 30, and Sylgard 184 are processed as reported in section DEA as 200 µm films by the automatic film applicator ZAA 2300 (Zehnter, Switzerland). ELASTOSIL 2030 membrane with 100 µm thickness is used as received. The membranes were cut into samples according to DIN 53504 (5 per material) and tensile testing is performed by the testing machine Z005/TN (ZwickRoell GmbH & Co.KG, Germany). Stress/strain curves are used to calculate the Young's moduli E_i of each material by linear fitting up to a strain of 10% (see **Table 1**).

Recording of the Displacement (Static/Dynamic), Velocity, and Acceleration

To investigate the influence of membrane pre-stretch and mechanical stiffness of the silicone material, used for the body, on the bending displacement (static), bending amplitude and frequency behavior (dynamic) of the robotic structure, a series of experiments, measuring the bending displacement for a voltage range up to 5 kV are conducted. Velocity and acceleration are measured during dynamic experiments. The experimental setup is shown in **Figure 6A**. The actuator is attached to a mount and the electrodes are connected to two channels of the high voltage power supply. A smartphone camera with a high-speed sensor is mounted vertically above the setup to capture videos of the actuator at a speed of 480 fps and a resolution of 720p. **Figure 6B** shows three captured video frames of the robotic structure at distinct displacements, depending on the voltage and frequency of the square waves. The driving voltage of the actuator is increased from 3,000 to 5,000 V in steps of 500 V using two channels of the power supply. For each voltage, a frequency, ranging from 2 Hz to 10 Hz, is applied. A step of 1 Hz is used for frequencies from 2 Hz to 6 Hz and from 8 Hz to 10 Hz. A step of 0.2 Hz is used for the frequencies from 6 Hz to 8 Hz to observe the resonance frequency carefully. A 180° phase-shift is maintained between the two channels, for maximum actuation. For each of the applied frequencies, a video of ∼5 s duration is captured. This procedure is repeated for robots with the body material Moldstar 30 and DEAs made from membranes having a pre-stretch of λ_{pre} = 1.1, 1.3, 1.5, and 1.7. The same process is repeated for DEAs with membranes stretched to λ_{pre} = 1.5 but different body materials (Sylgard 184 and Ecoflex 00-10). The **Video SM2** shows the dynamic displacement of a robotic structure from the camera's perspective as a reference.

MATLAB Tool for Video Analysis

The video data is extracted (in the form of text files) from the captured videos using a MATLAB GUI tool for all experiments. 300 frames of each video are processed to extract necessary data. The steps of processing for each frame are shown in **Figure 7**. At first, a frame of the original video is converted into a binary image and its complement. After removing irregularities, the final image is received. The robot size is used to calibrate distance

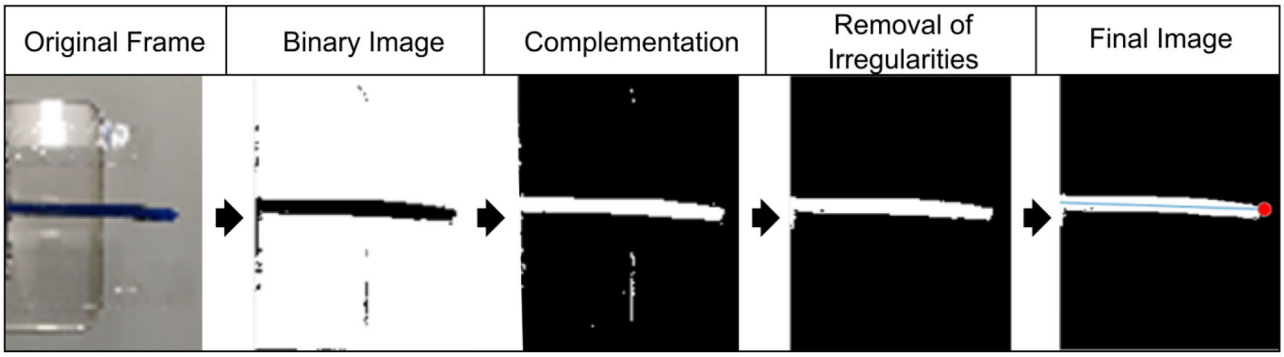

FIGURE 7 | Video analysis with processing steps to realize binary images for automated displacement, velocity, and acceleration measurements. The robot size was used to calibrate distance measurements.

measurements. Furthermore, the position of the tip of the robotic structure is found in pixels and written to the text file. The amplitude is calculated in pixels and then converted to distance in millimeters with the appropriate correction factor. This finally allows the displacement, the velocity, and the acceleration of the robotic structures to be derived. The velocity is measured at the zero position and the acceleration at the largest displacement of the robotic structure.

Blocking Force

The blocking forces, which the soft robotic structure can apply during static displacement, is measured using a force sensor ($F_{Max} = 2$ N, type 8432-5002-V0F00000, by burster präzisionsmesstechnik gmbh & co kg, Germany). The sensor is moved precisely to the tip of the robotic structure, using a *x-y* micrometer stage, until a minimum contact force is detected. The blocking force measurements is conducted for all samples and conditions investigated during static measurements described in section Recording of the Displacement (static/dynamic), Velocity, and Acceleration.

RESULTS AND DISCUSSION

Static Displacement

Bending behavior of the soft robotic structure is investigated with regards to the mechanical influence of the silicone body under static actuation at different applied voltages. **Figure 8A** depicts the displacement of robotic structures made of the three body materials, Ecoflex 00-10, Moldstar 30, and Sylgard 184, which differ in mechanical stiffness and density. The DEA membranes are uniformly stretched to $\lambda_{pre} = 1.5$. The voltage vs. displacement curves show the typical quadratic behavior. As Sylgard 184 is stiffer than the other materials, the displacement 3.1 mm at 5 kV is only half of the displacement of the softer structures with 6.1–6.2 mm. Interestingly, the structure with the highly flexible Ecoflex 00-10 did not achieve higher displacement values. The reason is explained in the end of this section. Instead, increasing the stiffness of the body material enhances the blocking force of the robotic structure, as can be seen in **Figure 8B**.

Additionally to a variation of the silicone body material, we conduct investigation regarding different pre-stretched DEA membranes $\lambda_{pre} = 1.1, 1.3, 1.5, 1.7$ with uniformly chosen silicone body material Moldstar 30 and measured the robot's displacement (see **Figure 8C**). Here, a distinct increase of displacement from about 2 ($\lambda_{pre} = 1.1$)−7 mm ($\lambda_{pre} = 1.7$) at 5 kV can be observed when the membrane pre-stretch is increased. A higher pre-stretch caused a better electromechanical coupling since the membrane layer of the capacitor structure got thinner, which increased the resulting thickness strain ε_{zz} of the activated DE membrane, see Equation (3). This reduces the mechanical stress applied to the silicone body. Large differences of the mechanical stress values between the activated and non-activated DEA enhance the robot's displacement. Furthermore, hyperelastic materials like silicone elastomer ELASTOSIL 2030 show a minimum Young's modulus in stress-strain curves at a certain pre-stretch due to high non-linearity. This allows a higher displacement at a certain pre-stretch value. In **Figure 8D**, the pre-stretch change from $\lambda_{pre} = 1.1$–1.7 facilitates nearly four times higher blocking force up to 4 mN ($\lambda_{pre} = 1.7$) during actuation at 5 kV, which can be explained by a better electromechanical coupling and a stiffening of the silicone membrane.

Furthermore, we carried out analytical calculations for the robot bending with the three different silicone body materials and varied the applied pre-stretch, described in section Bending Mechanism and Analytical Modeling. The calculated displacement values nicely fit to the experimental values. Deviations may be a result of fabrication variation, the influence of the silicone glue that is not considered in the analytical model and variation in the actual material stiffnesses. The large difference between experimental and simulation results for the Ecoflex 00-10 silicone body material can be attributed to the very low Young's modulus of this material that results in an undefined collapsing of the pre-stretch valued structure. Compare the actuators with Ecoflex 00-10 and Sylgard 184 silicone bodies in **Supplementary Figure 7**. The respective post-buckling state cannot be captured by a linear model as proposed above. The required non-linear 3D model is part of our future works.

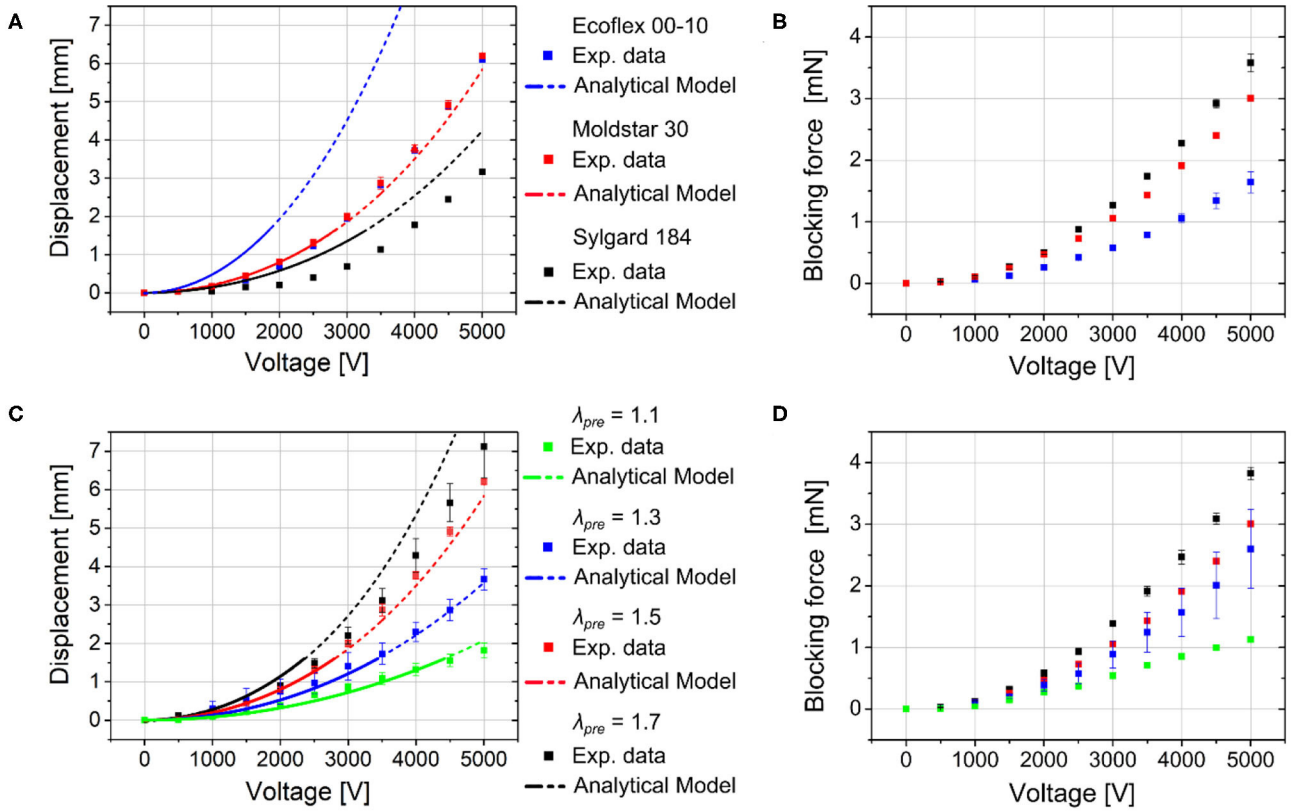

FIGURE 8 | Static displacements (data from experiment and analytical modeling) and applied blocking forces of the robotic structures depending on the applied voltage with **(A,B)** different silicone body materials (Ecoflex 00-10, Moldstar 30, Sylgard 184) with constant pre-stretched DE membrane ($\lambda_{pre} = 1.5$) and **(C,D)** varied pre-stretch ($\lambda_{pre} = 1.1, 1.3, 1.5, 1.7$) of the DEA silicone membranes with Moldstar 30 as silicone body material.

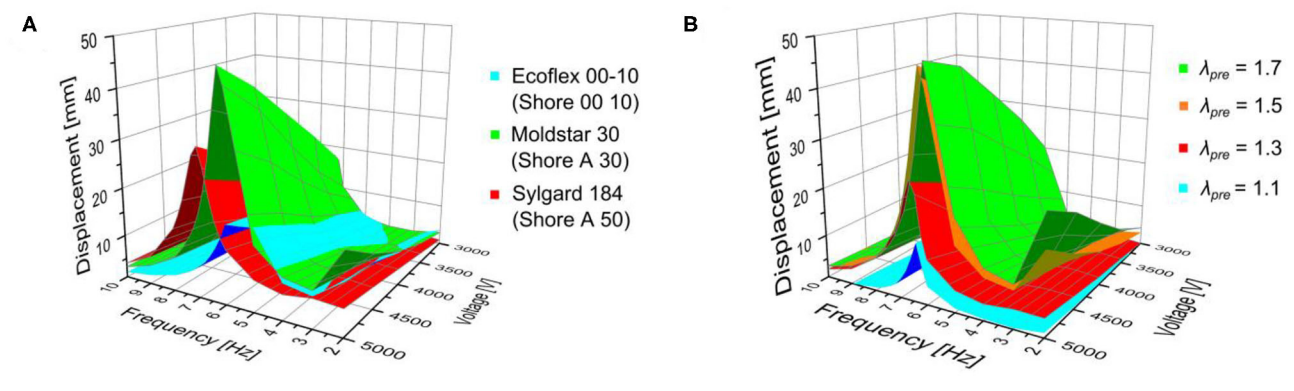

FIGURE 9 | Results of the investigation concerning the dynamic displacement depending on the applied voltage and frequency of the robotic structures with **(A)** different silicone body materials (Ecoflex 00-10, Moldstar 30, Sylgard 184) with uniformly pre-stretched DE membrane ($\lambda_{pre} = 1.50$) and **(B)** varied pre-stretch ($\lambda_{pre} = 1.1, 1.3, 1.5, 1.7$) of the DEA silicone membranes with Moldstar 30 as silicone body material.

Due to the assumptions and linearization used in the analytical model, it is only valid for voltages up to $\sim 2,000\ V$, even though the similarity between analytical and experimental results seems acceptable up to $5,000\ V$. Therefore, only displacement values up to $0.5 \cdot t_b$ can be reasonably compared with the experimental results. This is denoted by the dashed line for the modeling results.

However, due to the acceptable agreement with the experimental results, in the model's validity range, the model can be used to design this kind of actuator, i.e., the influence of

different parameters can be compared in order to enhance the actuator performance.

For further insights about the role of the parts of the structure, a full three-dimensional model must be derived, which will be part of our future works. There, also the non-linearity of kinematics and material can be captured.

Dynamic Displacement

The investigations of the static actuation manifest a strong dependency of the robotic structure's actuation behavior on the membrane pre-stretch and silicone body material. Simultaneously, switching from static to dynamic (here: oscillatory) actuation mode is supposed to enhance the bending and displacement behavior as resonance effects multiply the achievable displacement values. **Figure 9A** depicts the dynamic displacement (here: amplitude) of the soft robotic structures with different body materials (Ecoflex 00-10, Moldstar 30, Sylgard 184) and uniformly chosen membrane pre-stretch $\lambda_{pre} = 1.5$. The dynamic displacements are shown in 3D charts and depending on the applied voltage and frequency, on which both DEAs operate 180° phase-shifted. The maximum displacements of all three actuator types are achieved at the 5 kV voltage maximum, but show distinct frequency maxima or resonance frequencies at 5 Hz and 17.2 mm (Ecoflex 00-10), 6.2 Hz and 46.6 mm (Moldstar 30) as well as 7 Hz and 31.2 mm (Sylgard 184). The resonance frequencies are arranged in a way which can be expected from silicone body materials with low to high stiffness. Herein, Moldstar 30 seems to be the optimal body material enabling high actuation with our system. Additional 2D charts in **Supplementary Figures 3**, **5**, and **Supplementary Figure 6** show the dynamic displacement of the three robots more precisely.

In addition to the variation of the different silicone body materials, we investigated the influence of membrane pre-stretch ($\lambda_{pre} = 1.1, 1.3, 1.5, 1.7$) on the dynamic displacement. Here, the silicone body material is Moldstar 30. In **Figure 9B**, the maximum displacements at 5 kV are increasing from 13.0 mm at 6.4 Hz ($\lambda_{pre} = 1.1$), 25.2 mm at 6.4 Hz ($\lambda_{pre} = 1.3$) to 46.6 mm at 6.2 Hz ($\lambda_{pre} = 1.5$), and stay nearly constant at 47.4 mm at 6 Hz ($\lambda_{pre} = 1.7$). Additional 2D charts in **Supplementary Figures 1**–**4** show the dynamic displacement of the four robots more precisely.

As can be seen from the experimental values for the frequency-amplitude relation in **Figure 9A**, the resonance frequency changes for different materials. This can be attributed to (i) the change in Young's modulus, (ii) the different resulting length due to the coupling with the pre-stretched DEA and (iii) the different density of the materials. (i)–(iii) can be found in Equation (7). However, another effect that leads to a change in resonance frequency is a change in the dampening parameters, which will be part of our future investigations.

For different pre-stretches, only very minor variations can be found in **Figure 9B**. This is due to the fact that the effects (i) and (ii) above counteract: For higher pre-stretch, the Young's modulus gets smaller. At the same time, the length of the structure gets smaller, which influences ω_r in the 4th order. The quantification of this effect will be part of future studies.

The main influencing parameters to the resonance frequencies $\omega_{r,i}$ (for i the eigenmodes 1 and 2) can be estimated from the equation for linear oscillations

$$\omega_{r,i} = \kappa_i^2 \sqrt{\frac{E_x I_{yy}}{mL^4}} \tag{7}$$

where E_x is the Young's modulus in x-direction, I_{yy} the moment of inertia around the y-axis, m the mass and L the beam length.

Furthermore, we also measured the maximum velocity v_{max} and maximum acceleration a_{max} of the robotic structure. The data can be found in **Supplementary Figures**. The frequency depending behavior regarding the v_{max} and a_{max} values equals the dynamic displacement. By varying the DE membrane pre-stretch from $\lambda_{pre} = 1.1$–1.7 and using the same silicone body material Moldstar 30, both properties raise from $v_{max} = 1.7$–6.5 m/s and $a_{max} = 11$–38 m/s^2, at an activation voltage of 5 kV. At the same time, the lowest values of v_{max} and a_{max} are obtained with the silicone body material Ecoflex 00-10 and a pre-stretch of $\lambda_{pre} = 1.5$.

CONCLUSION

Artificial muscles based on DEAs have a great potential use in robotic systems, as they are soft, lightweight and are able to undergo large strokes. Here, we present a soft robotic structure, possessing a bioinspired skeleton, integrated into a soft body element, with an antagonistic working DEA artificial muscle pair. The finger-sized robotic structure (60 mm) showed an anisotropic, biomorphic bending behavior, due to stiff bone-like PLA struts, integrated into a silicone body element. During the experimental evaluation of the robot, a distinct biomorphic bending curvature is realized and can be analytically modeled using the Classical Laminate Theory. Depending on the optimized pre-stretch ($\lambda_{pre} = 1.5$–1.7) of the DEA membrane and stiffness of the silicone body material, fast and large dynamic displacements of about 47 mm are accomplished. In the same way, it was possible to optimize the blocking force from 1 to 4 mN. The investigations show how different parameters could improve the actuator performance of the robot for future application. In this way, it is reasonable to integrate our system in a real application like swimming robots with a fish tail.

DATA AVAILABILITY STATEMENT

The datasets generated for this study are available on request to the corresponding author.

AUTHOR CONTRIBUTIONS

MF and E-FMH conducted the concept, design, setup, and experiments of the project. AE and TW developed the analytical model of the bending mechanism. SL executed the experiments. AR provided advice about the fundamentals of this research topic. All authors composed through written, intellectual, or experimental contributions which approve of

its publication, contributed to the article, and approved the submitted version.

FUNDING

We gratefully acknowledge the financial support by the German Research Foundation (DFG) through the Research Grant for Sound sources based on dielectric elastomers (No. 397404199) and the Independent Junior Research Group Multifunctional dielectric elastomer electronics for next generation soft robotics (No. 418669083). We also thank the German Academic Exchange Service (DAAD) for the WISE scholarship (No. B137AB21611) and the Open Access Funding by the Publication Fund of the TU Dresden and SLUB.

ACKNOWLEDGMENTS

We thank Wacker Chemie AG for providing the silicone membrane material ELASTOSIL 2030. We acknowledge Katherine Wilson for manuscript editing help.

SUPPLEMENTARY MATERIAL

The Supplementary Material for this article can be found online at: https://www.frontiersin.org/articles/10.3389/frobt.2020.510757/full#supplementary-material

Supplementary Video SM1 | Performance of the dynamic bending behavior.

Supplementary Video SM2 | Performance of the dynamic bending behavior during measurement shown in slow-motion.

REFERENCES

Araromi, O. A., Gavrilovich, I., Shintake, J., Rosset, S., Richard, M., Gass, V., et al. (2015). Rollable multisegment dielectric elastomer minimum energy structures for a deployable microsatellite gripper. *IEEE/ASME Trans. Mech.* 20, 438–446. doi: 10.1109/TMECH.2014.2329367

Ashby, J., Rosset, S., Henke, E.-F. M., and Anderson, I. (2019). Inflatable dielectric elastomer robots for space. *Proc.* SPIE 10966, 218–229. doi: 10.1117/12.2514227

Bar-Cohen, Y. (2016). *Biomimetics: Nature-Based Innovation*. Boca Raton, FL: CRC Press Inc. doi: 10.1201/b11230

Berlinger, F., Duduta, M., Gloria, H., Clarke, D., Nagpal, R., and Wood, R. (2018). "A modular dielectric elastomer actuator to drive miniature autonomous underwater vehicles," in *2018 IEEE International Conference on Robotics and Automation (ICRA)* (Brisbane, QLD), 3429–3435. doi: 10.1109/ICRA.2018.8461217

Biot, M. A. (1963). Surface instability of rubber in compression. *Appl. Sci. Res. Sect. A* 12, 168–182. doi: 10.1007/BF03184638

Christianson, C., Goldberg, N. N., Deheyn, D. D., Cai, S., and Tolley, M. T. (2018). Translucent soft robots driven by frameless fluid electrode dielectric elastomer actuators. *Sci. Rob.* 3:eaat1893. doi: 10.1126/scirobotics.aat1893

Ehrenhofer, A., Bingel, G., Paschew, G., Tietze, M., Schroeder, R., Richter, A., et al. (2016). Permeation control in hydrogel-layered patterned PET membranes with defined switchable pore geometry - experiments and numerical simulation. *Sens. Actuators B Chem.* 232, 499–505. doi: 10.1016/j.snb.2016.03.152

Ehrenhofer, A., Elstner, M., and Wallmersperger, T. (2018). *Normalization of hydrogel swelling behavior for sensoric and actuatoric applications*. *Sens. Actuators B Chem*. 255, 1343–1353. doi: 10.1016/j.snb.2017.08.120

Ehrenhofer, A., and Wallmersperger, T. (2020). Shell-forming stimulus-active hydrogel composite membranes: concept and modeling. *Micromachines* 11:541. doi: 10.3390/mi11060541

Goh, S. C.-K., and Lau, G.-K. (2010). Dielectric elastomeric bimorphs using electrolessly deposited silver electrodes. *Proc. SPIE* 7642, 339–350. doi: 10.1117/12.847415

Gu, G.-Y., Zhu, J., Zhu, L.-M., and Zhu, X. (2017). A survey on dielectric elastomer actuators for soft robots. *Bioinspiration Biomimetics* 12:11003. doi: 10.1088/1748-3190/12/1/011003

Henke, E.-F. M., Schlatter, S., and Anderson, I. A. (2017). Soft dielectric elastomer oscillators driving bioinspired robots. *Soft Rob.* 4, 353–366. doi: 10.1089/soro.2017.0022

Katzschmann, R., Marchese, A., and Rus, D. (2016). "Hydraulic autonomous soft robotic fish for 3D swimming," in *Experimental Robotics*, eds M. Hsieh, O. Khatib, and V. Kumar (Cham: Springer), 405–420. doi: 10.1007/978-3-319-23778-7_27

Kleo, M., Foerster-Zuegel, F., Schlaak, H. F., and Wallmersperger, T. (2020). Thermo-electro-mechanical behavior of dielectric elastomer actuators: experimental investigations, modeling and simulation. *Smart Mater. Struct.* 29:085001. doi: 10.1088/1361-665X/ab8a6b

Kofod, G. (2008). The static actuation of dielectric elastomer actuators: how does pre-stretch improve actuation? *Sens. Actuators D Appl. Phys.* 41:215405. doi: 10.1088/0022-3727/41/21/215405

Kulikov, G. M., and Carrera, E. (2008). Finite deformation higher-order shell models and rigid-body motions. *Int. J. Solids Struct.* 45, 3153–3172. doi: 10.1016/j.ijsolstr.2008.01.020

Marshall, P. T. (1980). *Physiology of Mammals and Other Vertebrates*. Cambridge: Cambridge University Express.

Pelrine, R. E., Kornbluh, R. D., and Joseph, J. P. (1998). Electrostriction of polymer dielectrics with compliant electrodes as a means of actuation. *Sens. Actuators A Phys.* 64, 77–85. doi: 10.1016/S0924-4247(97)01657-9

Reddy, J. N. (2003). Mechanics of laminated composite plates and shells: theory and analysis. Boca Raton, FL: CRC Press. doi: 10.1201/b12409

Rosset, S., Araromi, O. A., Shintake, J., and Shea, H. R. (2014). Model and design of dielectric elastomer minimum energy structures. *Smart Mater. Struct.* 23:085021. doi: 10.1088/0964-1726/23/8/085021

Rosset, S., and Shea, H. R. (2013). Flexible and stretchable electrodes for dielectric elastomer actuators. *Appl. Phys. A* 110, 281–307. doi: 10.1007/s00339-012-7402-8

Schlatter, S., Illenberger, P., and Rosset, S. (2018). Peta-pico-Voltron: an open-source high voltage power supply. *HardwareX* 4:e00039. doi: 10.1016/j.ohx.2018.e00039

Shepherd, R. F., Ilievski, F., Choi, W., Morin, S. A., Stokes, A. A., and Mazzeo, A. D. (2011). Multigait soft robot. *Proc. Natl. Acad. Sci. U.S.A.* 108, 20400–20403. doi: 10.1073/pnas.1116564108

Wehner, M., Truby, R. L., Fitzgerald, D. J., Mosadegh, B., Whitesides, G. M., Lewis, J. A., et al. (2016). An integrated design and fabrication strategy for entirely soft, autonomous robots. *Nature* 536:451. doi: 10.1038/nature19100

Conflict of Interest: E-FMH was employed by the company PowerON Ltd.

The remaining authors declare that the research was conducted in the absence of any commercial or financial relationships that could be construed as a potential conflict of interest.

Advantages of publishing in Frontiers

OPEN ACCESS
Articles are free to read for greatest visibility and readership

FAST PUBLICATION
Around 90 days from submission to decision

HIGH QUALITY PEER-REVIEW
Rigorous, collaborative, and constructive peer-review

TRANSPARENT PEER-REVIEW
Editors and reviewers acknowledged by name on published articles

Frontiers
Avenue du Tribunal-Fédéral 34
1005 Lausanne | Switzerland

Visit us: www.frontiersin.org
Contact us: frontiersin.org/about/contact

REPRODUCIBILITY OF RESEARCH
Support open data and methods to enhance research reproducibility

DIGITAL PUBLISHING
Articles designed for optimal readership across devices

FOLLOW US
@frontiersin

IMPACT METRICS
Advanced article metrics track visibility across digital media

EXTENSIVE PROMOTION
Marketing and promotion of impactful research

LOOP RESEARCH NETWORK
Our network increases your article's readership